

Hydrodynamic and Water Quality Model Study of San Juan Bay Estuary

by Barry W. Bunch, Carl F. Cerco, Mark S. Dortch

Environmental Laboratory
U.S. Army Engineer Research and Development Center
3909 Halls Ferry Road
Vicksburg, MS 39180-6199

Billy H. Johnson, Keu W. Kim
Coastal and Hydraulics Laboratory
U.S. Army Engineer Research and Development Center
3909 Halls Ferry Road
Vicksburg, MS 39180-6199

Final report

Approved for public release; distribution is unlimited

20000615 027

Prepared for U.S. Army Engineer District, Jacksonville
Jacksonville, FL 32232-0019

Engineer Research and Development Center Cataloging-in-Publication Data

Hydrodynamic and water quality model study of San Juan Bay estuary / by Barry W. Bunch ... [et al.] ; prepared for U.S. Army Engineer District, Jacksonville.

298 p. : ill. ; 28 cm. — (ERDC ; TR-00-1)

Includes bibliographic references.

1. Hydrodynamics — Mathematical models. 2. Estuaries — Puerto Rico — San Juan Bay — Mathematical models. 3. San Juan Bay (P.R.) 4. Water quality — Puerto Rico — San Juan Bay — Testing. I. Bunch, Barry W. II. United States. Army. Corps of Engineers. Jacksonville District. III. Engineer Research and Development Center (U.S.) IV. Series: ERDC TR ; 00-1.
TA7 E8 no.ERDC TR-00-1

The contents of this report are not to be used for advertising, publication, or promotional purposes. Citation of trade names does not constitute an official endorsement or approval of the use of such commercial products.

The findings of this report are not to be construed as an official Department of the Army position, unless so designated by other authorized documents.



PRINTED ON RECYCLED PAPER

Contents

Preface	xi
1—Introduction	1
Background and Site Description	1
Objective and Scope	3
2—Approach	5
3—The Hydrodynamic Model	10
General	10
CH3D-WES Description	11
Boundary Conditions	24
Initial Conditions	34
Numerical Grid	36
4—Water Quality Model Formulation.	37
Introduction	37
Conservation of Mass Equation	39
Algae	40
Organic Carbon	54
Phosphorus.	58
Nitrogen	64
Chemical Oxygen Demand.	70
Dissolved Oxygen.	70
Salinity	72
Temperature	72
Fecal Coliform.	73
Glossary	73
Predictive Sediment Submodel	78
5—Water Quality Model Input.	85
Hydrodynamics	85
Meteorological Data	86
Initial Conditions	87
Boundary Concentrations and Loading Estimates	88

6—Hydrodynamic Model Adjustment and Skill Assessment	102
Tide Reproduction	103
Salinity Reproduction.	106
Reproduction of the Exchange Between Canals	113
Model Coefficients	115
Conclusions	121
7—Water Quality Model Calibration and Skill Assessment	122
Scatter Plots	125
Longitudinal Transect Comparisons.	130
Time Series Comparisons	148
Calibration Conclusions	164
8—Management Scenarios	166
Methods	166
Scenario Descriptions.	167
Hydrodynamic Model Results	171
Water Quality Model Results	206
9—Conclusions and Recommendations	271
10—References	274
Appendix A: Transformed Horizontal Momentum Diffusion Terms . .	A1
Appendix B: Scenario Average Concentrations and Percent Change from Base Condition.	B1
SF 298	

List of Figures

Figure 1-1. The San Juan Bay and Estuary system, San Juan, PR . .	2
Figure 2-1. Water quality stations, San Juan Bay Estuary, summer 1995	8
Figure 2-2. Locations of management alternatives (scenarios) in the San Juan Bay Estuary system.	9
Figure 3-1. Numerical grid of San Juan estuarine system	17
Figure 3-2. San Juan Airport wind data	26
Figure 3-3. Freshwater inflows.	27
Figure 3-4. ADCIRC numerical grid	34
Figure 3-5. ADCIRC grid near Puerto Rico.	35

Figure 3-6.	Tide computed by ADCIRC and applied on ocean boundary	35
Figure 4-1.	The Monod formulation for nutrient-limited growth . . .	42
Figure 4-2.	Effect of temperature on algal production.	44
Figure 4-3.	Exponential temperature function	45
Figure 4-4.	The ammonium preference function	49
Figure 4-5.	Carbon-to-nitrogen ratio (mean and standard error) of seston in upper Chesapeake Bay	52
Figure 4-6.	Carbon-to-phosphorus ratio (mean and standard error) of seston in upper Chesapeake Bay	52
Figure 4-7.	Model algal phosphorus-to-carbon ratio.	53
Figure 4-8.	Model carbon cycle	55
Figure 4-9.	Effect of nitrate and dissolved oxygen on denitrification rate	57
Figure 4-10.	Model phosphorus cycle	59
Figure 4-11.	Effect of algal biomass and nutrient concentration on hydrolysis and mineralization	61
Figure 4-12.	Chemostat simulation with and without variable phosphorus stoichiometry.	63
Figure 4-13.	Model nitrogen cycle	65
Figure 4-14.	Effect of dissolved oxygen and ammonium concentration on nitrification rate	68
Figure 4-15.	Model dissolved oxygen cycle	71
Figure 4-16.	Sediment model schematic	79
Figure 4-17.	Sediment model layers and definitions	81
Figure 5-1.	Water quality model grid, reduced from hydrodynamic model grid	87
Figure 5-2.	Flows observed at Hato Rey, Rio Piedras, June-September 1995	91
Figure 5-3.	Flows for Baldorioty de Castro Pump Station computed from pumping records for June-September 1995	93
Figure 5-4.	Model sub-basins of the San Juan Bay Estuary System with model locations of freshwater inflows indicated by the arrows	93
Figure 5-5.	Observed flows for Rio Piedras at Hato Rey versus observed rainfall plotted with the best-fit regression line	96

Figure 5-6.	Computed flows based on pumping records for Baldorioty de Castro Pump Station versus observed rainfall plotted with the best-fit regression line	96
Figure 6-1.	Location of data stations	102
Figure 6-2.	Comparison of computed and observed tide at S3	103
Figure 6-3.	Comparison of computed and observed tide at S4	104
Figure 6-4.	Comparison of computed and observed tide at S8	104
Figure 6-5.	Comparison of computed and observed tide at S9	105
Figure 6-6.	Comparison of computed and observed tide at S10 . . .	105
Figure 6-7.	Comparison of computed and observed tide at S6	106
Figure 6-8.	Comparison of computed and observed salinity at SJB-3	108
Figure 6-9.	Comparison of computed and observed salinity at SJB-5	109
Figure 6-10.	Comparison of computed and observed salinity at PN-1.	110
Figure 6-11.	Comparison of computed and observed salinity at S4 . .	111
Figure 6-12.	Comparison of computed and observed salinity at S5 . .	112
Figure 6-13.	Comparison of computed and observed salinity at S6 . .	113
Figure 6-14.	Comparison of computed and observed salinity at SC-1.	114
Figure 6-15.	Comparison of near surface computed and observed salinity at S8	115
Figure 6-16.	Comparison of computed and observed salinity at TL-1.	116
Figure 6-17.	Comparison of near surface computed and observed salinity at TL-3.	117
Figure 6-18.	Comparison of near surface computed and observed salinity at PL-1.	117
Figure 6-19.	Comparison of near surface computed and observed salinity at PL-2.	118
Figure 6-20.	Computed flux through Martin Pena Canal compared with USGS data	118
Figure 6-21.	Computed flux through Suarez Canal compared with USGS data	119
Figure 6-22.	Computed flux through Torrecilla-Pinones Canal compared with USGS data	119
Figure 6-23.	Comparison of computed flux at Range 2 with flux determined from ADCP data	120

Figure 6-24.	Comparison of computed flux at Range 4 with flux determined from ADCP data	120
Figure 6-25.	Comparison of computed flux at Range 6 with flux determined from ADCP data	121
Figure 7-1.	Calibration period scatter plots.	126
Figure 7-2.	Longitudinal transect and observation stations used for preparing calibration-period average transect plots . . .	131
Figure 7-3.	Calibration-period average, longitudinal transect plot of computed and observed water quality variables resulting from model calibration for summer 1995	132
Figure 7-4.	Location of clams in the WQM.	139
Figure 7-5.	Longitudinal transect calibration period average benthic algae	145
Figure 7-6.	Longitudinal transect calibration period average sediment fluxes.	146
Figure 7-7.	Laguna Los Corozos (Northern Laguna San José) calibration period time series.	149
Figure 7-8.	Cano Martin Pena station MP-2 calibration period time series	152
Figure 7-9.	Laguna Condado station LC-1 calibration period time series	156
Figure 7-10.	Cano San Antonio station SA-1 calibration period time series	159
Figure 7-11.	Computed and observed water quality variables at stations PL1 and PL2 (Laguna de Pinones) resulting from model calibration for summer 1995	161
Figure 8-1.	Comparison of flux through Martin Pena Canal between Scenarios 1a and 1b	172
Figure 8-2.	Comparison of flux through Suarez Canal between Scenarios 1a and 1b	173
Figure 8-3.	Comparison of tide at S6 between Scenarios 1a and 1b .	174
Figure 8-4.	Comparison of salinity at S4 between Scenarios 1a and 1b	175
Figure 8-5.	Comparison of salinity at S8 between Scenarios 1a and 1b	176
Figure 8-6.	Comparison of salinity at S6 between Scenarios 1a and 1b	177

Figure 8-7.	Comparison of tide at S6 between Scenarios 1a and 1c	177
Figure 8-8.	Comparison of flux at Range 2 between Scenarios 1a and 1c	178
Figure 8-9.	Comparison of flux at Range 4 between Scenarios 1a and 1c	179
Figure 8-10.	Comparison of salinity at S4 between Scenarios 1a and 1c	180
Figure 8-11.	Comparison of salinity at S6 between Scenarios 1a and 1c	181
Figure 8-12.	Comparison of salinity at S8 between Scenarios 1a and 1c	182
Figure 8-13.	Comparison of flux at Range 2 between Scenarios 1a and 2	183
Figure 8-14.	Comparison of flux at Range 4 between Scenarios 1a and 2	184
Figure 8-15.	Comparison of tide at S6 between Scenarios 1a and 2	185
Figure 8-16.	Comparison of salinity at S4 between Scenarios 1a and 2	186
Figure 8-17.	Comparison of salinity at S6 between Scenarios 1a and 2	187
Figure 8-18.	Comparison of salinity at S8 between Scenarios 1a and 2	188
Figure 8-19.	Comparison of tide at S6 between Scenarios 1a and 3	189
Figure 8-20.	Comparison of flux at Range 4 between Scenarios 1a and 3	190
Figure 8-21.	Comparison of flux at Range 2 between Scenarios 1a and 3	191
Figure 8-22.	Comparison of salinity at S4 between Scenarios 1a and 3	192
Figure 8-23.	Comparison of salinity at S6 between Scenarios 1a and 3	193
Figure 8-24.	Comparison of salinity at S8 between Scenarios 1a and 3	194
Figure 8-25.	Comparison of flux at Range 4 between Scenarios 1a and 4	195
Figure 8-26.	Comparison of tide at S6 between Scenarios 1a and 4	196

Figure 8-27. Comparison of flux at Range 2 between Scenarios 1a and 4	197
Figure 8-28. Comparison of salinity at S4 between Scenarios 1a and 4	198
Figure 8-29. Comparison of salinity at S6 between Scenarios 1a and 4	199
Figure 8-30. comparison of salinity at S8 between Scenarios 1a and 4	200
Figure 8-31. Comparison of tide at S6 between Scenarios 1a and 6b .	201
Figure 8-32. Comparison of flux at Range 2 between Scenarios 1a and 6b	202
Figure 8-33. Comparison of flux at Range 4 between Scenarios 1a and 6b	203
Figure 8-34. Comparison of salinity at S4 between Scenarios 1a and 6b	204
Figure 8-35. Comparison of salinity at S6 between Scenarios 1a and 6b	205
Figure 8-36. Comparison of salinity at S8 between Scenarios 1a and 6b	206
Figure 8-37. Simulation averaged transect plots and sediment flux plots comparing Scenario 1b with Scenario 1a	209
Figure 8-38. Simulation averaged transect plots comparing Scenario 1c with Scenario 1a	217
Figure 8-39. Simulation averaged transect plots comparing Scenario 2 with Scenario 1a	224
Figure 8-40. Simulation averaged transect plots comparing Scenario 3 with Scenario 1a	231
Figure 8-41. Simulation averaged transect plots comparing Scenario 4 with Scenario 1a	238
Figure 8-42. Simulation averaged transect plots comparing Scenario 5a with Scenario 1a	245
Figure 8-43. Simulation averaged transect plots comparing Scenario 5b with Scenario 1a	251
Figure 8-44. Simulation averaged transect plots comparing Scenario 6a with Scenario 1a	258
Figure 8-45. Simulation averaged transect plots comparing Scenario 6b with Scenario 1a	265

List of Tables

Table 4-1.	Water Quality Model State Variables	37
Table 4-2.	Terms in Kinetics Equations	74
Table 4-3.	Sediment Model State Variables and Fluxes	80
Table 5-1.	Ocean Boundary Concentrations	89
Table 5-2.	SJBE Sub-Basins and Areas	94
Table 5-3.	SJBE Sub-Basin Curve Numbers.	97
Table 5-4.	SJBE Sub-Basin Flow Estimation Methods	98
Table 5-5.	Uniform Runoff Concentrations	99
Table 5-6.	Modified Runoff Concentrations	100
Table 6-1.	Comparison of Harmonic Constituents of Tide Relative to San Juan Bay Tide	106
Table 7-1.	Parameter Values	122
Table 8-1.	Scenario Meteorological Conditions.	167
Table 8-2.	Management Water Quality Scenarios.	168
Table 8-3.	ICM Grid for Each Scenario	168
Table 8-4.	Scenarios Uniform Initial Conditions for Water Column	207
Table 9-1.	Summary of Impacts for Each Management Scenario . .	272

Preface

A hydrodynamic and water quality model study of San Juan Bay Estuary, Puerto Rico, was conducted from January 1996 through May 1999. This study was part of the United States Environmental Protection Agency's (USEPA) National Estuary Program. It was managed by the U.S. Army Engineer District, Jacksonville (CESAJ), and was sponsored by the USEPA Region II through the San Juan Bay Estuary Program (SJBEP), San Juan, Puerto Rico, and by the Caribbean Environment and Development Institute of San Juan, Puerto Rico, through a Cooperative Research and Development Agreement with the U.S. Army Engineer Research and Development Center (ERDC). Messrs. A. J. Salem, G. M. Strain, and James Duck were Chief, Acting Chief, and Chief, respectively, Planning Division, CESAJ, and Ms. Teré Rodríguez and Ms. Edna Villanueva were Directors, SJBEP. Mr. Mitch Granat of Planning Division, CESAJ, Mr. Jorge Tous of the Jacksonville District's Antilles Office, and Messrs. Héctor Abreu-Cintrón and Luis Jorge Rivera-Herrera of the SJBEP were the technical points of contact for this study.

Dr. Mark S. Dortch, Chief, Water Quality and Contaminant Modeling Branch (WQCMB), Environmental Processes and Effects Division (EPED), Environmental Laboratory (EL), ERDC, was the study manager and ERDC technical point of contact. The hydrodynamic modeling portion of this study was conducted by Drs. Billy H. Johnson and Keu W. Kim of the Waterways and Estuaries Division (WED), of the ERDC Coastal and Hydraulics Laboratory (CHL), under the general supervision of Dr. William H. McAnally, Chief, WED. The water quality modeling portion of this study was conducted by Drs. Carl F. Cerco and Barry W. Bunch of the WQCMB, EL, under the direct supervision of Dr. Dortch and the general supervision of Dr. Richard E. Price, Chief, EPED. Drs. Bunch and Kim conducted most of the day-to-day modeling tasks.

Dr. Jorge Capella, Mr. Aurelio Mercado, and Dr. Jorge Corredor from the University of Puerto Rico Marine Sciences Department, and Dr. Richard Signell from the U.S. Geological Survey in Woods Hole, MA, were members of the SJBEP Modeling Evaluation Group, which provided very valuable assistance for the study's model adjustment and skill assessment tasks. The SJBEP Management Committee and the Scientific and Technical Advisory Committee selected the management scenarios modeled and evaluated in the study.

This report was prepared by Drs. Bunch, Cerco, Dortch, Johnson, and Kim. The order of the authors is alphabetical and does not represent the amount of contribution provided by each to this study. Each author provided significant contributions to this study. However, Drs. Bunch and Johnson did provide the greatest amount of written contributions to the report.

At the time of publication of this report, Director of CHL was Dr. James R. Houston, Acting Director of EL was Dr. John W Keeley, and Acting Director of ERDC was Dr. Lewis E. Link. Commander of ERDC was COL Robin R. Cababa, EN.

This report should be cited as follows:

Bunch, B. W., Cerco, C. F., Dortch, M. S., Johnson, B. H., and Kim, K. W. (2000). "Hydrodynamic and Water Quality Model Study of San Juan Bay Estuary," ERDC TR-00-1, U.S. Army Engineer Research and Development Center, Vicksburg, MS.

The contents of this report are not to be used for advertising, publication, or promotional purposes. Citation of trade names does not constitute an official endorsement or approval of the use of such commercial products.

1 Introduction

Background and Site Description

Urbanization and anthropogenic influences from metropolitan areas of San Juan, Puerto Rico, have significantly impacted the water quality of the San Juan Bay Estuary (SJBE) system. Water quality impacts consist of eutrophication (i.e., nutrient enrichment), depressed dissolved oxygen (DO) concentrations, high concentrations of fecal coliform bacteria (FCB), an indicator of pathogens, and the presence of toxic substances. Portions of the SJBE system may have less than adequate flushing characteristics to assimilate pollutant loadings.

The San Juan Metropolitan area includes thirteen municipalities located on the north coast of Puerto Rico. Within this region, the municipalities of Toa Baja, Cataño, Guaynabo, Bayamón, San Juan, Trujillo Alto, Carolina, and Loiza share part of their territories with the SJBE or its watershed. Over 700,000 people live in the 240-km² SJBE drainage basin, of which 215 km² is land and 25 km² is covered with water.

The SJBE consists of five embayments (see Figure 1-1). From west to east these include: Bahía de San Juan, Laguna del Condado, Laguna San José (including Laguna Los Corozos), Laguna La Torrecilla, and Laguna de Piñones. San Juan Bay (ca. 7 km²) contains navigation channels, and the shoreline is highly developed. Laguna del Condado is a relatively small lagoon adjacent to an ocean inlet which keeps it well flushed. Laguna San José (4.6 km²) is the innermost lagoon which is shallow (mean depth of 1.5 m) and has the least tidal fluctuation of 5-10 cm with the tidal range in San Juan Bay and Laguna La Torrecilla being about 60 cm. As a result Laguna San José experiences little tidal flushing. Laguna La Torrecilla (2.5 km²) is connected to the ocean by Boca De Cangrejos and is bordered mostly by mangrove trees. Laguna de Piñones is connected to Laguna La Torrecilla through a small tidal creek with a width and depth of less than 5 m and 1 m, respectively. As a result, as in Laguna San José, tidal flushing in Laguna de Piñones is also small. Laguna de Piñones is surrounded by a large mangrove forest which can influence water quality in that lagoon.

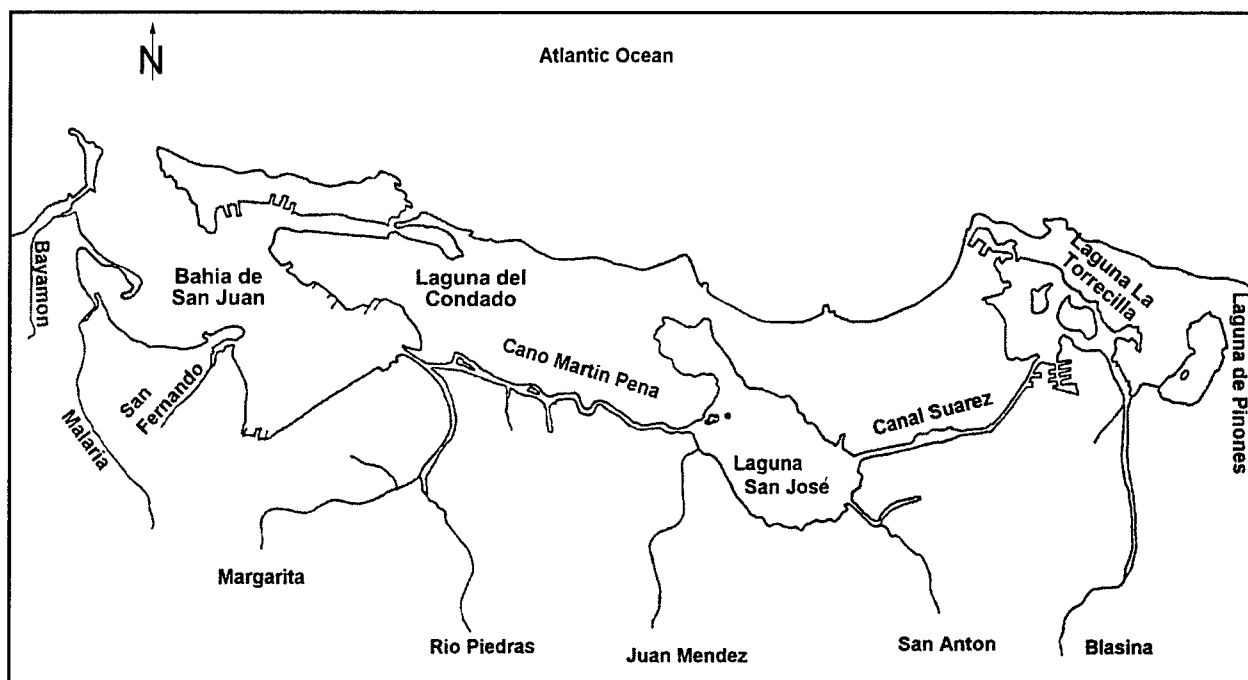


Figure 1-1. The San Juan Bay and Estuary system, San Juan, PR

The bay and lagoons are connected by narrow channels as shown in Figure 1-1. The two most distinct channels are Caño Martín Peña and Canal Suárez. Caño Martín Peña, which connects Laguna San José and San Juan Bay, is about 6 km long with a width that varies from a few meters at its eastern end to about 100 m at its western end with a dredged depth of 3.6 m. The average depth of the canal is about 1.2 m. The narrow, shallow constriction along the eastern end of Caño Martín Peña is due to sedimentation and debris and greatly impedes flushing of Laguna San José. As a result, the eastern portion of Caño Martín Peña and Laguna San José have the poorest water quality. Canal Suárez, which connects Laguna San José and Laguna La Torrecilla, is approximately 4 km long with widths ranging from greater than 30 m to less than 5 m where a major road crosses the canal. Depths of Canal Suárez range from as great as 10 m where dredging has taken place to less than 1 m at the narrow constriction. This constriction contributes to the reduced tidal range in Laguna San José. The SJBE system opens to the ocean at three locations, San Juan Bay, Laguna del Condado, and Laguna La Torrecilla.

Portions of the system have been altered due to dredging. An 11.9-m- (39-ft-) deep navigation channel traverses the interior and the perimeter of San Juan Bay. Borrow pits exist within Laguna del Condado, Laguna San José, and Laguna La Torrecilla where sand and fill mining occurred for the development of residential and service facilities, such as the Luis Muñoz Marín International Airport. The borrow pits are as deep as 10-18 m and are chemically stratified. Thus, the waters in the pits are low in DO and high in dissolved substances, including nutrients and chemical oxygen demand.

Treated municipal wastewater has been discharged off the coast since 1986. However, pollutants still enter the SJBE system from combined sewer overflows; runoff from residential, agricultural, and industrialized areas; faulty sewage lines; and un-sewered residential areas. Caño Martín Peña receives considerable untreated domestic wastes from adjacent residential areas. Storm water is collected and pumped directly into the SJBE or indirectly through its tributaries by a total of 12 pump stations that have a combined maximum capacity of over 900,000 gpm (56.8 m³/s). Pumped storm water is untreated and can contain pollutants. Additionally, pollutant loads can enter via freshwater inflow tributaries which enter the system through the Puerto Nuevo River, Malaria Channel, and three creeks, Juan Méndez, San Antón, and Blasina (see Figure 1-1). Freshwater flows are quite flashy as they are driven by local rainfall, and their water quality is dominated by local wash-off. There are no significant waste-water dischargers in the system, although there are two cooling water discharges from power plants.

Habitat loss has occurred within the system as a result of direct (e.g., construction, dredging, filling) and indirect impacts. Increased sediment runoff and eutrophication have increased water turbidity to the extent that benthic primary production is no longer possible in many locations. Water quality is poor in some areas of the system due to eutrophication and FCB contamination. Solid waste disposal is a problem within Caño Martín Peña as a result of inadequate waste collection from low income areas lining the canal.

Objective and Scope

San Juan Bay Estuary is one of the estuarine systems included in the U.S. Environmental Protection Agency's National Bay and Estuary Program (NEP; U.S. Environmental Protection Agency 1993). The NEP was started in 1987 as part of the Clean Water Act to protect and restore estuaries while supporting economic and recreational activities.

One of the goals of the San Juan Bay Estuary Program (SJBEP) and the Environmental Quality Board of Puerto Rico included the development of a hydrodynamic and a water quality model of the SJBE system for use in determining effective alternatives for water quality improvement and predicting the impacts of future development. The study reported herein was conducted to satisfy this goal. The objective of this study included development of such models and application of the models to evaluate the effectiveness of management alternatives on water quality improvement. Management alternatives considered included methods to increase system flushing and reduce pollutant loadings.

This study included four components: (1) bathymetric surveys; (2) hydrodynamic field data collection; (3) water quality data collection; and (4) hydrodynamic and water quality modeling. The first three

components were necessary to conduct the fourth. Recent bathymetric surveys were necessary for model input since considerable dredging, filling, and sedimentation had occurred since the last survey. Bathymetric data collection was conducted through contract by CESAJ. Recent data collection efforts did not contain the information required for hydrodynamic and water quality model calibration, thus, it was necessary to conduct components (2) and (3). These two efforts and the resulting data are documented by Kennedy et al. (1996) and Fagerburg (1998). Much of the data collected from components (2) and (3) are shown within this report where model results are compared against field observations to assess model accuracy.

There are many potential future uses for these models for evaluating the effects of changes in system hydrology, structural features, and/or pollutant loadings on circulation and water quality. These models can serve as valuable tools to help guide management and monitoring of the SJBE.

This report presents the approach, descriptions of the hydrodynamic and water quality models, including their input data, adjustment/calibration and skill assessment, methods used for and results of management scenario simulations, and conclusions and recommendations.

2 Approach

Depths within SJBES range from about 1 m to 20 m. Since the water column density and related water quality variables experience significant variation over the water depth in the deeper channels and borrow areas, a three-dimensional (3D) model was recommended. However, shallow areas were represented as vertically mixed (i.e., one layer), and the connecting channels were represented as laterally mixed (i.e., one segment wide) in some areas.

Numerical, 3D hydrodynamic and water quality models were used to simulate the effects of strategies to increase flushing and reduce pollutant loadings. The hydrodynamic model (HM) and the water quality model (WQM) were indirectly coupled without feedback. This means that the HM was executed and results were saved for subsequent use by the WQM to drive its transport terms. Hydrodynamic results were saved as hourly averages and used to provide hourly hydrodynamic updates to the WQM. Feedback from the WQM to the HM was not necessary since temperature and salinity, which affect water density and thus the hydrodynamics, were included in the HM simulations. Other water quality variables simulated by the WQM have an insignificant effect on water density. The models used the same computational grid but different time steps. The HM time step was one minute, whereas the WQM time step was variable and on the order of tens of minutes.

The 3D numerical hydrodynamic model, CH3D-WES (Curvilinear Hydrodynamics in 3 Dimensions, WES version), was used for this study. The WES version of a former model (CH3D) was developed by Johnson et al. (1991 and 1993). Physical processes in the model include tides, wind, density effects, freshwater inflows, turbulence, and the effect of the earth's rotation. As its name implies, CH3D-WES makes hydrodynamic computations on a curvilinear or boundary-fitted planform grid. However, the vertical dimension is Cartesian which allows for modeling density stratification on relatively coarse grids. Shallow areas can be modeled with one layer which effectively treats such areas in a vertically averaged sense.

The CE-QUAL-ICM (referred to as ICM) multi-dimensional, water quality model (Cерco and Cole 1995) was used for this study. ICM uses the integrated compartment method (thus ICM) for numerical treatment, which

is the same as a finite volume approach. This model was originally developed during a study of Chesapeake Bay (Cерco and Cole 1993 and 1994, Cerco 1995a and 1995b) and has subsequently been applied to other systems, including lower Green Bay (Mark et al. 1993), Newark Bay (Cерco and Bunch 1997 and Cerco, Bunch, and Letter 1999), New York Bight (Hall and Dortch 1994), Indian River and Rehoboth Bay, Delaware (Cерco et al. 1994 and Cerco and Seitzinger 1997). This model can and has been linked to a variety of hydrodynamic models for transport. However, the most common linkage is to CH3D-WES. The WQM has multiple water quality state variables, including temperature, salinity, DO, various forms of nitrogen, phosphorus, silica, and carbon, suspended solids, and phytoplankton. The model also includes a benthic sediment diagenesis submodel (DiToro and Fitzpatrick 1993) that simulates the decay and mineralization of bottom organic matter (e.g., settled algae) and the resulting nutrient and DO fluxes between the sediments and water column. The sediment diagenesis submodel dynamically couples sediment-water column interactions. For example, pollutant loading changes eventually affect sediment oxygen demand, which affects water column DO. Thus, this approach extends the credibility of the model for predicting future water quality. For this study, the WQM included the following 16 state variables:

- temperature
- salinity
- dissolved oxygen
- phytoplankton (one group)
- dissolved organic carbon
- particulate organic carbon
- particulate organic nitrogen
- dissolved organic nitrogen
- nitrate+nitrite nitrogen
- ammonium nitrogen
- particulate organic phosphorus
- dissolved organic phosphorus
- total inorganic phosphorus (with partitioning to dissolved and particulate phases)
- chemical oxygen demand (released from sediments)
- total suspended solids
- fecal coliform bacteria

In previous applications, models would be calibrated with one data set, then run with another independent data set, without changing any model parameters to verify model accuracy and adequacy for making predictions. In practice, if the verification was considered insufficiently accurate by the modelers, the parameters would be adjusted, and both the calibration and verification data sets would be re-run to assess accuracy of each. This process would be repeated until the model demonstrated acceptable

accuracy for both the calibration and verification periods using the same coefficients. If the modelers were furnished a third data set, then all three periods would be used. In fact, modelers are data hungry and will use data whenever available to adjust/calibrate their models, with the hope of finding *universal* coefficients that are satisfactory for all periods. This procedure is basically the same as using all available data sets for model adjustment/calibration and assessing the accuracy, or *skill*, of the calibration. Therefore, the term "verification" has been recently dropped from the process and replaced with "skill assessment." As an example, the Chesapeake Bay model (Cercio and Cole 1994) was calibrated and the skill assessed for a continuous three-year period, rather than calibrating for one or two years and verifying for another. This was a truly tough test of the model since it was run continuously for the three years where errors from one year were passed to the next. The model evaluation group for the Chesapeake Bay study knew that essentially the modelers would use all three years anyway to calibrate the model, so why not just calibrate all three years together? Thus, calibration/adjustment and skill assessment were conducted in the Chesapeake Bay study rather than calibration and verification, and this was the approach used in the present study.

The terms model adjustment and model calibration are used for the HM and WQM, respectively. The primary difference in these terms is that HM adjustment is limited to a few parameters, whereas WQM calibration can involve varying a host of parameters that affect water quality kinetic rates and transfers. Due to study funding constraints, it was possible to collect data from only one time period for use in model adjustment/calibration and skill assessment. Ideally, it is desirable to have data from multiple time periods, or to have data from a long period of time so that the model can be evaluated for a large range of conditions.

HM and WQM adjustment/calibration were accomplished with data collected over approximately two months during the summer of 1995. Summer conditions generally result in the most severe water quality conditions due to increased stratification and warmer water. The hydrodynamic data collection period extended from 22 June 1995 through 19 August 1995. The water quality data collection period extended from 26 June 1995 through 2 September 1995. Locations where surface water quality was sampled during this period are shown in Figure 2-1. Both models were applied for this approximately two-month period during model adjustment/calibration and skill assessment.

Each management scenario simulation was conducted using conditions from the summer of 1995 for boundary conditions for freshwater flows, tides, winds, meteorological, and water quality. However, it was necessary to run the WQM longer than the summer season in order to bring the system to a new state caused by altered circulation and/or loadings. Thus, for each simulation scenario, numerous runs of the WQM were made where each successive run used results from the previous run as initial conditions. This process was continued until water quality variables reached a new equilibrium condition, which required approximately eight months of

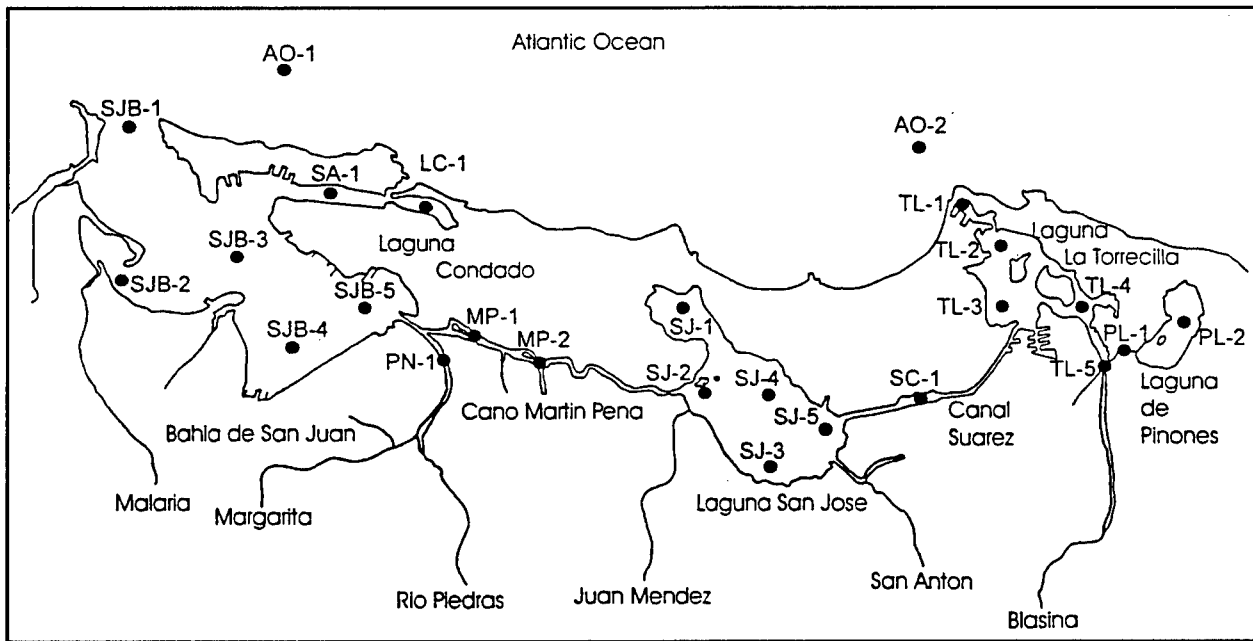


Figure 2-1. Water quality stations, San Juan Bay Estuary, summer 1995

water quality model simulation time. This procedure required using the HM output record repeatedly, or looping the hydrodynamics, to drive the WQM for longer periods. This approach approximated the long-term, steady-state response of the system to various management alternatives. The WQM required a relatively short time to reach equilibrium compared to other systems, which required on the order of several years. The part of the reason for this is believed to be due to the fact that relatively small changes in nutrient loadings to the system and/or system flushing characteristics were evaluated which required less time to reach equilibrium. Additionally, the model was repeatedly applied to warm-water conditions which accelerate reaction rates thus decreasing the time to reach equilibrium.

The results of each management scenario were then compared with results for a baseline scenario (Scenario 1a) which represented present conditions for circulation and loadings. The methods used in conducting scenario simulations are explained in more detail in Chapter 4. Looping the hydrodynamics to drive the water quality model to a long-term, steady-state, summer condition for scenario evaluations is considered a conservative approach, i.e., providing results that favor degraded rather than improved water quality, since summer conditions, which favor degraded water quality, do not persist repeatedly for long time frames. Management Scenarios 1b and 1c involved channel expansions in Caño Martín Peña. Scenario 2 involved filling dredged material borrow pits primarily in Laguna San José. Scenarios 3 and 4 evaluated channel expansion and a one-way tide gate in Canal Suárez, respectively. Scenarios 5a and 5b consisted of reductions of un-sewered loads to Caño Martín Peña and

removal of pump station loads at the Baldorioty de Castro outfall in northern Laguna San José, respectively. Scenarios 6a and 6b were limited combinations of the above scenarios. The location of each management alternative is shown on the map of Figure 2-2.

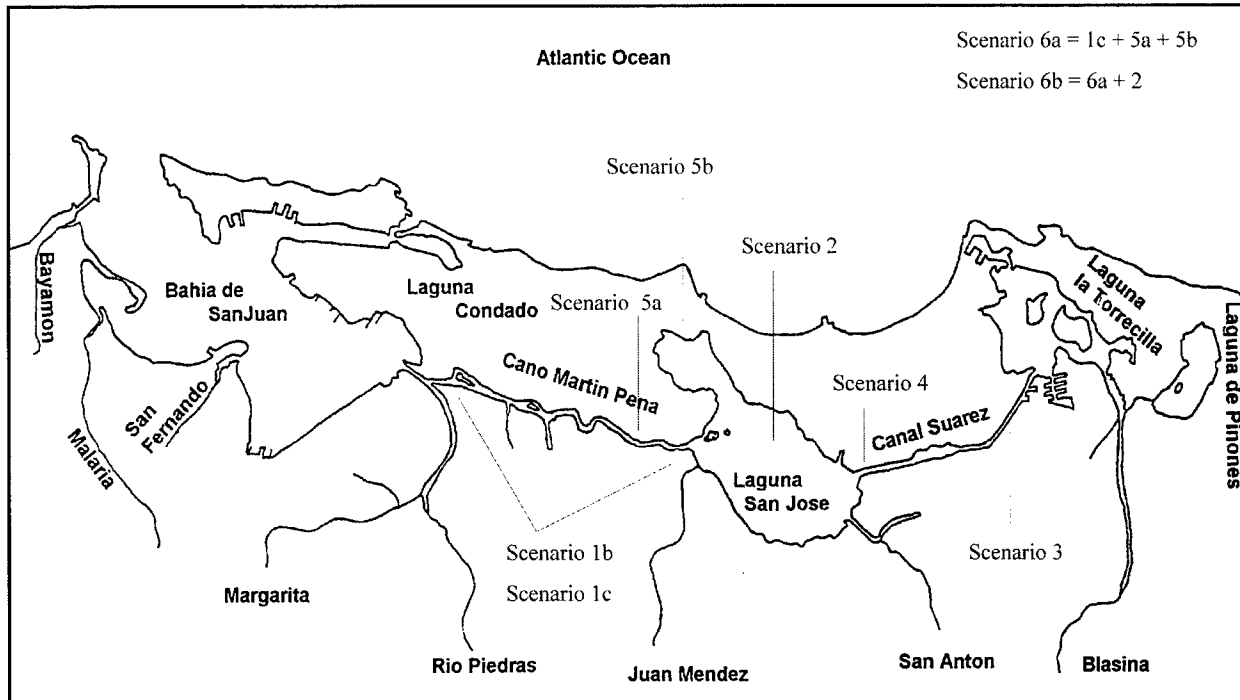


Figure 2-2. Locations of management alternatives (scenarios) in the San Juan Bay Estuary system

3 The Hydrodynamic Model

General

As noted, a 3D numerical hydrodynamic model of the San Juan Bay Estuary System has been developed to provide flow fields to the 3D water quality model of the system. As discussed in Chapter 2, to aid in model adjustment and skill assessment and to provide boundary conditions for production runs, a field data-collection effort was conducted during June-August 1995 (Fagerburg 1998). Water-surface elevations, salinity, and water-velocity data were collected at several locations. The short-term data were collected over 17-19 August 1995 when the crew went back to remove the long-term instruments. These data included Acoustic Doppler Current Profiler (ADCP) data collected over several ranges in an attempt to define the water flux through the connecting canals of the system. Model adjustment has primarily revolved around reproducing the observed tides throughout the system, reproducing the extreme stratification in salinity that often exists in the canals, and reproducing the net flux through the Martín Peña and Suárez Canals.

The verified numerical hydrodynamic model has been used to generate flow fields for various scenarios expected to improve the water quality of San José Lagoon. These include widening and deepening the Martín Peña Canal, removing a bridge from Suárez Canal that severely restricts the tidal flow, filling dredged holes throughout the system, and installing a tide gate in the Suárez Canal.

Discussions of the model adjustment and skill assessment effort and results from the scenario runs are presented in Chapters 6 and 8, respectively. In this chapter, theoretical details of the 3D numerical model are provided along with discussions of the computational grid and boundary forcings employed in its application to the San Juan Bay Estuary System.

CH3D-WES Description

The basic model (CH3D) was originally developed by Sheng (1986) for the U.S. Army Engineer Waterways Experiment Station (WES) but was extensively modified in its application to Chesapeake Bay. These modifications have consisted of different basic formulations as well as substantial recoding for more efficient computing. As its name implies, CH3D-WES makes hydrodynamic computations on a curvilinear or boundary-fitted planform grid. Physical processes impacting bay-wide circulation and vertical mixing that are modeled include tides, wind, density effects (salinity and temperature), freshwater inflows, turbulence, and the effect of the earth's rotation.

Adequately representing the vertical turbulence is crucial to a successful simulation of stratification/destratification. What is referred to as a $k-\epsilon$ turbulence model is employed. The boundary-fitted coordinates feature of the model provides enhancement to fit the irregular shoreline configuration of the San Juan Estuary system and permits adoption of an accurate and economical grid schematization. The solution algorithm employs an external mode consisting of vertically averaged equations to provide the solution for the free surface to the internal mode consisting of the full 3-D equations. Model details are discussed below.

Basic Equations

The basic equations for an incompressible fluid in a right-handed Cartesian coordinate system (x, y, z) are:

$$\frac{\partial u}{\partial x} + \frac{\partial v}{\partial y} + \frac{\partial w}{\partial z} = 0 \quad (3.1)$$

$$\begin{aligned} \frac{\partial u}{\partial t} + \frac{\partial u^2}{\partial x} + \frac{\partial uv}{\partial y} + \frac{\partial uw}{\partial z} = & fv - \frac{1}{\rho} \frac{\partial p}{\partial x} + \frac{\partial}{\partial x} \left(A_H \frac{\partial u}{\partial x} \right) \\ & + \frac{\partial}{\partial y} \left(A_H \frac{\partial u}{\partial y} \right) + \frac{\partial}{\partial z} \left(A_v \frac{\partial u}{\partial z} \right) \end{aligned} \quad (3.2)$$

$$\begin{aligned} \frac{\partial v}{\partial t} + \frac{\partial uv}{\partial x} + \frac{\partial v^2}{\partial y} + \frac{\partial vw}{\partial z} = & -fu - \frac{1}{\rho} \frac{\partial p}{\partial y} + \frac{\partial}{\partial x} \left(A_H \frac{\partial v}{\partial x} \right) \\ & + \frac{\partial}{\partial y} \left(A_H \frac{\partial v}{\partial y} \right) + \frac{\partial}{\partial z} \left(A_v \frac{\partial v}{\partial z} \right) \end{aligned} \quad (3.3)$$

$$\frac{\partial p}{\partial z} = -\rho g \quad (3.4)$$

$$\begin{aligned} & \frac{\partial T}{\partial t} + \frac{\partial uT}{\partial x} + \frac{\partial vT}{\partial y} + \frac{\partial wT}{\partial z} \\ &= \frac{\partial}{\partial x} \left(K_H \frac{\partial T}{\partial x} \right) + \frac{\partial}{\partial y} \left(K_H \frac{\partial T}{\partial y} \right) + \frac{\partial}{\partial z} \left(K_v \frac{\partial T}{\partial z} \right) \end{aligned} \quad (3.5)$$

$$\begin{aligned} & \frac{\partial S}{\partial t} + \frac{\partial uS}{\partial x} + \frac{\partial vS}{\partial y} + \frac{\partial wS}{\partial z} \\ &= \frac{\partial}{\partial x} \left(K_H \frac{\partial S}{\partial x} \right) + \frac{\partial}{\partial y} \left(K_H \frac{\partial S}{\partial y} \right) + \frac{\partial}{\partial z} \left(K_v \frac{\partial S}{\partial z} \right) \end{aligned} \quad (3.6)$$

$$\rho = \rho(T, S) \quad (3.7)$$

where

(u, v, w) = velocities in x-, y-, z-directions

t = time

f = Coriolis parameter defined as $2\Omega \sin \phi$ where Ω is the rotational speed of the earth and ϕ = latitude

ρ = density

p = pressure

A_H, K_H = horizontal turbulent eddy coefficients

A_v, K_v = vertical turbulent eddy coefficients

g = gravitational acceleration

T = temperature

S = salinity

Equation 3.4 implies that vertical accelerations are negligible. Thus, the pressure is hydrostatic.

Various forms of the equation of state can be used for Equation 3.7. In the present model, Equation 3.8 is used:

$$\rho = P / (\alpha + 0.698 P) \quad (3.8)$$

where

$$P = 5890 + 38T - 0.375T^2 + 3S$$

$$\alpha = 1779.5 + 11.25T - 0.0745T^2$$

and T is in degrees Celsius ($^{\circ}\text{C}$), S is in parts per thousand (ppt), and ρ is in g/cm^3 .

Working with the dimensionless form of the governing equations makes it easier to compare the relative magnitude of various terms in the equations. Therefore, the following dimensionless variables are used:

$$(u^*, v^*, w^*) = (u, v, wX_r / Z_r) / U_r$$

$$(x^*, y^*, z^*) = (x, y, zX_r / Z_r) / X_r$$

$$(\tau_x^*, \tau_y^*) = (\tau_x^w, \tau_y^w) / \rho_o f Z_r U_r$$

$$t^* = tf$$

$$\zeta^* = g\zeta / fU_r X_r = \zeta / S_r$$

$$\rho^* = (\rho - \rho_o) / (\rho_r - \rho_o)$$

$$T^* = (T - T_o) / (T_r - T_o)$$

$$A_H^* = A_H / A_{Hr}$$

$$A_v^* = A_v / A_{vr}$$

$$K_H^* = K_H / K_{Hr}$$

$$K_v^* = K_v / K_{vr}$$

where

$$(\tau_x^w, \tau_y^w) = \text{wind stress in x-, y-directions}$$

$$\zeta = \text{water-surface elevation}$$

$$\rho_o, T_o = \text{typical values for the water density and temperature}$$

and S_r , T_r , U_r , ρ_r , X_r , Z_r , A_{Hr} , A_{vr} , K_{Hr} , and K_{vr} are arbitrary reference values of the salinity, temperature, velocity, density, horizontal dimension, vertical dimension, horizontal viscosity, vertical viscosity, horizontal diffusion, and vertical diffusion, respectively. This then yields the following dimensionless parameters in the governing equations:

a. Vertical Ekman number:

$$E_v = A_{vr} / fZ_r^2$$

b. Lateral Ekman number:

$$E_H = A_{Hr} / fX_r^2$$

c. Vertical Prandtl (Schmidt) number:

$$Pr_v = A_{vr} / K_{vr}$$

d. Lateral Prandtl (Schmidt) number:

$$Pr_H = A_{Hr} / K_{Hr}$$

e. Froude number:

$$F_r = U_r / (gZ_r)^{1/2} \quad (6.26)$$

f. Rossby number:

$$R_o = U_r / fX_r$$

g. Densimetric Froude number:

$$Fr_D = F_r / \sqrt{\epsilon}$$

where

$$\epsilon = (\rho_r - \rho_o) / \rho_o$$

External-Internal Modes

The basic equations (Equations 3.1 through 3.8) can be integrated over the depth to yield a set of vertically integrated equations for the water surface, ζ , and unit flow rates U and V in the x - and y -directions. Using the dimensionless variables (asterisks have been dropped) and the parameters previously defined, the vertically integrated equations constituting the external mode are:

$$\frac{\partial \zeta}{\partial t} + \beta \left(\frac{\partial U}{\partial x} + \frac{\partial V}{\partial y} \right) = 0 \quad (3.9)$$

$$\frac{\partial U}{\partial t} = -H \frac{\partial \zeta}{\partial x} + \tau_{sx} - \tau_{bx} + V$$

$$\begin{aligned}
& -R_o \left[\frac{\partial}{\partial x} \left(\frac{UU}{H} \right) + \frac{\partial}{\partial y} \left(\frac{UV}{H} \right) \right] \\
& + E_H \left[\frac{\partial}{\partial x} \left(A_H \frac{\partial U}{\partial x} \right) + \frac{\partial}{\partial y} \left(A_H \frac{\partial U}{\partial y} \right) \right] \\
& - \frac{R_o}{Fr_D^2} \frac{H^2}{2} \frac{\partial \rho}{\partial x}
\end{aligned} \tag{3.10}$$

$$\begin{aligned}
\frac{\partial V}{\partial t} &= -H \frac{\partial \zeta}{\partial y} + \tau_{sy} - \tau_{by} - U \\
& - R_o \left[\frac{\partial}{\partial x} \left(\frac{UV}{H} \right) + \frac{\partial}{\partial y} \left(\frac{VV}{H} \right) \right] \\
& + E_H \left[\frac{\partial}{\partial x} \left(A_H \frac{\partial V}{\partial x} \right) + \frac{\partial}{\partial y} \left(A_H \frac{\partial V}{\partial y} \right) \right] \\
& - \frac{R_o}{Fr_D^2} \frac{H^2}{2} \frac{\partial \rho}{\partial y}
\end{aligned} \tag{3.11}$$

where

$$\beta = gZ_r / f^2 X_r^2 = (R_o / F_r)^2$$

H = total depth

τ_s, τ_b = surface and bottom shear stresses

As will be discussed later, the major purpose of the external mode is to provide the updated water-surface field.

The dimensionless form of the internal mode equations from which the 3-D velocity, salinity, and temperature fields are computed are:

$$\begin{aligned}
\frac{\partial hu}{\partial t} &= -h \frac{\partial \zeta}{\partial x} + E_v \frac{\partial}{\partial z} \left(A_v \frac{\partial hu}{\partial z} \right) + hv \\
& - R_o \left(\frac{\partial hu u}{\partial x} + \frac{\partial huv}{\partial y} + \frac{\partial huw}{\partial z} \right)
\end{aligned}$$

$$\begin{aligned}
& + E_H \left[\frac{\partial}{\partial x} \left(A_H \frac{\partial hu}{\partial x} \right) + \frac{\partial}{\partial y} \left(A_H \frac{\partial hu}{\partial y} \right) \right] \\
& - \frac{R_o}{Fr_D^2} \left(\int_z^\zeta \frac{\partial \rho}{\partial x} dz \right)
\end{aligned} \tag{3.12}$$

$$\begin{aligned}
\frac{\partial hv}{\partial t} &= -h \frac{\partial \zeta}{\partial y} + E_v \frac{\partial}{\partial z} \left(A_v \frac{\partial hv}{\partial z} \right) - hu \\
& - R_o \left(\frac{\partial hvu}{\partial x} + \frac{\partial hvv}{\partial y} + \frac{\partial hvw}{\partial z} \right) \\
& + E_H \left[\frac{\partial}{\partial x} \left(A_H \frac{\partial hv}{\partial x} \right) + \frac{\partial}{\partial y} \left(A_H \frac{\partial hv}{\partial y} \right) \right] \\
& - \frac{R_o}{Fr_D^2} \left(\int_z^\zeta \frac{\partial \rho}{\partial y} dz \right)
\end{aligned} \tag{3.13}$$

$$w_{k+1/2} = w_{k-1/2} - \left(\frac{\partial uh}{\partial x} + \frac{\partial vh}{\partial y} \right) \tag{3.14}$$

$$\begin{aligned}
\frac{\partial hT}{\partial t} &= \frac{E_v}{Pr_v} \frac{\partial}{\partial z} \left(K_v \frac{\partial T}{\partial z} \right) - R_o \left(\frac{\partial huT}{\partial x} + \frac{\partial hvT}{\partial y} + \frac{\partial hwT}{\partial z} \right) \\
& + \frac{E_H}{Pr_H} \left[\frac{\partial}{\partial x} \left(K_H \frac{\partial hT}{\partial x} \right) + \frac{\partial}{\partial y} \left(K_H \frac{\partial hT}{\partial y} \right) \right]
\end{aligned} \tag{3.15}$$

$$\begin{aligned}
\frac{\partial hS}{\partial t} &= \frac{E_v}{Pr_v} \frac{\partial}{\partial z} \left(K_v \frac{\partial S}{\partial z} \right) - R_o \left(\frac{\partial huS}{\partial x} + \frac{\partial hvS}{\partial y} + \frac{\partial hwS}{\partial z} \right) \\
& + \frac{E_H}{Pr_H} \left[\frac{\partial}{\partial x} \left(K_H \frac{\partial hS}{\partial x} \right) + \frac{\partial}{\partial y} \left(K_H \frac{\partial hS}{\partial y} \right) \right]
\end{aligned} \tag{3.16}$$

In these equations h is the thickness of an internal layer, w is the vertical component of the velocity, and $k+1/2$ and $k-1/2$ represent the top and bottom, respectively, of the k^{th} vertical layer.

Boundary-Fitted Equations

To better resolve complex geometries in the horizontal directions, the CH3D-WES makes computations on the boundary-fitted or generalized curvilinear planform grid shown in Figure 3-1. This necessitates the transformation of the governing equations into boundary-fitted coordinates (ξ, η) . If only the x - and y -coordinates are transformed, a system of equations similar to those solved by Johnson (1980) for vertically averaged flow fields is obtained. However, in CH3D-WES not only are the x - and y -coordinates transformed into the (ξ, η) curvilinear system, but also the velocity is transformed such that its components are perpendicular to the (ξ, η) coordinate lines; i.e., contravariant components of the velocity are computed. This is accomplished by employing the following definitions for the components of the Cartesian velocity (u, v) in terms of contravariant components \bar{u} and \bar{v}

$$u = x_{\xi} \bar{u} + x_{\eta} \bar{v}$$

$$v = y_{\xi} \bar{u} + y_{\eta} \bar{v}$$

along with the following expressions for replacing Cartesian derivatives

$$f_x = \frac{1}{J} \left[(fy_{\eta})_{\xi} - (fy_{\xi})_{\eta} \right]$$

$$f_y = \frac{1}{J} \left[-(fx_{\eta})_{\xi} + (fx_{\xi})_{\eta} \right]$$

where J is the Jacobian of the transformation defined as

$$J = x_{\xi} y_{\eta} - x_{\eta} y_{\xi}$$

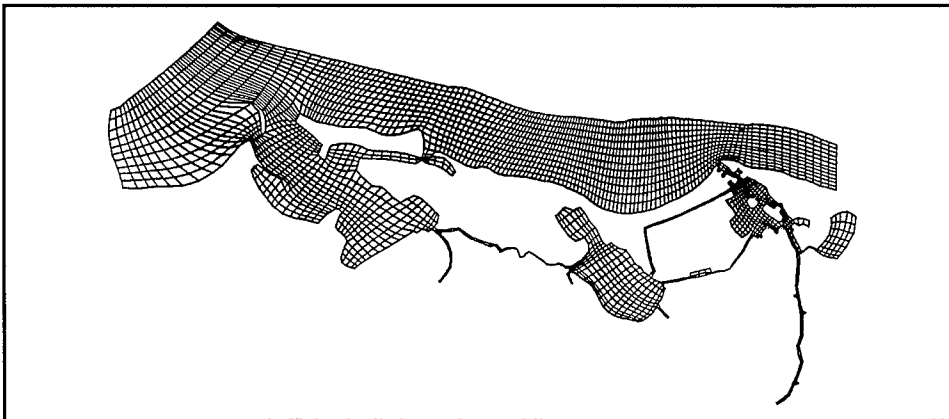


Figure 3-1. Numerical grid of San Juan estuarine system

With the governing equations written in terms of the contravariant components of the velocity, boundary conditions can be prescribed on a boundary-fitted grid in the same manner as on a Cartesian grid since \bar{u} and \bar{v} are perpendicular to the curvilinear cell faces (e.g., at a land boundary, either \bar{u} or \bar{v} is set to zero).

Initially the vertical dimension was handled through the use of what is commonly called a sigma-stretched grid. However, with a sigma-stretched grid, the bottom layer in one column communicates with the bottom layer in an adjacent column. Thus, if depth changes are rather coarsely resolved, channel stratification cannot be maintained. As a result, the governing equations, Equations 3.17-3.21, presented for solution on the Cartesian or z-plane in the vertical direction are the ones constituting the internal mode.

With both the Cartesian coordinates and the Cartesian velocity transformed, the following boundary-fitted equations for \bar{u} , \bar{v} , w , S , and T to be solved in each vertical layer are obtained.

$$\begin{aligned}
\frac{\partial \bar{h}\bar{u}}{\partial t} = & -h \left(\frac{G_{22}}{J^2} \frac{\partial \xi}{\partial \xi} - \frac{G_{12}}{J^2} \frac{\partial \xi}{\partial \eta} \right) + \frac{h}{J} (G_{12} \bar{u} + G_{22} \bar{v}) + \frac{R_o x_\eta}{J^2} \left[\frac{\partial}{\partial \xi} (J y_\xi \bar{h} \bar{u} \bar{u} \right. \\
& + J y_\eta \bar{h} \bar{u} \bar{v}) + \frac{\partial}{\partial \eta} (J y_\xi \bar{h} \bar{u} \bar{v} + J y_\eta \bar{h} \bar{v} \bar{v}) \left. \right] - \frac{R_o y_\eta}{J^2} \left[\frac{\partial}{\partial \xi} (J x_\xi \bar{h} \bar{u} \bar{u} + J x_\eta \bar{h} \bar{u} \bar{v}) \right. \\
& + \frac{\partial}{\partial \eta} (J x_\xi \bar{h} \bar{u} \bar{v} + J x_\eta \bar{h} \bar{v} \bar{v}) \left. \right] - R_o \left[(w \bar{u})_{top} - (w \bar{u})_{bot} \right] \\
& + E_v \left[\left(A_v \frac{\partial \bar{u}}{\partial z} \right)_{top} - \left(A_v \frac{\partial \bar{u}}{\partial z} \right)_{bot} \right] - \frac{R_o h}{Fr_D^2} \left[\int_z^\xi \left(\frac{G_{22}}{J^2} \frac{\partial \rho}{\partial \xi} \right. \right. \\
& \left. \left. - \frac{G_{12}}{J^2} \frac{\partial \rho}{\partial \eta} \right) dz \right] + \text{Horizontal Diffusion}
\end{aligned} \tag{3.17}$$

$$\begin{aligned}
\frac{\partial \bar{h}\bar{v}}{\partial t} = & -h \left(-\frac{G_{21}}{J^2} \frac{\partial \xi}{\partial \xi} + \frac{G_{11}}{J^2} \frac{\partial \xi}{\partial \eta} \right) - \frac{h}{J} (G_{11} \bar{u} + G_{21} \bar{v}) - \frac{R_o x_\xi}{J^2} \left[\frac{\partial}{\partial \xi} (J y_\xi \bar{h} \bar{u} \bar{u} \right. \\
& + J y_\eta \bar{h} \bar{u} \bar{v}) + \frac{\partial}{\partial \eta} (J y_\xi \bar{h} \bar{u} \bar{v} + J y_\eta \bar{h} \bar{v} \bar{v}) \left. \right] + \frac{R_o y_\xi}{J^2} \left[\frac{\partial}{\partial \xi} (J x_\xi \bar{h} \bar{u} \bar{u} + J x_\eta \bar{h} \bar{u} \bar{v}) \right. \\
& + \frac{\partial}{\partial \eta} (J x_\xi \bar{h} \bar{u} \bar{v} + J x_\eta \bar{h} \bar{v} \bar{v}) \left. \right] - R_o \left[(w \bar{v})_{top} - (w \bar{v})_{bot} \right]
\end{aligned}$$

$$+E_v \left[\left(A_v \frac{\partial \bar{v}}{\partial z} \right)_{top} - \left(A_v \frac{\partial \bar{v}}{\partial z} \right)_{bot} \right] - \frac{R_o h}{Fr_D^2} \left[\int_z^{\xi} \left(-\frac{G_{2l}}{J^2} \frac{\partial \rho}{\partial \xi} + \frac{G_{1l}}{J^2} \frac{\partial \rho}{\partial \eta} \right) dz \right]$$

+ *Horizontal Diffusion* (3.18)

$$w_{top} = w_{bot} - \frac{1}{J} \left(\frac{\partial J \bar{u} h}{\partial \xi} + \frac{\partial J \bar{v} h}{\partial \eta} \right)$$

(3.19)

$$\frac{\partial h S}{\partial t} = \frac{E_v}{Pr_v} \left[\left(K_v \frac{\partial S}{\partial z} \right)_{top} - \left(K_v \frac{\partial S}{\partial z} \right)_{bot} \right] - \frac{R_o}{J} \left(\frac{\partial h J \bar{u} S}{\partial \xi} + \frac{\partial h J \bar{v} S}{\partial \eta} \right)$$

- $R_o \left[(wS)_{top} - (wS)_{bot} \right] + \text{Horizontal Diffusion}$ (3.20)

$$\frac{\partial h T}{\partial t} = \frac{E_v}{Pr_v} \left[\left(K_v \frac{\partial T}{\partial z} \right)_{top} - \left(K_v \frac{\partial T}{\partial z} \right)_{bot} \right] - \frac{R_o}{J} \left(\frac{\partial h J \bar{u} T}{\partial \xi} + \frac{\partial h J \bar{v} T}{\partial \eta} \right)$$

- $R_o \left[(wT)_{top} - (wT)_{bot} \right] + \text{Horizontal Diffusion}$ (3.21)

where

$$\begin{aligned} G_{11} &= x_{\xi}^2 + y_{\xi}^2 \\ G_{22} &= x_{\eta}^2 + y_{\eta}^2 \\ G_{12} &= G_{21} = x_{\xi} x_{\eta} + y_{\xi} y_{\eta} \end{aligned}$$

Similarly, the transformed external mode equations become:

$$\frac{\partial \bar{\zeta}}{\partial t} + \beta \left(\frac{\partial \bar{U}}{\partial \xi} + \frac{\partial \bar{V}}{\partial \eta} \right) = 0$$

(3.22)

$$\begin{aligned} \frac{\partial \bar{U}}{\partial t} &= -\frac{H}{J^2} \left(G_{22} \frac{\partial \bar{\zeta}}{\partial \xi} - G_{12} \frac{\partial \bar{\zeta}}{\partial \eta} \right) \\ &+ \frac{1}{J} (G_{12} \bar{U} + G_{22} \bar{V}) + \frac{R_o x_n}{J^2 H} \left[\frac{\partial}{\partial \xi} (J y_{\xi} \bar{U} \bar{U} + J y_{\eta} \bar{U} \bar{V}) + \frac{\partial}{\partial \eta} (J y_{\xi} \bar{U} \bar{V} + J y_{\eta} \bar{V} \bar{V}) \right] \end{aligned}$$

$$\begin{aligned}
& -\frac{R_o y_\eta}{J^2} \left[\frac{\partial}{\partial \xi} (J x_\xi \bar{U}\bar{U} + J x_\eta \bar{U}\bar{V}) + \frac{\partial}{\partial \eta} (J x_\xi \bar{U}\bar{V} + J x_\eta \bar{V}\bar{V}) \right] \\
& + \tau_{s\xi} - \tau_{b\xi} - \frac{R_o}{Fr_D^2} \frac{H^2}{2} \left(G_{22} \frac{\partial \rho}{\partial \xi} - G_{12} \frac{\partial \rho}{\partial \eta} \right) \\
& + \text{Horizontal Diffusion}
\end{aligned} \tag{3.23}$$

$$\begin{aligned}
\frac{\partial \bar{V}}{\partial t} = & -\frac{H}{J^2} \left(-G_{21} \frac{\partial \xi}{\partial \xi} + G_{11} \frac{\partial \xi}{\partial \eta} \right) - \frac{1}{J} (G_{11} \bar{U} + G_{21} \bar{V}) \\
& -\frac{R_o x_\xi}{J^2 H} \left[\frac{\partial}{\partial \xi} (J y_\xi \bar{U}\bar{U} + J y_\eta \bar{U}\bar{V}) + \frac{\partial}{\partial \eta} (J y_\xi \bar{U}\bar{V} + J y_\eta \bar{V}\bar{V}) \right] \\
& +\frac{R_o y_\xi}{J^2 H} \left[\frac{\partial}{\partial \xi} (J x_\xi \bar{U}\bar{U} + J x_\eta \bar{U}\bar{V}) + \frac{\partial}{\partial \eta} (J x_\xi \bar{U}\bar{V} + J x_\eta \bar{V}\bar{V}) \right] \\
& + \tau_{s\eta} - \tau_{b\eta} - \frac{R_o}{Fr_D^2} \frac{H^2}{2} \left(-G_{21} \frac{\partial \rho}{\partial \xi} + G_{11} \frac{\partial \rho}{\partial \eta} \right) \\
& + \text{Horizontal Diffusion}
\end{aligned} \tag{3.24}$$

where \bar{U} and \bar{V} are contravariant components of the vertically averaged velocity.

Equations 3.22-3.24 are solved first to yield the water-surface elevations, which are then used to evaluate the water-surface slope terms in the internal mode equations. The horizontal diffusion terms are given in Appendix A.

Numerical Solution Algorithm

Finite differences are used to replace derivatives in the governing equations, resulting in a system of linear algebraic equations to be solved in both the external and internal modes. A staggered grid is used in both the horizontal and vertical directions of the computational domain. In the horizontal directions, a unit cell consists of a ξ -point in the center ($\xi_{i,j}$), a U-point on its left face ($U_{i,j}$), and a V-point on its bottom face ($V_{i,j}$). In the vertical direction, the vertical velocities are computed at the “full” grid points. Horizontal velocities, temperature, salinity, and density are computed at the “half” grid points (half grid spacing below the full points).

The external mode solution consists of the surface displacement and vertically integrated contravariant unit flows \bar{U} and \bar{V} . All of the terms in the transformed vertically averaged continuity equation are treated implicitly whereas only the water-surface slope terms in the transformed vertically averaged momentum equations are treated implicitly. If the external mode is used purely as a vertically averaged model, the bottom friction is also treated implicitly. Those terms treated implicitly are weighted between the new and old time-steps. The resulting finite difference equations are then factored such that a ξ -sweep followed by an η -sweep of the horizontal grid yields the solution at the new time-step.

Writing Equations 3.11 as

$$\frac{\partial \zeta}{\partial t} + \beta \left(\frac{\partial \bar{U}}{\partial \xi} + \frac{\partial \bar{V}}{\partial \eta} \right) = 0 \quad (3.25)$$

$$\frac{\partial \bar{U}}{\partial t} + \frac{H}{J^2} G_{22} \frac{\partial \zeta}{\partial \eta} = M \quad (3.26)$$

$$\frac{\partial \bar{V}}{\partial t} + \frac{H}{J^2} G_{11} \frac{\partial \zeta}{\partial \xi} = N \quad (3.27)$$

where M and N are the remaining terms in Equations 3.10 and 3.11, the ξ -sweep is

$$\begin{aligned} \xi - \text{sweep} &\rightarrow \zeta_{ij}^* + \frac{\beta \theta \Delta t}{\Delta \xi} (\bar{U}_{i+1,j}^* - \bar{U}_{ij}^*) \\ &= \zeta_{ij}^n (1 - \theta) \frac{\Delta t}{\Delta \xi} (\bar{U}_{i+1,j}^n - \bar{U}_{ij}^n) \frac{\Delta t}{\Delta \eta} (\bar{V}_{ij+1}^n - \bar{V}_{ij}^n) \end{aligned} \quad (3.28)$$

where θ is a parameter determining the degree of implicitness and

$$\bar{U}_{ij}^{n+1} + \frac{\theta \Delta t H G_{22}}{\Delta \xi J^2} (\zeta_{ij}^* - \zeta_{i-1,j}^*) = \bar{U}_{ij}^n - (1 - \theta) \frac{\Delta t H G_{22}}{\Delta \xi J^2} (\zeta_{ij}^n - \zeta_{i-1,j}^n) + \Delta t M^n \quad (3.29)$$

The η -sweep then provides the updated ζ and \bar{V} at the $n + 1$ time level.

$$\eta - \text{sweep} \rightarrow \zeta_{ij}^{n+1} + \frac{\beta \theta \Delta t}{\Delta \eta} (\bar{V}_{i,j+1}^{n+1} - \bar{V}_{ij}^{n+1}) = \zeta_{i,j}^*$$

$$-(1-\theta)\frac{\Delta t}{\Delta \eta}(\bar{V}_{i,j+1}^n - \bar{V}_{i,j}^n) + \frac{\Delta t}{\Delta \eta}(\bar{V}_{i,j+1}^n - \bar{V}_{i,j}^n) \quad (3.30)$$

and

$$\begin{aligned} \bar{V}_{i,j}^{n+1} + \frac{\theta \Delta t H G_{II}}{\Delta \eta J^2} (\zeta_{i,j+1}^{n+1} - \zeta_{i,j}^{n+1}) \\ = V_{i,j}^n - (1-\theta) \frac{\Delta t H G_{II}}{\Delta \eta J^2} (\zeta_{i,j+1}^n - \zeta_{i,j}^n) + \Delta t N^n \end{aligned} \quad (3.31)$$

A typical value of θ of 0.55 yields stable and accurate solutions.

The internal mode consists of computations from Equations 3.17-3.21 for the three velocity components \bar{u} , \bar{v} , and w , salinity, and temperature. The same time-step size is used for both internal and external modes. The only terms treated implicitly are the vertical diffusion terms in all equations and the bottom friction and surface slope terms in the momentum equations. Values of the water-surface elevations from the external mode are used to evaluate the surface slope terms in Equations 3.17 and 3.18. As a result, the extremely restrictive speed of a free-surface gravity wave is removed from the stability criteria. Roache's second upwind differencing is used to represent the convective terms in the momentum equations, whereas a spatially third-order scheme developed by Leonard (1979) called QUICKEST is used to represent the advective terms in Equations 3.20 and 3.21 for salinity and temperature, respectively. For example, if the velocity on the right face of a computational cell is positive, then with QUICKEST the value of the salinity used to compute the flux through the face is

$$\begin{aligned} S_R = \frac{1}{2}(S_{i,j,k} + S_{i+1,j,k}) - \frac{1}{6} \left[1 - \left(\frac{\bar{U}_{i+1,j,k} \Delta t}{\Delta \xi} \right)^2 \right] (S_{i+1,j,k} - 2S_{i,j,k} + S_{i-1,j,k}) \\ - \frac{1}{2} \frac{U_{i+1,j,k} \Delta t}{\Delta \xi} (S_{i+1,j,k} - S_{i,j,k}) \end{aligned} \quad (3.32)$$

Turbulence Parameterization

The effect of vertical turbulence is modeled using the concept of eddy viscosity and diffusivity to parameterize the velocity and density correlation terms that arise from a time averaging of the governing equations. The eddy coefficients are computed through the implementation of what is referred to as a $k-\epsilon$ turbulence model. This model is a two-equation model for the computation of the kinetic energy of the turbulence (k) and the

dissipation of the turbulence (ϵ). Both time evolution and vertical diffusion are retained, and the effects of surface wind shear, bottom shear, velocity gradient turbulence production, dissipation, and stratification are included. The basic idea behind the k - ϵ turbulence model (Rodi 1980) is that the vertical eddy viscosity coefficient can be related to the turbulent kinetic energy per unit mass, k , and its rate of dissipation, ϵ , and an empirical coefficient ($c_v = 0.09$) by:

$$A_z = c_v \frac{k^2}{\epsilon} \quad (3.33)$$

The transport equation for the turbulence quantities are:

$$\frac{\partial(k)}{\partial t} - \frac{\partial}{\partial z} \left(A_z \frac{\partial k}{\partial z} \right) = (P_z - \epsilon + G) \quad (3.34)$$

$$\frac{\partial(\epsilon)}{\partial t} - \frac{\partial}{\partial z} \left(\frac{A_z}{\sigma_\epsilon} \frac{\partial \epsilon}{\partial z} \right) = \left(c_1 \frac{\epsilon}{k} P_z - c_2 \frac{\epsilon^2}{k} \right) \quad (3.35)$$

in which $\sigma_\epsilon = 1.3$, $c_1 = 1.44$, and $c_2 = 1.92$ (Rodi 1980). The source and sink terms on the right-hand side of Equations 3.34 and 3.35 represent mechanical production of turbulence due to velocity gradients, P_z , and buoyancy production or destruction in the stable stratified condition, G . Surface (s) and bottom (b) boundary conditions for the turbulence quantities are specified as:

$$k_{s,b} = \frac{U_*^2}{\sqrt{c_v}} \quad (3.36)$$

$$\epsilon_{s,b} = \frac{U_*^3}{\kappa \frac{\Delta z}{2}} \quad (3.37)$$

where κ is the von Karman constant ($= 0.4$). The friction velocity used for the surface boundary condition is defined as the square root of the resultant wind shear stress divided by the water density. The bottom friction velocity is computed in an identical way with the wind shear stress being replaced by the bottom shear stress. The suppression of the vertical diffusivity by stratification is given by:

$$K_z = A_z (1 + 3R_i)^{-2} \quad (3.38)$$

where R_i is the Richardson Number (Bloss et al. 1988).

Therefore, the Prandtl Number becomes

$$P_r = (1 + 3R_i)^2 \quad (3.39)$$

Boundary Conditions

The boundary conditions at the free surface are

$$A_v \left(\frac{\partial \bar{u}}{\partial z}, \frac{\partial \bar{v}}{\partial z} \right) = (\tau_{s_s}, \tau_{s_n}) / \rho = (CW_{s_s}^2, CW_{s_n}^2) \quad (3.40)$$

$$\frac{\partial T}{\partial z} = \frac{Pr}{E_v} K(T - T_e) \quad (3.41)$$

$$\frac{\partial S}{\partial z} = 0 \quad (3.42)$$

whereas the boundary conditions at the bottom are

$$A_v \left(\frac{\partial \bar{u}}{\partial z}, \frac{\partial \bar{v}}{\partial z} \right) = (\tau_{b_s}, \tau_{b_n}) / \rho = \frac{U_r}{A_{vr}} Z_r C_d (\bar{u}_1^2 + \bar{v}_1^2)^{1/2} (\bar{u}_1, \bar{v}_1) \quad (3.43)$$

$$\frac{\partial T}{\partial z} = 0 \quad (3.44)$$

$$\frac{\partial S}{\partial z} = 0 \quad (3.45)$$

where

C = surface drag coefficient

W = wind speed

K = surface heat exchange coefficient

T_e = equilibrium temperature

C_d = bottom friction coefficient

\bar{u}_1, \bar{v}_1 = values of the horizontal velocity components next to the bottom

With z_l equal to one-half the bottom layer thickness, C_d is given by

$$C_d = k^2 [\ln(z_l / z_0)]^{-2} \quad (3.46)$$

where

k = von Karman constant

z_0 = bottom roughness height

As can be seen from Equation 3.40, the surface shear stress is computed from wind data. Figure 3-2 shows the hourly wind data recorded for each study month at the San Juan International Airport. These data were assumed to be constant over the numerical grid (Figure 3-1).

Manning's formulation is employed for the bottom friction in the external mode equations if the model is used purely to compute vertically averaged flow fields. As presented by Garratt (1977), the surface drag coefficient is computed from

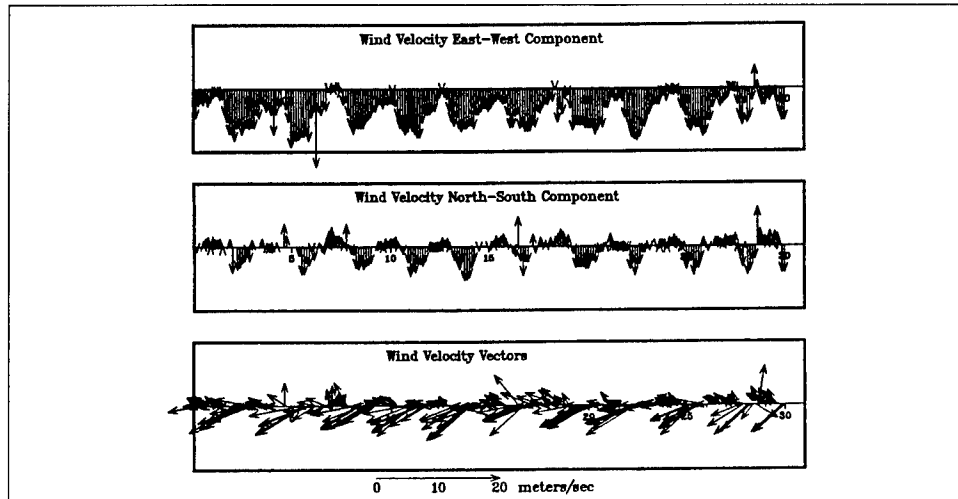
$$C = (0.75 + 0.067W) \times 10^{-3} \quad (3.47)$$

with the maximum allowable value being 0.003.

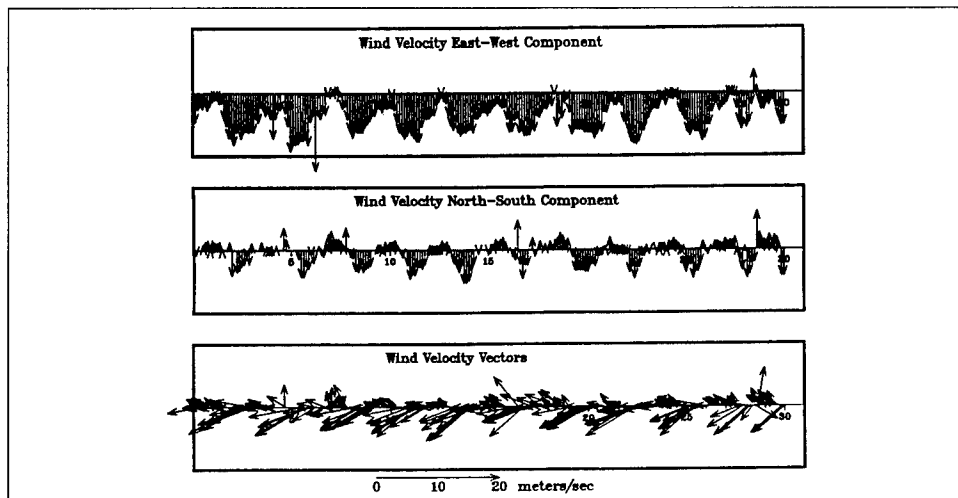
As discussed by Edinger, Brady, and Geyer (1974), the surface heat exchange coefficient, K , and the equilibrium temperature, T_e , are computed from the meteorological data (wind speed, cloud cover, dry bulb air temperatures, and either wet bulb air temperature or relative humidity). However, it should be noted that temperature was not computed in this study. Since there was virtually no change in the temperature during the simulation period, a constant temperature was input and used in the computation of the water density.

At river boundaries, the freshwater inflow and its temperature are prescribed and the salinity is normally assumed to be zero. Freshwater inflows into the San Juan Estuary system occur primarily through the Puerto Nuevo River, Juan Mendez Creek, San Anton Creek, Blasima Creek, and the Malaria Channel (Figure 1-1). As can be seen from an inspection of Figure 3-3, these inflows are quite flashy and, as will be seen in Chapter 6, can result in high salinity stratification in parts of the system. A discussion of the inflow of these data is presented in Chapter 5. The locations of these inflows are shown in Figure 5-4.

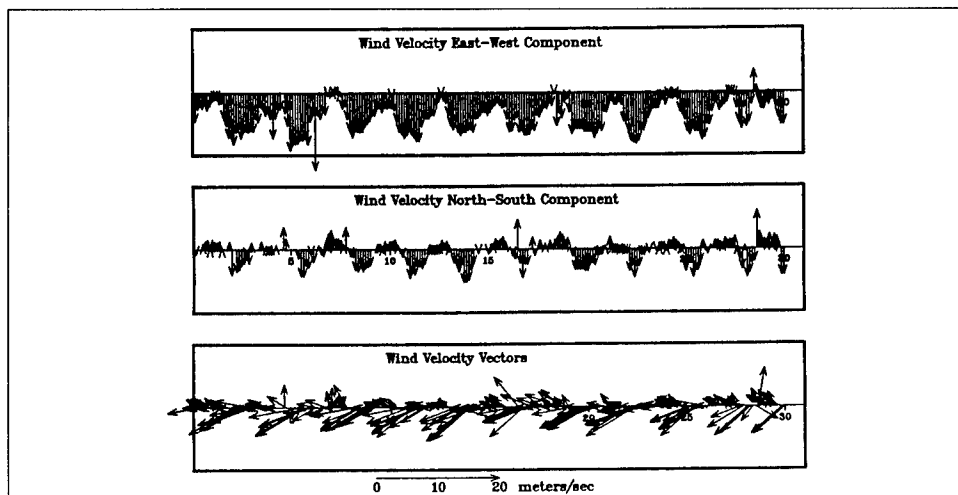
At an ocean boundary, the water-surface elevation is prescribed along with time-varying vertical distributions of salinity and temperature. To prescribe water surface elevations along the open ocean portion of the numerical grid shown in Figure 3-1, a global vertically averaged model called ADCIRC (Westerink et al. 1992) was applied. Figure 3-4 shows the ADCIRC grid which covers the Gulf of Mexico, the Carribean, and a portion of the Atlantic Ocean. A blowup of the grid surrounding Puerto Rico is shown in Figure 3-5. Time-varying water-surface elevations were saved from the ADCIRC model at several locations along the open ocean grid in Figure 3-1. These elevations reflect both the astronomical tide as well as



a. June

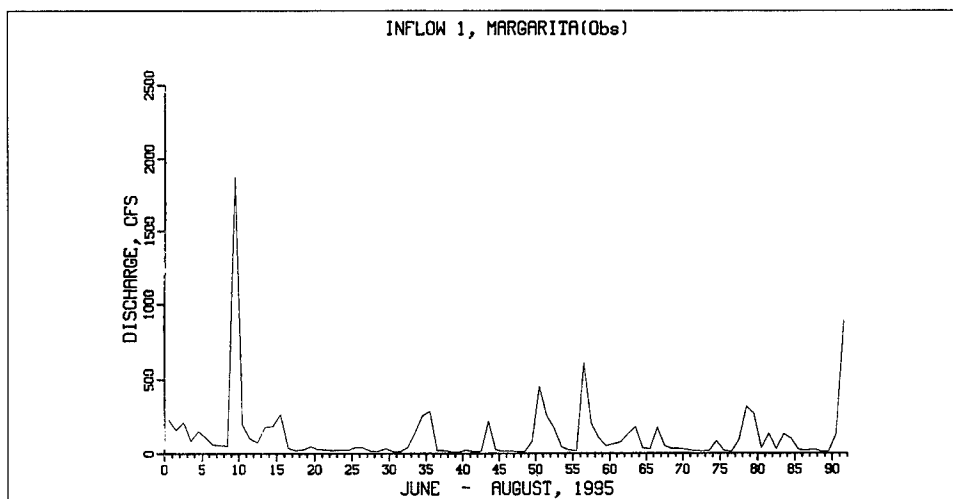


b. July

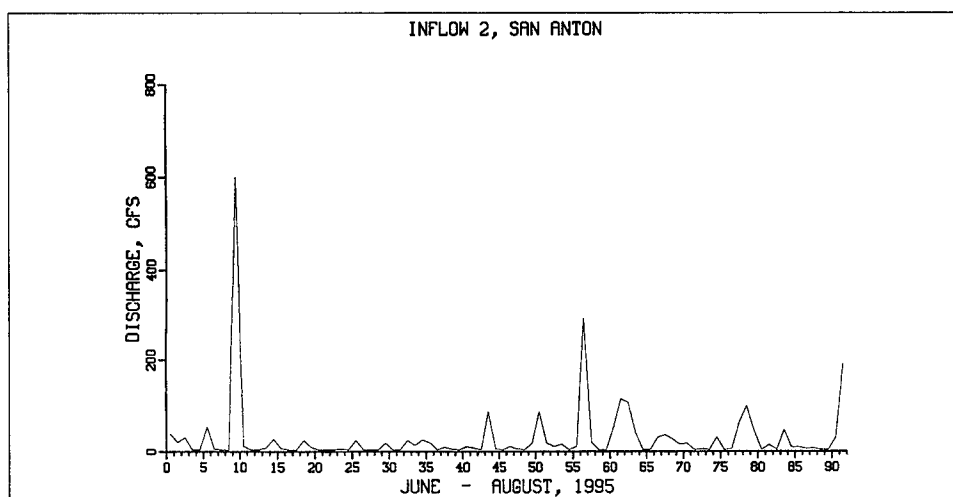


c. August

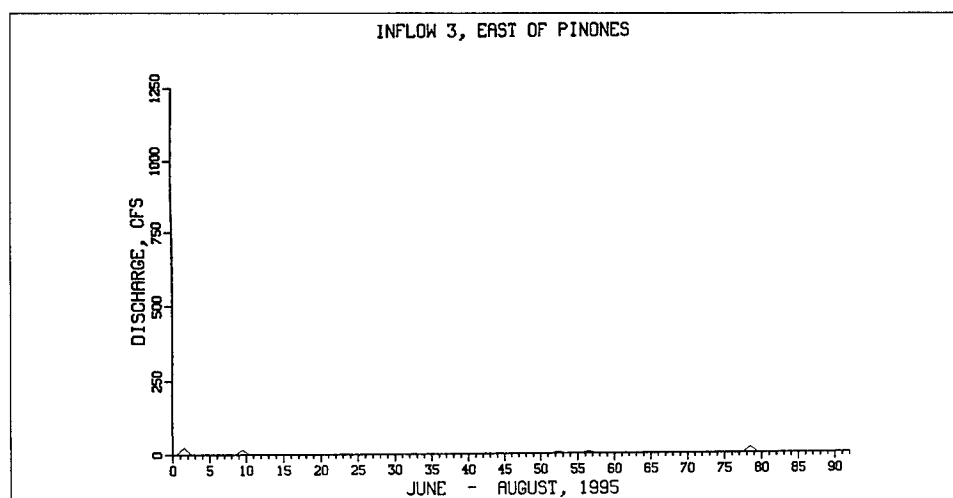
Figure 3-2. San Juan Airport wind data



a. Inflow 1

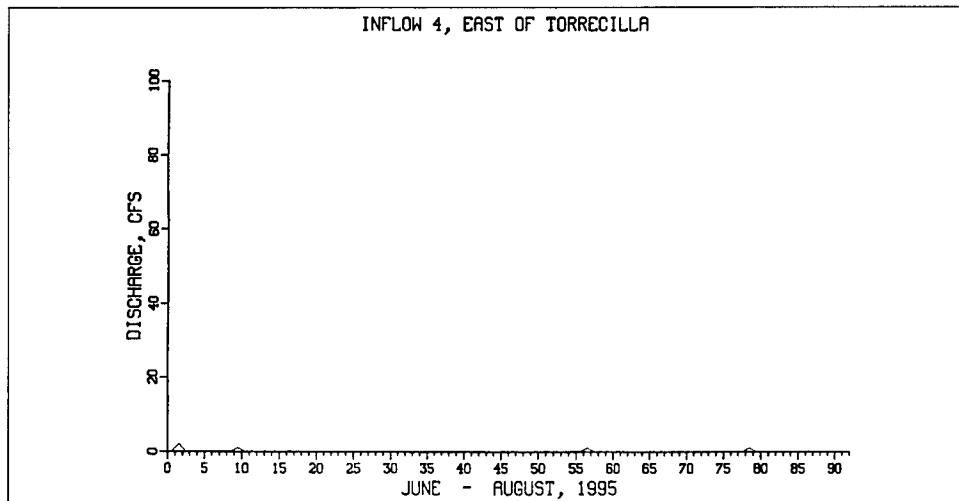


b. Inflow 2

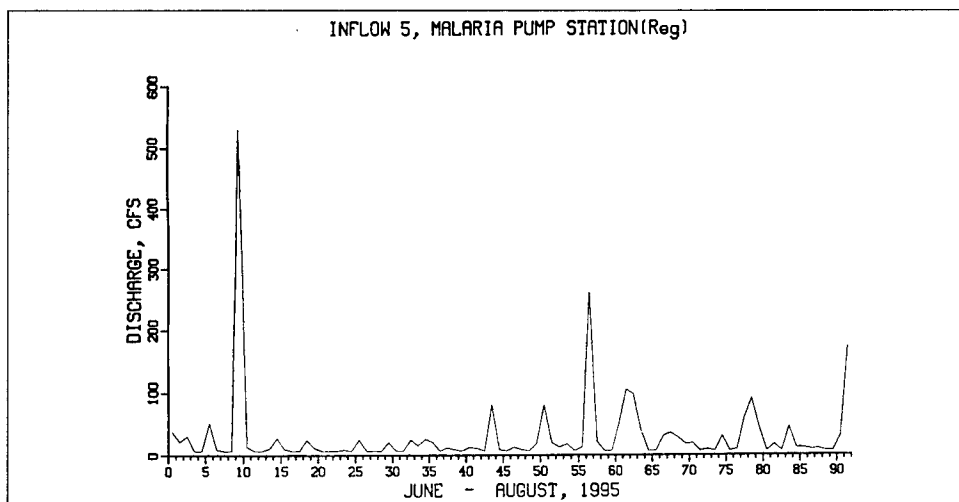


c. Inflow 3

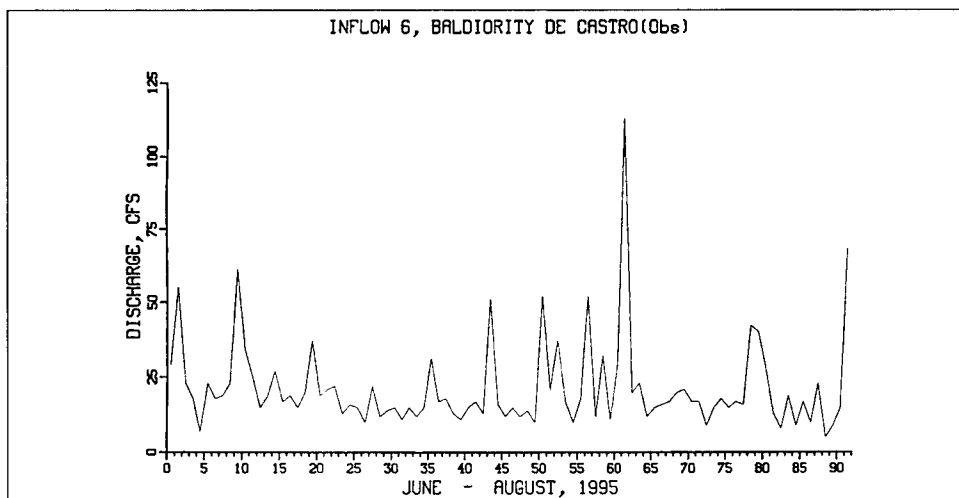
Figure 3-3. Freshwater inflows (continued)



d. Inflow 4

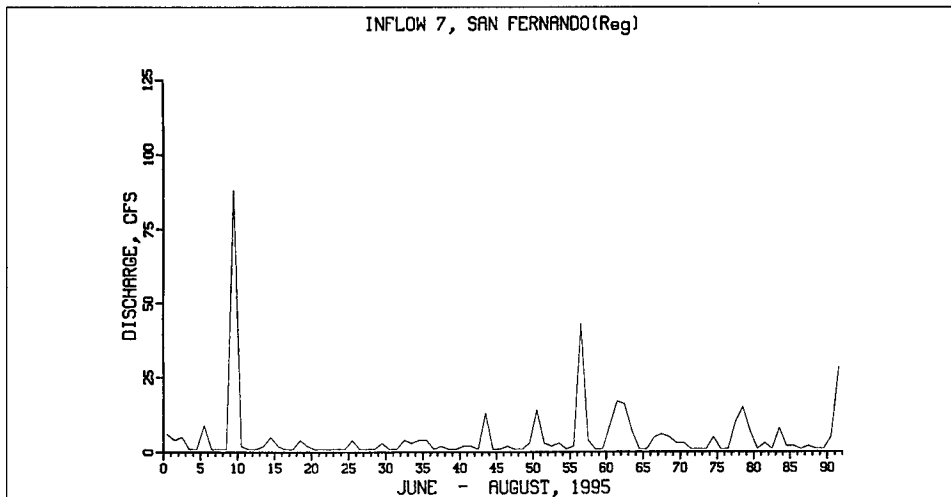


e. Inflow 5

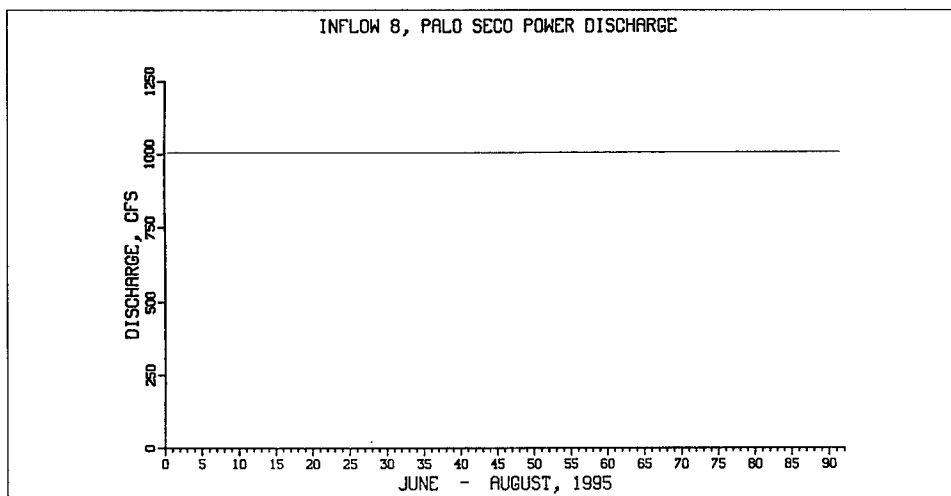


f. Inflow 6

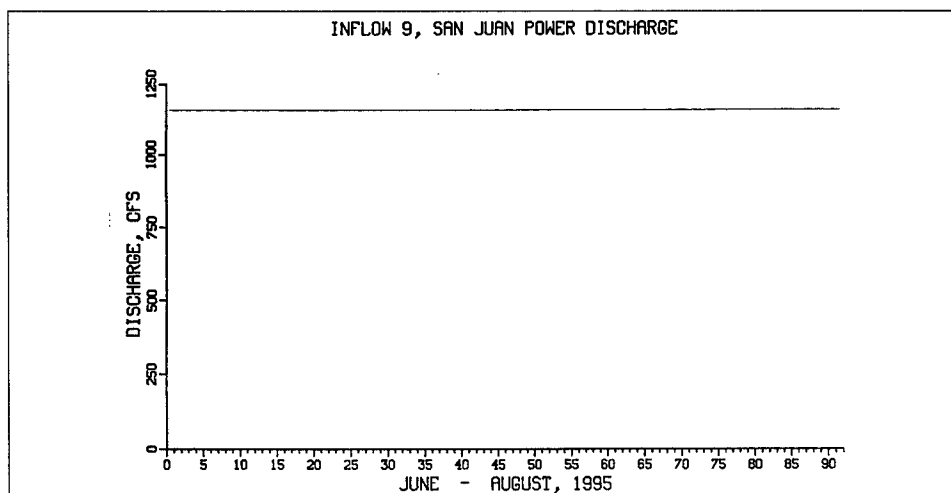
Figure 3-3. Continued



g. Inflow 7

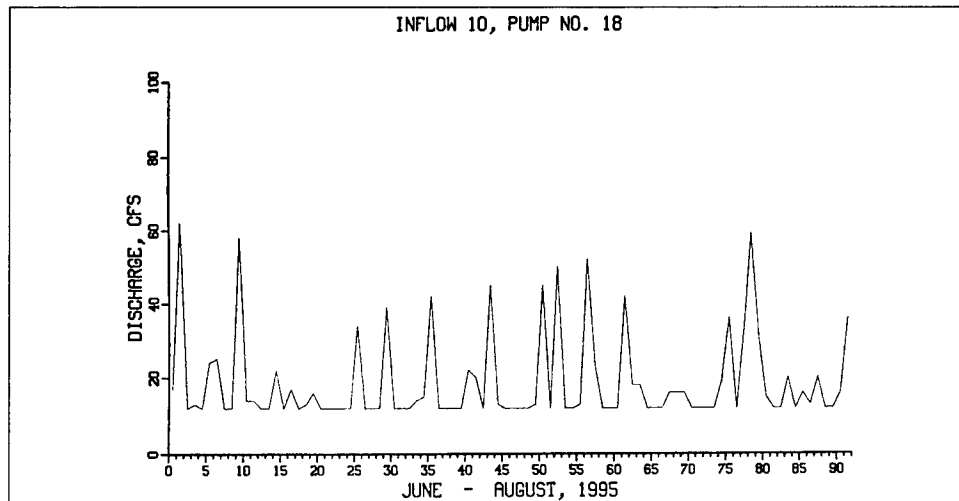


h. Inflow 8

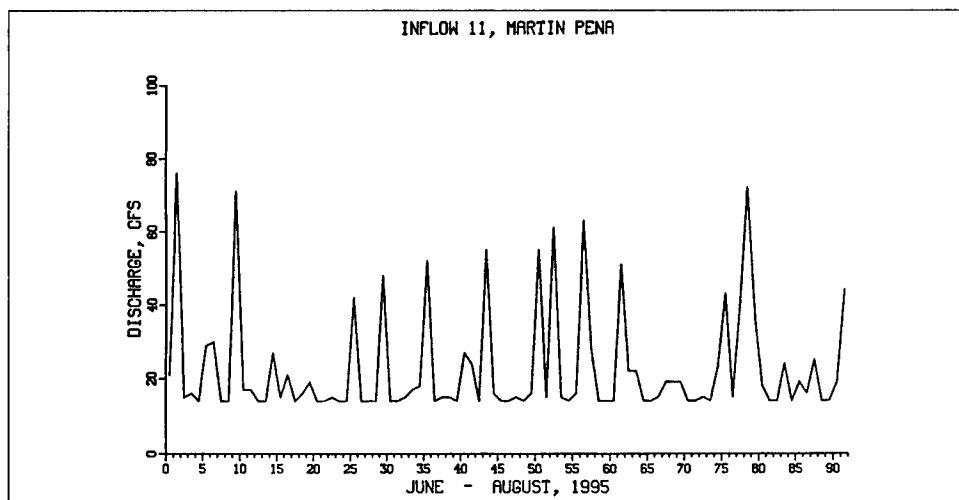


i. Inflow 9

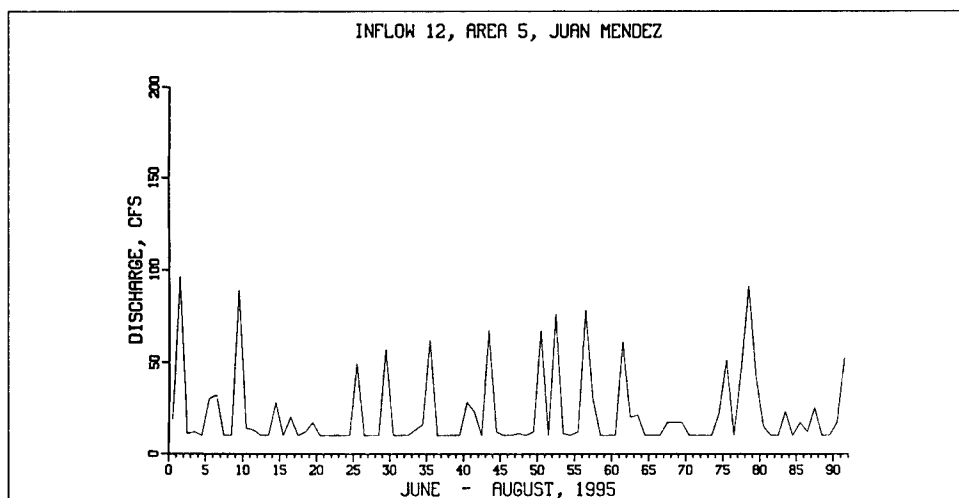
Figure 3-3. Continued



j. Inflow 10

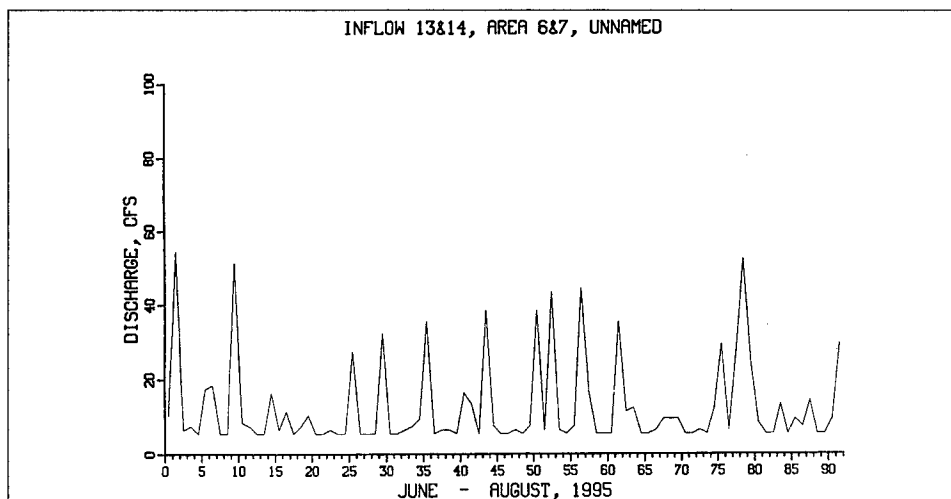


k. Inflow 11

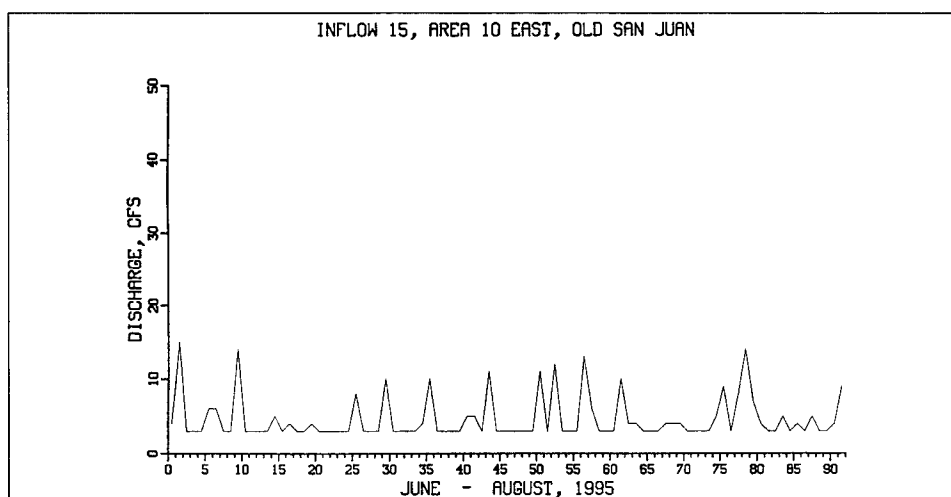


l. Inflow 12

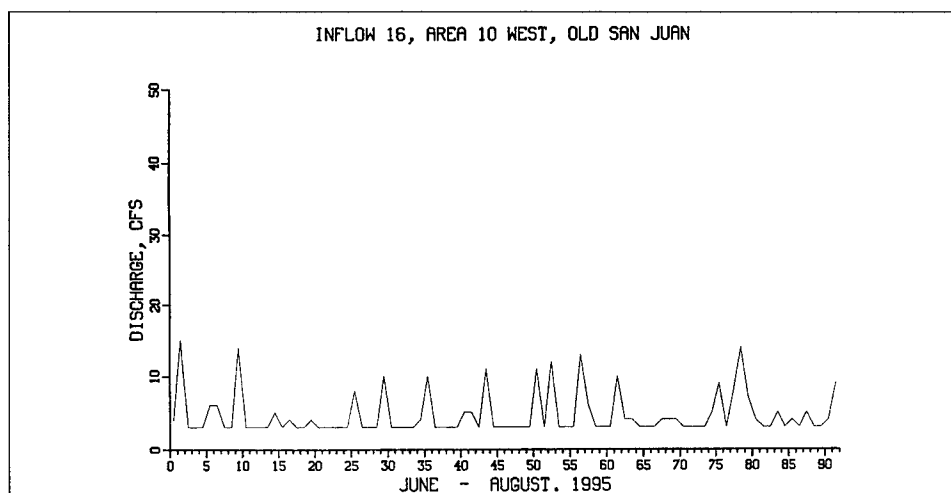
Figure 3-3. Continued



m. Inflow 13 & 14

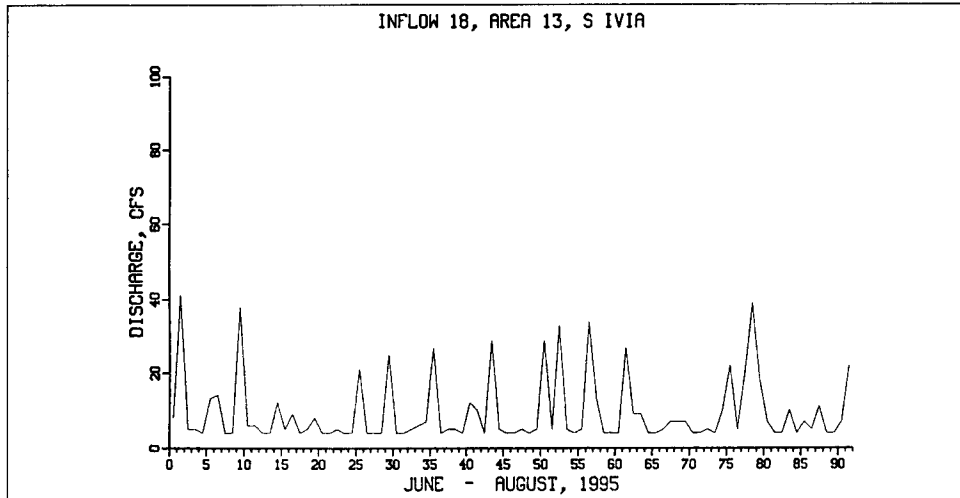


n. Inflow 15

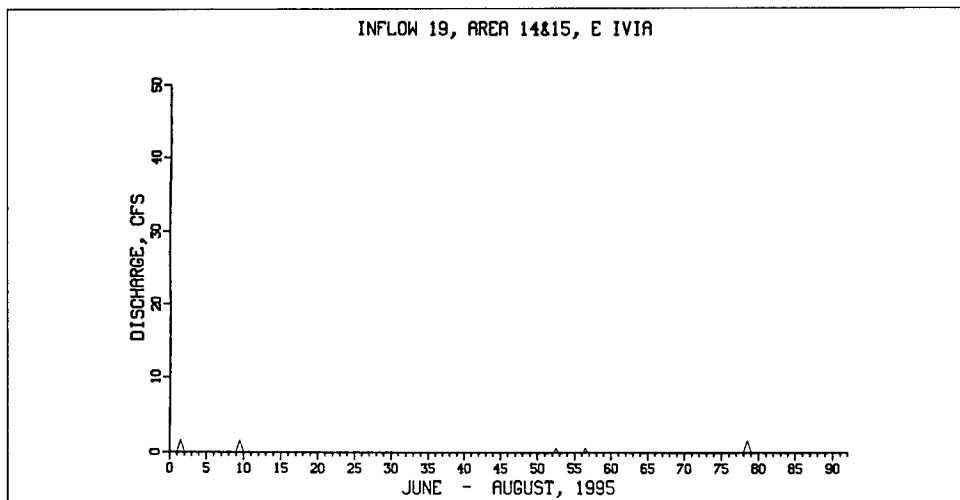


o. Inflow 16

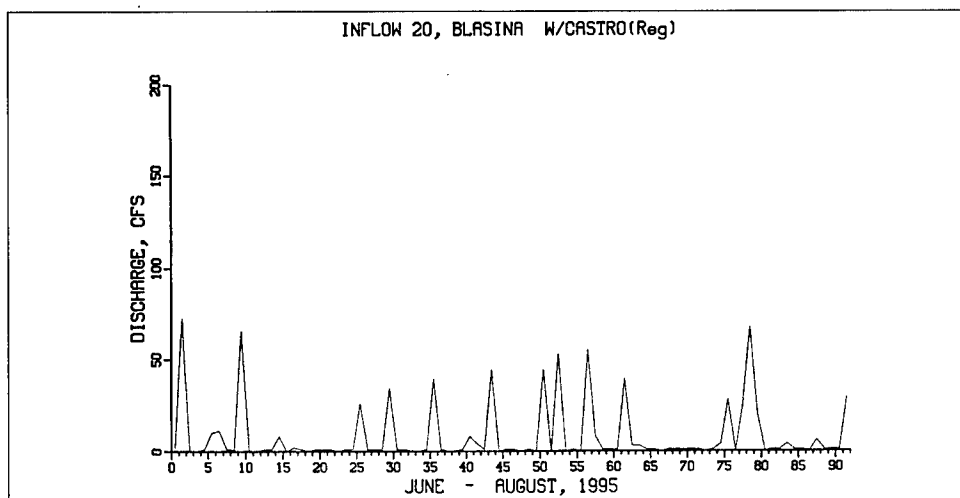
Figure 3-3. Continued



p. Inflow 18

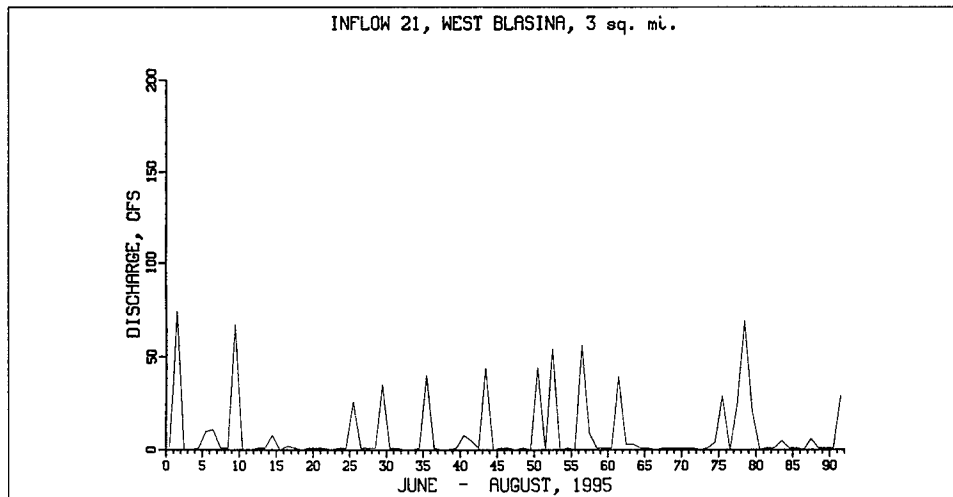


q. Inflow 19

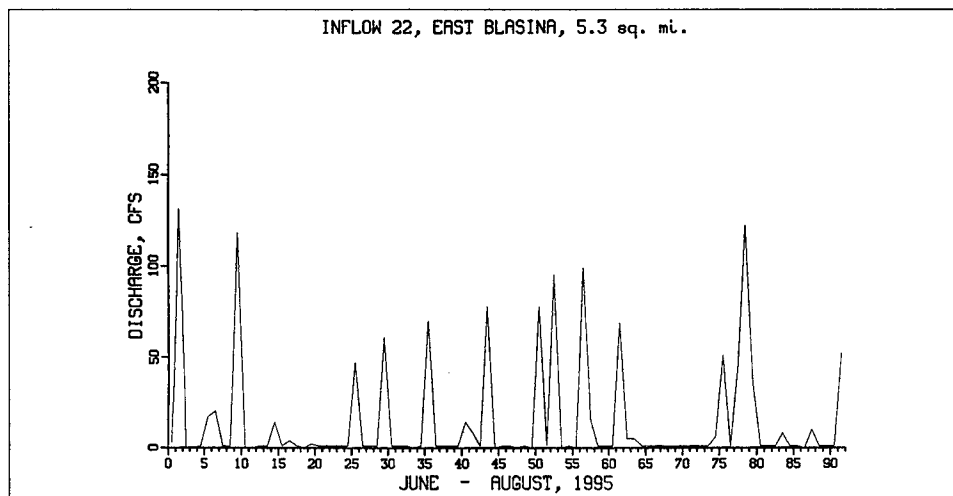


r. Inflow 20

Figure 3-3. Continued



s. Inflow 21



t. Inflow 22

Figure 3-3. Concluded

wind effects. An example of the water-surface elevations computed by ADCIRC and used in the CH3D-WES simulation is given in Figure 3-6.

The vertical distribution of salinity along the open ocean grid was specified from data collected by Fagerburg (1998). Since the temperature was specified as a constant, temperatures were not required to be specified along the ocean boundary of the grid. During flood, the specified values of salinity are employed, whereas during ebb, interior values are advected out of the grid. Along a solid boundary, the normal component of the velocity and the viscosity and diffusivity are set to zero.

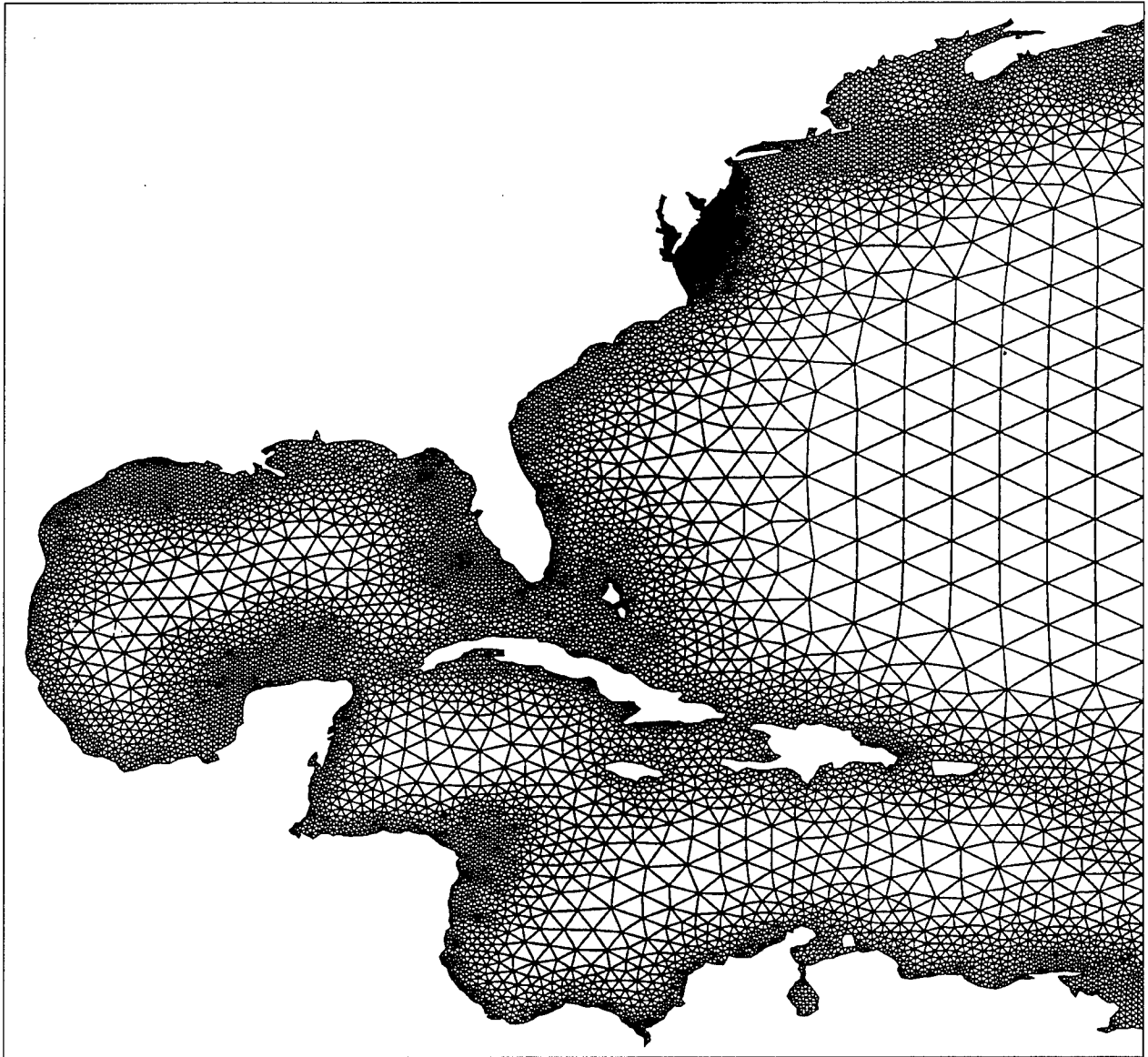


Figure 3-4. ADCIRC numerical grid

Initial Conditions

At the start of a model run, the values of ζ , \bar{u} , \bar{v} , w , \bar{U} , and \bar{V} are all set to zero. Values of the salinity and temperature are read from input files. These initial fields are generated from known data at a limited number of locations. Once the values in individual cells are determined by interpolating from the field data, the resulting 3-D field is smoothed several times. Generally, the salinity and temperature fields are frozen for the first few days of a simulation.

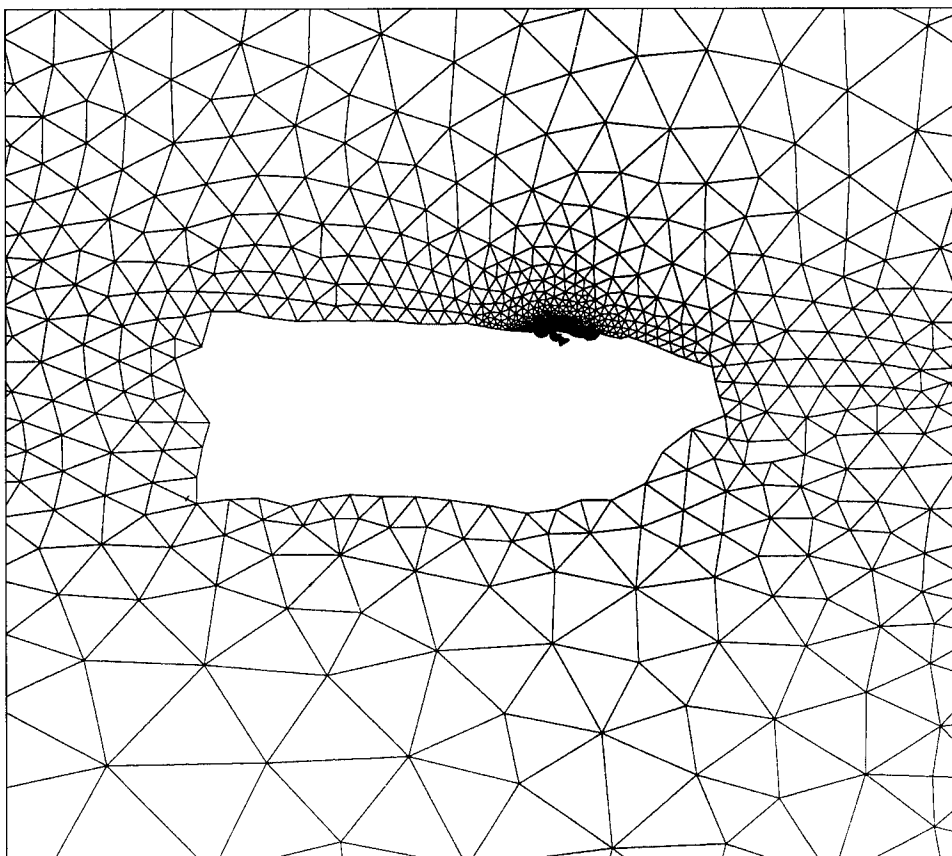


Figure 3-5. ADCIRC grid near Puerto Rico

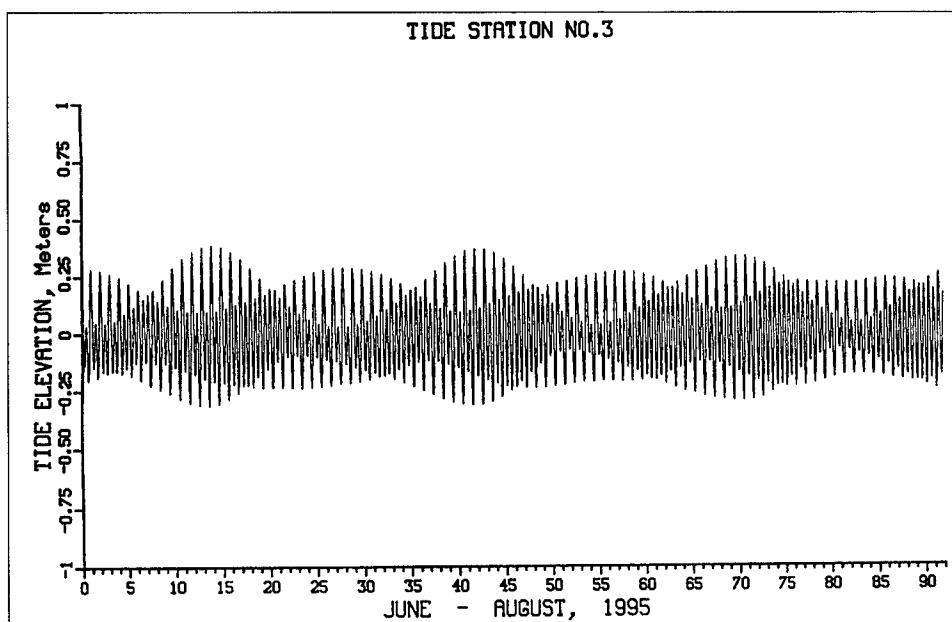


Figure 3-6. Tide computed by ADCIRC and applied on ocean boundary

Numerical Grid

The first step in any numerical modeling study is the generation of a suitable grid that captures the geometry of the modeled system. A map of the San Juan Bay Estuary system is shown in Figure 1-1 with the planform numerical boundary-fitted grid of the system illustrated in Figure 3-1. The numerical grid contains 2690 planform cells with a maximum of 30 vertical layers. Each layer is 3 ft (0.91 m) thick except for the top layer which varies with the tide. With much of the system being very shallow, many of the planform cells are represented by one layer. Thus, the computations involve a mixture of 3D as well as vertically averaged computations. With a total of 28,200 computational cells and a computational time step of 60 seconds, a 3-month simulation requires about 12 CPU hours on a 400 Mhz DEC Alpha work station.

4 Water Quality Model Formulation

Introduction

Kinetics for CE-QUAL-ICM were developed for application of the model to Chesapeake Bay (Cерco and Cole 1994). Model formulations are robust, however, and widely applicable. The model can be configured for specific applications by enabling various user-specified options. The description of the kinetics provided here is for the model as applied to the SJBE system. Descriptions of the complete kinetics are provided by Cerco and Cole (1994, 1995).

The central issues in eutrophication modeling are primary production of carbon by algae and concentration of dissolved oxygen. Primary production provides the energy required by the ecosystem to function. Excessive primary production is detrimental, however, since its decomposition, in the water and sediments, consumes oxygen. Dissolved oxygen is necessary to support the life functions of higher organisms and is considered an indicator of the "health" of estuarine systems. In order to predict primary production and dissolved oxygen, a large suite of model state variables is necessary (Table 4-1).

Table 4-1.
Water Quality Model State Variables

Temperature	Salinity
Fecal Coliform Bacteria	Algae
Dissolved Organic Carbon	Labile Particulate Organic Carbon
Refractory Particulate Organic Carbon	Ammonium
Nitrate	Dissolved Organic Nitrogen
Labile Particulate Organic Nitrogen	Refractory Particulate Organic Nitrogen
Total Phosphorus	Dissolved Organic Phosphorus
Labile Particulate Organic Phosphorus	Refractory Particulate Organic Phosphorus
Chemical Oxygen Demand	Dissolved Oxygen

Eutrophication, however, is not the only problem in the San Juan Estuary. Contamination with human and animal waste is also an issue. Consequently, fecal coliform bacteria were added to the suite of eutrophication variables.

Temperature

In some systems, temperature can be a primary determinant of the rate of biochemical reactions. Reaction rates increase as a function of temperature although extreme temperatures result in the mortality of organisms.

Salinity

Salinity is a conservative tracer that provides verification of the transport component of the model and facilitates examination of conservation of mass. Salinity also influences the dissolved oxygen saturation concentration and is used in the determination of kinetics constants that differ in saline and fresh water.

Fecal Coliform Bacteria

Fecal coliform bacteria are commonly found in human and animal waste. Although these organisms are harmless, they indicate waters are contaminated by waste matter.

Algae

Algae are represented in San Juan Estuary as a single group and quantified as carbonaceous biomass. Chlorophyll concentrations, for comparison with observations, are obtained through division of computed biomass by the carbon-to-chlorophyll ratio.

Organic Carbon

Three organic carbon state variables are considered: dissolved, labile particulate, and refractory particulate. Labile and refractory distinctions are based upon the time scale of decomposition. Labile organic carbon decomposes on a time scale of days to weeks while refractory organic carbon requires more time. Labile organic carbon decomposes rapidly in the water column or the sediments. Refractory organic carbon decomposes slowly, primarily in the sediments, and may contribute to sediment oxygen demand years after deposition.

Phosphorus

As with carbon and nitrogen, organic phosphorus is considered in three states: dissolved, labile particulate, and refractory particulate. Only a single mineral form, total phosphate, is considered. Total phosphate exists as two states within the model ecosystem: dissolved phosphate and phosphate incorporated in algal cells. Equilibrium partition coefficients are used to distribute the total among the states.

Nitrogen

Nitrogen is first divided into organic and mineral fractions. Organic nitrogen state variables are: dissolved organic nitrogen, labile particulate organic nitrogen, and refractory particulate organic nitrogen. Two mineral nitrogen forms are considered: ammonium and nitrate. Both are utilized to fulfill algal nutrient requirements although ammonium is preferred from thermodynamic considerations. The primary reason for distinguishing the two is that ammonium is oxidized by nitrifying bacteria into nitrate. This oxidation can be a significant sink of oxygen in the water column and sediments. An intermediate in the complete oxidation of ammonium, nitrite, also exists. Nitrite concentrations are usually much less than nitrate and for modeling purposes nitrite is combined with nitrate. Hence the nitrate state variable actually represents the sum of nitrate plus nitrite.

Chemical Oxygen Demand

Chemical oxygen demand is the concentration of reduced substances that are oxidizable by inorganic means. The primary component of chemical oxygen demand is sulfide released from sediments. Oxidation of sulfide to sulfate may remove substantial quantities of dissolved oxygen from the water column.

Dissolved Oxygen

Dissolved oxygen is required for the existence of higher life forms. Oxygen availability determines the distribution of organisms and the flows of energy and nutrients in an ecosystem. Dissolved oxygen is a central component of the water-quality model.

Conservation of Mass Equation

The foundation of CE-QUAL-ICM is the solution to the three-dimensional mass-conservation equation for a control volume. The control-volume structure was selected to allow maximum flexibility in linkage of CE-QUAL-ICM to alternate hydrodynamic models. Control

volumes in CE-QUAL-ICM correspond to cells in x-y-z space on the CH3D grid. CE-QUAL-ICM solves, for each volume and for each state variable, the conservation of mass equation:

$$\frac{\delta V_i C_i}{\delta t} = \sum_{j=1}^n Q_j C_j^* + \sum_{j=1}^n A_j D_j \frac{\delta C}{\delta x_j} + \sum S_i \quad (4.1)$$

where

- V_i = volume of ith control volume (m^3)
- C_i = concentration in ith control volume ($gm\ m^{-3}$)
- Q_j = volumetric flow across flow face j of ith control volume ($m^3\ sec^{-1}$)
- C_j^* = concentration in flow across flow face j ($gm\ m^{-3}$)
- A_j = area of flow face j (m^2)
- D_j = diffusion coefficient at flow face j ($m^2\ sec^{-1}$)
- n = number of flow faces attached to ith control volume
- S_i = external loads and kinetic sources and sinks in ith control volume ($gm\ sec^{-1}$)
- t, x = temporal and spatial coordinates

Solution to the mass-conservation equation is via the finite-difference method using the QUICKEST algorithm (Leonard 1979) in the horizontal directions and a Crank-Nicolson scheme in the vertical direction.

The majority of this chapter details with the kinetics portion of the mass-conservation equation for each state variable. Parameters are defined where they first appear. All parameters are listed, in alphabetical order, in a glossary (see Table 4-2). For consistency with reported rate coefficients, kinetics are detailed using a temporal dimension of days. Within the CE-QUAL-ICM code, kinetics sources and sinks are converted to a dimension of seconds before employment in the mass-conservation equation.

Algae

Algae play a central role in the carbon and nutrient cycles that comprise the model ecosystem. Sources and sinks of algae are:

- Growth (production)
- Basal metabolism
- Predation
- Settling

The governing equation for algal biomass is:

$$\frac{\delta}{\delta t} B = \left(P - BM - PR - W Sa \frac{\delta}{\delta z} \right) B \quad (4.2)$$

where

B = algal biomass, expressed as carbon (gm C m⁻³)

P = production (day⁻¹)

BM = basal metabolism (day⁻¹)

PR = predation (day⁻¹)

WSa = settling velocity (m day⁻¹)

z = vertical coordinate (m)

Production

Production by phytoplankton is determined by the availability of nutrients, by the intensity of light, and by the ambient temperature. The effects of each are considered to be multiplicative:

$$P = PM f(N)f(I)f(T) \quad (4.3)$$

where

PM = production under optimal conditions (day⁻¹)

f(N) = effect of suboptimal nutrient concentration ($0 \leq f \leq 1$)

f(I) = effect of suboptimal illumination ($0 \leq f \leq 1$)

f(T) = effect of suboptimal temperature ($0 \leq f \leq 1$)

Nutrients

Carbon, nitrogen, and phosphorus are the primary nutrients required for algal growth. Inorganic carbon is usually available in excess and is not considered in the model. The effects of the remaining nutrients on growth are described by the formulation commonly referred to as "Monod kinetics" (Monod 1949). In the Monod formulation (Figure 4-1) growth is dependent upon nutrient availability at low nutrient concentrations but is independent of nutrients at high concentrations. A key parameter in the formulation is the "half-saturation concentration." Growth rate is half the maximum when available nutrient concentration equals the half-saturation concentration. Liebig's "law of the minimum" (Odum 1971) indicates growth is determined by the nutrient in least supply:

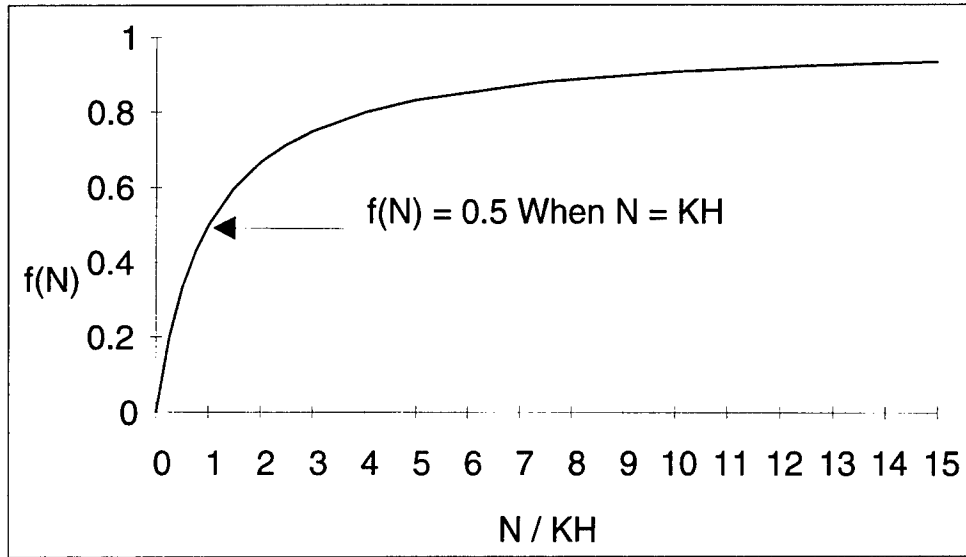


Figure 4-1. The Monod formulation for nutrient-limited growth

$$f(N) = \text{minimum} \left(\frac{NH_4 + NO_3}{KHn + NH_4 + NO_3}, \frac{PO_4d}{KHp + PO_4d} \right) \quad (4.4)$$

where

NH_4 = ammonium concentration (gm N m^{-3})

NO_3 = nitrate concentration (gm N m^{-3})

KHn = half-saturation constant for nitrogen uptake (gm N m^{-3})

PO_4d = dissolved phosphate concentration (gm P m^{-3})

KHp = half-saturation constant for phosphorus uptake (gm P m^{-3})

Light

Algal production increases as a function of light intensity until an optimal intensity is reached. Numerous options are available for a function which represents the increase of production as a function of light intensity. The function employed here is analogous to the Monod function used to compute nutrient limitations:

$$f(I) = \frac{I}{Ih + I} \quad (4.5)$$

where

I = illumination rate (Langley's day^{-1})

Ih = half-saturation illumination (Langley's day^{-1})

Equation 4.5 describes the instantaneous light limitation at a point in space. The model, however, computes processes integrated over discrete time intervals and aggregated spatially into model segments. Therefore, the equation must be integrated over an appropriate time interval and averaged over the thickness of each model segment. The integration interval selected is one day. This interval does not preclude computation steps less than a day but frees the model from accounting for illumination in "real time." Daily averaging does preclude computation of diurnal fluctuations in algal production. This restriction is not severe, however, since the classic equations for algal growth are not appropriate for short time scales.

Assuming light intensity declines exponentially with depth, the integrated, averaged form of Equation 4.5 is:

$$f(I) = \frac{FD}{K_{ess}\Delta z} \ln \left(\frac{I_h + I_o e^{-K_{ess} z_1}}{I_h + I_o e^{-K_{ess} z_2}} \right) \quad (4.6)$$

where

I_o = daily illumination at water surface (Langley's day⁻¹)

FD = fractional daylength ($0 \leq FD \leq 1$)

K_{ess} = total light attenuation coefficient (m⁻¹)

Δz = model segment thickness (m)

z_1 = distance from water surface to top of model segment (m)

z_2 = distance from water surface to bottom of model segment (m)

Light attenuation in the water column is composed of two fractions: a background value dependent on water color and concentration of suspended particles, and extinction due to light absorption by ambient chlorophyll:

$$K_{ess} = K_{eb} + K_{chl} \frac{B}{CChl} \quad (4.7)$$

where

K_{eb} = background light attenuation (m⁻¹)

K_{chl} = light attenuation coefficient for chlorophyll 'a' (m² mg⁻¹)

$CChl$ = algal carbon-to-chlorophyll ratio (gm C mg⁻¹ chl)

Temperature

Algal production increases as a function of temperature until an optimum temperature or temperature range is reached. Above the optimum, production declines until a temperature lethal to the organisms is attained. Numerous functional representations of temperature effects are available. Inspection of growth versus temperature curves indicates a function similar to a Gaussian probability curve. (Figure 4-2 provides a good fit to observations.)

$$\begin{aligned} f(T) &= e^{-KTg1(T-Tm)^2} \text{ when } T \leq Tm \\ &= e^{-KTg2(Tm-T)^2} \text{ when } T > Tm \end{aligned} \quad (4.8)$$

where

T = temperature ($^{\circ}\text{C}$)

Tm = optimal temperature for algal growth ($^{\circ}\text{C}$)

$KTg1$ = effect of temperature below Tm on growth ($^{\circ}\text{C}^{-2}$)

$KTg2$ = effect of temperature above Tm on growth ($^{\circ}\text{C}^{-2}$)

Basal Metabolism

As employed here, basal metabolism is the sum of all internal processes that decrease algal biomass. A portion of metabolism is respiration which may be viewed as a reversal of production. In respiration, carbon and nutrients are returned to the environment accompanied by the consumption of dissolved oxygen. A second internal sink of biomass is the excretion of dissolved organic carbon.

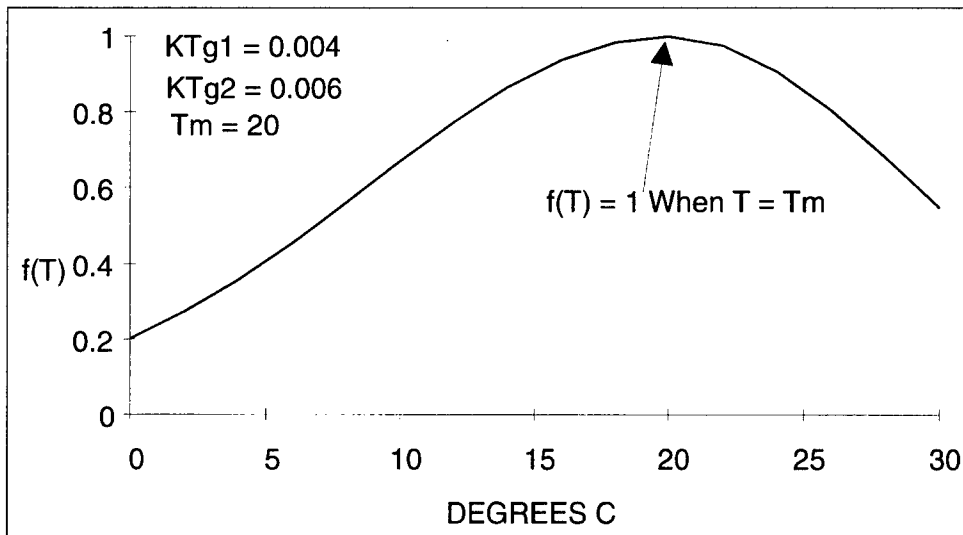


Figure 4-2. Effect of temperature on algal production

Respiration cannot proceed in the absence of oxygen. Basal metabolism cannot decrease in proportion to oxygen availability, however, or algae would approach immortality under anoxic conditions. To solve this dilemma, basal metabolism is considered to be independent of dissolved oxygen concentration but the distribution of metabolism between respiration and excretion is oxygen-dependent. When oxygen is freely available, respiration is a large fraction of the total. When oxygen is restricted, excretion becomes dominant. Formulation of this process is detailed in the following text that describes algal effects on carbon and dissolved oxygen.

Basal metabolism is commonly considered to be an exponentially increasing (Figure 4-3) function of temperature:

$$BM = BMr e^{KTb(T-Tr)} \quad (4.9)$$

where

BMr = metabolic rate at Tr (day^{-1})

KTb = effect of temperature on metabolism ($^{\circ}\text{C}^{-1}$)

Tr = reference temperature for metabolism ($^{\circ}\text{C}$)

Predation

Detailed specification of predation within the water column requires predictive modeling of zooplankton biomass and activity. Absence of data prohibited the modeling of zooplankton in the San Juan Estuary. Consequently, a constant predation rate was specified. This specification implicitly assumed zooplankton biomass is a constant fraction of algal biomass. Zooplankton activity was assumed to be influenced by temperature. The temperature effect was represented by an exponential relationship

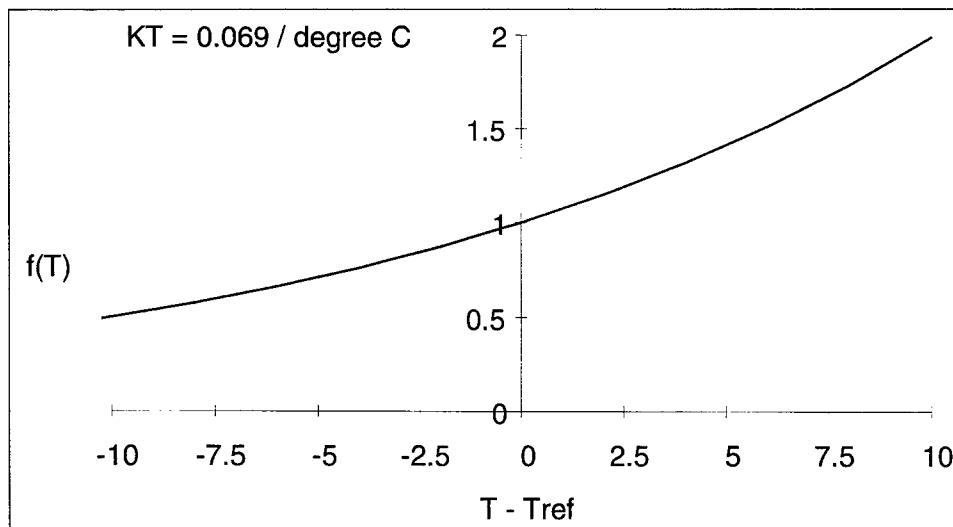


Figure 4-3. Exponential temperature function

(Figure 4-3). The predation formulation is identical to basal metabolism. The difference in predation and basal metabolism lies in the distribution of the end products of these processes.

$$PR = BPR e^{KTb(T-Tr)} \quad (4.10)$$

where

$$BPR = \text{predation rate at } Tr \text{ (day}^{-1}\text{)}$$

Macrobenthic Grazing

A second form of predation on algae is grazing by filter-feeding organisms which inhabit the sediment-water interface. As with zooplankton, detailed specification of predation by macrobenthos requires predictive modeling of macrobenthic activity and biomass. In the absence of a benthos model, a formulation was specified which converted macrobenthic grazing into an equivalent settling rate:

$$WSmb = MBGM FR \frac{DO}{KHomb + DO} \quad (4.11)$$

where

$$WSmb = \text{equivalent settling rate (m day}^{-1}\text{)}$$

$$MBGM = \text{macrobenthic biomass (gm C m}^{-2}\text{)}$$

$$FR = \text{filtering rate (m}^{-3} \text{ gm}^{-1} \text{ C day}^{-1}\text{)}$$

$$DO = \text{dissolved oxygen concentration (gm DO m}^{-3}\text{)}$$

$$KHomb = \text{dissolved oxygen concentration at which macrobenthic grazing is halved (gm DO m}^{-3}\text{)}$$

Macrobenthic grazing is implemented only in the model cells which interface with the bottom. Biomass is specified based on the observed distribution of benthos in the system. Incorporation of dissolved oxygen into the relationship accounts for the cessation of filtering and eventual demise of benthos under anoxic conditions. Algal biomass filtered from the water column is routed into the sediment diagenesis portion of the model package.

Effect of Algae on Organic Carbon

During production and respiration, algae primarily take up and produce carbon dioxide, an inorganic form not considered in the model. A small fraction of basal metabolism is exuded as dissolved organic carbon, however, and in the model this fraction increases as dissolved oxygen becomes scarce. Algae also produce organic carbon through the effects of predation. Zooplankton take up and redistribute algal carbon through grazing, assimilation, respiration, and excretion. Since zooplankton are not included in the model, routing of algal carbon through zooplankton is simulated by empirical distribution coefficients. The effects of algae on organic carbon are expressed:

$$\frac{\delta}{\delta t} DOC = \quad (4.12)$$

$$\left[FCD + (1 - FCD) \left(\frac{KHr}{KHr + DO} \right) BM + FCDP PR \right]$$

$$\frac{\delta}{\delta t} LPOC = FCLP PR B \quad (4.13)$$

$$\frac{\delta}{\delta t} RPOC = FCRP PR B \quad (4.14)$$

where

DOC = dissolved organic carbon concentration (gm C m⁻³)

DO = dissolved oxygen concentration (gm O₂ m⁻³)

LPOC = labile particulate organic carbon concentration (gm C m⁻³)

RPOC = refractory particulate organic carbon concentration (gm C m⁻³)

FCD = fraction of basal metabolism exuded as dissolved organic carbon

KHr = half-saturation concentration for algal dissolved organic carbon excretion (gm O₂ m⁻³)

FCDP = fraction of dissolved organic carbon produced by predation

FCLP = fraction of labile particulate carbon produced by predation

FCRP = fraction of refractory particulate carbon produced by predation

The sum of the three predation fractions must equal unity.

Effect of Algae on Phosphorus

Algae take up dissolved phosphate during production and release dissolved phosphate and organic phosphorus through mortality. As with carbon, the fate of algal phosphorus released by metabolism and predation is represented by distribution coefficients. Since the total phosphate state variable includes both intra- and extracellular phosphate, no explicit representation of the effect of algae on phosphate is necessary. Distribution of total phosphate is determined by partition coefficients as detailed in the Phosphorus section of this chapter. The equations that express the effects of algae on organic phosphorus are:

$$\frac{\delta}{\delta t} DOP = (BM FPD + PR FPD) APC B \quad (4.15)$$

$$\frac{\delta}{\delta t} LPOP = (BM FPL + PR FPL) APC B \quad (4.16)$$

$$\frac{\delta}{\delta t} RPOP = (BM FPR + PR FPR) APC B \quad (4.17)$$

where

DOP = dissolved organic phosphorus concentration (gm P m^{-3})

LPOP = labile particulate organic phosphorus concentration
(gm P m^{-3})

RPOP = refractory particulate organic phosphorus concentration
(gm P m^{-3})

APC = phosphorus-to-carbon ratio of all algal groups ($\text{gm P gm}^{-1} \text{C}$)

FPD = fraction of dissolved organic phosphorus produced by
metabolism

FPL = fraction of labile particulate phosphorus produced by
metabolism

FPR = fraction of refractory particulate phosphorus produced by
metabolism

FPDP = fraction of dissolved organic phosphorus produced by
predation

FPLP = fraction of labile particulate phosphorus produced by
predation

FPRP = fraction of refractory particulate phosphorus produced by
predation

The sums of the metabolism and respiration fractions must each be less than or equal to unity.

Effect of Algae on Nitrogen

Algae take up ammonium and nitrate during production and release ammonium and organic nitrogen through mortality. Nitrate is internally reduced to ammonium before synthesis into biomass occurs (Parsons et al. 1984). Trace concentrations of ammonium inhibit nitrate reduction so that, in the presence of ammonium and nitrate, ammonium is utilized first. The "preference" of algae for ammonium can be expressed empirically (Thomann and Fitzpatrick 1982):

$$PN = NH_4 \frac{NO_3}{(KHn + NH_4)(KHn + NO_3)} + NH_4 \frac{KHn}{(NH_4 + NO_3)(KHn + NO_3)} \quad (4.18)$$

where

PN = algal preference for ammonium uptake ($0 \leq PN \leq 1$)

The ammonium preference function (Figure 4-4) has two limiting values. When nitrate is absent, the preference for ammonium is unity. When ammonium is absent, the preference is zero. In the presence of ammonium and nitrate, the preference depends on the abundance of both forms relative to the half-saturation constant for nitrogen uptake. When both ammonium and nitrate are abundant, the preference for ammonium approaches unity. When ammonium is scarce but nitrate is abundant, the preference decreases in magnitude and a significant fraction of algal nitrogen requirement comes from nitrate.

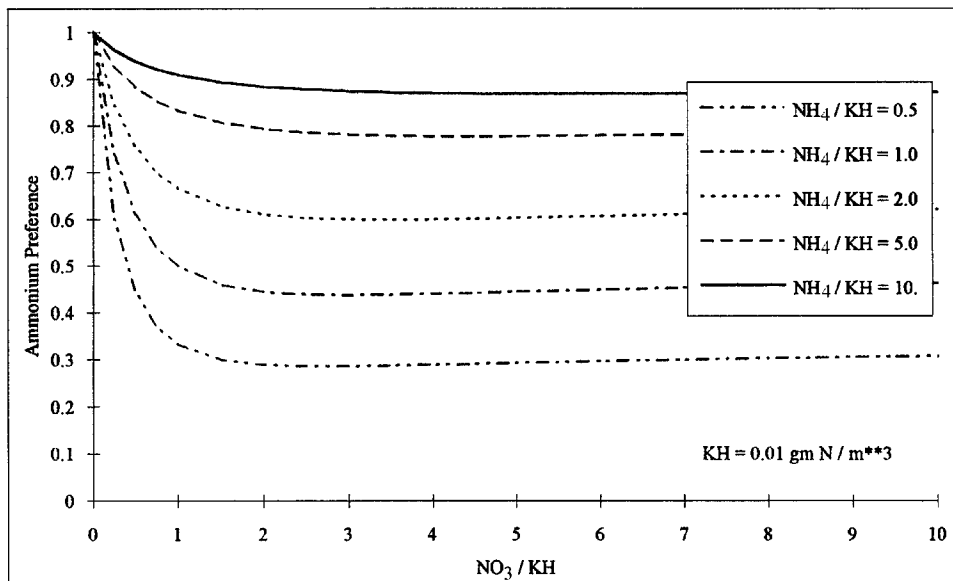


Figure 4-4. The ammonium preference function

The fate of algal nitrogen released by metabolism and predation is represented by distribution coefficients. The effects of algae on the nitrogen state variables are expressed:

$$\frac{\delta}{\delta t} NH_4 = (BM FNI + PR FNIP - PN P) ANC B \quad (4.19)$$

$$\frac{\delta}{\delta t} NO_3 = (PN - 1)P ANC B \quad (4.20)$$

$$\frac{\delta}{\delta t} DON = (BM FND + PR FNDP) ANC B \quad (4.21)$$

$$\frac{\delta}{\delta t} LPON = (BM FNL + PR FNLP) ANC B \quad (4.22)$$

$$\frac{\delta}{\delta t} RPON = (BM FNR + PR FNRP) ANC B \quad (4.23)$$

where

DON = dissolved organic nitrogen concentration ($gm\ N\ m^{-3}$)

LPON = labile particulate organic nitrogen concentration ($gm\ N\ m^{-3}$)

RPON = refractory particulate organic nitrogen concentration
($gm\ N\ m^{-3}$)

ANC = nitrogen-to-carbon ratio of algae ($gm\ N\ gm^{-1}\ C$)

FNI = fraction of inorganic nitrogen produced by metabolism

FND = fraction of dissolved organic nitrogen produced by
metabolism

FNL = fraction of labile particulate nitrogen produced by
metabolism

FNR = fraction of refractory particulate nitrogen produced by
metabolism

FNIP = fraction of inorganic nitrogen produced by predation

FNDP = fraction of dissolved organic nitrogen produced by predation

FNLP = fraction of labile particulate nitrogen produced by predation

FNRP = fraction of refractory particulate nitrogen produced by
predation

The sums of the metabolism fractions and the predation fractions must each equal unity.

Algal Stoichiometry

Algal biomass is quantified in units of carbon. In order to express the effects of algae on nitrogen and phosphorus, the ratios of nitrogen-to-carbon and phosphorus-to-carbon in algal biomass must be specified. Global mean values of these ratios are well known (Redfield et al. 1966). Algal composition varies, however, especially as a function of nutrient availability. As nitrogen and phosphorus become scarce, algae adjust their composition so that smaller quantities of these vital nutrients are required to produce carbonaceous biomass (Droop 1973; DiToro 1980; Parsons et al. 1984).

Observations from upper Chesapeake Bay were examined to assess the potential variability of algal stoichiometry. Data employed were collected by the Maryland Department of the Environment from June 1985 to December 1987. This subset of the monitoring database was selected since it contained direct laboratory analysis of particulate nutrients. Examination was restricted to surface (≤ 2 m) data to maximize the fraction of algae in the particulate analyses. The ratio of particulate carbon-to-nitrogen was plotted as a function of ammonium plus nitrate concentration (Figure 4-5). The ratio of particulate carbon-to-phosphorus was plotted as a function of dissolved phosphate concentration (Figure 4-6). (These ratios were plotted to correspond to conventional reporting of algal composition. Their inverses are used in the model.) The variation of carbon-to-nitrogen stoichiometry in the upper Bay was small. No altered composition as a function of diminished nutrient availability was evident. As a consequence of these observations, the model formulation specified constant algal nitrogen-to-carbon ratio, ANC. Large variations in carbon-to-phosphorus ratio occurred, however. The carbon-to-phosphorus ratio in seston more than doubled as dissolved phosphate concentration diminished. To account for this effect, a variable algal phosphorus-to-carbon ratio, APC, was specified in the model.

Calculation of APC requires specification of three parameters:

- APCmin = minimum phosphorus-to-carbon ratio ($\text{gm P gm}^{-1} \text{C}$);
- APCmax = maximum phosphorus-to-carbon ratio ($\text{gm P gm}^{-1} \text{C}$);
and
- PO₄dmax = dissolved phosphate concentration at which algal phosphorus-to-carbon ratio achieves its maximum value (gm P m^{-3}).

The minimum phosphorus-to-carbon ratio is assumed to occur when dissolved phosphate is zero. The ratio increases linearly from the minimum to the maximum which occurs when dissolved phosphate equals PO₄dmax:

$$APC = APC_{\min} + \frac{APC_{\max} - APC_{\min}}{PO_4 d_{\max}} PO_4 d \quad (4.24)$$

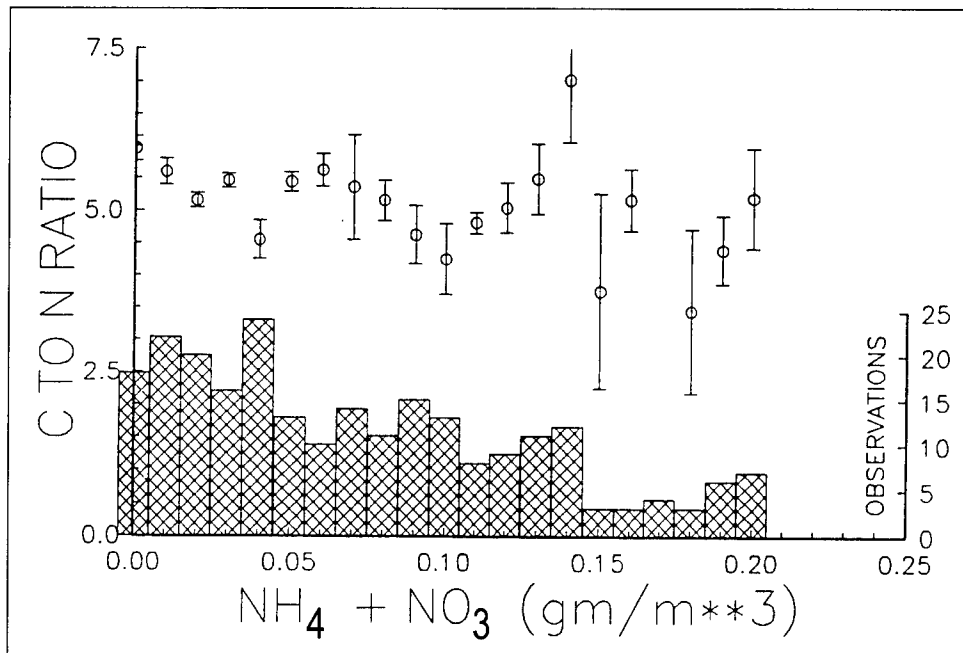


Figure 4-5. Carbon-to-nitrogen ratio (mean and standard error) of seston in upper Chesapeake Bay. Bars show number of observations

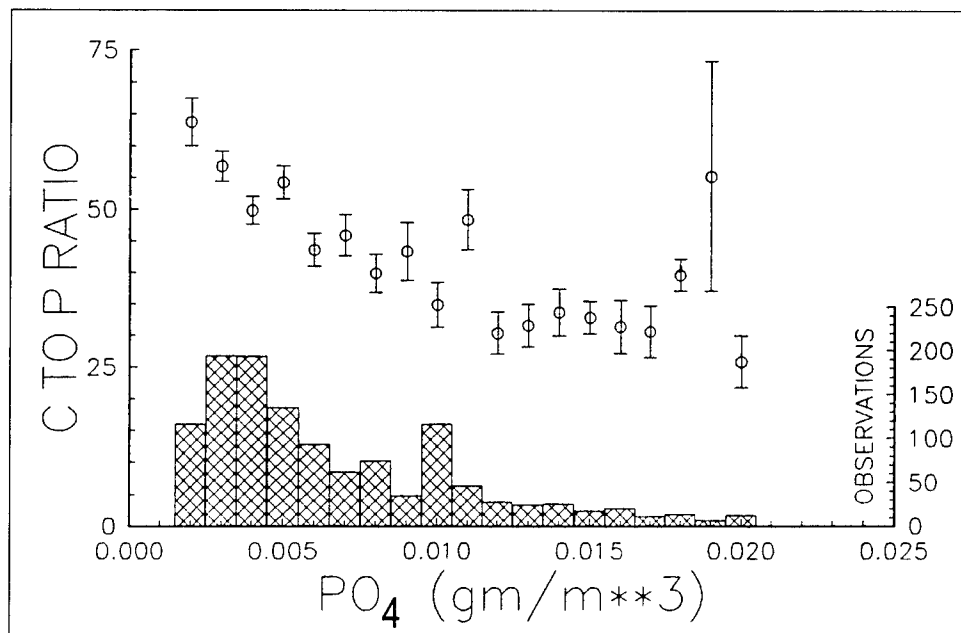


Figure 4-6. Carbon-to-phosphorus ratio (mean and standard error) of seston in upper Chesapeake Bay. Bars show number of observations

where

$$\text{APC} = \text{algal phosphorus-to-carbon ratio (gm P gm}^{-1}\text{ C)}$$

When dissolved phosphate exceeds $\text{PO}_4 \text{dmax}$, APC is held at its maximum value (Figure 4-7).

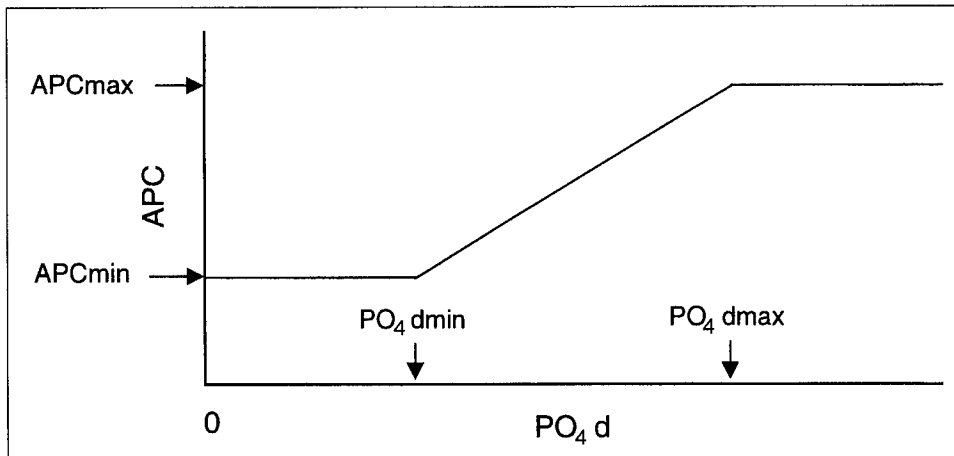
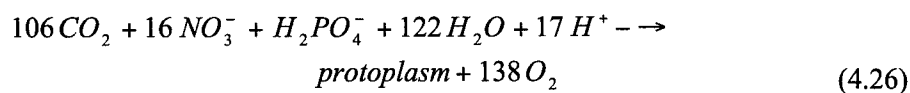
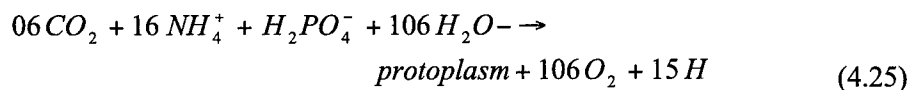


Figure 4-7. Model algal phosphorus-to-carbon ratio

Effect of Algae on Dissolved Oxygen

Algae produce oxygen during photosynthesis and consume oxygen through respiration. The quantity produced depends on the form of nitrogen utilized for growth. More oxygen is produced, per unit of carbon fixed, when nitrate is the algal nitrogen source than when ammonium is the source. Equations describing algal uptake of carbon and nitrogen and production of dissolved oxygen (Morel 1983) are:



When ammonium is the nitrogen source, one mole oxygen is produced per mole carbon dioxide fixed. When nitrate is the nitrogen source, 1.3 moles oxygen are produced per mole carbon dioxide fixed.

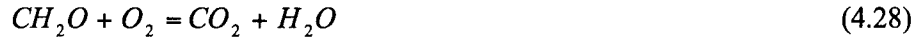
The equation that describes the effect of algae on dissolved oxygen in the model is:

$$\frac{\delta}{\delta t} DO = \left[(1.3 - 0.3 PN)P - (1 - FCD) \frac{DO}{KHr + DO} BM \right] AOCR B \quad (4.27)$$

where

AOCR = dissolved oxygen-to-carbon ratio in respiration
(2.67 gm O₂ gm⁻¹ C)

The magnitude of AOCR is derived from a simple representation of the respiration process:



The quantity (1.3 - 0.3 PN) is the photosynthesis ratio and expresses the molar quantity of oxygen produced per mole carbon fixed. The photosynthesis ratio approaches unity as the algal preference for ammonium approaches unity.

Organic Carbon

Organic carbon undergoes innumerable transformations in the water column. The model carbon cycle (Figure 4-8) consists of the following elements:

- Phytoplankton production
- Phytoplankton exudation
- Predation on phytoplankton
- Dissolution of particulate carbon
- Heterotrophic respiration
- Denitrification
- Settling

Algal production is the primary carbon source although carbon also enters the system through external loading. Predation on algae releases particulate and dissolved organic carbon to the water column. A fraction of the particulate organic carbon undergoes first-order dissolution to dissolved organic carbon. The remainder settles to the sediments. Dissolved organic carbon produced by phytoplankton exudation, by predation, and by dissolution is respired or denitrified at a first-order rate to inorganic carbon. No carbon is recycled from the sediments to the water column although oxygen demand created by carbon diagenesis is included in the model.

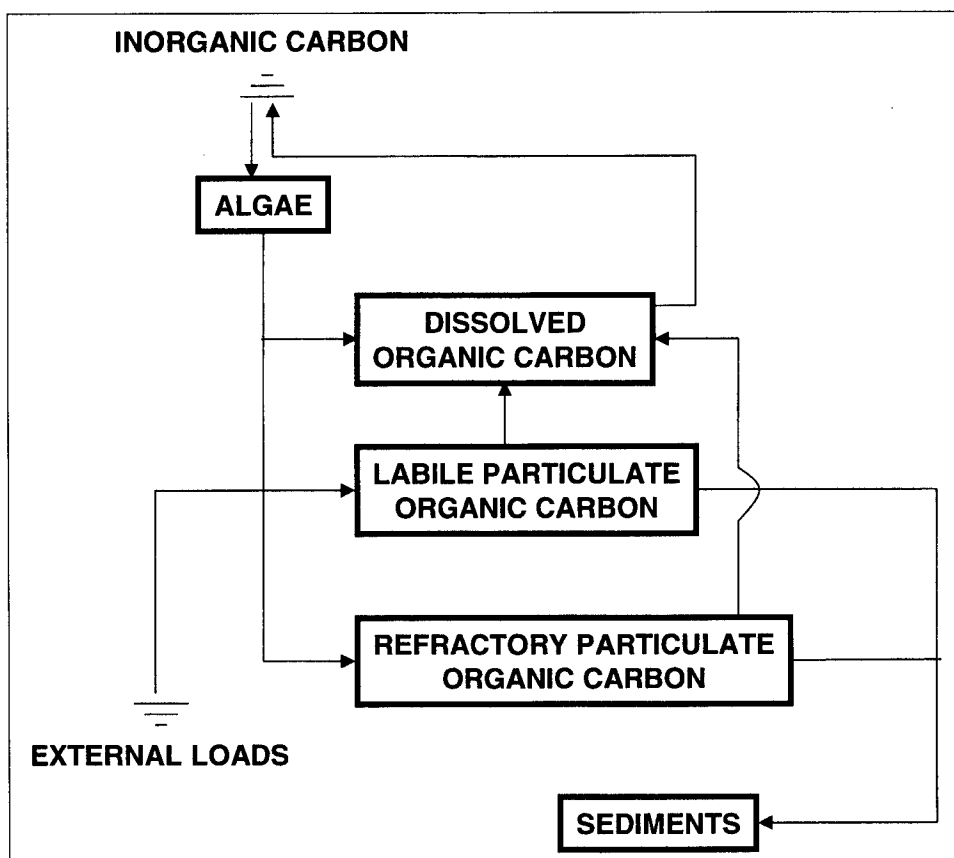


Figure 4-8. Model carbon cycle

Dissolution and Respiration Rates

Dissolution and respiration rates depend on the availability of carbonaceous substrate and on heterotrophic activity. Heterotrophic activity and biomass have been correlated with algal activity and biomass across a wide range of natural systems (Bird and Kalff 1984; Cole et al. 1988). Consequently, algal biomass can be incorporated into dissolution and respiration rate formulations as a surrogate for heterotrophic activity. The correlation between algae and heterotrophs occurs because algae produce labile carbon that fuels heterotrophic activity. Dissolution and respiration processes do not require the presence of algae, however, and may be fueled entirely by external carbon inputs. Representation of dissolution and respiration in the model allows specification of algal-dependent and algal-independent rates:

$$K_{doc} = K_{dc} + K_{dcalg} B \quad (4.29)$$

where

K_{doc} = respiration rate of dissolved organic carbon (day^{-1})

K_{dc} = minimum respiration rate (day^{-1})

K_{dcalg} = constant that relates respiration to algal biomass
($m^3 \text{ gm}^{-1} \text{ C day}^{-1}$)

$$K_{lpoc} = K_{lc} + K_{lcalg} B \quad (4.30)$$

where

K_{lpoc} = dissolution rate of labile particulate organic carbon (day^{-1})

K_{lc} = minimum dissolution rate (day^{-1})

K_{lcalg} = constant that relates dissolution to algal biomass
($m^3 \text{ gm}^{-1} \text{ C day}^{-1}$)

$$K_{rpoc} = K_{rc} + K_{rcalg} B \quad (4.31)$$

where

K_{rpoc} = dissolution rate of refractory particulate organic carbon
(day^{-1})

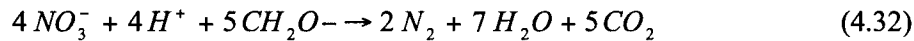
K_{rc} = minimum dissolution rate (day^{-1})

K_{rcalg} = constant that relates dissolution to algal biomass
($m^3 \text{ gm}^{-1} \text{ C day}^{-1}$)

An exponential function (Figure 4-3) relates dissolution and respiration to temperature.

Denitrification

As oxygen is depleted from natural systems, oxidation of organic matter is affected by the reduction of alternate oxidants (referred to as “alternate electron acceptors”). The sequence in which alternate acceptors are employed is determined by the thermodynamics of oxidation-reduction reactions. The first substance reduced in the absence of oxygen is nitrate. A representation of the denitrification reaction can be obtained by balancing standard half-cell redox reactions (Stumm and Morgan 1981):



Equation 4-32 describes the stoichiometry of the denitrification reaction. The kinetics of the reaction, represented in the model, are first-order. The dissolved organic carbon respiration rate, K_{doc} , is modified so that significant decay via denitrification occurs only when nitrate is freely available and dissolved oxygen is depleted (Figure 4-9). A parameter is included so that the anoxic respiration rate is slower than oxic respiration:

$$\text{Denit} = \frac{K_{Hodoc}}{K_{Hodoc} + \text{DO}} \frac{\text{NO}_3}{K_{Hndn} + \text{NO}_3} A_{\text{ANOX}} K_{doc} \quad (4.33)$$

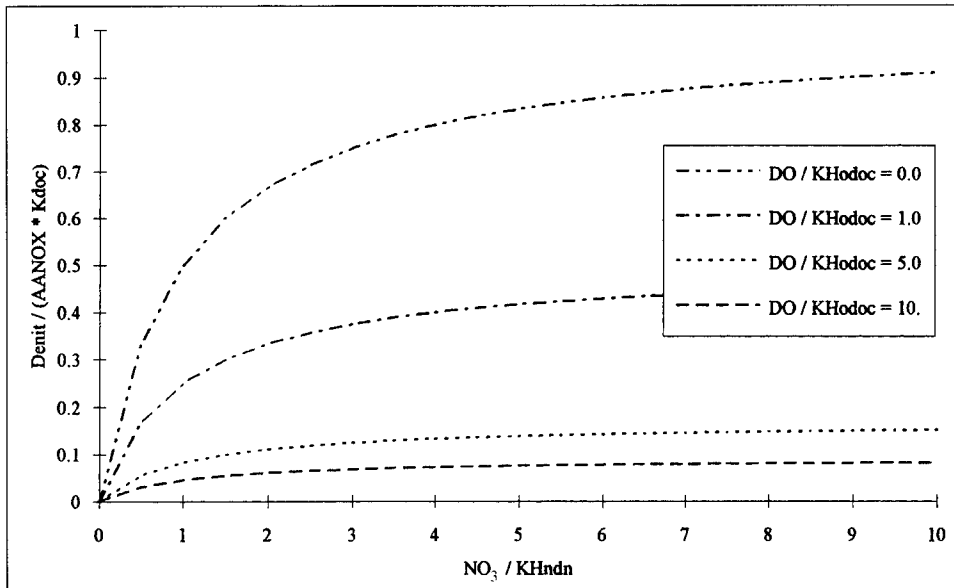


Figure 4-9. Effect of nitrate and dissolved oxygen on denitrification rate

where

Denit = denitrification rate of dissolved organic carbon (day^{-1})

AANOX = ratio of denitrification to oxic carbon respiration rate
($0 \leq \text{AANOX} \leq 1$)

KHodoc = half-saturation concentration of dissolved oxygen required
for oxic respiration ($\text{gm O}_2 \text{ m}^{-3}$)

KHdn = half-saturation concentration of nitrate required for
denitrification (gm N m^{-3})

An exponential function (Figure 4-3) relates denitrification to temperature. Parameter values in the function are the same as those for dissolved organic carbon respiration.

Dissolved Organic Carbon

The complete representation of all dissolved organic carbon sources and sinks in the model ecosystem is:

$$\begin{aligned} \frac{\delta}{\delta t} \text{DOC} = & \left(\text{FCD} + (1 - \text{FCD}) \frac{\text{Khr}}{\text{Khr} + \text{DO}} \text{BM} + \text{FCDP PR} \right) \text{B} \\ & + \text{Klpoc LPOC} + \text{Krpoc RPOC} - \frac{\text{DO}}{\text{KHodoc} + \text{DO}} \text{Kdoc DOC} \\ & - \text{Denit DOC} \end{aligned} \quad (4.34)$$

Labile Particulate Organic Carbon

The complete representation of all labile particulate organic carbon sources and sinks in the model ecosystem is:

$$\frac{\delta}{\delta t} LPOC = FCLP PR B - Klpoc LPOC - WSl \frac{\delta}{\delta z} LPOC \quad (4.35)$$

where

WSl = settling velocity of labile particles ($m \text{ day}^{-1}$)

Refractory Particulate Organic Carbon

The complete representation of all refractory particulate organic carbon sources and sinks in the model ecosystem is:

$$\frac{\delta}{\delta t} RPOC = FCRP PR B - Krpoc RPOC - Wsr \frac{\delta}{\delta z} RPOC \quad (4.36)$$

where

Wsr = settling velocity of refractory particles ($m \text{ day}^{-1}$)

Phosphorus

The model phosphorus cycle (Figure 4-10) includes the following processes:

- Algal production and metabolism
- Predation
- Hydrolysis of particulate organic phosphorus
- Mineralization of dissolved organic phosphorus
- Settling

External loads provide the ultimate source of phosphorus to the system. Dissolved phosphate is incorporated by algae during growth and released as phosphate and organic phosphorus through respiration and predation. A portion of the particulate organic phosphorus hydrolyzes to dissolved organic phosphorus. The balance settles to the sediments. Dissolved organic phosphorus is mineralized to phosphate. Within the sediments, particulate phosphorus is mineralized and recycled to the water column as dissolved phosphate.

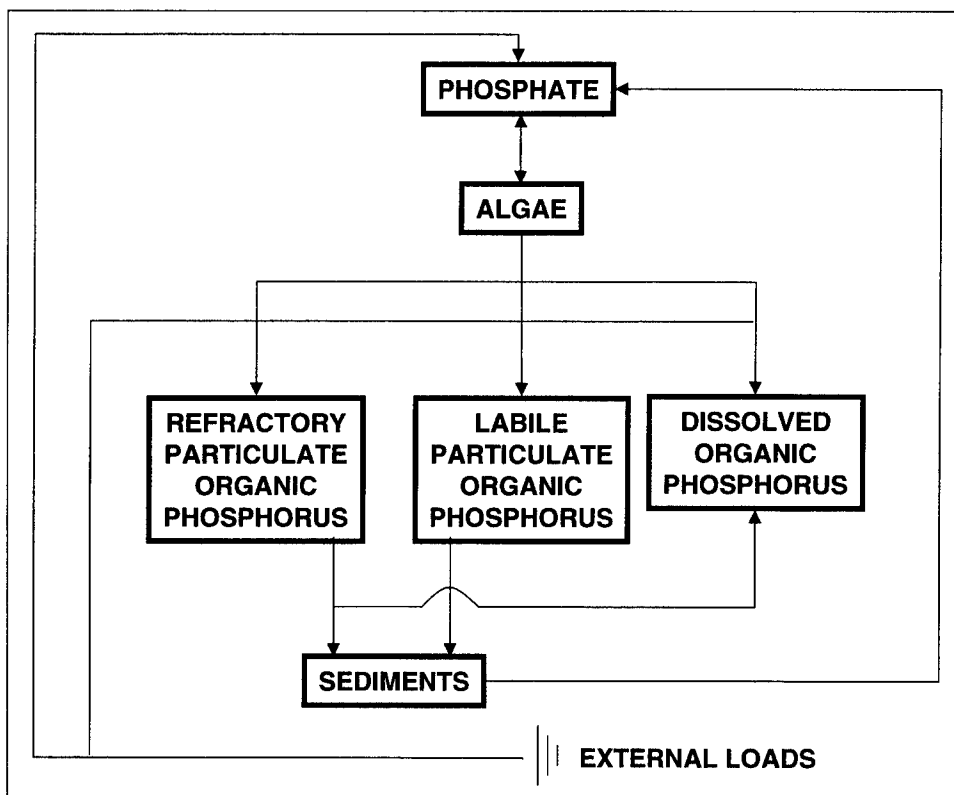


Figure 4-10. Model phosphorus cycle

Effects on phosphorus of algal production, metabolism, and predation have already been detailed. Descriptions of hydrolysis and mineralization and of the total phosphate system follow.

Hydrolysis and Mineralization

Within the model, hydrolysis is defined as the process by which particulate organic substances are converted to dissolved organic form. Mineralization is defined as the process by which dissolved organic substances are converted to dissolved inorganic form. Conversion of particulate organic phosphorus to phosphate proceeds through the sequence of hydrolysis and mineralization. Direct mineralization of particulate organic phosphorus does not occur.

Mineralization of organic phosphorus is mediated by the release of nucleotidase and phosphatase enzymes by bacteria (Ammerman and Azam 1985; Chrost and Overbeck 1987) and algae (Matavulj and Flint 1987; Chrost and Overbeck 1987; Boni et al. 1989). Since the algae themselves release the enzyme and since bacterial abundance is related to algal biomass, the rate of organic phosphorus mineralization is related, in the model, to algal biomass. A most remarkable property of the enzyme process is that alkaline phosphatase activity is inversely proportional to ambient phosphate concentration (Chrost and Overbeck 1987; Boni et al. 1989).

Put in different terms, when phosphate is scarce, algae stimulate production of an enzyme that mineralizes organic phosphorus to phosphate. This phenomenon is simulated by relating mineralization to the algal phosphorus nutrient limitation. Mineralization is highest when algae are strongly phosphorus limited and is least when no limitation occurs.

Expressions for mineralization and hydrolysis rates are:

$$K_{dop} = K_{dp} + \frac{K_{Hp}}{K_{Hp} + PO_4 d} K_{dpalg} B \quad (4.37)$$

where

K_{dop} = mineralization rate of dissolved organic phosphorus (day^{-1})

K_{dp} = minimum mineralization rate (day^{-1})

K_{dpalg} = constant that relates mineralization to algal biomass
($\text{m}^3 \text{gm}^{-1} \text{C day}^{-1}$)

$$K_{lpop} = K_{lp} + \frac{K_{Hp}}{K_{Hp} + PO_4 d} K_{lpalg} B \quad (4.38)$$

where

K_{lpop} = hydrolysis rate of labile particulate phosphorus (day^{-1})

K_{lp} = minimum hydrolysis rate (day^{-1})

K_{lpalg} = constant that relates hydrolysis to algal biomass
($\text{m}^3 \text{gm}^{-1} \text{C day}^{-1}$)

$$K_{rpop} = K_{rp} + \frac{K_{Hp}}{K_{Hp} + PO_4 d} K_{rpalg} B \quad (4.39)$$

where

K_{rpop} = hydrolysis rate of refractory particulate phosphorus (day^{-1})

K_{rp} = minimum hydrolysis rate (day^{-1})

K_{rpalg} = constant that relates hydrolysis to algal biomass
($\text{m}^3 \text{gm}^{-1} \text{C day}^{-1}$)

An exponential function (Figure 4-3) relates mineralization and hydrolysis rates to temperature.

Potential effects of algal biomass and nutrient limitation on mineralization and hydrolysis rates are shown in Figure 4-11. When nutrient concentration greatly exceeds the half-saturation concentration for algal uptake, the rate roughly equals the minimum. Algal biomass has little influence. As nutrient becomes scarce relative to the half-saturation concentration,

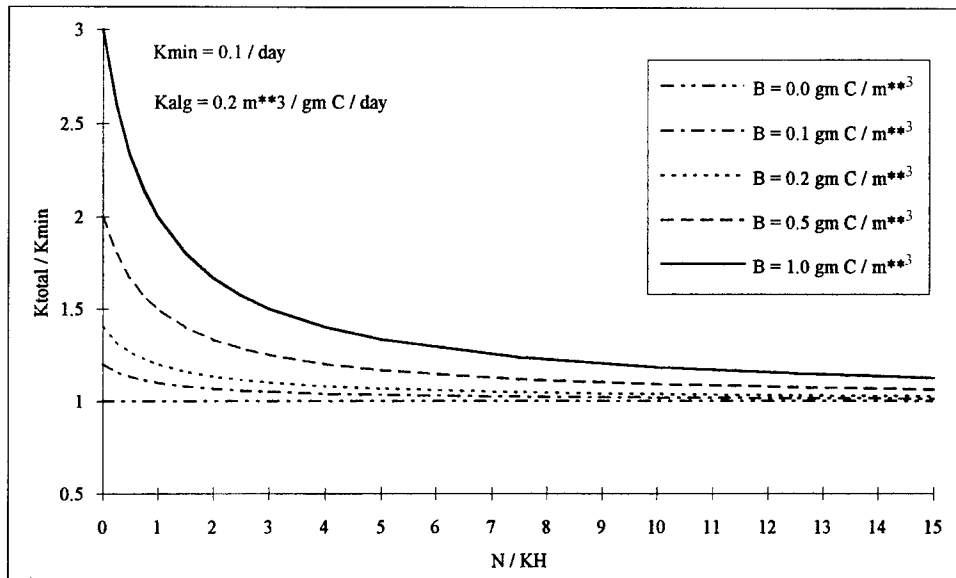


Figure 4-11. Effect of algal biomass and nutrient concentration on hydrolysis and mineralization

the rate increases. The magnitude of increase depends on algal biomass. Factor of two to three increases are feasible.

The Total Phosphate System

One fraction of total phosphorus in the water column is phosphorus incorporated in algal biomass. This fraction is computed in the model as the product of algal biomass and APC, the phosphorus-to-carbon ratio. In the environment, algae adjust their phosphorus content in response to external conditions. Algal phosphorus content is high when external phosphorus is abundant, and phosphorus content is low when phosphorus is scarce. The adaptation of algae to their environment indicates phosphorus-to-carbon ratio should be a variable in the model. Treatment of the ratio as a variable, however, greatly complicates computation of phosphorus transport due to the mixture of algal masses of different composition. The complication is avoided if intracellular and extracellular phosphorus are treated and transported as a single state variable. Intracellular and extracellular concentrations are determined by equilibrium partitioning of their sum.

The model phosphate state variable is defined as the sum of dissolved phosphate and algal phosphorus content:

$$PO_4t = PO_4d + PO_4a \quad (4.40)$$

where

PO_4t = total phosphate (gm P m^{-3})

PO_4d = dissolved phosphate (gm P m^{-3})

PO_4a = algal phosphorus (gm P m^{-3})

Computation of Algal Phosphorus

Algal phosphorus is defined:

$$PO_4 a = APC B \quad (4.41)$$

The phosphorus-to-carbon ratio is calculated by the empirical function expressed in Equation 4.24.

The expressions 4.24 and 4.40 form a set of simultaneous equations in which APC depends on $PO_4 d$ and $PO_4 d$ depends on APC. The equations can be solved directly for APC:

$$APC = \frac{APCMIN + APCRAT PO_4 t}{1 + APCRAT B} \quad (4.42)$$

in which:

$$APCRAT = \frac{APCMAX - APCMIN}{PO_4 d \max} \quad (4.43)$$

The computation of APC takes place only when $PO_4 d < PO_4 d_{\max}$. Otherwise, APC takes the value APCMAX.

Effect of Variable Phosphorus Stoichiometry

The effect of the variable phosphorus-to-carbon ratio and the operation of the total phosphate system is best seen by an example. The model was applied to a chemostat supplied with unlimited inorganic nitrogen. Phosphorus recycling was eliminated in the water and sediments so that only the initial phosphate was available to the algae. The chemostat was simulated for thirty days. Midway through the simulation, a phosphate load, equivalent to the initial mass in the chemostat, was injected. Simulations were conducted with and without variable stoichiometry.

Algal production was initially identical with and without variable stoichiometry (Figure 4-12). As dissolved phosphate became scarce in the constant-stoichiometry chemostat, algal production diminished so that respiration exceeded growth prior to day five. Biomass decreased until the phosphate injection at day fifteen. In the variable-stoichiometry chemostat, algae responded to diminished phosphate availability by reducing their phosphorus-to-carbon ratio. Because less phosphorus was required per unit carbonaceous biomass formed, growth exceeded respiration beyond day five and maximum biomass exceeded biomass formed under constant stoichiometry. Upon injection of new phosphate, algal production increased with and without variable stoichiometry. Algae with variable stoichiometry responded with increased phosphorus-to-carbon ratio as well as increased production. As a result of the altered ratio,

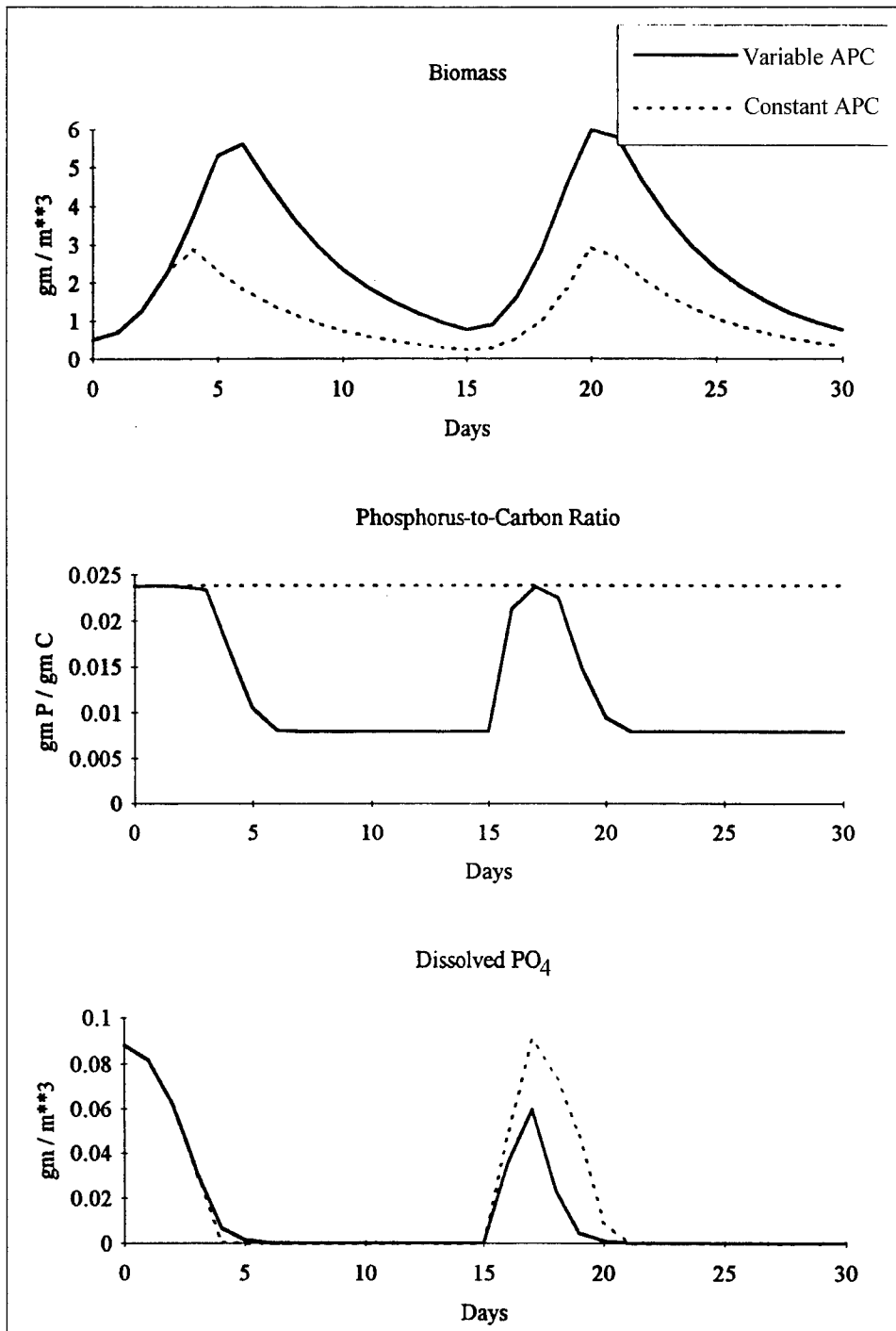


Figure 4-12. Chemostat simulation with and without variable phosphorus stoichiometry

dissolved phosphate peaked at a lower concentration in the presence of variable stoichiometry. The ability of algae to diminish phosphorus-to-carbon ratio still allowed algae in the variable-stoichiometry chemostat to exceed biomass formed in the constant-stoichiometry chemostat, however.

Phosphate

Once the interactions of dissolved and algal phosphate are made explicit, the balance of the equations describing phosphorus are straightforward summations of previously described sources and sinks:

$$\frac{\delta}{\delta t} PO_4 t = -WSa \frac{\delta}{\delta z} APC B + Kdop DOP \quad (4.44)$$

Algal uptake and release of phosphate represents an exchange of phosphate fractions rather than a phosphate source or sink. Consequently, no algal source or sink terms are included in the phosphate mass-conservation equation. The settling term is required to represent the settling of particulate phosphate incorporated in algal biomass.

Dissolved Organic Phosphorus

$$\begin{aligned} \frac{\delta}{\delta t} DOP = & (BM FPD + PR FPDO) APC B \\ & + Klpop LPOP + Krop RPOP - Kdop DOP \end{aligned} \quad (4.45)$$

Labile Particulate Organic Phosphorus

$$\begin{aligned} \frac{\delta}{\delta t} LPOP = & (BM FPL + PR FPLP) APC B \\ & - Klpop LPOP - WSl \frac{\delta}{\delta z} LPOP \end{aligned} \quad (4.46)$$

Refractory Particulate Organic Phosphorus

$$\begin{aligned} \frac{\delta}{\delta t} RPOP = & (BM FPR + PR FPRP) APC B \\ & - Krop RPOP - WSr \frac{\delta}{\delta z} RPOP \end{aligned} \quad (4.47)$$

Nitrogen

The model nitrogen cycle (Figure 4-13) includes the following processes:

- Algal production and metabolism
- Predation
- Hydrolysis of particulate organic nitrogen
- Mineralization of dissolved organic nitrogen
- Settling

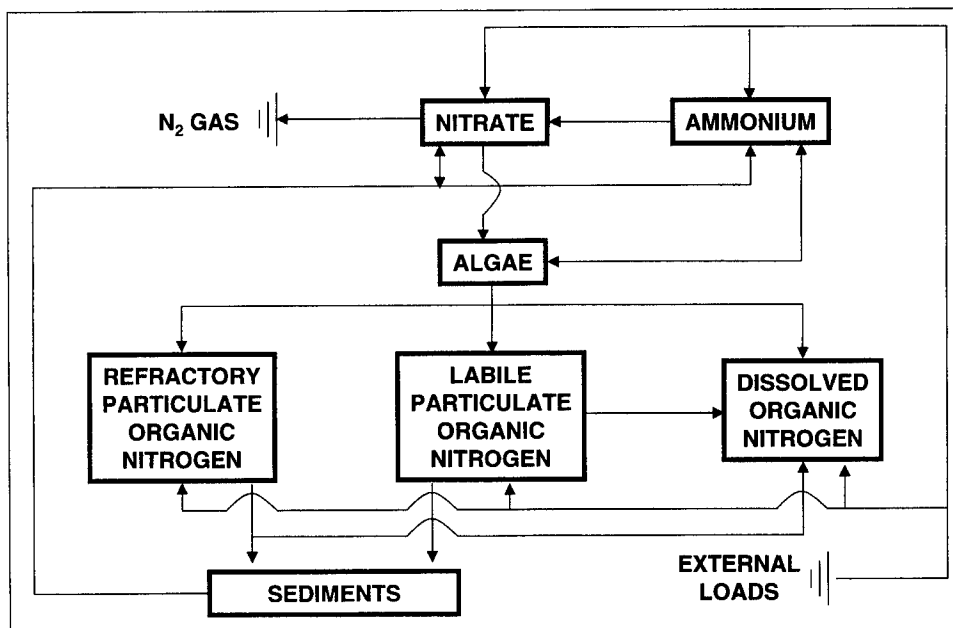


Figure 4-13. Model nitrogen cycle

- Nitrification
- Denitrification

External loads provide the ultimate source of nitrogen to the system. Inorganic nitrogen is incorporated by algae during growth and released as ammonium and organic nitrogen through respiration and predation. A portion of the particulate organic nitrogen hydrolyzes to dissolved organic nitrogen. The balance settles to the sediments. Dissolved organic nitrogen is mineralized to ammonium. In an oxygenated water column, a fraction of the ammonium is subsequently oxidized to nitrate through the nitrification process. In anoxic water, nitrate is lost to nitrogen gas through denitrification. Particulate nitrogen that settles to the sediments is mineralized and recycled to the water column, primarily as ammonium. Nitrate moves in both directions across the sediment-water interface, depending on relative concentrations in the water column and sediment interstices.

Effects on nitrogen of algal production, metabolism, and predation have already been detailed. Descriptions of hydrolysis, mineralization, nitrification, and denitrification follow.

Hydrolysis and Mineralization

In the model, particulate organic nitrogen is converted to the dissolved organic form via hydrolysis. Dissolved organic nitrogen is converted to ammonium through mineralization. Conversion of particulate nitrogen to ammonium proceeds through the sequence of hydrolysis and mineralization. Direct mineralization of particulate nitrogen does not occur. The

argument for accelerated hydrolysis and mineralization during nutrient-limited conditions is not as clear for nitrogen as for phosphorus. The same formulations are made available for nitrogen as for phosphorus, however. Accelerated processes can be activated or deactivated through parameter selection. The nitrogen hydrolysis and mineralization formulations are:

$$K_{don} = K_{dn} + \frac{KHn}{KHn + NH_4 + NO_3} K_{dnalg} B \quad (4.48)$$

where

K_{don} = mineralization rate of dissolved organic nitrogen (day^{-1})

K_{dn} = minimum mineralization rate (day^{-1})

K_{dnalg} = constant that relates mineralization to algal biomass
($\text{m}^3 \text{ gm}^{-1} \text{ C day}^{-1}$)

$$K_{lpon} = K_{ln} + \frac{KHn}{KHn + NH_4 + NO_3} K_{lnalg} B \quad (4.49)$$

where

K_{lpon} = hydrolysis rate of labile particulate nitrogen (day^{-1})

K_{ln} = minimum hydrolysis rate (day^{-1})

K_{lnalg} = constant that relates hydrolysis to algal biomass
($\text{m}^3 \text{ gm}^{-1} \text{ C day}^{-1}$)

$$K_{rpon} = K_{rn} + \frac{KHn}{KHn + NH_4 + NO_3} K_{rnalg} B \quad (4.50)$$

where

K_{rpon} = hydrolysis rate of refractory particulate nitrogen (day^{-1})

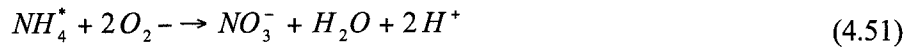
K_{rn} = minimum hydrolysis rate (day^{-1})

K_{rnalg} = constant that relates hydrolysis to algal biomass
($\text{m}^3 \text{ gm}^{-1} \text{ C day}^{-1}$)

An exponential function (Figure 4-3) relates mineralization and hydrolysis rates to temperature.

Nitrification

Nitrification is a process mediated by specialized groups of autotrophic bacteria that obtain energy through the oxidation of ammonium to nitrite and oxidation of nitrite to nitrate. A simplified expression for complete nitrification (Tchobanoglous and Schroeder 1987) is:



The equation indicates that two moles of oxygen are required to nitrify one mole of ammonium into nitrate. The simplified equation is not strictly true, however. Cell synthesis by nitrifying bacteria is accomplished by the fixation of carbon dioxide so that less than two moles of oxygen are consumed per mole ammonium utilized (Wezernak and Gannon 1968).

The kinetics of complete nitrification are modeled as a function of available ammonium, dissolved oxygen, and temperature:

$$NT = \frac{DO}{KH_{ont} + DO} \frac{NH_4}{KH_{nnt} + NH_4} f(T) NTm \quad (4.52)$$

where

NT = nitrification rate (gm N m⁻³ day⁻¹)

KH_{ont} = half-saturation constant of dissolved oxygen required for nitrification (gm O₂ m⁻³)

KH_{nnt} = half-saturation constant of NH₄ required for nitrification (gm N m⁻³)

NT_m = maximum nitrification rate at optimal temperature (gm N m⁻³ day⁻¹)

The kinetics formulation (Figure 4-14) incorporates the products of two "Monod" functions. The first function diminishes nitrification at low dissolved oxygen concentration. The second function expresses the influence of ammonium concentration on nitrification. When ammonium concentration is low, relative to KH_{nnt}, nitrification is proportional to ammonium concentration. For NH₄ << KH_{nnt}, the reaction is approximately first-order. (The first-order decay constant ≈ NT_m/KH_{nnt}.) When ammonium concentration is large, relative to KH_{nnt}, nitrification approaches a maximum rate. This formulation is based on a concept proposed by Tuffey et al. (1974). Nitrifying bacteria adhere to benthic or suspended sediments. When ammonium is scarce, vacant surfaces suitable for nitrifying bacteria exist. As ammonium concentration increases, bacterial biomass increases, vacant surfaces are occupied, and the rate of nitrification increases. The bacterial population attains maximum density when all surfaces suitable for bacteria are occupied. At this point, nitrification proceeds at a maximum rate independent of additional increase in ammonium concentration.

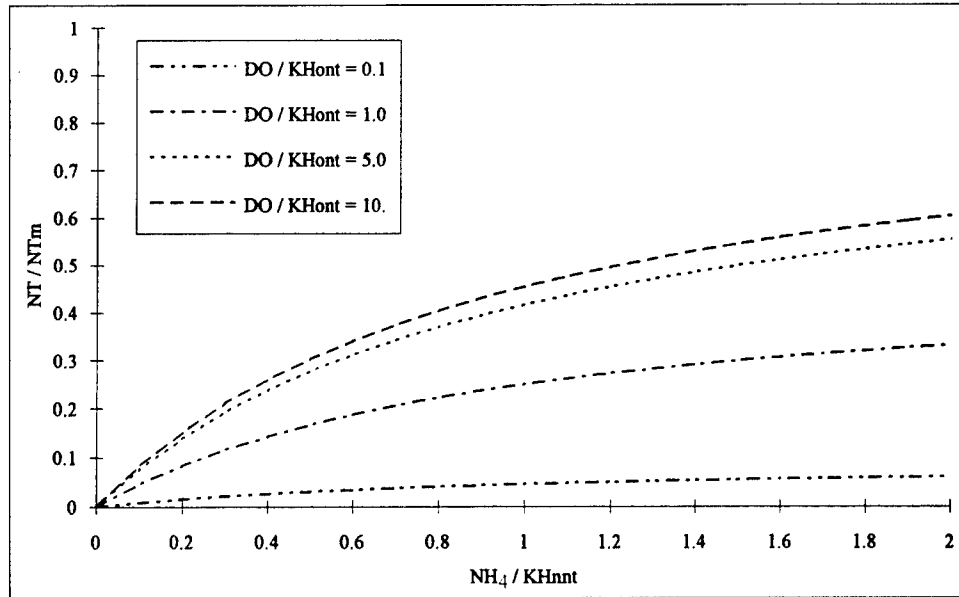


Figure 4-14. Effect of dissolved oxygen and ammonium concentration on nitrification rate

The optimal temperature for nitrification may be less than peak temperatures that occur in coastal waters. To allow for a decrease in nitrification at superoptimal temperature, the effect of temperature on nitrification is modeled in the Gaussian form of Equation 4.8.

Effect of Nitrification on Ammonium

$$\frac{\delta}{\delta t} NH_4 = -NT \quad (4.53)$$

Effect of Nitrification on Nitrate

$$\frac{\delta}{\delta t} NO_3 = NT \quad (4.54)$$

Effect of Nitrification on Dissolved Oxygen

$$\frac{\delta}{\delta t} DO = -AONT NT \quad (4.55)$$

where

AONT = mass dissolved oxygen consumed per mass
ammonium-nitrogen nitrified ($4.33 \text{ gm O}_2 \text{ gm}^{-1} \text{ N}$)

Effect of Denitrification on Nitrate

The effect of denitrification on dissolved organic carbon has been described. Denitrification removes nitrate from the system in stoichiometric proportion to carbon removal:

$$\frac{\delta}{\delta t} NO_3 = -ANDC \text{ Denit DOC} \quad (4.56)$$

where

ANDC = mass nitrate-nitrogen reduced per mass dissolved organic carbon oxidized ($0.933 \text{ gm N gm}^{-1} \text{ C}$)

Nitrogen Mass Balance Equations

The mass-balance equations for nitrogen state variables are written by summing all previously described sources and sinks:

Ammonium

$$\begin{aligned} \frac{\delta}{\delta t} NH_4 = & (BM \text{ FNI} + PR \text{ FNIP} - PN \text{ P})ANC \text{ B} \\ & + Kdon \text{ DON} - NT \end{aligned} \quad (4.57)$$

Dissolved Organic Nitrogen

$$\begin{aligned} \frac{\delta}{\delta t} DON = & (BM \text{ FND} + PR \text{ FNDP})ANC \text{ B} \\ & + Klpon \text{ LPON} + Krpon \text{ RPON} - Kdon \text{ DON} \end{aligned} \quad (4.58)$$

Labile Particulate Organic Nitrogen

$$\begin{aligned} \frac{\delta}{\delta t} LPON = & (BM \text{ FNL} + PR \text{ FNL P})ANC \text{ B} \\ & - Klpon \text{ LPON} - WSl \frac{\delta}{\delta z} LPON \end{aligned} \quad (4.59)$$

Refractory Particulate Organic Nitrogen

$$\begin{aligned} \frac{\delta}{\delta t} RPON = & (BM \text{ FNR} + PR \text{ FNR P})ANC \text{ B} \\ & - Krpon \text{ RPON} - WSr \frac{\delta}{\delta z} RPON \end{aligned} \quad (4.60)$$

Nitrate

$$\frac{\delta}{\delta t} NO_3 = (PN - 1)P \text{ ANC } B + NT - \text{ANDC Denit DOC} \quad (4.61)$$

Chemical Oxygen Demand

Chemical oxygen demand is the concentration of reduced substances that are oxidizable through inorganic means. The source of chemical oxygen demand in saline water is sulfide released from sediments. A cycle occurs in which sulfate is reduced to sulfide in the sediments and reoxidized to sulfate in the water column. In freshwater, methane is released to the water column by the sediment model. Both sulfide and methane are quantified in units of oxygen demand and are treated with the same kinetics formulation:

$$\frac{\delta}{\delta t} COD = - \frac{DO}{KHocod + DO} Kcod COD \quad (4.62)$$

where

COD = chemical oxygen demand concentration (gm O₂-equivalents m⁻³)

KHocod = half-saturation concentration of dissolved oxygen required for exertion of chemical oxygen demand (gm O₂ m⁻³)

Kcod = oxidation rate of chemical oxygen demand (day⁻¹)

An exponential function (Figure 4-3) describes the effect of temperature on exertion of chemical oxygen demand.

Dissolved Oxygen

Sources and sinks of dissolved oxygen in the water column (Figure 4-15) include:

- Algal photosynthesis
- Atmospheric reaeration
- Algal respiration
- Heterotrophic respiration
- Nitrification
- Chemical oxygen demand

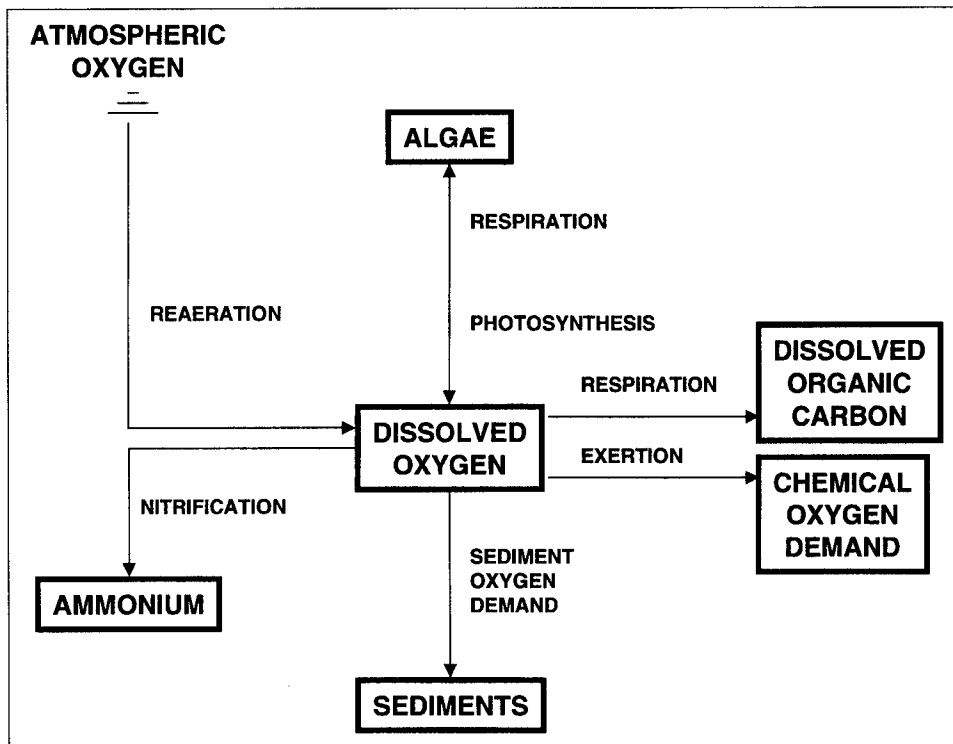


Figure 4-15. Model dissolved oxygen cycle

Reaeration

The rate of reaeration is proportional to the dissolved oxygen deficit in model segments that form the air-water interface:

$$\frac{\delta}{\delta t} DO = \frac{Kr}{\Delta z} (DOs - DO) \quad (4.63)$$

where

Kr = reaeration coefficient ($m \text{ day}^{-1}$)

DOs = dissolved oxygen saturation concentration ($gm \text{ O}_2 \text{ m}^{-3}$)

In shallow water (e.g. free-flowing streams), the reaeration coefficient depends largely on turbulence generated by bottom shear stress (O'Connor and Dobbins 1958). In deeper systems (e.g. estuaries), however, wind effects may dominate the reaeration process (O'Connor 1983). The reaeration coefficient is also influenced by temperature (ASCE 1961) and salinity (Wen et al. 1984). No universal formula for evaluation of the reaeration coefficient exists. In the model, the reaeration coefficient is treated as a user-supplied parameter.

Saturation dissolved oxygen concentration diminishes as temperature and salinity increase. An empirical formula that describes these effects (Genet et al. 1974) is:

$$DO_s = 14.5532 - 0.38217 T + 0.0054258 T^2 - CL(1.665 \times 10^{-4} - 5.866 \times 10^{-6} T + 9.796 \times 10^{-8} T^2) \quad (4.64)$$

where

CL = chloride concentration (= salinity/1.80655)

Summary of Dissolved Oxygen Sources and Sinks

The complete kinetics for dissolved oxygen are:

$$\begin{aligned} \frac{\delta}{\delta t} DO = & \left((13 - 0.3PN)P - \frac{DO}{KHr + DO} BM \right) AOCR B \\ & - AONT NT - \frac{DO}{KHodoc + DO} AOCR Kdoc DOC \\ & - \frac{DO}{KHocod + DO} Kcod COD + \frac{Kr}{\Delta z} (DO_s - DO) \end{aligned} \quad (4.65)$$

Salinity

No internal sources or sinks of salinity exist. Salinity is included to verify proper transport and linkage to the HM.

Temperature

A conservation of internal energy equation can be written analogous to the conservation of mass equation. The only source or sink of internal energy considered is exchange with the atmosphere. Although solar radiation can penetrate several meters into the water column, radiation-induced increases in internal energy are here assigned entirely to the surface model layer.

For practical purposes, the internal-energy equation can be written as a conservation of temperature equation. Change of temperature due to atmospheric exchange is considered proportional to the temperature difference between the water surface and a theoretical equilibrium temperature (Edinger et al. 1974):

$$\frac{\delta}{\delta t} T = \frac{KT}{\rho C_p \Delta z} (T_e - T) \quad (4.66)$$

where

T_e = equilibrium temperature ($^{\circ}\text{C}$)

KT = heat exchange coefficient ($\text{watt m}^{-2} \text{ }^{\circ}\text{C}^{-1}$)

C_p = specific heat of water ($4200 \text{ watt sec kg}^{-1} \text{ }^{\circ}\text{C}^{-1}$)

ρ = density of water (1000 kg m^{-3})

Fecal Coliform

Mortality of fecal coliform bacteria in the environment is represented as a first-order loss process:

$$\frac{\delta}{\delta t} FC = -K_{fc} FC \quad (4.67)$$

where

K_{fc} = decay rate of fecal coliform (day^{-1})

Glossary

Table 4-2 presents a glossary of terms employed in water-column kinetics described in this chapter.

Table 4-2.
Terms in Kinetics Equations

Symbol	Definition	Units
A_j	Area of flow face j	m^2
AANOX	Ratio of denitrification to oxic carbon respiration rate	
ANC	Nitrogen-to-carbon ratio of algae	$gm\ N\ gm^{-1}\ C$
AOCR	Dissolved oxygen-to-carbon ratio in respiration	$gm\ O_2\ gm^{-1}\ C$
AONT	Mass dissolved oxygen consumed per mass ammonium nitrified	$gm\ O_2\ gm^{-1}\ N$
ANDC	Mass nitrate-nitrogen consumed per mass carbon oxidized	$gm\ N\ gm^{-1}\ C$
APC	Algal phosphorus-to-carbon ratio	$gm\ P\ gm^{-1}\ C$
APCmin	Minimum phosphorus-to-carbon ratio	$gm\ P\ gm^{-1}\ C$
APCmax	Maximum phosphorus-to-carbon ratio	$gm\ P\ gm^{-1}\ C$
APCRAT	Change in phosphorus-to-carbon ratio per unit change in dissolved phosphate	C^{-1}
BMr	Basal metabolic rate of algae at reference temperature T_r	day^{-1}
BPR	Predation rate on algae at reference temperature T_r	day^{-1}
B	Biomass of algae	$gm\ C\ m^{-3}$
C_i	Concentration in ith control volume	$gm\ m^{-3}$
C_j^*	Concentration in flow across face j	$gm\ m^{-3}$
CChl	Carbon-to-chlorophyll ratio of algae	$gm\ C\ mg^{-1}\ chl$
CL	Chloride concentration	ppt
COD	concentration of chemical oxygen demand	$gm\ m^{-3}$
C_p	specific heat of water	$watt\ sec\ kg^{-1}\ ^\circ C^{-1}$
D_j	Diffusion coefficient at flow face j	$m^2\ sec^{-1}$
Denit	Denitrification rate of dissolved organic carbon	day^{-1}
DO	Dissolved oxygen	$gm\ O_2\ m^{-3}$
DOC	Dissolved organic carbon	$gm\ C\ m^{-3}$
DON	Dissolved organic nitrogen	$gm\ N\ m^{-3}$
DOP	Dissolved organic phosphorus	$gm\ P\ m^{-3}$
DOs	Saturation dissolved oxygen concentration	$gm\ O_2\ m^{-3}$
FCD	Fraction of basal metabolism exuded as dissolved organic carbon by algae	$0 \leq FCDx \leq 1$
FCDP	Fraction of dissolved organic carbon produced by predation	$0 \leq FCDP \leq 1$
FCLP	Fraction of labile particulate carbon produced by predation	$0 \leq FCLP \leq 1$
FCRP	Fraction of refractory particulate carbon produced by predation	$0 \leq FCRP \leq 1$
FD	Daylight fraction of total daylength	$0 \leq FD \leq 1$
$f(I)$	Effect of suboptimal illumination on algal production	$0 \leq f(I) \leq 1$

(Sheet 1 of 5)

Table 4-2. Continued

Symbol	Definition	Units
f(N)	Effect of suboptimal nutrient concentration on algal production	$0 \leq f(N) \leq 1$
FNI	Fraction of inorganic nitrogen produced by metabolism of algae	$0 \leq FNI_x \leq 1$
FNIP	Fraction of inorganic nitrogen produced by predation	$0 \leq FNIP \leq 1$
FND	Fraction of dissolved organic nitrogen produced by metabolism of algae	$0 \leq FND_x \leq 1$
FNDP	Fraction of dissolved organic nitrogen produced by predation	$0 \leq FNDP \leq 1$
FNL	Fraction of labile particulate nitrogen produced by metabolism of algae	$0 \leq FNL_x \leq 1$
FNLP	Fraction of labile particulate nitrogen produced by predation	$0 \leq FNLP \leq 1$
FNR	Fraction of refractory particulate nitrogen produced by metabolism of algae	$0 \leq FNR_x \leq 1$
FNRP	Fraction of refractory particulate nitrogen produced by predation	$0 \leq FNRP \leq 1$
FPD	Fraction of dissolved organic phosphorus produced by metabolism by algae	$0 \leq FPD_x \leq 1$
FPDP	Fraction of dissolved organic phosphorus produced by predation	$0 \leq FPDP \leq 1$
FPI	Fraction of inorganic phosphorus produced by metabolism of algae	$0 \leq FPI \leq 1$
FPIP	Fraction of inorganic phosphorus produced by predation	$0 \leq FPIP \leq 1$
FPL	Fraction of labile particulate phosphorus produced by metabolism of algae	$0 \leq FPL_x \leq 1$
FPLP	Fraction of labile particulate phosphorus produced by predation	$0 \leq FPLP \leq 1$
FPR	Fraction of refractory particulate phosphorus produced by metabolism of algae	$0 \leq FPR_x \leq 1$
FPRP	Fraction of refractory particulate phosphorus produced by predation	$0 \leq FPRP \leq 1$
FR	Macrobenthic filtration rate	$\text{m}^3 \text{gm}^{-1} \text{C day}^{-1}$
f(T)	Effect of suboptimal temperature on algal production	$0 \leq f(T) \leq 1$
I	Illumination rate	Langley's day^{-1}
Ih	Illumination rate at which algal production is halved	Langley's day^{-1}
Io	Daily illumination at water surface	Langley's day^{-1}
Kcod	Oxidation rate of chemical oxygen demand	day^{-1}
Kdc	Minimum respiration rate of dissolved organic carbon	day^{-1}
Kdcalg	Constant that relates respiration rate to algal biomass	$\text{m}^3 \text{gm}^{-1} \text{C day}^{-1}$
Kdn	Minimum mineralization rate of dissolved organic nitrogen	day^{-1}
Kdnalg	Constant that relates mineralization rate to algal biomass	$\text{m}^3 \text{gm}^{-1} \text{C day}^{-1}$
Kdoc	Dissolved organic carbon respiration rate	day^{-1}

(Sheet 2 of 5)

Table 4-2. Continued

Symbol	Definition	Units
Kdon	Dissolved organic nitrogen mineralization rate	day ⁻¹
Kdop	Dissolved organic phosphorus mineralization rate	day ⁻¹
Kdp	Minimum mineralization rate of dissolved organic phosphorus	day ⁻¹
Kdpalg	Constant that relates mineralization rate to algal biomass	m ³ gm ⁻¹ C day ⁻¹
Keb	Background light attenuation	m ⁻¹
Kechl	Light attenuation coefficient for chlorophyll 'a'	m ² mg ⁻¹
Kess	Total light attenuation	m ⁻¹
Kfc	Decay rate of fecal coliform	day ⁻¹
KHn	Half-saturation concentration for nitrogen uptake by algae	gm N m ⁻³
KHndn	Half-saturation concentration of nitrate required for denitrification	gm N m ⁻³
KHnnt	Half-saturation concentration of NH ₄ required for nitrification	gm N m ⁻³
KHocod	Half-saturation concentration of dissolved oxygen required for exertion of COD	gm O ₂ m ⁻³
KHodoc	Half-saturation concentration of dissolved oxygen required for oxic respiration	gm O ₂ m ⁻³
KHomb	Dissolved oxygen concentration at which macrobenthic grazing is halved	gm O ₂ m ⁻³
KHont	Half-saturation concentration of dissolved oxygen required for nitrification	gm O ₂ m ⁻³
KHp	Half-saturation concentration for phosphorus uptake by algae	gm P m ⁻³
KHr	Half-saturation concentration for dissolved organic carbon excretion by algae	gm O ₂ m ⁻³
Klc	Minimum dissolution rate of labile particulate carbon	day ⁻¹
Klcalg	Constant that relates dissolution rate to algal biomass	m ³ gm ⁻¹ C day ⁻¹
Kln	Minimum dissolution rate of labile particulate nitrogen	day ⁻¹
Klnalg	Constant that relates dissolution rate to algal biomass	m ³ gm ⁻¹ C day ⁻¹
Klp	Minimum dissolution rate of labile particulate phosphorus	day ⁻¹
Klpalg	Constant that relates dissolution rate to algal biomass	m ³ gm ⁻¹ C day ⁻¹
Klpoc	Labile particulate organic carbon dissolution rate	day ⁻¹
Klpon	Labile particulate organic nitrogen hydrolysis rate	day ⁻¹
Klpop	Labile particulate organic phosphorus hydrolysis rate	day ⁻¹
Kr	Reaeration coefficient	m day ⁻¹
Krc	Minimum dissolution rate of refractory particulate carbon	day ⁻¹
Krcalg	Constant that relates dissolution rate to algal biomass	m ³ gm ⁻¹ C day ⁻¹
Krn	Minimum dissolution rate of refractory particulate nitrogen	day ⁻¹
Krnalg	Constant that relates dissolution rate to algal biomass	m ³ gm ⁻¹ C day ⁻¹

(Sheet 3 of 5)

Table 4-2. Continued

Symbol	Definition	Units
Krp	Minimum dissolution rate of refractory particulate phosphorus	day ⁻¹
Krpalg	Constant that relates dissolution rate to algal biomass	m ³ gm ⁻¹ C day ⁻¹
Krpoc	Refractory particulate organic carbon dissolution rate	day ⁻¹
Krpon	Refractory particulate organic nitrogen hydrolysis rate	day ⁻¹
Krpop	Refractory particulate organic phosphorus hydrolysis rate	day ⁻¹
KT	Surface heat exchange coefficient	watt m ⁻² °C ⁻¹
KTb	Effect of temperature on basal metabolism of algae	°C ⁻¹
KTcod	Effect of temperature on oxidation of chemical oxygen demand	°C ⁻¹
KTg1	Effect of temperature below Tm on growth of algae	°C ⁻²
KTg2	Effect of temperature above Tm on growth of algae	°C ⁻²
KThdr	Constant that relates hydrolysis rates to temperature	°C ⁻¹
KTmnl	Constant that relates mineralization rates to temperature	°C ⁻¹
KTnt1	Effect of temperature below Tmnt on nitrification	°C ⁻²
KTnt2	Effect of temperature above Tmnt on nitrification	°C ⁻²
LPOC	Labile particulate organic carbon	gm C m ⁻³
LPON	Labile particulate organic nitrogen	gm N m ⁻³
LPOP	Labile particulate organic phosphorus	gm P m ⁻³
MBGM	Macrobenthic biomass	gm C m ⁻²
NH ₄	Ammonium concentration	gm N m ⁻³
NO ₃	Nitrate+nitrite concentration	gm N m ⁻³
NT	Nitrification rate	gm N m ⁻³ day ⁻¹
NTm	Maximum nitrification rate at optimal temperature	gm N m ⁻³ day ⁻¹
PM	Production rate of algae under optimal conditions	day ⁻¹
PN	Preference for ammonium uptake by algae	0 ≤ PN ≤ 1
PO ₄ a	Phosphate in algal biomass	gm P m ⁻³
PO ₄ d	Dissolved phosphate concentration	gm P m ⁻³
PO ₄ dmax	Dissolved phosphate concentration at which algal phosphorus-to-carbon ratio achieves its maximum value	gm P m ⁻³
PO ₄ t	Total phosphate concentration	gm P m ⁻³
PR	Rate of predation on algae	day ⁻¹
P	Production rate of algae	day ⁻¹
Q _j	Volumetric flow across flow face j	m ³ sec ⁻¹
RPOC	Refractory particulate organic carbon	gm C m ⁻³
RPON	Refractory particulate organic nitrogen	gm N m ⁻³

(Sheet 4 of 5)

Table 4-2. Concluded		
Symbol	Definition	Units
RPOP	Refractory particulate organic phosphorus	gm P m ⁻³
S	Salinity	ppt
S _i	External loads and kinetics sources and sinks in ith control volume	gm sec ⁻¹
t	Temporal coordinate	sec
T	temperature	°C
T _e	Equilibrium temperature	°C
T _m	Optimal temperature for growth of algae	°C
T _{mnt}	Optimal temperature for nitrification	°C
T _r	Reference temperature for metabolism	°C
T _{rcod}	Reference temperature for COD oxidation	°C
T _{rhdr}	Reference temperature for hydrolysis	°C
T _{rmnl}	Reference temperature for mineralization	°C
V _i	Volume of ith control volume	m ³
WS _i	Settling velocity of labile particles	m day ⁻¹
WS _r	Settling velocity of refractory particles	m day ⁻¹
WS _a	Settling velocity of algae	m day ⁻¹
WS _{mb}	Equivalent settling rate induced by macrobenthic grazing	m day ⁻¹
x	Spatial coordinate	m
z	Vertical coordinate	m
z ₁	Distance from water surface to top of model segment	m
z ₂	Distance from water surface to bottom of model segment	m
Δz	Model segment thickness	m
ρ	Density of water	kg m ⁻³
<i>(Sheet 5 of 5)</i>		

Predictive Sediment Submodel

The predictive sediment submodel was developed as one component of the Chesapeake Bay eutrophication model study (Cерco and Cole 1994). The need for a predictive benthic sediment model was made apparent by the results of a preceding steady-state model study of the bay (HydroQual 1987). The study indicated sediments were the dominant source of phosphorus and ammonium during the summer period of minimum dissolved oxygen. Increased sediment oxygen demand and nutrient releases were implicated in a perceived dissolved oxygen decline from 1965 to 1985. No means existed to predict how these sediment processes would respond to

nutrient load reductions, however. Neither was the time scale for completion of the responses predictable.

For management purposes, a sediment model was required with two fundamental capabilities: (1) predict effects of management actions on sediment-water exchange processes, and (2) predict time scale for alterations in sediment-water exchange processes.

The model (Figure 4-16) was driven by net settling of organic matter from the water column to the sediments. In the sediments, the model simulated the diagenesis (decay) of the organic matter. Diagenesis produced oxygen demand and inorganic nutrients. Oxygen demand, as sulfide (in salt water) or methane (in fresh water), took three paths out of the sediments: export to the water column as chemical oxygen demand, oxidation at the sediment-water interface as sediment oxygen demand, or burial to deep, inactive sediments. Inorganic nutrients produced by diagenesis took two paths out of the sediments: release to the water column, or burial to deep, inactive sediments.

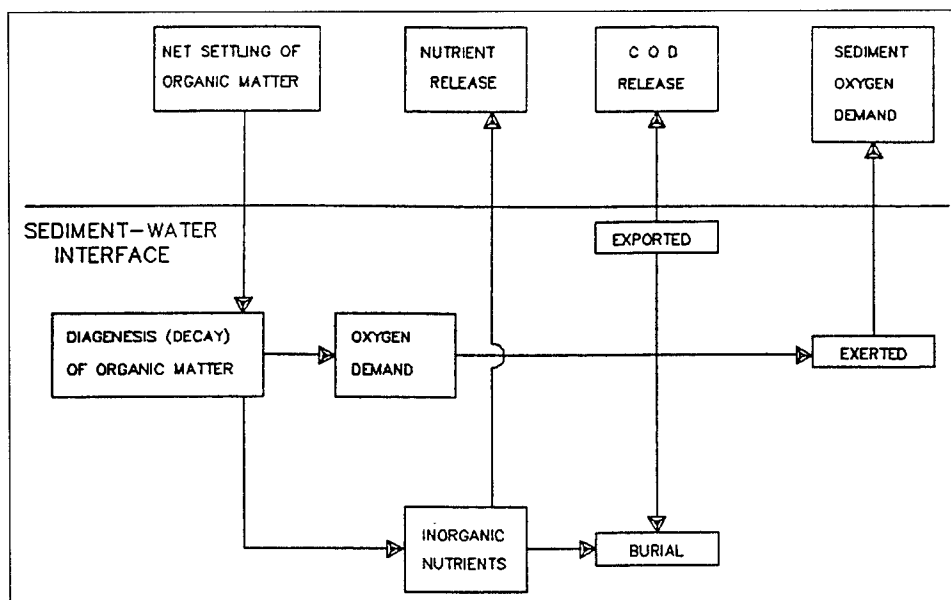


Figure 4-16. Sediment model schematic

Additional details of the model, required to understand the coupling of the sediment submodel to the model of the water column, are provided below. Complete model documentation is provided by DiToro and Fitzpatrick (1993). A listing of sediment model state variables and predicted sediment-water fluxes is provided in Table 4-3.

Table 4-3.
Sediment Model State Variables and Fluxes

State Variable	Sediment-Water Flux
Temperature	
Particulate Organic Carbon	Sediment Oxygen Demand
Sulfide/Methane	Release of Chemical Oxygen Demand
Particulate Organic Nitrogen	
Ammonium	Ammonium Flux
Nitrate	Nitrate Flux
Particulate Organic Phosphorus	
Phosphate	Phosphate Flux

Description of Sediment Model

Benthic sediments are represented as two layers with a total depth of 10 cm (Figure 4-17). The upper layer, in contact with the water column, may be oxic or anoxic depending on dissolved oxygen concentration in the water. The lower layer is permanently anoxic. The thickness of the upper layer is determined by the penetration of oxygen into the sediments. At its maximum thickness, the oxic layer depth is only a small fraction of the total.

The sediment model consists of three basic processes. The first is deposition of particulate organic matter from the water column to the sediments. Due to the negligible thickness of the upper layer, deposition proceeds from the water column directly to the lower, anoxic layer. Within the lower layer, organic matter is subject to the second basic process, diagenesis (or decay). The third basic process is flux of substances produced by diagenesis to the upper sediment layer, to the water column, and to deep, inactive sediments. The flux portion of the model is the most complex. Computation of flux requires consideration of reactions in both sediment layers, of partitioning between particulate and dissolved fractions in both layers, of sedimentation from the upper to lower layer and from the lower layer to deep inactive sediments, of particle mixing between layers, of diffusion between layers, and of mass transfer between the upper layer and the water column.

Deposition

Deposition is one process which couples the model of the water column with the model of the sediments. Consequently, deposition is represented in both the sediment and water-column models. In the water column, deposition is represented with a modification of the mass-balance equation applied only to cells that interface the sediments:

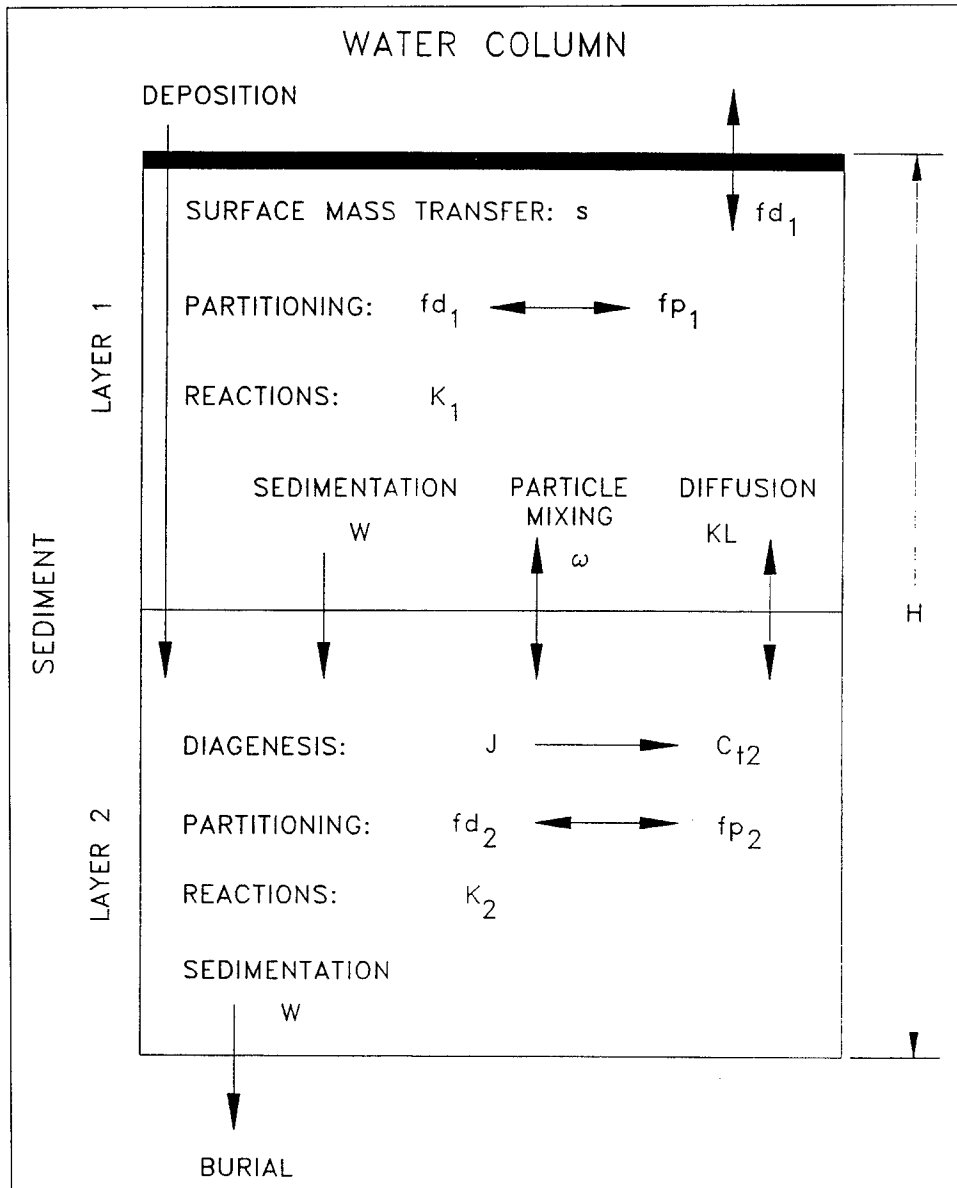


Figure 4-17. Sediment model layers and definitions

$$\frac{\delta C}{\delta t} = [\text{transport}] + [\text{kinetics}] + \frac{WS}{\Delta z} C_{up} - \frac{W_{net}}{\Delta z} C \quad (4.68)$$

where

C = concentration of particulate constituent (gm m^{-3})

WS = settling velocity in water column (m day^{-1})

C_{up} = constituent concentration two cells above sediments (gm m^{-3})

W_{net} = net settling to sediments (m day^{-1})

Δz = cell thickness (m)

Net settling to the sediments may be greater or lesser than settling in the water column. Sediment resuspension is implied when settling to the sediments is less than settling through the water column. Net settling that exceeds particle settling velocity implies active incorporation of particles into sediment by biota or other processes.

Diagenesis

Organic matter in the sediments is divided into three G classes or fractions, in accordance with principles established by Westrich and Berner (1984). Division into G classes accounts for differential decay rates of organic matter fractions. The G1, labile, fraction has a half life of 20 days. The G2, refractory, fraction has a half life of one year. The G3, inert, fraction undergoes no significant decay before burial into deep, inactive sediments. Each G class has its own mass-conservation equation:

$$H \frac{\delta G_i}{\delta t} = W_{net} f_i C - W G_i - H K_i G_i \theta_i^{(T-20)} \quad (4.69)$$

where

H = total thickness of sediment layer (m)

G_i = concentration organic matter in G class i (gm m^{-3})

f_i = fraction of deposited organic matter assigned to G class i

W = burial rate (m day^{-1})

K_i = decay rate of G class i (day^{-1})

θ_i = constant that expresses effect of temperature on decay of G class i

Since the G3 class is inert, $K_3 = 0$.

Total diagenesis is the rate at which oxygen demand and nutrients are produced by diagenesis of the G1 and G2 fractions:

$$J = H [K_1 G_1 \theta_1^{(T-20)} + K_2 G_2 \theta_2^{(T-20)}] \quad (4.70)$$

where

J = total diagenesis ($\text{gm m}^{-2} \text{day}^{-1}$)

Flux

Total diagenesis provides the driving force for the flux portion of the model. Computation of flux requires mass-balance equations for oxygen demand and nutrients in both sediment layers. The upper layer is thin such that a steady-state approximation is appropriate:

$$s \, fd_1 \, Ct_1 = \omega (fp_2 Ct_2 - fp_1 Ct_1) + KL (fd_2 Ct_2 - fd_1 Ct_1) - W Ct_1 \pm \sum K_1 \quad (4.71)$$

where

Ct_1 = total concentration in upper layer (gm m^{-3})

Ct_2 = total concentration in lower layer (gm m^{-3})

fd_1 = dissolved fraction of total substance in upper layer
($0 \leq fd \leq 1$)

fd_2 = dissolved fraction of total substance in lower layer

fp_1 = particulate fraction of total substance in upper layer = $1 - fd_1$

fp_2 = particulate fraction of total substance in lower layer

s = sediment-water mass-transfer coefficient (m day^{-1})

ω = particle mixing velocity (m day^{-1})

KL = diffusion velocity for dissolved fraction (m day^{-1})

$\sum K_1$ = sum of all sources and sinks due to reactions in upper layer
($\text{gm m}^{-2} \text{ day}^{-1}$)

The left-hand side of Equation 4-71 represents flux to the water column under the assumption that dissolved concentration in the water column is negligibly small compared to the sediments. The assumption is made here for notational simplicity. Effects of concentration in the overlying water are computed in the sediment model code. The terms on the right-hand side are mass transport due to particle mixing, diffusion of dissolved substance, deposition to the lower layer, and reactive sources and sinks. The reactions include, for example, the oxidation of sulfide that results in sediment oxygen demand. The equation states that flux to the water column, deposition from surficial sediments, and reactive sources and sinks are balanced by mixing and diffusion from deeper sediments.

The mass balance equation for the lower layer accounts for temporal concentration variations:

$$\begin{aligned} \frac{\delta Ct_2}{\delta t} = & \frac{J}{H} - \frac{\omega}{H} (fp_2 Ct_2 - fp_1 Ct_1) - \frac{KL}{H} (fd_2 Ct_2 - fd_1 Ct_1) \\ & + \frac{W}{H} (Ct_1 - Ct_2) \pm \sum K_2 \end{aligned} \quad (4.72)$$

where

$$\Sigma K_2 = \text{sum of all sources and sinks due to reactions in lower layer} \\ (\text{gm m}^{-2} \text{ day}^{-1})$$

The first term on the right of Equation 4.72 represents the diagenetic source of oxygen demand or nutrient. The second term represents exchange of the particulate fraction with the upper layer. The third term represents exchange of the dissolved fraction with the upper layer. The fourth term represents deposition of total substance from the upper layer to the lower layer and burial from the lower layer to deep, inactive sediments. The last term is the sum of all internal sources and sinks due to reactions.

The mass balance equations, with appropriate sources and sinks, are solved within the sediment model for sulfide, methane, ammonium, nitrate, phosphate, and silica. Details of the reactions and solution scheme may be found in the model documentation (DiToro and Fitzpatrick 1993).

The water-quality and sediment models interact on a time scale equal to the integration time step of the water-quality model. After each integration, predicted particle deposition, temperature, nutrient and dissolved oxygen concentrations are passed from the water-quality model to the sediment model. The sediment model computes sediment-water fluxes of dissolved nutrients and oxygen based on predicted diagenesis and concentrations in the sediments and water. The computed sediment-water fluxes are incorporated by the water-quality model into appropriate mass balances and kinetic reactions.

5 Water Quality Model Input

The CE-QUAL-ICM (ICM) requires various forms of information in order to accurately predict water quality. Types of input data required include hydrodynamic, meteorological, initial conditions, boundary conditions and external loadings, and also parameters. Descriptions of these inputs for this study are presented below. Parameters include kinetic rate coefficients, half saturation constants, stoichiometry, and other coefficients used in water quality reactions. Parameters used in this study are presented in Chapter 7.

Hydrodynamics

CH3D-WES (see Chapter 3) was the source for all hydrodynamic information for ICM during this study. The hydrodynamic information generated by CH3D can be described as time-invariant and time-varying. Time-invariant data are the information obtained from CH3D which do not change, or are constant, during the ICM simulation. Time-varying data are information which change during the simulation and which must be updated in ICM at each hydrodynamic update interval.

Time-invariant hydrodynamic data consist of: cell areas (m^2) in planform, i.e., in the horizontal plane; initial cell volumes (m^3) for all computational cells; distances (m) between neighboring cell centroids; and initial subsurface horizontal flow-face areas (m^2) between all cells. With the z-plane version of CH3D-WES, which was used for this study, the horizontal flow-face areas and volumes of cells below the surface layer do not change over time. However, since the surface layer thicknesses increase and decrease with the tides, horizontal flow-face areas and cell volumes in the surface layer do change over time.

Time-varying data consist of three-dimensional flows (m^3/sec) between computational cells, horizontal flow-face areas (m^2) for surface layer cells, cell volumes (m^3) for the surface layer, and vertical diffusivities (m^2/sec) between layers. The flows, facial areas, and diffusivities are updated within ICM at each hydrodynamic update interval, but they are held constant in ICM between hydrodynamic updates. Volumes are used for

comparison purposes during each hydrodynamic update to ensure that the internally computed volume of ICM is consistent with CH3D-WES volumes, i.e., to check for preservation of volume conservation.

A calibrated version of CH3D-WES must be applied for the same period over which the WQM is to be applied. A processor is appended as subroutines to the CH3D-WES source code. The processor computes time-averaged flows, surface layer flow-face areas, and vertical diffusivities throughout the ICM grid for each hydrodynamic update interval and then writes these values to an output file that is subsequently used by ICM. For the SJBE study, the averaging interval, or hydrodynamic update interval was fifteen minutes. Processing the hydrodynamic information separately and storing it in a file allows a set of hydrodynamic information to be generated once and used repeatedly for WQM application. Details of the hydrodynamic model and its application are covered in Chapter 3.

For this study, a one-to-one correspondence of the HM and WQM grids was used, i.e., the same grid was used for both models. Since water levels are used to drive the ocean boundaries of the HM, the outermost row of cells is not used within the WQM grid. It is possible for the WQM to use either a coarser overlay of the HM grid or an entirely different grid and project mass conserving flow fields from the HM grid to the WQM. The latter approach has been developed recently and is still undergoing testing.

For this study, a modification was made to the grid. The areas of concern in this study were in the interior bays and canals of the system and not the offshore regions. There are large differences in depth (and the number of layers) between the areas of concern and the offshore waters. Numerous areas in the interior of the system had depths of approximately 3 ft and were modeled as one layer. Offshore regions were over 90 ft deep or 30 layers. The large numbers of cells required offshore resulted in un-necessarily long computational requirements. To alleviate this problem, an additional four rows of cells were removed along the ocean boundary. The final grid shown in Figure 5-1 contained 1,923 surface cells and 10,600 total cells. The deepest portion of the reduced grid was directly offshore of the mouth of San Juan Bay which was 30 layers or approximately 90 ft deep.

Meteorological Data

ICM utilizes meteorological information in the computation of temperature and algal growth. Daily meteorological observations were obtained for the National Weather Service Station at the San Juan International Airport for the period May through September 1995. Data obtained consisted of daily average values for dry bulb temperature, wet bulb temperature, cloud cover, and wind speed. With this information values for equilibrium temperature, heat exchange coefficient, daily solar illumination, and

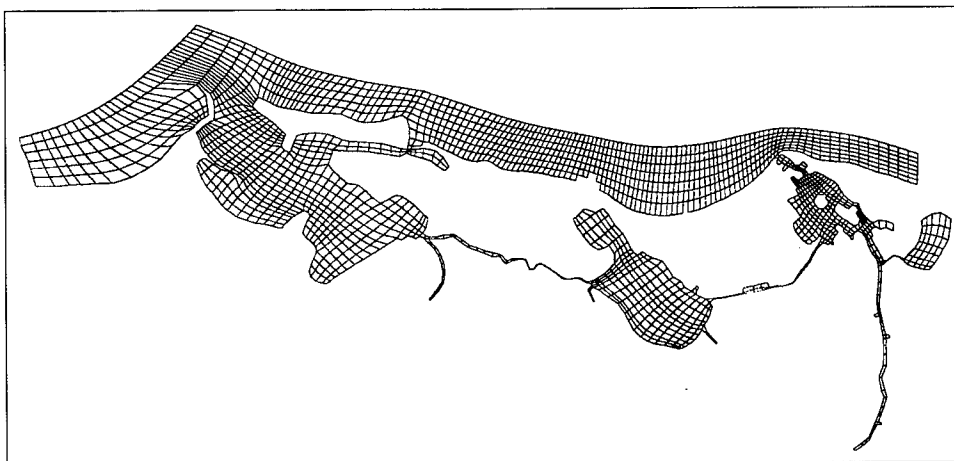


Figure 5-1. Water quality model grid, reduced from hydrodynamic model grid

fractional day length were computed. Details of the computational procedures used are found in Edinger et al. (1974).

Initial Conditions

ICM requires initial concentrations for all modeled constituents in all water column and sediment cells. These values must be realistic, otherwise model results can be biased by the initial conditions and may not fully reflect the loading and hydrodynamic processes occurring during simulation. Appropriate initial conditions for the sediment model are especially crucial since sediment model cells respond more slowly to changes in the loads and processes than does the water column.

Initial conditions were generated by spinning up the model. Spinning up was accomplished by initiating model calibration with a set of uniform initial conditions for water column cells based upon sampling data. Initial conditions in the sediments were specified in a similar manner. ICM was run using the calibration period hydrodynamics, loads, and boundary conditions. At the end of the first calibration run, the concentrations of all constituents in all water column and sediment cells were stored in a binary file. This file was then used as the initial conditions for a second calibration run. At the completion of the second calibration run, concentrations for all cells were again written to a binary file which was used as the initial conditions for the third calibration run. This process was repeated in subsequent calibration runs until a quasi steady-state condition (in terms of initial conditions) was reached in both the water column and sediment cells. This process required approximately 12 runs. Once a quasi steady-state set of initial conditions existed, all subsequent runs were made using the same set of initial conditions. The same iterative procedure was used to establish initial conditions for scenario runs. The scenario simulation period was run multiple times using results from the previous run to

establish a new set of initial conditions. The process was repeated until a quasi steady-state set of initial conditions existed between runs.

Boundary Concentrations and Loading Estimates

Water quality boundary conditions for this study can be divided into two forms, ocean and terrestrial. Atmospheric loadings were not included. Ocean boundary conditions are concentrations set along the open ocean boundary. These concentrations are used for all flow conditions during which flow is coming into the water quality model grid at the edge of the grid along the ocean boundary. Terrestrial boundary concentrations or loads are specified for inflows entering the water quality model grid from tributary headwaters, local, nonpoint source runoff directly from land into the bays, and point source loads. Point source loads are usually used to account for discharges from treatment plants, wastewater, combined sewer overflows, pumping plants, and other sources of pollutants at specified locations. Point and nonpoint source loadings are usually treated as loads, which means they are input as mass/time (the product of flow times concentration) at the appropriate grid locations and are not tied to a HM tributary inflow. Boundary concentrations are usually specified to the WQM for tributaries since flows are passed from the HM to the WQM for all tributaries. However, for this study, the tributary loads were computed and input for all constituents, except temperature and DO for which concentration boundary conditions were input.

Ocean Boundary Concentrations

The values used for the ocean boundary were obtained from the data collected at stations AO-1 and AO-2 (Kennedy et al., 1996). Analysis of data at these stations indicates that there is little variation in the data between the stations, and there was no vertical stratification. Nutrient levels were low relative to levels inside the SJBE system. Consequently, these data were averaged and a single value was determined which was used for all ocean boundary faces (Table 5-1). Ocean boundary concentrations varied over time and were updated periodically as shown in Table 5-1.

Table 5-1.
Ocean Boundary Concentrations

Parameter	Day 0	Day 38	Day 52	Day 66	Day 81
Temperature, °C	28.0	28.0	28.3	28.2	28.9
Salinity, ppt	37.9	36.6	36.2	37.9	37.1
Total Suspended Solids, mg/l	0.0	0.0	0.0	0.0	0.0
Chlorophyll-a, µg/l	0.48	0.37	0.48	0.23	0.50
DOC, mg/l	3.12	0.94	3.15	8.47	1.98
POC, mg/l	0.38	0.43	0.38	1.50	0.32
NH ₄ , mg/l	0.0	0.09	0.0	0.03	0.16
NO ₃ , mg/l	0.01	0.01	0.0	0.0	0.0
TON, mg/l	0.0	0.0	0.0	0.0	0.0
TIP, mg/l	0.002	0.002	0.001	0.001	0.003
DOP, mg/l	0.003	0.017	0.0	0.007	0.007
POP, mg/l	0.001	0.006	0.003	0.0	0.004
DO, mg/l	6.2	6.1	5.9	5.3	4.8

Loading Estimates

External loads of constituents are separated into two categories, point source and nonpoint source. Point source loads are traditionally defined as those which are attributable to a single location or "point." Examples include effluent pipes from municipal or industrial wastewater treatment facilities. Nonpoint source loads are defined as those whose origin is distributed over a widely spaced area. A traditional example is runoff from a local subwatershed along the model shoreline. Nonpoint source loads can also include loads which are truly point source in nature but which occur in the watershed and not at the model boundary.

When commencing this study, an extensive effort was made to identify significant point source and nonpoint source loads for the SJBE system. Many possible sources of pollution were identified as reasons for poor water quality in various regions of the system. Unfortunately, little documentation was discovered which substantiated these theories. Part of the problem is that in some cases it is hard to quantify the loads due to their distributed nature. Other cases, such as sewer pump station overflows, are intermittent and the quantity of water and load cannot be easily determined. In other instances, data on concentration or flow were lacking.

A review of EPA permit records indicated that there were no major municipal wastewater treatment plants or industrial point source dischargers for nutrients or oxygen-depleting substances that were releasing effluents directly into the SJBE system. Treatment plant effluents are removed via a Puerto Rico Aqueduct and Sewer Authority (PRASA) pipeline for ocean disposal beyond the boundary of the water quality model grid. Two Puerto Rico Electric Power Association (PREPA) power plants

discharge cooling water to San Juan Bay. The net effect of these two power plants is that they increase the temperature of the cooling water. Therefore, all of the external loads can be considered as nonpoint source loads.

Estimation of Flows. While there are officially no major point source dischargers to the system, the system receives significant loads in the form of runoff loads from the adjacent watershed and storm water pump stations. Prior to estimation of these loads, two pieces of information are required, flow and concentration. Two forms of flow data were available, Rio Piedras (see Figure 1-1) flow records and storm water pump station records.

Rio Piedras at Hato Rey flow records for the period being modeled were obtained from the USGS. The frequency of these data were 15 minutes. A review of the records for the calibration period indicated that observed flows varied from 0.11 to 236.6 m³/s (4 to 8355 ft³/s), see Figures 5-2a through 5-2d for June through September 1995. Daily averages of flow were used in the hydrodynamic model for the Rio Piedras inflow.

Records for storm water pump stations operated by the Puerto Rico Department of Natural Resources were obtained. The only pump station whose records overlapped the calibration period was the Baldorioty de Castro Pump Station on San José Lagoon. (Records for the calibration period for the other pump stations were unavailable.) Information on these records consisted of hours of operation for pumps from which the daily pumping duration could be obtained. The daily total water volume pumped was determined by multiplying the pump capacity by the daily pumping duration. This volume was then converted into an equivalent daily flow rate as shown in Figure 5-3.

The SJBE watershed was divided into 21 sub-basins as shown in Figure 5-4 based upon information extracted from USGS topographic maps. Areas for each sub-basin were determined and are listed in Table 5-2. Freshwater flows were introduced in the HM at each location where there is an arrow shown in Figure 5-4. There are more arrows than sub-basins since flows were put in and taken out at two power plants and in several cases more than one flow location was used for a sub-basin. For all cases, except Caño Martín Peña, the HM inflow was treated as a tributary (i.e., quantity with momentum). For Caño Martín Peña, inflow was distributed along the canal as a lateral flow, i.e., no momentum.

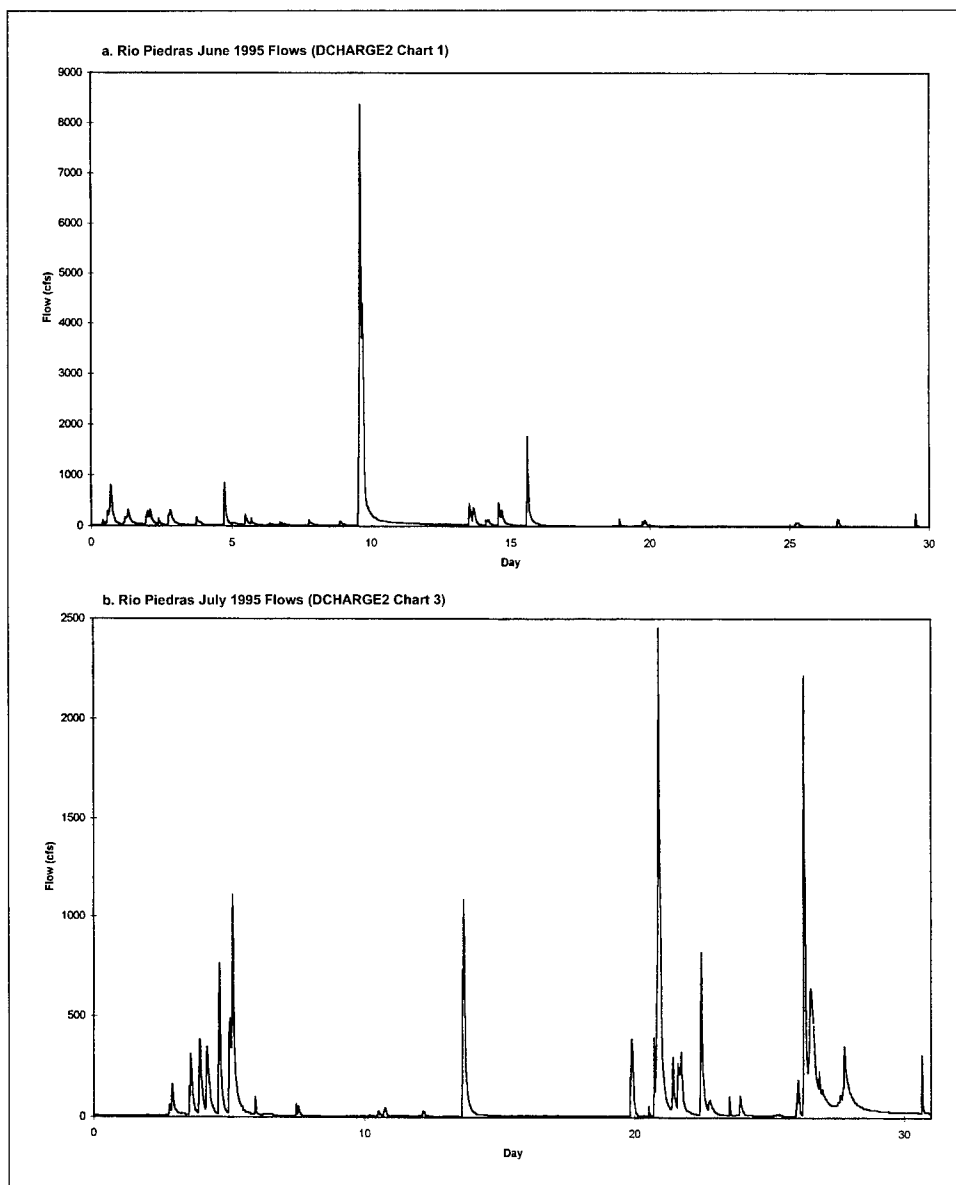


Figure 5-2. Flows observed at Hato Rey, Rio Piedras, June-September 1995 (continued)

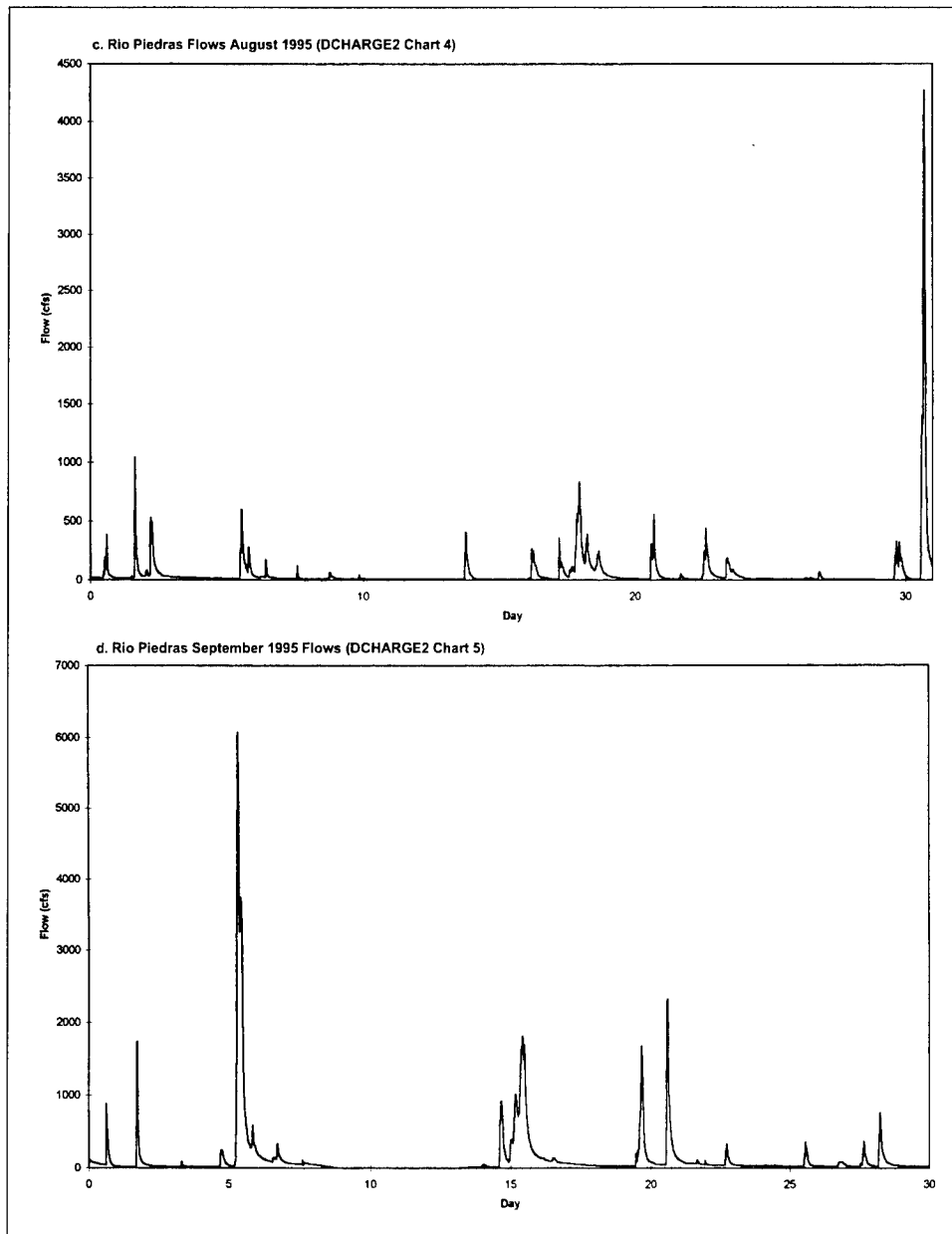


Figure 5-2. (concluded)

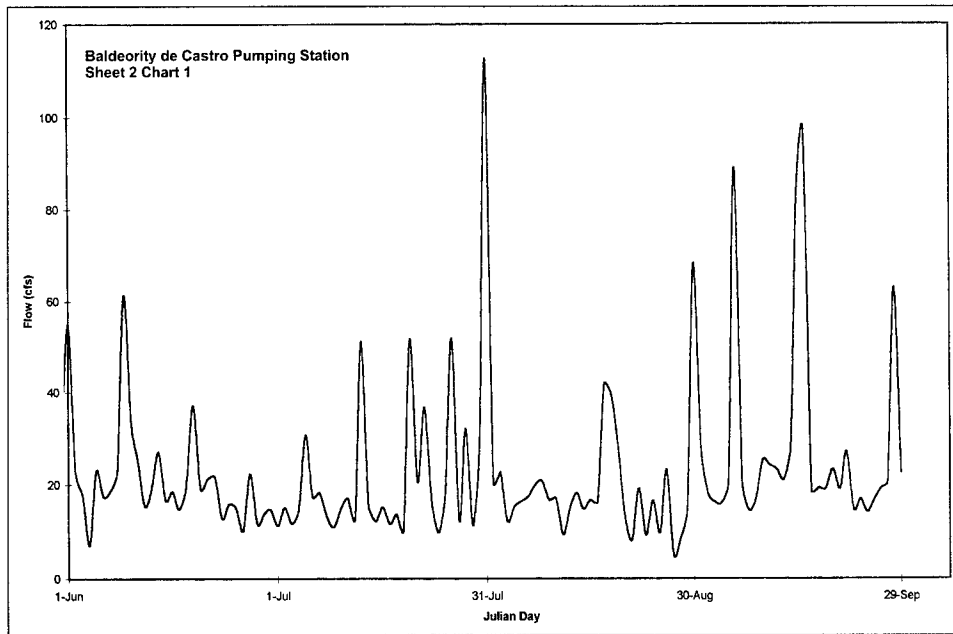


Figure 5-3. Flows for Baldeority de Castro Pump Station computed from pumping records for June-September 1995

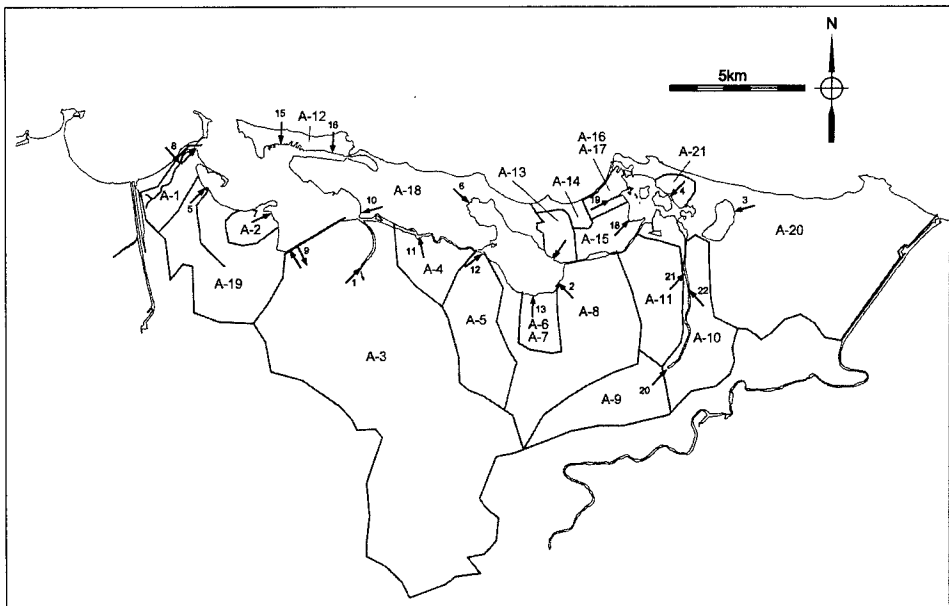


Figure 5-4. Model sub-basins of the San Juan Bay Estuary System with model locations of freshwater inflows indicated by the arrows

**Table 5-2.
SJBE Sub-Basins and Areas**

Sub-basin	Name	Size (mi ²)
A1	Bayamon	1.35
A2	San Fernando	1.0
A3	Rio Piedras	27.1
A4	Martin Peña	2.3
A5	Juan Mèndez	3.2
A6	Unnamed creek sw Laguna San José	0.9
A7	Unnamed creeks Laguna San José	0.9
A8	Quebrada San Antòn	6.8
A9	Quebrada Blasina	2.96
A10	Eastern Blasina	5.3
A11	Western Blasina	3.0
A12	Old San Juan	0.9
A13	Western End of Airport	0.9
A14	Northern End of Airport	0.45
A15	Southern End of Airport	1.35
A16	Eastern End of Airport 1	0.22
A17	Eastern End of Airport 2	0.23
A18	Santurce	5.86
A19	Malaria	6.0
A20	Piñones	13.0
A21	East of Torrecilla	1.0

Using the USGS gaged flow records from Hato Rey and the Baldorioty de Castro Pump Station pumping records, flow relationships were derived for each sub-basin of the watershed. However, prior to the derivation of any flow relationships, the observed flows for the two locations had to be converted to inches per day of runoff. This was accomplished by dividing the equivalent daily volume of flow by the area of the respective sub-basin expressed in square feet. The resulting height of runoff was then converted from ft/day to in./day. Sub-basin area used for the Rio Piedras regression was the area upstream of the USGS flow gage at Hato Rey (15.2 mi²). A contributing area of 1.94 mi² was used for the Baldorioty de Castro sub-basin.

Rainfall records for the calibration period were available from the National Weather Service station at the San Juan International Airport and for a number of USGS rainfall collection stations in the basin. Using rainfall records from the USGS rain gage at Rio Piedras and flow records from the USGS flow gage at Hato Rey, a type II regression was performed to determine a relationship between rainfall and runoff. A similar procedure was followed using pumping records from Baldorioty de Castro Pump Station and National Weather Service rainfall records. The rainfall-runoff

relationships developed for Rio Piedras at Hato Rey and Baldorioty de Castro Pump Station, respectively, are

$$q_p = 0.046 + 0.7468 * \text{rain} \quad (5.1)$$

where

q_p = Rio Piedras flow at Hato Rey, inches/day
rain = daily rainfall observed at the Rio Piedras rain gage,
inches/day

and

$$q_B = 0.232 + 0.9 * \text{rain} \quad (5.2)$$

where

q_B = Baldorioty de Castro Pump Station flow, inches/day
rain = daily rainfall observed at the San Juan International Airport,
inches/day

Figures 5-5 and 5-6 show the relationship between Equations 5.1 and 5.2 and the observed rainfall and flow. The first term in Equations 5.1 and 5.2 represents a base flow and the second a runoff flow. The base flow occurs whether there is any rainfall or not. Runoff flow only occurs when there has been rainfall. The values computed in the above equations are in inches per day of flow which were converted to ft^3/s for each sub-basin by the following relationship

$$Q = 5.093 \times 10^{-3} q A_{\text{Basin}} \quad (5.3)$$

where

A_{Basin} = measured area of sub-basin in mi^2

Initially, Equations 5.1 - 5.3 were used to compute runoff flows for all sub-basins for which there were no observed flows, which included all the sub-basins except for Rio Piedras and the Baldorioty de Castro Pump Station. For Rio Piedras, flows observed at Hato Rey were multiplied by 1.78 to account for contributions from the portion of the watershed below the stream gage.

Refinements were made to several of the other sub-basins after tests with the hydrodynamic model indicated that the predicted inflows were too high to maintain proper salinity. Because water levels and flows through transects compared favorably with measured data, it was assumed that estimated flows were probably too high rather than ocean exchange too low. Inflows for the several sub-basins around Quebrada Blasina and Laguna de Piñones were computed using the SCS Curve Number Method (Mississippi

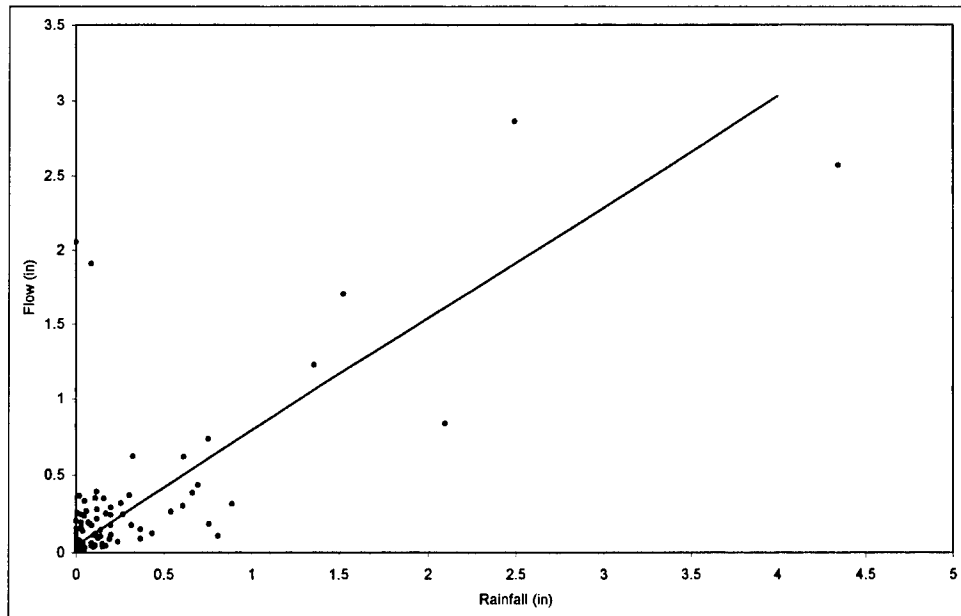


Figure 5-5. Observed flows for Rio Piedras at Hato Rey versus observed rainfall plotted with the best-fit regression line

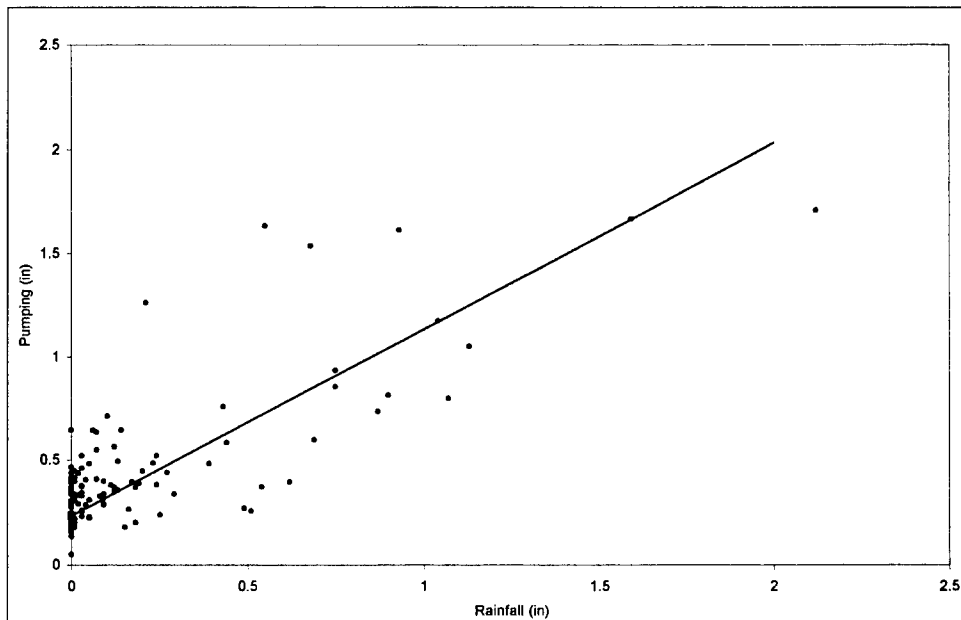


Figure 5-6. Computed flows based on pumping records for Baldorioty de Castro Pump Station versus observed rainfall plotted with the best-fit regression line

Department of Environmental Quality et al. 1994) to estimate runoff flows per unit area (inches/day).

$$q = \frac{\left(\text{rain} + 0.2 * \left(\frac{1000}{CN} - 10 \right) \right)^2}{\text{rain} + 0.8 * \left(\frac{1000}{CN} - 10 \right)} \quad (5.4)$$

where

rain = rainfall at International Airport, inches/day

CN = SCS Curve Number

Curve Numbers were selected based on land use, land cover, and soil type and are shown in Table 5-3. The unit areal flows computed from Equation 5.4 were used with Equation 5.3 to calculate volumetric flows (m³/sec). Rationale for re-computing flows for these basins was twofold. The region east of Piñones is undeveloped and flat and would therefore have a longer retention time and slower response than the developed, hilly Rio Piedras watershed. Secondly, flows for the region surrounding Laguna de Piñones were being over-predicted by the regression developed from the Baldorioty de Castro Pump Station. The Santurce region served by the Baldorioty de Castro Pump Station is a highly developed region of the San Juan metropolitan area. Due to limited infiltration as a result of impervious land cover, this region has a high percentage of runoff (90%). In addition, there is a substantial base flow which is thought to be due to leaking sewer pipes and undocumented sewer connections to the storm-water collection system. Neither the base flow nor the high runoff coefficient for the Baldorioty de Castro regression was appropriate for the Piñones and Blasina sub-basins.

Table 5-3.
SJBE Sub-Basin Curve Numbers

Sub-Basin	Name	SCS Curve Number
A9	Quebrada Blasina	98
A10	Eastern Blasina	98
A11	Western Blasina	98
A13	Western End of Airport	84
A16	Eastern End of Airport 1	86
A17	Eastern End of Airport 2	86
A20	Piñones	76
A21	East of Torrecilla	76

Flows for the remaining regions were analyzed in conjunction with hydrodynamic calibration runs. It became apparent that the estimated inflows were also too high in the interior of the system, specifically San José Lagoon. In order to improve the salinity predictions in San José, base flows for the sub-basins flowing into San José were reduced by 50%. Table 5-4 summarizes the sources of and methods used to obtain runoff for each sub-basin.

Table 5-4.
SJBE Sub-Basin Flow Estimation Methods

Sub-Basin	Name	Method
A1	Bayamon	Rio Piedras Regression
A2	San Fernando	Rio Piedras Regression
A3	Rio Piedras	USGS Observed Flows
A4	Martin Peña	Baldorioty de Castro Regression
A5	Juan Mendez	Baldorioty de Castro Regression
A6	Unnamed creek sw Laguna San José	Baldorioty de Castro Regression
A7	Unnamed creek sw Laguna San José	Baldorioty de Castro Regression
A8	Quebrada San Anton	Baldorioty de Castro Regression
A9	Quebrada Blasina	SCS Curve Number Method
A10	Eastern Blasina	SCS Curve Number Method
A11	Western Blasina	SCS Curve Number Method
A12	Old San Juan	SCS Curve Number Method
A13	Western End of Airport	SCS Curve Number Method
A14	Northern End of Airport	SCS Curve Number Method
A15	Southern End of Airport	SCS Curve Number Method
A16	Eastern End of Airport 1	SCS Curve Number Method
A17	Eastern End of Airport 2	SCS Curve Number Method
A18	Santurce	Baldorioty de Castro Records and Regression
A19	Malaria	Rio Piedras Regression
A20	Piñones	SCS Curve Number Method
A21	East of Torrecilla	SCS Curve Number Method

Runoff Concentrations. Runoff concentrations are required to set tributary boundary concentrations and/or to compute tributary and local runoff loads. Most of the runoff entering into the San Juan estuaries system is not routinely sampled. As a result, the most comprehensive database available for the calibration period was the tributary sampling conducted in conjunction with the open water monitoring study conducted for model calibration (Kennedy et al. 1996). Due to the limited number of observations on any one tributary and the similarity of most of the watershed, the data for all were combined together into a database from which a single average value was determined and used (see Table 5-5) for each constituent concentration. These values were held constant for the duration of the calibration simulation and applied with the following exceptions discussed below to estimate all loads, including tributary inflows, local, storm-water runoff, and storm-water pumping plant discharges. With this approach, loads vary with flow since they are the product of flow and concentration. However,

the limited information on loadings to the system is a major source for model error and uncertainty and a recognized future monitoring need.

Table 5-5.
Uniform Runoff Concentrations

Constituent	Value Used
Temperature, °C	27.9
Salinity, ppt	0.0
Total Suspended Solids, mg/l	12.0
DOC, mg/l	13.2
POC, mg/l	2.0
NH ₄ , mg/l	1.035
NO ₃ , mg/l	0.15
TON, mg/l	0.16
DIP, mg/l	0.23
DOP, mg/l	0.025
POP, mg/l	0.20
DO, mg/l	5.84
Fecal Coliform, mpn/100ml	1.6×10^6

Exceptions to uniform concentrations are presented in Table 5-6. Exceptions included DO concentrations in the flows from Malaria Canal where DO was set to 2.0 mg/l instead of the 5.84 mg/l value used elsewhere (Table 5-5). The highest DO observation in Malaria during the sampling study was 2.53 mg/l, while the lowest was 0.5 mg/l. Malaria is reputed to have poor water quality resulting from sewage overflows and discharges and as such warrants a lower DO concentration. Headwater boundary TSS concentrations on the Rio Piedras were set to 114 mg/l while those on the Quebrada San Anton were set to 57 mg/l. TSS levels in these two streams were much higher than the other tributaries. Chlorophyll loads were introduced for only the sub-basins shown in Table 5-6, whereas for other sub-basins, the chlorophyll load was zero. Finally, fecal coliform bacteria levels for Rio Bayamon were set to 215 mpn/100 ml. This value is the average of the samples collected in that stream. The reason that Rio Bayamon observations were so low is unclear. Rio Bayamon serves as the receptor for cooling water discharges from the Palo Seco Power Plant, one of two power plants in the SJBE System. The intake water for this plant comes from offshore and should have very low levels of fecal coliform. The power plant uses approximately 650×10^6 gal/day or $28.5 \text{ m}^3/\text{s}$ ($1,006 \text{ ft}^3/\text{s}$), which when discharged to the Rio Bayamon would then simply be diluting the upstream fecal coliform levels thereby resulting in the low counts obtained during sampling. Tributary loads for Rio Bayamon were computed using only the computed tributary flow based upon drainage area.

**Table 5-6.
Modified Runoff Concentrations**

Sub-Basin	DO mg/l	TSS mg/l	Chlorophyll $\mu\text{g/l}$	Fecal Coliform mpn/100 ml
Rio Piedras	5.84	112	3.33	1.6×10^6
Malaria	2.0	12	2.5	1.6×10^6
Bayamon	5.84	12	82	215
San Fernando	5.84	12	27	1.6×10^6
Quebrada Blasina	5.84	12	1	1.6×10^6
Runoff into Eastern Blasina	5.84	12	1	1.6×10^6
Runoff into Western Blasina	5.84	12	1	1.6×10^6
Runoff into Caño Martín Peña	5.84	12	4	1.6×10^6
Juan Méndez	5.84	47	3	1.6×10^6
Un-named creeks sw Laguna San José	5.84	12	4	1.6×10^6
Un-named creeks Laguna San José	5.84	12	4	1.6×10^6
Quebrada San Antón	5.84	12	11	1.6×10^6
Runoff into Airport area	5.84	12	4	1.6×10^6
Runoff into Laguna de Piñones	5.84	12	1	1.6×10^6

The second power plant located in the system, the San Juan Power Plant, withdraws and discharges to San Juan Bay near the Military Terminal. The maximum cooling water flow for this facility is 700×10^6 gal/day or $32.8 \text{ m}^3/\text{s}$ ($1159 \text{ ft}^3/\text{s}$). These power plants are treated as a special type of boundary in the WQM. At the intakes, water is removed from the model grid. The water is then returned to the model at the outfall location without any change in water quality other than a temperature increase of 5°C resulting from process unit cooling. Concentrations of other constituents are introduced unchanged at the outfall.

Initial sub-basin loads to the WQM were computed by multiplying the daily flows for each sub-basin by the concentrations for the various constituents indicated in Tables 5-5 and 5-6. It is pointed out that for all sub-basins not indicated in Table 5-6, the uniform concentrations of Table 5-5 were used to compute loads. Additional loads were identified and implemented during calibration and are discussed in Chapter 7.

The model requires that loads of organic carbon, nitrogen, and phosphorus be split into model state variables. These variables represent dissolved organic, labile particulate organic, and refractory particulate organic constituents. Laboratory analyses do not always directly indicate these splits. In that case, values observed in other systems are adapted and refined, if necessary, in the model calibration process.

Dissolved organic carbon (DOC) was directly analyzed. Particulate organic carbon (POC) was obtained by subtracting DOC from total organic carbon. POC was split evenly between labile and refractory fractions. This split includes more labile material than is normally employed. In Chesapeake Bay, for example, the split is 10% labile and 90% refractory. More labile material was required in San Juan to create oxygen demand and match observed low dissolved oxygen concentrations in system bottom waters. The split suggests loads to the SJBE system contain more fresh organic matter (algal, raw sewage) than runoff to temperate estuaries.

Total organic nitrogen (TON) was obtained by subtracting ammonium from total Kjeldahl nitrogen (TKN). Guidance for splitting TON into dissolved and particulate forms was obtained from ammonium and TKN data collected in receiving waters adjacent to tributaries. The split was 10% dissolved and 90% particulate. Particulate organic nitrogen was split evenly into labile and refractory fractions, consistent with the splits for POC.

The majority of phosphorus observations in the tributaries were of total phosphorus (TP) and total dissolved phosphorus (TDP). Roughly 20% of the observations also included dissolved inorganic phosphorus (DIP) and particulate inorganic phosphorus (PIP). The DIP measures were used to guide specification of DIP in the loads. Subtraction of DIP from TDP yielded concentration of dissolved organic phosphorus (DOP) for use in the model. Subtraction of TDP from TP yielded total particulate phosphorus. The total particulate phosphorus included labile and refractory organic particles as well as particulate inorganic particles. PIP contains mineral forms that are not biologically available. Since the model does not include detailed representation of PIP chemistry, PIP is assigned to the refractory particulate organic fraction. Consequently, the split of particulate phosphorus into labile and refractory fractions included more refractory matter than for carbon or nitrogen. The splits used in the model were 12.5% labile and 87.5% refractory.

6 Hydrodynamic Model Adjustment and Skill Assessment

As previously discussed, a field data collection effort provided data for boundary conditions as well as interior data for comparison with model results (Fagerburg 1998). Water-surface elevations, salinity, and water-velocity data were collected at several locations throughout the system during June-August 1995. Both long-term as well as short-term data were collected. The short-term data were collected over 17-19 August 1995 when the crew returned to remove the long-term instruments. These data included ADCP data collected over several ranges in an attempt to define the water flux through the connecting canals of the system. Due to fouling of the long-term meters, very little useful long-term velocity and salinity data were obtained. Most salinity data employed were collected by Kennedy et al. (1996) during their collection of water quality data. Locations of data stations used in the skill assessment of CH3D are shown in Figure 6-1. Assessing the ability of the numerical model to simulate the hydrodynamics of the system has primarily revolved around reproducing the observed tides throughout the system, reproducing the extreme stratification in salinity that often exists during storm events, and reproducing the net flux through Caño Martín Peña and Canal Suárez.

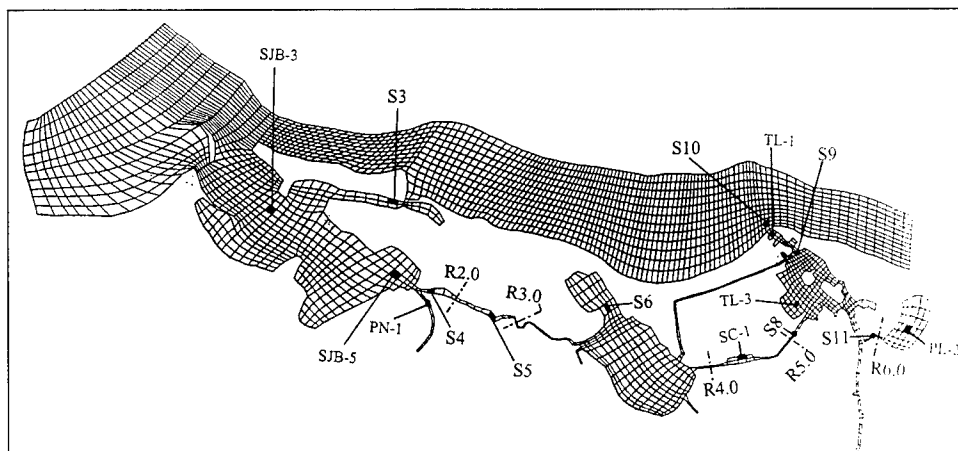


Figure 6-1. Location of data stations

Tide Reproduction

As illustrated in Figure 3-6, the tide in San Juan Harbor is mixed, with the M2 component being the largest. To better illustrate comparisons of the observed and computed tides throughout the system, comparisons for a three-day period in July 1995 are shown in Figures 6-2 - 6-6. It can be seen that the range and phase are reproduced fairly well, with phase errors on the order of perhaps 30 minutes occurring in some places. Figure 6-7 shows the computed and observed tide at a station in Laguna San José. The extreme reduction in the tide in Laguna San José as a result of the constriction in the eastern end of Martín Peña Canal and a bridge constriction in Canal Suárez is clearly illustrated. Obviously, there is little tidal flushing of Laguna San José, resulting in the poor water quality observed there.

Table 6-1 shows a comparison of the M2 and O1 computed and observed harmonic components of the tides at stations in San Juan Bay, Laguna San José, Laguna La Torrecilla, and Laguna de Piñones. Phasing is relative to the tide in San Juan Harbor. The letter **R** stands for the ratio of the ranges and **L** is the lag in phase in hours. It can be seen that the greatest reduction is in the higher frequency components. This agrees with the analytical analysis for a simplified co-oscillating system. Generally the comparison of the computed constituents with those determined from the observed data is good.

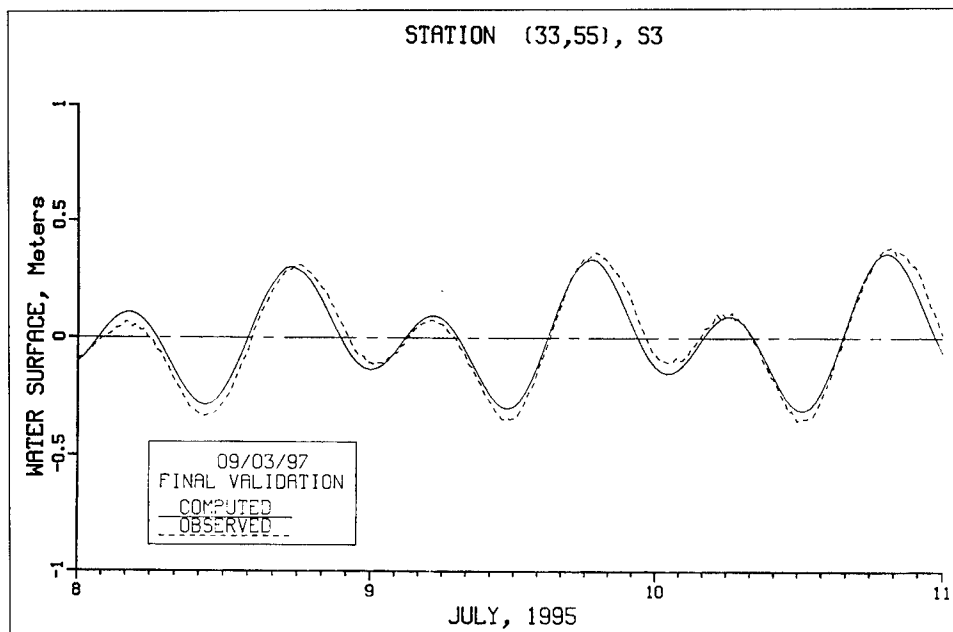


Figure 6-2. Comparison of computed and observed tide at S3

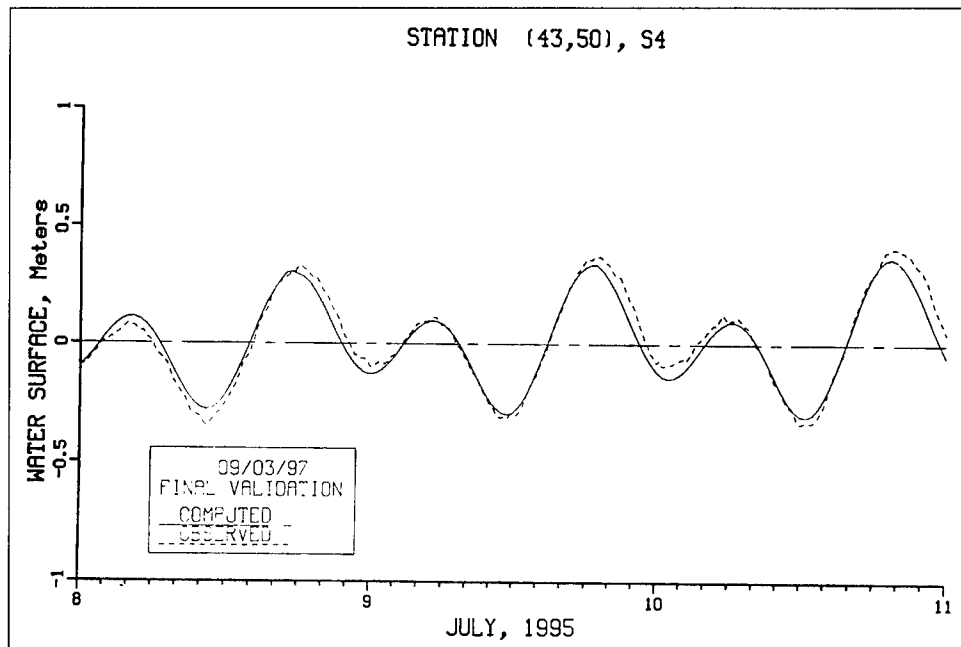


Figure 6-3. Comparison of computed and observed tide at S4

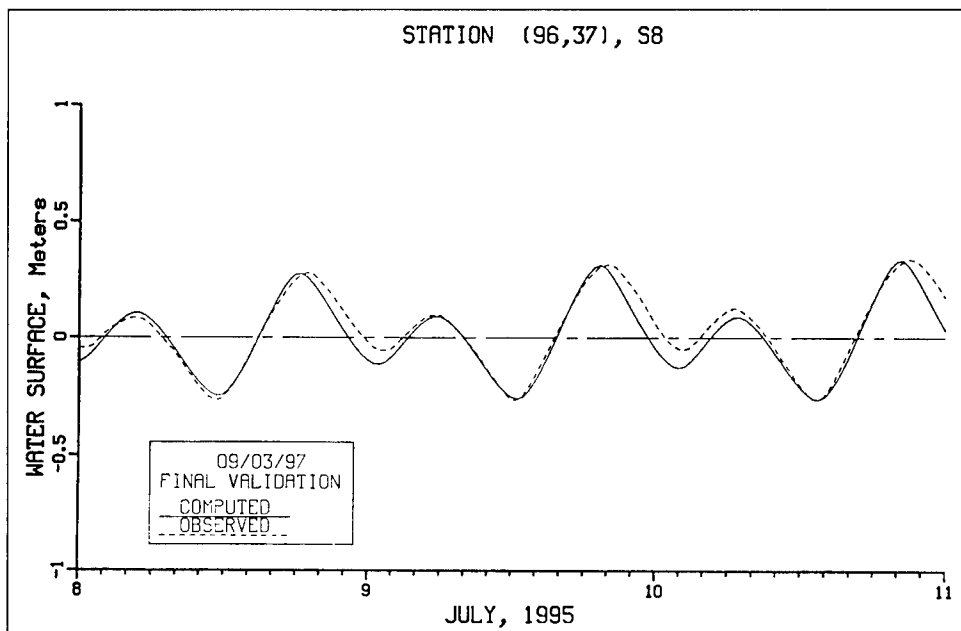


Figure 6-4. Comparison of computed and observed tide at S8

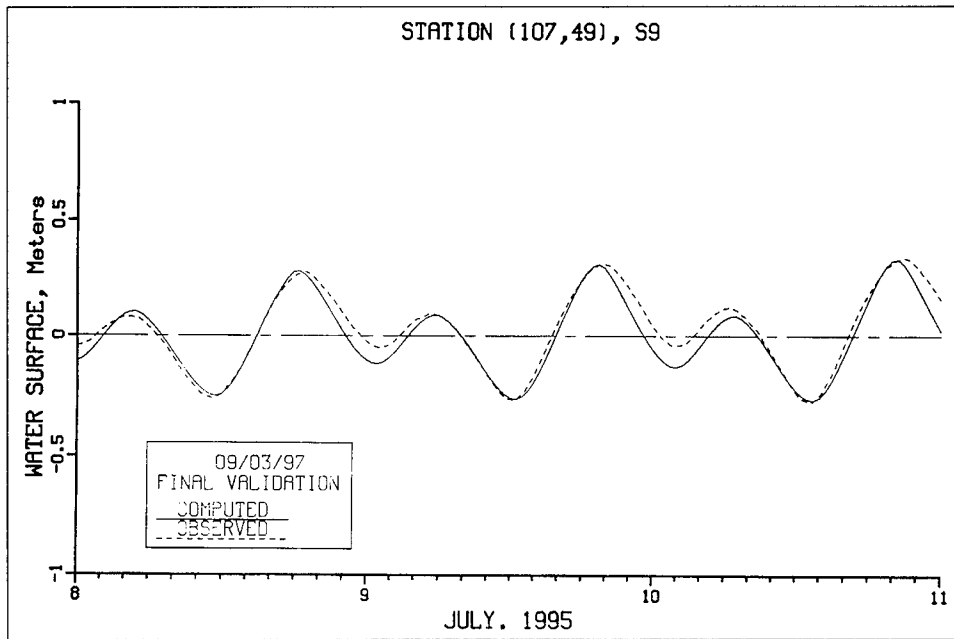


Figure 6-5. Comparison of computed and observed tide at S9

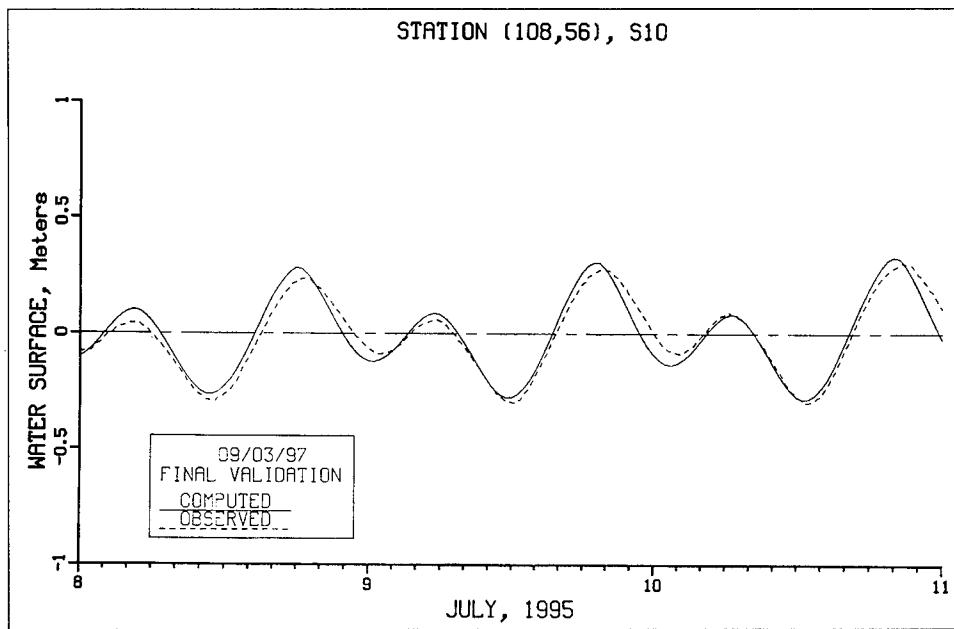


Figure 6-6. Comparison of computed and observed tide at S10

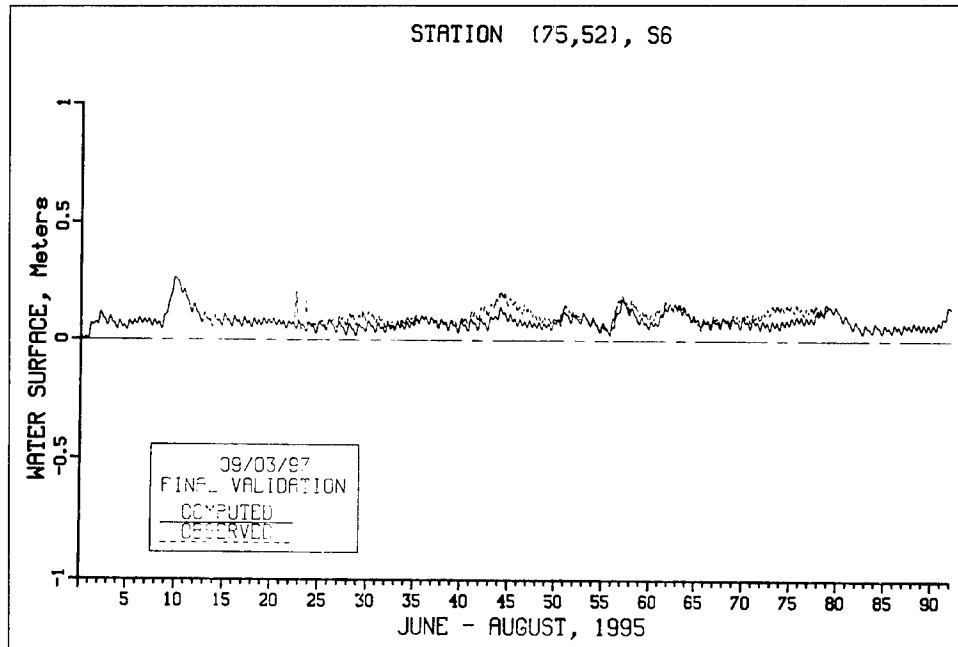


Figure 6-7. Comparison of computed and observed tide at S6

Table 6-1.
Comparison of Harmonic Constituents of Tide Relative to
San Juan Bay Tide

Location	M2				O1			
	Model		Data		Model		Data	
	R	L	R	L	R	L	R	L
San José	0.06	3.69	0.06	3.85	0.16	5.42	0.10	6.47
Torrecilla	0.90	0.37	0.81	0.41	0.92	0.64	0.87	0.83
Piñones	0.12	4.01	0.12	3.67	0.23	6.01	0.23	6.18

Salinity Reproduction

The numerical model was run for the period 1 June - 31 August 1995. Boundary forcings are presented and discussed in Chapter 3. Although initial conditions on water-surface elevation and water velocity aren't too important since the effect of those initial conditions are flushed from the system within a few tidal cycles, the specification of the initial salinity field is much more important. Model stability was fairly sensitive to the initial salinity prescribed. In previous applications of CH3D, this behavior has not been observed. To overcome this problem, the model was initiated with a constant salinity over the entire grid and run for the month of June. The computed salinity field was then saved and used as the initial salinity field in all subsequent simulations for the entire three months. This

procedure yielded an initial salinity field that was close to observed data and resulted in a stable model.

Figures 6-8 through 6-19 show the ability of the numerical model to reproduce salinity throughout the system. In most plots, both near-surface salinity (layer 30) and near-bottom (layers less than 30) are shown. However, in some locations the depth is so shallow, e.g., Station S6 in Laguna San José (Figure 6-13), that only near-surface salinity is presented. An inspection of the salinity plots reveals that the Kennedy data (Kennedy et al. 1996) are the primary salinity data available for skill assessment. Due to fouling of the long-term meters in the tropical waters of the SJBE system, most of the salinity data from those meters weren't useful. Figure 6-15 which shows a comparison of salinity at Station S8 collected by a long-term meter with model results is an example. Some salinity data collected during the 17-19 August short-term survey were of use, e.g., see Figure 6-11.

During periods of high freshwater inflow, a freshwater lens of 30-60 cm flows on the surface of some portions of the system, resulting in high salinity stratification. An example of this occurring can be observed in the western end of Martín Peña Canal. Field data show that the surface salinity is reduced to 5-10 ppt with salinity near the bottom being greater than 30 ppt. Figure 6-10 illustrates the model's ability to reproduce this extreme stratification after a large freshwater inflow event (relative to other flows during the study period) that occurred around the 9th of June (see Figure 3-4 showing the freshwater inflows). Note that the Kennedy data displayed in the salinity plots labeled near surface (layer 30) were collected at 0.5 m and 1.0 m, whereas the model results correspond to the middle of the top layer, which varies in thickness with the tide. The observed extreme stratification is reproduced well in the numerical model even though each layer in the vertical is 0.91 m thick.

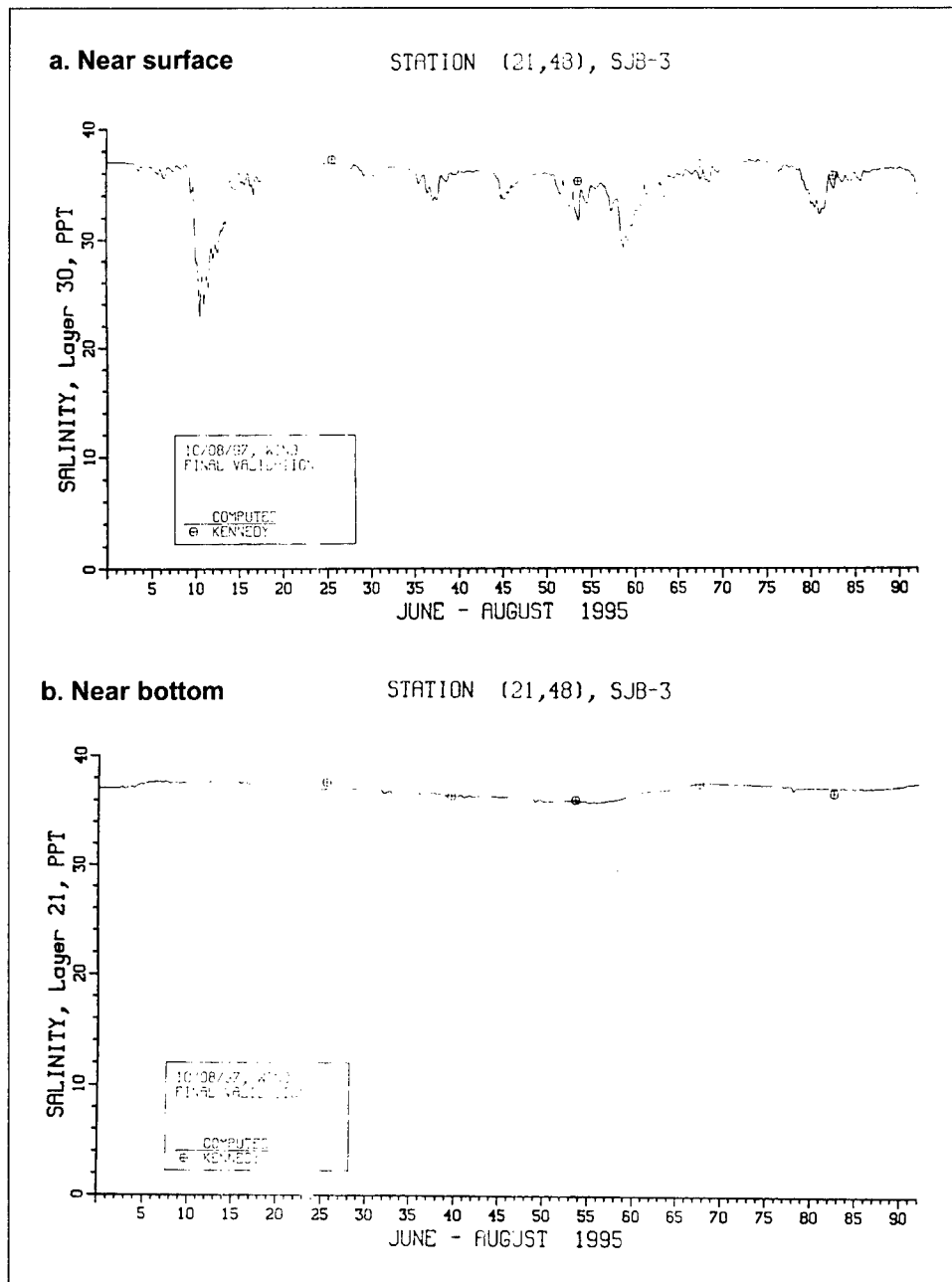


Figure 6-8. Comparison of computed and observed salinity at SJB-3

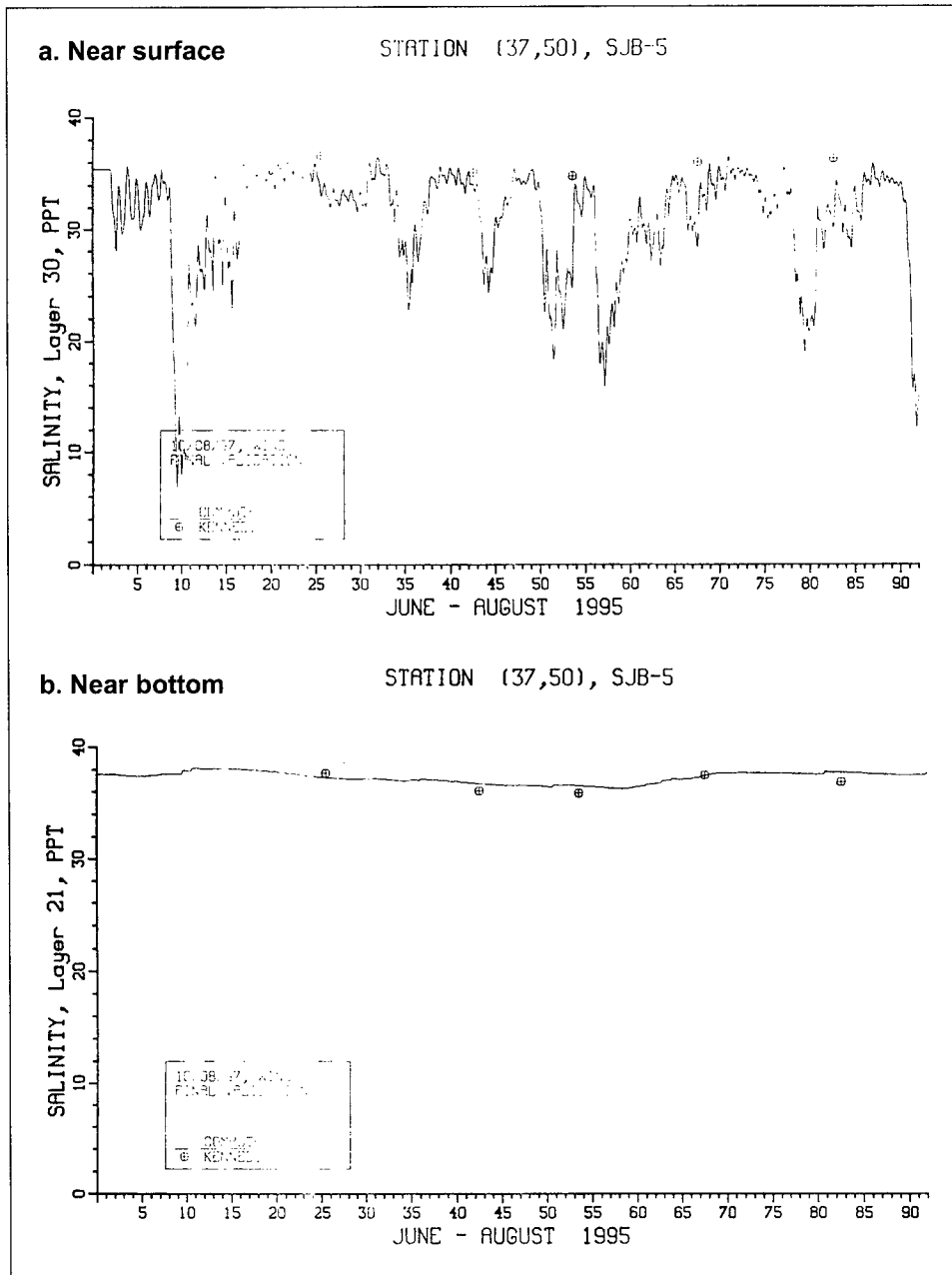


Figure 6-9. Comparison of computed and observed salinity at SJB-5

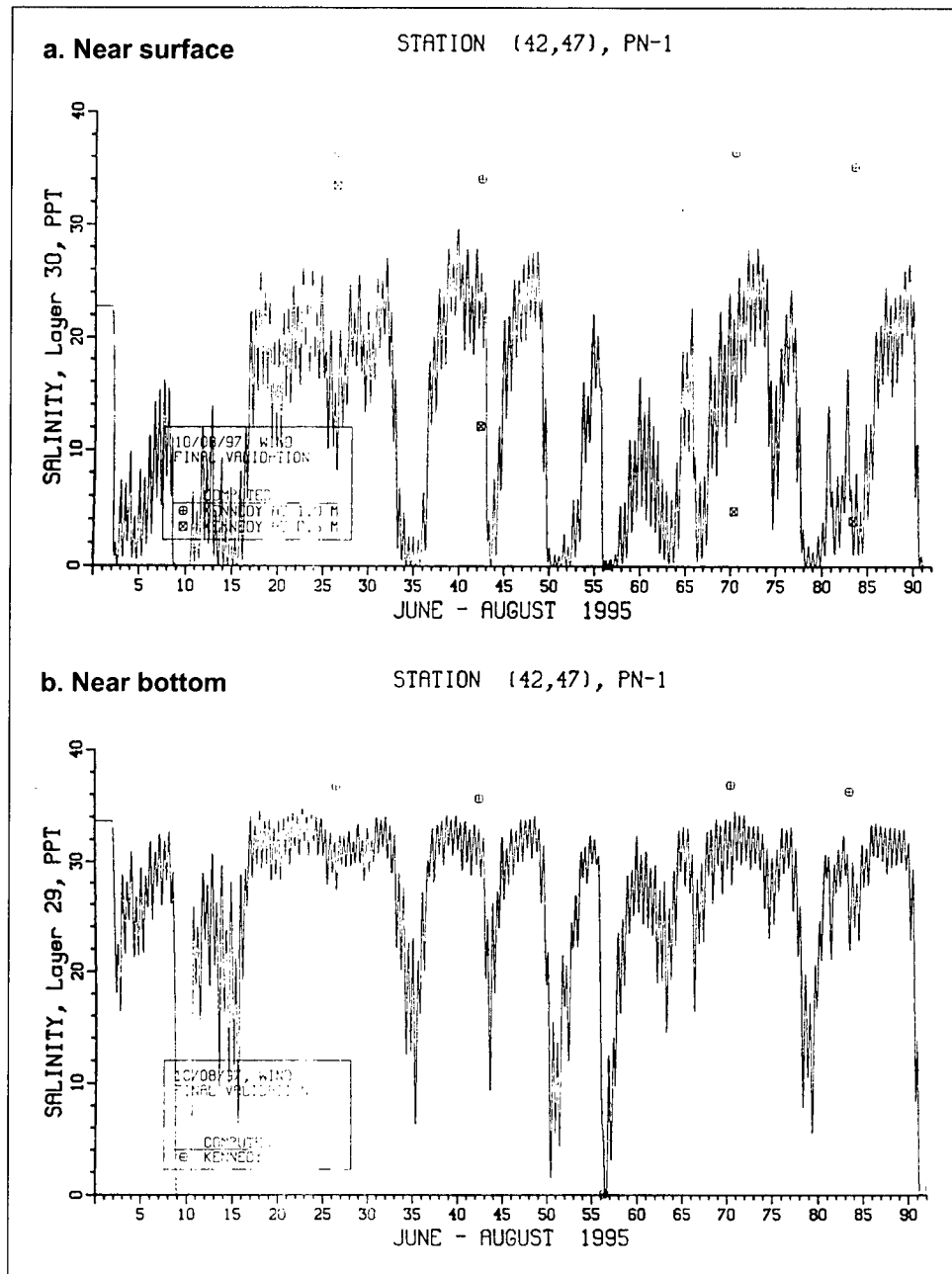


Figure 6-10. Comparison of computed and observed salinity at PN-1

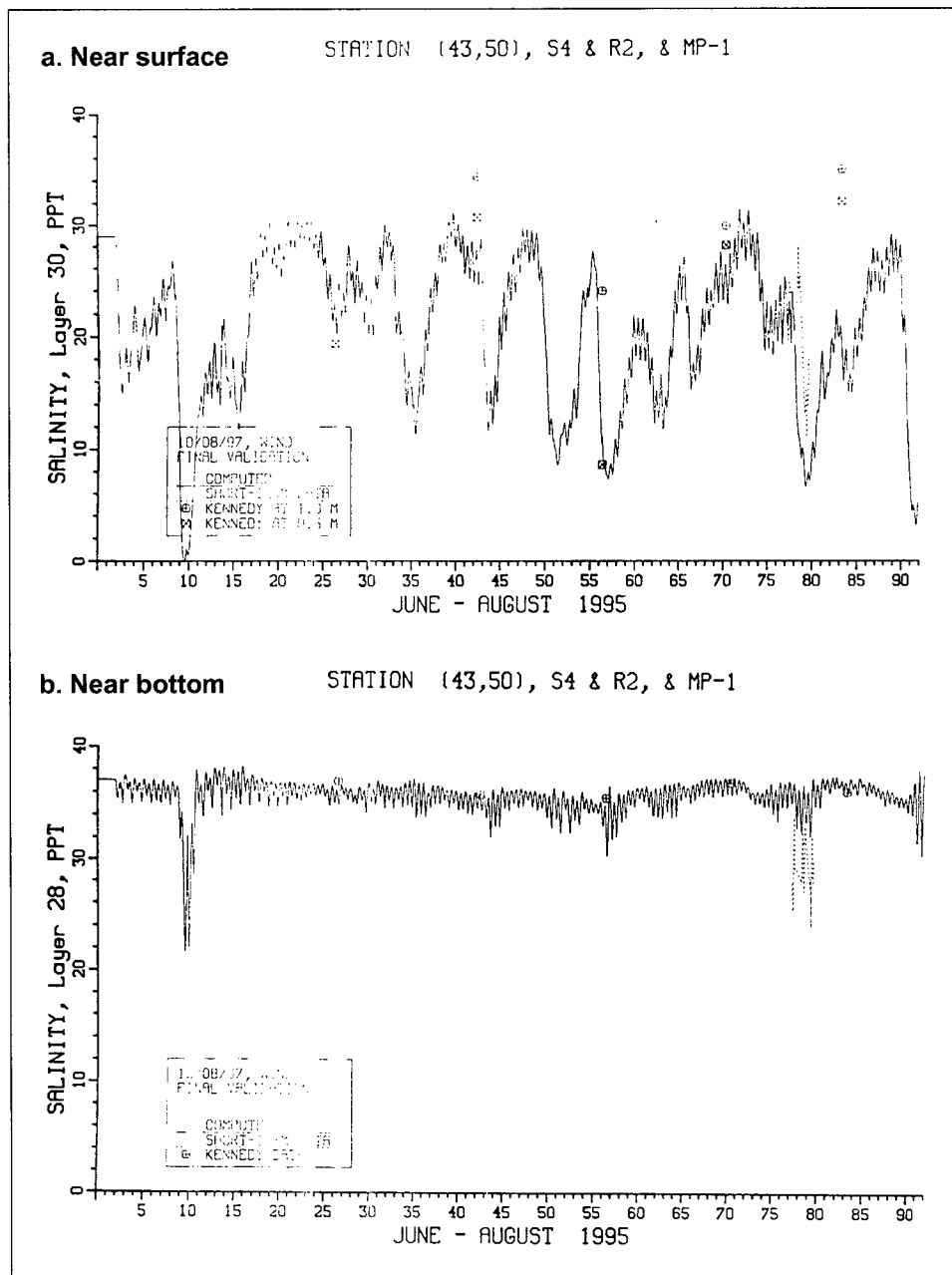


Figure 6-11. Comparison of computed and observed salinity at S4

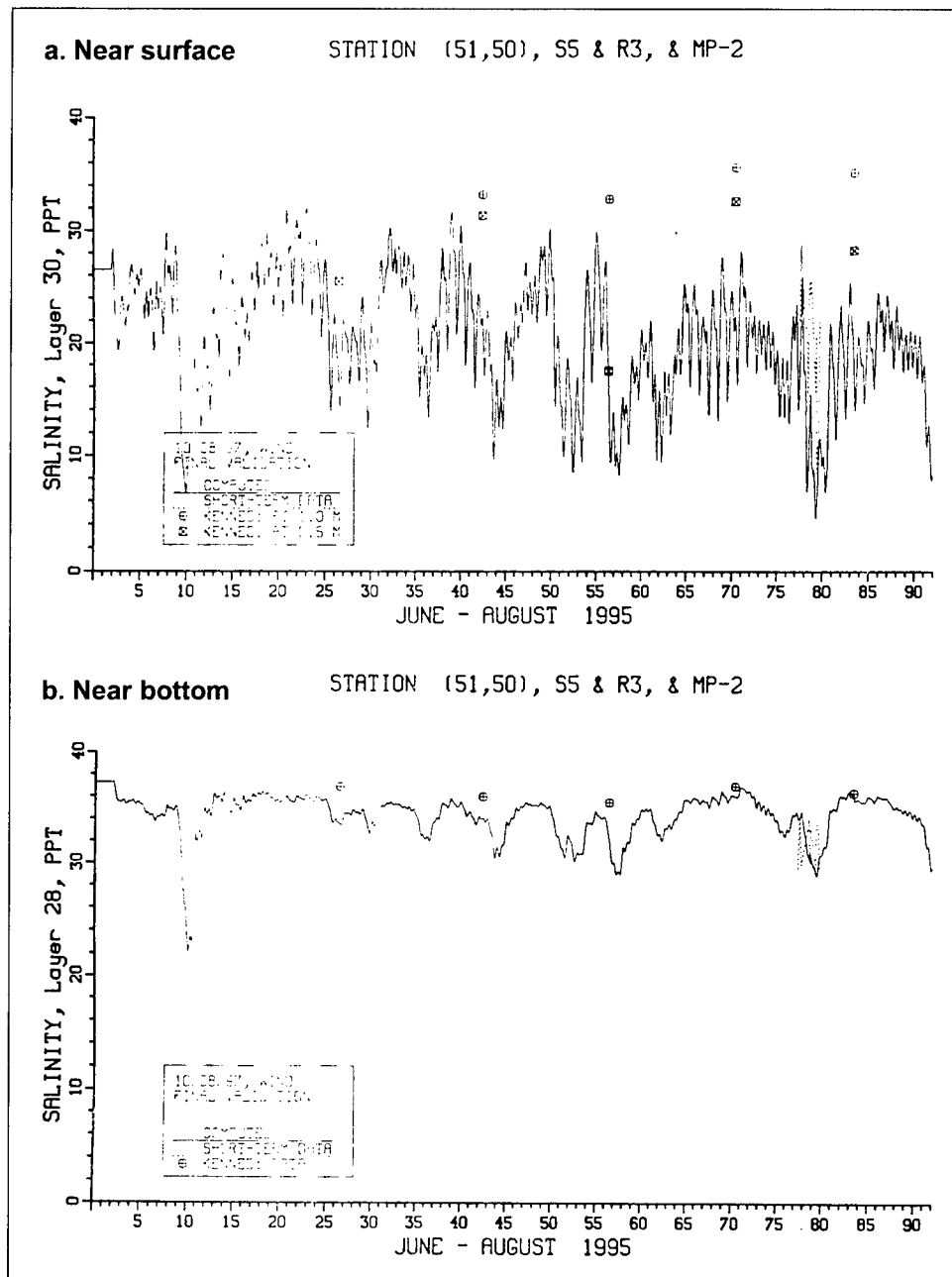


Figure 6-12. Comparison of computed and observed salinity at S5

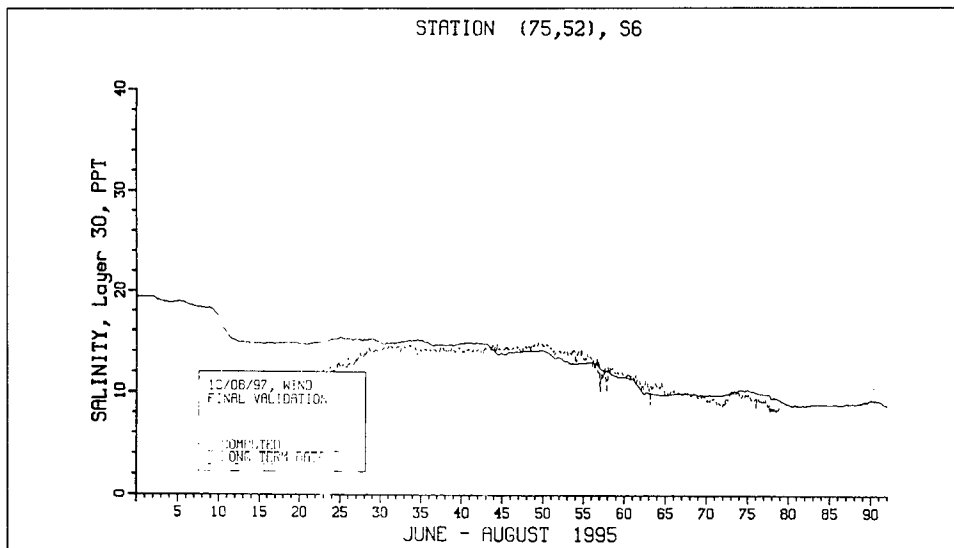


Figure 6-13. Comparison of computed and observed salinity at S6

Reproduction of the Exchange Between Canals

An important component of the skill assessment of the model is the illustration that the model can accurately compute the exchange between the various lagoons, especially the exchange between San Juan Bay and Laguna San José and between Laguna La Torrecilla and Laguna San José since this will have a major impact on water quality computations in Laguna San José and the viability of various management strategies to improve flushing. Figures 6-20 through 6-22 show the computed flux at the eastern end of Martín Peña Canal, the western end of Canal Suárez and between Laguna La Torrecilla and Laguna de Piñones. Total flux volumes in cubic meters for the entire three months have been computed and are shown on the plots. The net flux through Caño Martín Peña is about 1/4 of that through Canal Suárez and is directed toward San Juan Bay, whereas the flux through Canal Suárez is directed toward Torrecilla. The net flux through the Torrecilla - Piñones canal is directly into Torrecilla. These fluxes, of course, represent the sum of the net freshwater inflows into the various lagoons minus the volume of water evaporated. An evaporation rate of 82 in./yr was assumed in the computations.

The bounds on flux determined from a USGS survey (Ellis et. al. 1976) over one tidal cycle in 1974 are superimposed on the plots. It can be seen that the computed bounds in Canal Suárez and the Torrecilla - Piñones canal agree with the USGS data quite well. The bounds on the computed flux through Martín Peña Canal don't agree as well, but conditions in the eastern end of Martín Peña are different from those that existed in 1974. Significant sedimentation and the disposal of debris has occurred in this part of the system since 1974, resulting in the eastern end of Caño Martín Peña becoming clogged. As a result, special model adjustments were necessary as discussed in the next section.

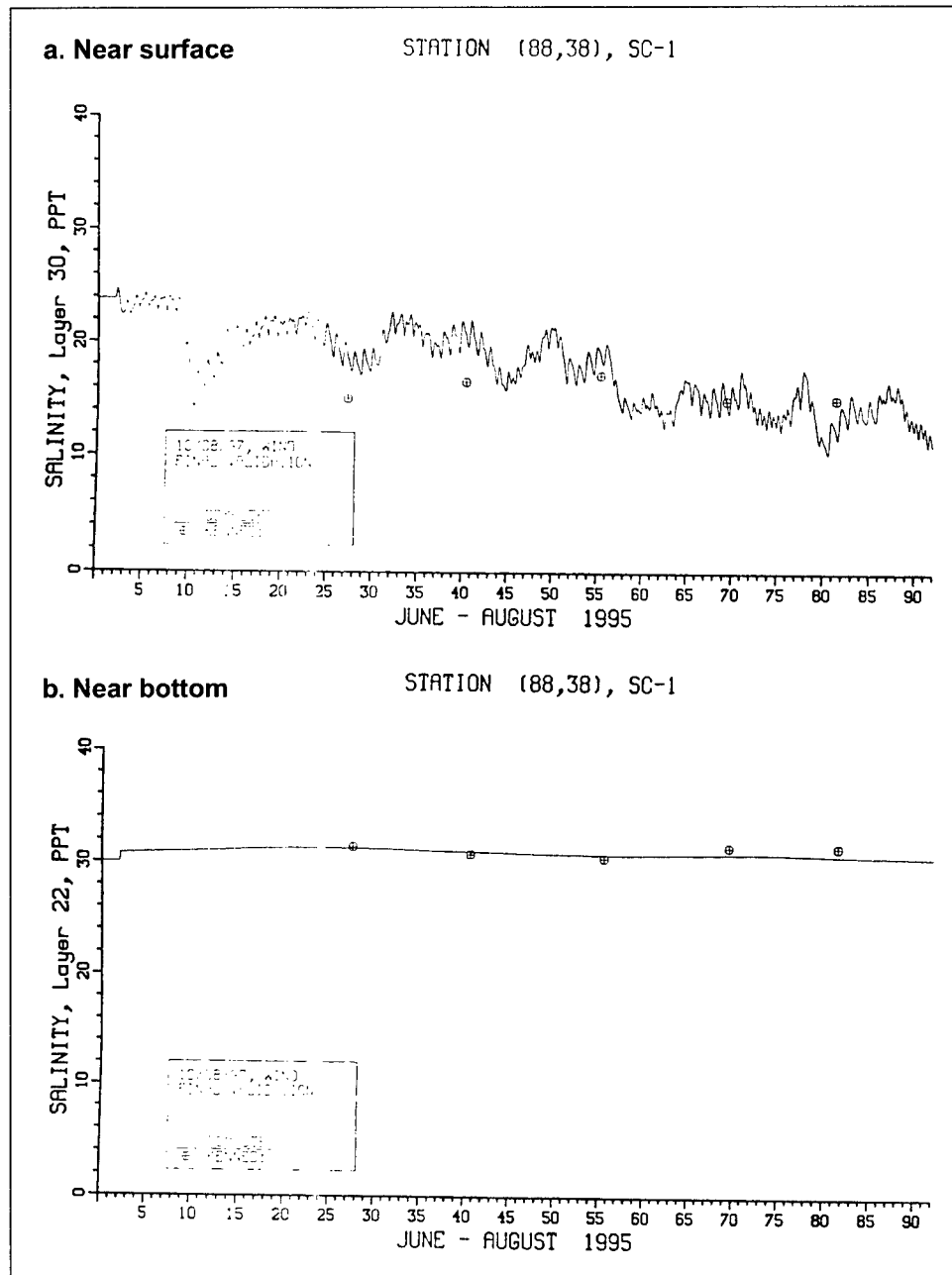
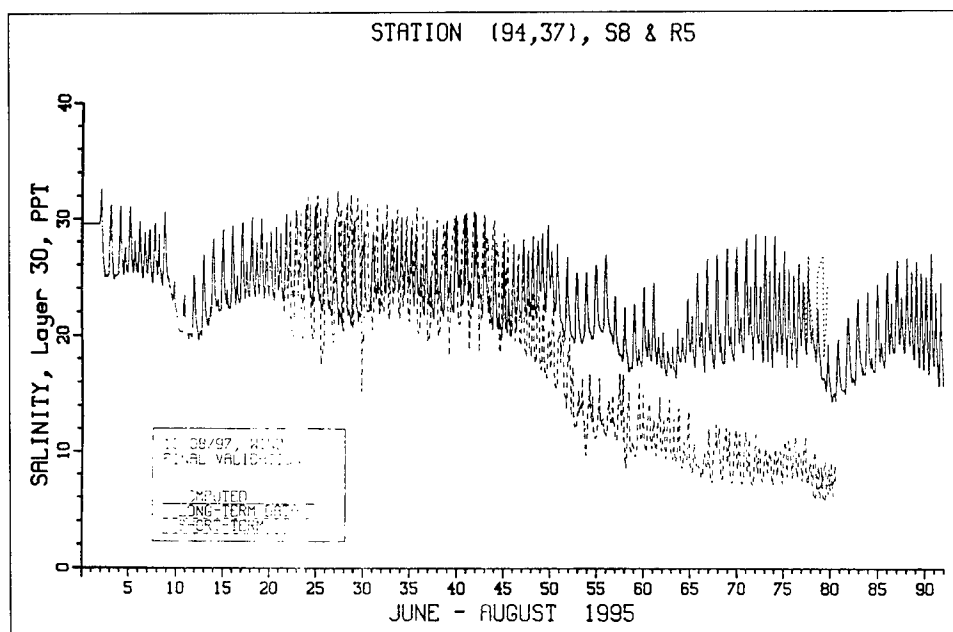


Figure 6-14. Comparison of computed and observed salinity at SC-1



Figures 6-23 through 6-25 show comparisons of computed flux in Martín Peña Canal, Canal Suárez, and the Torrecilla-Piñones canal with the flux determined from the ADCP data collected during 17-19 August 1995. Generally the agreement is quite good and, with the USGS data agreement, increases confidence that the hydrodynamic model computes the proper exchange between the various bodies of water comprising the SJBE system.

Model Coefficients

The only model parameters available for variation during skill assessment of the hydrodynamic model are the bottom friction, or drag coefficient, horizontal diffusion coefficient, and minimum and maximum values of the vertical diffusion coefficients for momentum and salinity. The value of the bottom drag coefficient was set to 0.002 throughout most of the system. The major exception was in the eastern end of Caño Martín Peña and the canal connecting Torrecilla and Laguna de Piñones. As previously discussed, the eastern end of Martín Peña is severely constricted with debris such as old refrigerators that have been dumped into the canal over the past few years. Values of the bottom drag coefficient specified in these areas were 0.0075 and 0.0040, respectively.

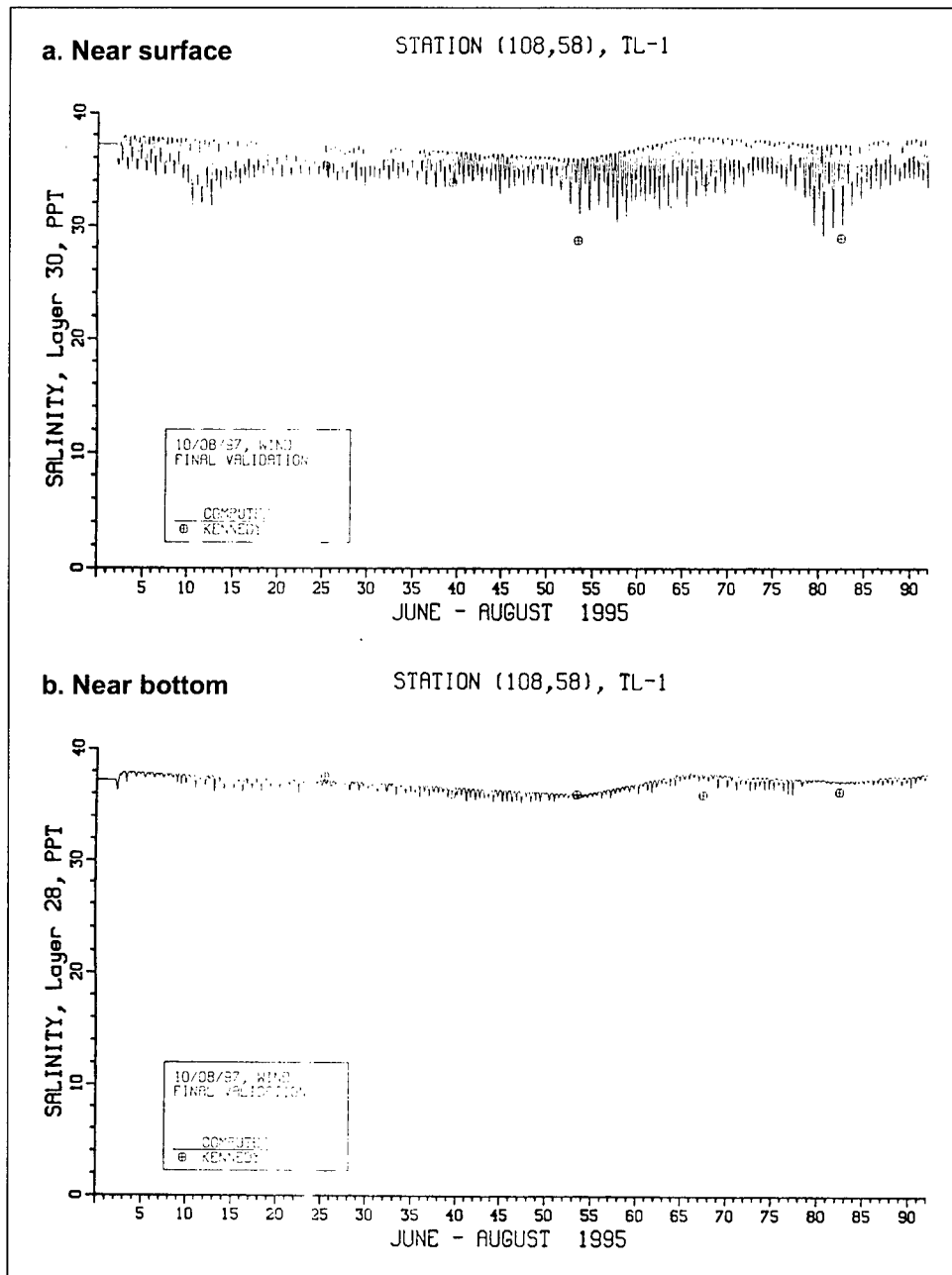


Figure 6-16. Comparison of computed and observed salinity at TL-1

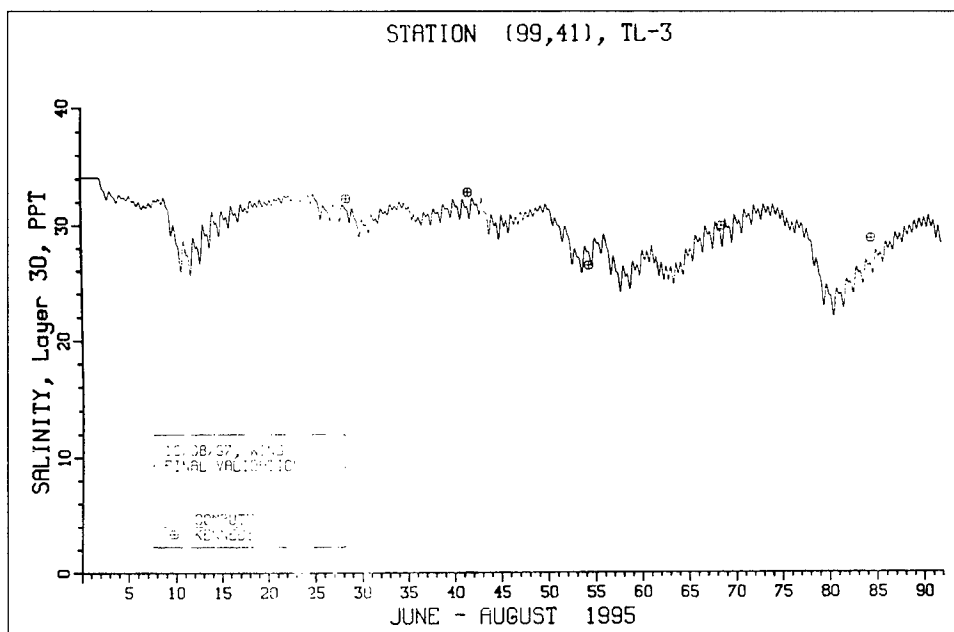


Figure 6-17. Comparison of near surface computed and observed salinity at TL-3

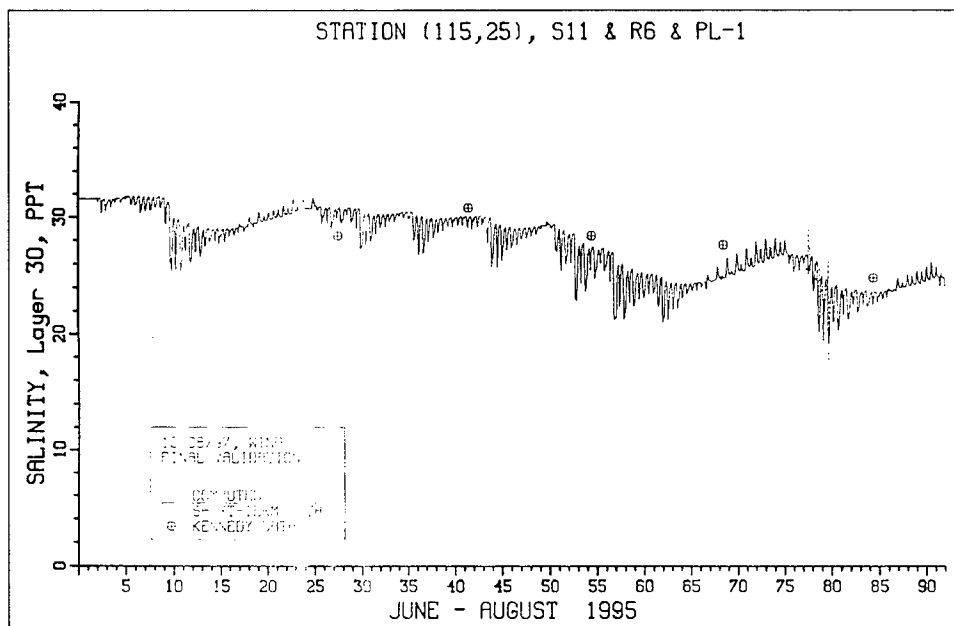


Figure 6-18. Comparison of near surface computed and observed salinity at PL-1

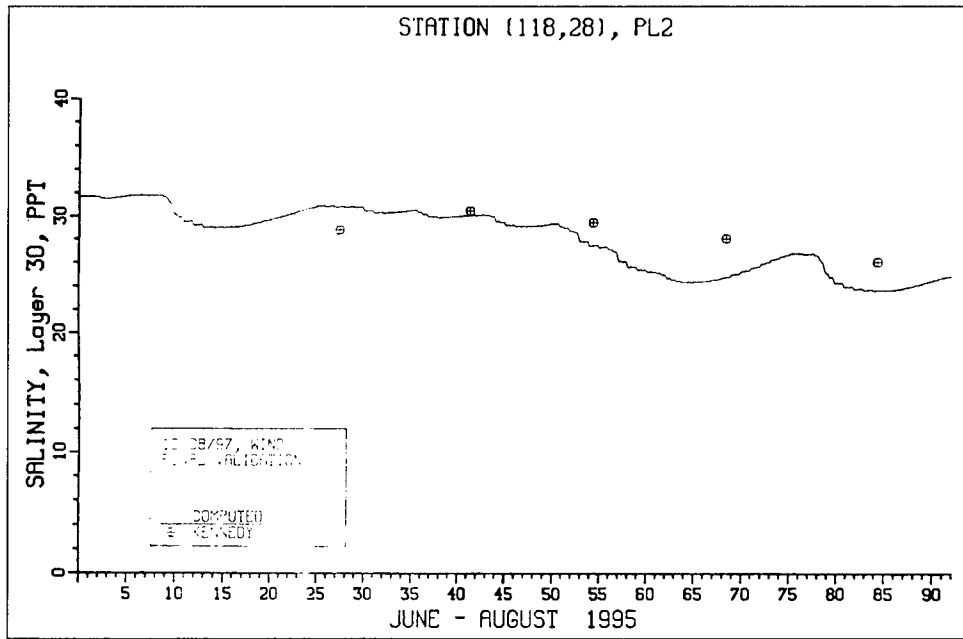


Figure 6-19. Comparison of near surface computed and observed salinity at PL-2

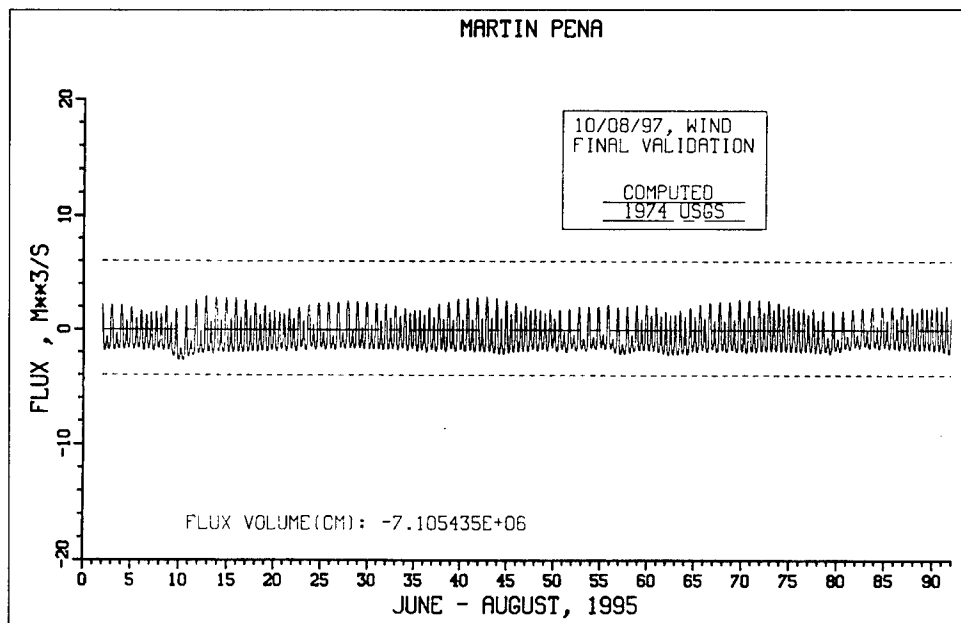


Figure 6-20. Computed flux through Martin Pena Canal compared with USGS data

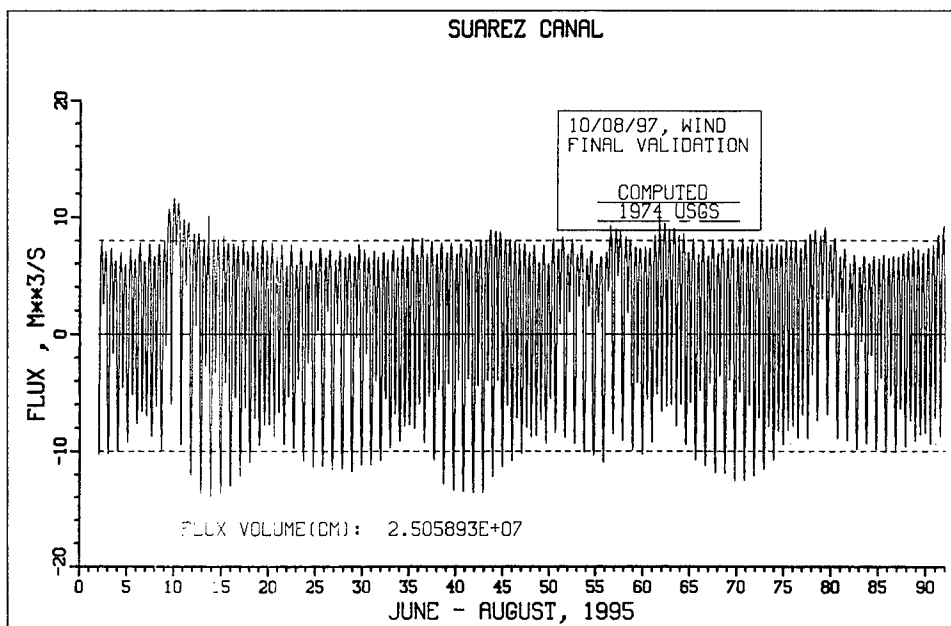


Figure 6-21. Computed flux through Suarez Canal compared with USGS data

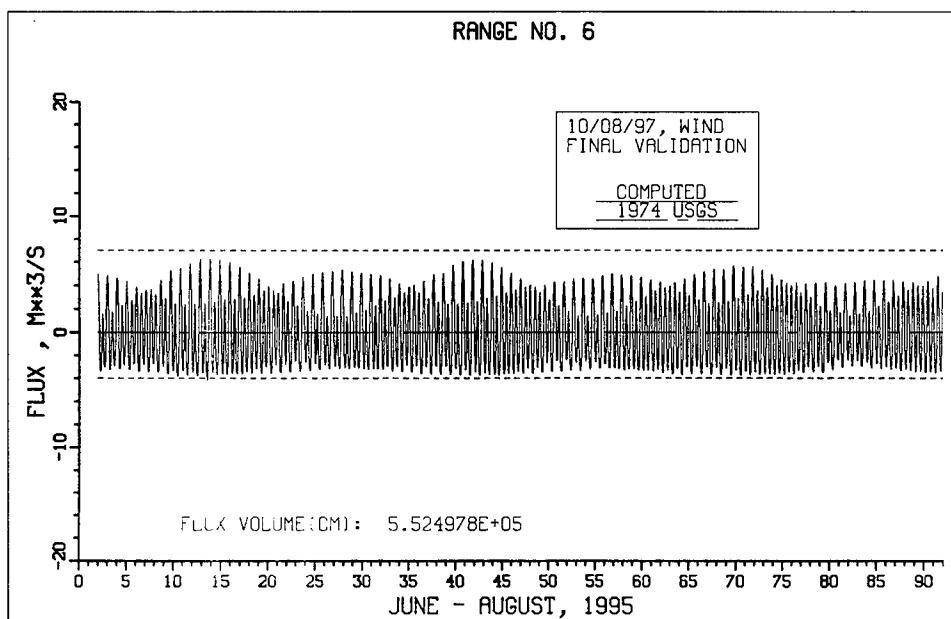


Figure 6-22. Computed flux through Torrecilla - Pinones Canal compared with USGS data

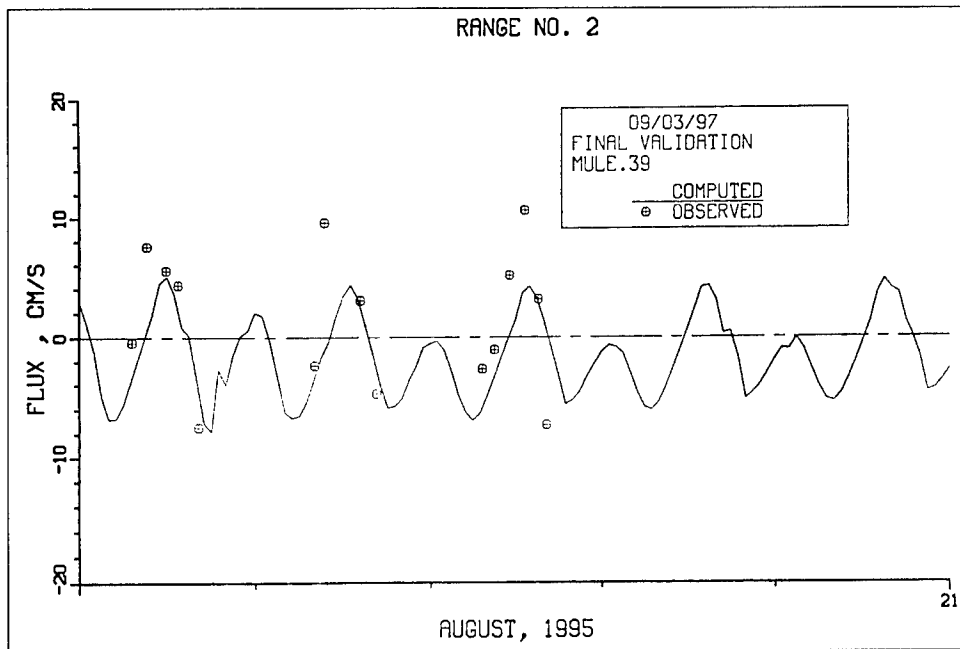


Figure 6-23. Comparison of computed flux at Range 2 with flux determined from ADCP data

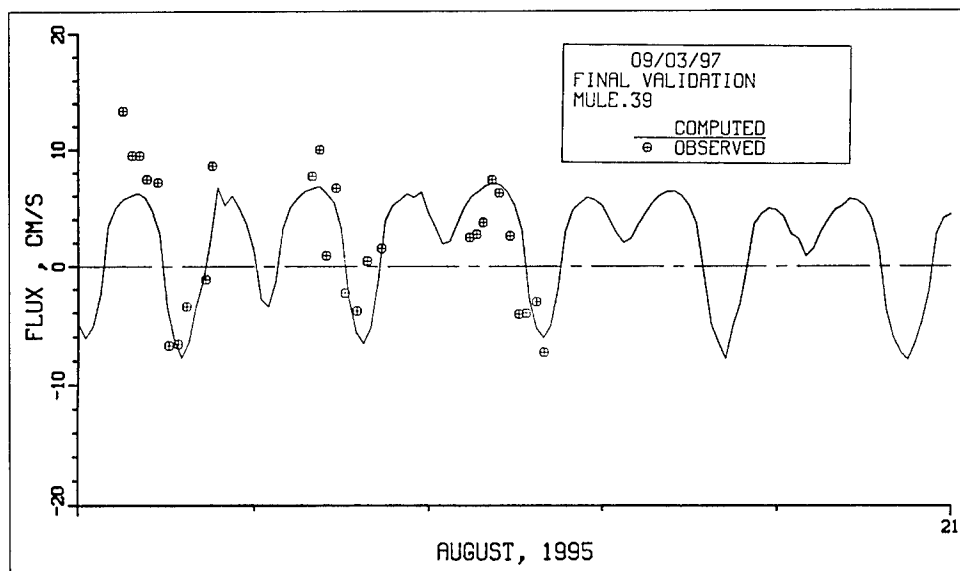


Figure 6-24. Comparison of computed flux at Range 4 with flux determined from ADCP data

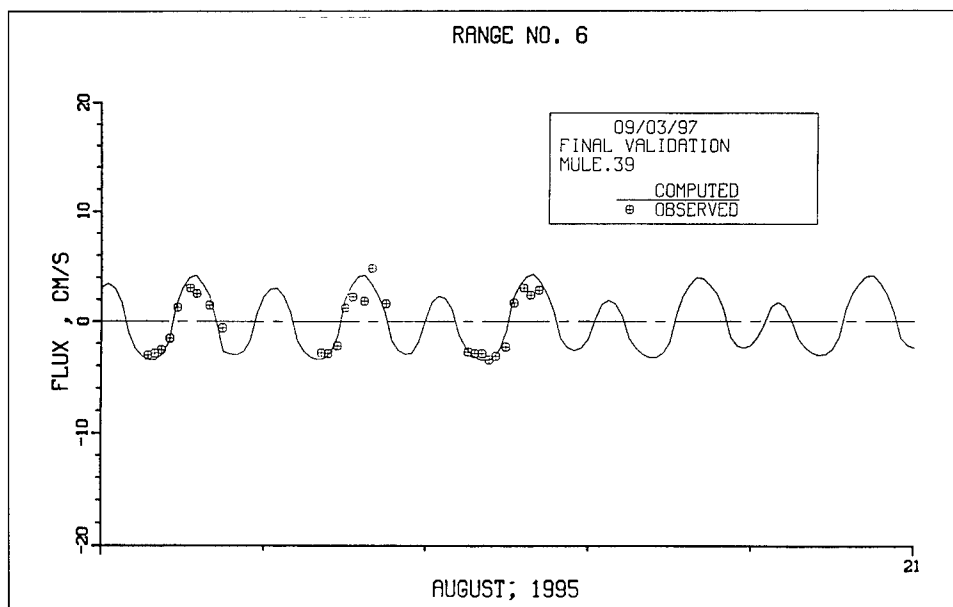


Figure 6-25. Comparison of computed flux at Range 6 with flux determined from ADCP data

The horizontal diffusion coefficient is the same in both horizontal directions. The value selected was $10 \text{ m}^2/\text{sec}$. This value is typical of values employed in other studies as well as values reported in the literature by other modelers.

With the coefficients in the vertical turbulence k-e model being considered as universal coefficients, the only parameters available for variation are the bounds on the computed vertical eddy viscosity and diffusion coefficients. The minimum values specified for the vertical viscosity and vertical diffusivity were 5 and $0.001 \text{ cm}^2/\text{sec}$, respectively, whereas, the maximum value for both was set to $500 \text{ cm}^2/\text{sec}$. These minimum and maximum limits are the same as previously employed in a study on Chesapeake Bay (Johnson et. al. 1991).

Conclusions

Skill assessment of the hydrodynamic model focused on illustrating the ability of the model to reproduce tides throughout the SJBE system; to reproduce the salinity throughout the modeled system, with particular focus on reproducing the extreme stratification that develops during storm events; and to properly compute the exchange of water between the various lagoons in the system. Although data for comparison with the model were limited due to fouling of the long-term meters by the warm tropical waters of the SJBE system, enough data were available to create confidence that the hydrodynamic model reproduces the basic hydrodynamics of the SJBE system so that model results can be used to provide transport for the water quality model.

7 Water Quality Model Calibration and Skill Assessment

The purpose of calibration is to demonstrate that the model can adequately simulate observed conditions. Once this is done, then the model can be used as a predictive tool to determine what effect a proposed action might have. Over 50 simulations were made during calibration. During these simulations, kinetic coefficients were adjusted within accepted tolerances, estimated loads were reviewed and adjusted if necessary, and new processes were added to the WQM. The results presented here represent the culmination of the knowledge gained during the 50 plus calibration simulations. Listed in Table 7-1 are values for the calibration parameters described in Chapter 4 and Table 4-2.

The period 1 June through 31 August 1995 was used for WQM calibration. Model calibration was assessed via plots of model output and observed data. Scatter plots of model output and observed data provide an indication of overall model performance. Calibration period-average longitudinal transect plots were used during calibration as they are indicative of model performance at a variety of locations during the simulation. Time-series plots for selected locations demonstrate the WQM output agreement with observations in specific locations over time.

**Table 7-1.
Parameter Values**

Symbol	Value	Units
AANOX	0.5	
ANC	0.167	gm N gm ⁻¹ C
AOCR	2.67	gm O ₂ gm ⁻¹ C
AONT	4.33	gm O ₂ gm ⁻¹ N
ANDC	0.933	gm N gm ⁻¹ C
APCmin	0.01	gm P gm ⁻¹ C
APCmax	0.024	gm P gm ⁻¹ C

(Sheet 1 of 3)

Table 7-1. (Continued)

Symbol	Value	Units
BMr	0.01	day ⁻¹
BPR	0.215	day ⁻¹
CChl	60	gm C mg ⁻¹ chl
FCD	0.0	0 ≤ FCDx ≤ 1
FCDP	0.1	0 ≤ FCDP ≤ 1
FCLP	0.55	0 ≤ FCLP ≤ 1
FCRP	0.35	0 ≤ FCRP ≤ 1
FNI	0.0	0 ≤ FNix ≤ 1
FNIP	0.0	0 ≤ FNIP ≤ 1
FND	1.0	0 ≤ FNDx ≤ 1
FNDP	0.1	0 ≤ FNDP ≤ 1
FNL	0.0	0 ≤ FNLx ≤ 1
FNLP	0.55	0 ≤ FNLP ≤ 1
FNR	0.0	0 ≤ FNRx ≤ 1
FNRP	0.35	0 ≤ FNRP ≤ 1
FPD	1.0	0 ≤ FPDx ≤ 1
FPDP	0.5	0 ≤ FPDP ≤ 1
FPI	0.0	0 ≤ FPI ≤ 1
FPIP	0.2	0 ≤ FPIP ≤ 1
FPL	0.0	0 ≤ FPLx ≤ 1
FPLP	0.2	0 ≤ FPLP ≤ 1
FPR	0.0	0 ≤ FPRx ≤ 1
FPRP	0.1	0 ≤ FPRP ≤ 1
FR	5.6	m ⁻³ gm ⁻¹ C day ⁻¹
Ih	50	Langley's day ⁻¹
Kcod	30	day ⁻¹
Kdc	0.025 to 0.25	day ⁻¹
Kdcalg	0.0	m ³ gm ⁻¹ C day ⁻¹
Kdn	0.2 to 2.0	day ⁻¹
Kdnalg	0.0	m ³ gm ⁻¹ C day ⁻¹
Kdp	0.05	day ⁻¹
Kdpalg	0.2	m ³ gm ⁻¹ C day ⁻¹
Keb	0.09 to 2.8	m ⁻¹
Kechl	0.029	m ² mg ⁻¹
Kfc	5.0	day ⁻¹
KHn	0.01	gm N m ⁻³
KHndn	0.1	gm N m ⁻³
KHnnt	1.0	gm N m ⁻³
KHocod	0.5	gm O ₂ m ⁻³
KHodoc	0.5	gm O ₂ m ⁻³
KHomb	2.0	gm O ₂ m ⁻³
KHont	1.0	gm O ₂ m ⁻³

(Sheet 2 of 3)

Table 7-1. (Concluded)		
Symbol	Value	Units
KHp	0.001	gm P m ⁻³
KHr	0.5	gm O ₂ m ⁻³
Klc	0.15 to 1.5	day ⁻¹
Klcalg	0.0	m ³ gm ⁻¹ C day ⁻¹
Kln	0.3 to 3.0	day ⁻¹
Klnalg	0.0	m ³ gm ⁻¹ C day ⁻¹
Klp	0.075	day ⁻¹
Klpalg	0.0	m ³ gm ⁻¹ C day ⁻¹
Kr	2.44	m day ⁻¹
Krc	0.005	day ⁻¹
Krcalg	0.0	m ³ gm ⁻¹ C day ⁻¹
Krn	0.005	day ⁻¹
Krnalg	0.0	m ³ gm ⁻¹ C day ⁻¹
Krp	0.005	day ⁻¹
Krpalg	0.0	m ³ gm ⁻¹ C day ⁻¹
KTb	0.069	°C ⁻¹
KTcod	0.041	°C ⁻¹
KTg1	0.008	°C ⁻²
KTg2	0.01	°C ⁻²
KThdr	0.069	°C ⁻¹
KTmhl	0.069	°C ⁻¹
KTnt1	0.09	°C ⁻²
KTnt2	0.09	°C ⁻²
MBGM	0.0 to 0.16	gm C m ⁻²
NTm	0.07 to 0.7	gm N m ⁻³ day ⁻¹
PM	3.0	day ⁻¹
PO ₄ dmax	0.01	gm P m ⁻³
Tm	30	°C
Tmnt	30	°C
Tr	30	°C
Trcod	23	°C
Trhdr	20	°C
Trmnl	20	°C
WSl	0.3	m day ⁻¹
WSr	0.3	m day ⁻¹
WSa	0.05	m day ⁻¹
(Sheet 3 of 3)		

Scatter Plots

Figure 7-1 contains calibration period scatter plots. The locations of circles indicate the correlation between model predictions and observed data. A perfect match between model and observed data is indicated by the diagonal line on each graph. Circles above the line indicate that the model is overpredicting for that observation. Circles below the line indicate that the model is underpredicting the observation. Observations used in these plots were typically obtained by means of a grab sample or in situ measurement and reflect the conditions in the water column at that instant. Model outputs used in these plots are the daily averages of the constituents of interest in cells corresponding to the sample site location. Some of the scatter in these plots can be attributed to the phasing resulting from comparison of instantaneous observations with daily average model results. Shown with each plot are the mean error (ME), absolute mean error (AME), root mean square (RMS) error, and relative error (RE) which is expressed as percent.

The mean error is a summary of the model tendency to overestimate or underestimate the observed data. Mean error can be zero even though large discrepancies exist in individual model-data comparisons. Mean error is computed as follows:

$$ME = \frac{\sum(O - P)}{n} \quad (7-1)$$

where

ME = mean error

O = observation

P = model prediction

n = number of observations

The absolute mean error is a measure of the average discrepancy between observations and model results. No differentiation is made between overestimation or underestimation. Absolute mean error is computed as follows:

$$AME = \frac{\sum|O - P|}{n} \quad (7-2)$$

where

AME = absolute mean error

The root mean square error is an indication of the average discrepancy between observations and model results. It is computed as follows:

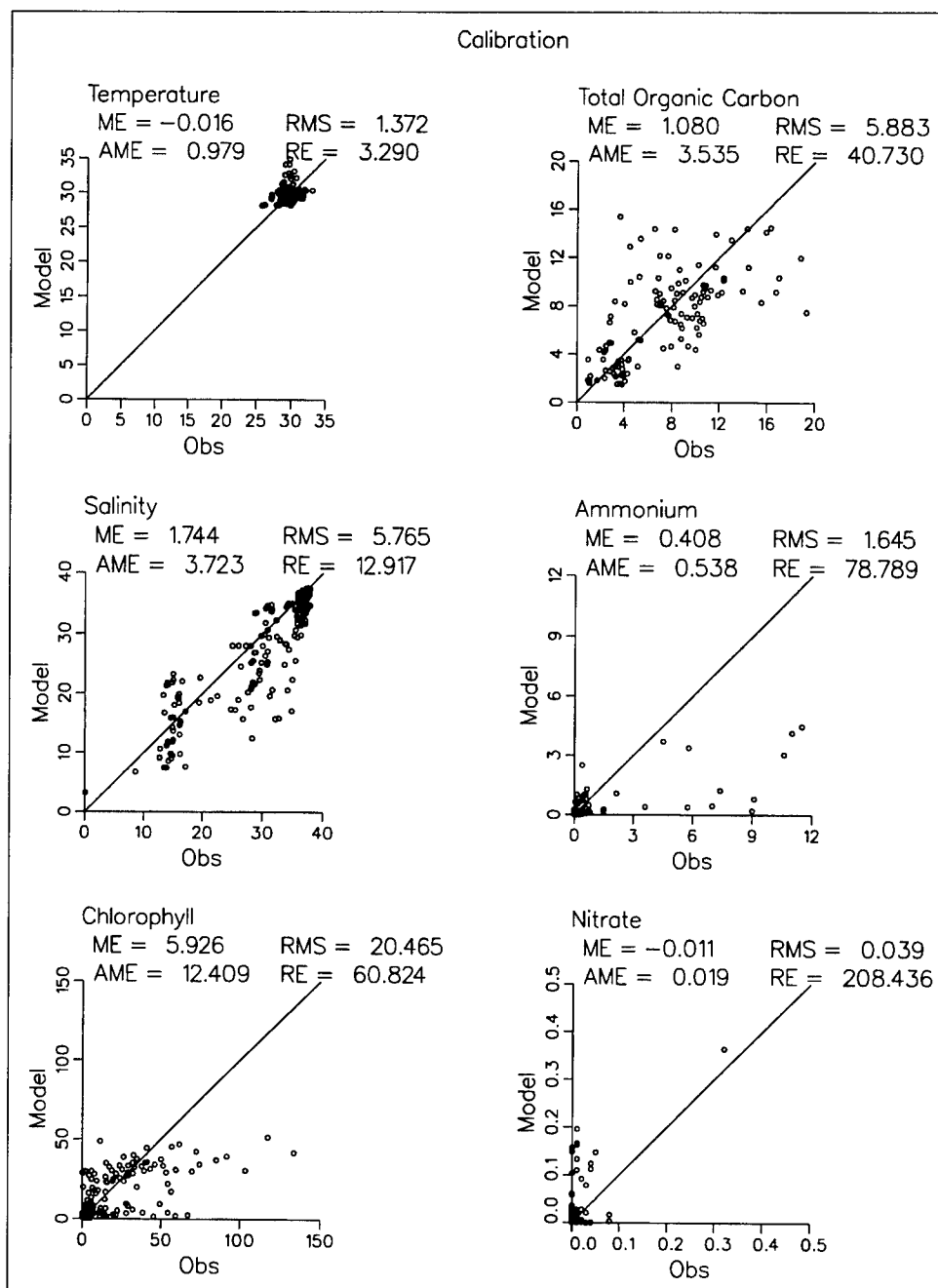


Figure 7-1. Calibration period scatter plots (continued)

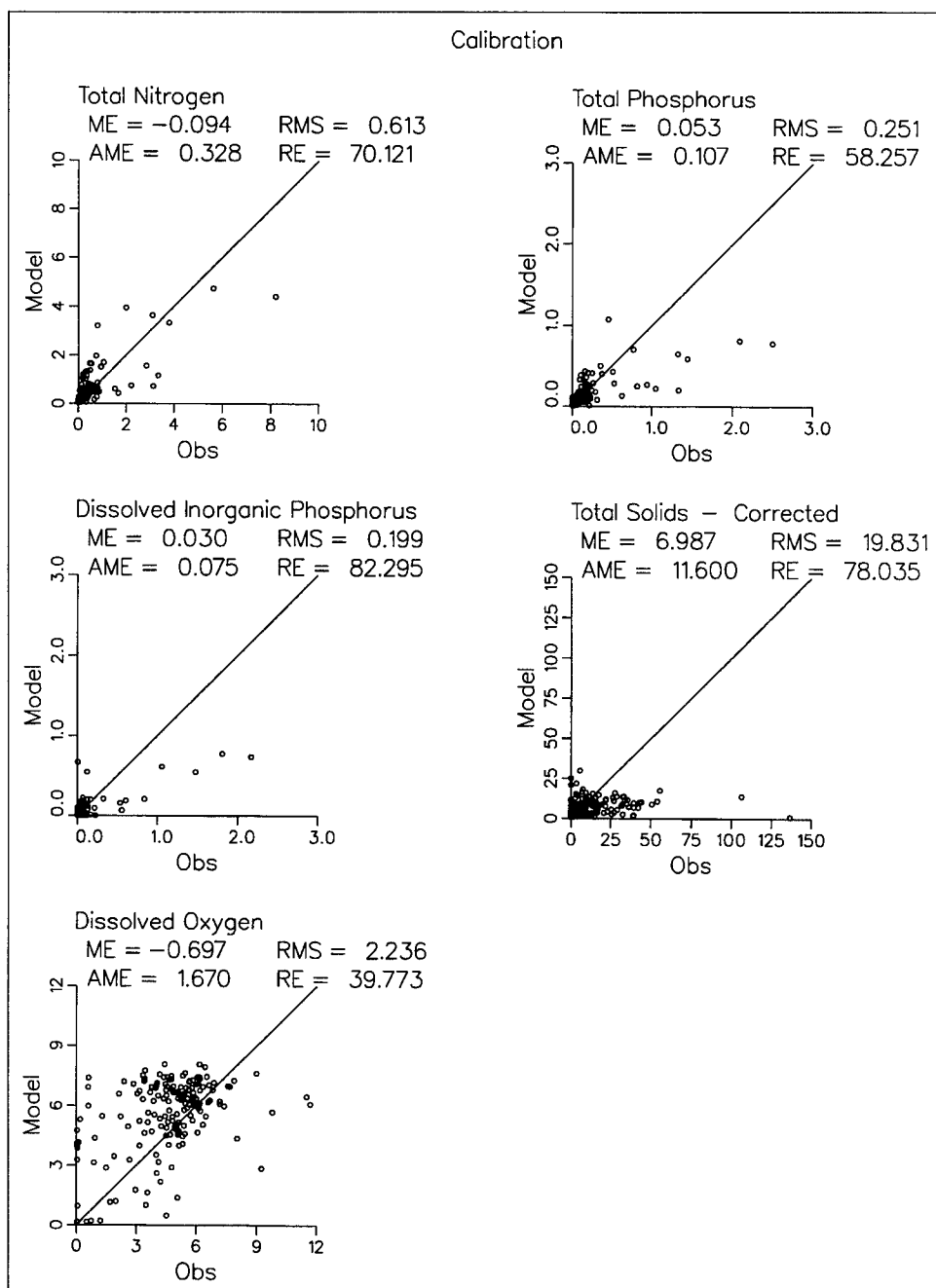


Figure 7-1. (concluded)

$$RMS = \sqrt{\frac{\sum (O - P)^2}{n}} \quad (7-3)$$

where

RMS = root mean square

The relative error is the absolute mean error normalized by the magnitude of the observations. It is expressed as a percent and is computed as follows:

$$RE = \frac{\sum |O - P|}{\sum O} \quad (7-4)$$

where

RE = relative error

Overall, the model does well for all constituents. The scatter plot for temperature indicates that the model results are in agreement with observations. The scatter plot for salinity indicates that model predictions agree reasonably well over a range of conditions. While not evident from these plots, ICM underpredicts salinity in Caño Martín Peña, Laguna de Piñones, and the southern portion of Laguna La Torrecilla. Results for chlorophyll indicate that ICM underpredicts extremely high values (over 75 ug/l) but does reasonably well for lower values. The total organic carbon scatter plot exhibits a significant amount of variability around the diagonal indicating that the model is reasonable over a range of conditions but underpredicts some high values.

The ammonium scatter plot indicates that the model underpredicts when concentrations are greater than 1 mg/l. Concentrations of this level and higher were typically only observed in borrow pits in the interior of the SJBE system. Observed nitrate concentrations were low with most being at or just above detection levels. The model indicates a few higher nitrate concentrations but most are very low, as are the observations. Model predictions agreed well with observations for total nitrogen over the 0- to 3-mg/l range but overpredict for the few observations greater than 3 mg/l.

Model predictions for dissolved inorganic phosphorus and total phosphorus are good with the exception of the model underpredicting concentrations exceeding 1 mg/l.

Overall the model overpredicts DO by about 0.70 mg/l, primarily on the surface in the eastern portion of the system, possibly due to overestimation of reaeration. Generally, bottom DO predictions agree favorably with observations. ICM underpredicts DO when concentrations are greater than 8 mg/l, which are supersaturated DO concentrations for the temperature and salinity of this system. Dissolved oxygen supersaturation is a result of

photosynthesis during daylight hours. The model uses calculated daily-average light; thus, photosynthesis and its contribution to DO production are daily-average values, whereas photosynthesis actually follows a sinusoidal pattern that peaks during daylight hours. All observations were collected during the day. Therefore, the model always tends to underpredict DO when supersaturated conditions prevail.

The scatter plot reveals that the WQM overpredicted anoxic and hypoxic conditions in some cases. Upon further investigation it was determined that half of these cases were occurring at stations in upper Laguna La Torrecilla, Blasina Canal, and in the canal leading to Laguna de Piñones. All five bottom observations at TL-5 indicated DO levels lower than 1 mg/l. Corresponding WQM results ranged from 3.14 to 5.3 mg/l. Dissolved oxygen observations in Piñones Canal at station PL-1 ranged from 0.6 mg/l to 3.7 mg/l. Corresponding model predictions ranged from 6.6 to 7.2 mg/l. Reasons for the poor model performance at these locations are several. First, Piñones Canal is influenced by the mangroves which it flows through. Loadings from the mangroves are not accounted for in the model. Second, Piñones Canal is modeled as one layer deep in the model which precludes any simulated stratification. Loads from Piñones Canal are discharged into Blasina Canal at TL-5 which would impact water quality at that location. Furthermore, observations at TL-5 indicate that the water column is stratified. Although Blasina Canal is modeled with two layers, this amount of resolution was insufficient to resolve the rather strong stratification observed in the field in this reach.

Model DO overprediction occurred at station MP-2 in Caño Martín Peña in the surface layer. Surface water at this station was influenced by thin, freshwater lenses which were too thin for the model to accurately resolve. Finally, there are stations where the model computed anoxic DO when anoxic DO existed, such as the bottom layer of MP-2. However, plots of anoxic observations against anoxic model predictions on the scatter plot yielded a single point rather than multiple points, which gives a false impression that the model rarely computes low DO when low, observed DO conditions existed.

The remaining cases where low DO conditions were overpredicted were distributed among the sampling stations. Three were from the bottom of Laguna San José at different sampling stations, one at the bottom of Laguna del Condado, and one at the bottom of San Antonio Canal. Reasons for overpredictions at any of these stations would be speculative. One of these overpredictions occurred at station SJ-1 (Laguna Los Corozos) whose time series results are shown in Figure 7-7. No clear reason is evident for this overprediction. This observation was the first at this station. All subsequent observations were much higher and agreed favorably with model results. Possibly, the first sample was obtained in a slightly different location or in a slug of "dirty water" recently discharged from the Baldorioty de Castro Pump Station.

Total suspended solids scatter plots indicate that the model performs reasonably well. During model calibration a problem with the total suspended solids data was discovered. Total suspended solids data had been collected and filtered but not rinsed with distilled water. Since some of the samples were collected in waters that were saline, the filtered material contained salt. When the filter was dried the salt remained and its weight was incorrectly attributed to suspended solids. In an attempt to compensate for this error, observed total suspended solids data were corrected by using the following relationship.

$$TSS_{new} = TSS_{obs} - \frac{C_{sal}}{C_{ocean}} TSS_{ocean} \quad (7.5)$$

where

TSS_{new} = new total suspended solids concentration

TSS_{obs} = observed total suspended solids concentration

C_{sal} = observed salinity at sampling location

C_{ocean} = observed salinity at ocean boundary

TSS_{ocean} = observed total suspended solids concentration at AO-1 and AO-2 (see Figure 2-1)

With this correction implemented, the agreement of model predictions and observations improved. ICM still underpredicted observations greater than 25 mg/l. All total suspended solids data presented in this report have been corrected in the manner described above.

Longitudinal Transect Comparisons

Calibration period-average longitudinal transect plots were made for a transect beginning at the mouth of San Juan Bay, passing through Caño Martín Peña, Laguna San José, Canal Suárez, ending at the mouth of Laguna La Torrecilla (see Figure 7-2). The route of this transect was selected so as to pass through five of the major features of the SJBE system. Two transects are shown for each constituent. One transect is for cells in the surface layer while the other is for cells in the bottom layer. Due to the bathymetry of the system, there are locations where the grid is only one layer thick which results in the same cell appearing in both the surface and bottom transects. Locations where this occurs include eastern Caño Martín Peña, Laguna San José, and Laguna La Torrecilla. The model average for the calibration period is shown on the transect plots as a solid line. The range of model predictions during the simulation is illustrated by the shaded region. Average values of sampling observations are indicated as a circle while the ranges of observations are indicated by the vertical bar through the circle. The model results presented here are averages over the

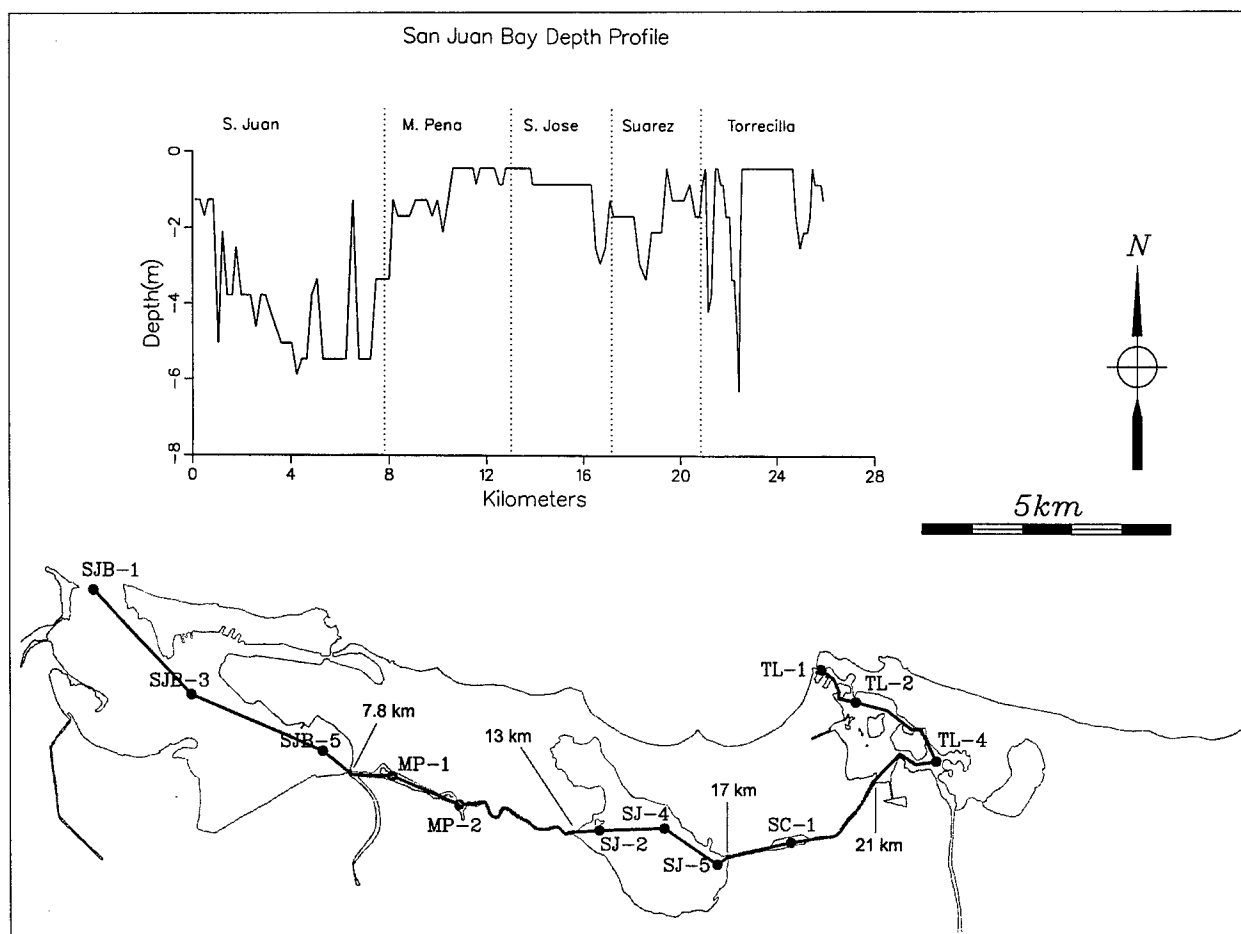


Figure 7-2. Longitudinal transect and observation stations used for preparing calibration-period average transect plots

whole calibration period and as such do not relate the effects of any temporal activity which might be reflected in the observed data.

Overall, as these plots indicate (see Figure 7-3), the model performs well. There are locations where the line denoting the model calibration average and the average of the observed data do not agree. However, the model does capture most of the means of the observations and their range.

As indicated in the description of the transect route, this transect passes through water bodies with very different characteristics. San Juan Bay is well flushed via tidal exchange with the Atlantic Ocean at its mouth and a secondary channel on the northeastern side, i.e., Caño de San Antonio. Due to the extensive exchange with the ocean, water quality in San Juan Bay is similar to that of the ocean. Laguna San José, which is located along the middle of the transect is completely landlocked with only limited exchange with the ocean via Caño Martín Peña and Canal Suárez. As a result, salinity in Laguna San José is less than half of ocean values. Laguna La Torrecilla on the eastern end of the system is a transition region between the interior of the system and the ocean. Water quality near the

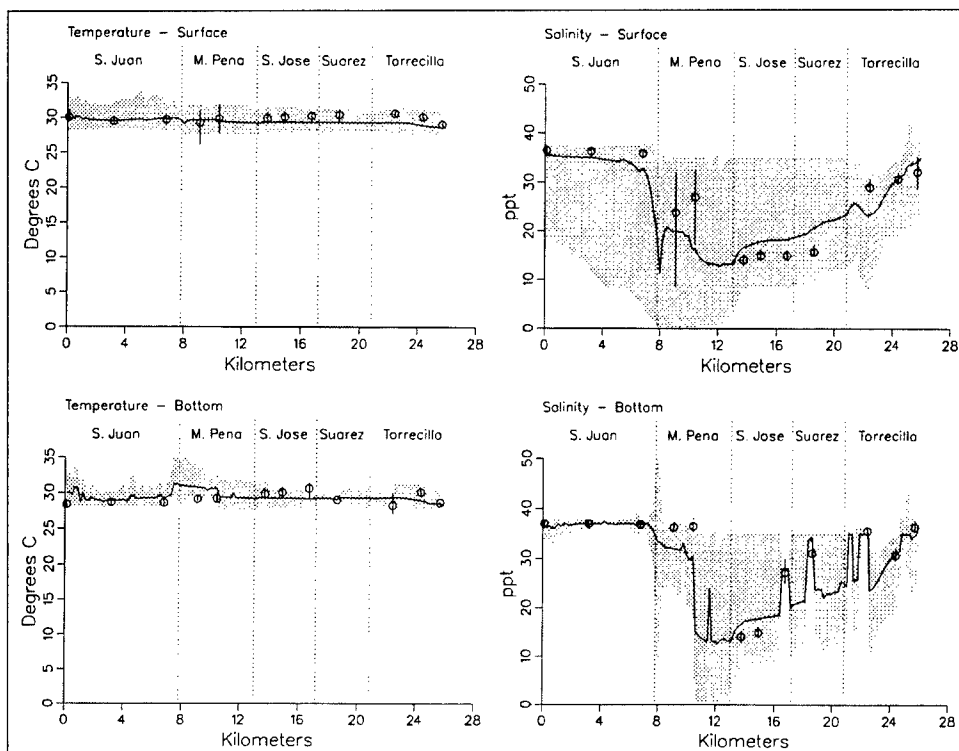


Figure 7-3. Calibration-period average, longitudinal transect plot of computed and observed water quality variables resulting from model calibration for summer 1995 (Sheet 1 of 8)

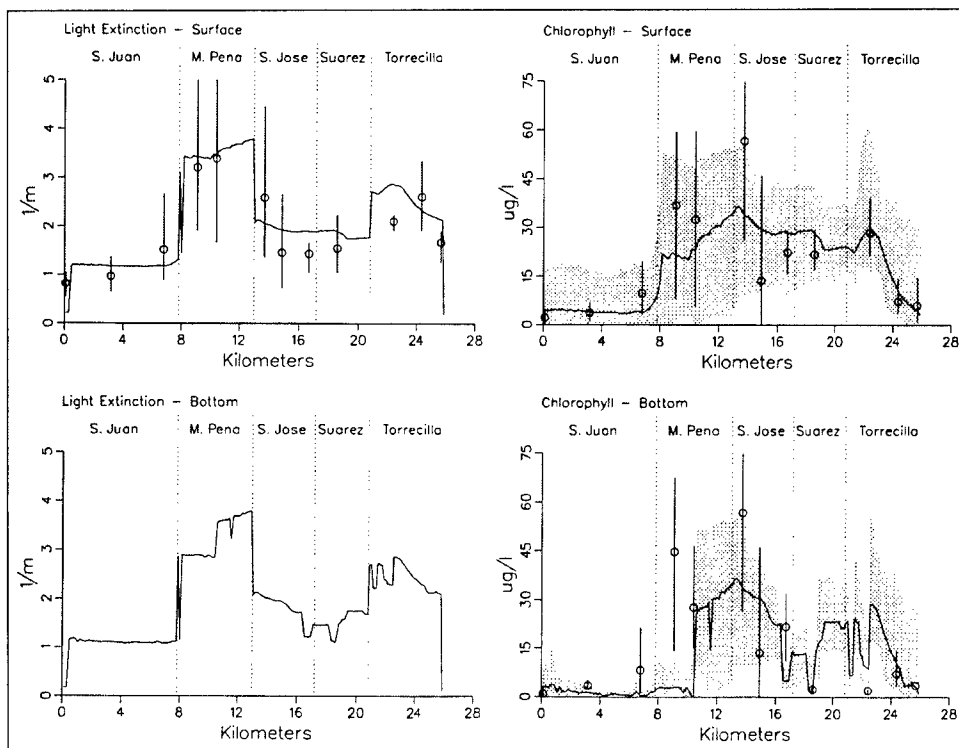


Figure 7-3. (Sheet 2 of 8)

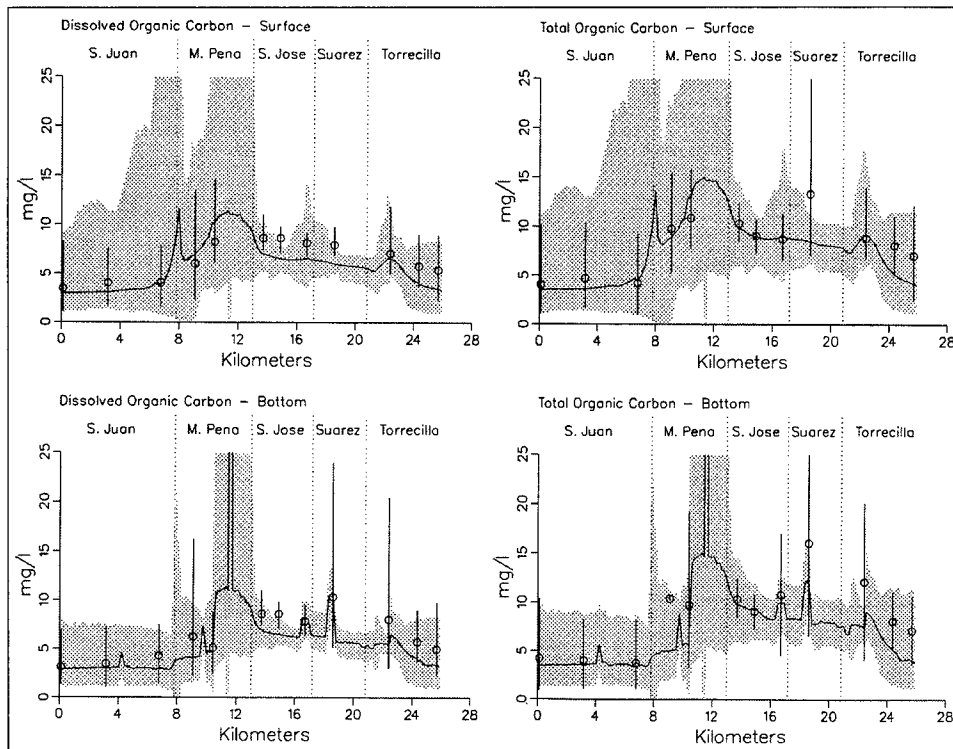


Figure 7-3. (Sheet 3 of 8)

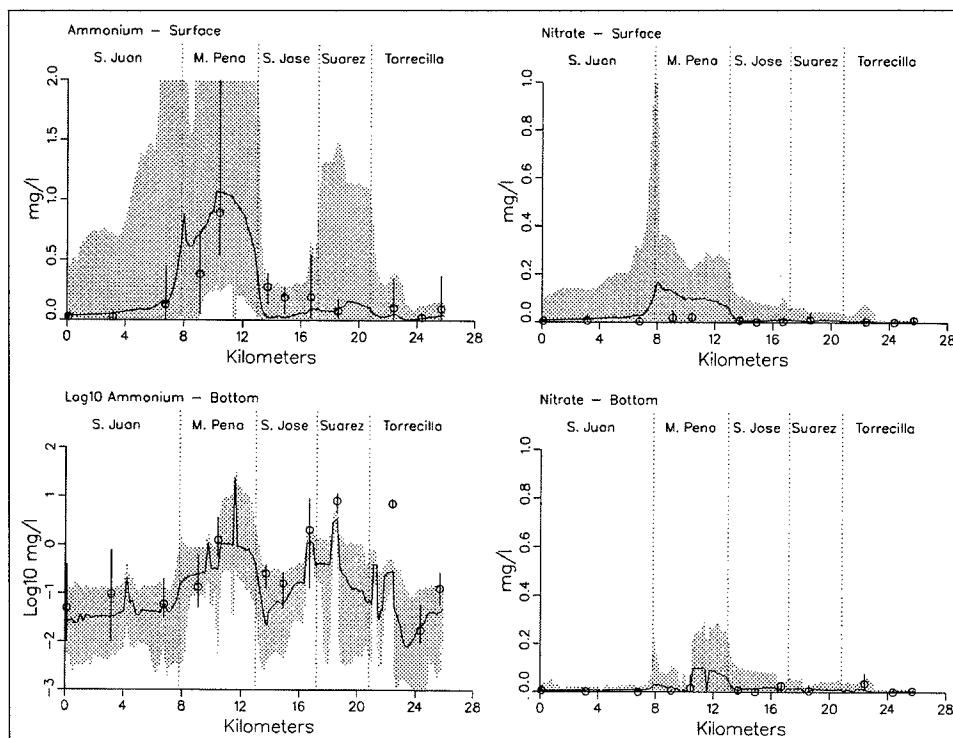


Figure 7-3. (Sheet 4 of 8)

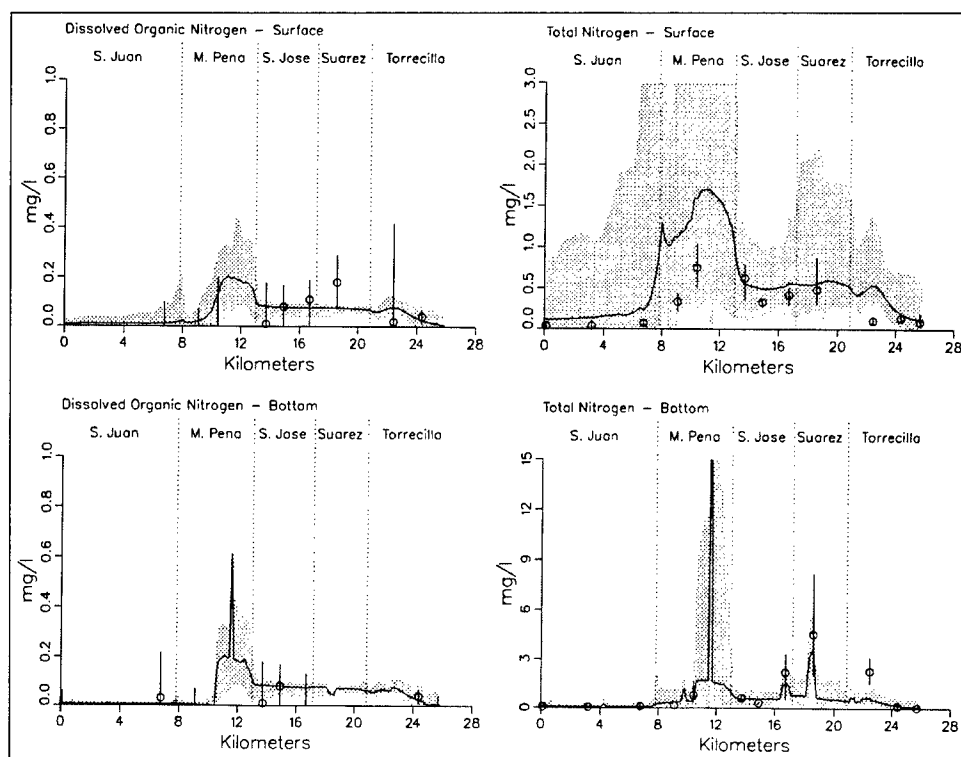


Figure 7-3. (Sheet 5 of 8)

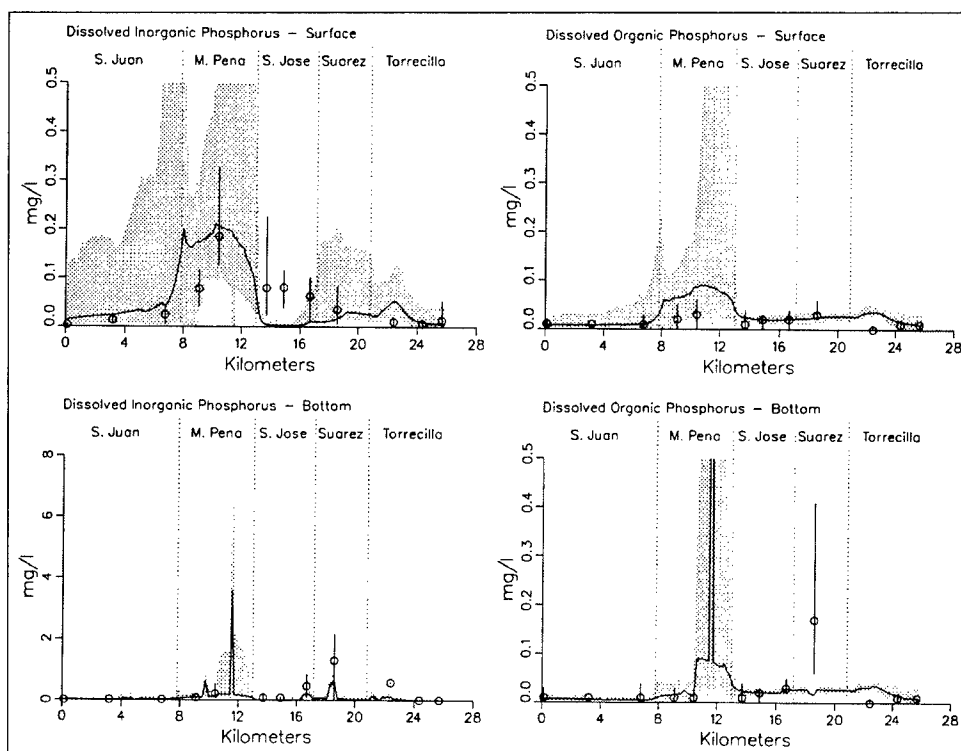


Figure 7-3. (Sheet 6 of 8)

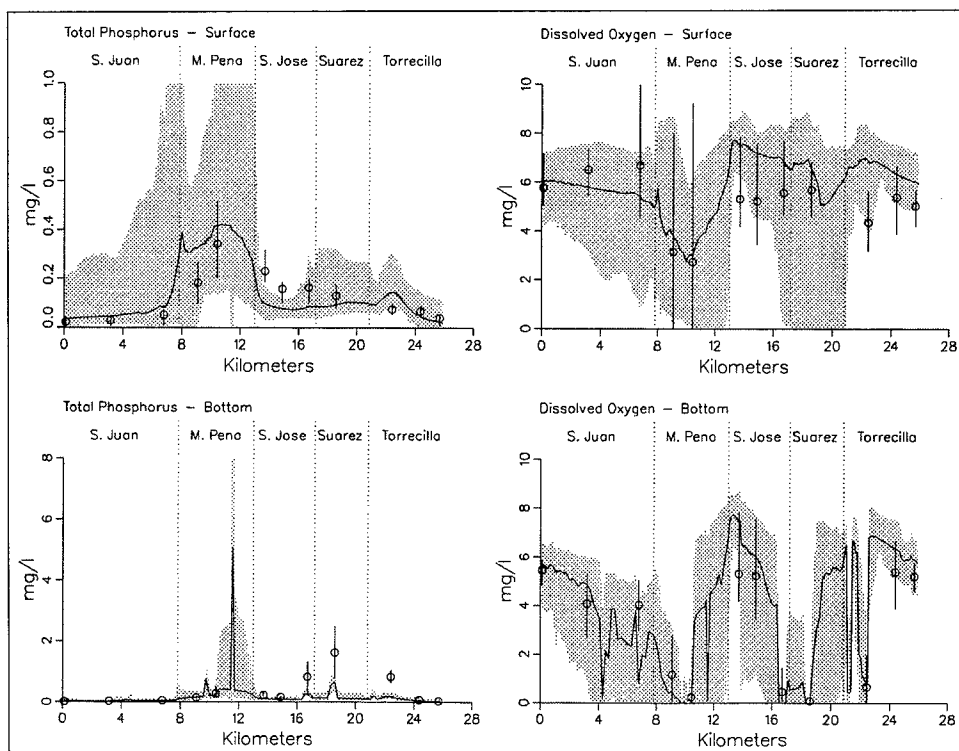


Figure 7-3. (Sheet 7 of 8)

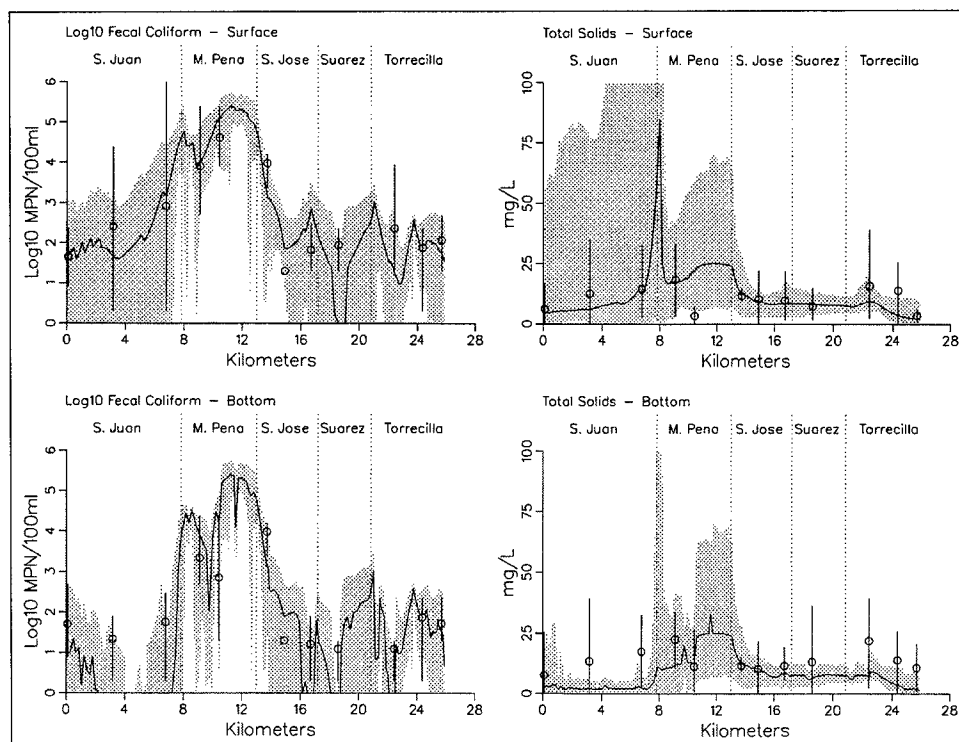


Figure 7-3. (Sheet 8 of 8)

mouth of Laguna La Torrecilla is similar to offshore conditions while water quality in the other areas is more like that found in Canal Suárez. Each constituent is discussed in the order it is presented in the transect plots.

Temperature

Temperature transect plots indicate that there is little variation in the model predictions for temperature along the transect, Figure 7-3. Likewise there was little variation in observed temperature readings. Model results agree favorably with observations indicating that the model is predicting temperature accurately. The lack of significant temperature differences between the surface and bottom transects is an indication that the system is not thermally stratified.

Salinity

Salinity transects, unlike the temperature transects, indicate significant variation. Model results and observed data for San Juan Bay exhibit average salinity approximately equal to that found offshore. Near the mouth of Caño Martín Peña, surface salinity drops in response to freshwater inflows from Rio Piedras and the flow from Caño Martín Peña. Bottom salinity decreases slightly in the dredged portion of Caño Martín Peña with the model average being lower than the observed data. However, the observed data for both surface and bottom samples at this location do fall within the range of model predictions.

The degree of variation in observed salinity supports the model results which indicate that there are significant swings in salinity as a result of fresher flows from eastern Caño Martín Peña and runoff into Laguna San José. These fresher flows remain near the surface and override the bottom waters of western Caño Martín Peña resulting in a 10- to 15-ppt difference in salinity between surface and bottom waters. Eastern Caño Martín Peña is shallow and modeled as one layer in most places. This results in the surface and bottom salinity plots being identical for this region. The only exception occurs near km 12 where there is a small hole. At this location, the model grid is two layers deep while the cells upstream and downstream are only one layer deep. The cell in the “hole” cannot have advection into or out of it due to the one-cell isolation. The only means for moving material into or out of this cell are diffusion and settling. Salinity being a dissolved substance does not settle but can diffuse depending upon the overlying water salinity. At the same time, salinity is not taken up by the sediments so the salinity that diffuses into the “hole” is only removed by diffusion when the overlying water is fresher.

Predicted surface salinity in Laguna San José is slightly higher than observations for the calibration period. The surface and bottom salinity values at SJ-2 and SJ-4 are identical as this is a location where the system

is relatively shallow and there is no stratification. At station SJ-5, there is a significant difference in surface and bottom salinity. This location is a dredge material borrow pit which is 6.8 m deep. These pits are located throughout Laguna San José, Canal Suárez, and Laguna La Torrecilla. Just as the small hole in Caño Martín Peña, these holes have limited exchange with surface waters. Some holes are large enough that they cover multiple model cells and can therefore accommodate advection which should allow these holes to freshen. However, observed data indicated that surface salinity at these holes was much lower than bottom salinity. Numerous theories were developed as to why the salinity in these holes should be so much higher than that at the surface. The theories included groundwater intrusion from the ocean into the holes. Whatever the mechanism, it was beyond the capability of CH3D and ICM to simulate it without modification.

In an attempt to incorporate the effects of these holes on water quality, the salinity in these deep holes was “nudged” toward higher values throughout the simulation. The same procedures were used in both the HM and WQM. During each model time-step iteration, the salinity in the holes where nudging was employed was adjusted toward a predetermined, higher concentration according to the relationship

$$C_{new} = C + 0.1 * (C_{nudge} - C) \quad (7.6)$$

where

C_{new} = new salinity concentration

C = previously computed salinity concentration

C_{nudge} = reference salinity concentration

The result of nudging was that these dredge material borrow pits became pseudo-salinity boundaries representing sources of ocean salinity. Nudging was only employed in cells located more than three layers deep in dredge material borrow pits. A value of $C_{nudge} = 28$ ppt was used for holes in Laguna San José while a value of $C_{nudge} = 35$ ppt was used for dredge borrow pits in Laguna La Torrecilla. In locations where nudging was employed, little fluctuation in salinity occurred. Examples of the effects of nudging can be seen in the bottom salinity transect plots between km 16 and km 24.

Transect salinity continues to increase as the transect passes through Canal Suárez. There is a slight decrease in salinity as the transect passes around an island in Laguna La Torrecilla in the vicinity of TL-4 at which time it is exposed more to the fresher Blasina flows. Salinity continues to rise as the transect continues through Torrecilla to the ocean.

Light Extinction

The background light extinction was specified spatially based upon observations. Model values vary some during the simulation due to the effects of algae. Only the model mean values are plotted in Figure 7-3 for interpretive purposes. These values were adjusted so that the model light extinction closely followed the observed. Although the model surface and bottom light extinction values are very similar for surface and bottom layers, the amount of light remaining in the bottom layers can be quite different from that in the surface layers. Light extinction measurements were taken only for the surface.

Chlorophyll

Modeled chlorophyll levels along the transect in San Juan Bay are low, averaging 4 $\mu\text{g/l}$. There is a slight gradient in the observed values in San Juan Bay with the observations near the mouth of Caño Martín Peña being the highest. The average and range of chlorophyll observations fall within the range of the WQM simulation for San Juan Bay. Chlorophyll levels increase significantly just inside Caño Martín Peña. Model levels remain constant throughout the western dredged portion of Martín Peña and begin to increase once the undredged eastern portion of the canal is reached.

Computed chlorophyll concentrations at the juncture between Caño Martín Peña and Laguna San José are the highest of any location on the transect. Chlorophyll concentrations remain high throughout San José and into Canal Suárez. Average chlorophyll observations in San José exhibited temporal and spatial variability which made calibration problematic. Attempts to make the WQM match the higher chlorophyll observations at SJ-2 would make it overpredict the much lower average at SJ-4 even more. Attempts to obtain a better match at SJ-4 would result in the WQM underpredicting even more at SJ-2 which in turn would cause lower chlorophyll predictions throughout Martín Peña. The surface waters of San José serve as an incubator for chlorophyll with ample light and nutrients to promote growth.

Macrobenthic grazing was added to the model in order to aid in chlorophyll calibration in Laguna San José. Benthic organisms remove algae via filtration of the overlying cell, consequentially, the waters above bivalve beds have lower levels of algae and other particulates. Light penetration increases in the waters above clam beds in response to the decrease in suspended matter.

Bivalve beds were observed at different locations in Laguna San José during the sampling study. Bivalves were placed into the southern half of Laguna San José in the WQM, Figure 7-4. Macrobenthic grazing is dependent upon dissolved oxygen levels. Bivalves require dissolved oxygen to live. In the WQM the higher the dissolved oxygen the better the conditions for grazing, the lower the dissolved oxygen the worse.

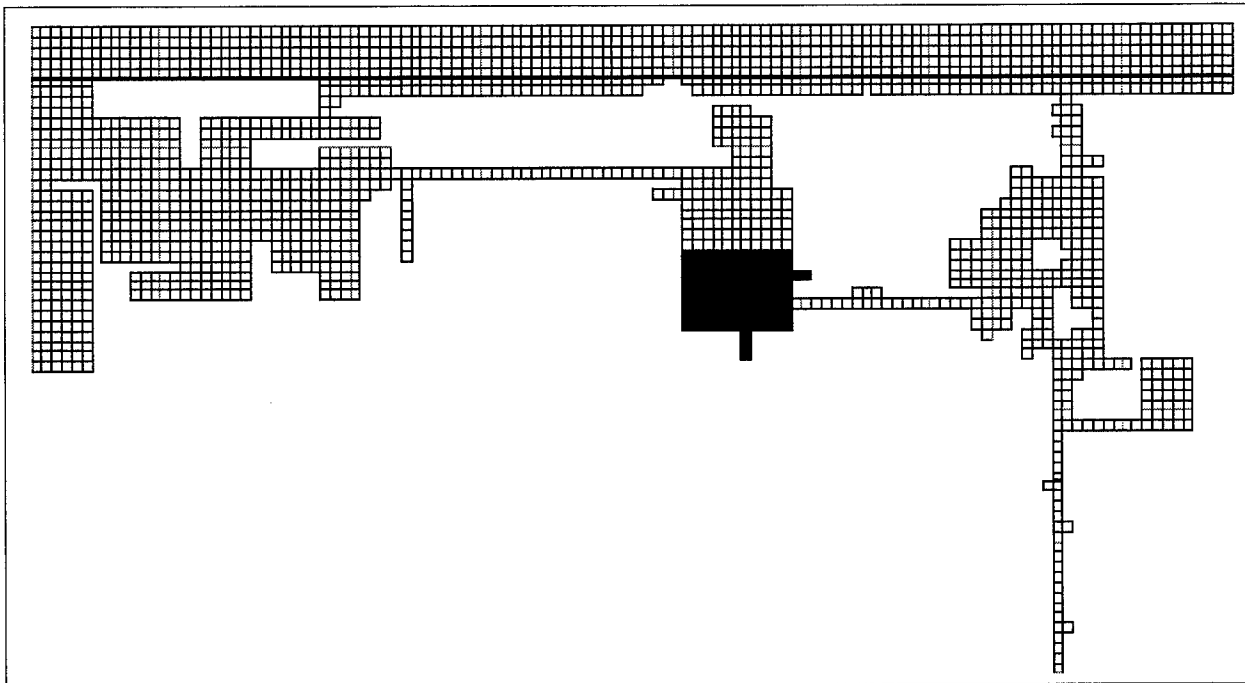


Figure 7-4. Location of clams in the WQM

Macrobenthic grazing will not occur in bottom cells with anoxic conditions even if bivalves are present.

Incorporation of macrobenthic grazing allowed greater spatial variability in Laguna San José chlorophyll concentrations. The net impact was that chlorophyll levels decreased in the southern portion of Laguna San José in the presence of the bivalve beds.

Canal Suárez chlorophyll levels were lower than either Laguna San José or Laguna La Torrecilla but still higher than any other location along the transect. Model surface chlorophyll concentrations along the transect in Torrecilla were highest at TL-4. Levels at TL-1 and TL-2 are relatively low reflecting the influence of the ocean water exchange through the Laguna La Torrecilla inlet.

Bottom chlorophyll concentrations along the transect are typically low. The exception occurs at locations where the model grid is only one layer deep which results in the same cell being on both the surface and bottom transects. Light limitation is the major limiting factor for algal growth in the deeper waters of the system with the exception of the regions offshore. Typically, algae found in the bottom waters were transported there by settling and vertical flows.

Organic Carbon

The WQM simulated three forms of organic carbon: dissolved, labile particulate, and refractory particulate. Results are shown for dissolved organic carbon (DOC) and total organic carbon (TOC) which is the sum of DOC and the two particulate fractions. The DOC and TOC transects have similar shapes which is expected since DOC is the major component of TOC. Concentrations at both the San Juan Bay and Laguna La Torrecilla inlets reflect the conditions offshore. The interior portions of the transect have elevated levels that are the result of anthropogenic loadings. The highest surface concentrations occur at the Rio Piedras - Caño Martín Peña confluence and in the eastern portion of Caño Martín Peña. The high concentrations at the Rio Piedras - Caño Martín Peña juncture result from the Rio Piedras loadings. Transect plots indicate that this load is rapidly disseminated into the waters of San Juan Bay by the combined Rio Piedras and Caño Martín Peña flows.

Surface DOC and TOC concentrations in eastern Caño Martín Peña are high as a result of the organic carbon component of the un-sewered loads. This region is reported to directly receive substantial discharges of untreated wastewater. The exact quantity was unknown and could only be estimated. Based upon calibration results and demographic information, a loading of 400 kg/day of organic carbon split evenly between dissolved and labile particulate fractions was distributed along the eastern half of Caño Martín Peña. In addition, loadings of 62.5 kg/day of ammonia, 37.5 kg/day of dissolved organic nitrogen, 12.5 kg/day of dissolved inorganic phosphorus, and 7.5 kg/day of dissolved organic phosphorus were also added. The carbon/nitrogen/phosphorus (C/N/P) ratio of this load was 20/5/1 which is typical of that indicated for medium strength wastewater (Metcalf and Eddy 1979). Based on a daily per-capita total organic carbon loading of 75 g/person/day (0.17 lb/person/day) this loading was equivalent to that of approximately 5300 persons. The un-sewered loadings into eastern Caño Martín Peña were required not only to bring the DOC and TOC up but to increase the levels of other nutrients and decrease dissolved oxygen. The impact of the un-sewered loads on these and other variables is discussed below in the corresponding sections.

Model surface DOC concentrations match observed data quite well throughout the system except for Laguna La Torrecilla where model predictions were slightly low. One possible explanation for the model being low in this region is that the model does not include the organic carbon loading coming from the mangroves around Torrecilla. Surface model DOC concentrations in San José and Canal Suárez are slightly low in comparison to observed data. However, model predictions for TOC at these stations indicate that the model average agrees with the observed averages at stations SJ-2, SJ-4, SJ-5, and SC-1. Any attempt to increase DOC concentrations in the model would increase TOC concentrations and result in a poorer model performance in San José and Canal Suárez.

Model bottom DOC levels are similar to surface levels for most of the transect. In the dredged western portion of western Caño Martín Peña, bottom DOC levels are lower than surface waters. A possible reason for this is that there is some salinity stratification in this portion of the canal which decreases surface-bottom water mixing. Over the remainder of the transect, model surface and bottom DOC concentrations are comparable except for holes and dredge material borrow pits. At these locations, DOC concentrations are elevated as a result of the dissolution of settled particulate organic carbon and the respiration and decay of algae that settle into these cells. As a result, the DOC levels in these holes are higher as there is no mechanism to readily remove the DOC other than vertical diffusion. Observed bottom DOC and TOC concentrations at SJ-5, SC-1 and TL-4 indicate elevated concentrations similar to those predicted by the model.

Nitrogen

Results for three model constituents, ammonium, nitrate, and dissolved organic nitrogen (DON) are shown as well as results for total nitrogen. The dominant feature of the nitrogen transects are the high observed values of ammonium in Caño Martín Peña. The high observed ammonium levels in Caño Martín Peña are further evidence of substantial discharges of untreated wastewater directly into Caño Martín Peña. The sources of this ammonium are direct loading, mineralization of DON, and diagenesis of settled particulate organic nitrogen in the sediments. Mineralization occurs in the water column but as indicated in the transect plots, little DON was observed in Caño Martín Peña. Diagenesis occurs in the sediments and is a likely source of the ammonium especially in the holes and dredged borrow pits. At these locations, particulate organic matter in these cells will eventually be settled and undergo diagenesis. The ammonium released can only be removed via diffusion. Consequentially observed ammonium levels greater than 1 mg/l were observed and predicted along the bottom.

In the deeper portions of Caño Martín Peña, Laguna San José, and Canal Suárez, sediments act as a source of ammonium to the water column. Model sediment fluxes of 25 mg/m²/day or greater are common in Laguna San José and Canal Suárez. Benthic algae in the shallow portions of the eastern portion of Caño Martín Peña and Laguna San José take up ammonium as it is being released from the sediments to the water column. Without these algae, ammonium levels in Caño Martín Peña and Laguna San José would be even higher. The spatial extent of the benthic algae is limited by the availability of light and nutrients.

Computed and observed nitrate levels were low throughout the system. The model slightly overpredicts nitrate in Caño Martín Peña, possibly due to under-estimation of sediment denitrification or algal uptake of nitrate. Computed and observed dissolved organic nitrogen is also relatively low with more present in the eastern half of the system. Surface transect plots indicate that model total nitrogen levels were higher in Caño Martín Peña

than observed values but agreed well with observations in Laguna San José. Total nitrogen transect plots for the bottom indicate that the model performs well for the whole system. Model predictions are low for the first station in Laguna La Torrecilla, TL-4, but this is mainly the result of the ammonium prediction for this station being low.

Phosphorus

Dissolved inorganic phosphorus (DIP) transects have a look similar to that of ammonium. Low predicted and observed surface concentrations occurred throughout the system with the exception of Caño Martín Peña. DIP concentrations approaching 0.2 mg/l were predicted for the length of Caño Martín Peña which matched well with observations at MP-2 but were slightly above the observations at MP-1. The sediments of the dredged western portion of Caño Martín Peña are a source of DIP with sediment flux rates reaching a maximum of 20 mg/m²/day near MP-2. Eastern Caño Martín Peña sediments serve as a sink for DIP with the benthic algae community at this location taking DIP from the water column. Eastern Caño Martín Peña receives a phosphorus loading of 20 kg/day as part of the un-sewered area loadings. Surface water predictions from the model are lower than observations in Laguna San José but are representative in Canal Suárez and Laguna La Torrecilla. The reason for low predictions in Laguna San José appear to be benthic and planktonic algal nutrient uptake. Much of Laguna San José is relatively shallow so that the bottom waters at certain locations receive adequate light for benthic algae to flourish. Where benthic algae are active their role is the sequestration of sediment releases of nutrients, notably DIP and ammonia. If conditions are appropriate, the benthic algae can uptake the complete sediment release of a nutrient and still remove nutrients from the overlying water column. Incorporation of benthic algae into the WQM improved the calibration by muting sediment releases at certain locations and increasing the uptake of nutrients from the water column.

Model predictions for DIP for the bottom transect agree well with observed data. Again the holes and dredged borrow pits have elevated levels of DIP which the model captures. Model results for surface water dissolved organic phosphorus indicate that the model slightly overpredicts in Caño Martín Peña but does well in the remainder of the system. Overall, transects for total phosphorus demonstrate that the model tracks well with the observed data for both surface and bottom waters throughout the system.

Dissolved Oxygen

Observed data for the surface water dissolved oxygen (DO) transect indicate that levels are relatively high throughout the system with the exception of Caño Martín Peña. The least variability in DO is observed at the stations located at the mouths of San Juan Bay and Laguna La Torrecilla. These locations are the most influenced by the ocean and therefore reflect ocean conditions of constant salinity, temperature, and low levels of algae. Model predictions for DO decrease slightly along the transect between the mouth of San Juan Bay and Caño Martín Peña. Averages for observed data at stations SJB-3 and SJB-5 are higher than model predictions along the surface but the range of observations overlap the range of model predictions. The highest of the observed DO concentrations exceed saturation and are indicative of the diurnal effects of algal photosynthesis. The inability of the WQM to capture DO supersaturation at these stations is probably due to the fact that ICM does not incorporate diurnal effects in the algal process computations.

Model surface calibration average and range match observed data well in Caño Martín Peña. Observed data in this region indicate large fluctuations in DO which the model is able to capture. Model surface DO levels increased in eastern Caño Martín Peña as a result of algal photosynthesis. Calibration averages were slightly higher than observed data averages in Laguna San José and Canal Suárez; however, the range of model predictions encompassed the observed averages.

Bottom water model calibration results indicate numerous locations with anoxic conditions. Portions of Caño Martín Peña are anoxic on the bottom due to high DO demands exceeding reaeration. Additionally, holes and dredged borrow pits are anoxic as a result of sediment releases of ammonium in addition to poor circulation and exchange with the aerated surface waters. Sediment oxygen demand (SOD) also removes DO from the water column but only in areas where the water has DO. Consequently, locations with high SODs are also locations where the bottom water is not anoxic but instead has adequate DO.

Fecal Coliform

The only source of fecal coliform bacteria in the model is from external loads. Once introduced to the system, fecal coliform can only be transported and die. Highest fecal coliform levels are found near the loading sources. The highest fecal coliform observation occurred in the interior of the system in Caño Martín Peña and western Laguna San José. Transect plots indicate that model output matches observations well for both the average and range throughout the system.

Total Suspended Solids

Total suspended solids (TSS) include both inorganic and organic suspended solids. TSS plots indicate that the model performs well along the transect. Model predictions are higher than observations at MP-2 but match observations at the closest two stations MP-1 and SJ-2. The dominant feature of the surface transect is the spike at km 8. This spike results from the Rio Piedras sediment load. As indicated by the plot, this load is disseminated rapidly in the system. The plot for the bottom transect indicates that the model performs well in the interior of the system but tends to be low in San Juan Bay and Laguna La Torrecilla.

Benthic Algae

ICM has no mechanism for the transport, transplantation, or propagation of benthic algae from one cell to another. Consequentially, benthic algae exist at the sediment water interface of every water column in the model. If the light or nutrients are inadequate, the algae are dormant and have no effect on water quality or sediment processes. Where nutrient and light levels are conducive the algae grow. The kinetic processes of benthic algae are similar to those of phytoplankton which were described earlier in Chapter 4. Specific information of benthic algal processes can be found in Cerco and Seitzinger (1998). As indicated in Figure 7-5, the presence of benthic algae in an appreciable amount is limited to relatively few locations along the transect. Nutrients are abundant for the length of the transect and throughout the SJBE system. However light at the sediment water interface is adequate at only a few locations. Most locations along the transect are too deep and the light extinction too high for appreciable levels of light to penetrate to the sediment water interface. The highest benthic algae biomass levels were at the mouths of San Juan Bay and Laguna La Torrecilla where levels approaching 20 g C/m^2 were computed. Light extinction at these locations is low as a result of water clarity and low chlorophyll levels. Adequate nutrients from the interior of the system are also available which allow the benthic algae to thrive. Two locations in the interior of the system, one in Laguna San José and one in Canal Suárez, also have elevated levels of benthic algae. Both of these locations are shallow and represented in the model as one layer deep. Benthic algae at the Laguna San José location receive ample nutrients from Caño Martín Peña while the Canal Suárez benthic algae receive nutrients exiting from Laguna San José via Canal Suárez.

In Laguna La Torrecilla and Caño Martín Peña there are locations where the benthic algal biomass is between 0.1 gm C/m^2 and 2 gm C/m^2 . Even at these levels the algae play an important role in the water quality of the system. At all locations along the transect where benthic algae are growing, it is sequestering sediment nutrient releases notably ammonium and phosphate. At these locations the sediments are sinks for ammonium and phosphate while at the locations where benthic algae are dormant the sediments can be sources.

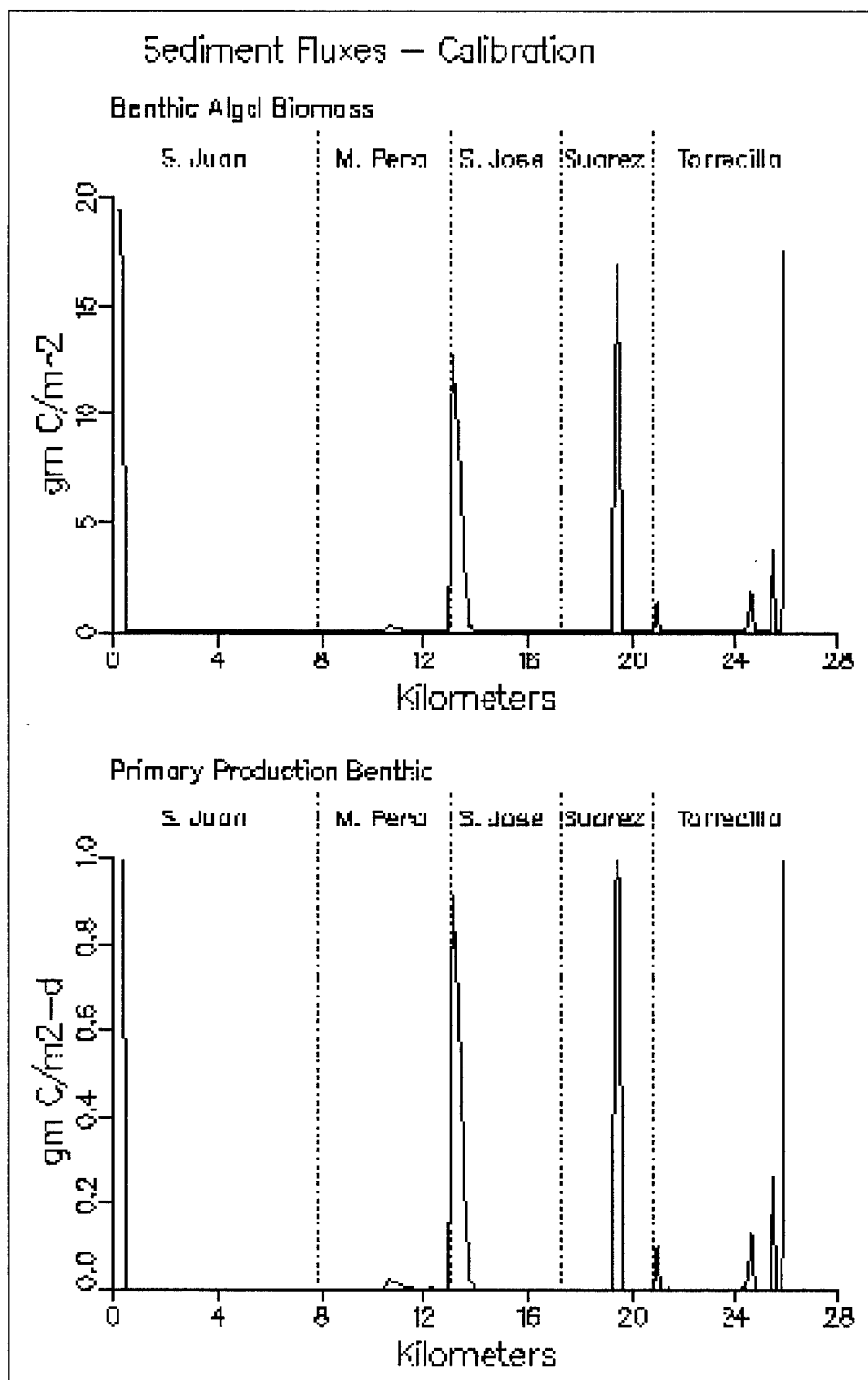


Figure 7-5. Longitudinal transect calibration period average benthic algae

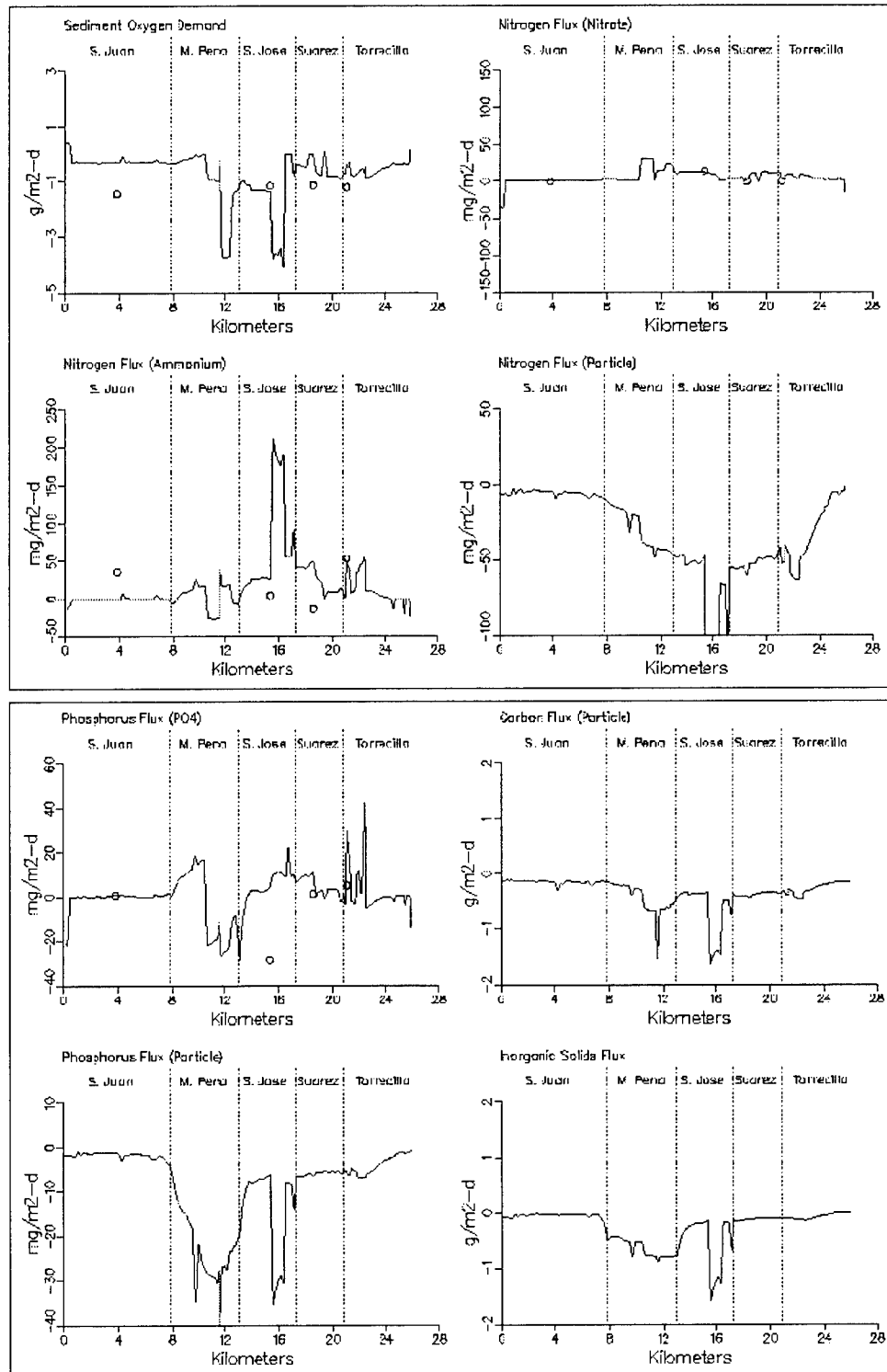


Figure 7-6. Longitudinal transect calibration period average sediment fluxes

Sediment Fluxes

Calibration period averages for sediment fluxes along the transect are shown in Figure 7-6. Negative values indicate that there is a transfer from the water column to the sediment while positive values indicate that there is a transfer from the sediments to the water column.

The calibration period average for sediment oxygen demand indicates that except for Caño Martín Peña and Laguna San José the sediment oxygen demand was between 0 and $-1 \text{ gm/m}^2\text{-day}$. In eastern Caño Martín Peña and eastern Laguna San José the sediment oxygen demand increases to $-4 \text{ gm/m}^2\text{-day}$. These high sediment oxygen demand rates occur in the vicinity of holes and borrow pits which have limited flushing. An oddity of sediment oxygen demand is that there must be oxygen present in the water column for the sediment oxygen demand to have a value as the sediment oxygen demand is indicative of the *transfer* of oxygen from the water column to the sediments. The processes that create a sediment oxygen demand continue in the absence of water column dissolved oxygen. Under these conditions, the demand is transported to the water column as a chemical oxygen demand. Consequently, the highest sediment oxygen demands are in the areas adjacent to the anoxic holes and borrow pits. The sediment oxygen demand in the cells comprising the anoxic pits and borrow holes are $0 \text{ gm/m}^2\text{-day}$. On both ends of the transect and at one location in Canal Suárez, the sediment oxygen demand was greater than $0 \text{ gm/m}^2\text{-day}$ which is indicative of the sediments being a dissolved oxygen source (i.e. releasing dissolved oxygen to the water column). Conditions at these locations (adequate light and nutrients) are conducive to benthic algal growth and photosynthesis which is the source of the dissolved oxygen.

Sediment ammonia fluxes along the transect varied from $-25 \text{ mg/m}^2\text{-day}$ to $200 \text{ mg/m}^2\text{-day}$. Locations where the ammonia flux was negative are due to the presence of active benthic algae which are taking up ammonia releases from the sediments and ammonia from the water column. Sediment fluxes for Caño Martín Peña, Laguna San José, and Canal Suárez indicate that the sediments in the interior of the system serve as an ammonia source. The highest fluxes tend to be associated with holes and borrow pits in which dissolved oxygen is low or absent.

The highest nitrate fluxes occur in the central portion of Caño Martín Peña on the western end of the undredged eastern portion. Fluxes approaching $30 \text{ mg/m}^2\text{-day}$ were predicted for this location. Lower positive fluxes were predicted along the remainder of the transect through Laguna San José, Canal Suárez, and Laguna La Torrecilla.

Particulate nitrogen flux results indicate that the Caño Martín Peña, Laguna San José, Canal Suárez, and Laguna La Torrecilla all are sinks for particulate nitrogen. The bathymetry of this portion of the system when combined with the proximity of the tributary and anthropogenic loads results in the high level of deposition occurring.

Phosphorus sediment flux plots had many similarities to the nitrogen sediment flux plots. Benthic algae located at the mouths of San Juan Bay and Laguna La Torrecilla cause the sediments at these locations to be phosphate sinks. There is little sediment flux of phosphate in San Juan Bay due to the low deposition rate of particulate phosphorus at this location and to the oxic bottom dissolved oxygen levels. The sediments of the dredged western end of Caño Martín Peña are a source of phosphate for the water column while the undredged eastern end is a sink. The bottom waters of the western end have low dissolved oxygen or are anoxic which contributes to the sediment phosphorus release. The eastern end of Caño Martín Peña has high dissolved oxygen due to reaeration and its shallow depth. In addition, this reach of Caño Martín Peña receives the un-sewered loads. These factors combine to cause the eastern part of Caño Martín Peña to act as a sink for dissolved inorganic phosphorus. The water column of Caño Martín Peña has the highest levels of dissolved inorganic phosphorus found in the SJBE system. Most of this phosphorus originates with the un-sewered and lateral inflow loads into Caño Martín Peña. Elevated dissolved inorganic phosphorus flux rates occur in eastern Laguna San José and Laguna La Torrecilla in the vicinity of hypoxic pits and dredge borrow pits.

Time Series Comparisons

Located in Laguna Los Corozos, which is in the northern portion of Laguna San José, is station SJ-1 (see Figure 2-1). This portion of the bay is the receiving water for the Baldorioty de Castro Pump Station. ICM results for temperature agree well with observations at SJ-1 for the duration of the calibration period, Figure 7-7. Surface salinity results indicated that ICM agrees favorably with the first three observations but slightly underpredicts observations at the end of the calibration period. ICM chlorophyll results agree well with the first four observations but are much lower than the fifth observed concentration of 92 mg/l. ICM results agreed well with surface ammonium and nitrate observations for SJ-1 which were low for the duration of the calibration period. The time series plot for total nitrogen indicates that overall the model is performing adequately for nitrogen at this station. Dissolved inorganic phosphorus results from ICM underpredict the first two observations but agree well with the last three. Time series of total phosphorus indicate that the model performs adequately.

Algal growth in the surface layer is limited by nitrogen availability more so than phosphorus. The average concentration of 0.01 mg/l of phosphorus available is more than adequate to maintain algal levels at their current state. Under some conditions, nitrogen is even more limiting than light at this location. Occasionally nitrogen limitation on algal growth relaxes when large flows and accompanying loads are discharged from the Baldorioty de Castro storm water pump station.

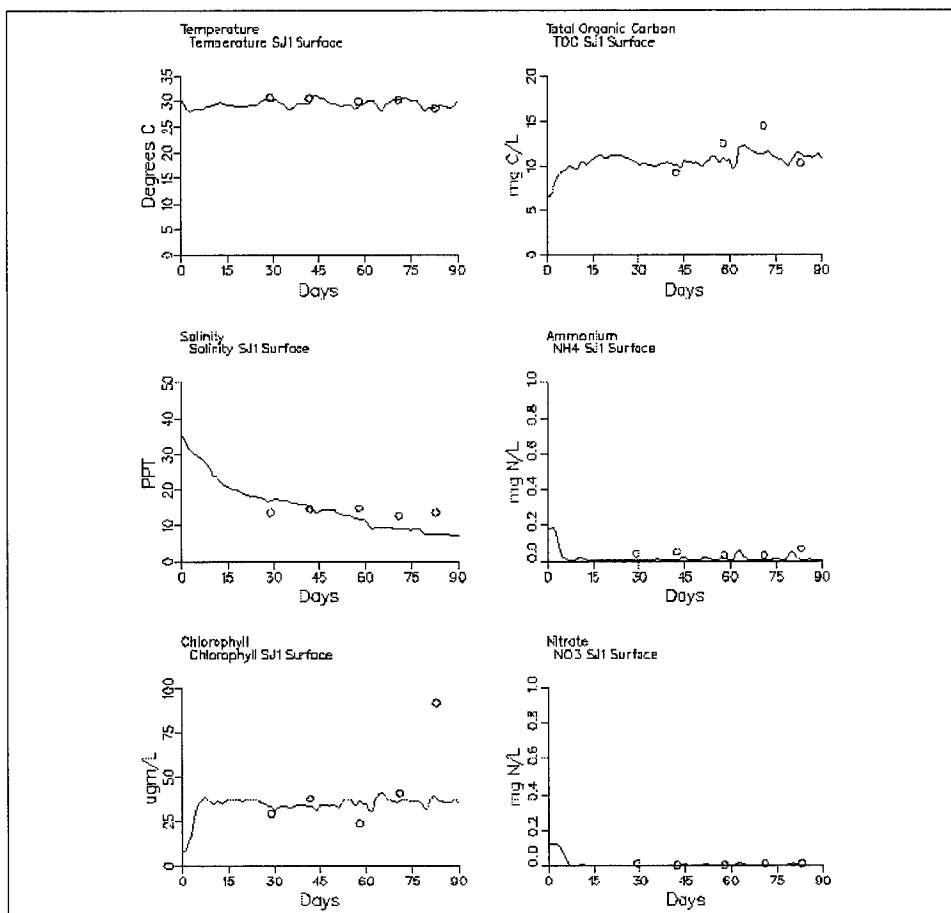


Figure 7-7. Laguna Los Corozos (Northern Laguna San José) calibration period time series (Sheet 1 of 4)

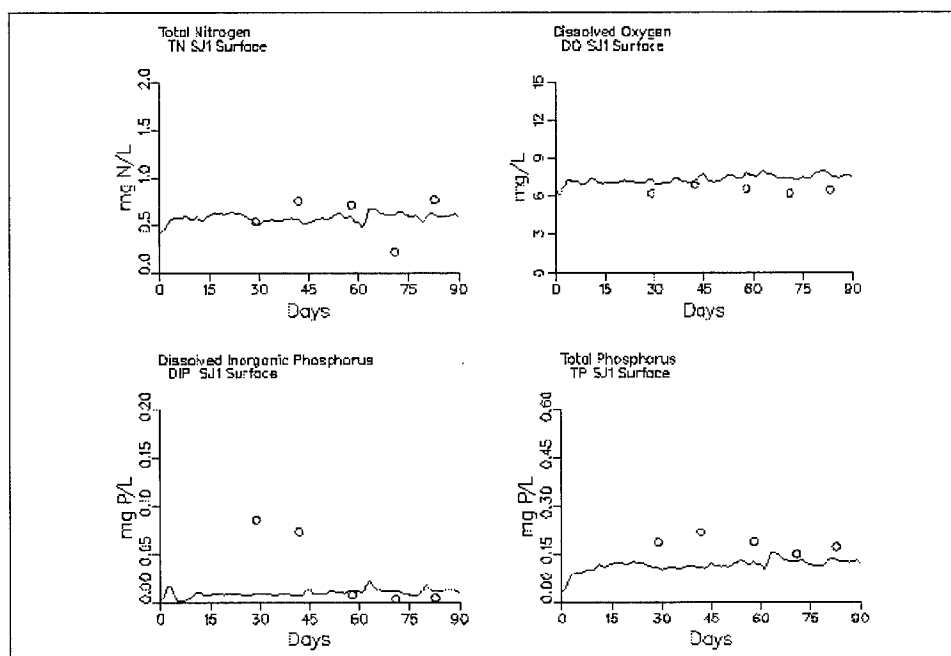


Figure 7-7. (Sheet 2 of 4)

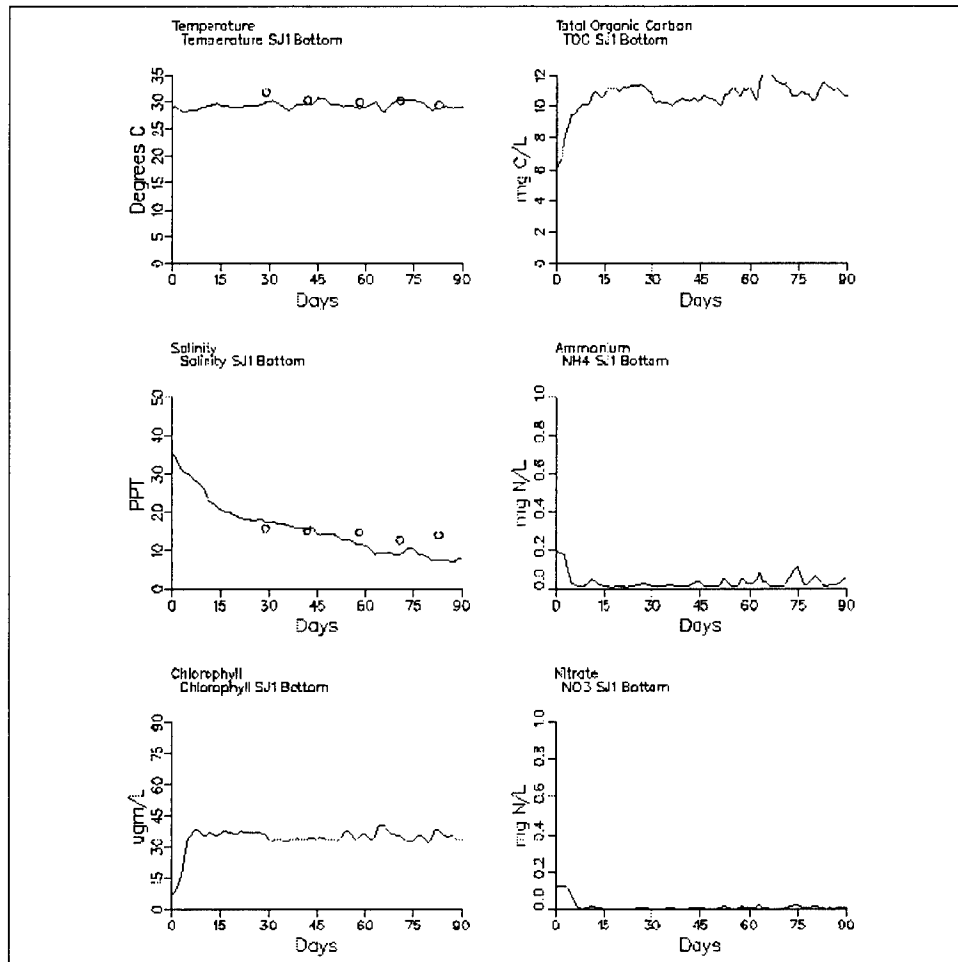


Figure 7-7. (Sheet 3 of 4)

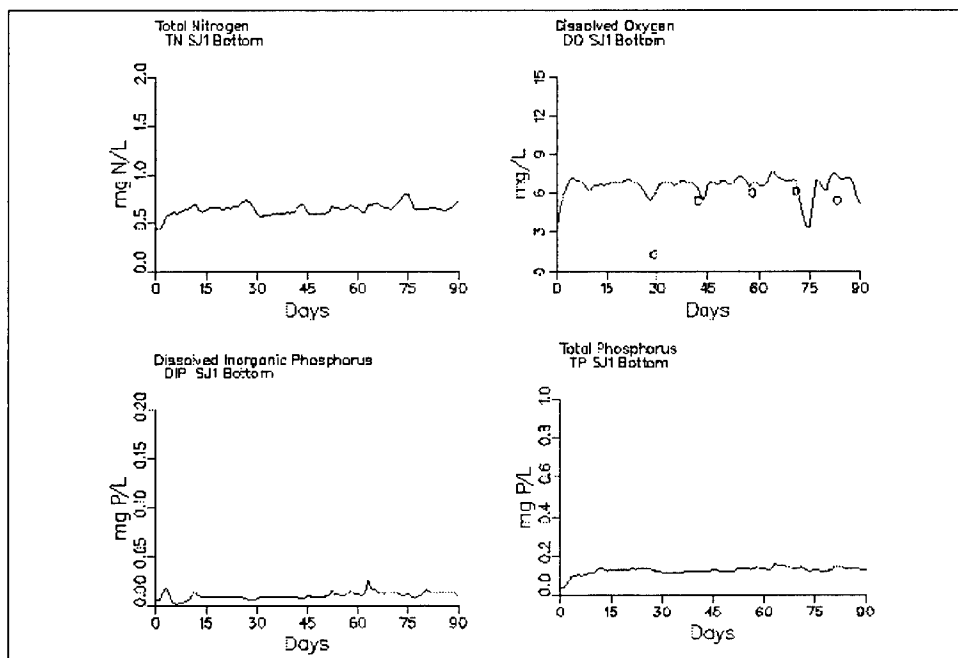


Figure 7-7. (Sheet 4 of 4)

Dissolved oxygen observations are slightly lower than model predictions in the surface layer. The model predictions are near saturation for the salinity and temperature conditions in this system. Sampling results indicate that the surface water dissolved oxygen was consistently around 6 mg/l. Both the model and the observed data indicate that dissolved oxygen levels are relatively high in spite of the high organic carbon concentrations. Algal photosynthesis maintains surface dissolved oxygen levels near saturation for the temperature and salinity conditions present. Dissolved oxygen results for the bottom layer indicate more variability than the dissolved oxygen in the surface layer. The observed data indicate that there was little difference in surface and bottom dissolved oxygen on four of the five sampling dates. This observation when combined with the salinity and temperature surface and bottom time series observations indicate that there is little stratification at this location.

Time series plots for station MP-2 located in Caño Martín Peña are shown in Figure 7-8. This station is located midway between San Juan Bay and Laguna San José at the eastern end of the dredged channel. Water quality at this location is affected by the conditions in Laguna San José, eastern Caño Martín Peña, the Caño Martín Peña watershed, and San Juan Bay.

ICM results for surface water temperature at MP-2 matched observed values well. Temperature predictions for the bottom layer were slightly higher than the observations. Surface salinity observations varied from 17.1 to 32.7 ppt. ICM surface salinity results also indicated significant variation but were still less than the observed data. Salinity swings of 10 ppt were repeatedly predicted at MP-2 during calibration. The timing of these salinity swings corresponds with the occurrence of increases in runoff in the Caño Martín Peña watershed in response to a storm event, Figure 3-3. It must be noted that the ICM results are daily averages while the salinity observations are instantaneous. As such, a portion of the difference between the ICM results and the observed salinities could be attributed to timing.

Bottom salinity observations at this station ranged from 35.4 to 37 ppt during the calibration period. Salinity observations this high indicate that salt water is intruding along the bottom of Caño Martín Peña. Station MP-2 is located near the farthest extent of the intrusion as it is at the end of the dredged section of the canal. ICM bottom salinity results, while lower than the observations, are consistently over 30 ppt. Just as with the surface salinity, some fluctuations are evident in response to runoff events in the Caño Martín Peña sub-basin. When both the surface and bottom observations are viewed together, it is evident that the surface salinity is consistently lower than the bottom salinity. This difference is due to the lower salinity "fresh" water from Laguna San José and eastern Caño Martín Peña overriding the denser high salinity water infiltrating up western Caño Martín Peña from San Juan Bay. A review of the salinity transect plots, Figure 7-3, indicates that this salinity stratification continues to the western end of Caño Martín Peña. Rio Piedras inflows aid in keeping the surface salinity decreased in western Caño Martín Peña.

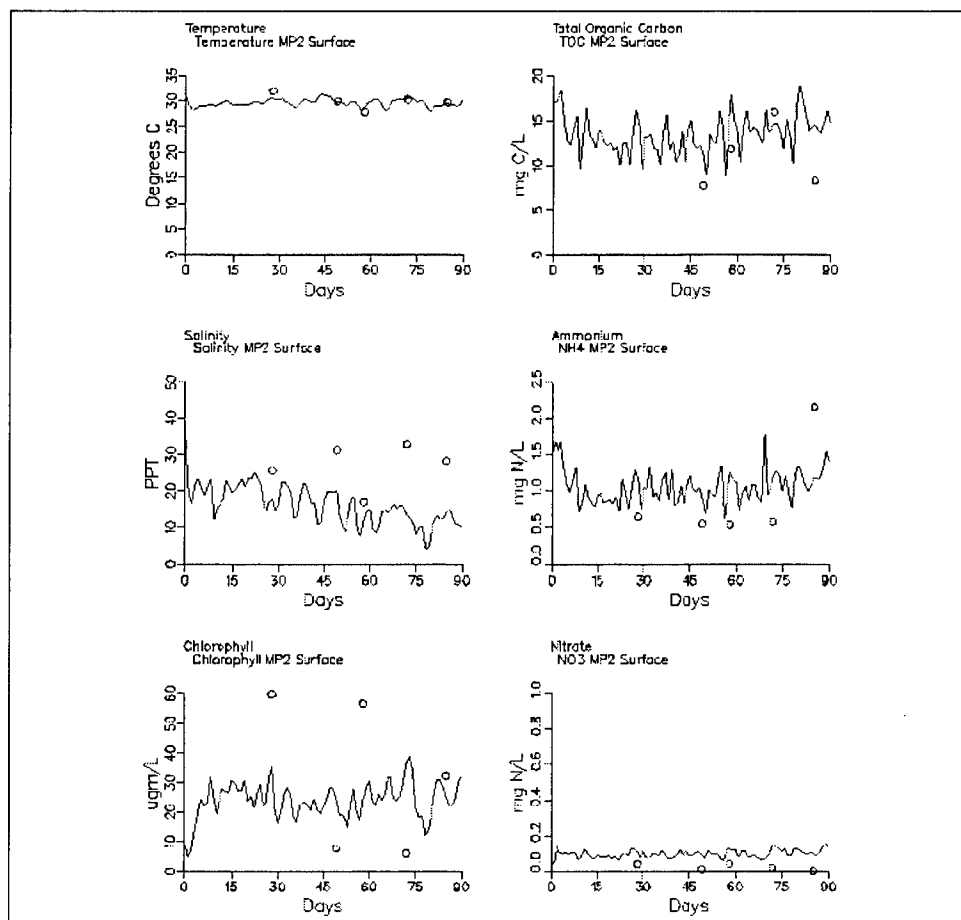


Figure 7-8. Caño Martín Peña station MP-2 calibration period time series (Sheet 1 of 4)

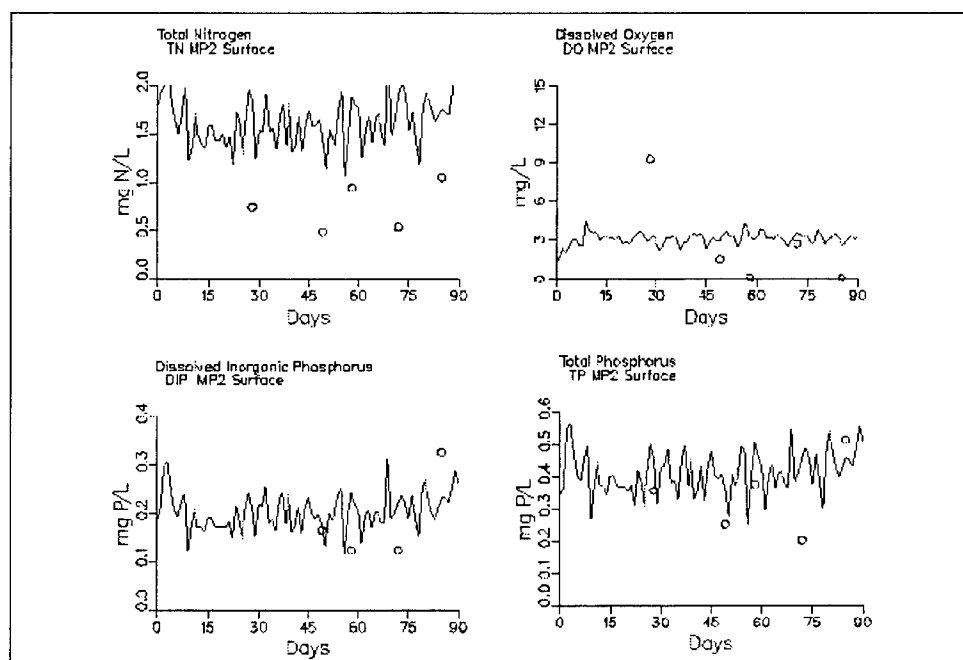


Figure 7-8. (Sheet 2 of 4)

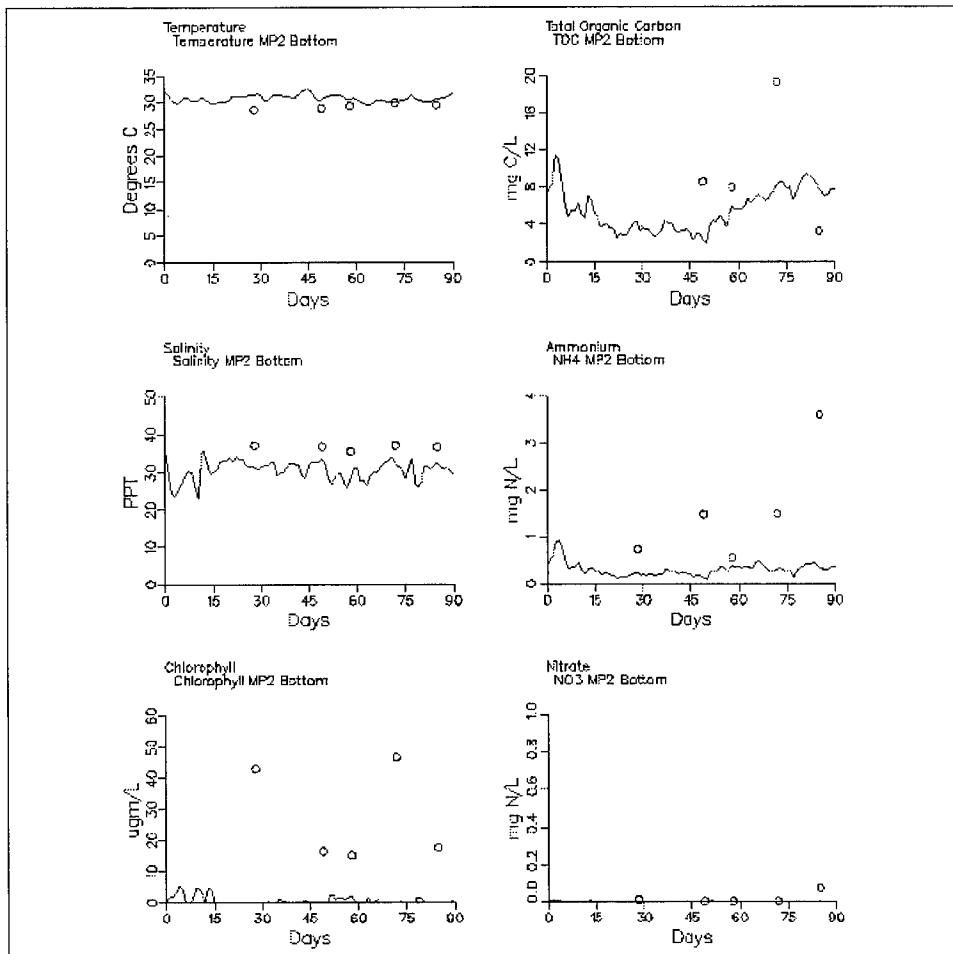


Figure 7-8. (Sheet 3 of 4)

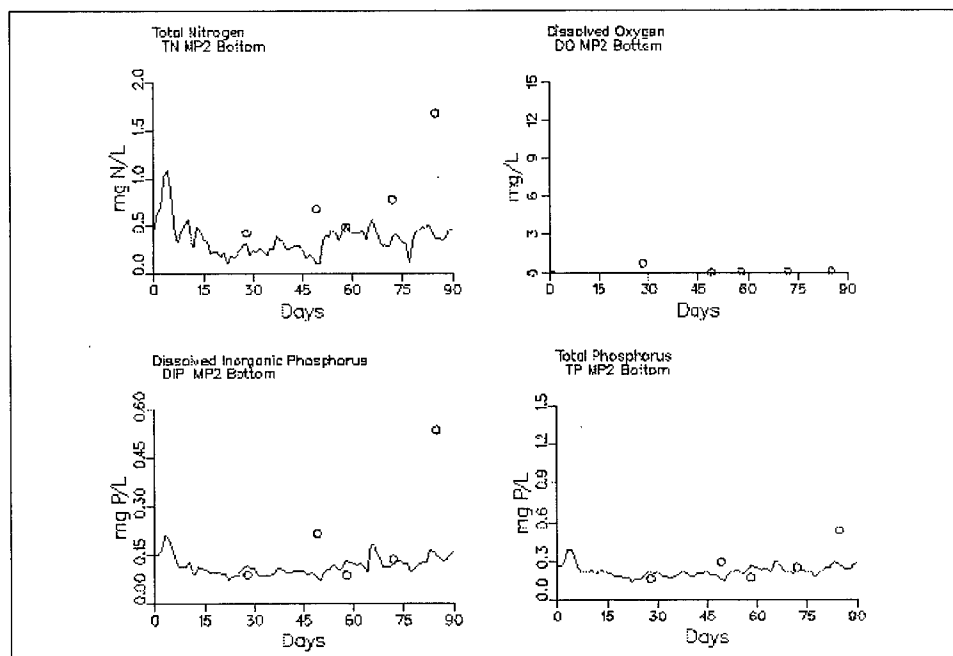


Figure 7-8. (Sheet 4 of 4)

Observed chlorophyll levels at MP-2 varied from 6 ug/l to 60 ug/l. Algae observed at station SJ-2 most likely originate in Laguna San José and are flushed down Caño Martín Peña by runoff-producing events. This is substantiated by the following. The two highest chlorophyll observations at MP-2 correspond to the lowest salinity concentrations. The lowest two chlorophyll observations correspond to the highest surface salinity observations. Runoff events generate higher flows in Caño Martín Peña which transport the chlorophyll quickly past MP-2. High light extinction and resulting low water column light levels in Caño Martín Peña are not conducive to algal growth, so the only way that elevated levels can exist is that they are generated elsewhere. ICM chlorophyll results exhibit significant variation in response to flow conditions. However, they do not indicate the degree of variability seen in the observations. As with salinity, this could be the result of comparing daily average model output with instantaneous observations at a location where things are sensitive to tidal action and flow conditions. Bottom chlorophyll observations exhibited significant variation too. Observations ranged from 15 ug/l to 47 ug/l. ICM chlorophyll results at this location are low. The only means by which algae can reach the bottom waters at station MP-2 are settling or transport with the intruding salt water. There are ample nutrients in the water to support algae but negligible light. The absence of light results in algal mortality before adequate time has passed for the algae to reach this location.

Total organic carbon surface observations ranged from 7.6 to 15.9 mg/l while bottom observations were between 7.9 mg/l and 19.3 mg/l. ICM results for the surface ranged from approximately 9 mg/l to 19 mg/l. The ICM results exhibited considerable variation in response to tidal action and eastern Caño Martín Peña flows but were representative of the observations. ICM bottom total organic carbon results were lower than the surface results and tended to be lower than the observed data. This is expected since the chlorophyll predictions were low at this location.

Observed ammonium levels in the surface water were elevated. Four of the observations were between 0.54 mg/l and 0.68 mg/l while the fifth was 2.15 mg/l. ICM results showed considerable fluctuation in response to hydrodynamic conditions but overall were representative of the observed data. Bottom water ammonia predictions were lower than the observations but still relatively high. Ammonium sediment flux rates at this station average 25 mg/m² day. Since the surface water ammonium levels are higher than the bottom water levels and the sediment flux of ammonia is not huge, it appears that the source of the ammonium in the surface water at MP-2 is eastern Caño Martín Peña. Little nitrate is found in the water at MP-2. ICM surface nitrate levels at MP-2 were slightly higher than the observations which were in the 0-mg/l to 0.04-mg/l range. ICM bottom nitrate predictions for MP-2 were essentially 0 mg/l which matched four of the five observations. Sediment nitrate fluxes at MP-2 were essentially 0 mg/m² day. Anoxic conditions along the bottom prevent nitrification from transforming ammonia into nitrate.

ICM dissolved oxygen concentrations in the surface fluctuated around 3 mg/l throughout the calibration period. Four of the observations during the calibration period were less than 3 mg/l with two being less than 0.12 mg/l. One observation was in excess of 9 mg/l which was in excess of saturation for the temperature and salinity at that time. A dissolved oxygen level this high results from algal photosynthesis. Bottom dissolved oxygen observations ranged from 0.04 mg/l to 0.79 mg/l. ICM results for bottom dissolved oxygen were 0 mg/l for the duration of the calibration period. When both surface and bottom dissolved oxygen concentrations are considered, ICM does a good job of matching observed conditions. The conditions existing at MP-2 result from two things. First, the high nutrient and organic carbon loading of eastern Caño Martín Peña. These oxygen-depleting substances remove the dissolved oxygen from the water faster than reaeration can replace it. Secondly, its location at the upper end of the dredging allows the waters from eastern Caño Martín Peña to override the denser waters infiltrating from San Juan Bay. Limited mixing between the surface and bottom waters at this location contributes to the dissolved oxygen depletion.

Overall ICM performs well at station MP-2. Conditions at this location are very dynamic. Major influences at this site are two. First is the flow from San José Bay into eastern Caño Martín Peña which is high in nutrients, algae, and oxygen demand. Second is the infiltration of salt water along the bottom of western Caño Martín Peña from San Juan Bay. ICM is able to reproduce many of the conditions observed during calibration even though conditions at this site are continually changing.

Station LC-1 is located in Laguna Condado. Temperature and salinity plots of results indicate that ICM matches observations in LC-1 well, Figure 7-9. Both temperature and salinity at this location reflect offshore conditions. ICM results match surface chlorophyll observations which are low, ranging from 0.5 to 3.2 ug/l. Total organic carbon observations for the surface and bottom exhibit the same behavior which mimics the observations at AO-1. ICM total organic carbon results indicate the same pattern as the observations. Ammonia observations at the surface ranged from 0 mg/l to 0.41 mg/l and from 0 mg/l to 0.6 mg/l at the bottom. ICM ammonia results were low, typically less than 0.05 mg/l in both the surface and bottom. ICM ammonia results were much lower than the extreme observations at this location. The validity of the extreme values at this station is uncertain since they are much greater than the TKN observations. At the end of the calibration period ICM ammonia concentrations are increasing in response to increases in the ammonia concentration specified at the ocean boundary. Nitrate levels, observed and computed in ICM, are near or are 0 mg/l for the duration of the calibration period in both surface and bottom waters. ICM dissolved inorganic phosphorus and total phosphorus levels agreed well with observations in both the surface and bottom waters at station LC-1. ICM dissolved oxygen results agreed well with all but one dissolved oxygen observation.

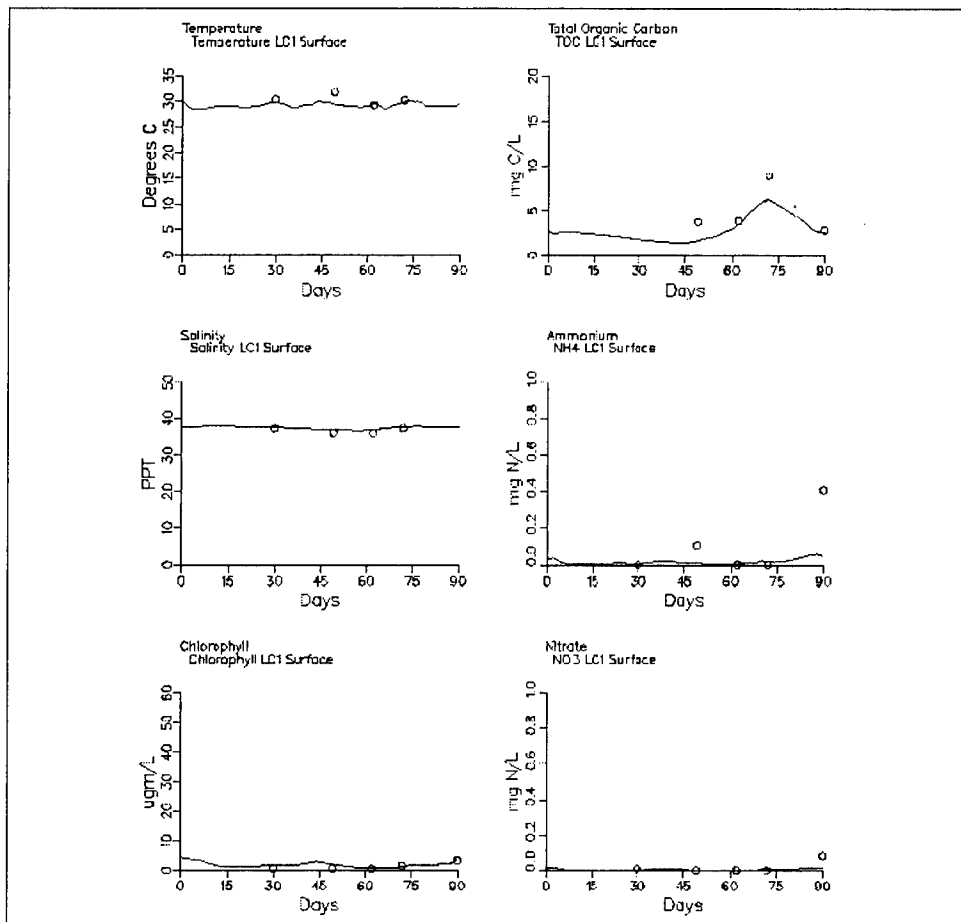


Figure 7-9. Laguna Condado station LC-1 calibration period time series (Sheet 1 of 4)

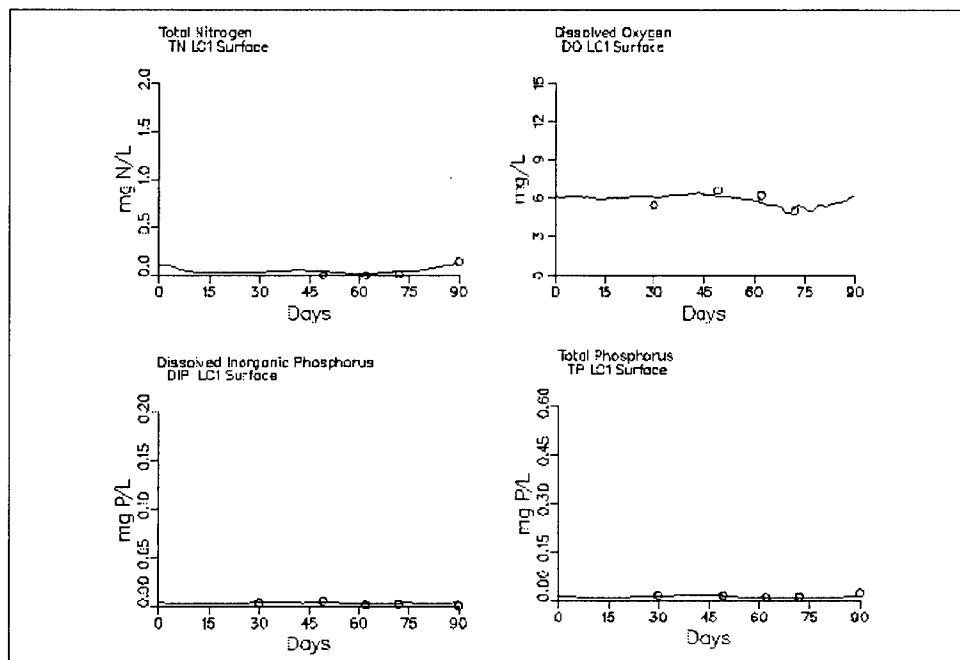


Figure 7-9. (Sheet 2 of 4)

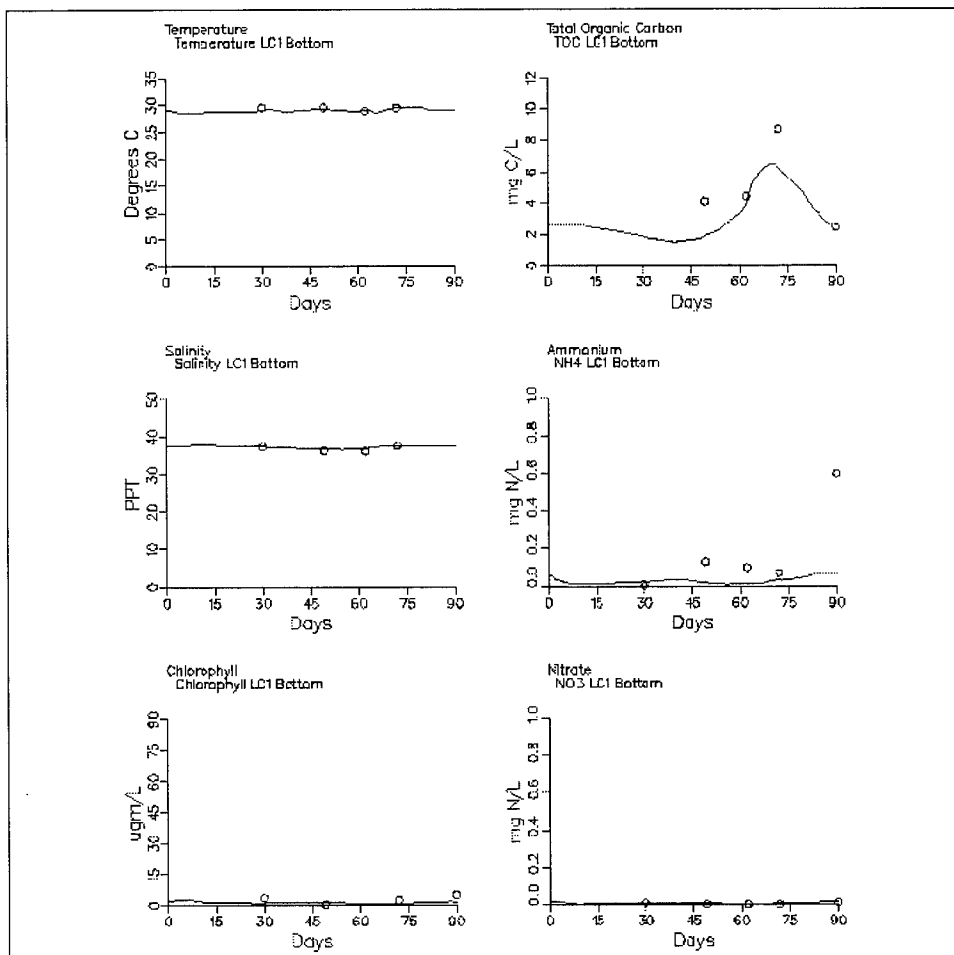


Figure 7-9. (Sheet 3 of 4)

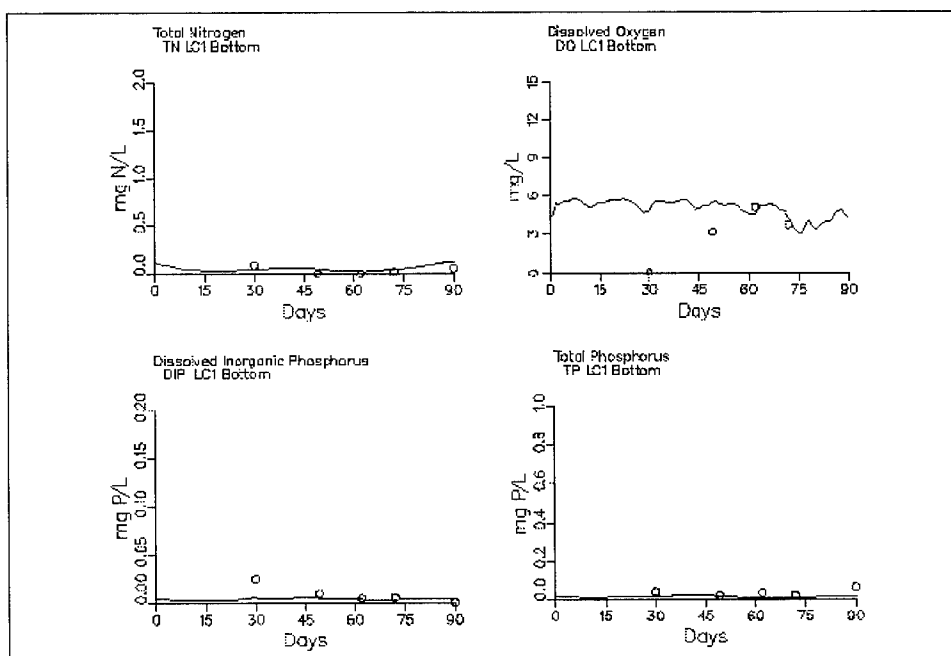


Figure 7-9. (Sheet 4 of 4)

Overall, the results indicate that ICM is performing well at this location. No attempts were made to calibrate ICM for Laguna Condado. A large part of ICM's performance at this location is attributable to the amount of exchange that occurs between Laguna Condado and the ocean. Constituent concentrations in Laguna Condado are similar to those specified at the ocean boundary. This is further evidence of the dominance of offshore conditions on this body.

Station SA-1 is located in Caño San Antonio which lies along the northeast side of San Juan Bay. Temperature and salinity observations in the surface and at the bottom at SA-1 location reflect conditions observed offshore at stations AO-1 and AO-2 indicating a high degree of exchange with the ocean. ICM results for both temperature and salinity correspond well with these observations, Figure 7-10. Surface chlorophyll observations were less than 5 ug/l. ICM chlorophyll results for the surface were typically 2 ug/l or less. Bottom water observations were less than 2.5 ug/l with the exception of one observation which was 17.6 ug/l. ICM results for the bottom of SA-1 indicated that chlorophyll levels were of 1-2 ug/l which agreed well with all but one observation. Total organic carbon surface and bottom observations at SA-1 demonstrated the same behavior observed at the offshore stations AO-1 and AO-2 with an increase in total organic carbon at calibration day 68. ICM results were similar to these observations. ICM results for ammonia, nitrate, and total nitrogen agreed well with both surface and bottom observations at SA-1. Dissolved organic phosphorus and total phosphorus ICM results likewise agreed well with surface and bottom observations at SA-1. Surface dissolved oxygen observations at SA-1 ranged from 5.16 to 9.78 mg/l while bottom dissolved oxygen levels ranged from 3.57 to 4.71 mg/l. As the ranges of observations indicate, the bottom dissolved oxygen concentration was considerably lower than the surface. ICM results adequately matched both surface and bottom dissolved oxygen levels when it is remembered that ICM results are daily averages and do not reflect any diurnal variation due to algal activity.

Laguna de Piñones is one of the major bodies of water in the SJBE system. Its location prevented its inclusion in the transect. Laguna de Piñones is located to the east of Laguna La Torrecilla and resides within a mangrove forest. Laguna de Piñones is connected to the southern end of Laguna La Torrecilla via a narrow canal. The region surrounding Laguna de Piñones is largely undeveloped and the flows and loads it receives are naturally occurring. Laguna de Piñones is shallow and was modeled as one layer in ICM.

Two stations are located in Laguna de Piñones. PL-1 is located in the canal that connects Laguna de Piñones and Laguna La Torrecilla. PL-2 is located on the eastern side of the lagoon. Model results indicate only slight fluctuations in temperature during the calibration period at both stations (Figure 7-11). Salinity predictions are adequate for the first portion of the calibration period but are low by day 90 of the simulation. This is indicative of freshwater flows from the watershed possibly being too high

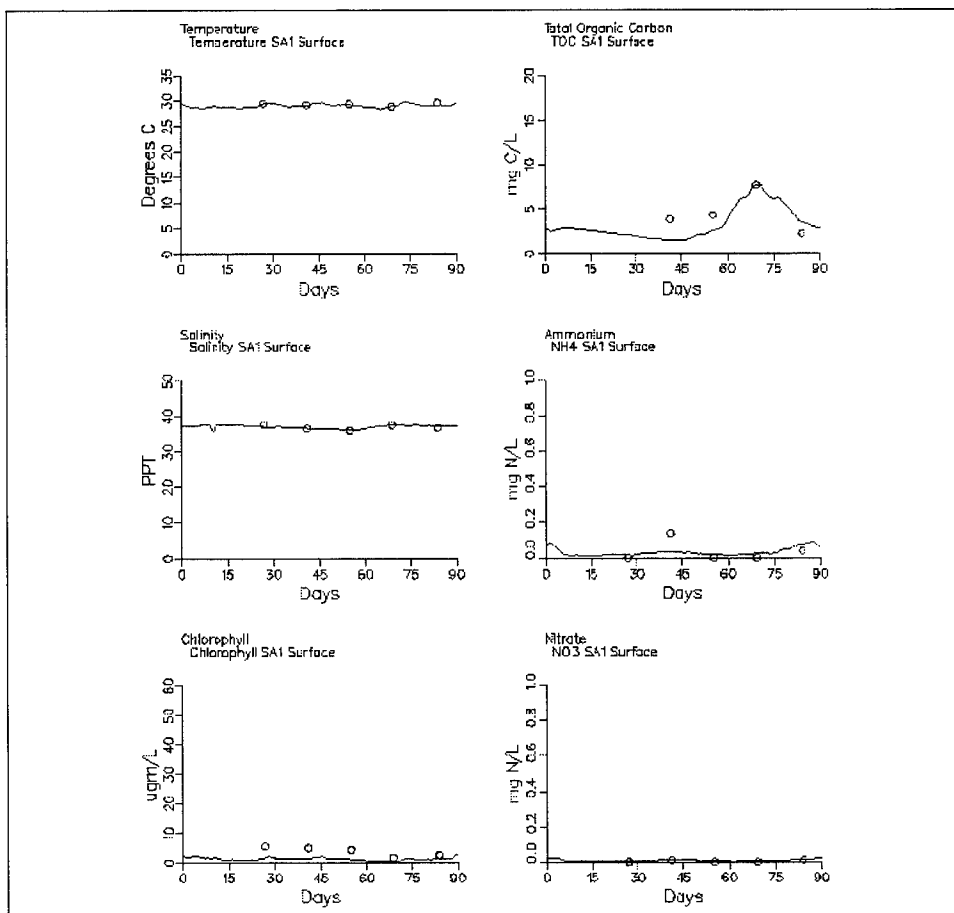


Figure 7-10. Caño San Antonio station SA-1 calibration period time series (Sheet 1 of 4)

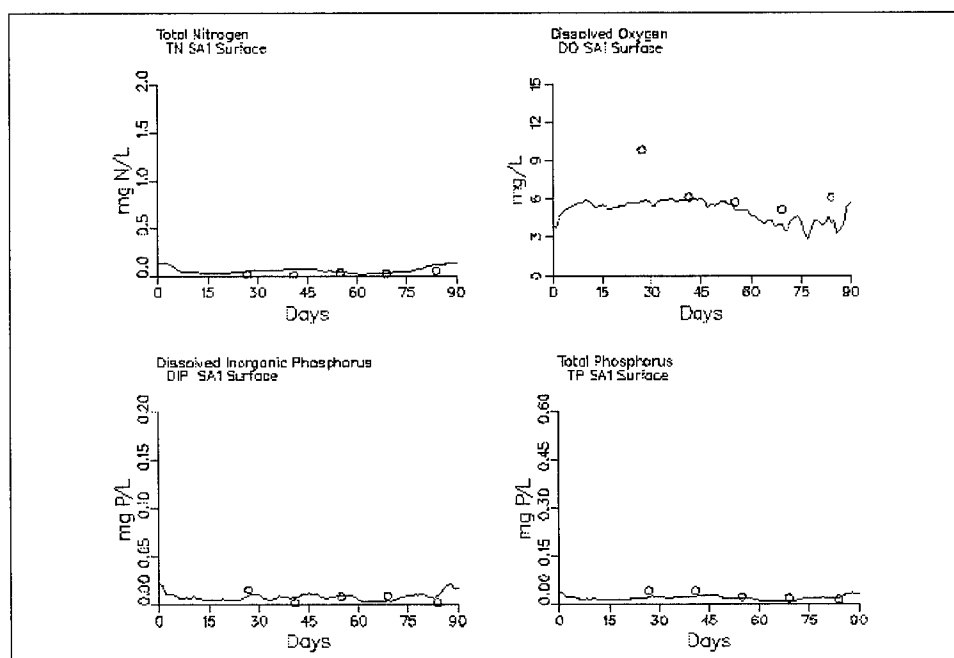


Figure 7-10. (Sheet 2 of 4)

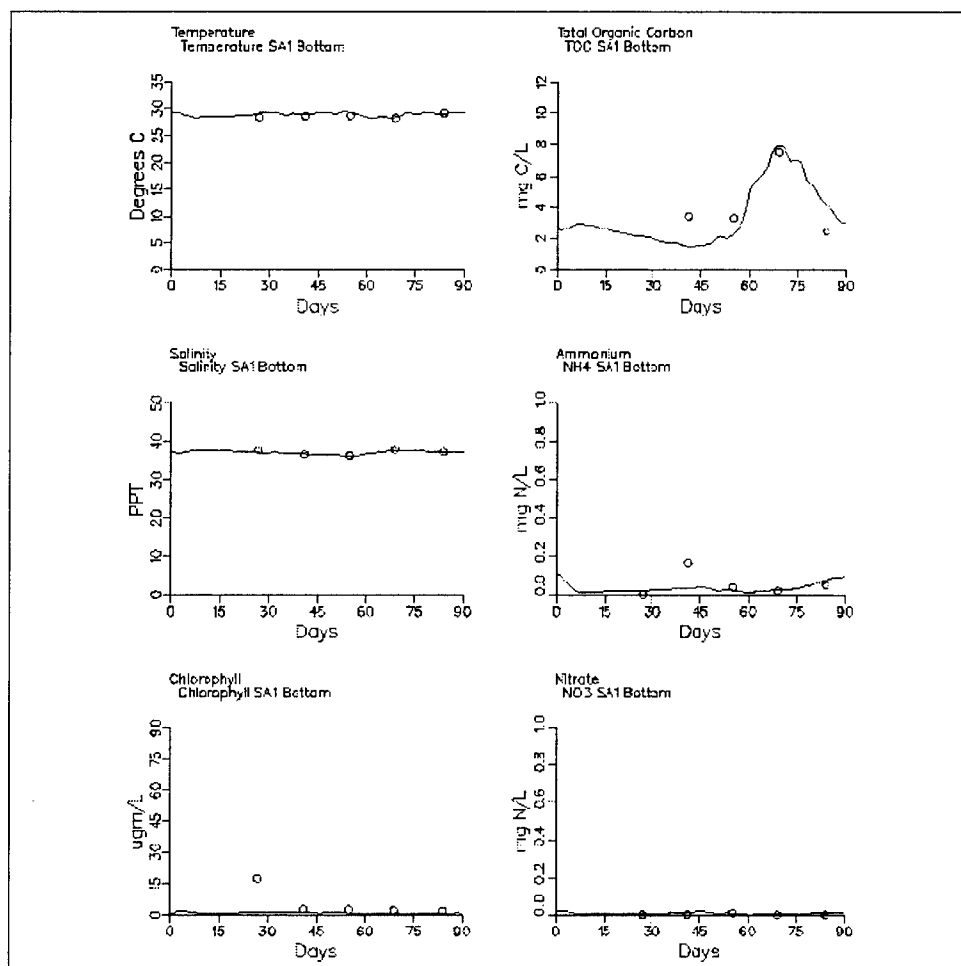


Figure 7-10. (Sheet 3 of 4)

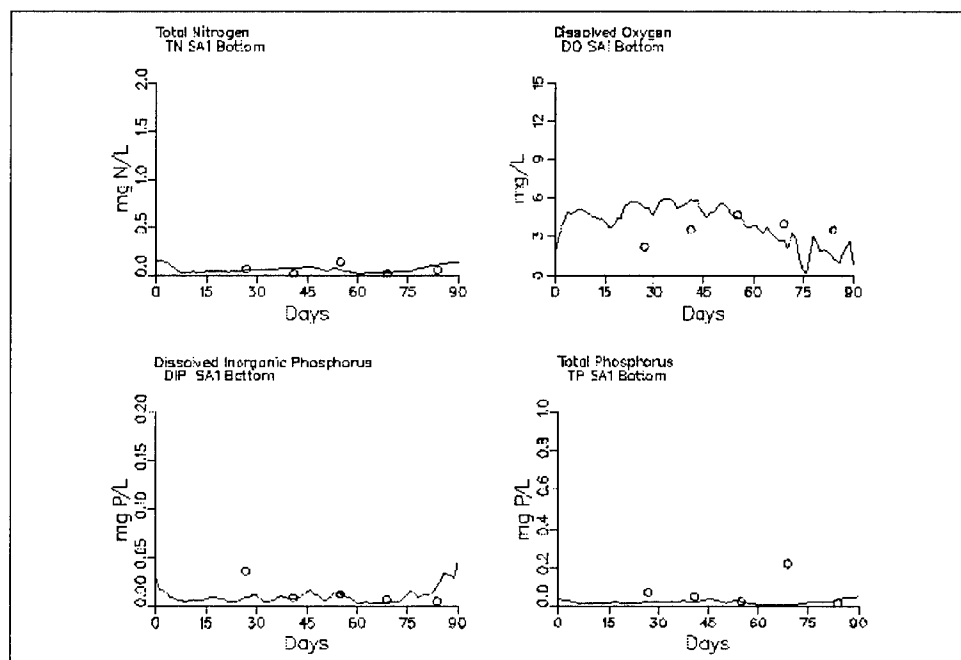


Figure 7-10. (Sheet 4 of 4)

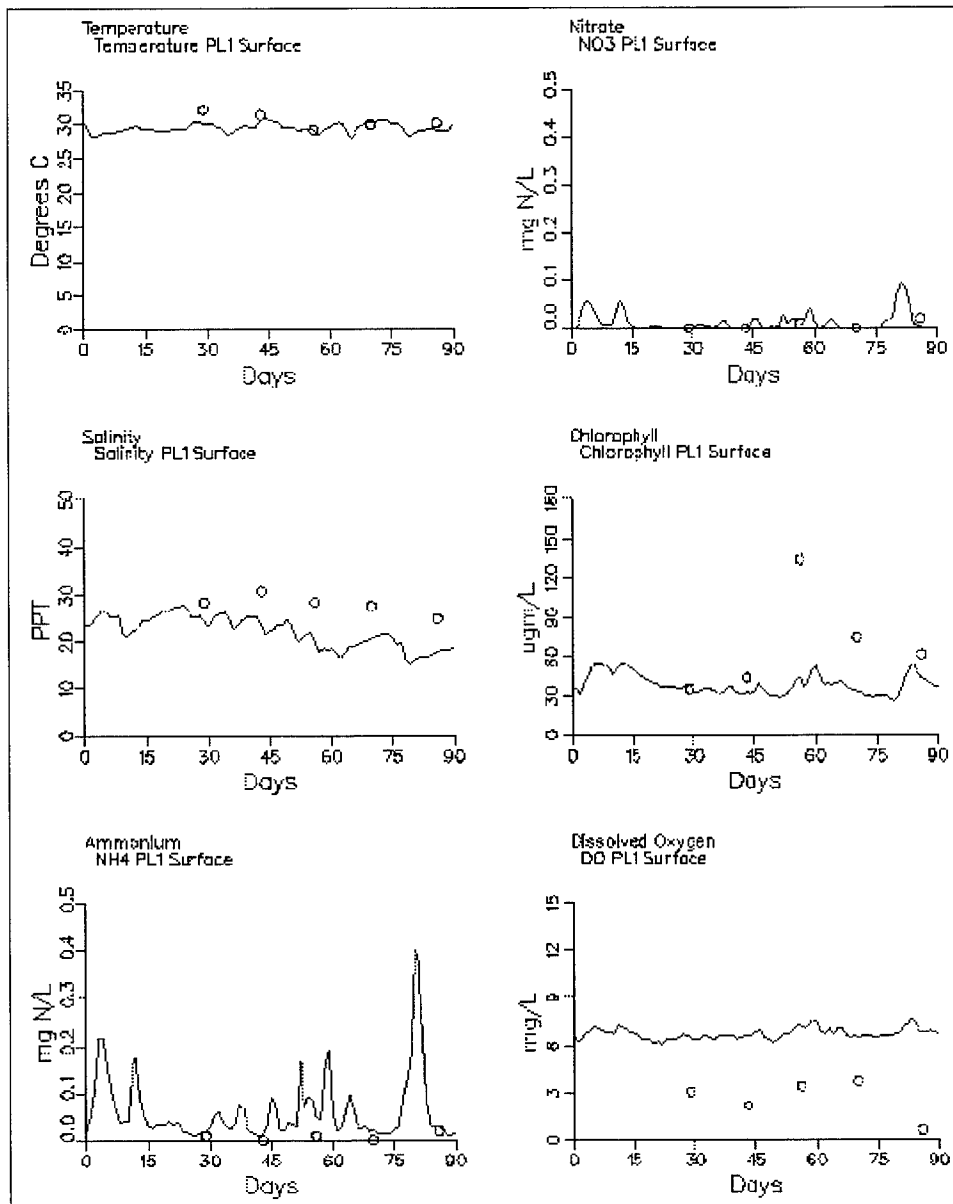


Figure 7-11. Computed and observed water quality variables at stations PL1 and PL2 (Laguna de Pinones) resulting from model calibration for summer 1995 (Sheet 1 of 4)

or too little salt water being able to enter Laguna de Piñones from Laguna La Torrecilla. Early on during calibration it was evident that the original loadings to Piñones were too low. Algae were too low as were nitrogen and organic carbon while dissolved oxygen was too high. Additional loads of nitrogen and carbon were added to the Piñones inflows to compensate for irregular inflow events and possible underestimation of loads. Organic carbon loads were increased from a daily average of 31.4 kg/d to 314.5 kg/day and total nitrogen loadings were increased from 4.5 kg/day to 36.1 kg/day. With these loads model chlorophyll predictions did increase but remained slightly low as a result of nutrient limitations retarding algal growth. Results for ammonium and dissolved inorganic phosphorus

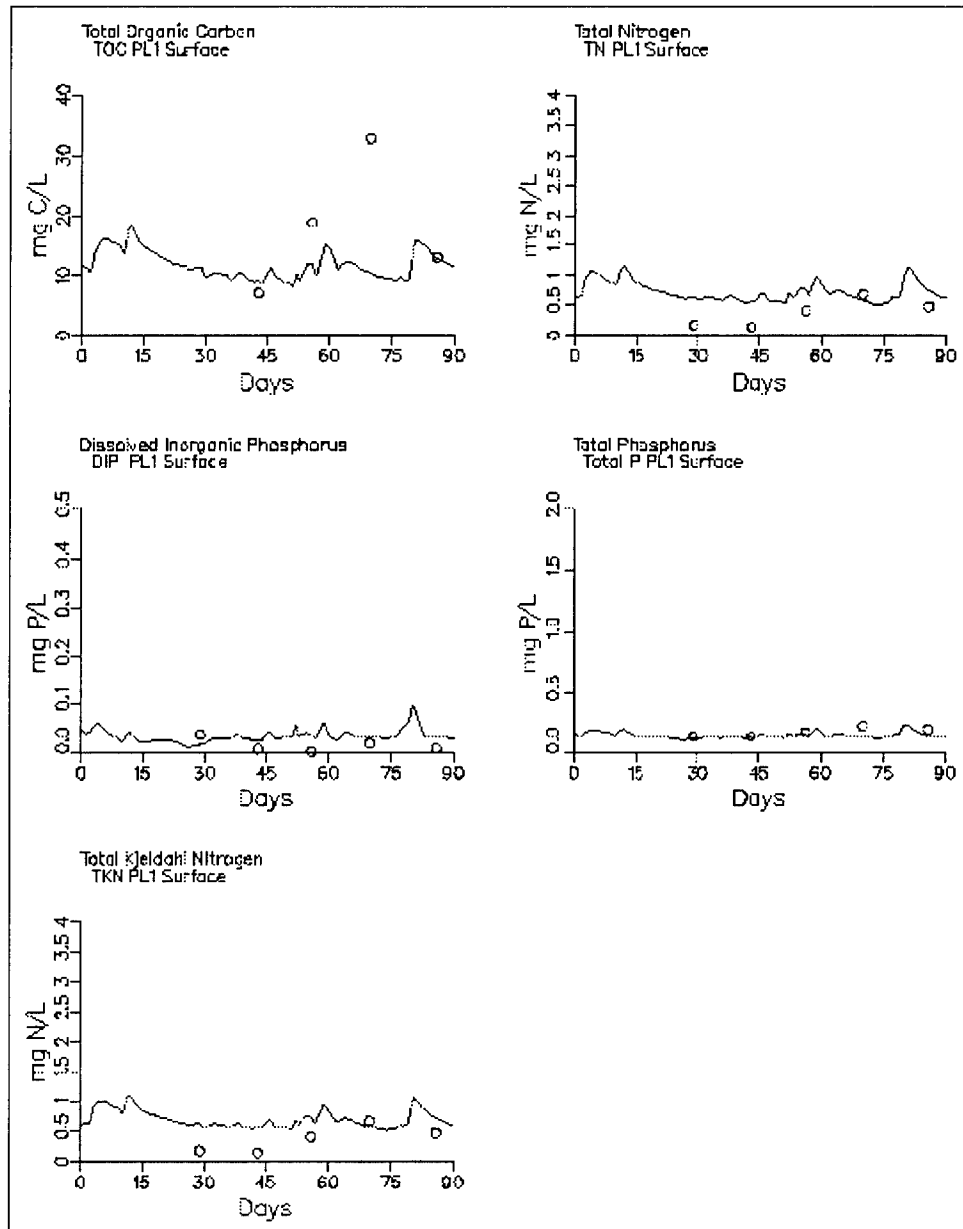


Figure 7-11. (Sheet 2 of 4)

indicate that as soon as a runoff event has deposited these nutrients into the system, algal growth (expressed by chlorophyll levels) increases until the nutrients are removed. At that time, chlorophyll levels cease to increase and actually begin to decrease until the next influx of nutrients occurs. Model predictions for total nitrogen and total phosphorus match the observations well. Model output for total organic carbon underpredicted the observed data continually even with the additional loading. Underprediction of TOC is possibly due to the presence of the mangrove forest which contributes organic carbon. No attempt was made to simulate the effects of the mangroves surrounding the lagoon. Model dissolved oxygen levels remained relatively constant throughout the

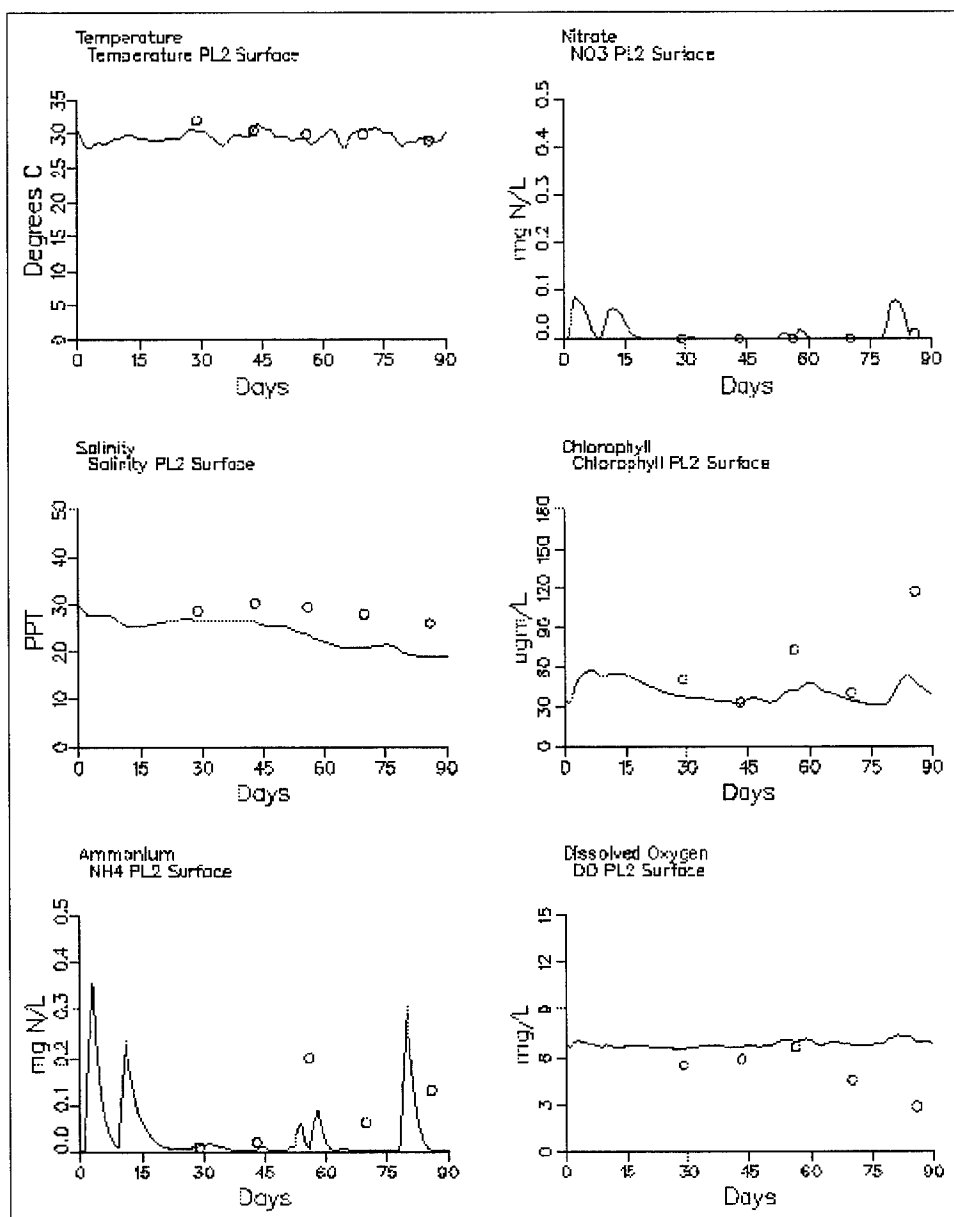


Figure 7-11. (Sheet 3 of 4)

calibration period and are overpredicted compared with observed, especially in the lagoon connecting canal. Possibly SOD is underpredicted due to TOC loadings from the mangroves, or the problem could be related to the inability of the model to resolve thin layers of stratification. Stratified water columns with thin (i.e., < 0.5 m) freshwater lenses are common in estuaries such as the SJBE.

Laguna de Piñones is located on the periphery of the SJBE system. None of the scenarios conducted involved Laguna de Piñones. Thus, the calibration results for Laguna de Piñones are adequate for the purposes of this study.

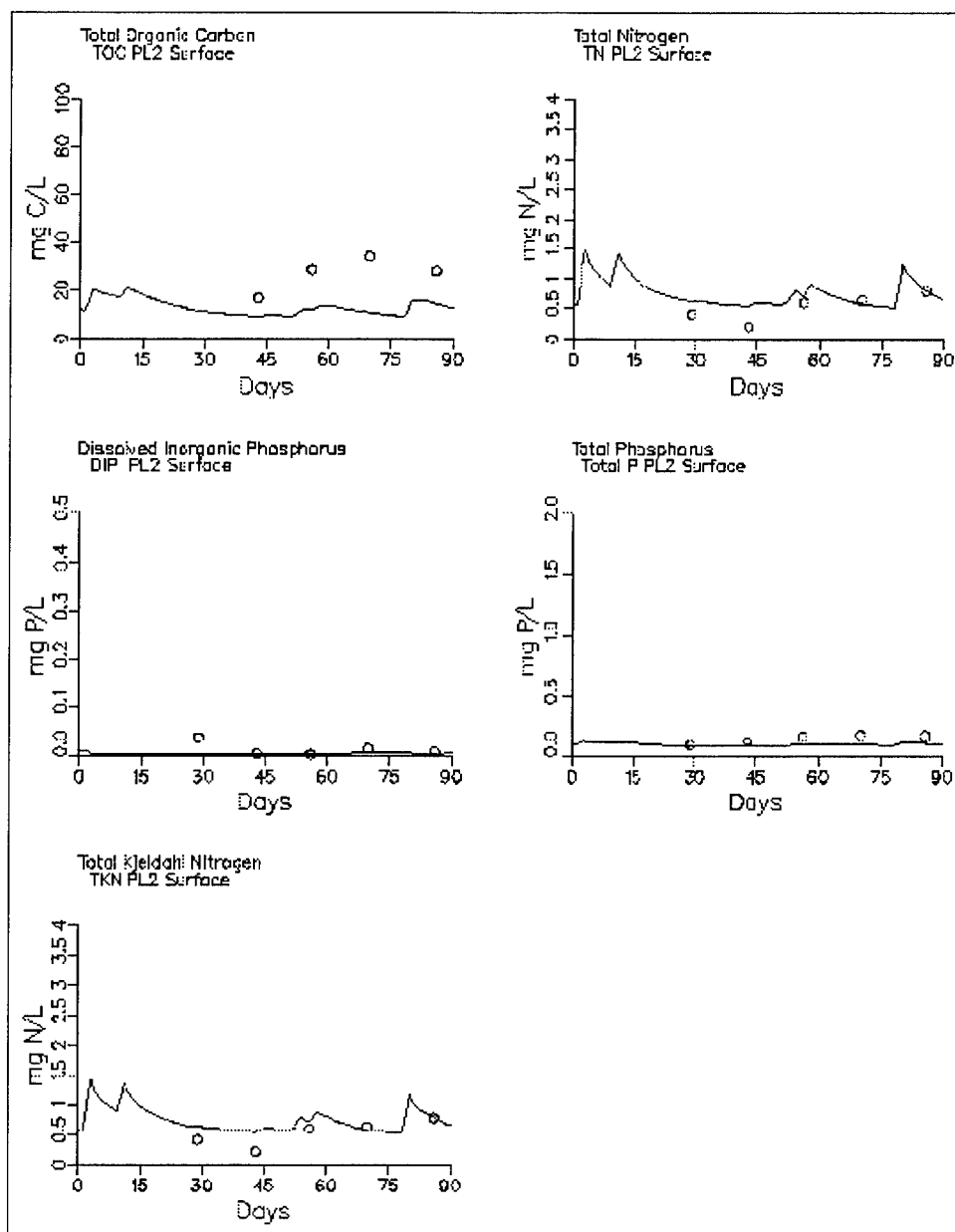


Figure 7-11. (Sheet 4 of 4)

Calibration Conclusions

Model calibration has resulted in a useful tool which adequately replicates observed behavior in the SJBE system. Though the SJBE system is not large it is very heterogenous with numerous bays, lagoons, and canals which complicated WQM calibration and affected performance. Often, attempts to improve calibration in one constituent or region had detrimental consequences on the calibration elsewhere. Further improvements in calibration were hindered by the limitations of the loading data. A comprehensive database of loading information did not exist and the loads used for calibration were estimates. The actual SJBE system is subjected to

highly variable (both spatially and temporally) loadings resulting from runoff events and localized anthropogenic loadings. Great effort was expended in developing and implementing loads in the WQM which would be representative of these conditions. However, these estimates might not always agree with actual loads resulting from short-term events. Consequently, model calibration is impacted as the WQM may not match observations at locations with large temporal fluctuations in water quality resulting from runoff.

Another consideration when reviewing calibration results is the scale at which processes occur in the real system. Vertical resolution in the WQM is limited to the layer thicknesses used in the hydrodynamic model which were in turn limited by model stability requirements. Consequentially, processes such as stratification in shallow water or the simulation of over-riding, thin, freshwater lenses are beyond the capability of the WQM to resolve.

Overall model calibration was judged to be acceptable for scenario testing by the modelers and the model review group. In scenario testing, the model is run with a modification (scenario) and the results compared to a simulation with no modifications (base) and the relative differences determined. Any calibration deficiencies are present in both the base and scenario simulations and therefore tend to cancel out when the focus is on relative differences between base and scenario results.

8 Management Scenarios

Methods

The model was used to evaluate the effectiveness of various management alternatives (i.e., scenarios) for improving water quality. This section describes the methods used for conducting the management scenario simulations.

The overall strategy consisted of developing a scenario test period (STP) that was used for all scenarios so that comparisons of the relative worth of various management options could be evaluated. Both the HM and WQM had to be executed for each scenario, since the flows from the HM are used to drive the WQM, and in most cases the proposed management alternative affects the flows. However, as discussed further below, it was not necessary to run the HM for the same length of time as the WQM since the HM output is saved and can be used in a repetitive fashion throughout the WQM simulation, as was done for WQM calibration. To properly compare different management options, the WQM was run until it reached an equilibrium condition, i.e., a cyclic, steady-state condition. As the hydrodynamics, inflows, and loadings of the STP were cycled multiple times through the WQM, the WQM eventually arrived at an equilibrium condition that was time-varying, but repeated itself for each STP cycle. The time to reach equilibrium depended on the time it took for the sediments and water column to reach equilibrium, which was on the order of about 8 months.

The calibration period of summer 1995 was chosen for the STP. This period was chosen since it allowed comparison of each scenario against baseline conditions that existed in 1995 when observed data were available. The STP extended for one complete lunar month (28.25 days) using the conditions extending from 10 July through 7 August 1995, which contained a storm event around 1 August. A few extra days were executed on the front end of each HM run for model spin-up. The observed conditions for tides, wind, and freshwater flows were used. Output from the HM was saved and used repeatedly by the WQM throughout the longer, multimonth WQM simulation. Thus, the hydrodynamics used for each month of the WQM simulation were identical for a given scenario. When recycling

hydrodynamics in this fashion, there is a requirement that the system water depths and volumes be nearly equivalent at the beginning and end of the HM simulation to avoid building up or depleting too much water over the long-term WQM simulation. This requirement was satisfied by carefully choosing the beginning and ending time for the STP.

Each WQM scenario STP was run for eight times to spin-up the new conditions, thus achieving a new dynamic steady-state. Only results from the final 28.25-day STP are presented here.

The STP constituent loadings for the WQM were the same as those used for the calibration, except for the loading reduction scenarios where loads were reduced. Meteorological conditions for the WQM for all scenarios were based upon the average July period of record observations at San Juan International Airport and are presented in Table 8-1. Observed, hourly varying July winds were used for the HM scenario runs since winds can affect residual circulation.

Table 8-1. Scenario Meteorological Conditions	
Dry Bulb Temperature	82°F
Dew Point Temperature	73°F
Wind Speed	8.5 mph
Cloud Cover	60%

Scenario Descriptions

Ten sets of simulations (Table 8-2) were run to assess the impact proposed remediation management strategies would have upon water quality. Scenario 1a was a base condition against which the other nine would be judged. Five scenarios (1b, 1c, 2, 3, and 4) involved some form of channel/bathymetric modification in either Caño Martín Peña, Laguna San José, or Canal Suárez and Laguna La Torrecilla which would result in a redistribution of flows. Scenarios 5a and 5b involved only loading reductions while scenarios 6a and 6b combined channel/bathymetric modifications and loading reductions. The channel/bathymetric modifications called for by many of these scenarios resulted in a reconfiguration of ICM grid (see Table 8-3) as well as running new conditions in the HM (see Table 8-2). The scenarios evaluated are described further below, and the results are discussed in the subsequent sections of this chapter.

**Table 8-2.
Management Water Quality Scenarios**

Scenario	Description	Hydrodynamic Scenario
1a	Base condition with approved dredging in San Juan Bay and Rio Piedras implemented	1a
1b	1a plus clearing and widening eastern end of Caño Martín Peña to 50 ft	1b
1c	1a plus widening Caño Martín Peña to 150 ft and deepening to 9 ft	1c
2	1a plus filling all dredge material borrow pits to 6-ft depth	2
3	1a plus removing the constriction at the Loiza Expressway bridge on Suárez Canal by widening by 100 ft and deepening to 12 ft	3
4	Conditions of Scenario 3 plus installation of 1-way tide gate in Canal Suárez	4
5a	1a plus loading reduction in Caño Martín Peña Canal (removal of un-sewered loadings)	1a
5b	1a plus loading reduction in San José (removal of Baldorioty de Castro pump station loadings)	1a
6a	1c plus 5a and 5b	1c
6b	6a plus 2	6b

**Table 8-3.
ICM Grid for Each Scenario**

Scenario	Surface Cells	Total Cells	Total Flow Faces	Horizontal Flow Faces
1a	1923	10731	28230	19422
1b	1923	10731	28230	19422
1c	1923	10769	28309	19463
2	1923	10341	27451	19033
3	1923	10734	28238	19427
4	1923	10734	28238	19427
5a	1923	10731	28230	19422
5b	1923	10731	28230	19422
6a	1923	10769	28309	19463
6b	1923	10379	27530	19047

Scenario 1a, Baseline Conditions

The baseline simulation was similar to conditions that existed during the summer of 1995 and used the same boundary conditions and loadings as those used for model calibration. The geometry and bathymetry of the system were the same as the *existing* conditions with the exception of minor geometric changes related to dredge and fill improvements that were approved and have either been implemented or are underway. These improvements involved deepening the San Juan Harbor channel to 11.9 m (39 ft) and deepening the Puerto Nuevo flood control channel to 7.32 m (24 ft). Scenario 1a served as the baseline, or *existing*, conditions against which all other scenarios were compared to evaluate their effectiveness.

Scenarios 1b and 1c, Channel Improvements in Caño Martín Peña

The eastern portion of Caño Martín Peña is considered to severely hinder flushing of the inner part of the system. Thus, two scenarios simulations were conducted to evaluate channel improvements for the eastern portion of Caño Martín Peña. The first channel improvement, Scenario 1b, consisted of clearing the channel to a nominal 15.2-m (50-ft) width from about 7 m (25 ft). The model bottom drag coefficient was also changed to reflect clearing of the channel for Scenario 1b. The second channel improvement, Scenario 1c, consisted of a channel widened to a minimum width of 45.7 m (150 ft) and deepened to a minimum depth of 2.74 m (9 ft). Both scenarios were run with all other conditions and configurations set the same as those for Scenario 1a. The HM grid was modified for each channel configuration, and the HM was executed for the STP to generate flows for the WQM. Then the WQM was run to equilibrium using the new HM output and *existing* loads for the STP.

Scenario 2, Filling of Submerged Borrow Pits

This scenario consisted of Scenario 1a conditions plus filling of submerged borrow pits within Laguna San José and Laguna La Torrecilla. These pits are the result of sand and fill mining for development of residential and service facilities. The deep holes have low DO and are sources for nutrients that diffuse from bottom sediments under low DO conditions. The bathymetry for model grids cells representing the pits was reduced to a depth of 1.83 m (6 ft). The HM was executed for the STP with the new depths. The WQM was then run to equilibrium using this HM output and *existing* loads.

Scenario 3, Loiza Epressway Bridge Constriction in Suárez Canal Removed

For the most part, Suárez Canal does not restrict flushing, with the exception of a constriction at the Loiza Expressway bridge, where the canal is only about 15 m (50 ft) wide and 0.91 m (3 ft) deep. Thus, a scenario was conducted to investigate removing the Loiza Expressway bridge constriction by enlarging the canal at the bridge to 30.5 m (100 ft) wide by 3.66 m (12 ft) deep. The HM grid was adjusted to represent the proposed Suárez Canal improvement, and the model was run using Scenario 1a conditions for all other geometric features and boundary conditions. The WQM was then run to equilibrium using this HM output and *existing* loads.

Scenario 4, Tide Gate in Suárez Canal with Bridge Constriction Removed

Scenario 4 investigated a tide gate installed and operated in Suárez Canal where the gate was open during flood flow through Suárez Canal and closed during ebb flow to force water out through Caño Martín Peña. The HM was modified to allow simulation of a tide gate operating in the western portion of Suárez Canal, and the HM was executed for the STP with the tide gate combined with Scenario 1a conditions plus the bridge constriction removed (Scenario 3). The bridge constriction was removed too for this scenario since this improvement is considered likely to occur if a tide gate is built. The WQM was then run to equilibrium using this HM output and *existing* loads.

Scenarios 5a and 5b, Loading Reductions

Considerable loadings of nutrients and fecal coliform bacteria occur within the SJBE system. Therefore, management actions to reduce these loadings is a potential effective means of improving water quality. To evaluate the effectiveness of loading reductions, it was necessary to conduct these simulations with *existing* conditions for other boundary conditions and system geometry and bathymetry. Therefore, the loading reductions were conducted with Scenario 1a hydrodynamics imposed. So it was not necessary to re-run the HM for Scenarios 5a and 5b. The loadings in the WQM prescribed in Scenario 1a were reduced as described below, and the WQM was run to a new equilibrium condition.

Scenario 5a consisted of eliminating local, nonpoint source loadings along Caño Martín Peña. These loads are significant and represent untreated sewage from un-sewered residential areas. Removing these loads is a very likely management scenario.

Scenario 5b consisted of diverting all pollutant loadings that enter Laguna San José via the Baldorioty de Castro storm water pump station.

The flows from the plant were still introduced, but the constituent concentrations were removed.

Scenarios 6a and 6b, Combinations

Following review of results from the previous scenarios, the SJBEP recommended two combination scenarios be run to evaluate the cumulative effectiveness.

Scenario 6a consisted of the combination of management alternatives prescribed by Scenarios 1c, 5a, 5b. Thus, Scenario 6a contained the improved Caño Martín Peña (45.7 m or 150 ft wide and 2.74 m or 9 ft deep) along with the elimination of loadings in Caño Martín Peña and from the Baldorioty de Castro storm water pump station. Otherwise, other geometry, bathymetry, and boundary conditions were the same as those for Scenario 1a. Thus, HM output from run 1c was used to drive the WQM to a new equilibrium condition using the reduced loadings for Scenarios 5a and 5b.

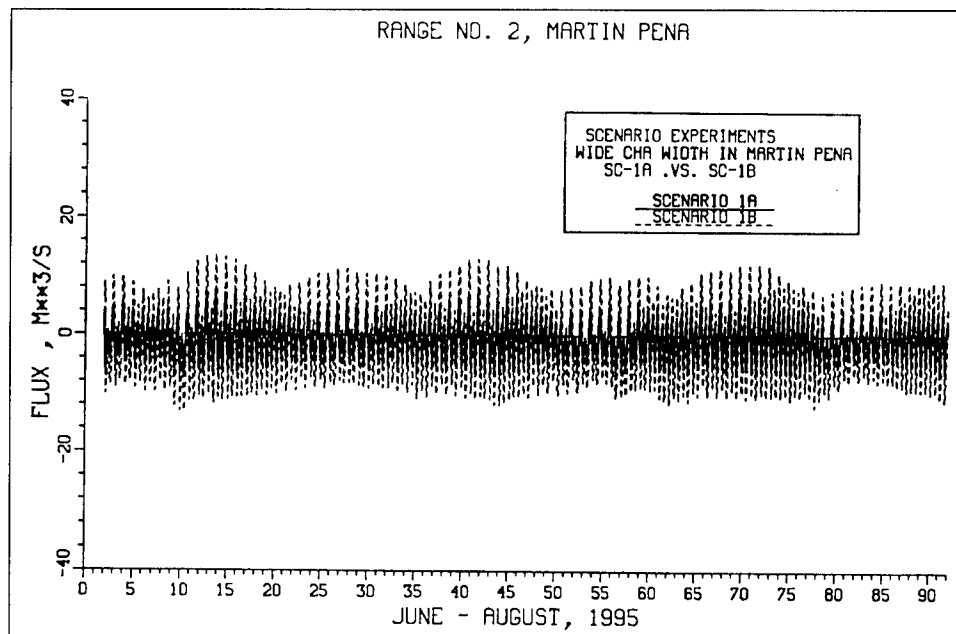
Scenario 6b consisted of the combination of management alternatives prescribed by Scenarios 1c, 2, 5a, and 5b. Thus, Scenario 6b included conditions for Scenario 6a plus Scenario 2, i.e., submerged borrow pits filled. Scenario 6b required re-running the HM with the combination of Scenarios 1c and 2 management alternatives. These HM results were used to drive the WQM to a new equilibrium condition with Scenarios 5a and 5b loading reductions imposed.

Hydrodynamic Model Results

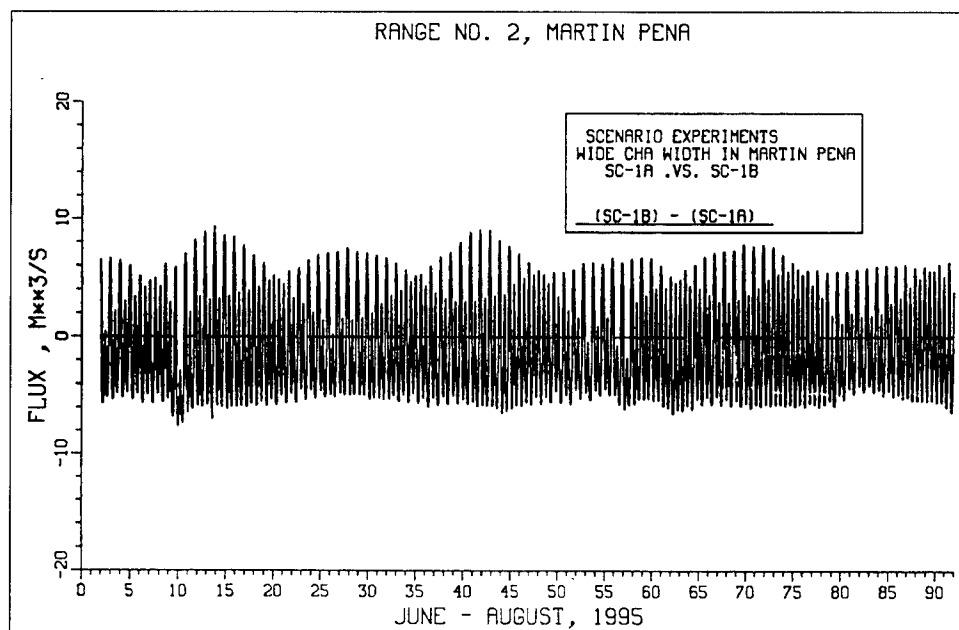
This section discusses the scenarios that were simulated by the HM. Comparisons of HM results from each of the scenarios with results from Scenario 1a are presented and discussed below.

Scenario 1b Results

As can be seen from Figures 8-1 and 8-2, the impact of slightly widening the eastern end of Martín Peña and reducing the friction is to increase the tidal flux through the Martín Peña Canal while slightly decreasing the flux through Canal Suárez. Figure 8-3 shows essentially no change in the tidal range in Laguna San José, but a slight setdown in the water level is computed. This is likely due to more of the Laguna San José freshwater inflow being able to move out of the lagoon more quickly through the improved Martín Peña Canal. As a result of the increased flow of freshwater, one might expect that the salinity in Martín Peña would decrease. Figure 8-4 shows this to be the case. Likewise, due to the decreased amount of San José freshwater inflow moving out through the Canal

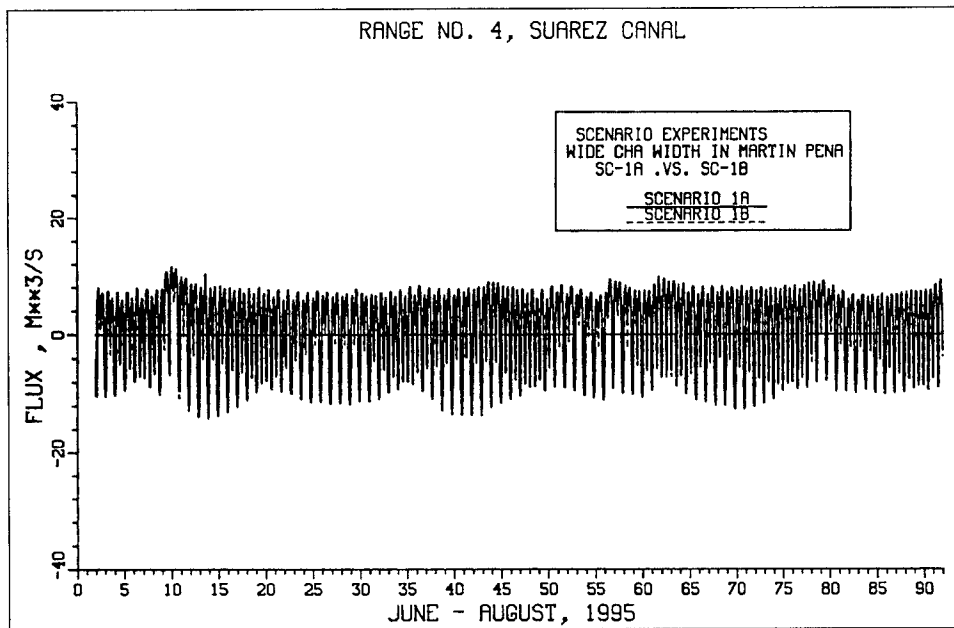


a. Both 1a and 1b

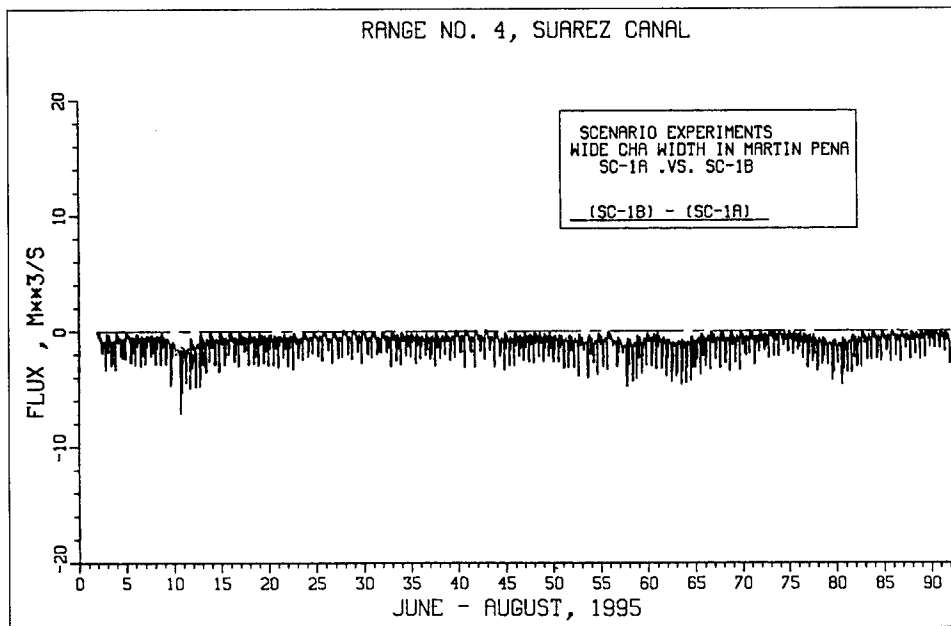


b. Difference between 1a and 1b

Figure 8-1. Comparison of flux through Martin Pena Canal between Scenarios 1a and 1b



a. Both 1a and 1b



b. Difference between 1a and 1b

Figure 8-2. Comparison of flux through Suarez Canal between Scenarios 1a and 1b

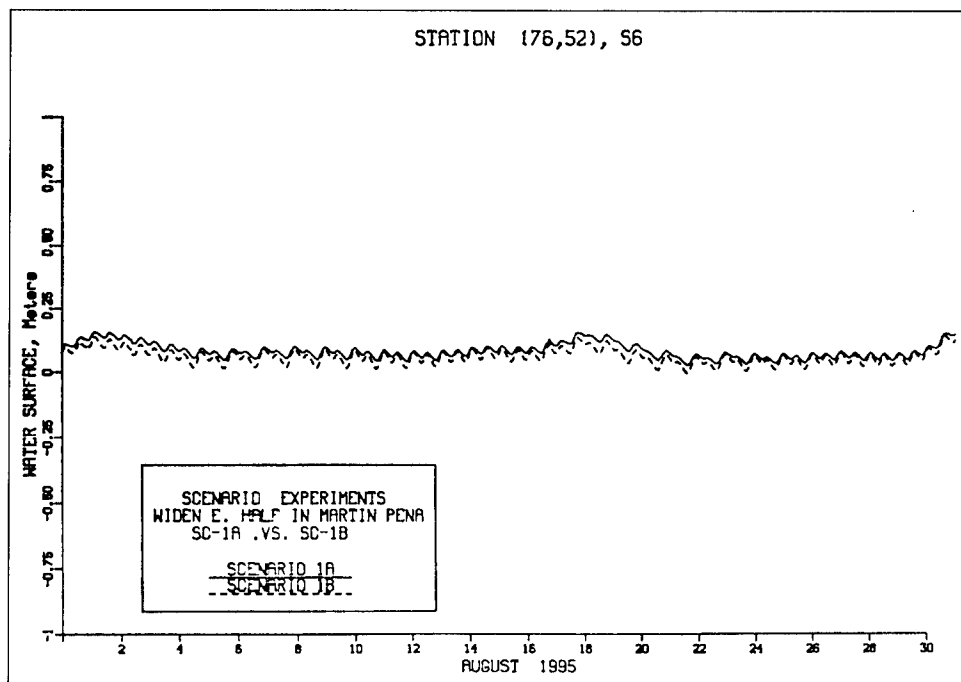


Figure 8-3. Comparison of tide at S6 between Scenarios 1a and 1b

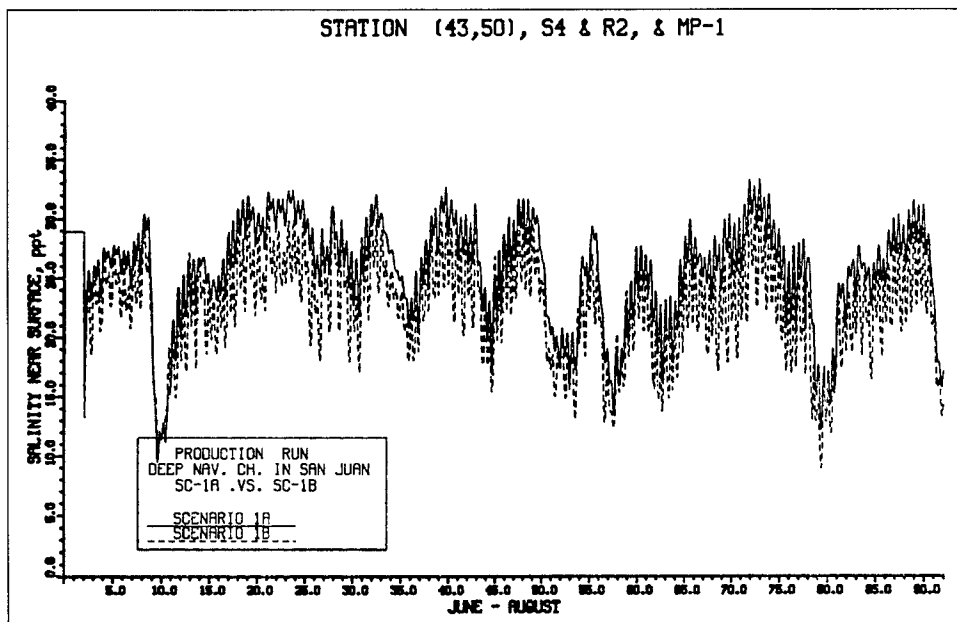
Suárez, Figure 8-5 shows that the salinity in Suarez increases. With the salinity in Suarez being higher, higher saline water flows into Laguna San José during flood, resulting in higher salinity in San José. This is illustrated in Figure 8-6.

Scenario 1c Results

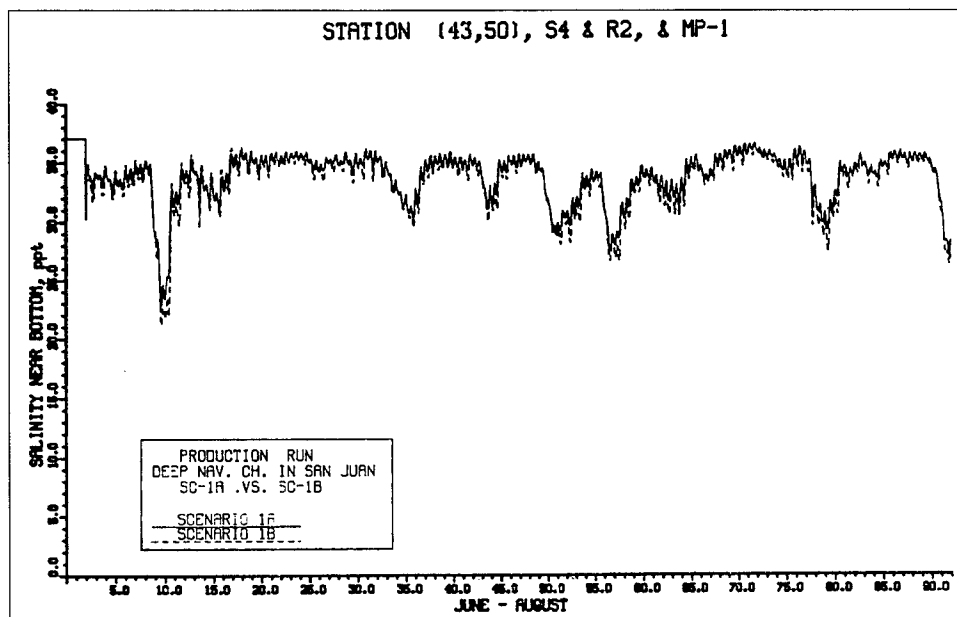
With a substantial increase in width and depth in Martín Peña Canal for this scenario, Figure 8-7 illustrates that the tide range in Laguna San José increases from less than 5 cm (0.164 ft) to 30-35 cm (0.984 - 1.148 ft). As illustrated in Figure 8-8, the tidal flushing between San Juan Bay and Laguna San José increases by more than an order of magnitude. However, as with Scenario 1b, improvements in Martín Peña Canal result in less flushing through Canal Suárez (Figure 8-9). With the tremendous increase in tidal flushing through Martín Peña Canal, the high saline waters of San Juan Bay move into Laguna San José, resulting in increases in salinity in Martín Peña and San José (Figures 8-10 and 8-11). Likewise, with the increased salinity in San José, as water moves from San José into Canal Suárez, salinity in Canal Suárez increases (Figure 8-12).

Scenario 2 Results

As illustrated in Figures 8-13 - 8-15, filling the holes in the system had virtually no impact on flux through the canals nor on the tidal range in Laguna San José. However, as shown in Figures 8-16 - 8-18, decreases in salinity in Martín Peña, San José, and Suarez were computed. Data from

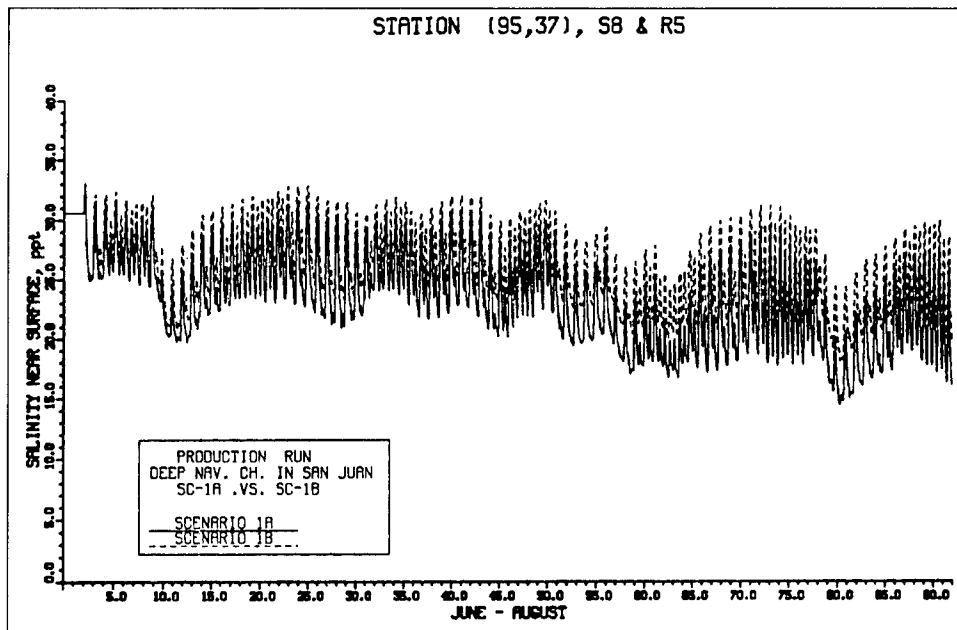


a. Near surface

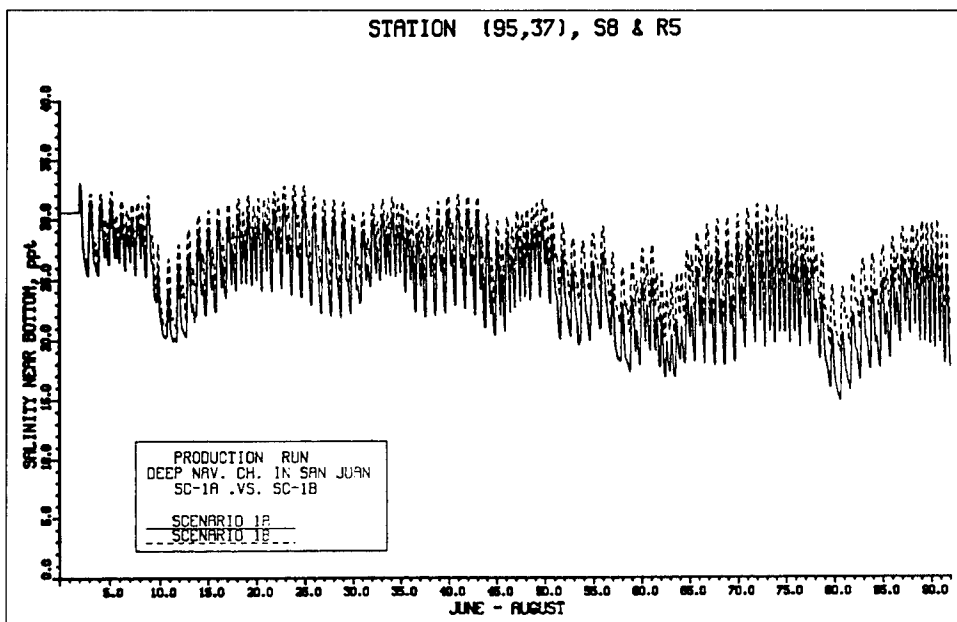


b. Near bottom

Figure 8-4. Comparison of salinity at S4 between Scenarios 1a and 1b



a. Near surface



b. Near bottom

Figure 8-5. Comparison of salinity at S8 between Scenarios 1a and 1b

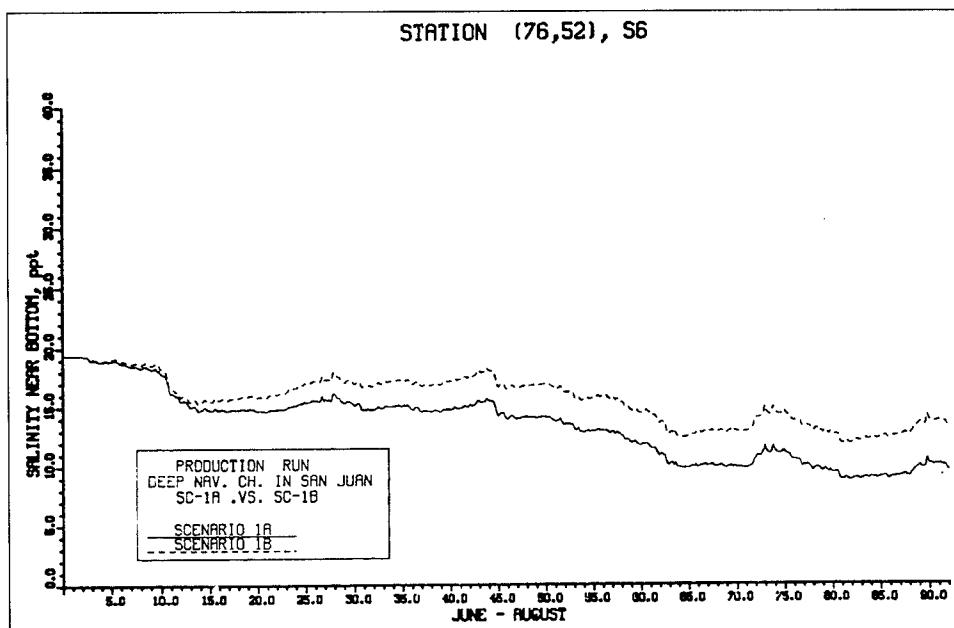


Figure 8-6. Comparison of salinity at S6 between Scenarios 1a and 1b

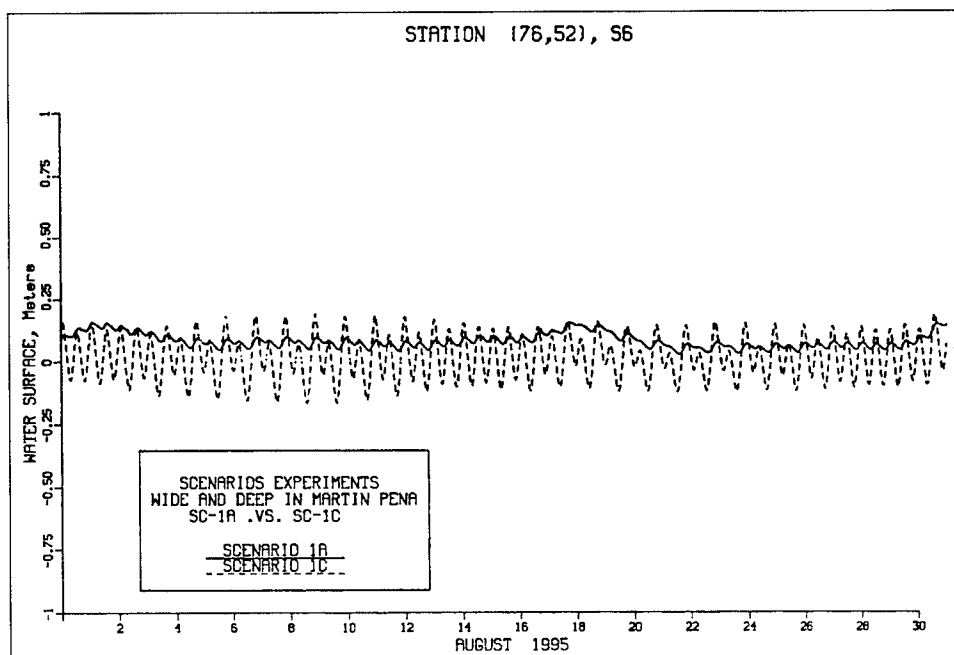
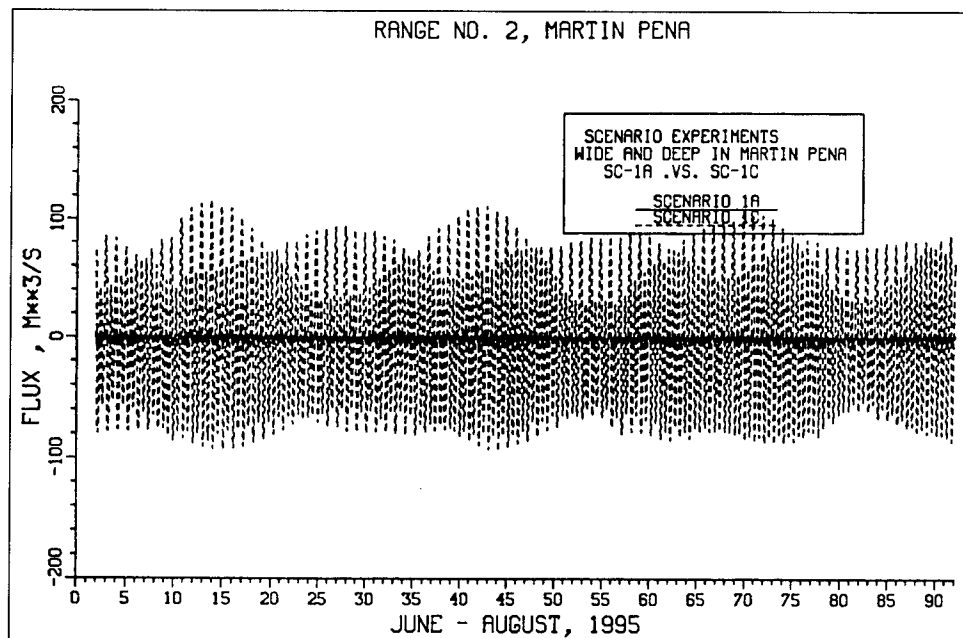
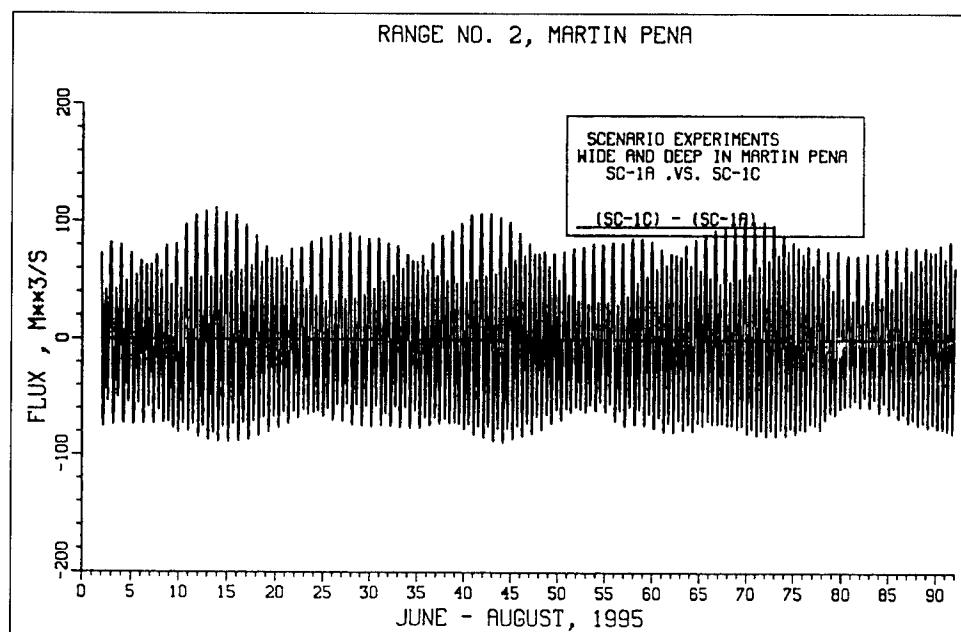


Figure 8-7. Comparison of tide at S6 between Scenarios 1a and 1c

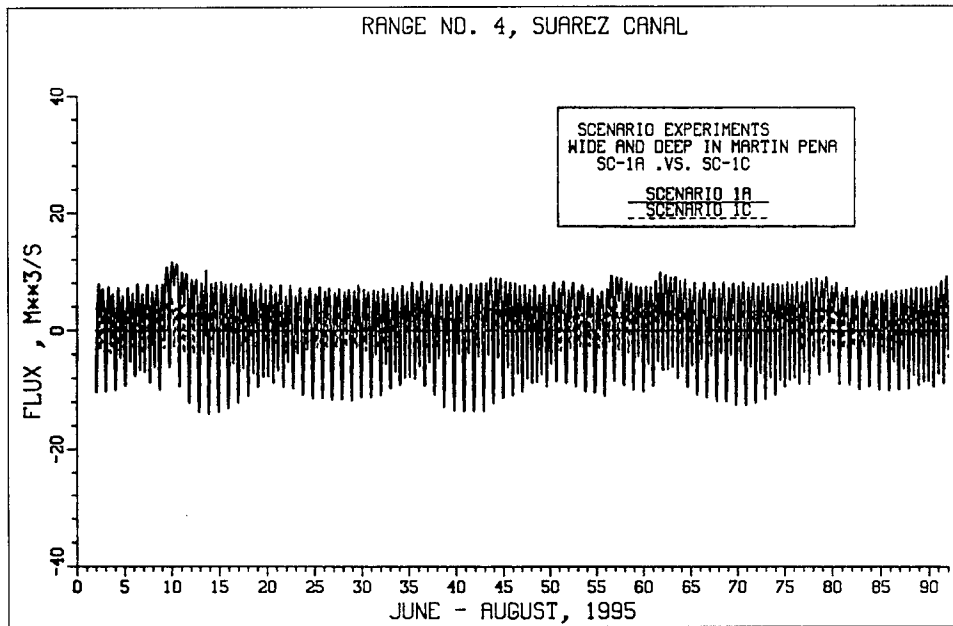


a. Both 1a and 1c

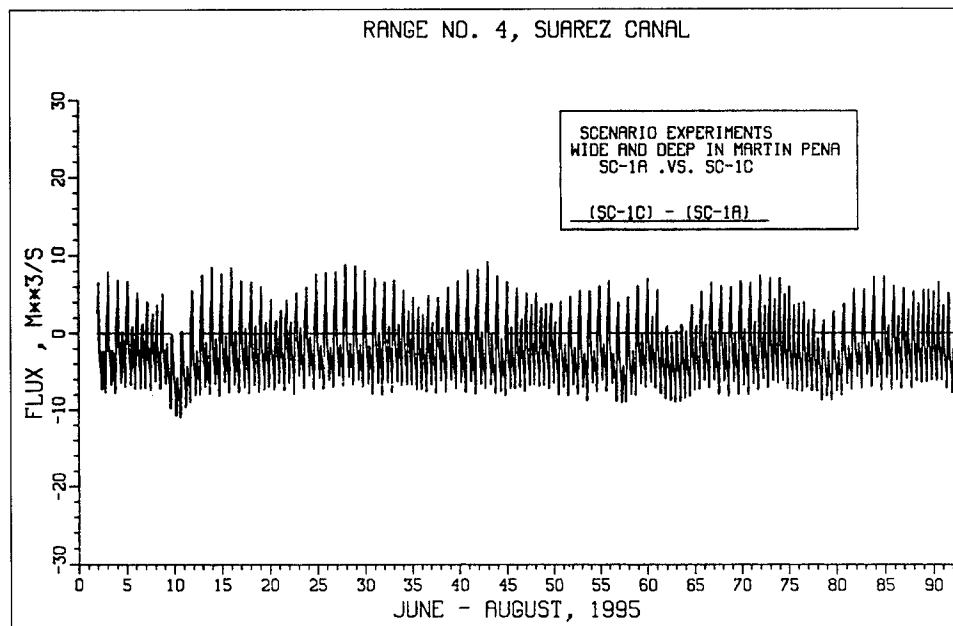


b. Difference between 1a and 1c

Figure 8-8. Comparison of flux at Range 2 between Scenarios 1a and 1c

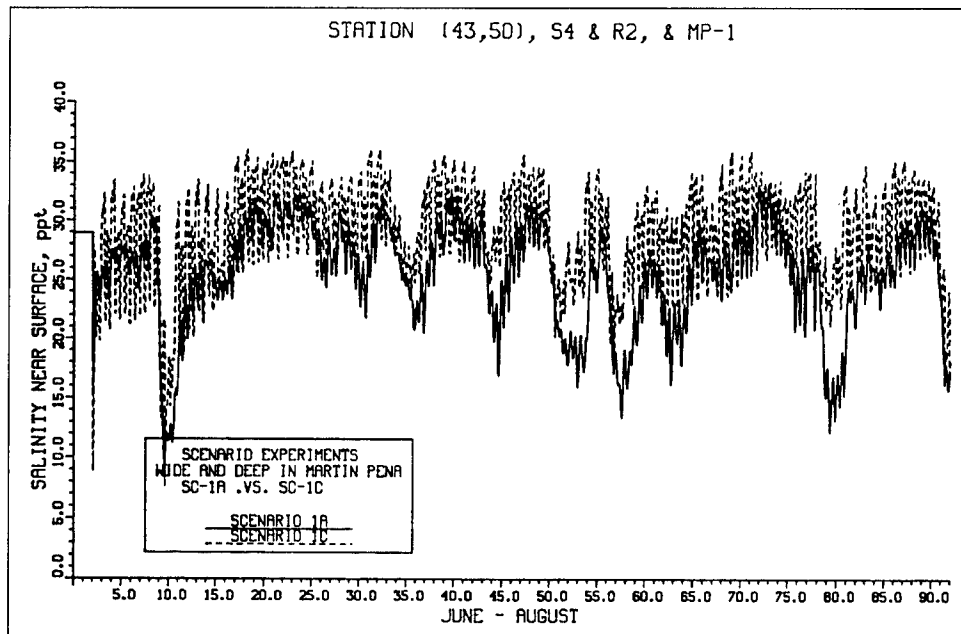


a. Both 1a and 1c

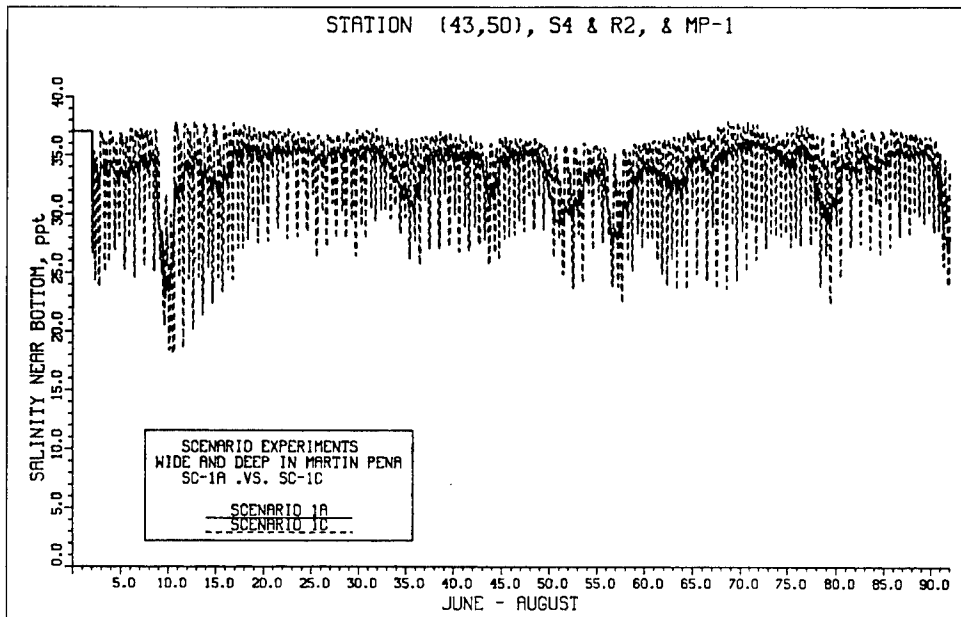


b. Difference between 1a and 1c

Figure 8-9. Comparison of flux at Range 4 between Scenarios 1a and 1c



a. Near surface



b. Near bottom

Figure 8-10. Comparison of salinity at S4 between Scenarios 1a and 1c

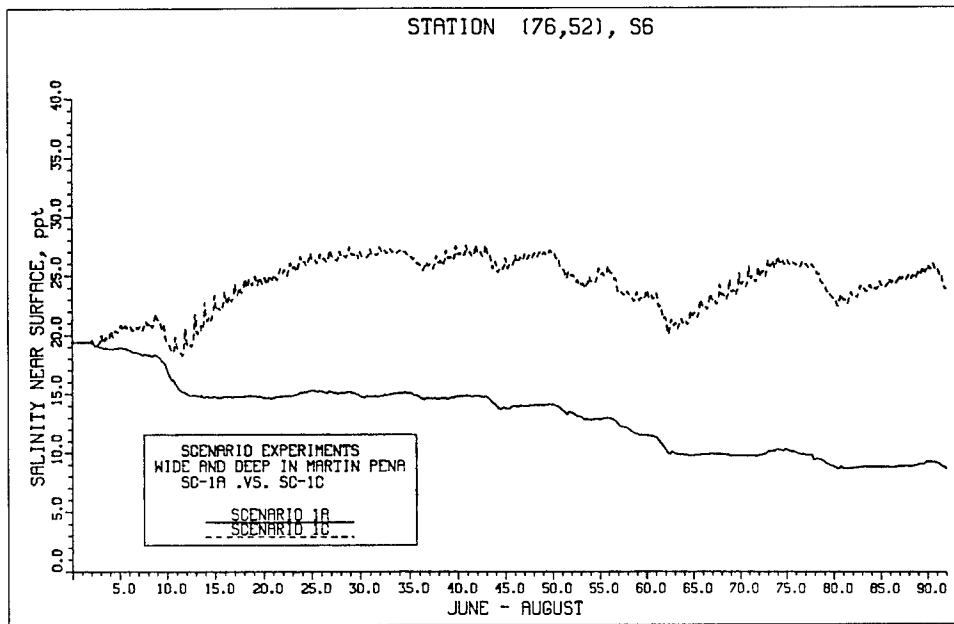
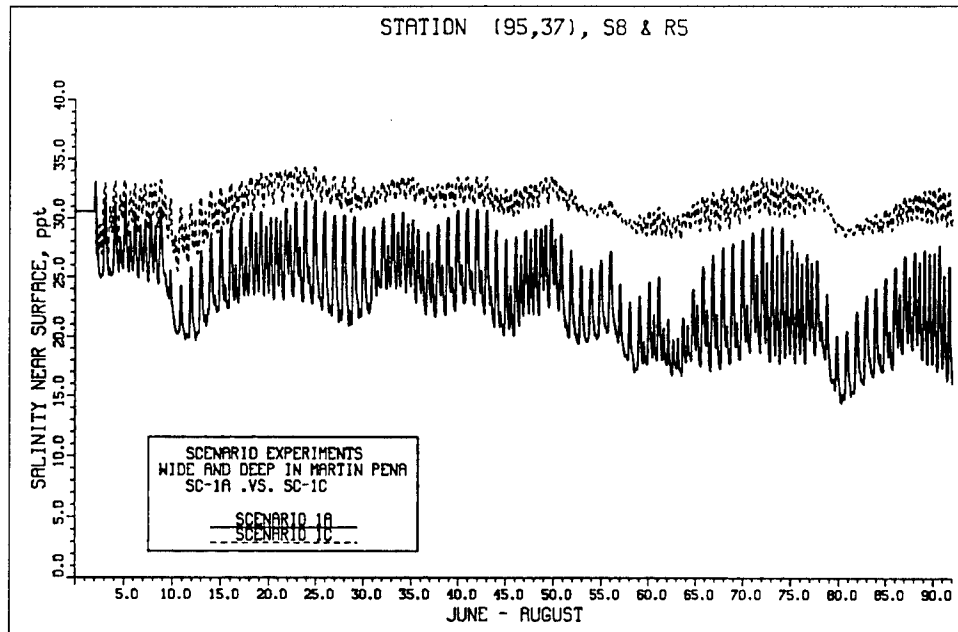


Figure 8-11. Comparison of salinity at S6 between Scenarios 1a and 1c

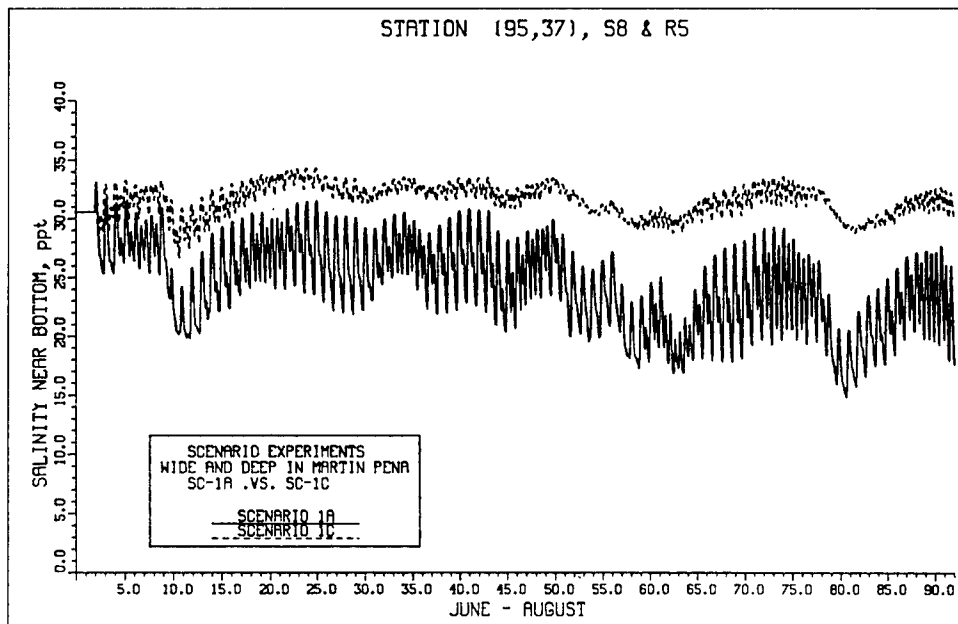
the field collection effort previously discussed show that high salinity exists in the dredged holes in Laguna San José and one hole in Canal Suárez. It has been speculated that high salinity groundwater from the ocean maintains the high salinity in the holes. To simulate this behavior in the model, salinity in the holes was nudged (see Chapter 7) to match the field data. Thus, when the holes were filled, this source of salinity was removed, resulting in the lower computed salinity in Laguna San José and Canal Suárez.

Scenario 3 Results

This scenario involved widening and deepening the constriction in Canal Suárez. As can be seen from Figure 8-19, opening this constriction results in the tide range in San José increasing from less than 5 cm (0.164 ft) to 20-25 cm (0.656 - 0.820 ft), with the resulting tidal flux through Canal Suárez (Figure 8-20) being increased by a factor of 5 or so. Figure 8-21 shows that the impact on the flux through Martín Peña is to increase the flux slightly on flood (water moving into Laguna San José). This results in the salinity in Martín Peña being slightly increased (Figure 8-22). With the increased tidal exchange between San José and Laguna La Torrecilla, salinity in both San José and Suarez increases (Figures 8-23 and 8-24). One noticeable exception in Suarez is around the 9th of June when a storm event resulted in a considerable runoff of freshwater into Laguna San José (see inflows in Figure 3-3). With the less constricted Canal Suárez, a larger portion of the San José freshwater inflow moves through the canal than before.

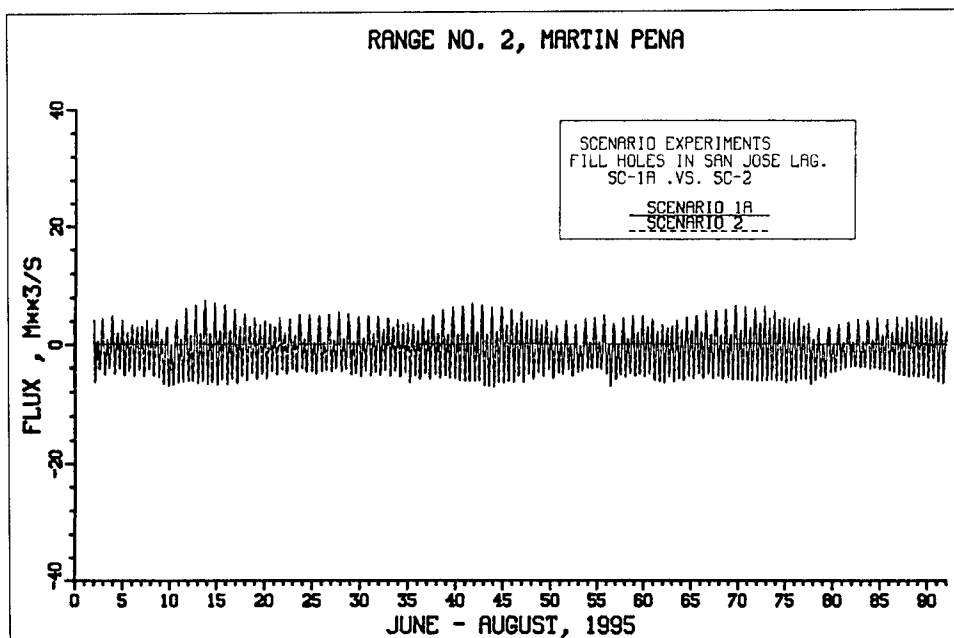


a. Near surface

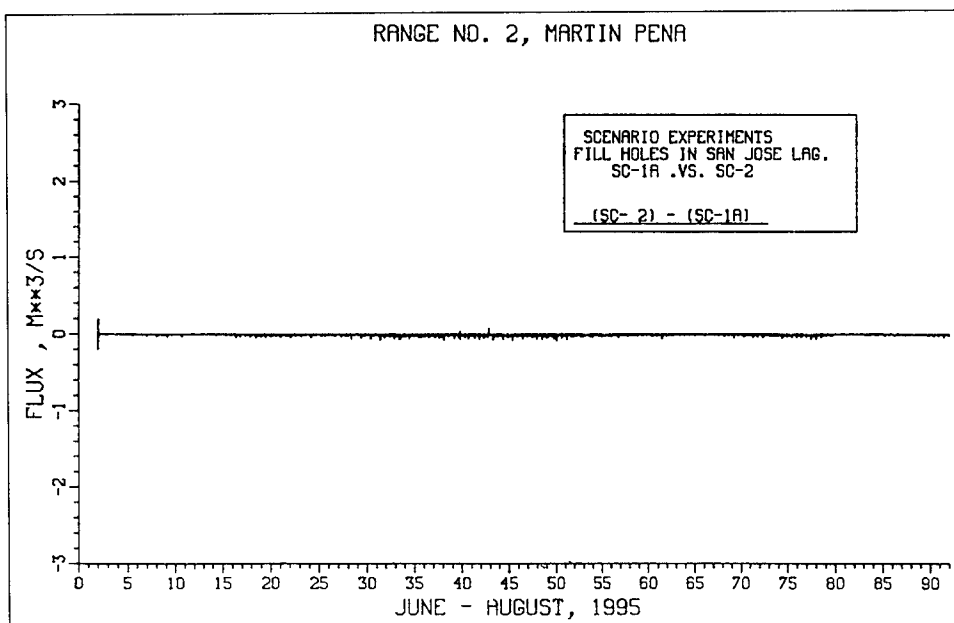


b. Near bottom

Figure 8-12. Comparison of salinity at S8 between Scenarios 1a and 1c

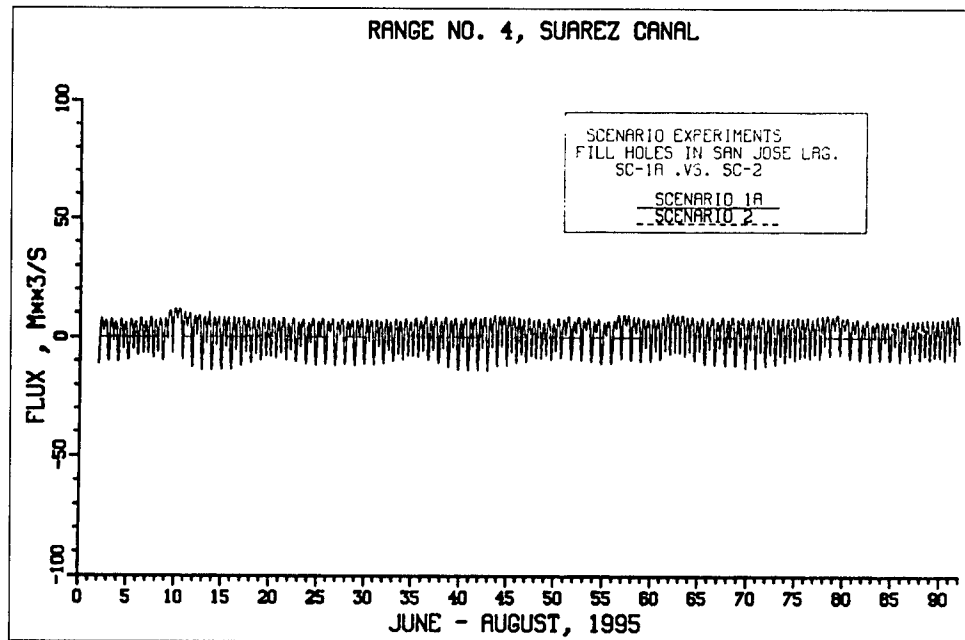


a. Both 1a and 2

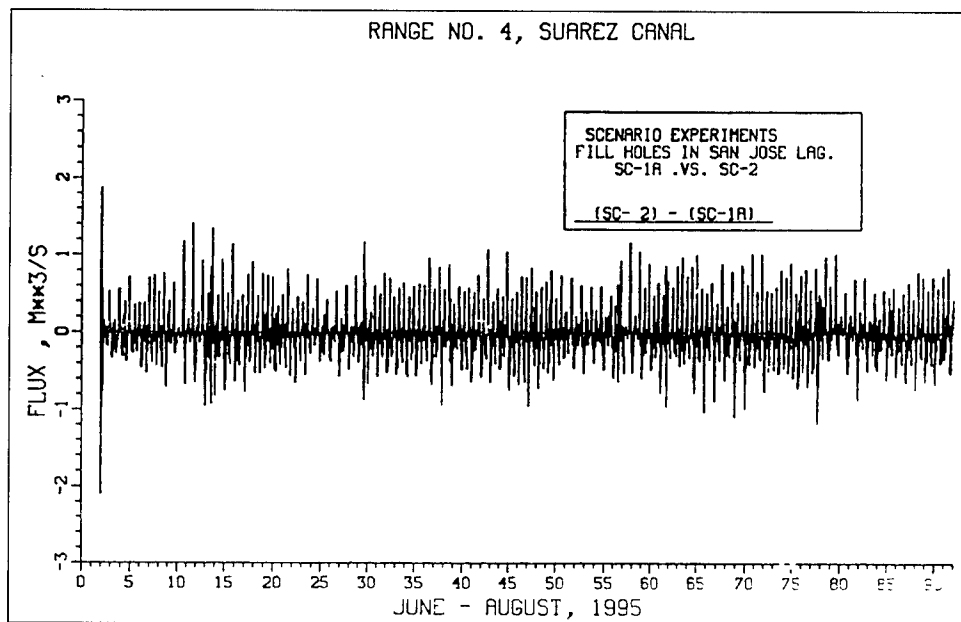


b. Difference between 1a and 2

Figure 8-13. Comparison of flux at Range 2 between Scenarios 1a and 2



a. Both 1a and 2



b. Difference between 1a and 2

Figure 8-14. Comparison of flux at Range 4 between Scenarios 1a and 2

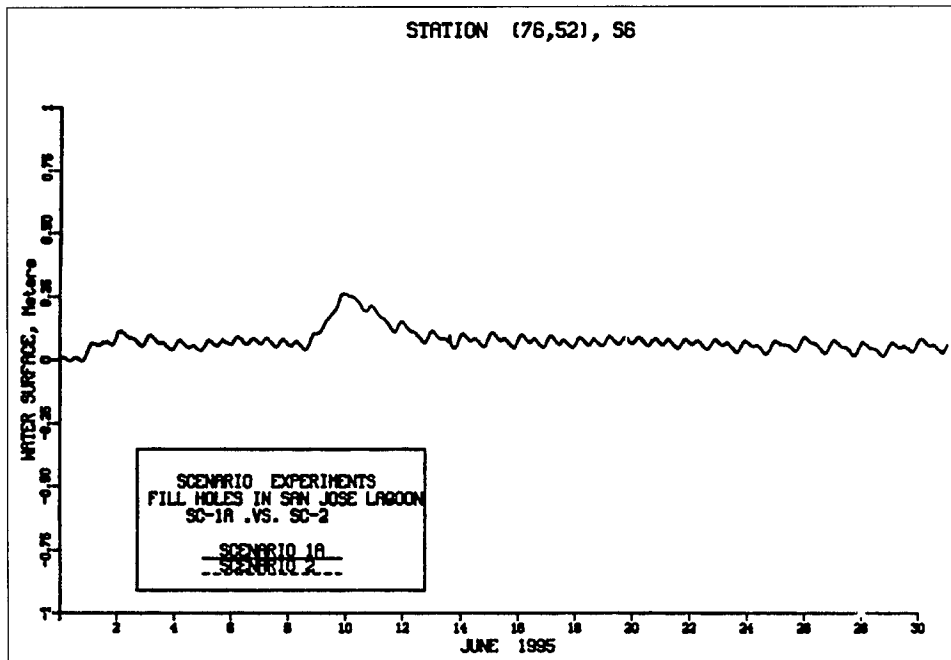
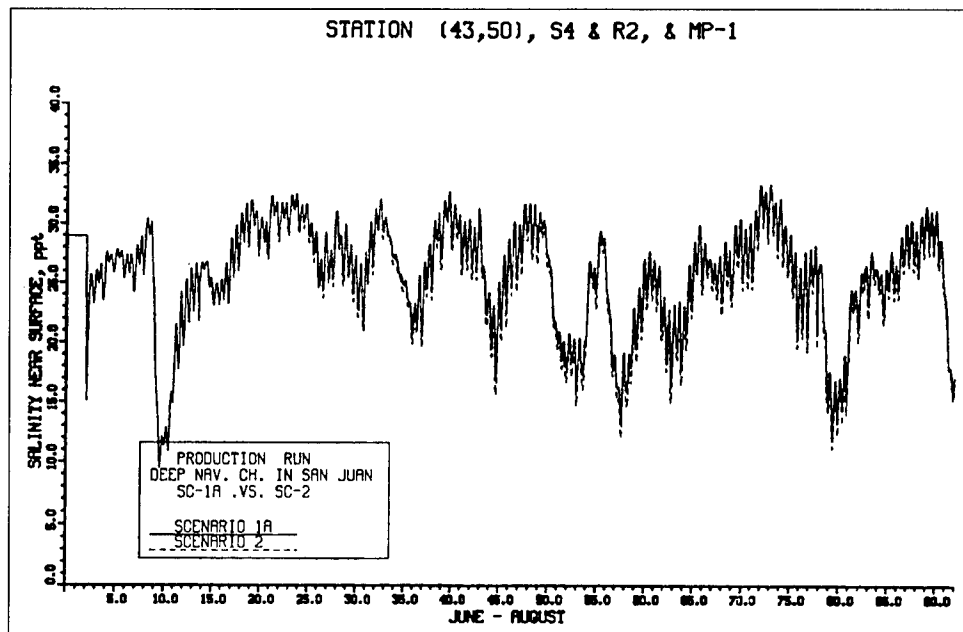


Figure 8-15. Comparison of tide at S6 between Scenarios 1a and 2

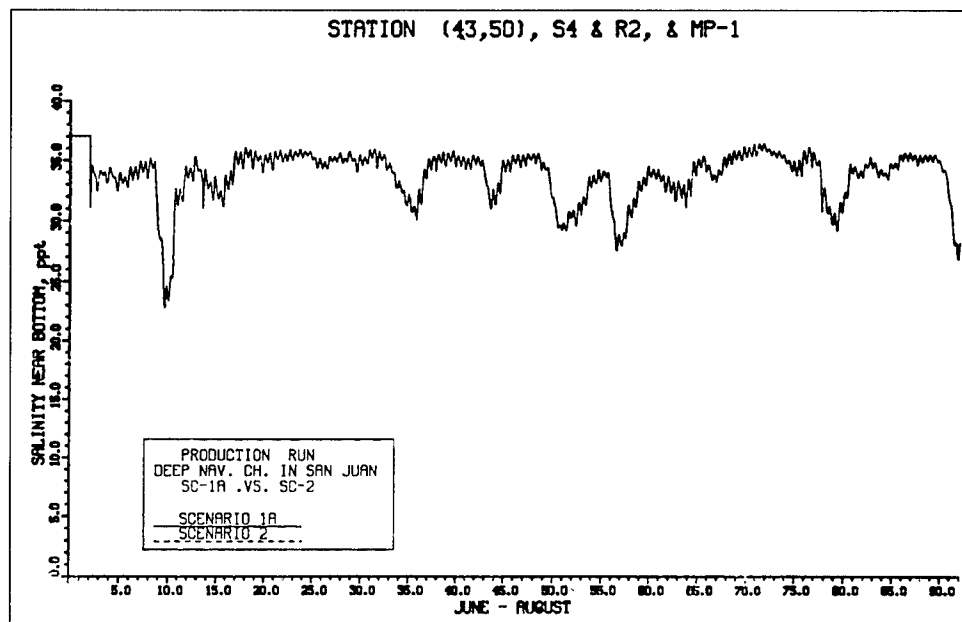
Scenario 4 Results

Scenario 4 has the Loiza Expressway bridge constriction removed in the Canal Suárez along with a tide gate installed in the canal. Simulation of the tide gate was accomplished by setting an internal boundary condition to cut off flow from San José through Canal Suárez to Torrecilla when the water surface elevation is higher on the San José side of the gate. The basic operation of the tide gate was expected to be such that tidal-floodwaters from Torrecilla would move into San José and would then be trapped in San José and forced to flow out through Martín Peña Canal. However, for the vast majority of the time, the water-surface elevation on the San José side of the gate remains higher than on the Torrecilla side of the gate, resulting in virtually no flux through Canal Suárez (Figure 8-25). Thus, only occasionally does the gate allow tidal-floodwaters from Laguna La Torrecilla into Laguna San José. The reason is that with the Martín Peña Canal so constricted, water can't easily pass out of San José, resulting in a buildup of the water-surface elevation in Laguna San José. This buildup of the San José water-surface elevation can be seen in Figure 8-26. Figure 8-27 shows the increased flux during ebb (water moving toward San Juan Bay) through Martín Peña.

An interesting observation from Figure 8-26 is that there is essentially no tidal fluctuation in Laguna San José with Canal Suárez blocked. Thus, the small tidal fluctuation observed in San José for the existing state of the system (Figure 6-7) is almost totally due to the tide moving through Canal Suárez. The tidal effect on Laguna San José due to Martín Peña Canal is essentially zero.



a. Near surface



b. Near bottom

Figure 8-16. Comparison of salinity at S4 between Scenarios 1a and 2

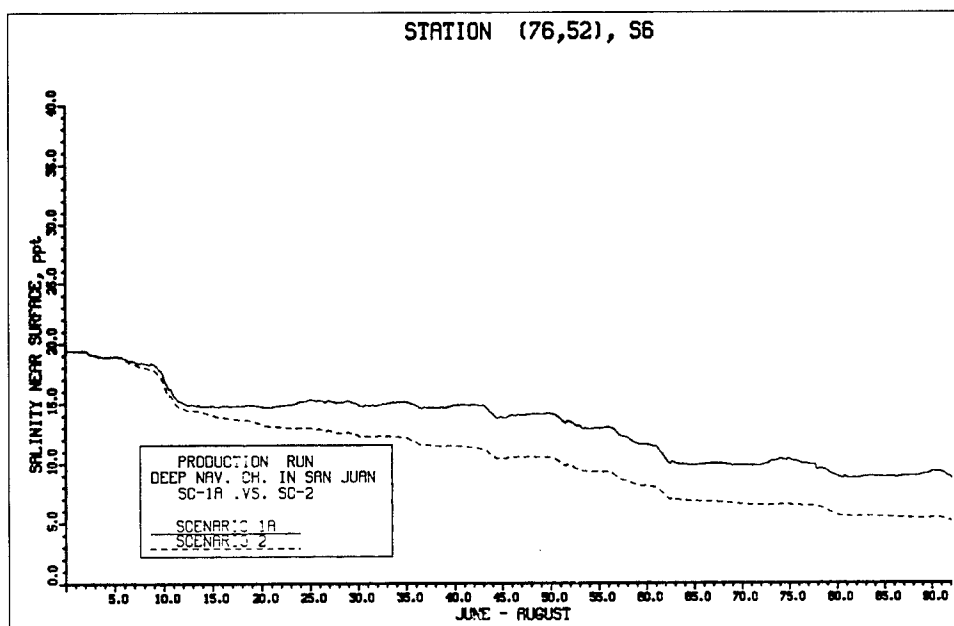
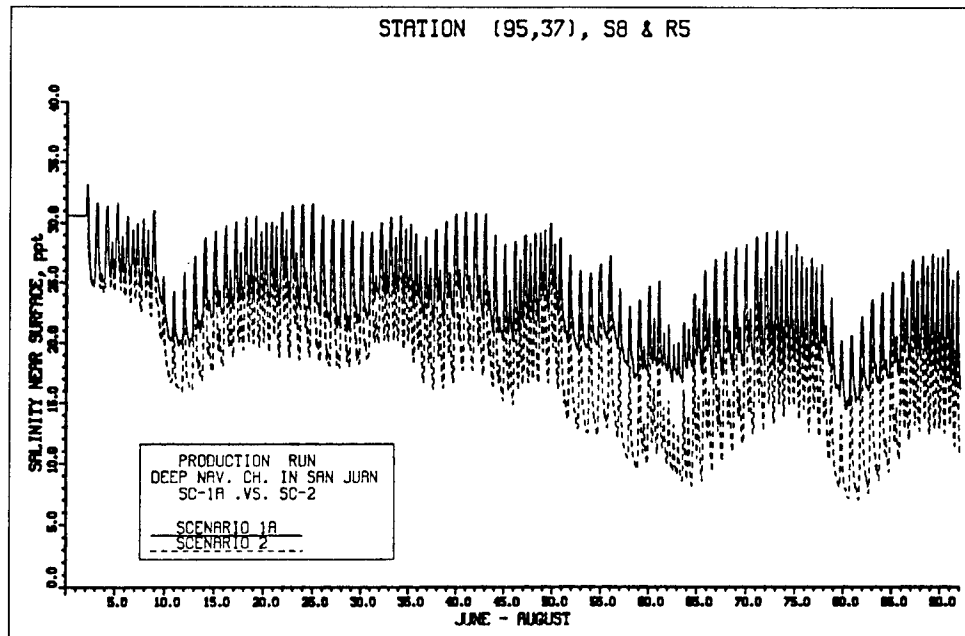


Figure 8-17. Comparison of salinity at S6 between Scenarios 1a and 2

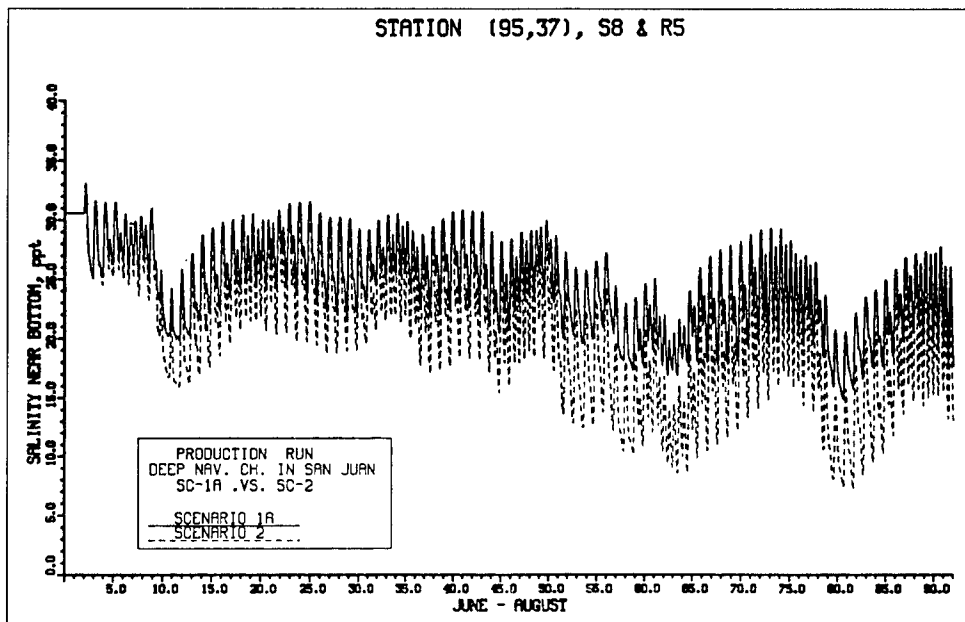
With all of the freshwater inflow into Laguna San José having to pass through Martín Peña Canal, Figure 8-28 shows that the impact is a reduction in salinity in Martín Peña. However, as illustrated in Figures 8-29 and 8-30, salinity in Laguna San José and Canal Suárez increases. With no flow from Laguna San José into Torecilla Lagoon, salinity in Suarez on the Torecilla side of the tide gate builds up. Thus, during the few times that tidal-flood flow in the Canal Suárez is allowed through the tide gate into San José, much higher salinity is flushed into San José, resulting in increased salinity in Laguna San José.

Scenario 6b Results

As previously discussed, this scenario is a combination of Scenario 1c and Scenario 2. In other words, the eastern end of Martín Peña is widened to a minimum of 150 ft (45.7 m) and deepened to 9 ft (2.74 m) and the dredged holes are filled. An inspection of the results from this scenario (Figures 8.31 -8.36) along with those from Scenario 1c (Figures 8.7 -8.12) reveals virtually no difference in the computed tide in Laguna San José nor in the computed flux and salinity in the Martín Peña and Canal Suarez from those obtained for Scenario 1c. Although Scenario 2 by itself does result in a decrease in salinity in Laguna San José and the connecting canals (Figures 8.16 - 8.18), evidently the hydrodynamic impact of Scenario 1c is so large that the influence of Scenario 2 is miniscule when the two are combined. An inspection of Figure 8.8 of the flux through Canal Martín Peña for Scenario 1c shows that during flood (flow into Canal Martín Peña from San Juan Bay) the average flux is about 50 m³/sec. Thus, on each flood cycle about 2.25 million m³ of high saline San Juan Bay water moves into Laguna San José. With the total volume of Laguna San



a. Near surface



b. Near bottom

Figure 8-18. Comparison of salinity at S8 between Scenarios 1a and 2

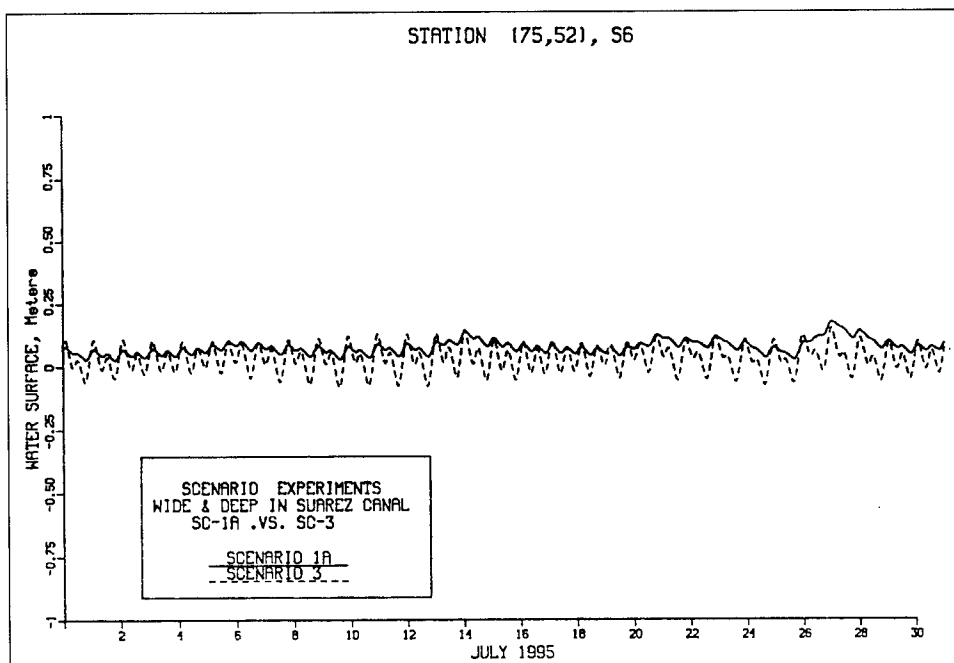


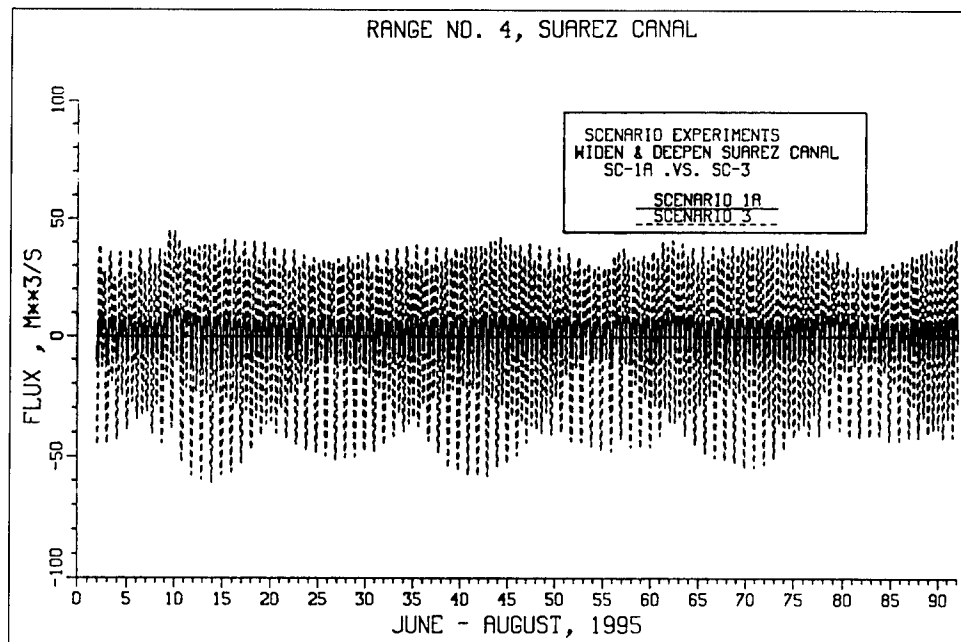
Figure 8-19. Comparison of tide at S6 between Scenarios 1a and 3

José being about 7.5 million m^3 , it only takes three to four flood cycles to totally replace the waters of Laguna San José. This illustrates the enormous impact of Scenario 1c.

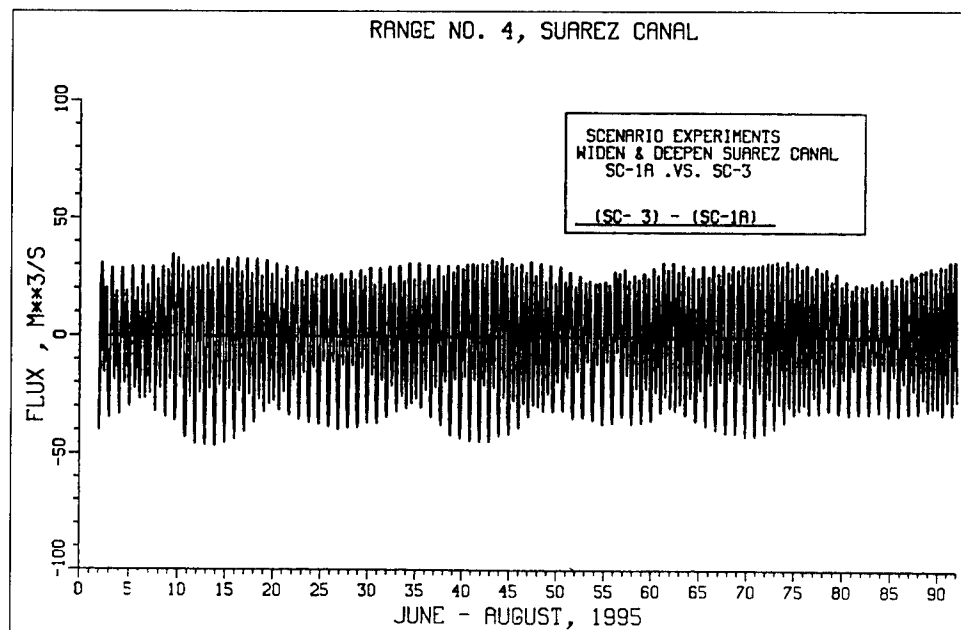
Conclusions

The major goal to be accomplished through physical changes to the SJBE system is to increase tidal flushing in Martín Peña Canal and Laguna San José. The results from the various scenarios discussed above show that Scenario 1c accomplishes this goal the best, if the desire is to increase the exchange between San José and San Juan Bay. Scenario 3 also significantly increases the tidal flushing of Laguna San José, but the exchange is with Laguna La Torrecilla waters rather than San Juan Bay waters. It is doubtful that mixing the relatively polluted San José waters with the relatively clean waters of Torrecilla is desirable.

The final scenario simulated was a combination of Scenario 1c and Scenario 2. Although Scenario 2 has little impact on tidal flushing in Laguna San José, the belief (from a HM perspective without including any benefits of pollutant load reductions) is that with the increased tidal flushing resulting from significantly widening and deepening the Martín Peña Canal, along with filling the highly polluted deep holes in San José and other areas of the system, the combination of Scenarios 1c and 2 offers the best hope for improving the water quality of Laguna San José.

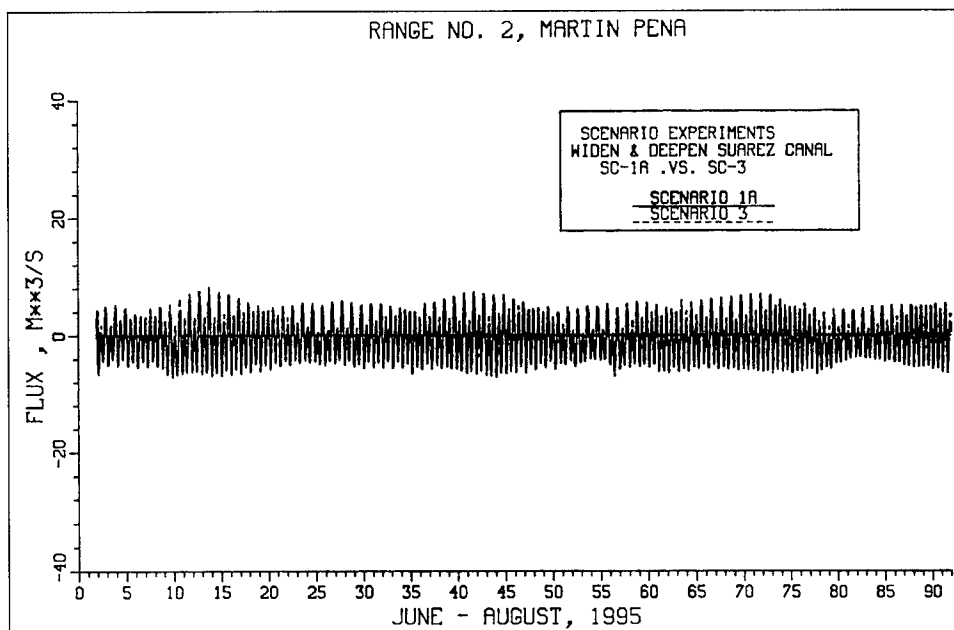


a. Both 1a and 3

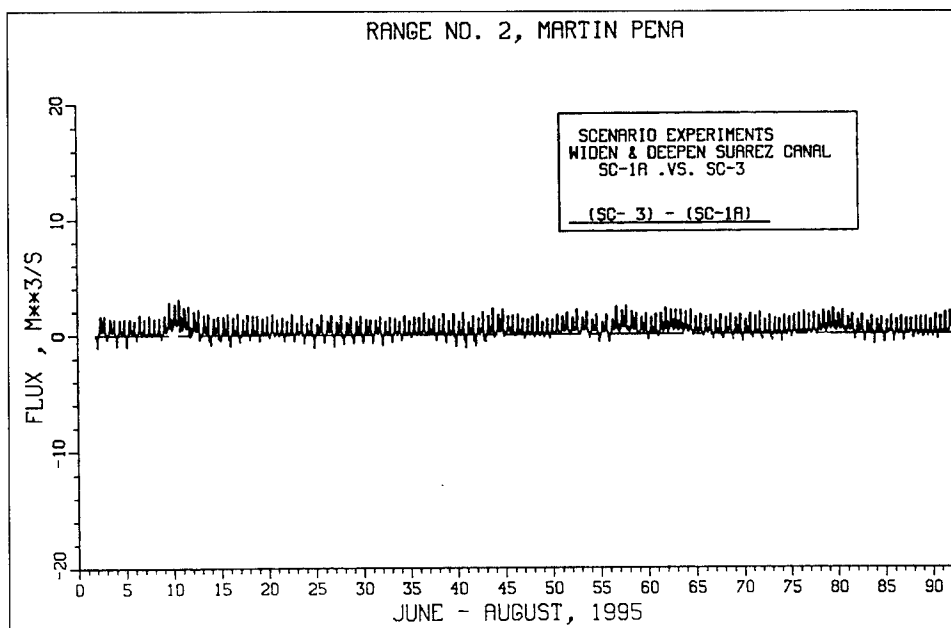


b. Difference between 1a and 3

Figure 8-20. Comparison of flux at Range 4 between Scenarios 1a and 3

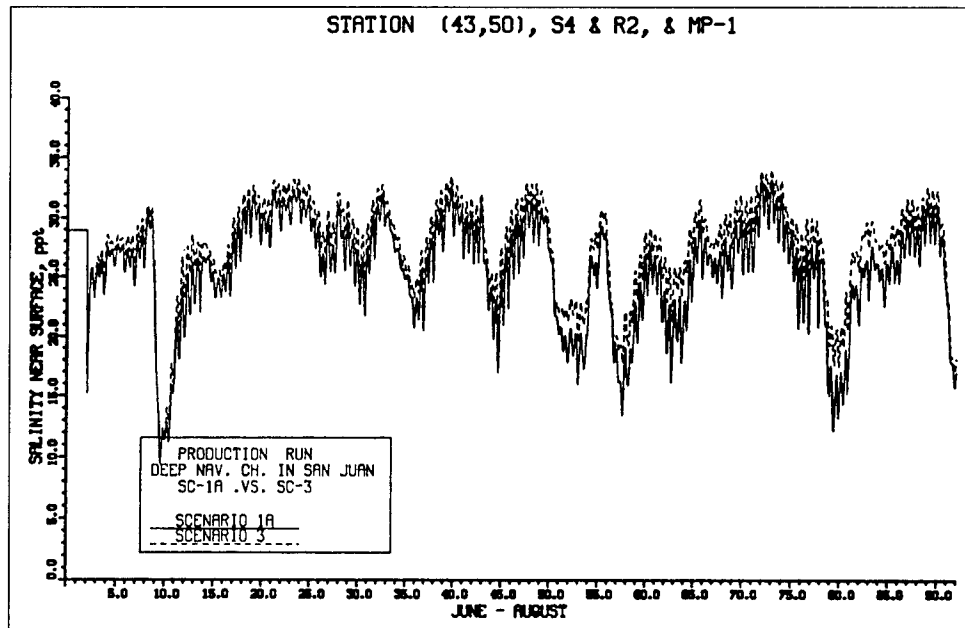


a. Both 1a and 3

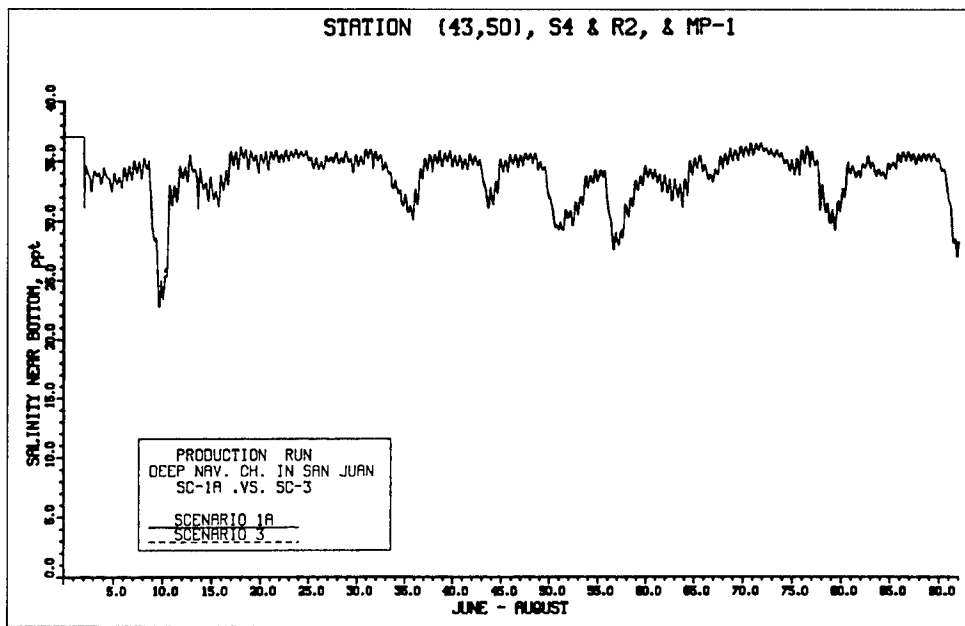


b. Difference between 1a and 3

Figure 8-21. Comparison of flux at Range 2 between Scenarios 1a and 3



a. Near surface



b. Near bottom

Figure 8-22. Comparison of salinity at S4 between Scenarios 1a and 3

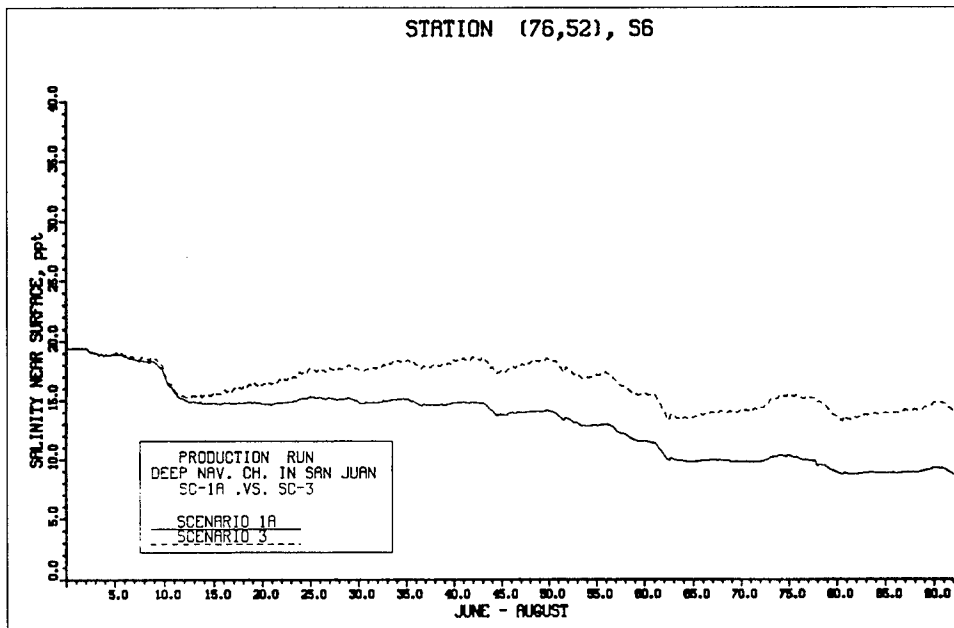
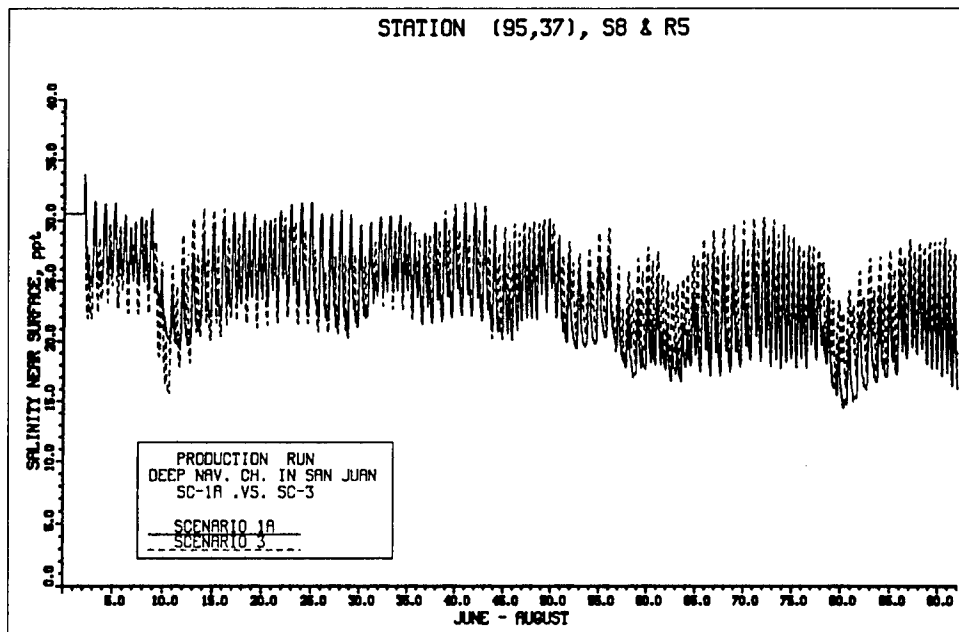
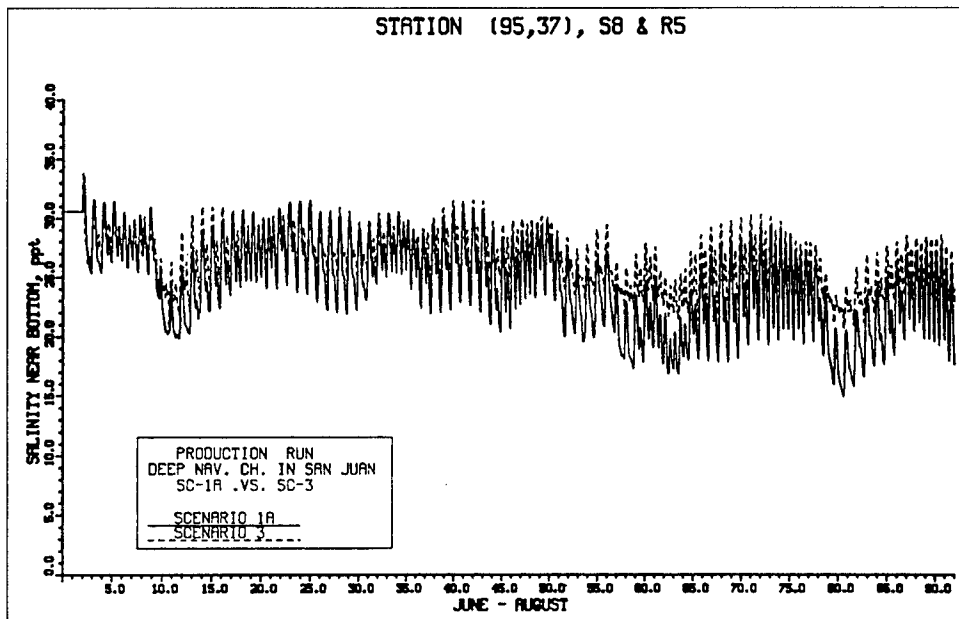


Figure 8-23. Comparison of salinity at S6 between Scenarios 1a and 3

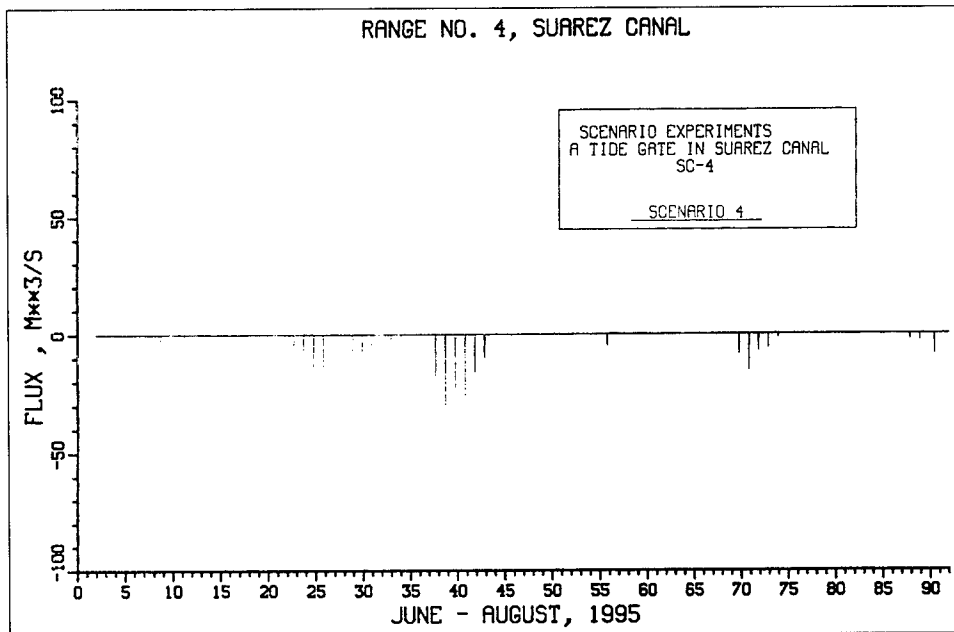


a. Near surface

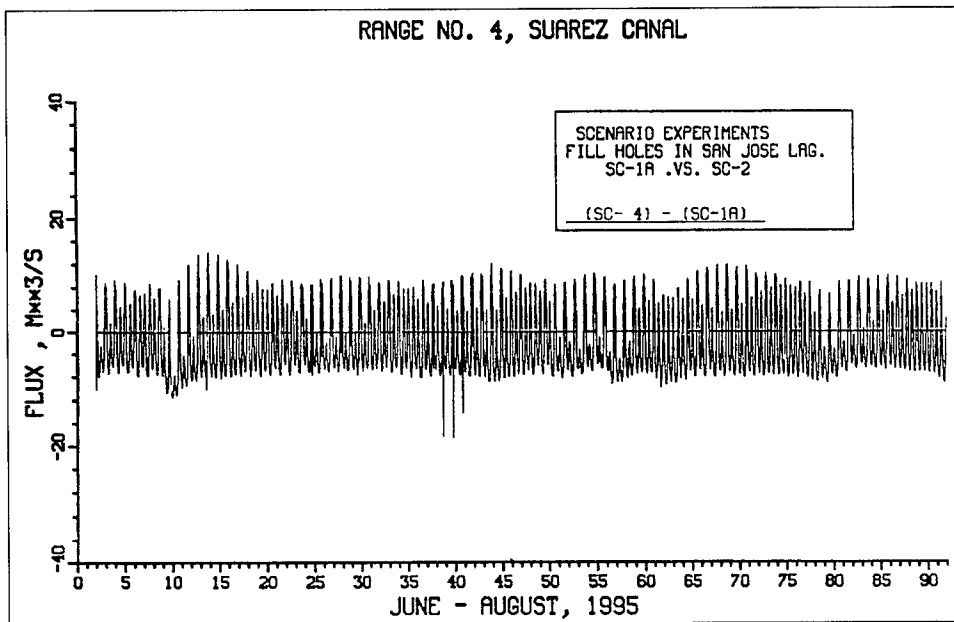


b. Near bottom

Figure 8-24. Comparison of salinity at S8 between Scenarios 1a and 3



a. Only 4



b. Difference between 1a and 4

Figure 8-25. Comparison of flux at Range 4 between Scenarios 1a and 4

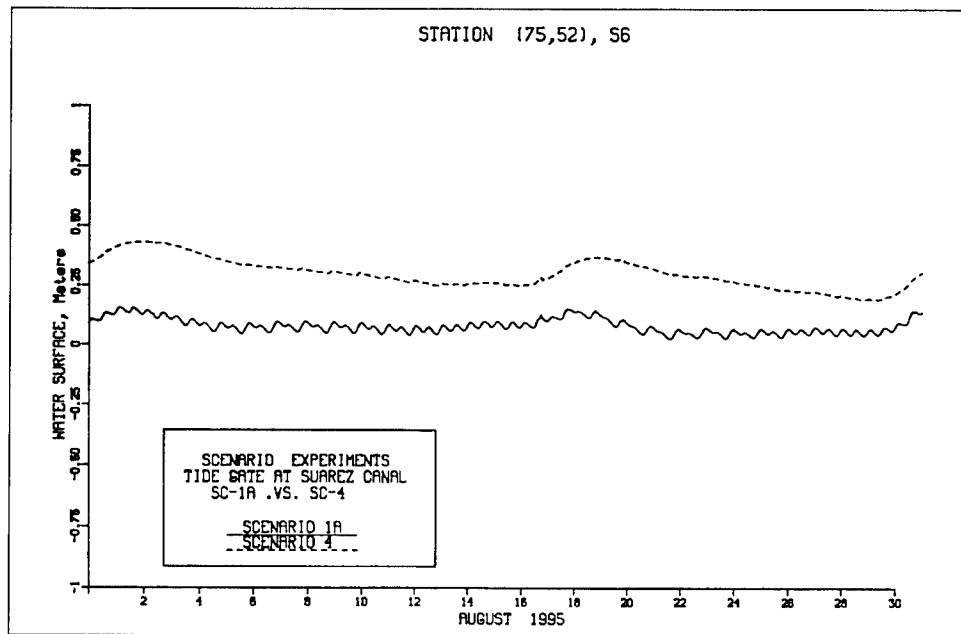
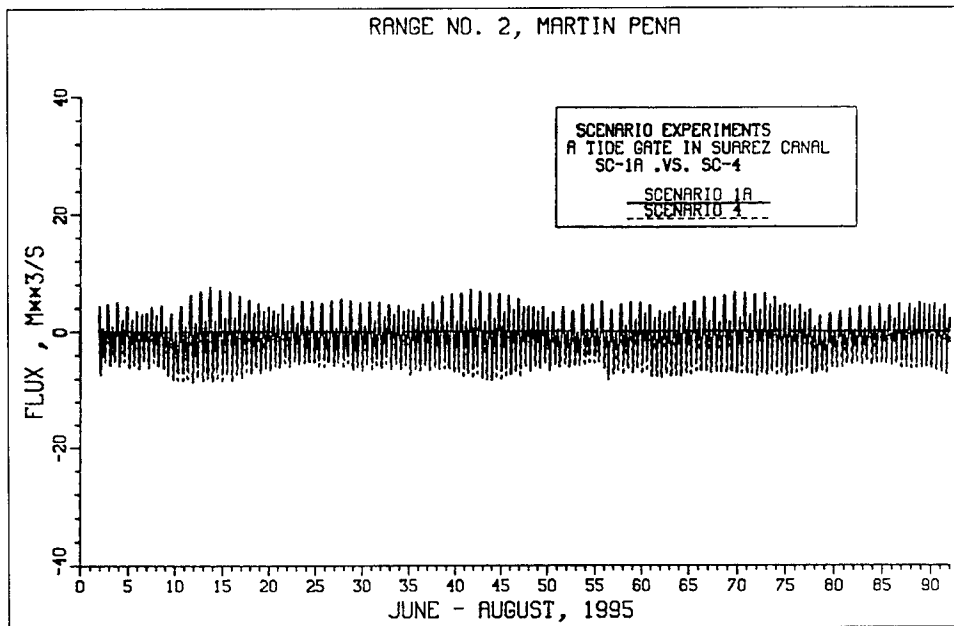
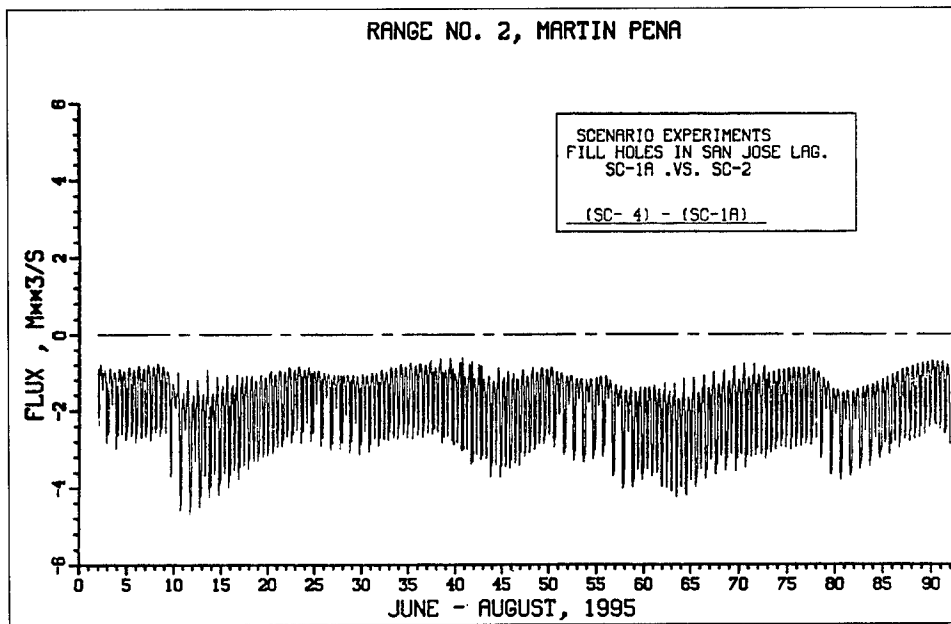


Figure 8-26. Comparison of tide at S6 between Scenarios 1a and 4

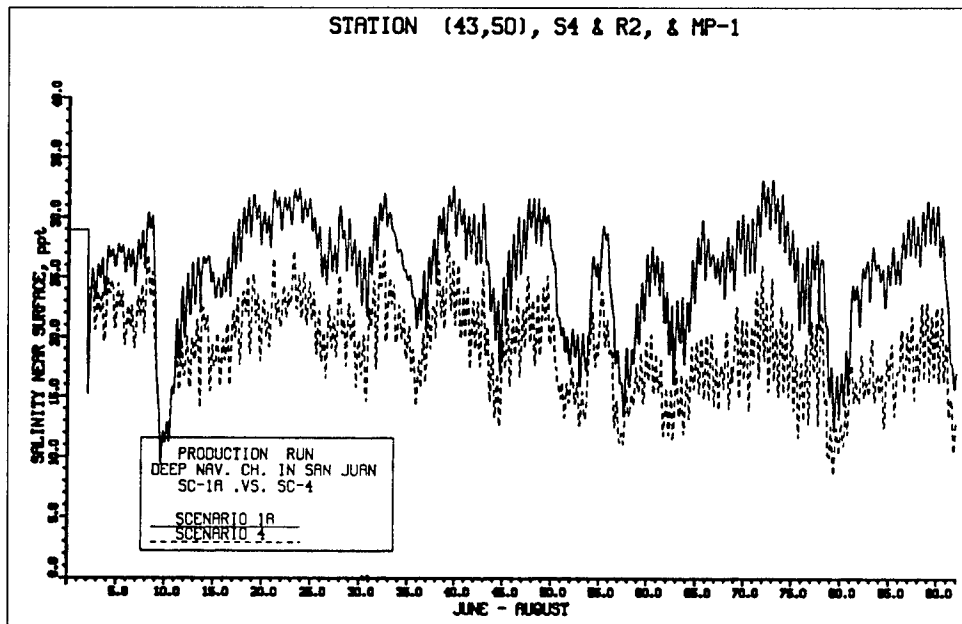


a. Both 1a and 4

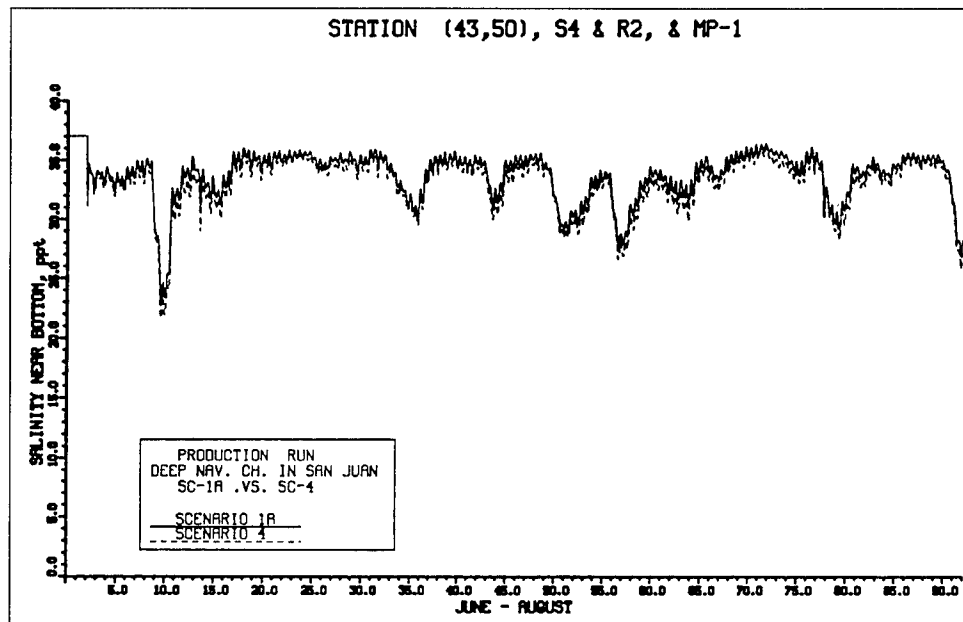


b. Difference between 1a and 4

Figure 8-27. Comparison of flux at Range 2 between Scenarios 1a and 4



a. Near surface



b. Near bottom

Figure 8-28. Comparison of salinity at S4 between Scenarios 1a and 4

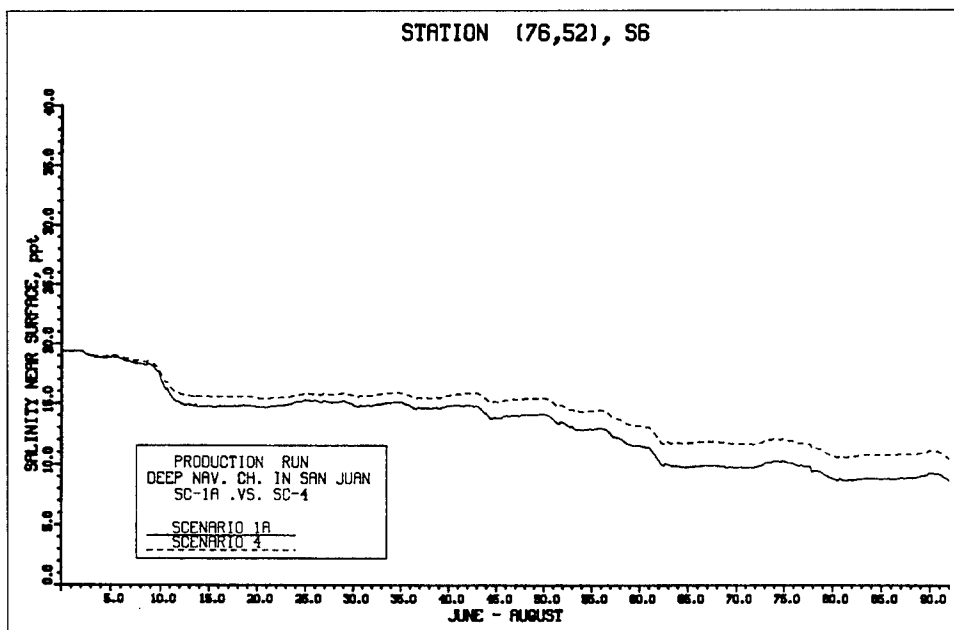
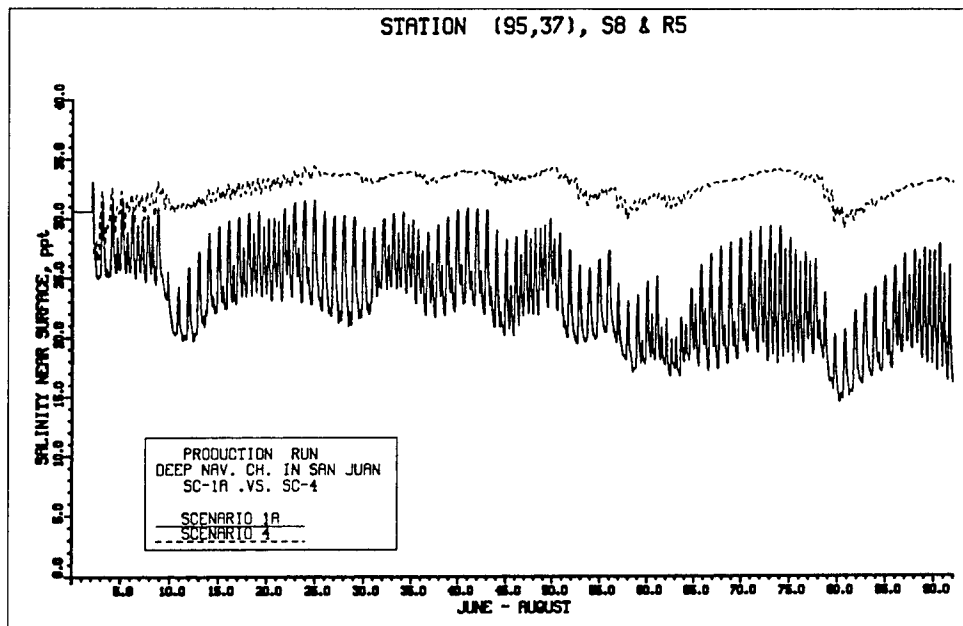
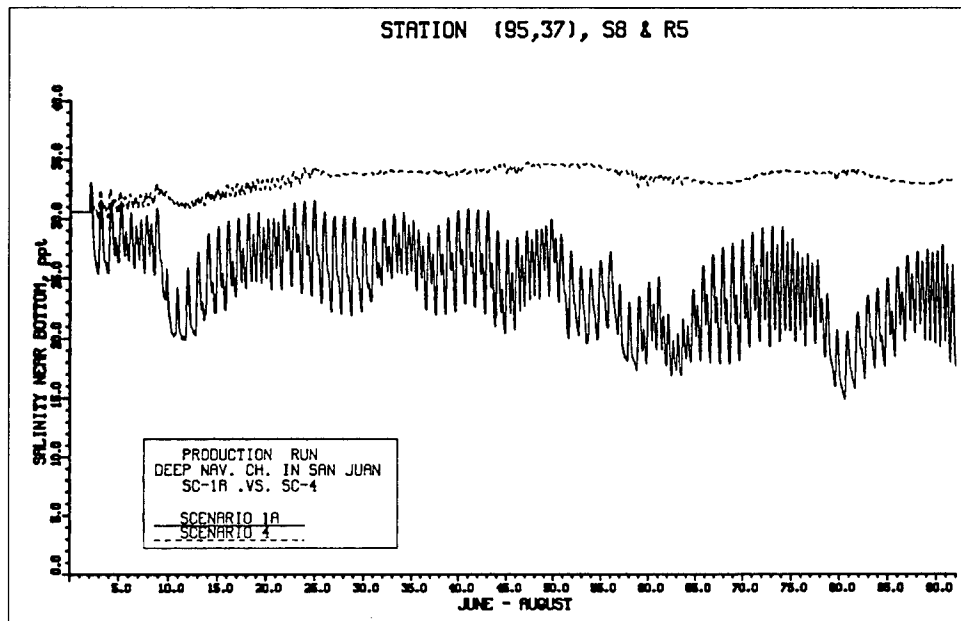


Figure 8-29. Comparison of salinity at S6 between Scenarios 1a and 4



a. Near surface



b. Near bottom

Figure 8-30. Comparison of salinity at S8 between Scenarios 1a and 4

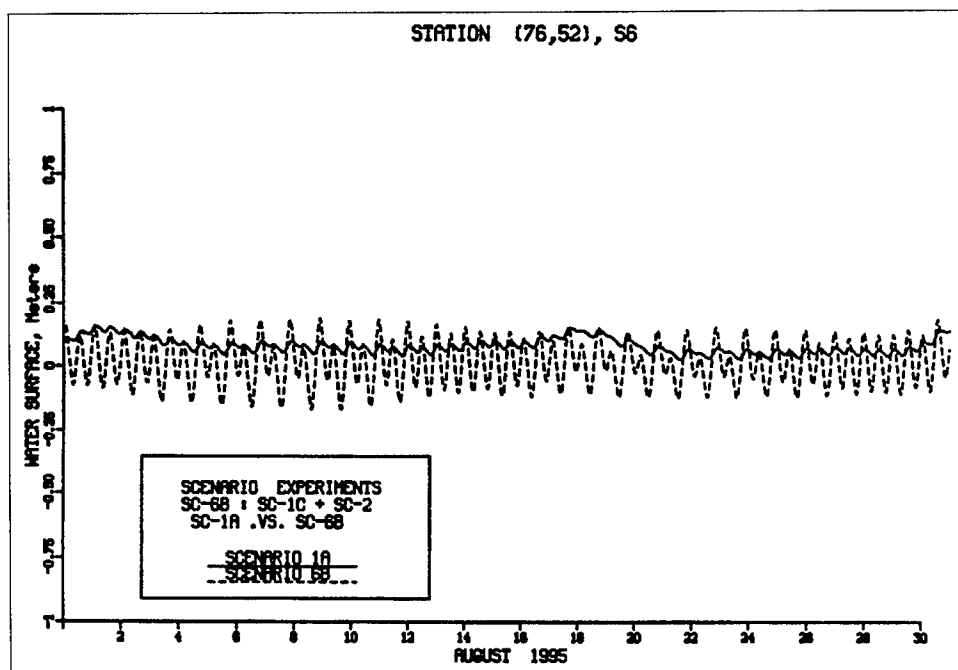
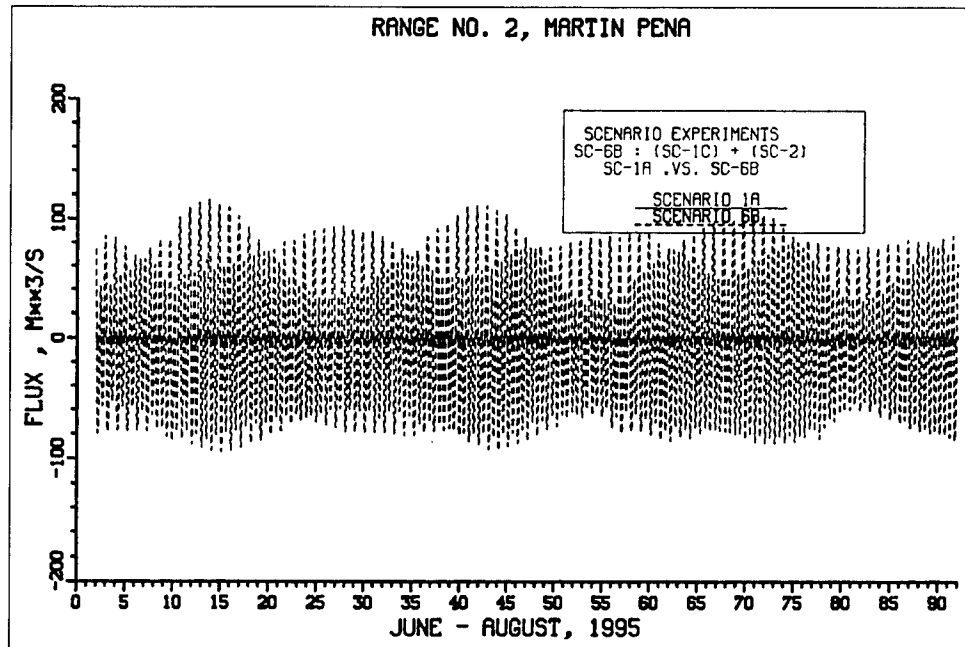
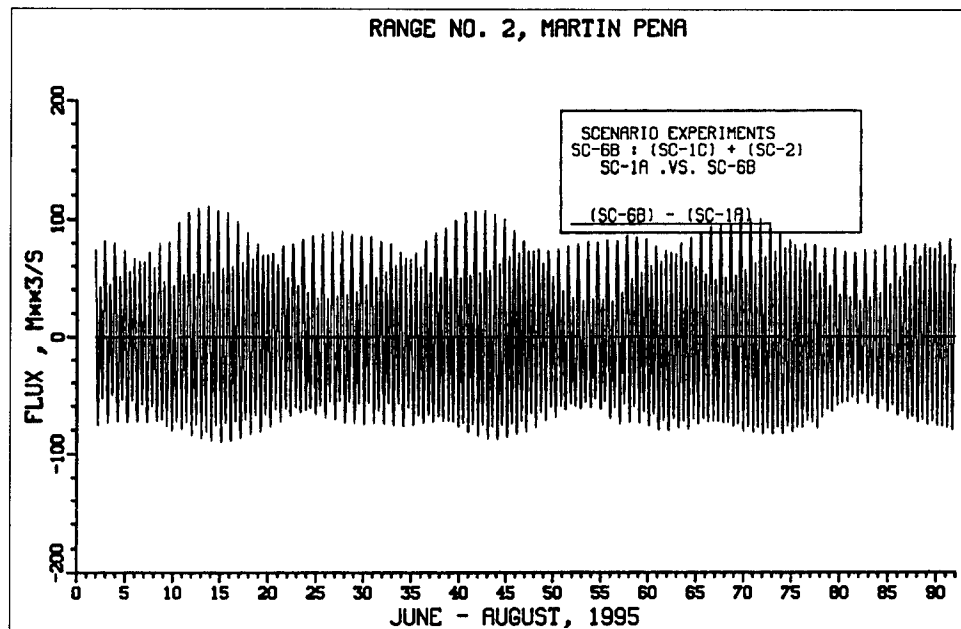


Figure 8-31. Comparison of tide at S6 between Scenarios 1a and 6b

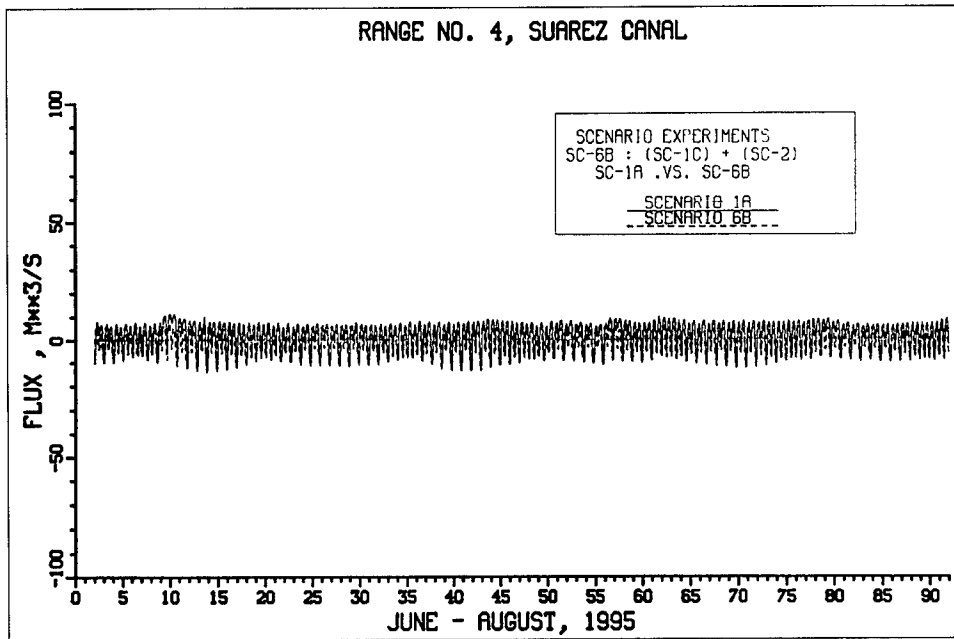


a. Both 1a and 6b

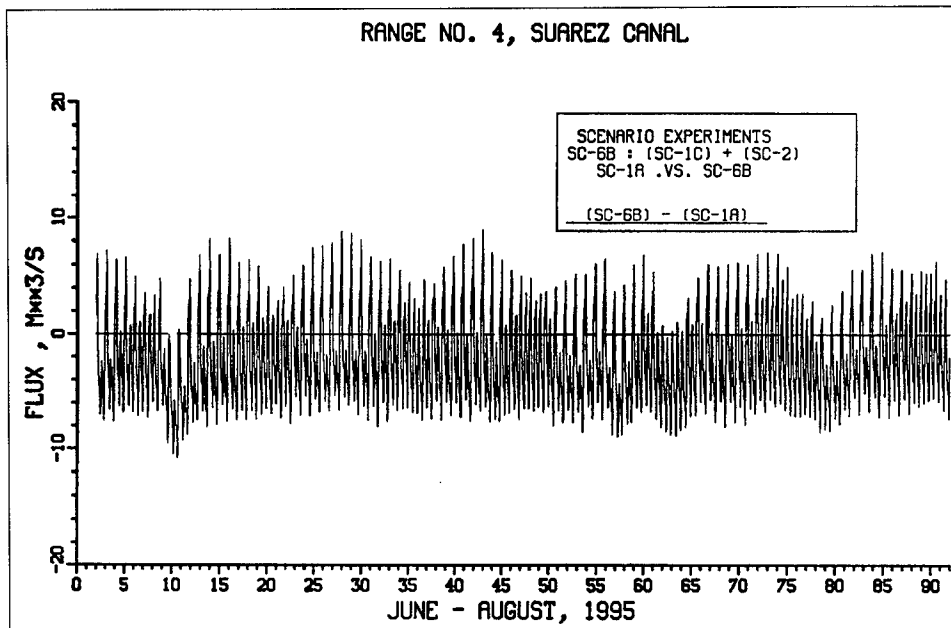


b. Difference between 1a and 6b

Figure 8-32. Comparison of flux at Range 2 between Scenarios 1a and 6b

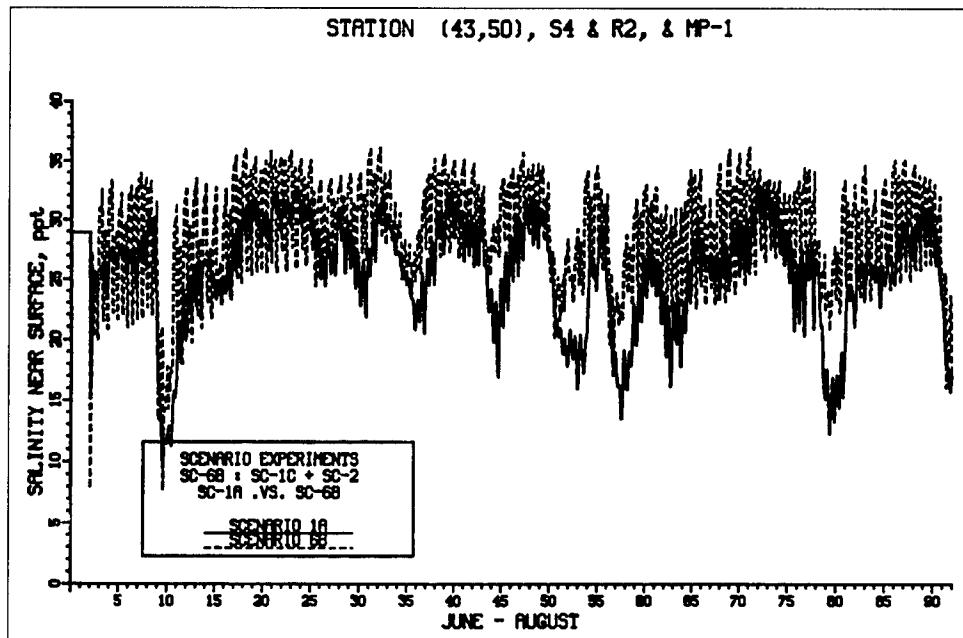


a. Both 1a and 6b

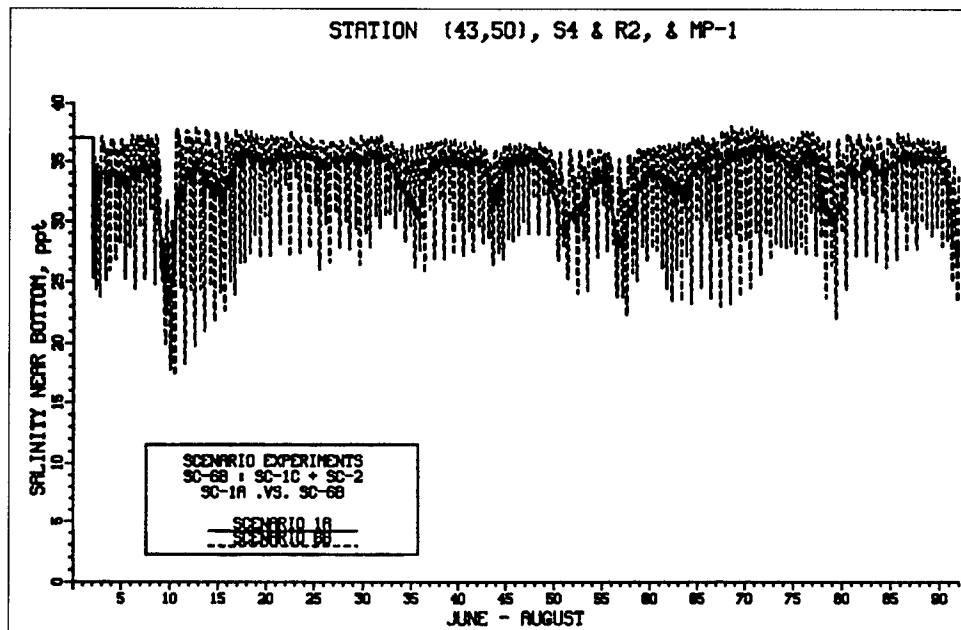


b. Difference between 1a and 6b

Figure 8-33. Comparison of flux at Range 4 between Scenarios 1a and 6b

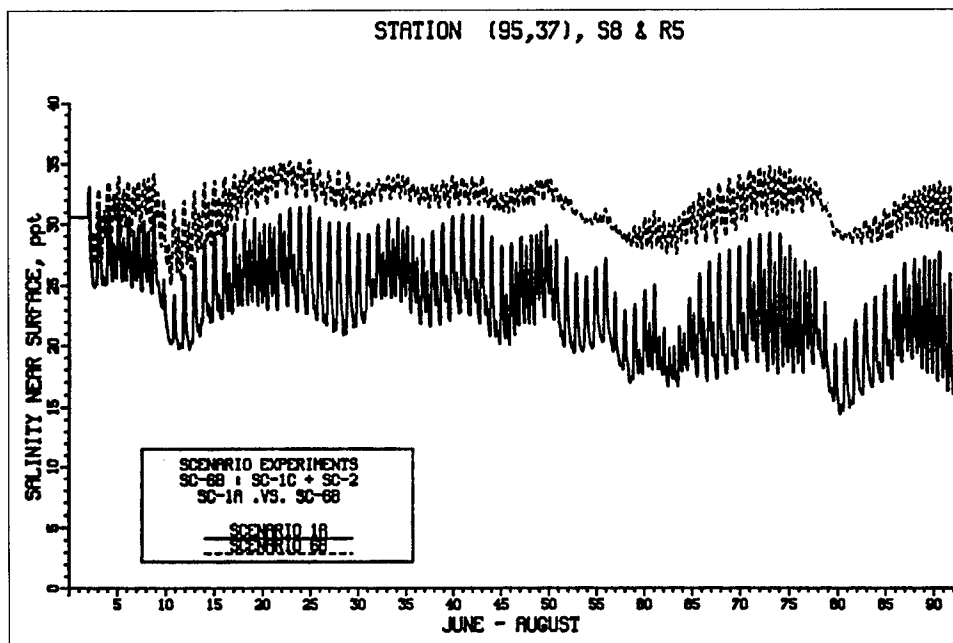


a. Near surface

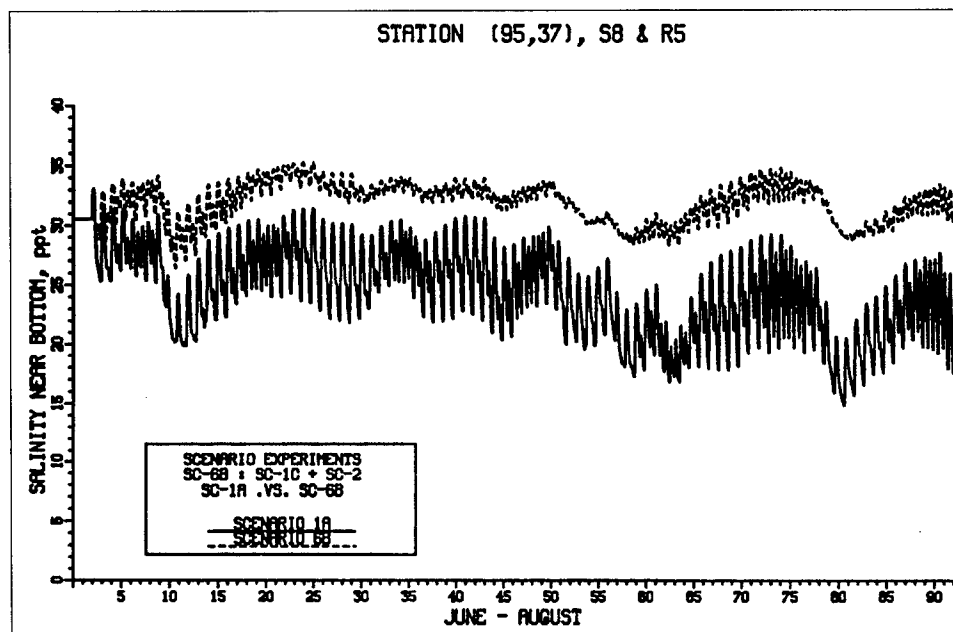


b. Near bottom

Figure 8-34. Comparison of salinity at S4 between Scenarios 1a and 6b



a. Near surface



b. Near bottom

Figure 8-36. Comparison of salinity at S8 between Scenarios 1a and 6b

Water Quality Model Results

All scenarios required a common set of initial conditions for the water column and the sediments so that any differences observed between the scenarios would be attributable to the modifications imposed by the scenario. Ideally, the spatially varying set of initial conditions for the water column and sediments generated during calibration would be used. Unfortunately, the addition and deletion of water quality cells resulting from channel modification caused the number of cells and cell numbering to vary among scenarios. All scenarios had the same plan view so the number of surface cells remained unchanged, only subsurface cells were added or deleted in response to scenario dredging and filling activities.

To circumvent the problems with cell numbers and numbering in the scenarios, each scenario began with a uniform set of initial conditions in the water column as shown in Table 8-4. The WQM was run for the duration of the scenario, the final concentrations saved to a file which was then used as the initial conditions for the next run of that scenario. Sediment initial conditions were more problematic. Since sediments respond more slowly to changes in flow patterns and loadings than the water column does, beginning each scenario with a spatially uniform set of sediment initial conditions was undesirable due to the length of simulation required to reach a dynamic steady-state condition. Instead, the first run of every scenario began with the same sediment initial conditions used during calibration. These had been established over numerous calibration runs and were in equilibrium with calibration water column conditions.

Scenario results were compared using the same longitudinal transect as used during calibration. Results from each scenario were averaged over the STP and plotted with results from the base scenario, 1a, in order to assess the impact resulting from the scenario. Since all conditions in the scenarios were identical except for the change mandated by that scenario, deviations between the results of an individual scenario and 1a were wholly due to the conditions of the scenario.

Results from Scenarios 1b through 4 indicate changes in water quality that are totally due to changes in circulation resulting from channel/bathymetric modifications in Caño Martín Peña, Laguna San José, Canal Suárez, and Laguna La Torrecilla. As such, results from these scenarios all have similar characteristics.

In the following sections, Scenarios 1b through 6b are discussed. Results from all are compared to the base scenario, 1a. Observations are made as to the effects of the scenario conditions on each water quality constituent.

Table 8-4.
Scenario Uniform Initial Conditions for Water Column

Constituent	Value	Units
Temperature	30	ppt
Salinity	30	°C
Total Solids	10	g m ⁻³
Algae	0.6	g m ⁻³
Dissolved Organic Carbon	5	g m ⁻³
Labile Particulate Organic Carbon	1	g m ⁻³
Refractory Particulate Organic Carbon	1	g m ⁻³
Ammonium	0.1	g m ⁻³
Nitrate	0.02	g m ⁻³
Dissolved Organic Nitrogen	0.05	g m ⁻³
Labile Particulate Organic Nitrogen	0.2	g m ⁻³
Refractory Particulate Organic Nitrogen	0.2	g m ⁻³
Total Phosphorus	0.03	g m ⁻³
Dissolved Organic Phosphorus	0.02	g m ⁻³
Labile Particulate Organic Phosphorus	0.04	g m ⁻³
Refractory Particulate Organic Phosphorus	0.04	g m ⁻³
Chemical Oxygen Demand	0.1	g m ⁻³
Dissolved Oxygen	6	g m ⁻³
Fecal Coliform	100	mpn/100ml

Scenario 1b

The WQM grid for Scenario 1b was the same as the one used in 1a as widening Caño Martín Peña did not change the number of cells or flow faces. Figure 8-37 indicates the effect Scenario 1b had on the various water quality constituents. Temperature was unchanged between Scenario 1a and 1b as was expected. Salinity levels in San Juan Bay were only slightly changed but both surface and bottom salinity levels along the remainder of the transect were altered significantly. Surface salinity in western Caño Martín Peña decreased slightly in Scenario 1b while salinity in the eastern portion increased. This is due to the widening of the channel promoting increased exchange between the eastern and western ends of the canal. Surface salinity increased in Laguna San José as a result of increased flushing with San Juan Bay through Caño Martín Peña. Net flow from Laguna San José to Caño Martín Peña increased from 0.5 m³/s to 1.45 m³/s. Surface salinity also increased in Canal Suárez and La Torrecilla as a result of more of the freshwater flows into Laguna San José being removed via Caño Martín Peña. Net flow from Laguna San José to Canal Suárez decreased from 1.98 m³/s to 1.08 m³/s. Bottom salinity also

increased throughout the interior portion of the system as a result of greater exchange with San Juan Bay and the ocean.

Chlorophyll levels in the surface layer of western Caño Martín Peña increased as a result of additional flushing from Laguna San José. Correspondingly, there were decreases in chlorophyll over the eastern end of the transect as a result of chlorophyll leaving Laguna San José. The redistribution in chlorophyll had a slight effect on predicted light extinction values in the interior portions of the system as the self-shading component was affected. Phytoplankton production decreased in San José from 6093 kg C/day in 1a to 5825 kg C/day in 1b as a result of lower algae levels due to increased flushing.

Transect plots for carbon indicate that levels in the interior portions of the system decrease in Scenario 1b. This results from increased exchanges between Caño Martín Peña and San Juan Bay and Laguna San José and Caño Martín Peña. Carbon daily flux rates between Laguna San José and Caño Martín Peña increase from 454 kg/day in 1a to 1311 kg/day in 1b, while daily flux rates from Caño Martín Peña to San Juan Bay increased from 4860 kg/day to 5674 kg/day. As a result of the widening of Caño Martín Peña, less carbon was leaving Laguna San José by Canal Suárez in 1b (769 kg/day) than in 1a (1631 kg/day) which results in a decrease in carbon levels expressed as DOC and TOC in Canal Suárez and Laguna La Torrecilla.

Results similar to those for carbon were seen for nitrogen and phosphorus. The widening of Caño Martín Peña in Scenario 1b resulted in more nitrogen and phosphorus leaving Laguna San José via Caño Martín Peña rather than through Canal Suárez. This did not have much effect on concentrations in Laguna San José as concentrations were already low. There was a slight decrease in sediment ammonium flux rates over the length of Canal Suárez which resulted in ammonium release for Scenario 1b dropping to 8.9 kg/day from 10.2 kg/day in 1a. Both surface and bottom ammonium concentrations in Canal Suárez dropped in response to this and the decrease in nitrogen fluxes from Laguna San José. Nitrogen levels in surface and bottom waters decreased in Caño Martín Peña as a result of increased flushing and a slight decrease in ammonium releases from 3.95 kg/day in 1a to 3.67 kg/day in 1b. Dissolved organic phosphorus and dissolved inorganic phosphorus concentrations dropped in both the surface and subsurface waters of Caño Martín Peña. Again the decrease appears to be the result of increased flushing moving the flow and loading out of Caño Martín Peña faster.

Dissolved oxygen levels improved considerably over the length of Caño Martín Peña in 1b. The largest increase occurred near the middle of Caño Martín Peña at the end of the dredged portion where dissolved oxygen levels increased from 3 mg/l to over 5.5 mg/l. Bottom dissolved oxygen levels increased slightly in eastern Caño Martín Peña, Canal Suárez, and Laguna La Torrecilla. Fecal coliform levels remained relatively unchanged along the transect except for a slight decrease in eastern Caño

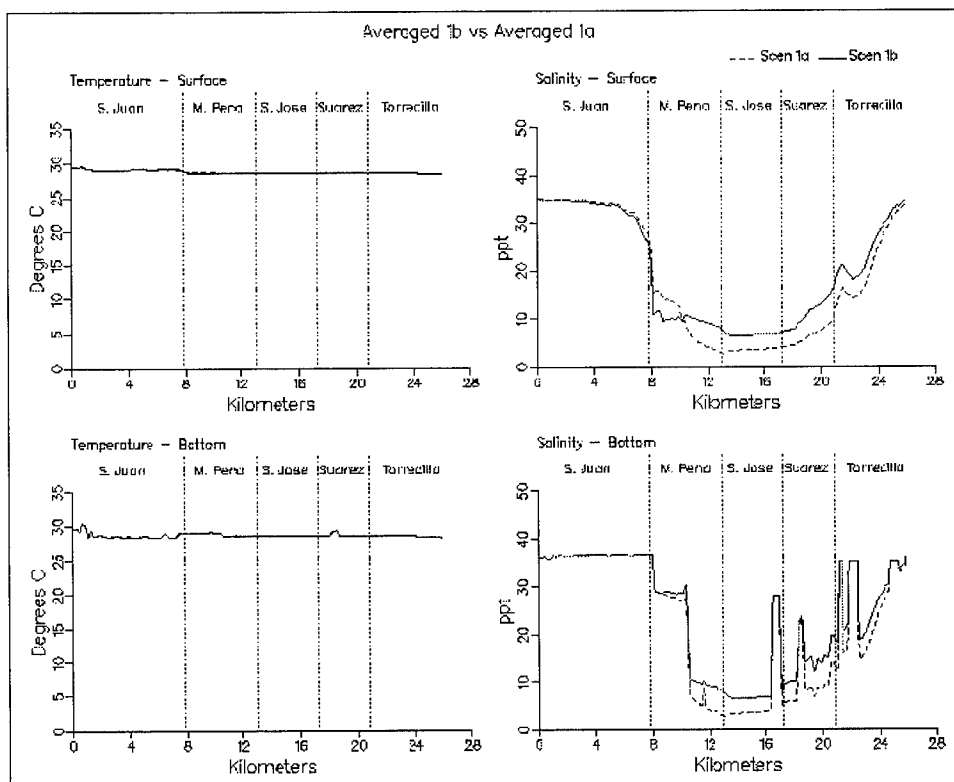


Figure 8-37. Simulation averaged transect plots and sediment flux plots comparing Scenario 1b with Scenario 1a (Sheet 1 of 11)

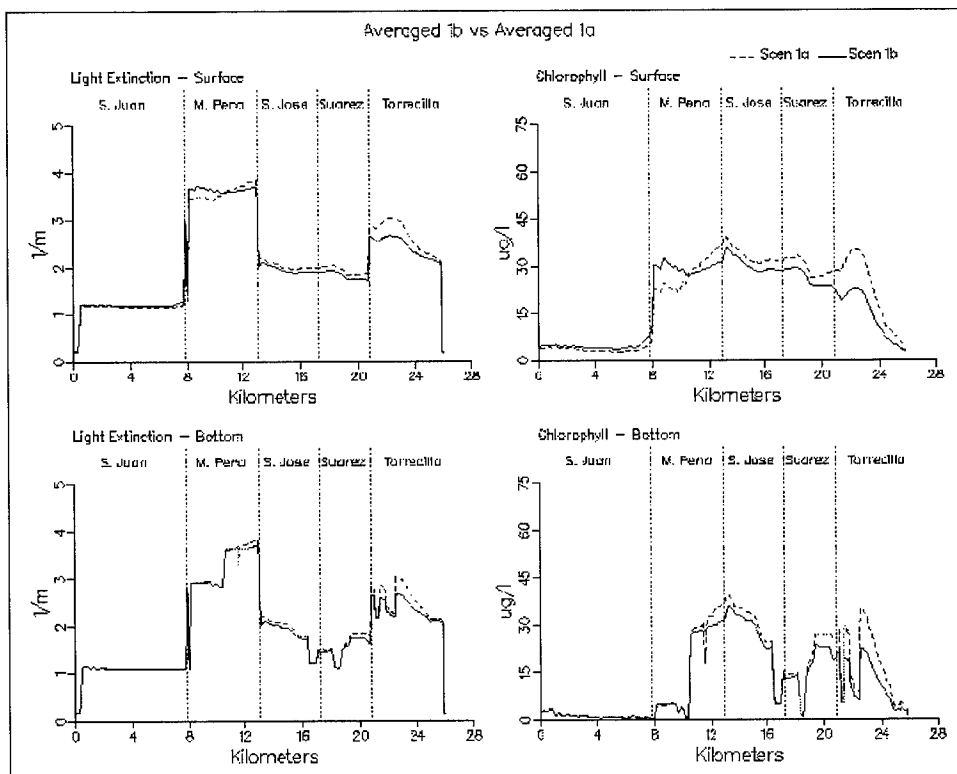


Figure 8-37. (Sheet 2 of 11)

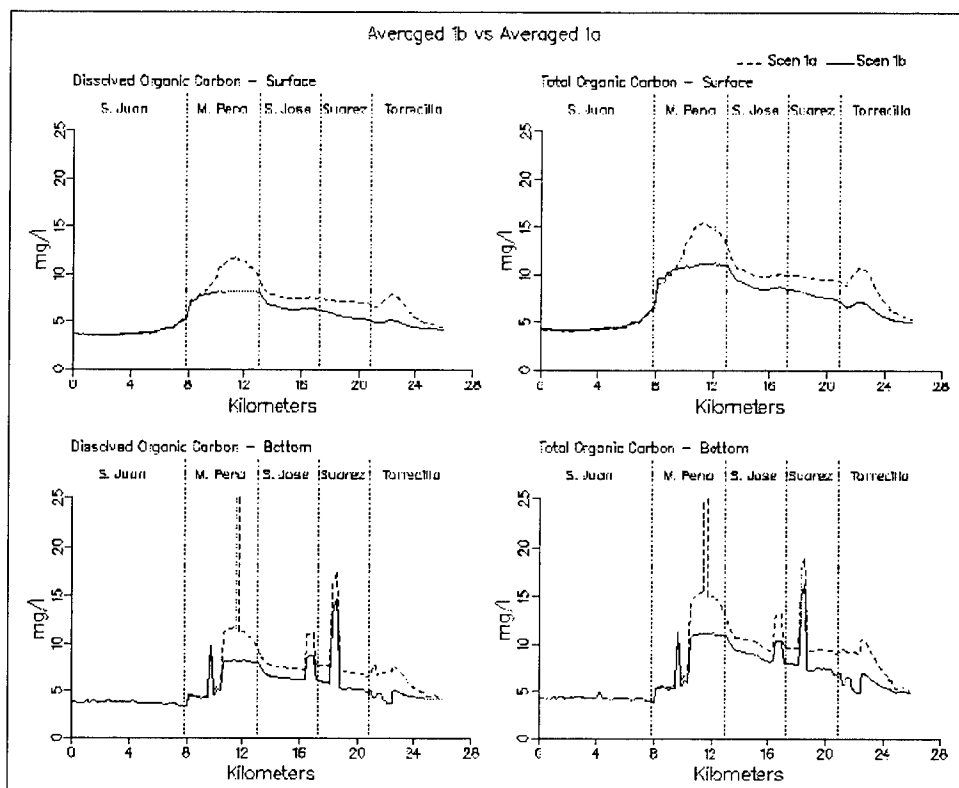


Figure 8-37. (Sheet 3 of 11)

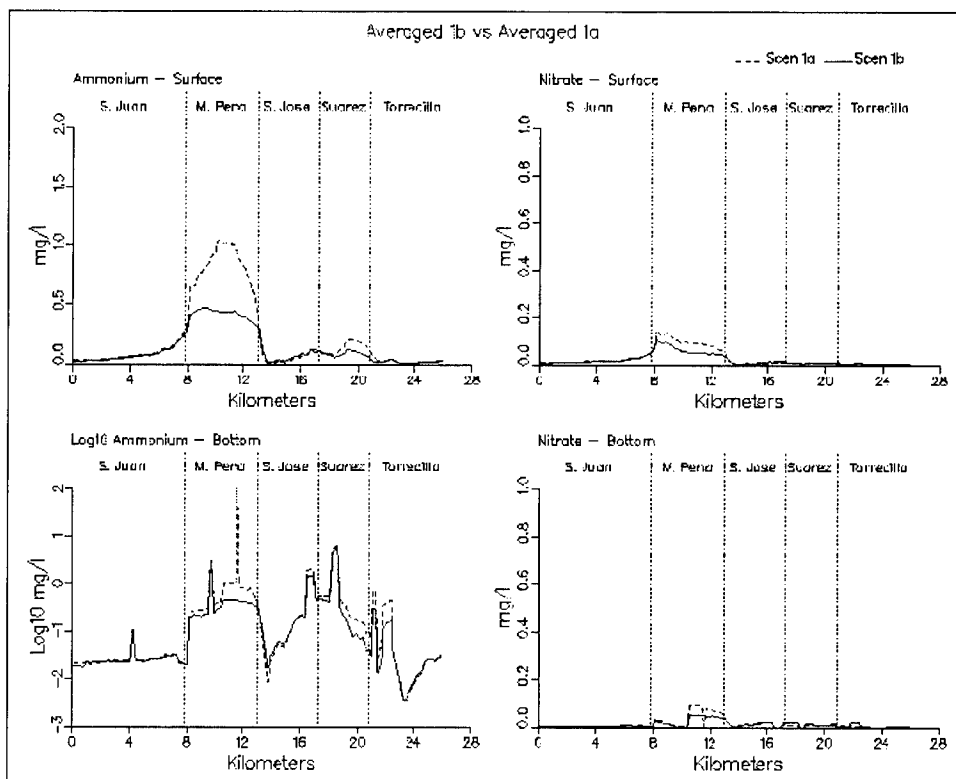


Figure 8-37. (Sheet 4 of 11)

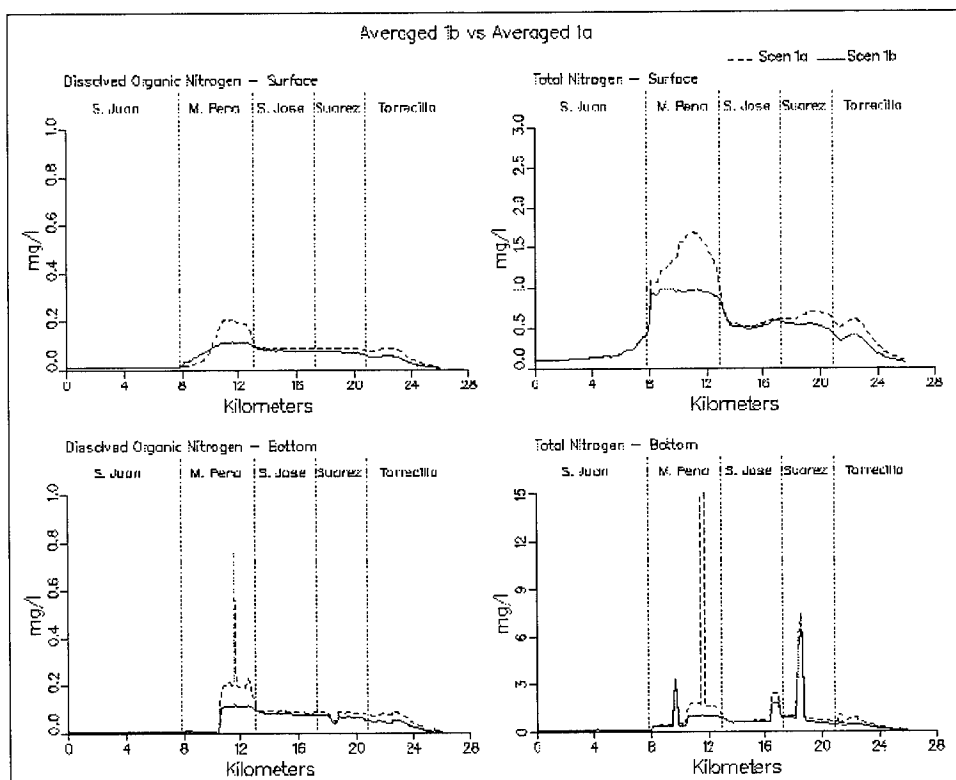


Figure 8-37. (Sheet 5 of 11)

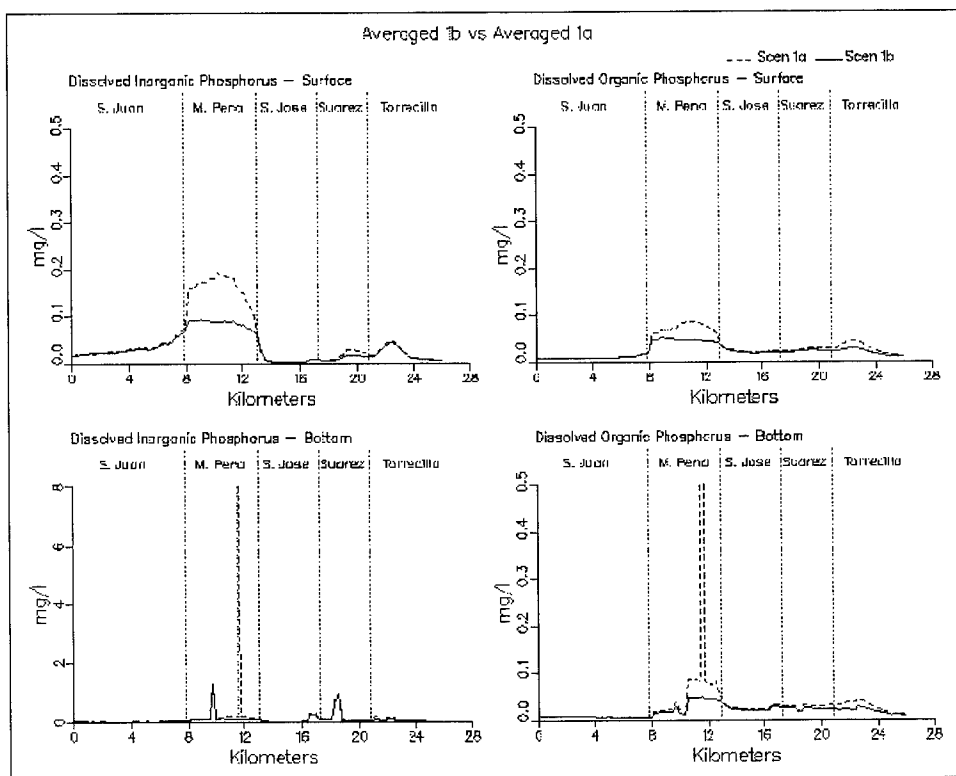


Figure 8-37. (Sheet 6 of 11)

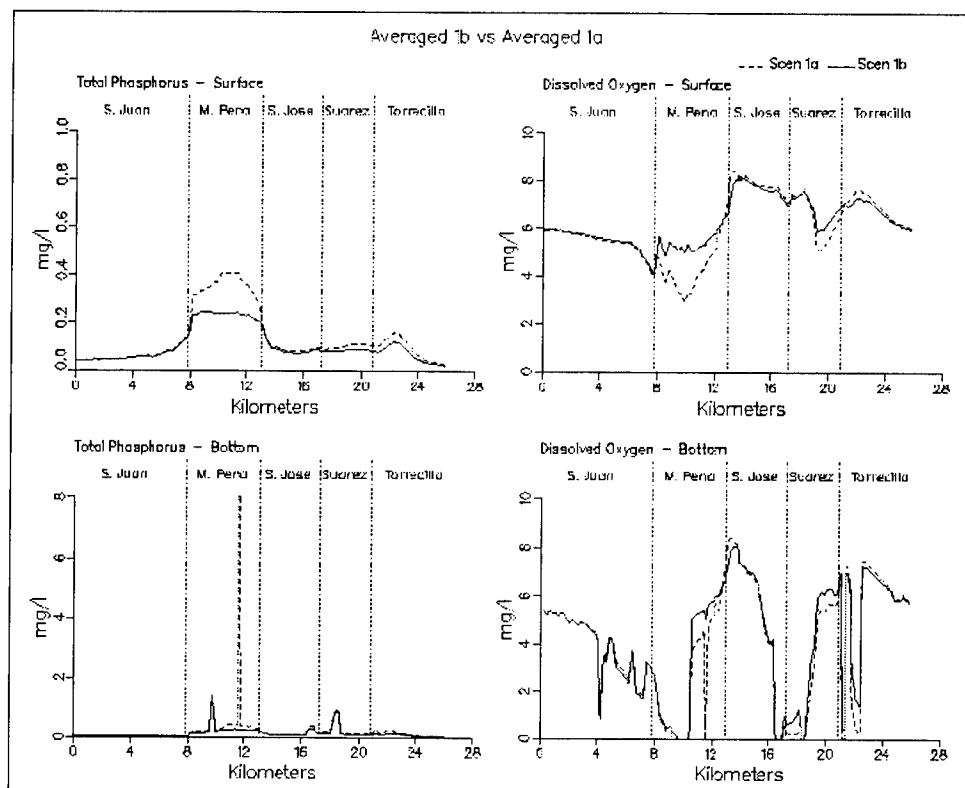


Figure 8-37. (Sheet 7 of 11)

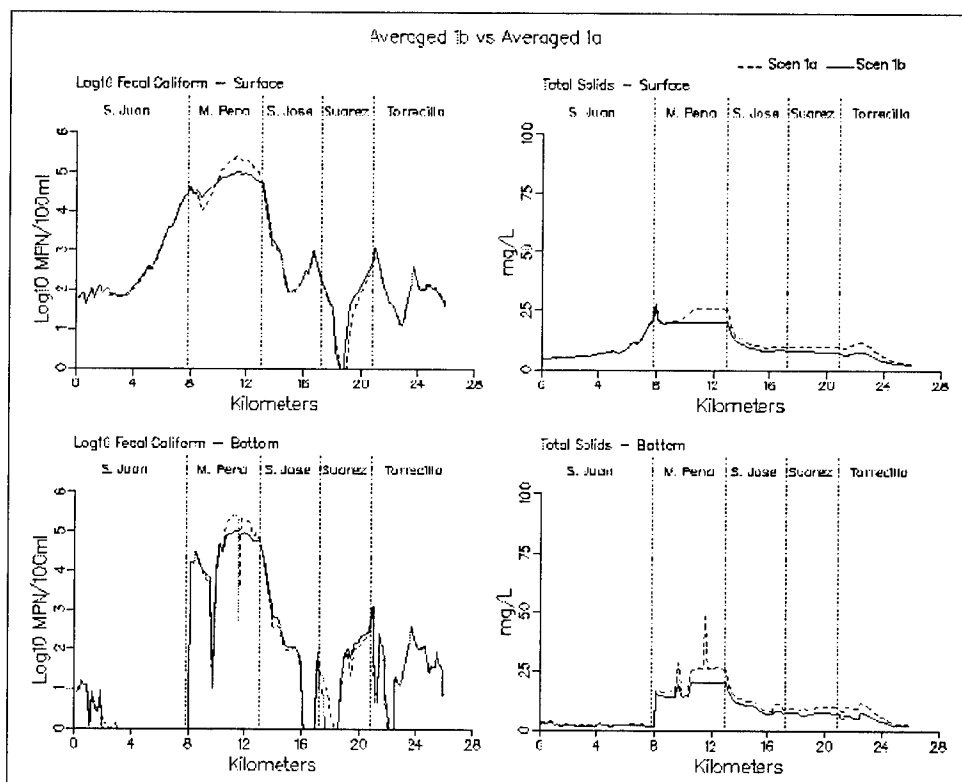


Figure 8-37. (Sheet 8 of 11)

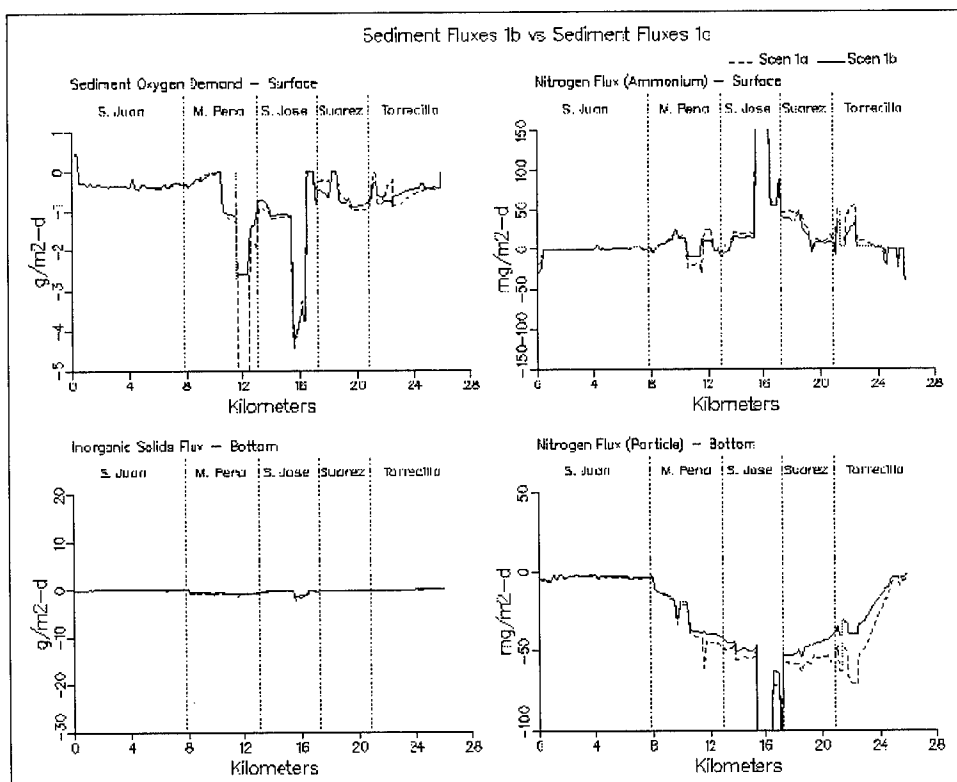


Figure 8-37. (Sheet 9 of 11)

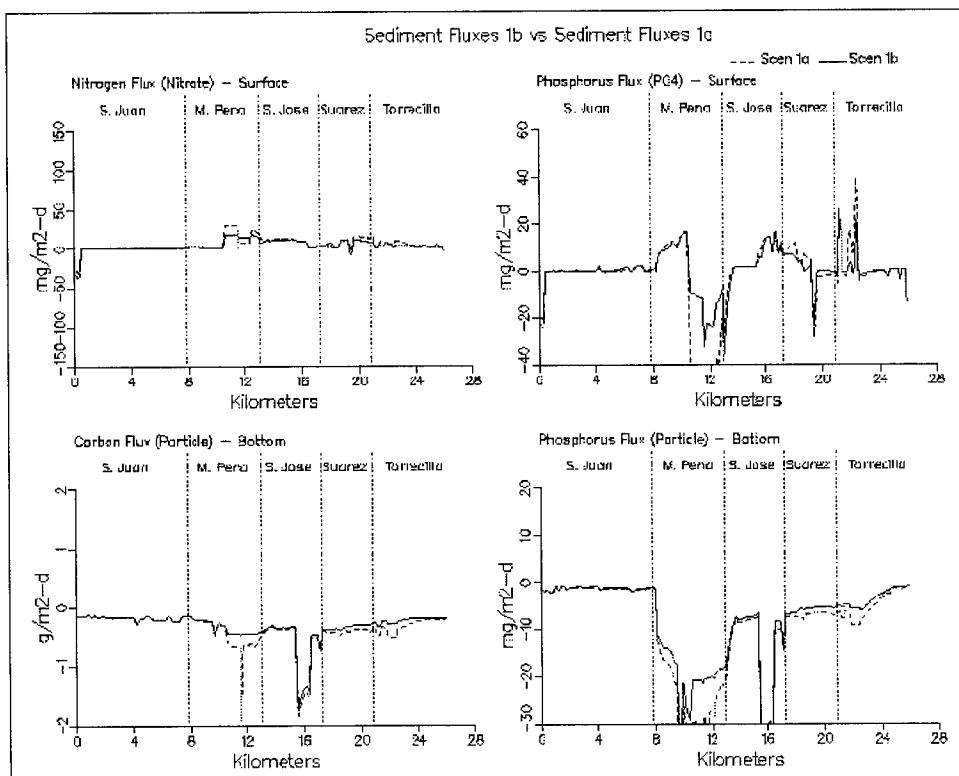


Figure 8-37. (Sheet 10 of 11)

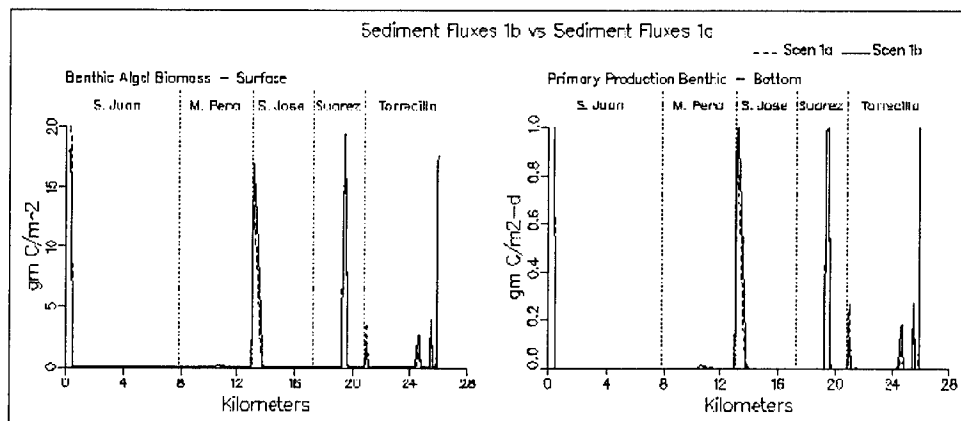


Figure 8-37. (Sheet 11 of 11)

Martín Peña as a result of increased flushing. Total solids transect plots also indicated decreases in the interior of the system as a result of additional flushing.

In summary, Scenario 1b resulted in an increase in the flow from Laguna San José through Caño Martín Peña. At the same time, there was a corresponding decrease in flow from Laguna San José through Canal Suárez. There were corresponding decreases in the mass of carbon, nitrogen, and phosphorus leaving Laguna San José via Canal Suárez which had the end result of improving water quality by decreasing nutrients and increasing salinity in Canal Suárez. The decrease in Laguna San José flow through Canal Suárez had the result of increasing ocean water influx through the Laguna La Torrecilla inlet which raised salinity levels. Nutrient levels in Caño Martín Peña were typically decreased by the nearly three-fold increase in flushing through the eastern end of the canal. The additional load due to the flux of Laguna San José waters through Caño Martín Peña was more than offset by the additional exchange with San Juan Bay.

Scenario 1c

The channel modifications for this scenario required that a new grid be generated (Table 8-3). Widening and deepening Caño Martín Peña had a significant effect on the distribution of flows from Laguna San José. Average discharge from Laguna San José through Caño Martín Peña increased to over $3 \text{ m}^3/\text{s}$. In the base Scenario 1a, discharge through this same path was only $0.5 \text{ m}^3/\text{s}$. Flow from Laguna San José via Canal Suárez in the base scenario had been nearly $2 \text{ m}^3/\text{s}$. In Scenario 1c, there is a reversal of the net flow so that there is now an average inflow of water from Canal Suárez to Laguna San José of $0.4 \text{ m}^3/\text{s}$. In effect, a clockwise circulation pattern has been established through the interior of the system from Laguna La Torrecilla to the mouth of San Juan Bay.

The change in circulation described above had significant effects upon water quality. Average salinity levels in Caño Martín Peña, Laguna San José, and Canal Suárez increased to approximately 23 ppt, Figure 8-38. There was a slight decrease in surface salinity in San Juan Bay as a result of more of the freshwater flows from Laguna San José being discharged through Caño Martín Peña. Bottom water salinity levels in Caño Martín Peña, Laguna San José, and Canal Suárez had increases similar to those of the surface waters, reaching concentrations of 25 ppt or greater. Chlorophyll levels in Caño Martín Peña, Laguna San José, Canal Suárez, and Laguna La Torrecilla decreased. Only San Juan Bay indicated any increase in chlorophyll when compared to Scenario 1a. Surface chlorophyll concentrations increased to 7 $\mu\text{g/l}$ in San Juan Bay as a result of chlorophyll from Laguna San José being transported down Caño Martín Peña. Phytoplankton production levels increased in San Juan Bay in 1c to 5300 kg C/day. In 1a, phytoplankton production levels were 3586 kg C/day. By comparison, phytoplankton production levels in Laguna San José were 5860 kg C/day in Scenario 1c and 6093 kg C/day in Scenario 1a. So while there was a significant change in chlorophyll levels between 1a and 1c in Laguna San José, the change was not the result of decreased algal activity but was instead the result of algae being discharged to San Juan Bay via Caño Martín Peña. A slight change in light extinction rates occurs along the transect as a result of changes in algal self-shading due to changes in algae concentration.

Surface dissolved organic carbon levels decreased in Caño Martín Peña, Laguna San José, Canal Suárez, and Laguna La Torrecilla. Concentrations in eastern Caño Martín Peña decreased from 12 mg/l to 5 mg/l. To some degree decreases in this area can be attributed to the canal dredging increasing receiving water volume for the un-sewered loadings. Total organic carbon levels showed results similar to those of dissolved organic carbon. Particulate organic carbon sediment deposition rates were decreased in eastern Caño Martín Peña from 0.5 g/m²-day to 0.1 g/m²-day. Carbon fluxes from Laguna San José to Caño Martín Peña in Scenario 1c were 3530 kg/day. Carbon fluxes from Canal Suárez to Laguna San José were 166 kg/day. Therefore, Canal Suárez transferred organic carbon into Caño Martín Peña for 1c.

Surface and bottom ammonium levels decreased all along the transect with the exception of a slight increase (0.05 mg/l) in the vicinity of station SJ-2 in Laguna San José. The greatest decreases in surface waters occurred in eastern Caño Martín Peña where ammonium levels decreased from as high as 1 mg/l to 0.1 mg/l. Surface levels decreased in western Caño Martín Peña but not to the same degree as in the eastern end of the canal. One possible explanation for this is the effects of the Rio Piedras inflows into Caño Martín Peña at its juncture with San Juan Bay. Ammonium levels decreased in the anoxic holes throughout the system. The most substantial decreases occurred in Caño Martín Peña as a result of the channelization removing the hole from the eastern end. The decreases in eastern Laguna San José, Canal Suárez, and Laguna La Torrecilla result from the clockwise circulation pattern established through the interior.

Nitrate levels decreased in the surface waters of Caño Martín Peña and were unchanged elsewhere. Dissolved organic nitrogen levels decreased along the transect from Caño Martín Peña eastward. An insignificant increase occurred in San Juan Bay at its confluence with Caño Martín Peña. Laguna San José discharged 186.7 kg/day of nitrogen into Caño Martín Peña and imported 5 kg/day from Canal Suárez.

Phosphorus results for Scenario 1c were similar to nitrogen results. Laguna San José discharged 15.3 kg/day of phosphorus into Caño Martín Peña and imported 2.3 kg/day from Canal Suárez. Dissolved inorganic phosphorus levels dropped in Caño Martín Peña surface waters and in the bottom waters all along the transect. Dissolved organic phosphorus levels also dropped in Caño Martín Peña in 1c and remained unchanged elsewhere along the transect. Total phosphorus results indicated the greatest decrease occurred in Caño Martín Peña. Slight decreases in total phosphorus occurred in Canal Suárez and Laguna La Torrecilla as a result of the flow reversal from 1a to 1c in Canal Suárez.

Surface dissolved oxygen levels increased in Caño Martín Peña to the 5-mg/l to 6-mg/l range in 1c. No bottom waters in Caño Martín Peña were anoxic in 1c although at least one location had an average dissolved oxygen less than 1 mg/l. Overall, bottom water dissolved oxygen levels in Caño Martín Peña were greater than 3 mg/l. Laguna San José, Canal Suárez, Laguna La Torrecilla all saw some degree of dissolved oxygen decrease in the surface and bottom waters. These decreases appear to be the result of diminished algal concentrations resulting in less photosynthesis. Bottom anoxic conditions at the confluence of Laguna San José and Canal Suárez were raised to a minimum of 2 mg/l and as high as 5 mg/l. Only the deep hole in Canal Suárez remained anoxic.

Fecal coliform levels decreased in Caño Martín Peña by an order of magnitude in part due to additional receiving water volume being present. Levels increased insignificantly in San Juan Bay as a result of additional flushing through Caño Martín Peña. A slight increase also occurred along the transect in Laguna San José as a result of Caño Martín Peña being opened. Total solids levels decreased throughout the system in 1c with the greatest decreases occurring in Caño Martín Peña.

In summary, Scenario 1c resulted in an increase in the discharge of Laguna San José through Caño Martín Peña. At the same time, there was a reversal in net flow in Suárez Canal which resulted in the establishment of a clockwise circulation pattern through the interior of the system. Canal Suárez exported nutrients into Laguna San José in 1c. All water quality variables, except DO, showed improvement in Scenario 1c when compared to 1a in all bodies of water examined. There were decreases in surface dissolved oxygen levels in Laguna San José, Canal Suárez, and Laguna La Torrecilla as a result of decreased algal photosynthesis. Nevertheless, surface dissolved oxygen levels in these waters remained in the 6-mg/l to 7-mg/l range and were the highest along the transect.

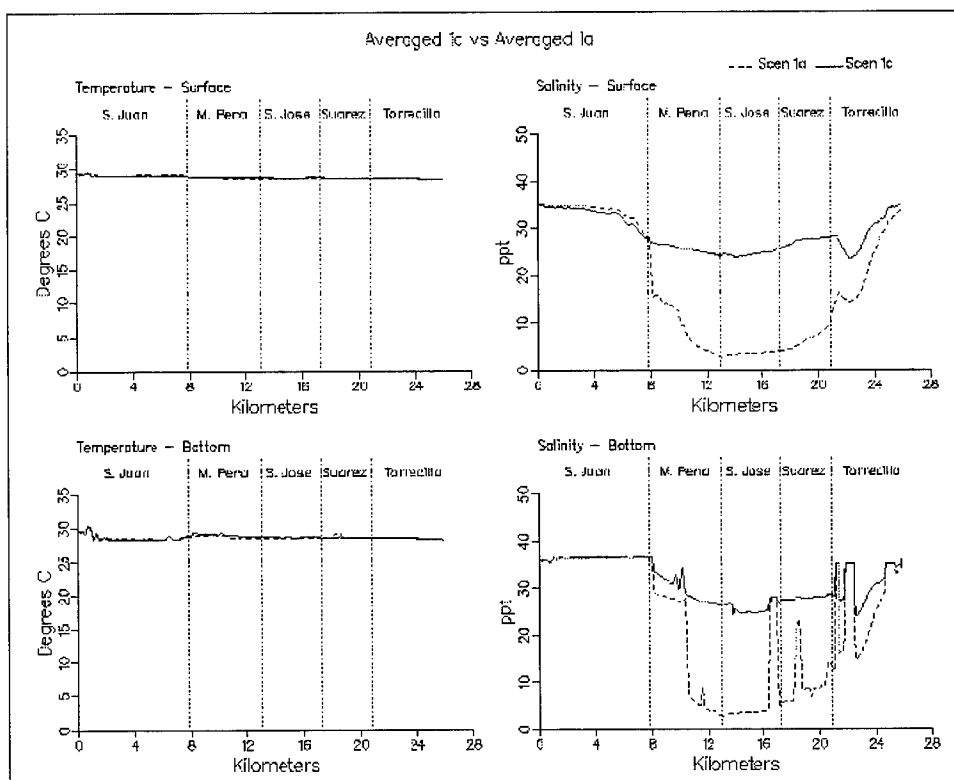


Figure 8-38. Simulation averaged transect plots comparing Scenario 1c with Scenario 1a (Sheet 1 of 11)

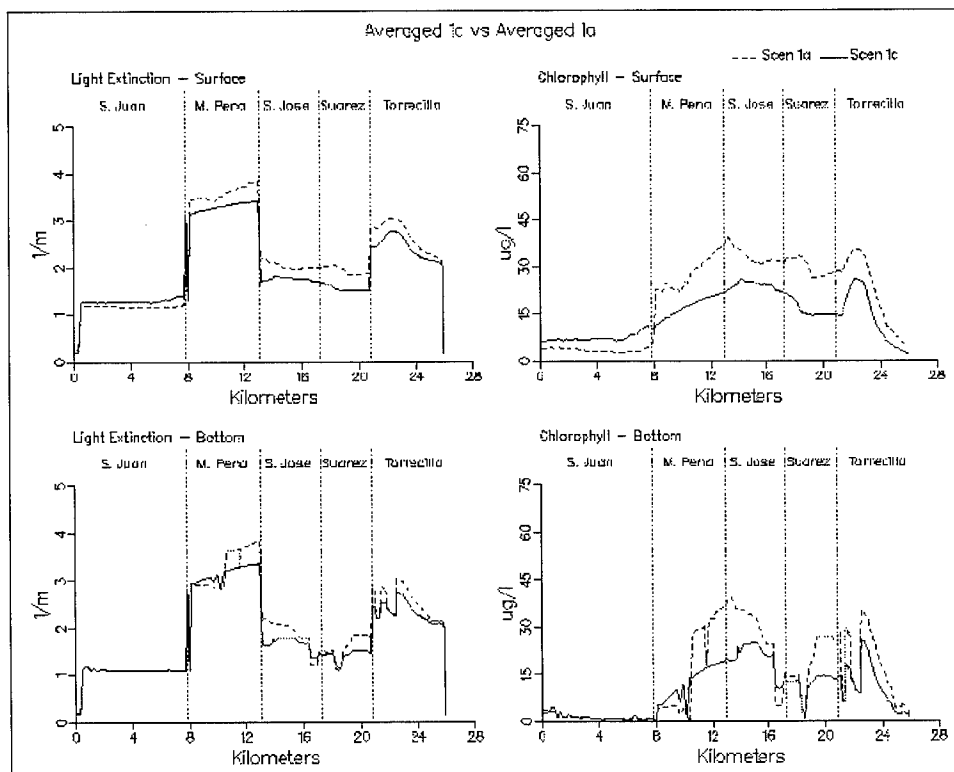


Figure 8-38. (Sheet 2 of 11)

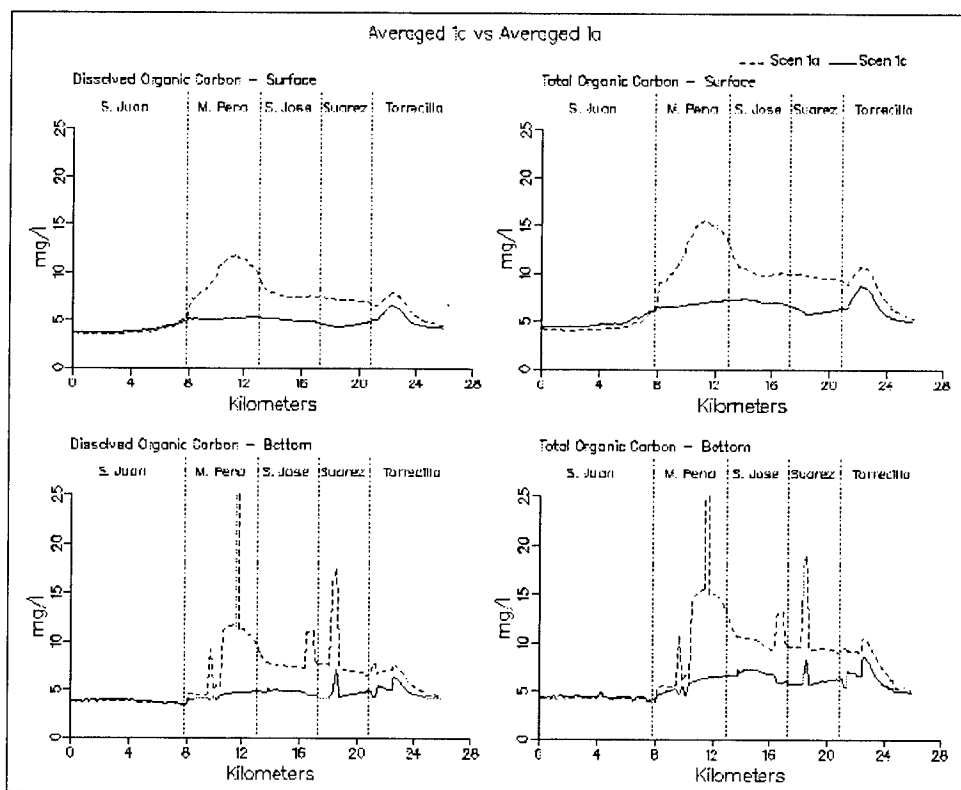


Figure 8-38. (Sheet 3 of 11)

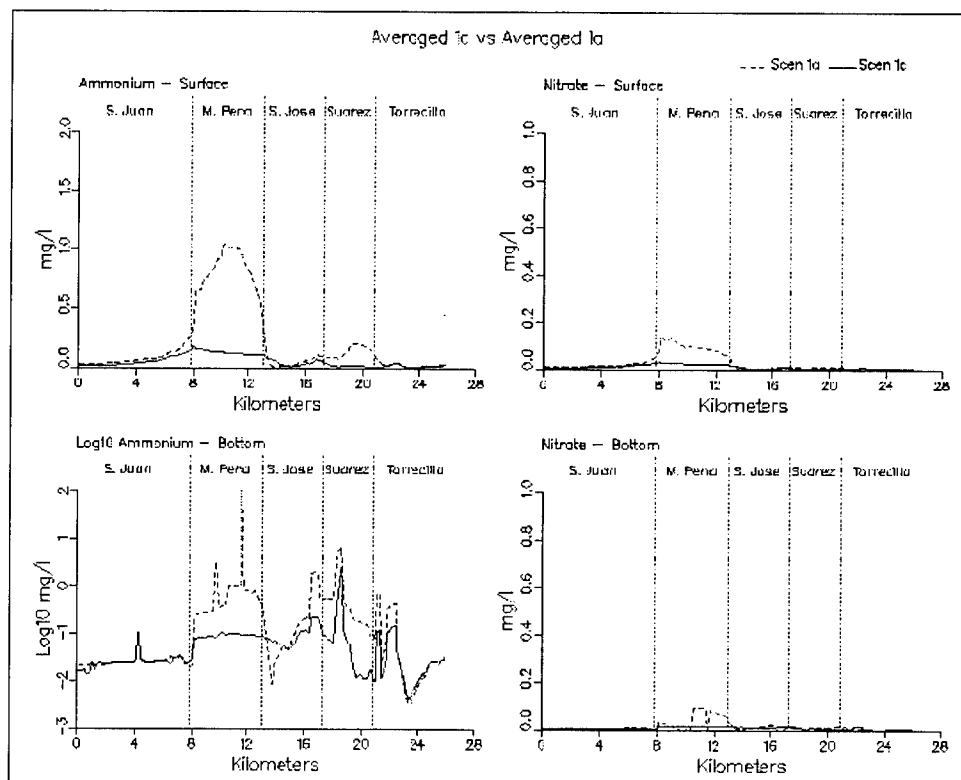


Figure 8-38. (Sheet 4 of 11)

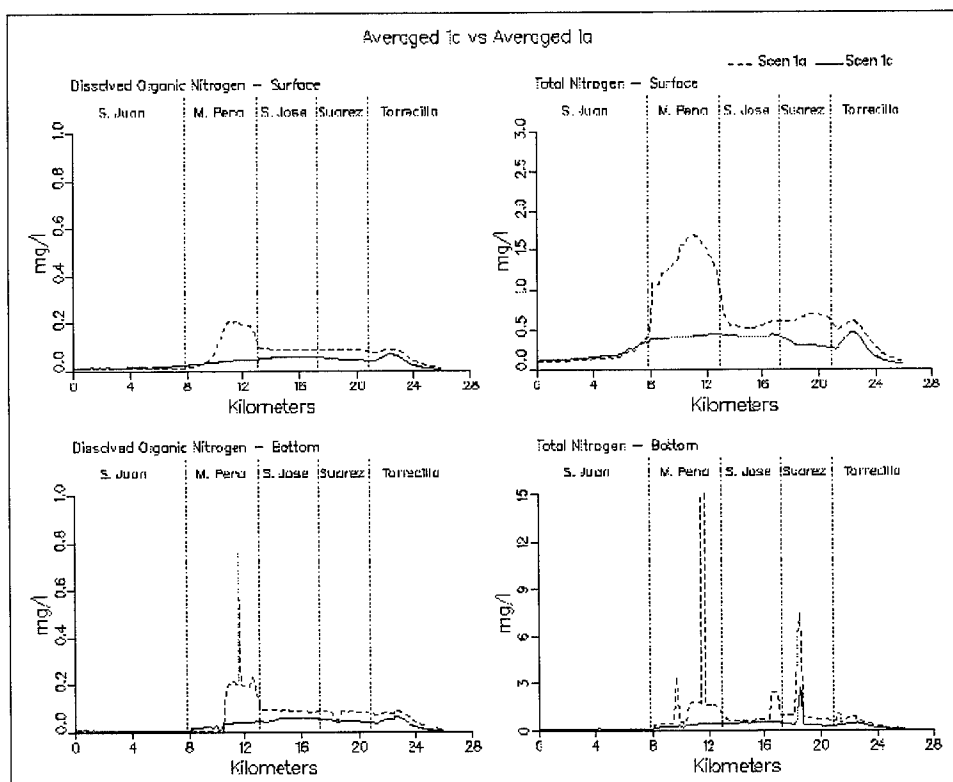


Figure 8-38. (Sheet 5 of 11)

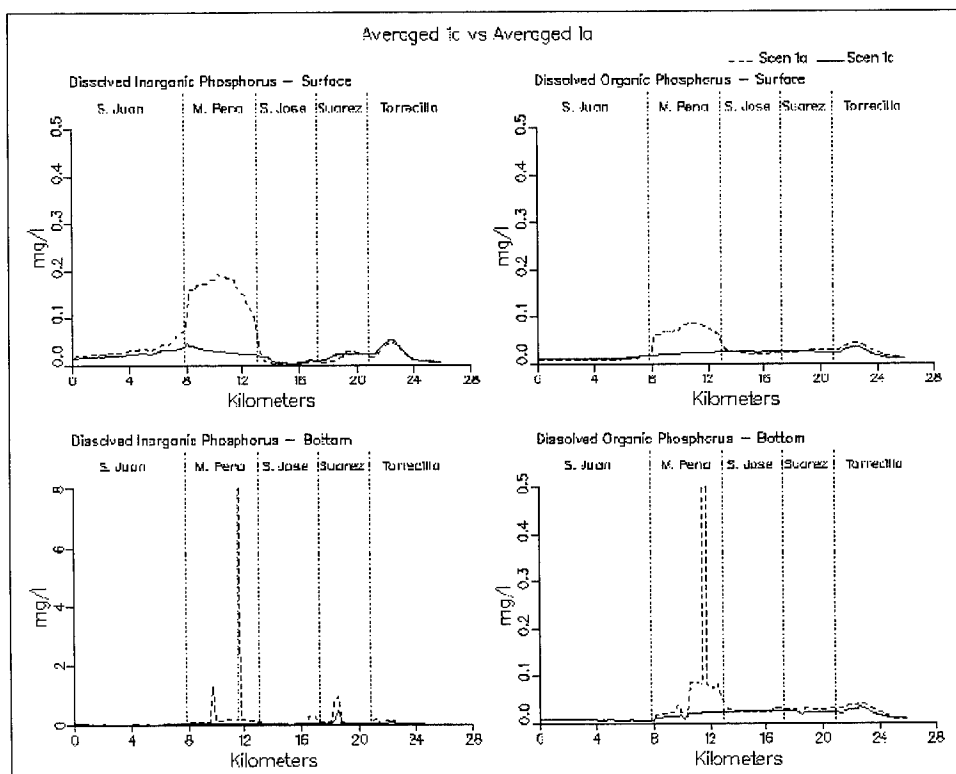


Figure 8-38. (Sheet 6 of 11)

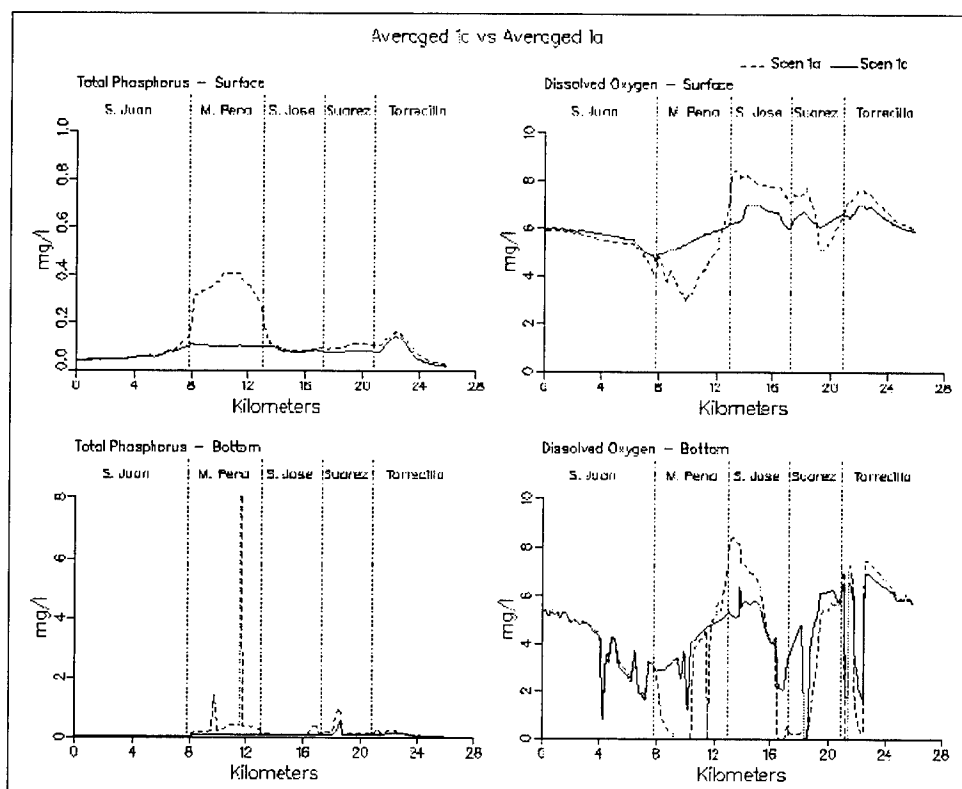


Figure 8-38. (Sheet 7 of 11)

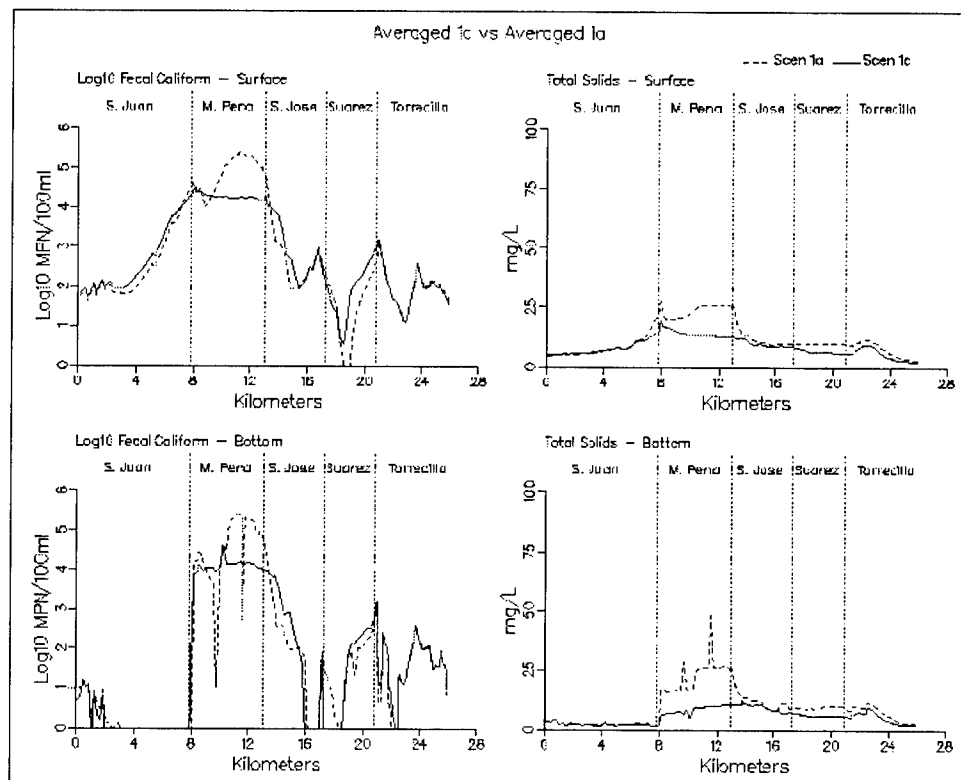


Figure 8-38. (Sheet 8 of 11)

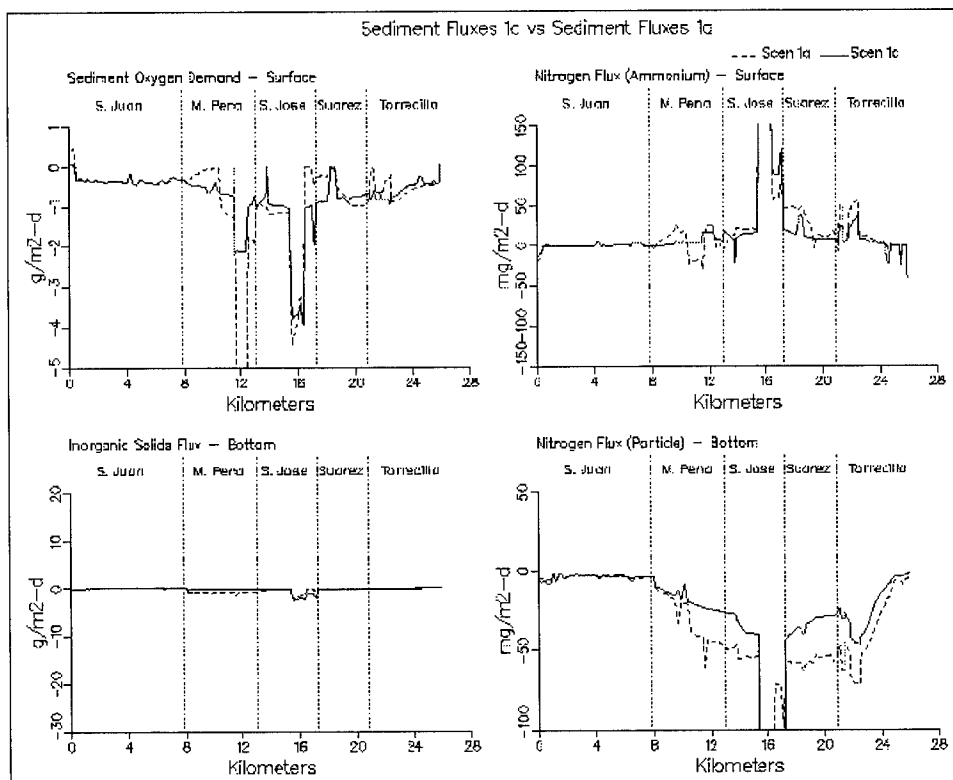


Figure 8-38. (Sheet 9 of 11)

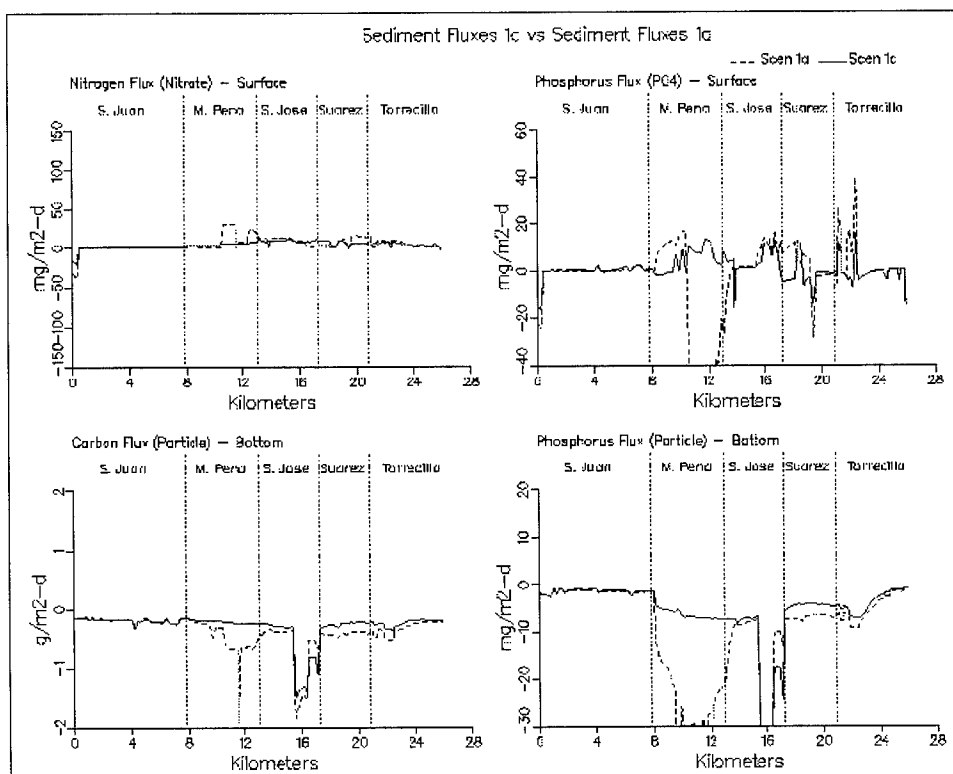


Figure 8-38. (Sheet 10 of 11)

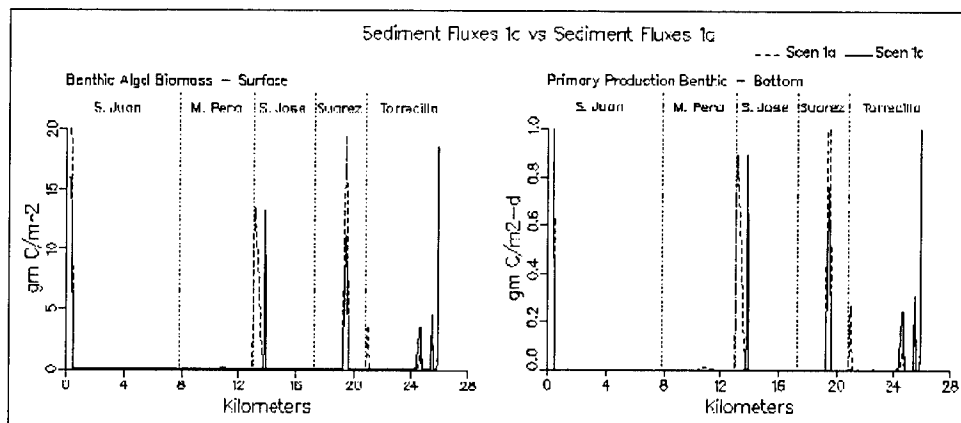


Figure 8-38. (Sheet 11 of 11)

Scenario 2

Scenario 2 was unique among scenarios in that nothing was done which would improve circulation and flushing of Laguna San José, Caño Martín Peña, or Canal Suárez. Neither would the features of Scenario 2 result in any decrease in tributary or runoff loads to the system. Instead, by filling the anoxic holes of Laguna San José, sediment nutrient fluxes and the oxygen demand arising from these holes should be decreased. The volume of Laguna San José in Scenario 1a was 12,781,933 m³ which was decreased to 9,507,690 m³ in Scenario 2. The distribution of flows leaving Laguna San José in Scenario 2 was identical to the flow distribution in 1a.

Results from Scenario 2 indicate that the surface temperatures in San Juan Bay are slightly cooler than 1a (Figure 8-39). Salinity transects show more differences. Filling in the holes resulted in there being no “nudging” of salinity. As a result, this internal salinity boundary condition was lost. The spin-up runs required to equilibrate the sediments effectively flushed the salt out of Laguna San José and Canal Suárez. As a result, the waters being flushed down Caño Martín Peña are too fresh and actually decrease the salinity of San Juan Bay.

Chlorophyll levels in Scenario 2 are much lower throughout the interior of the system. Tributary loads of chlorophyll are unchanged, thus the reason appears to be nutrient limitation. In Scenario 2, Laguna San José sediments take up 105.5 kg/day of ammonium and 28.9 kg/day of phosphate. In comparison, the sediments gave off 436 kg/day of ammonium and 20 kg/day of phosphate in Scenario 1a.

Dissolved organic carbon levels are decreased in Scenario 2 apparently as a result of the decrease in algae productivity. Carbon fluxes from Laguna San José to Caño Martín Peña were 329 kg/day. Fluxes from Laguna San José to Canal Suárez were 1060 kg/day.

Ammonium levels in Caño Martín Peña were unchanged in Scenario 2. Levels in Canal Suárez did drop to near 0 mg/l. Nitrate levels were unchanged throughout the system. Dissolved organic nitrogen levels decreased from the middle of Caño Martín Peña eastward in response to a decrease in algal levels. Total nitrogen levels indicated considerable decreases in Laguna San José and Canal Suárez when compared to Scenario 1a. Nitrogen fluxes from Laguna San José to Caño Martín Peña were 8.8 kg/day while fluxes from Laguna San José to Canal Suárez were 18.4 kg/day.

Dissolved inorganic phosphorus concentrations actually increased in Caño Martín Peña, Laguna San José, and Canal Suárez in Scenario 2. This is felt to be in response to the decreased levels of algae in Laguna San José. Also, the presence of phosphorus and the near absence of ammonium indicate that nitrogen is probably the limiting factor in algal growth. Dissolved organic phosphorus levels along the transect were relatively unchanged in Scenario 2. Total phosphorus levels were unchanged in Scenario 2 except for slight decreases in the eastern end of Canal Suárez. Phosphorus fluxes from Laguna San José to Caño Martín Peña in Scenario 2 were 2 kg/day. Phosphorus fluxes from Laguna San José to Canal Suárez were 12.9 kg/day.

Surface dissolved oxygen levels showed little change in Scenario 2. There were slight increases in DO in San Juan Bay but this is undoubtedly due to the decrease in salinity. Bottom dissolved oxygen levels increased significantly in Laguna San José as a result of the removal of the ammonium fluxes and sediment oxygen demand associated with the anoxic holes. Fecal coliform levels were unchanged. Total solids transect plots indicated a slight decrease in the interior system which is the result of decreased algal levels in these waters.

In summary, Scenario 2 improved water quality by removing internal nutrient sources which resulted in a decrease in algal concentrations. The extensive spin-up period resulted in the flushing of the salinity out of the interior of the system but does not appear to have influenced other water quality constituents significantly.

Scenario 3

Scenario 3 involved Scenario 1a plus removal of the bridge constriction on Canal Suárez. Net flow from Laguna San José to Canal Suárez increased from less than 2 m³/s in Scenario 1a to over 2.5 m³/s for Scenario 3. Flow from Laguna San José to Caño Martín Peña decreased from 0.5 m³/s in 1a to less than 0.1 m³/s in Scenario 3. In essence, all of Laguna San José's exchange with the ocean is via Canal Suárez in Scenario 3.

Results for Scenario 3 indicate that salinity increases in Caño Martín Peña, Laguna San José, and Canal Suárez when compared to 1a (Figure

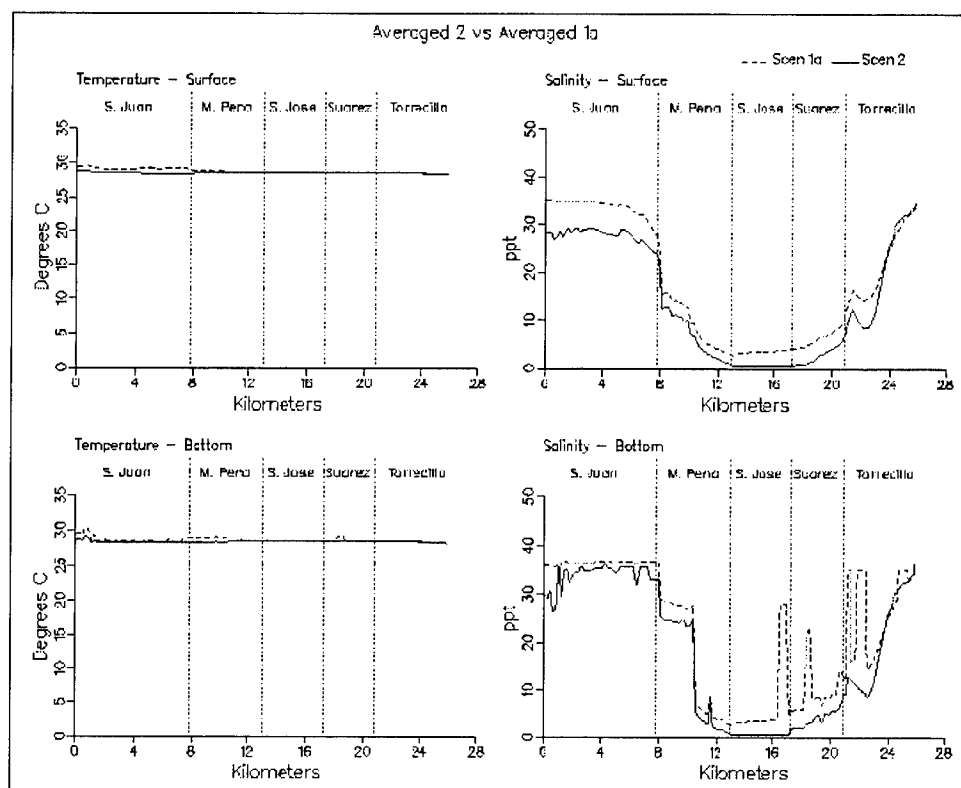


Figure 8-39. Simulation averaged transect plots comparing Scenario 2 with Scenario 1a (Sheet 1 of 11)

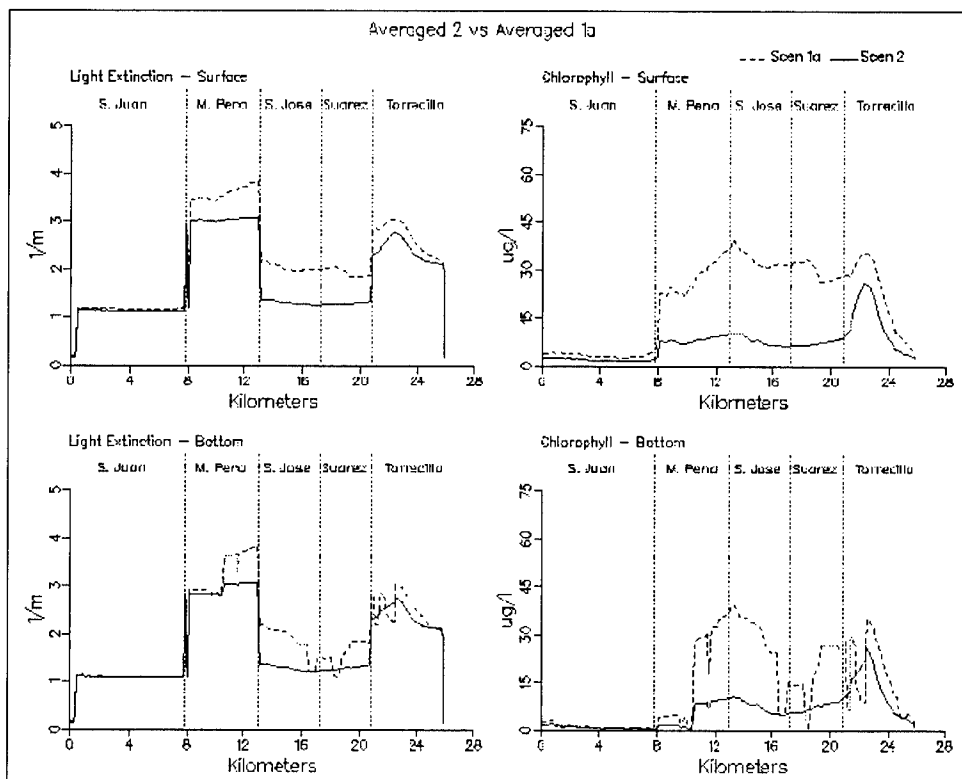


Figure 8-39. (Sheet 2 of 11)

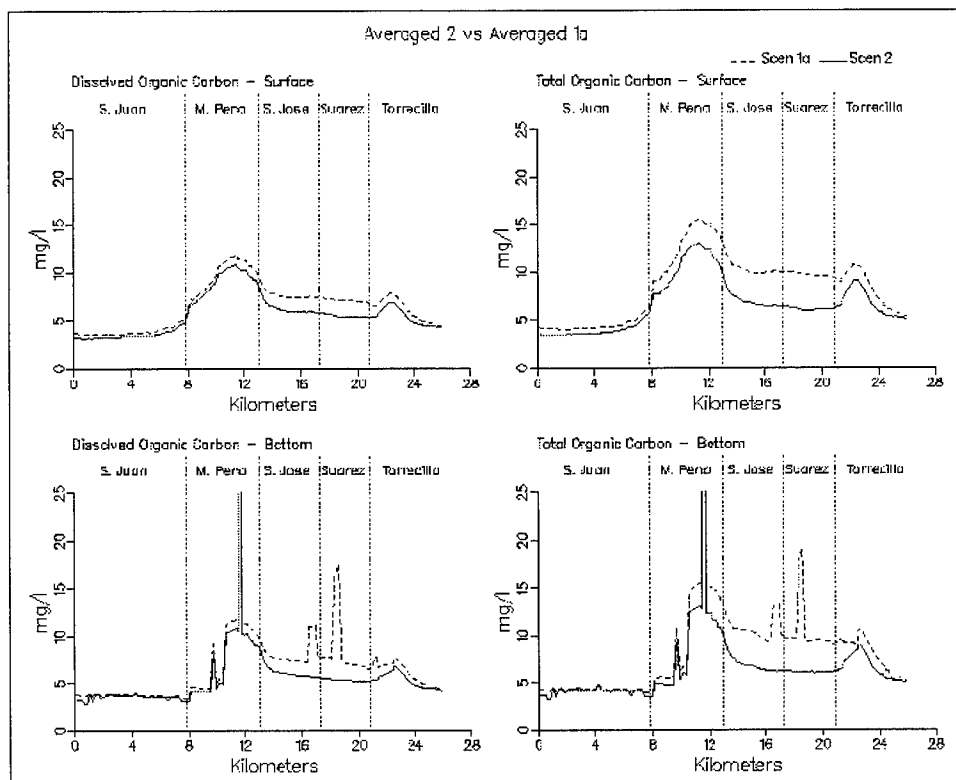


Figure 8-39. (Sheet 3 of 11)

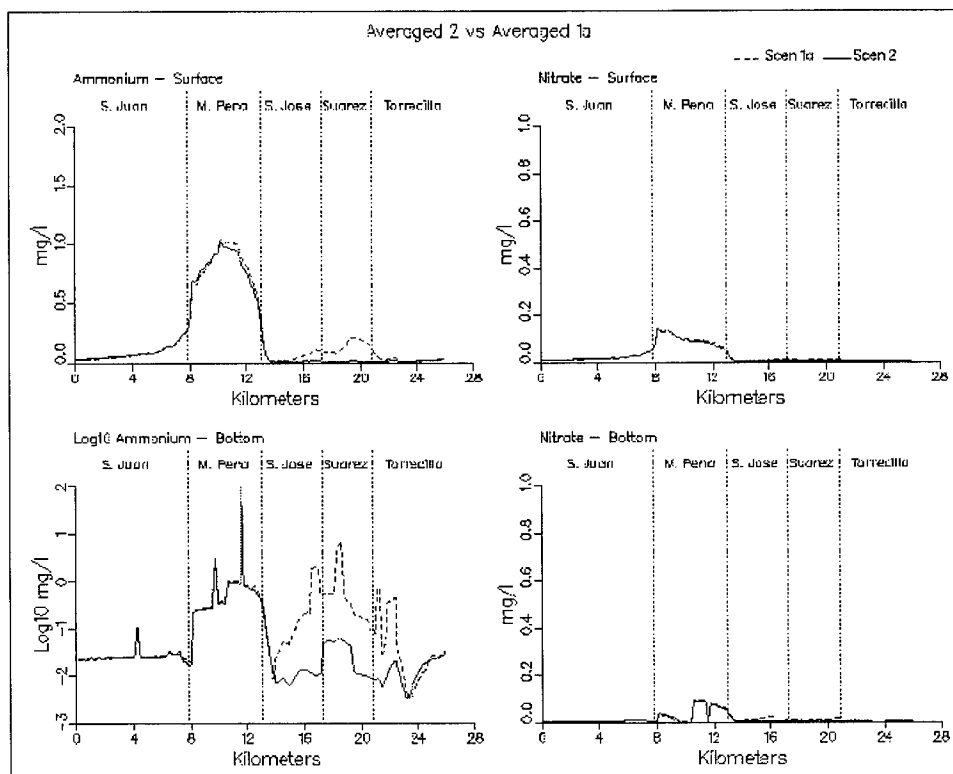


Figure 8-39. (Sheet 4 of 11)

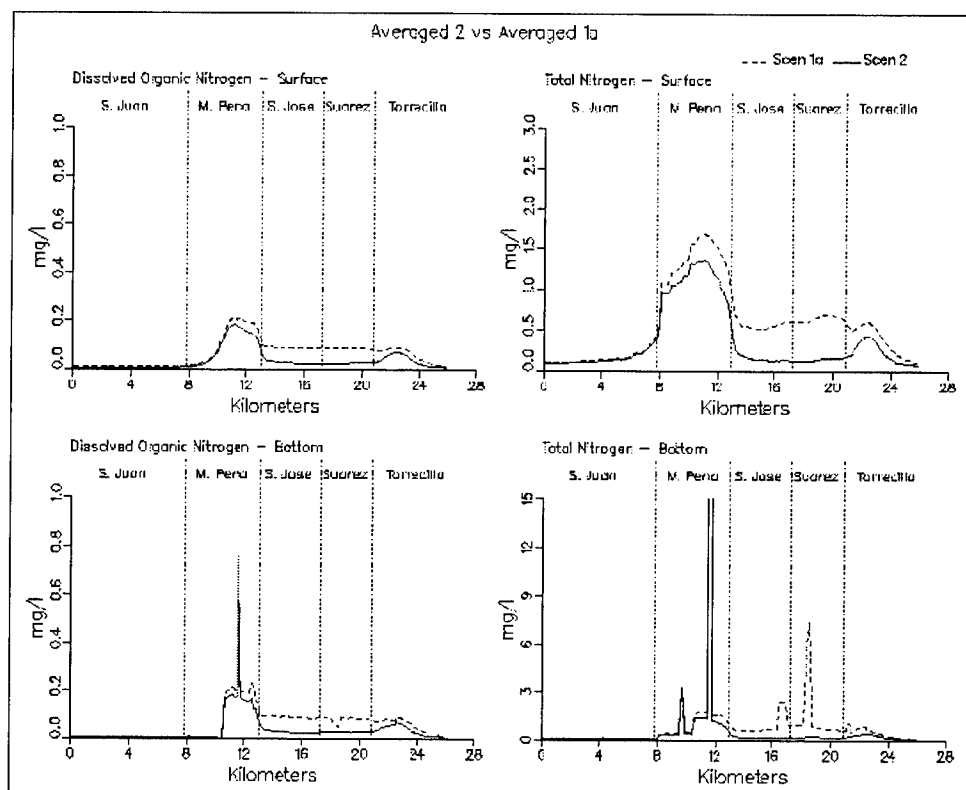


Figure 8-39. (Sheet 5 of 11)

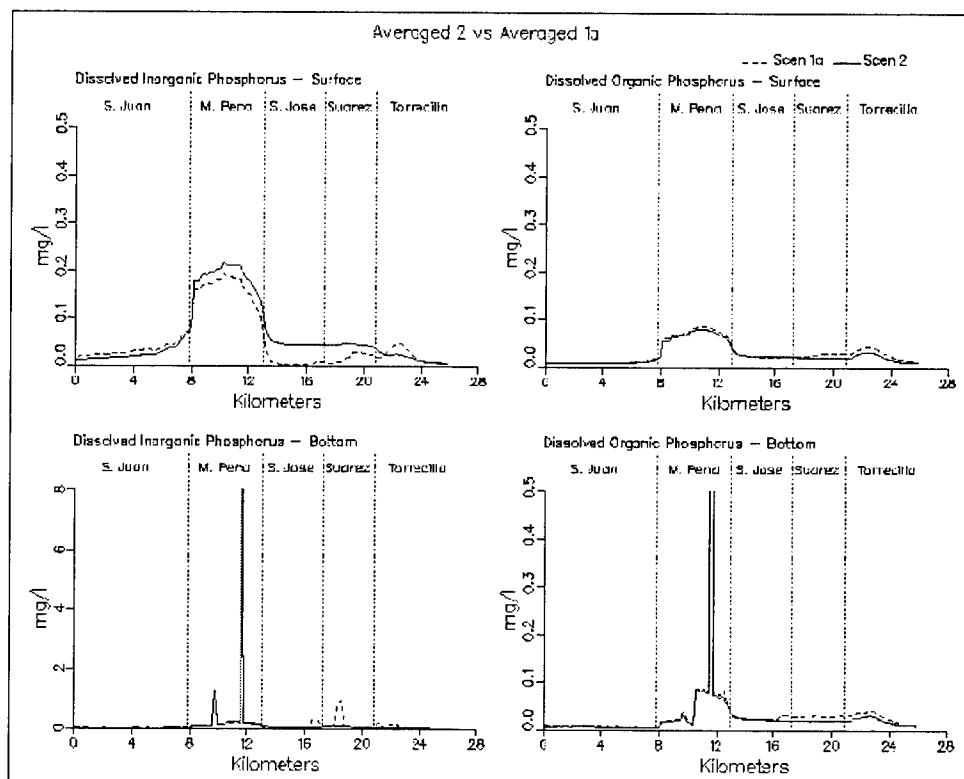


Figure 8-39. (Sheet 6 of 11)

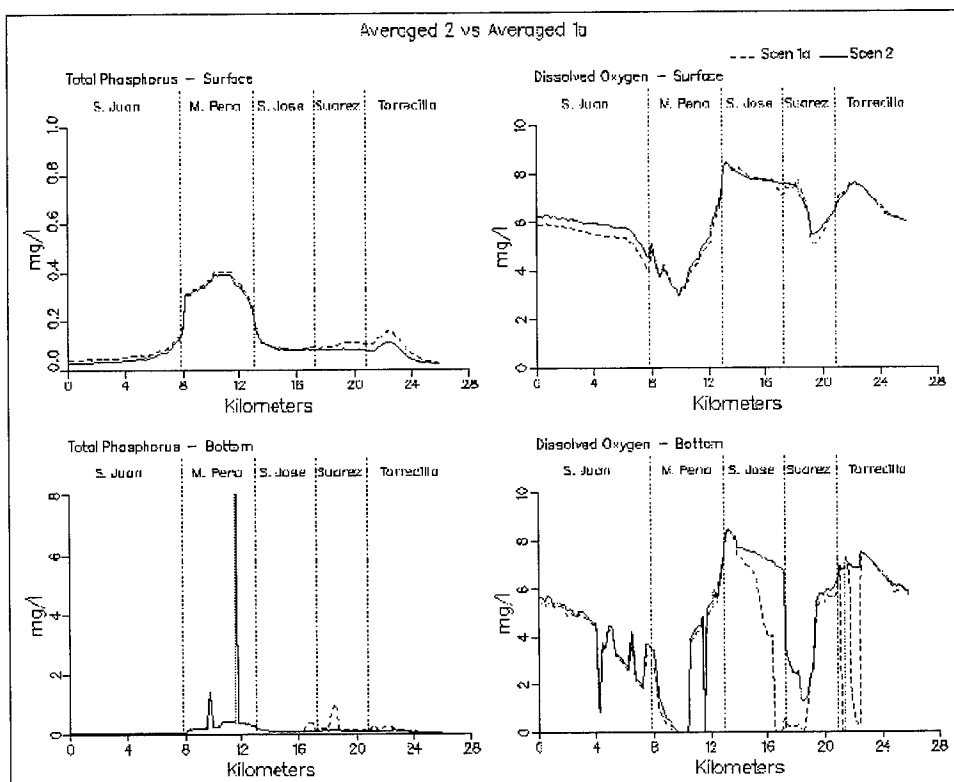


Figure 8-39. (Sheet 7 of 11)

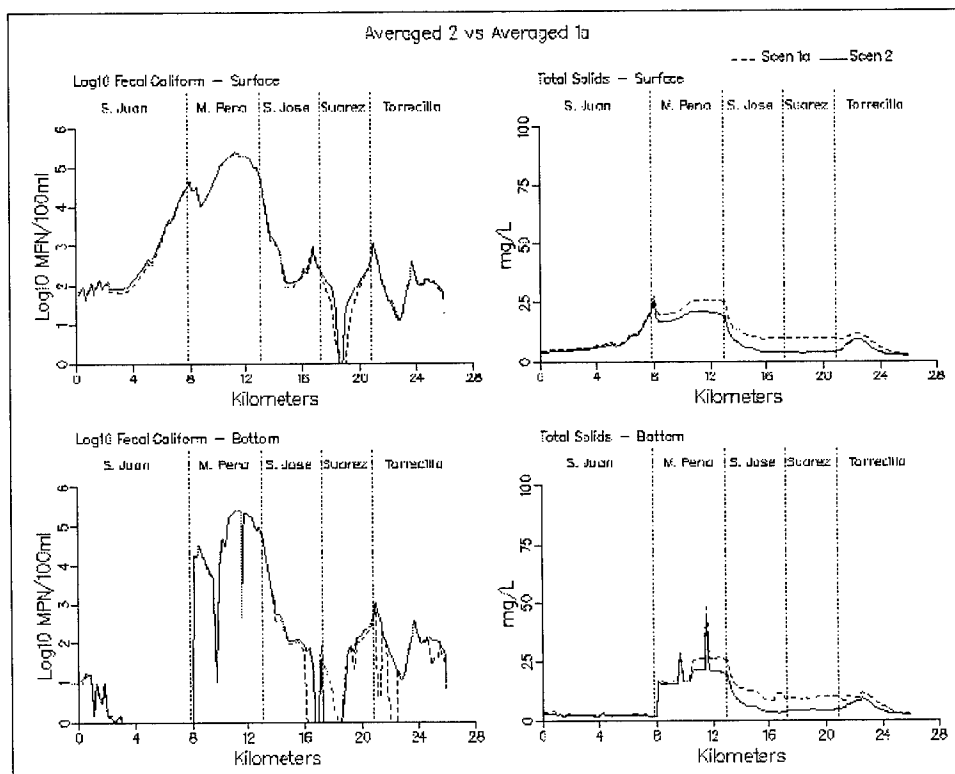


Figure 8-39. (Sheet 8 of 11)

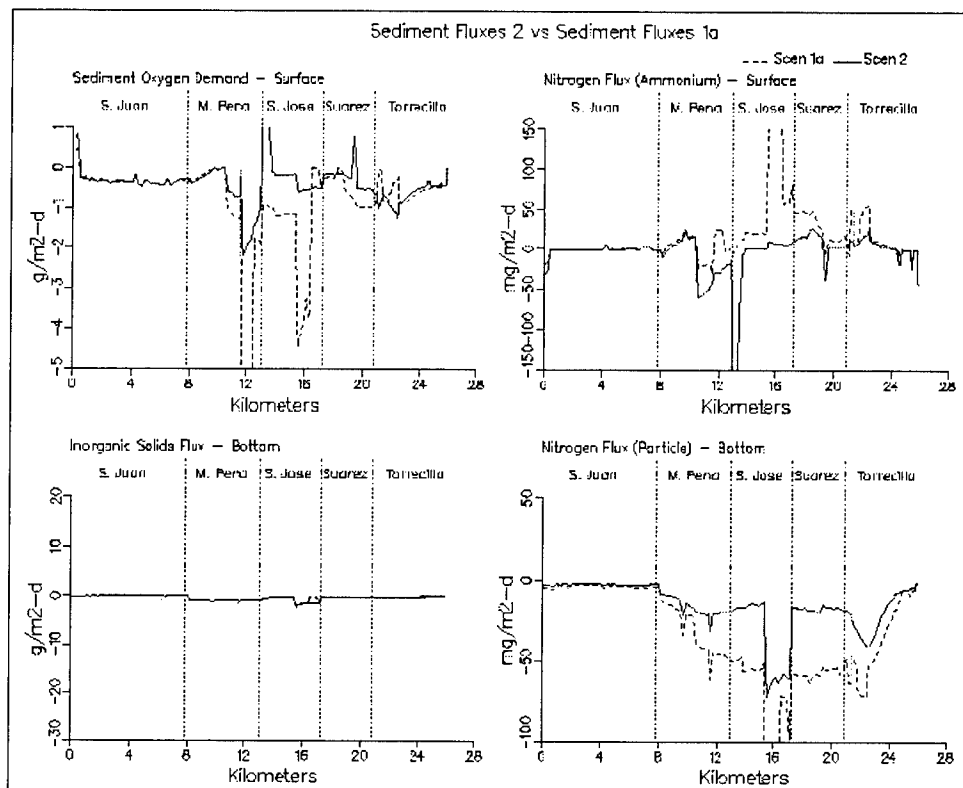


Figure 8-39. (Sheet 9 of 11)

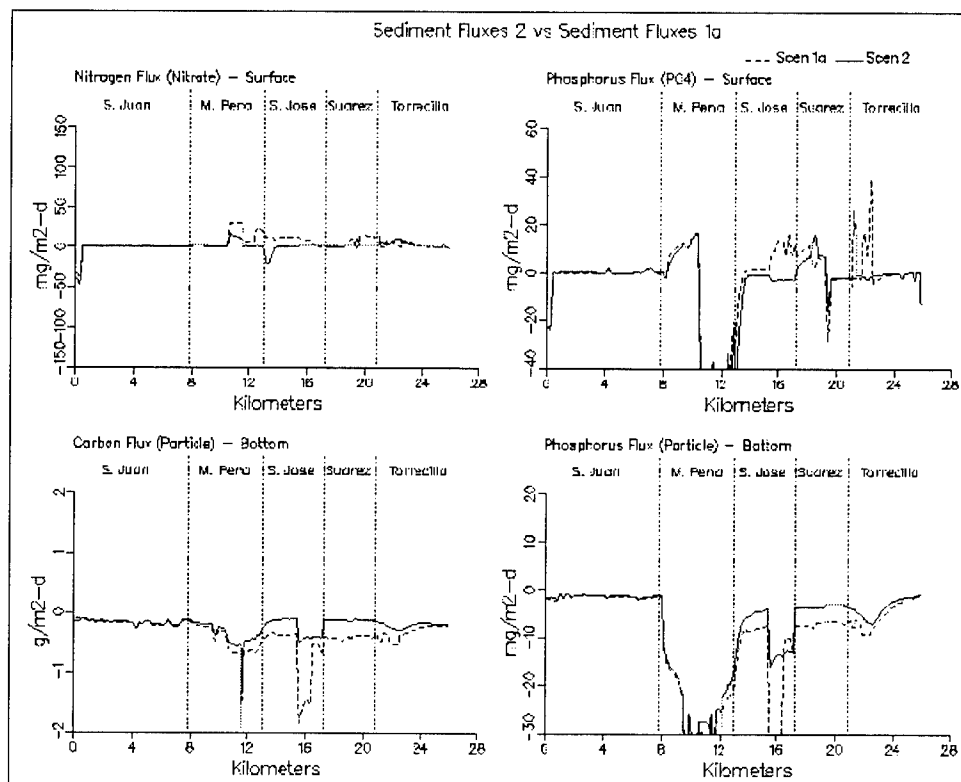


Figure 8-39. (Sheet 10 of 11)

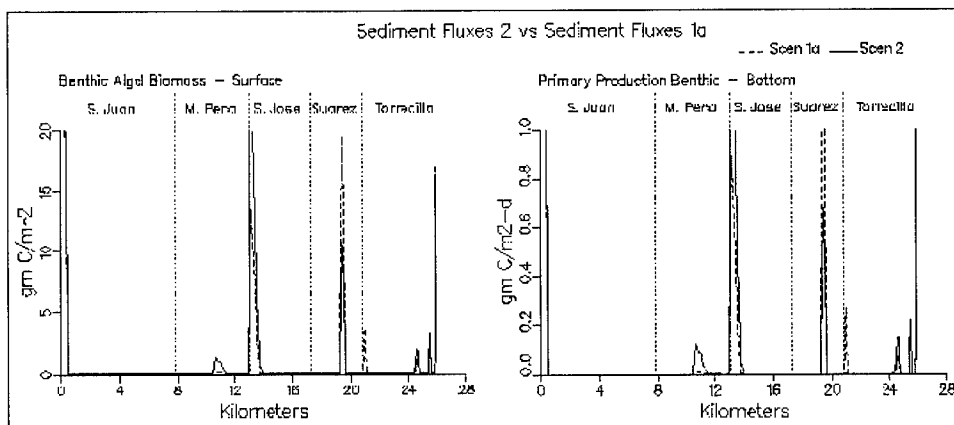


Figure 8-39. (Sheet 11 of 11)

8-40). Increases in Caño Martín Peña are probably the result of saltwater intrusion farther up the canal. Increases in Laguna San José and Canal Suárez result from more exchange with the ocean via Laguna La Torreçilla. Chlorophyll levels remained relatively unchanged in Laguna San José, Canal Suárez, and Laguna La Torreçilla in Scenario 3 compared to Scenario 1a, but decreased in western Caño Martín Peña by $10 \mu\text{g/l}$ due to bay water intrusion up the canal and less algae exchange with Laguna San José. Light extinction levels were unchanged except for Caño Martín Peña where there was a slight decrease due to a decrease in algal self-shading. Only slight changes were observed in organic carbon levels in Scenario 3. Surface dissolved organic carbon levels decreased slightly in western and increased slightly in the eastern portions of Caño Martín Peña. Although total organic carbon concentrations in Laguna San José in Scenario 3 are nearly identical to those in 1a, the flux of carbon from Laguna San José to Canal Suárez is 2261 kg/day versus 1631 kg/day in 1a. Caño Martín Peña actually exports a slight amount of carbon (35.5 kg/day) to Laguna San José in Scenario 3.

Surface water ammonium concentrations increased in the eastern undredged portion of Caño Martín Peña as a result of lower flushing from Laguna San José. Bottom water ammonium levels increased slightly in the undredged portion of Caño Martín Peña to 1 mg/l . Surface water ammonium levels in eastern Canal Suárez decreased from 0.2 mg/l to less than 0.1 mg/l . Bottom ammonia concentrations decreased the entire length of Canal Suárez in part due to a decrease in sediment ammonium fluxes in the western portion of the canal. Nitrate levels exhibited only the slightest change in Caño Martín Peña. Dissolved organic nitrogen levels were relatively unchanged in Scenario 3. Changes in transect plots for total nitrogen between 1a and Scenario 3 are attributable to the changes in ammonium concentrations in Caño Martín Peña and Canal Suárez. Laguna San José exported 178 kg/day of nitrogen through Canal Suárez in Scenario 3 versus 138 kg/day in Scenario 1a. Laguna San José also imported 38.2 kg/day from Caño Martín Peña in Scenario 3 where it had exported 7.5 kg/day in Scenario 1a.

Scenario 3 phosphorus results were similar to those of nitrogen. Increases occurred in dissolved inorganic phosphorus in the undredged eastern portion of Caño Martín Peña and decreases occurred in the eastern end of Canal Suárez. Bottom dissolved inorganic phosphorus levels decreased in the hole in Caño Martín Peña. Dissolved organic phosphorus levels increased slightly in eastern Caño Martín Peña. DIP and DOP levels elsewhere did not change. Laguna San José imported 9.4 kg/day of phosphorus from Caño Martín Peña and exported 23.4 kg/day through Canal Suárez.

Dissolved oxygen levels in Scenario 3 were similar to those in Scenario 1c. Dissolved oxygen decreased slightly in eastern Caño Martín Peña probably as a result of decreased photosynthesis. Surface dissolved oxygen levels did increase in the eastern portion of Canal Suárez. Anoxic conditions in the western end of Canal Suárez were relieved. Fecal coliform levels were unchanged throughout the system except for a slight increase in Canal Suárez. Little change in total solids transect plots occurred as a result of Scenario 3 modifications.

In summary, the modifications of Scenario 3 did little to improve overall water quality when compared to Scenario 1a. Salinity in Laguna San José was increased over 1a results. However, even though there was still a slight discharge from Laguna San José to Caño Martín Peña, Caño Martín Peña became a source of nutrients to Laguna San José. Nutrient concentrations increased in the undredged section of Caño Martín Peña with the diminished flushing from Laguna San José.

Scenario 4

Scenario 4 like Scenario 3 centered on modifications to Canal Suárez without any channel modifications elsewhere. In Scenario 4, a one-way tide gate was installed in the western section of Canal Suárez, along with the removal of the bridge constriction. The tide gate would allow flows in Canal Suárez to move in an east to west fashion but not west to east. This prevented Laguna San José from discharging via Canal Suárez and forced all flow leaving Laguna San José to exit via Caño Martín Peña. No additional channel modifications were made to Caño Martín Peña other than those performed for Scenario 1a.

Scenario 4 results indicated significant change in salinity when compared to results for Scenario 1a (see Figure 8-41). Salinity levels decreased in Caño Martín Peña in response to increased flow from Laguna San José. Average net flow from Laguna San José to Caño Martín Peña increased from 0.5 m³/s in Scenario 1a to 2.55 m³/s in Scenario 4. For comparisons' sake, the net discharge from Laguna San José to Caño Martín Peña in Scenario 1c where Caño Martín Peña had been widened and deepened was 3.05 m³/s. A net inflow of water from Canal Suárez to Laguna San José of 0.2 m³/s occurred in Scenario 4. Salinity levels on the ocean

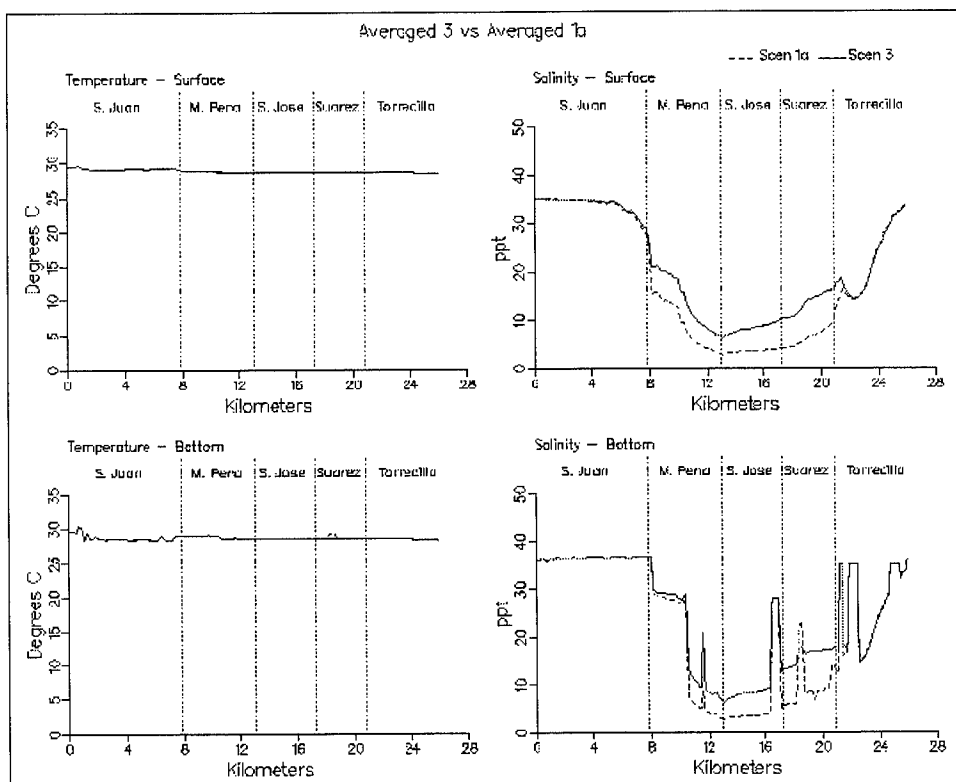


Figure 8-40. Simulation averaged transect plots comparing Scenario 3 with Scenario 1a (Sheet 1 of 11)

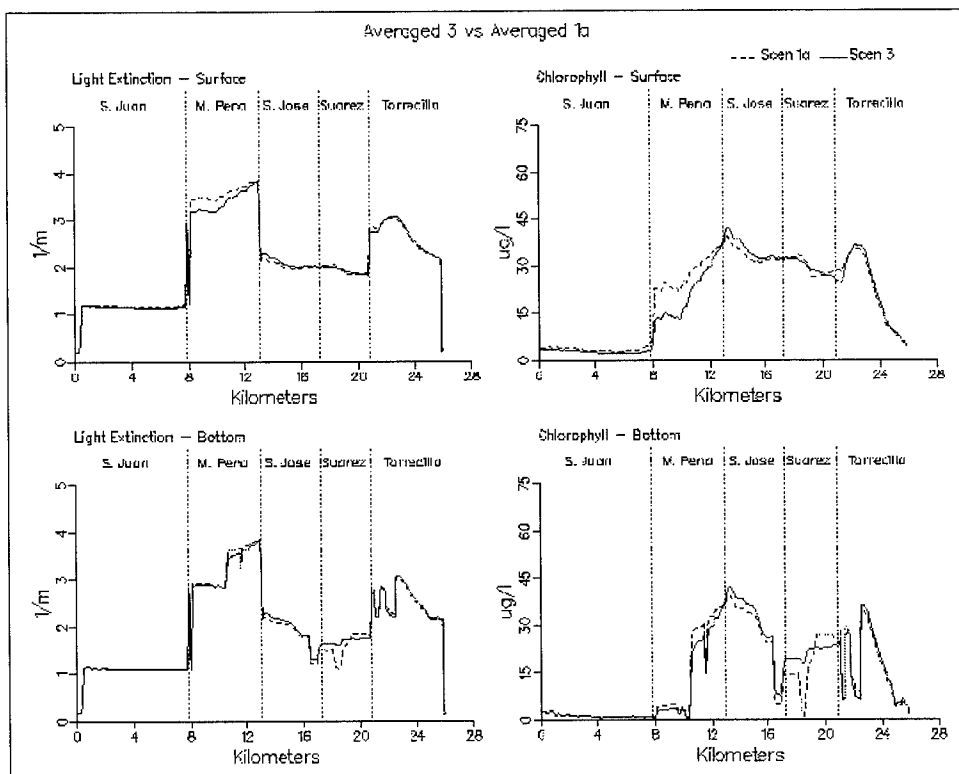


Figure 8-40. (Sheet 2 of 11)

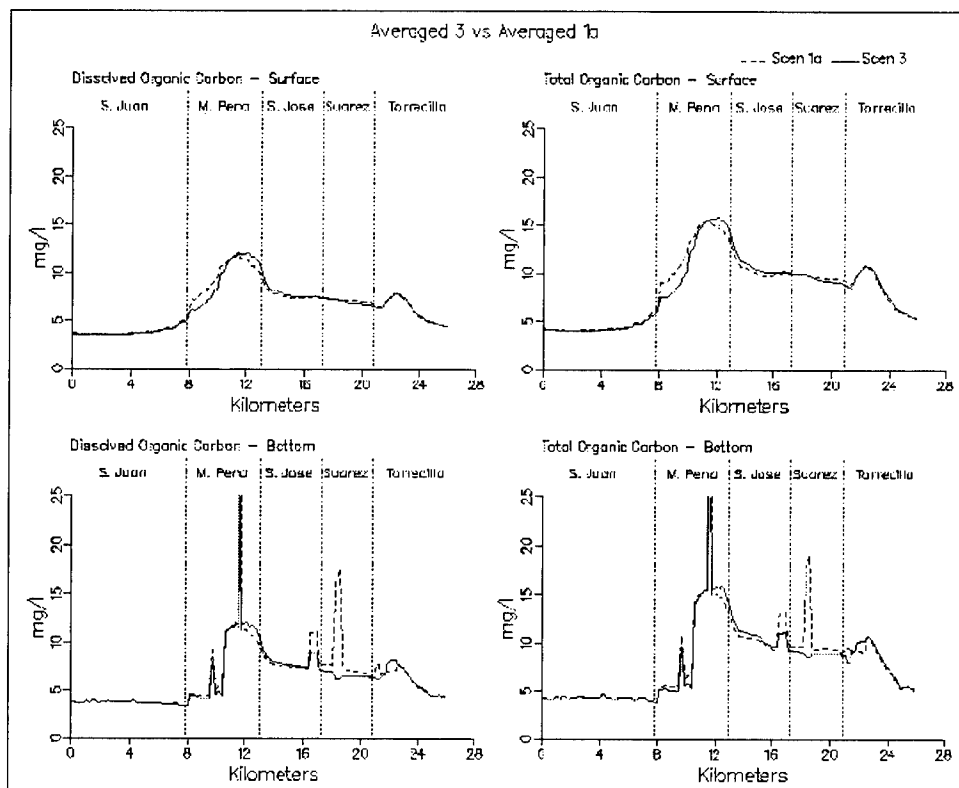


Figure 8-40. (Sheet 3 of 11)

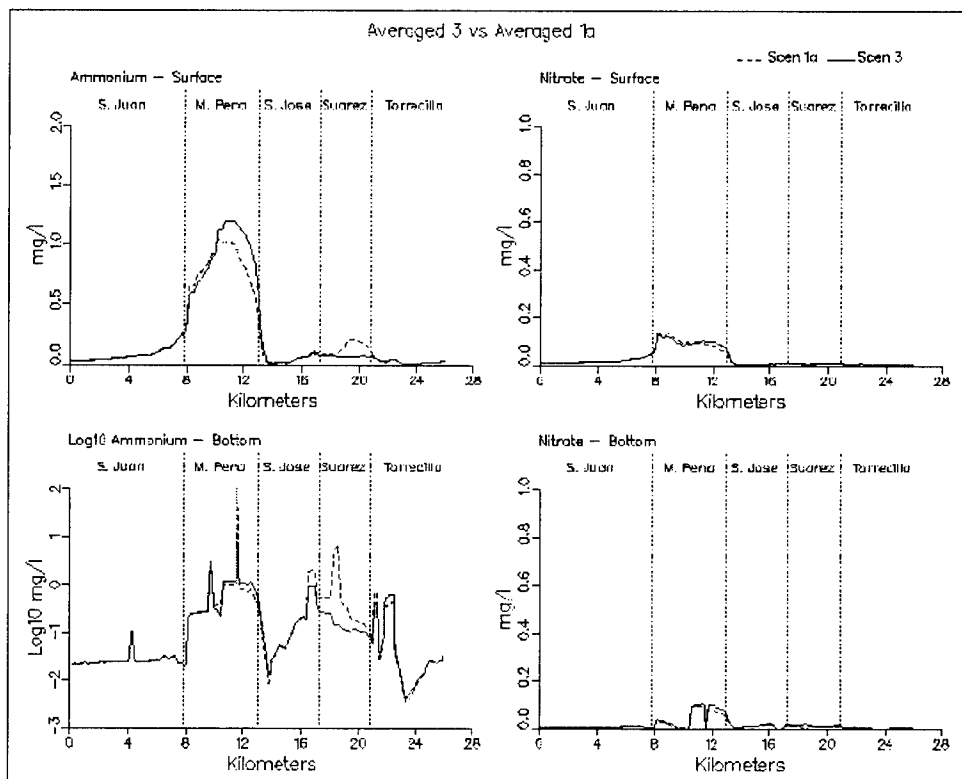


Figure 8-40. (Sheet 4 of 11)

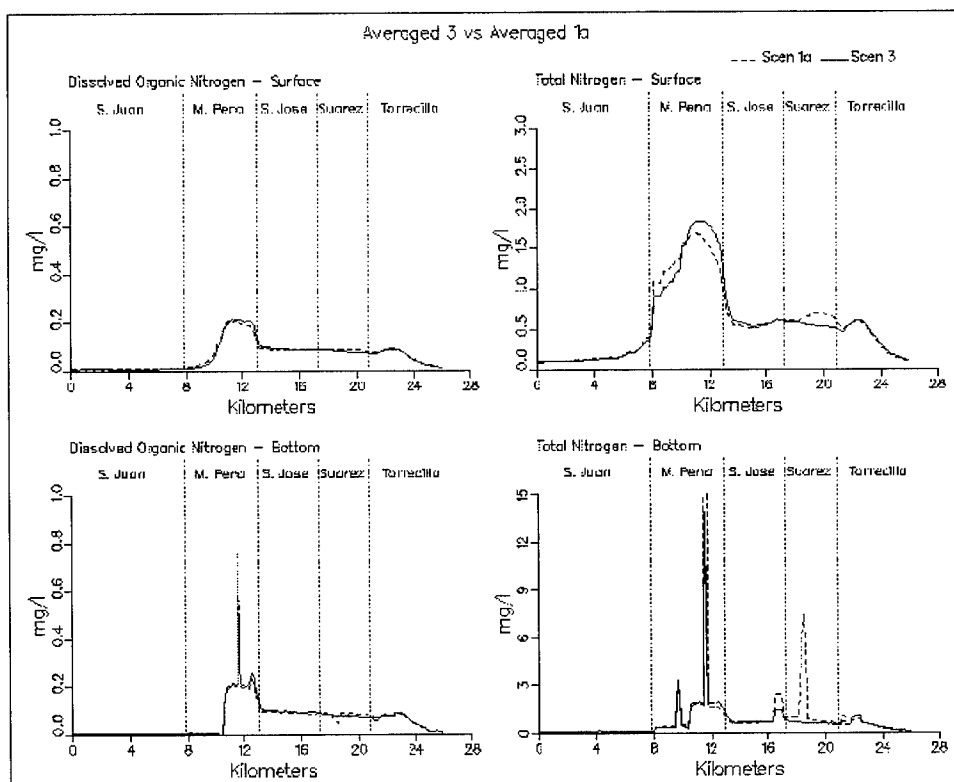


Figure 8-40. (Sheet 5 of 11)

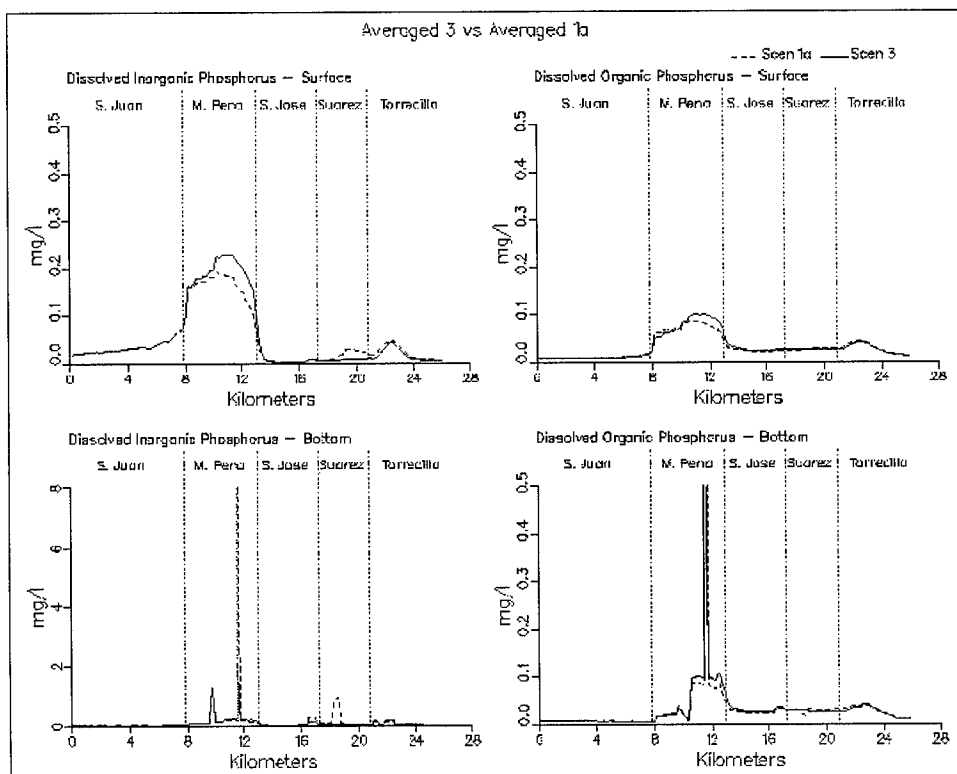


Figure 8-40. (Sheet 6 of 11)

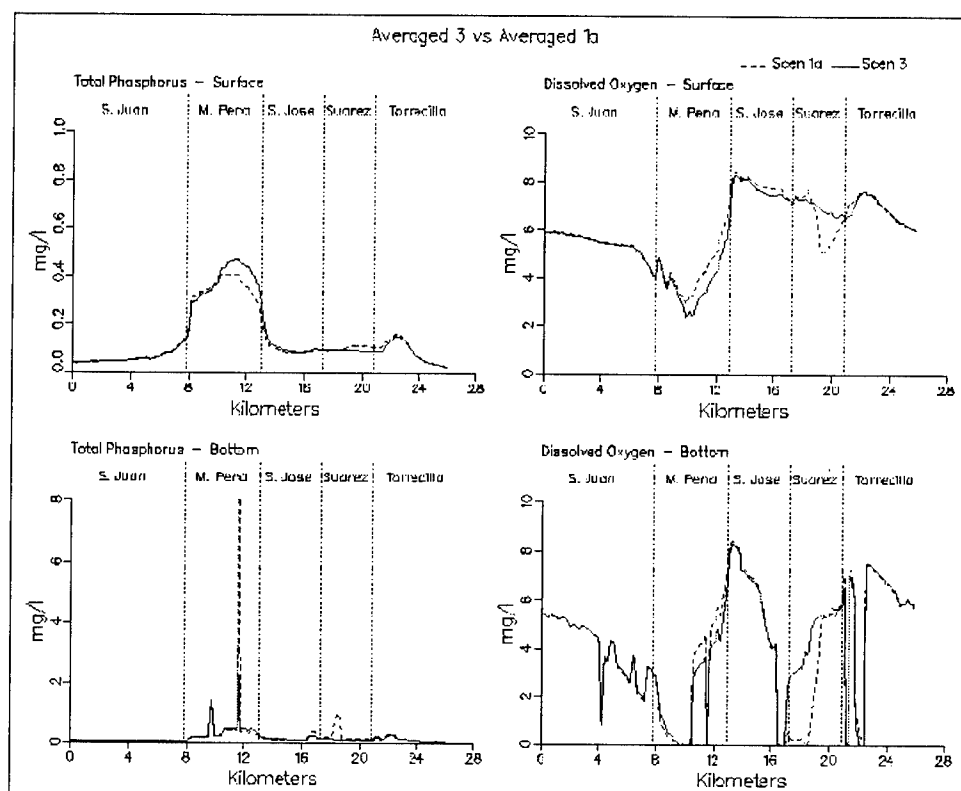


Figure 8-40. (Sheet 7 of 11)

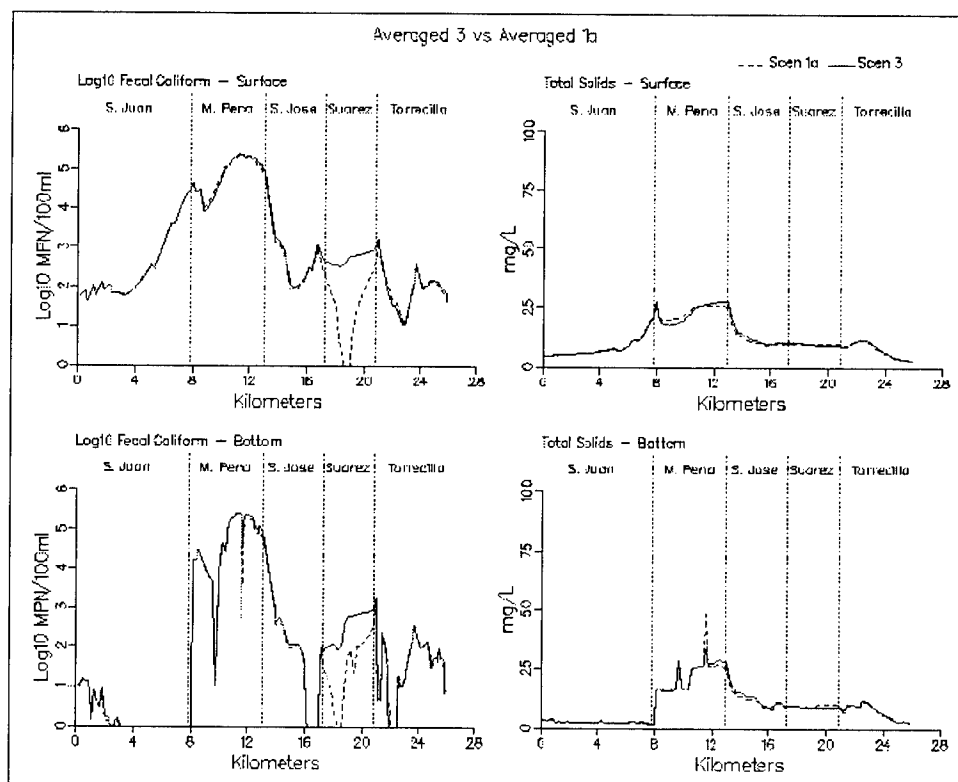


Figure 8-40. (Sheet 8 of 11)

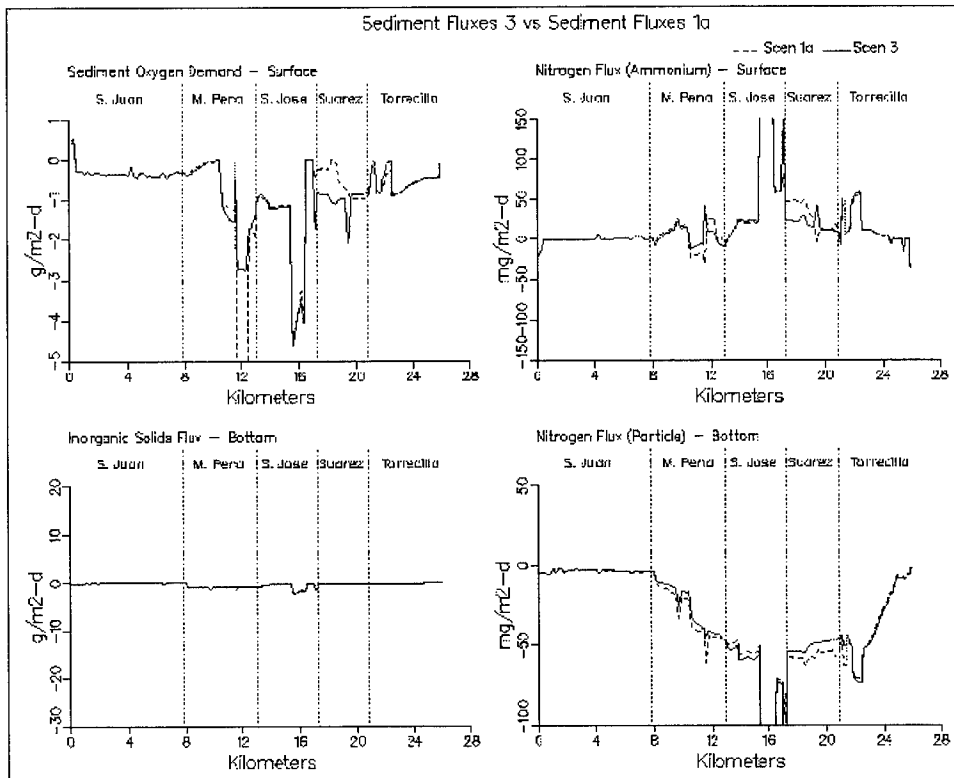


Figure 8-40. (Sheet 9 of 11)

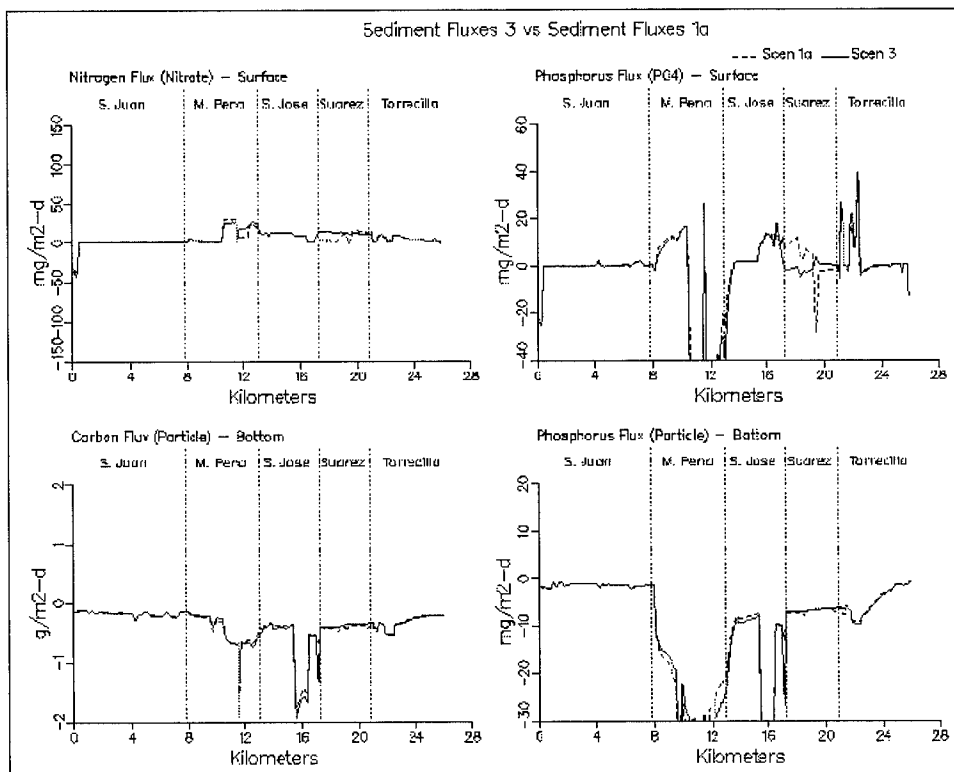


Figure 8-40. (Sheet 10 of 11)

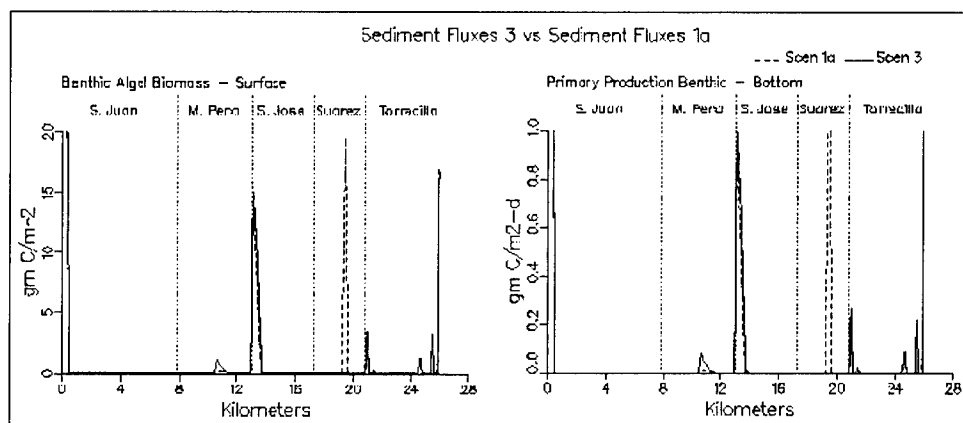


Figure 8-40. (Sheet 11 of 11)

side of the tide gate in Canal Suárez increased in response to the lack of flow from Laguna San José.

Chlorophyll results indicate that chlorophyll levels in Caño Martín Peña increased in Scenario 4. Laguna San José chlorophyll levels were relatively unchanged in comparison to 1a which indicates that the rise observed in Caño Martín Peña is due to the algae from Laguna San José being forced out through Caño Martín Peña. Addition of the tidal gate does not significantly decrease algae levels in Laguna San José. Chlorophyll levels do decrease on the ocean side of the tide gate in Canal Suárez once again because flows from Laguna San José are cut off.

Transect plots for carbon for Scenario 4 indicate patterns that are repeated in other water-quality constituents. The tide gate acts as a wall preventing waters from Laguna San José, which typically have higher concentrations of carbon, nitrogen, and phosphorus, from entering Canal Suárez. As a result, concentrations in Suárez decrease. Dissolved organic carbon concentrations on the ocean side of the tide gate decreased by 4 mg/l. Concentrations in eastern Caño Martín Peña also decreased but this decrease was in response to the increased flushing resulting from the higher flows. Total organic carbon profiles exhibited the same behavior as dissolved organic carbon. Carbon fluxes from Laguna San José to Caño Martín Peña were 2415 kg/day. Daily carbon imports from Canal Suárez to Laguna San José were 73 kg/day.

Surface ammonium concentrations decreased in Caño Martín Peña in response to the increased flushing and dilution through the canal. Surface ammonium concentrations on the ocean side of the tide gate decreased to nearly 0 mg/l. Bottom water ammonia concentrations at this location decreased to approximately 0.02 mg/l. This decrease is attributed to a decrease in particulate nitrogen deposition to the sediments and its subsequent decay and release as ammonium. Nitrate levels in the surface waters of Caño Martín Peña decreased by 0.05 mg/l. Dissolved organic nitrogen levels on the ocean side of the tide gate decreased to 0.05 mg/l while those

in Laguna San José were unchanged. Dissolved organic nitrogen levels in eastern Caño Martín Peña decreased, but concentrations on the western end increased as a result of the higher flows redistributing the un-sewered organic nitrogen loads. Total nitrogen daily fluxes from Laguna San José to Caño Martín Peña were 141 kg/day. Total daily imports of nitrogen from Canal Suárez were 2 kg/day.

Dissolved inorganic phosphorus levels in Caño Martín Peña decreased in Scenario 4. Levels on the ocean side of the tide gate increased in Canal Suárez in response to lower levels of algae. Higher levels of algae and increased dilution are probably the reason for the dissolved inorganic phosphorus decrease in Caño Martín Peña. Dissolved organic phosphorus levels indicated decreases in Caño Martín Peña with slight increases on the eastern side of Laguna San José. Concentrations on the ocean side of the tide gate were relatively unaffected. Daily phosphorus flux from Laguna San José to Caño Martín Peña were 32 kg/day. An average of 1 kg/day was imported from Canal Suárez to Laguna San José.

Dissolved oxygen levels increased in Scenario 4 in Caño Martín Peña as a result of the increased flushing of high dissolved oxygen concentration water from Laguna San José. Anoxic conditions that occurred in the bottom waters of western Caño Martín Peña were unaffected by the additional flushing. Dissolved oxygen levels on the ocean side of the tide gate decreased slightly as a result of decreased algal photosynthesis. Fecal coliform levels throughout most of the system remained unchanged except for Canal Suárez which saw a slight decrease as a result of loading from Laguna San José being cut off. Total solids levels decreased slightly in Caño Martín Peña as a result of additional flushing. Solids concentrations on the ocean side of the tide gate decreased slightly again because the source of the solids in Laguna San José had been cut off.

In summary, Scenario 4 tended to improve water quality conditions in Canal Suárez since it prevented the more polluted water from Laguna San José from entering. Any improvements seen in Caño Martín Peña appear to be due to increased flow through the canal resulting in an increased volume of receiving water for runoff.

Scenario 5a

In Scenario 5a the un-sewered loads were removed from Caño Martín Peña. These loads were not redirected any place but were simply removed from the model. A total of 400 kg/day of carbon, 100 kg/day of nitrogen, and 20 kg/day of phosphorus were removed. An additional reduction was made to the fecal coliform loading for the Martín Peña sub-basin to approximate the effect of removal of fecal coliform loading associated with these loads would have.

Scenario 5a was run using Scenario 1a hydrodynamics. Scenario 5a temperature and salinity were identical to those of 1a (see Figure 8-42).

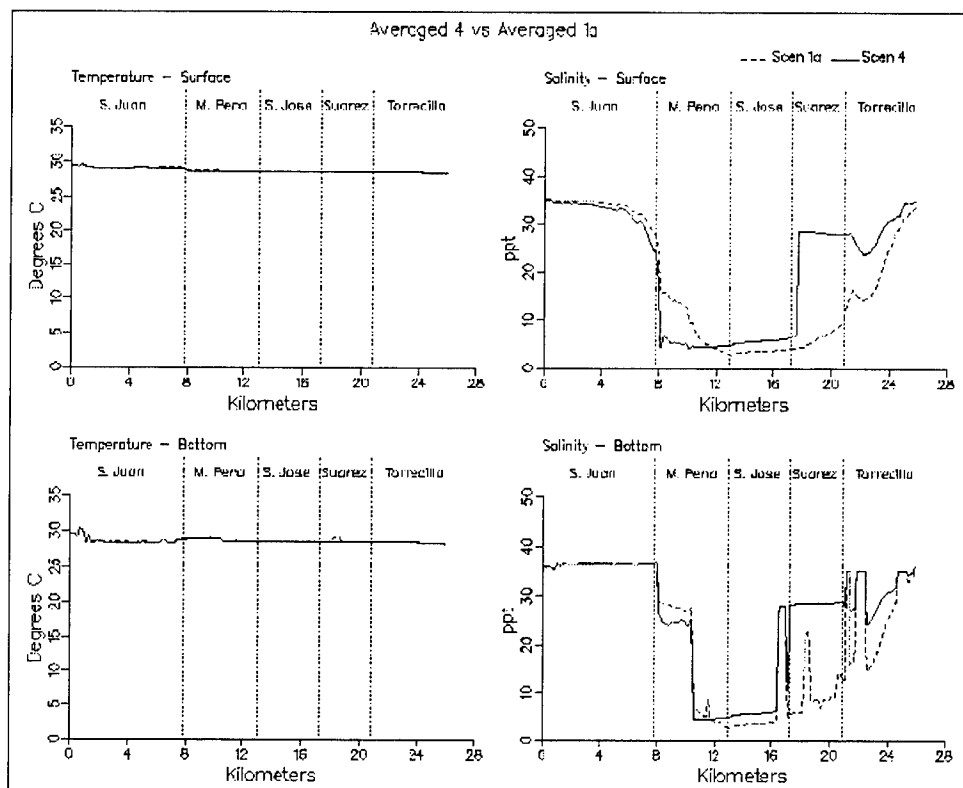


Figure 8-41. Simulation averaged transect plots comparing Scenario 4 with Scenario 1a (Sheet 1 of 11)

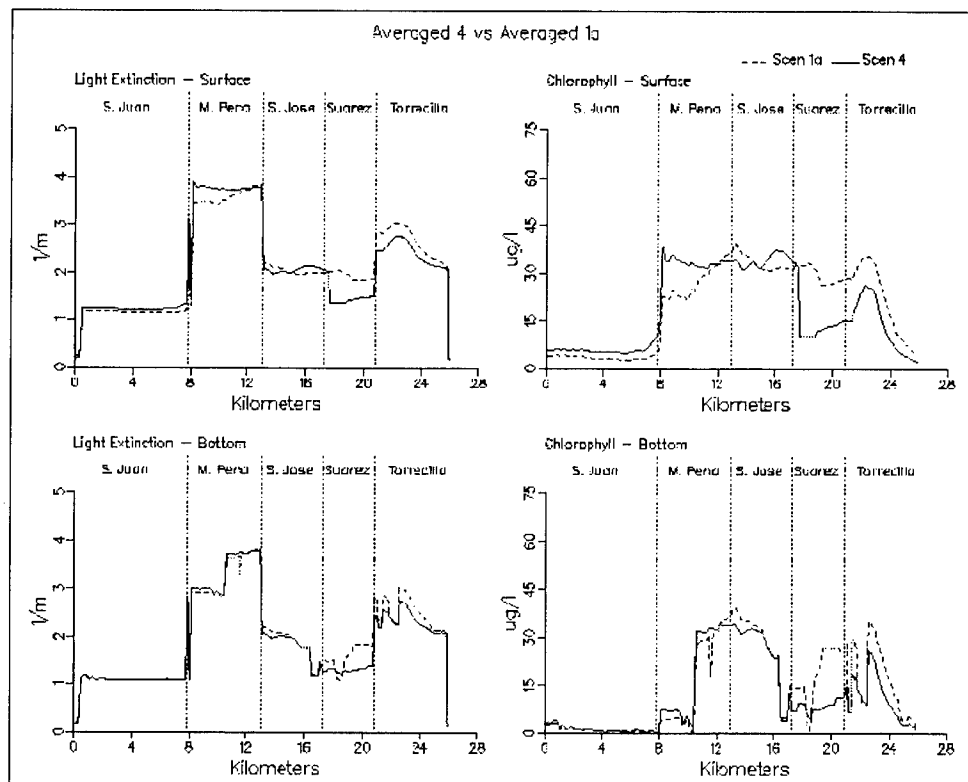


Figure 8-41. (Sheet 2 of 11)

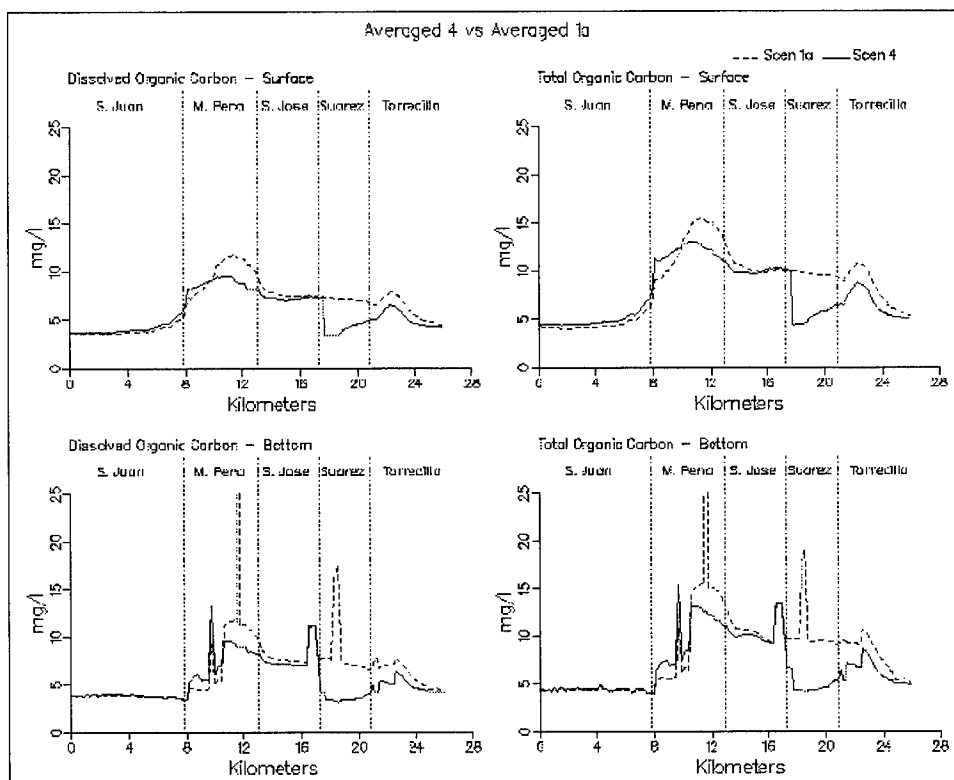


Figure 8-41. (Sheet 3 of 11)

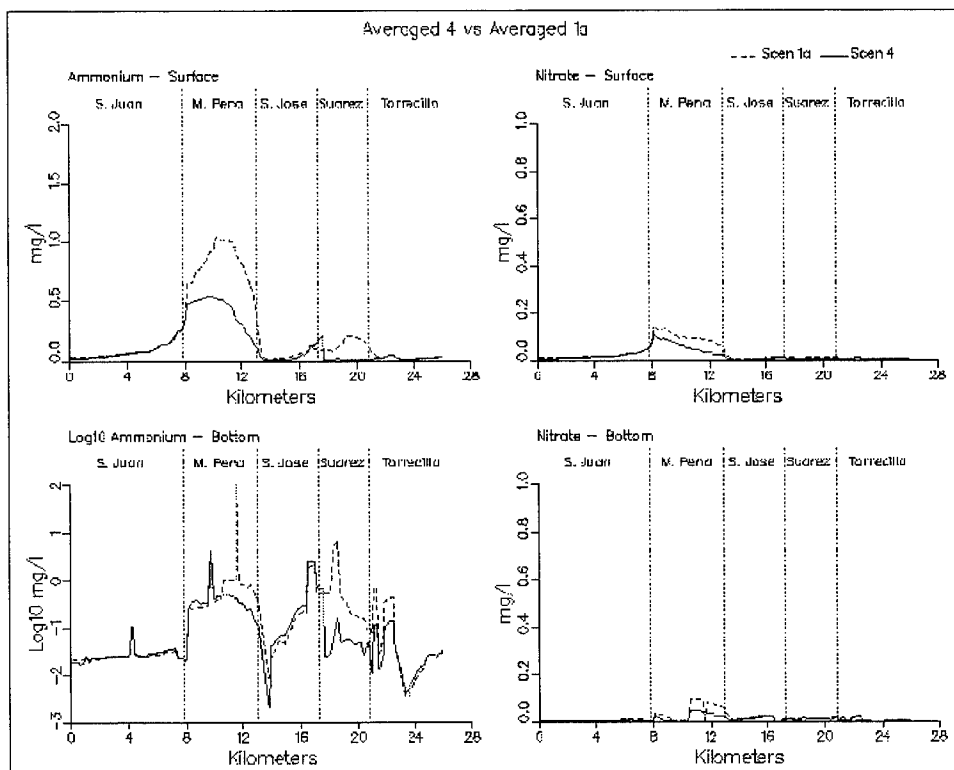


Figure 8-41. (Sheet 4 of 11)

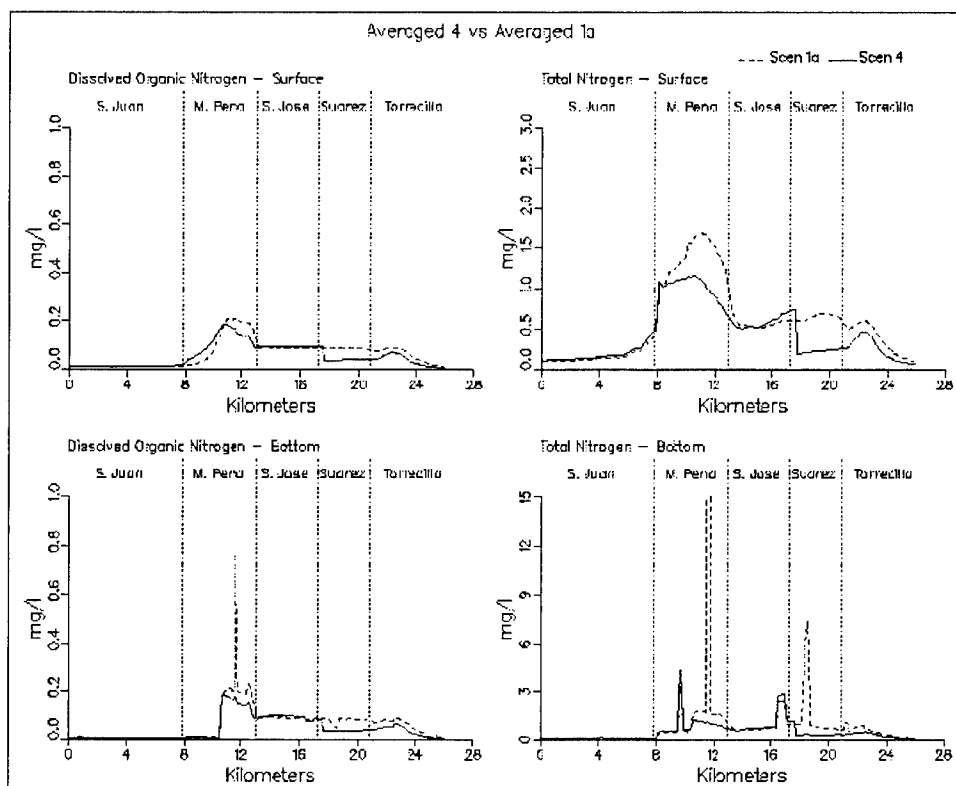


Figure 8-41. (Sheet 5 of 11)

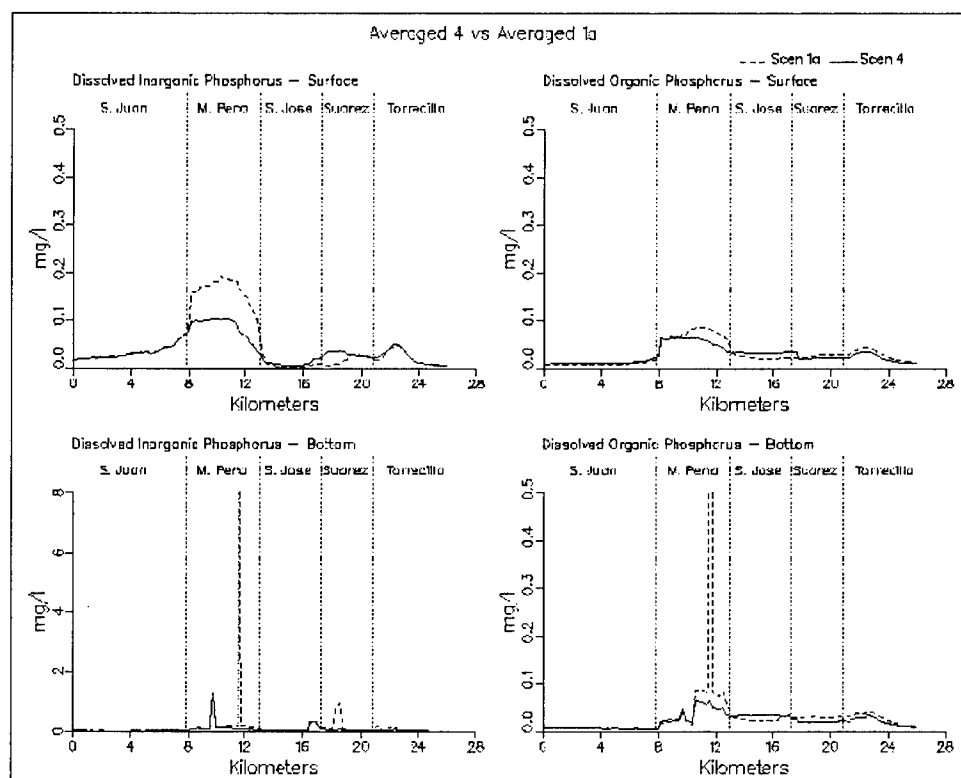


Figure 8-41. (Sheet 6 of 11)

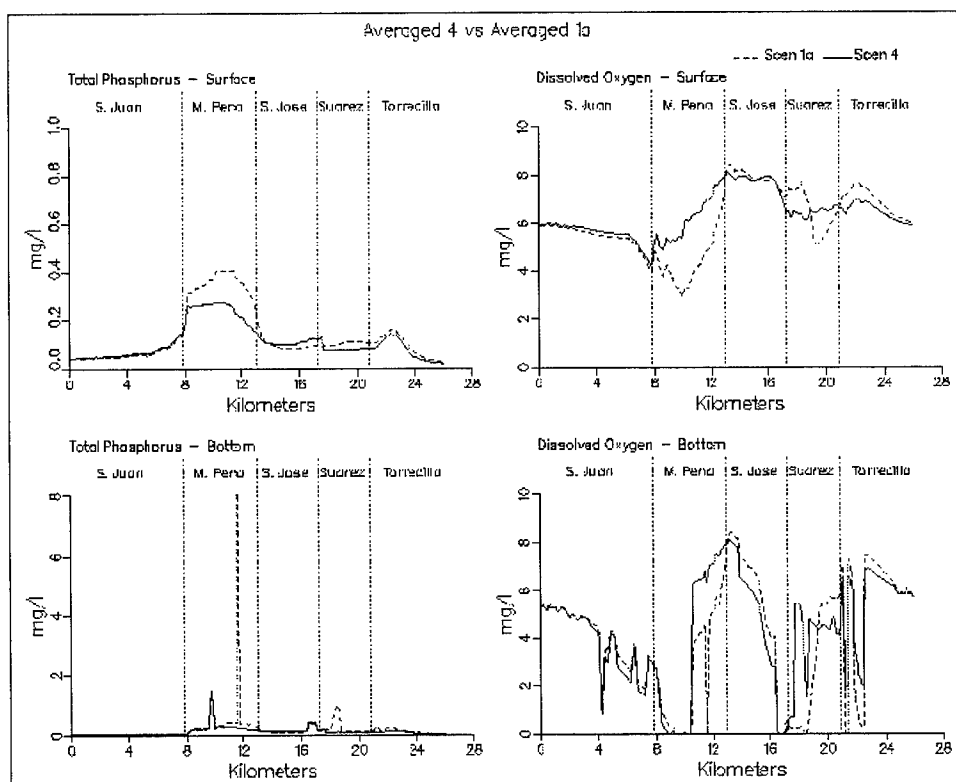


Figure 8-41. (Sheet 7 of 11)

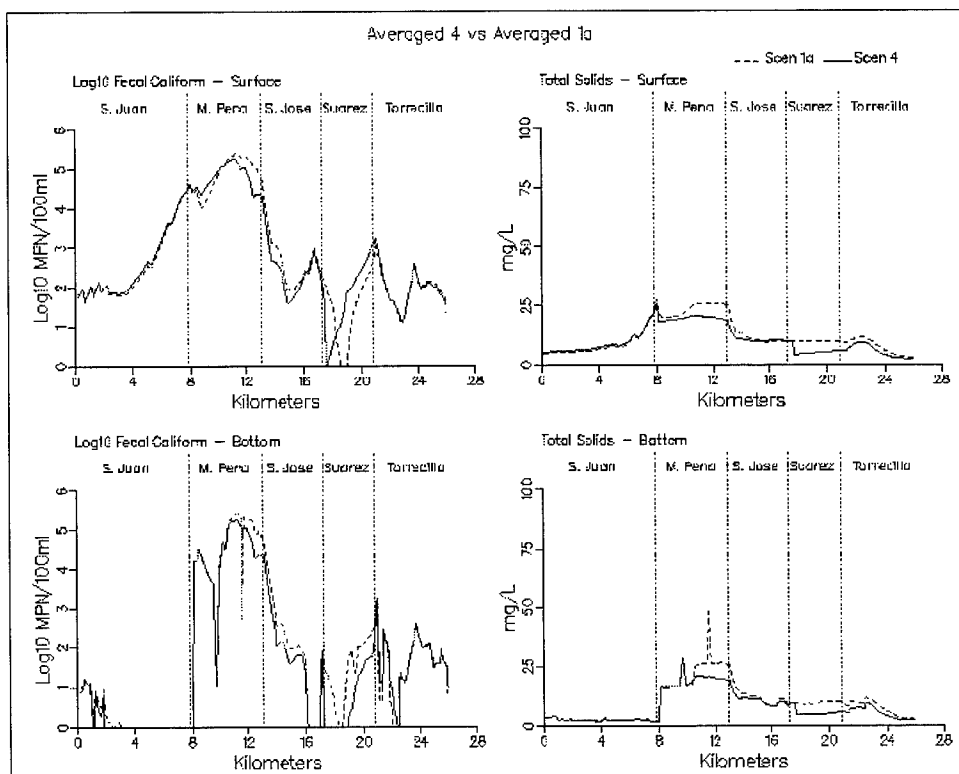


Figure 8-41. (Sheet 8 of 11)

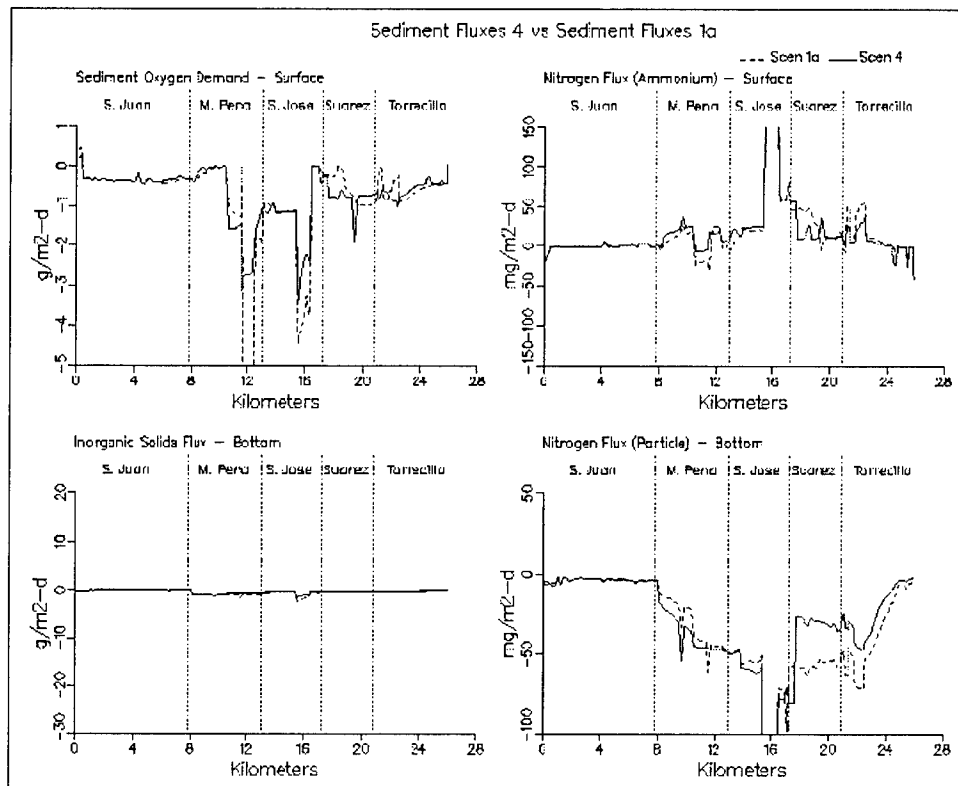


Figure 8-41. (Sheet 9 of 11)

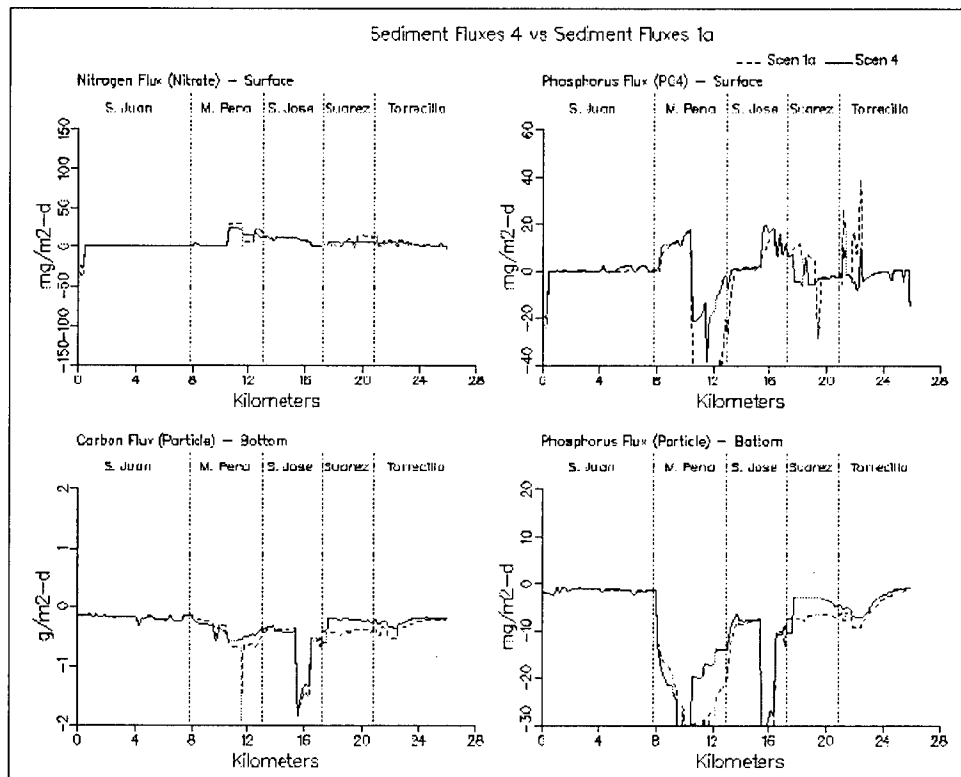


Figure 8-41. (Sheet 10 of 11)

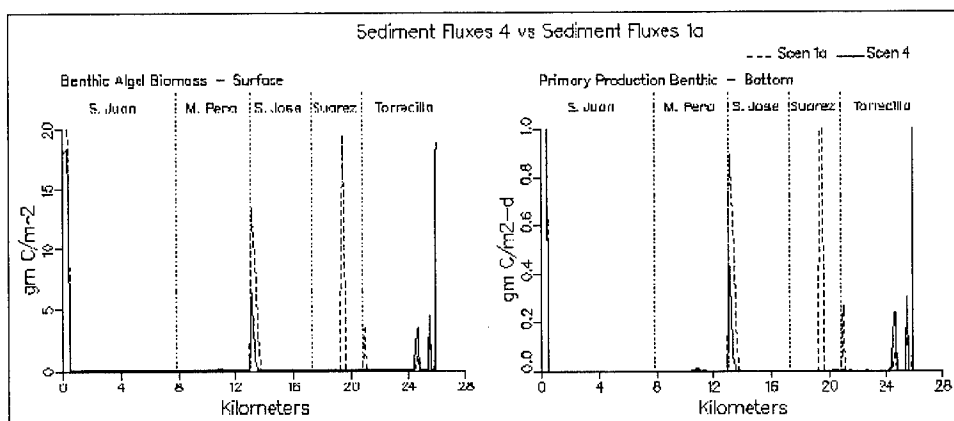


Figure 8-41. (Sheet 11 of 11)

Chlorophyll levels decreased slightly in Caño Martín Peña, Laguna San José, and Canal Suárez. The amount of the decrease was a maximum of 4 $\mu\text{g/l}$. Dissolved organic carbon levels decreased by 3 mg/l in Caño Martín Peña. Total carbon levels in Caño Martín Peña decreased by 4 mg/l . There was a slight decrease in DOC and TOC in Laguna San José and Canal Suárez.

Ammonium levels in Caño Martín Peña decreased from a maximum of 1.0 mg/l to 0.4 mg/l . No changes occurred elsewhere along the transect. Nitrate levels also decreased in Caño Martín Peña in response to the loading reduction. Dissolved organic nitrogen levels decreased significantly in Caño Martín Peña with the removal of the un-sewered loads. Surface total nitrogen levels decreased by nearly 1 mg/l in Caño Martín Peña. Concentrations at this location are still the highest along the transect.

Removal of the un-sewered loads resulted in a decrease in dissolved inorganic phosphorus levels in Caño Martín Peña of 0.1 mg/l , while dissolved organic phosphorus levels decreased to Laguna San José levels. No other significant change occurred in phosphorus concentrations elsewhere along the transect.

The DO transect indicates a slight improvement (0.3 mg/l) in Caño Martín Peña. No other changes were observed. Fecal coliform levels showed some decrease in Caño Martín Peña. Effects did not extend beyond the confluence of Caño Martín Peña and San Juan Bay. A slight increase in total solids resulting from a decrease in algae occurred in Caño Martín Peña.

In summary, impacts resulting from Scenario 5a conditions were confined for the most part to Caño Martín Peña. Other than in Caño Martín Peña, these effects were insignificant.

Scenario 5b

Scenario 5b like 5a involved a loading reduction. In this scenario, the loading reduction was the removal of loads originating from the Baldeorioty de Castro storm water pumping station. Upper Laguna San José serves as the receiving waters for this load. An average loading of 906 kg/day of carbon, 79.2 kg/day of nitrogen, and 27.2 kg/day of phosphorus was removed. All other conditions and loads were the same as those used in Scenario 1a. The pumping discharges remained without the loads.

Salinity and temperature were identical in Scenario 5b to those of 1a (see Figure 8-43). Chlorophyll levels decreased by a maximum of approximately 8 $\mu\text{g/l}$ in Laguna San José and Canal Suárez. Smaller decreases were predicted in Caño Martín Peña.

Dissolved organic carbon levels decreased approximately 2 mg/l in Laguna San José and Canal Suárez. Total organic carbon levels indicated a similar decrease. Carbon fluxes from Laguna San José to Caño Martín Peña were 369 kg/day. Carbon fluxes from Laguna San José to Canal Suárez were 1240 kg/day.

Neither ammonium nor nitrate discharges indicated any change along the transect in Scenario 5b when compared with Scenario 1a. Any ammonium discharged by the pump station is rapidly taken up and doesn't remain in the system long enough to influence ammonium concentrations along the transect. Dissolved organic nitrogen levels decreased slightly in response to lower chlorophyll levels in Laguna San José and Canal Suárez. Nitrogen flux rates from Laguna San José to Caño Martín Peña averaged 10.2 kg/day. Nitrogen flux rates from Laguna San José to Canal Suárez averaged 109.9 kg/day.

The only change in phosphorus levels along the transect in Scenario 5b occurred as a result of decreased algae levels. Dissolved inorganic phosphorus levels in Scenario 5b were unchanged from 1a. Dissolved organic phosphorus levels showed only the slightest decrease in Laguna San José. Phosphorus flux rates from Laguna San José to Caño Martín Peña averaged 1 kg/day. Phosphorus flux rates from Laguna San José to Canal Suárez averaged 15.5 kg/day.

Dissolved oxygen, fecal coliform, and total solids levels along the transect were relatively unaffected by the loading reductions of Scenario 5b.

In summary, the effects of the loading reduction of Scenario 5b were limited to a great extent to Laguna San José. The reduction in nutrients resulted in a decrease in algae which did affect organic carbon levels in Caño Martín Peña and Canal Suárez. Nitrogen levels were affected slightly in Laguna San José and Canal Suárez. Substantial impacts in nutrients were not observed along the transect since this loading reduction

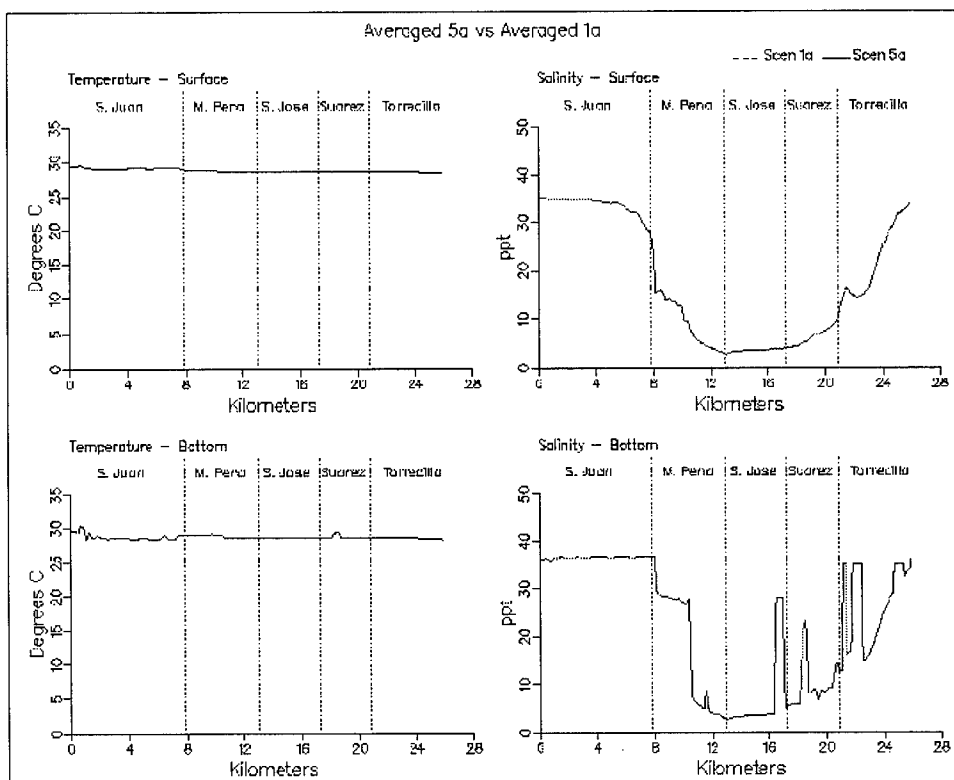


Figure 8-42. Simulation averaged transect plots comparing Scenario 5a with Scenario 1a (Sheet 1 of 11)

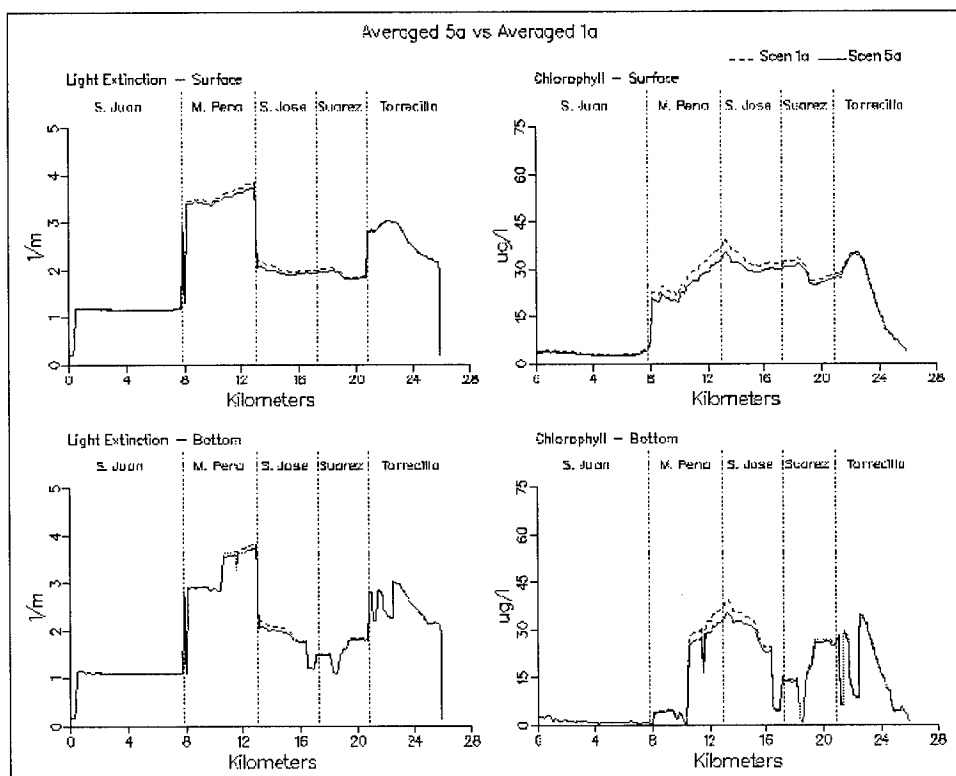


Figure 8-42. (Sheet 2 of 11)

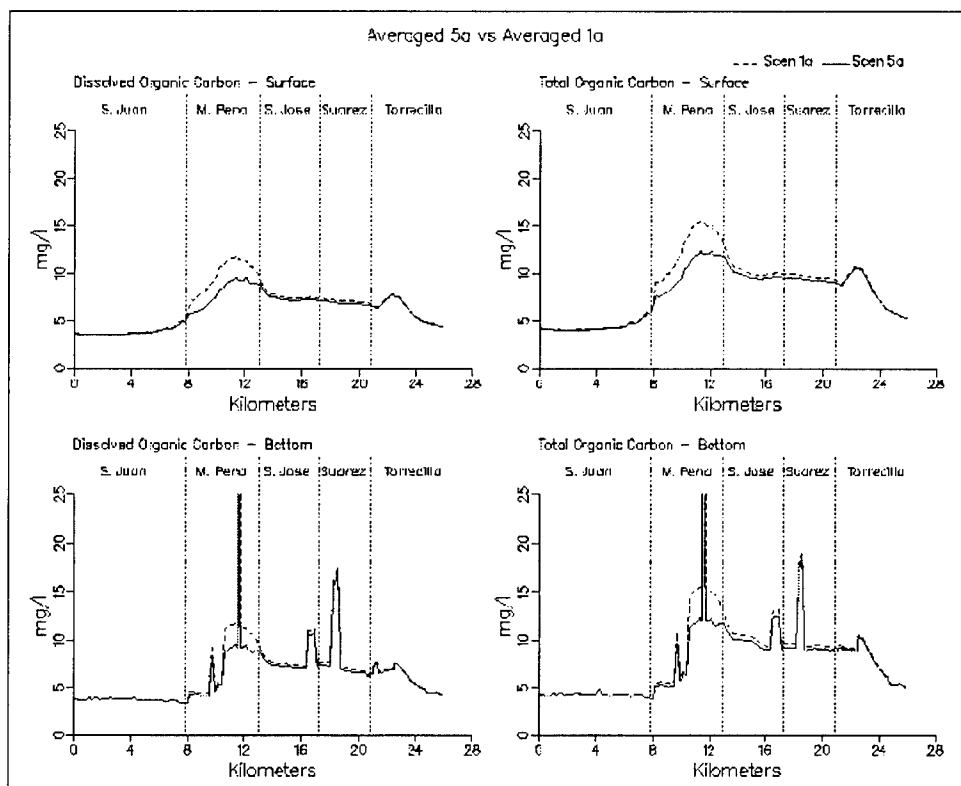


Figure 8-42. (Sheet 3 of 11)

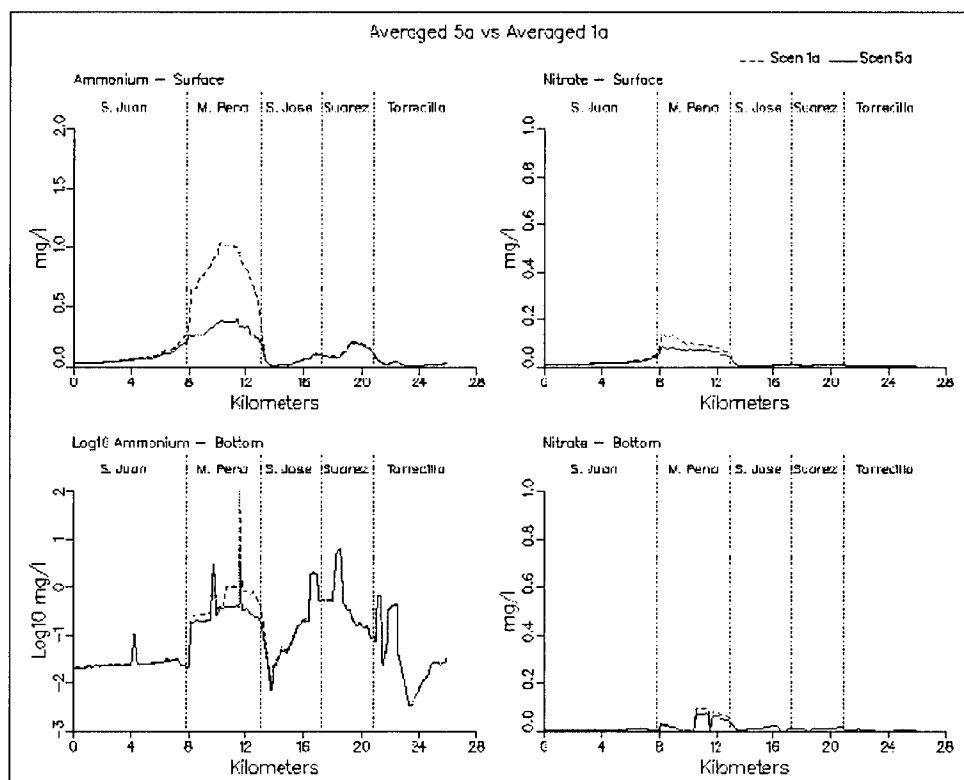


Figure 8-42. (Sheet 4 of 11)

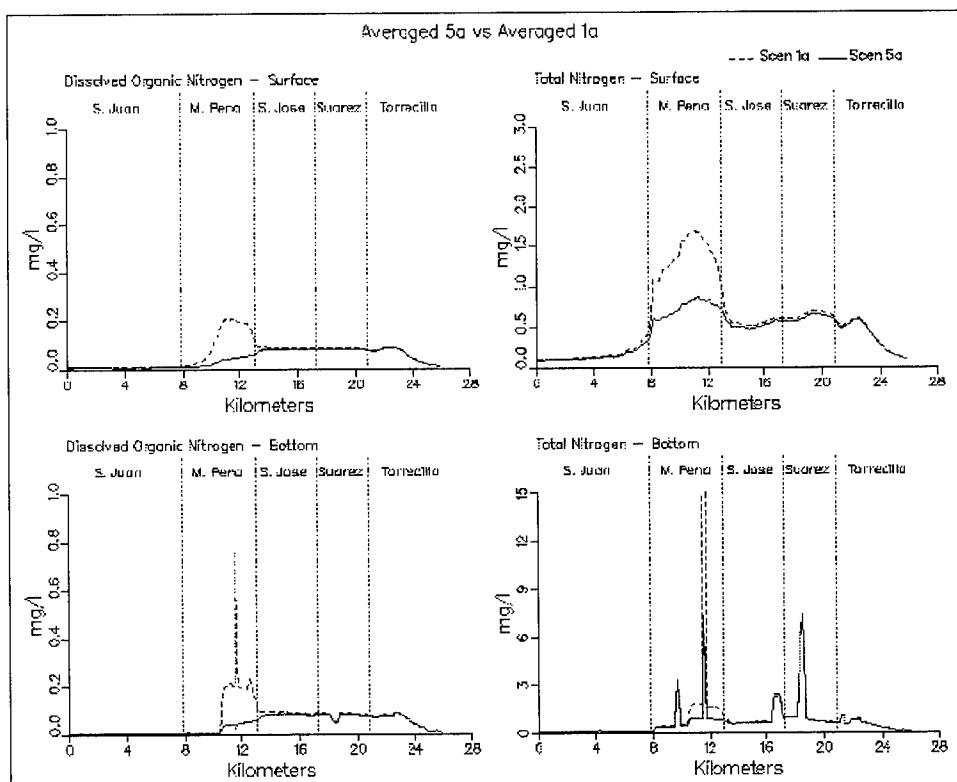


Figure 8-42. (Sheet 5 of 11)

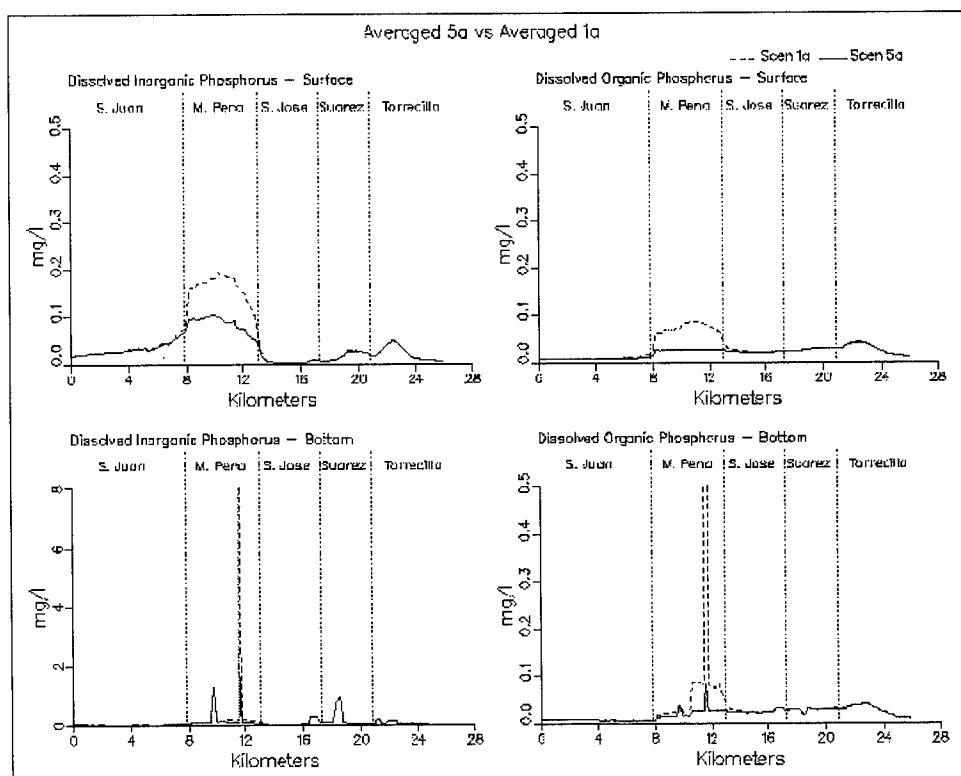


Figure 8-42. (Sheet 6 of 11)

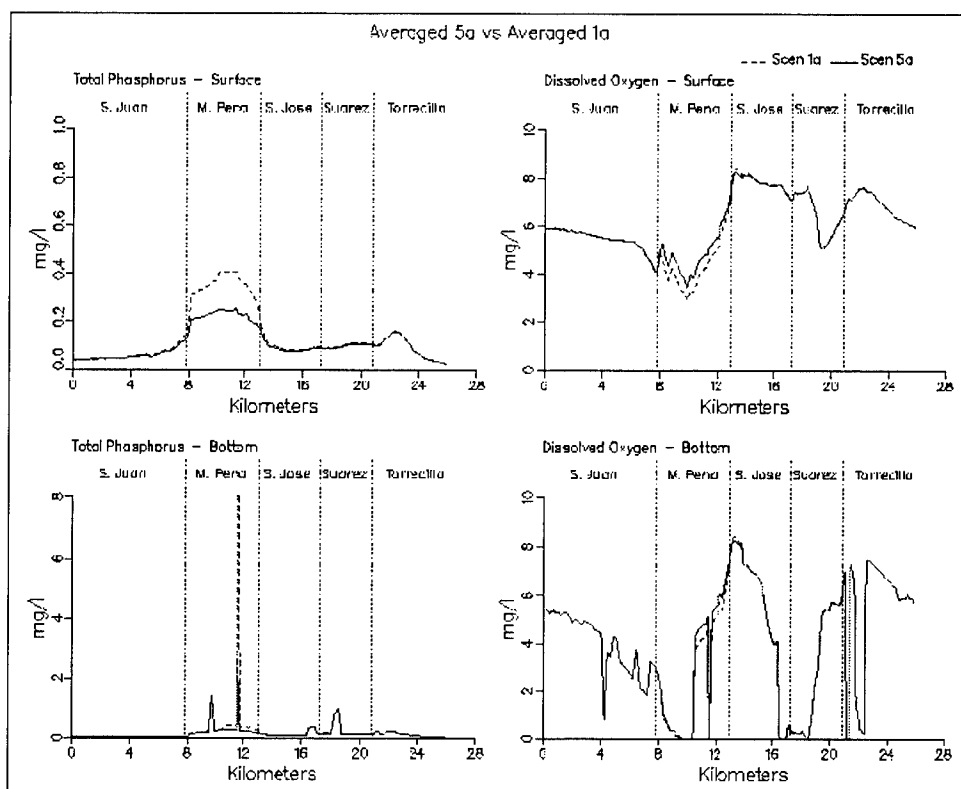


Figure 8-42. (Sheet 7 of 11)

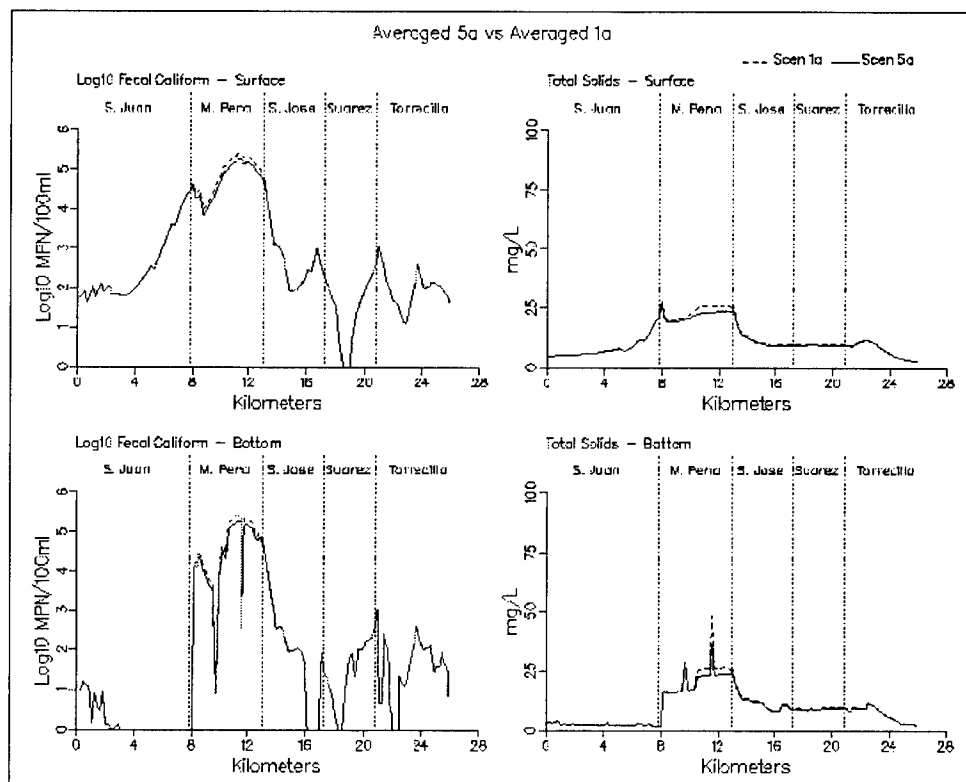


Figure 8-42. (Sheet 8 of 11)

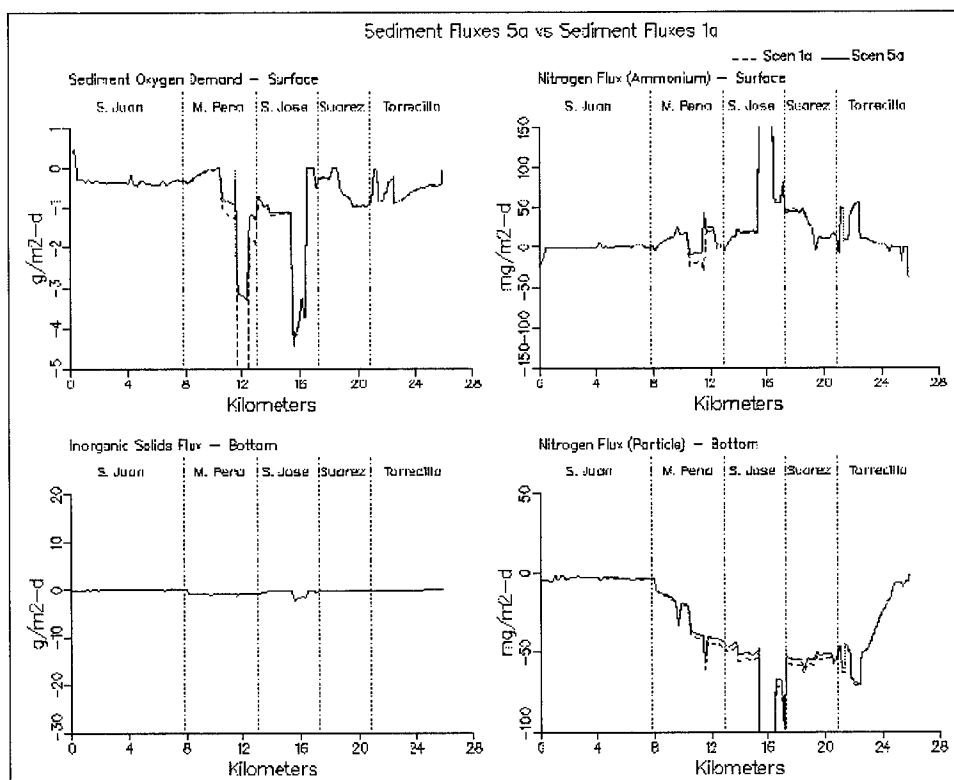


Figure 8-42. (Sheet 9 of 11)

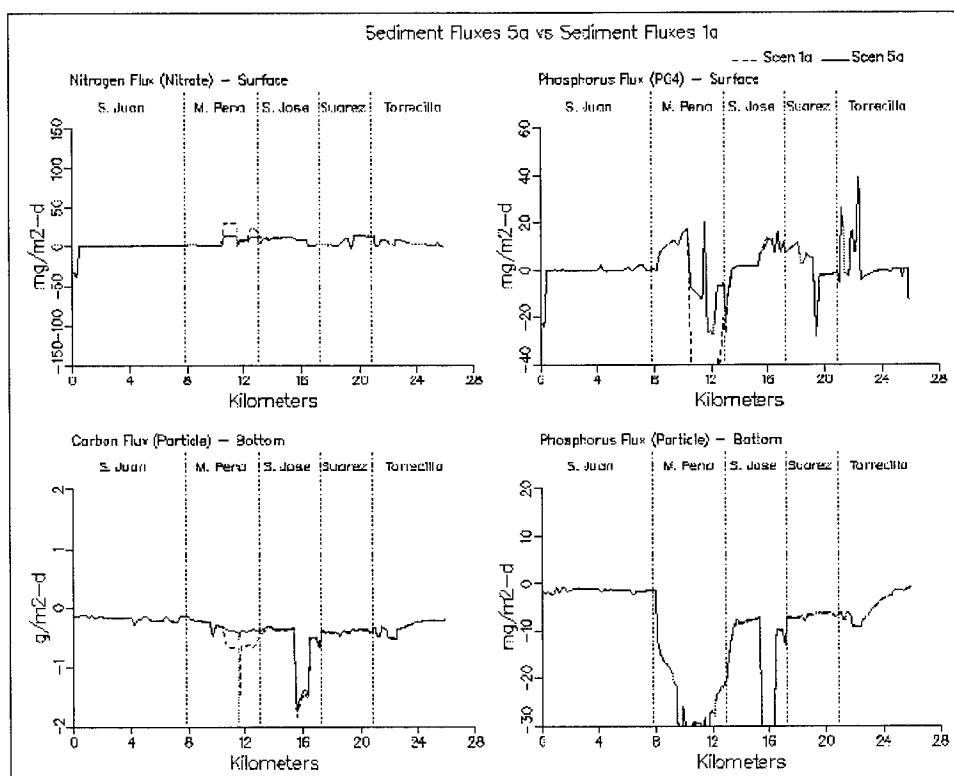


Figure 8-42. (Sheet 10 of 11)

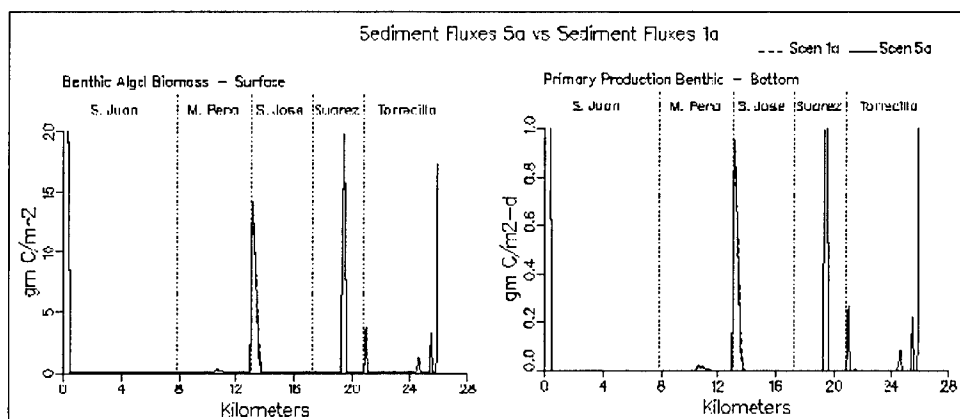


Figure 8-42. (Sheet 11 of 11)

is relatively far from the transect. Changes in nutrients loadings are rapidly compensated by algal uptake near the point of discharge.

Scenario 6a

Scenario 6a combined the loading reductions of Scenarios 5a and 5b with the channel modification to Caño Martín Peña of Scenario 1c. Since the loading reductions of 5a and 5b did not require the grid to be reconfigured, the grid and hydrodynamic data for Scenario 1c could be used for Scenario 6a. In essence, Scenario 6a is a repeat of Scenario 1c with loading reductions in Laguna San José and Caño Martín Peña.

As expected, temperature and salinity transects for Scenario 6a (see Figure 8-44) were identical to results for Scenario 1c. Chlorophyll levels for Scenario 6a are lower than those of Scenario 1a for all of the transect except San Juan Bay where levels increased by 3 $\mu\text{g/l}$. Chlorophyll levels in Laguna San José are typically 15 $\mu\text{g/l}$ lower than those of Scenario 1a with the greatest decrease occurring at the confluence of Caño Martín Peña and Laguna San José. At this location, chlorophyll levels were approximately 23 $\mu\text{g/l}$ lower in Scenario 6a than in Scenario 1a. Surface chlorophyll levels in Scenario 6a were lower than those predicted in Scenario 1c. The average surface chlorophyll level in Laguna San José was approximately 7 $\mu\text{g/l}$ lower in Scenario 6a than that in Scenario 1c. Chlorophyll levels decreased in Caño Martín Peña by 2 $\mu\text{g/l}$ on the western end and as much as 5 $\mu\text{g/l}$ on the eastern end in Scenario 6a when compared to results from Scenario 1c. A decrease of 6 $\mu\text{g/l}$ of chlorophyll occurred in western Canal Suárez in Scenario 6a when compared to Scenario 1c. The decreases in chlorophyll observed between Scenarios 6a and 1c result from the removal of the un-sewered loads for Caño Martín Peña and the loads for the Baldeoroty de Castro Pump Station. Since neither one of these sources input a chlorophyll load, the decrease in chlorophyll levels observed is the result of a decrease in nutrients.

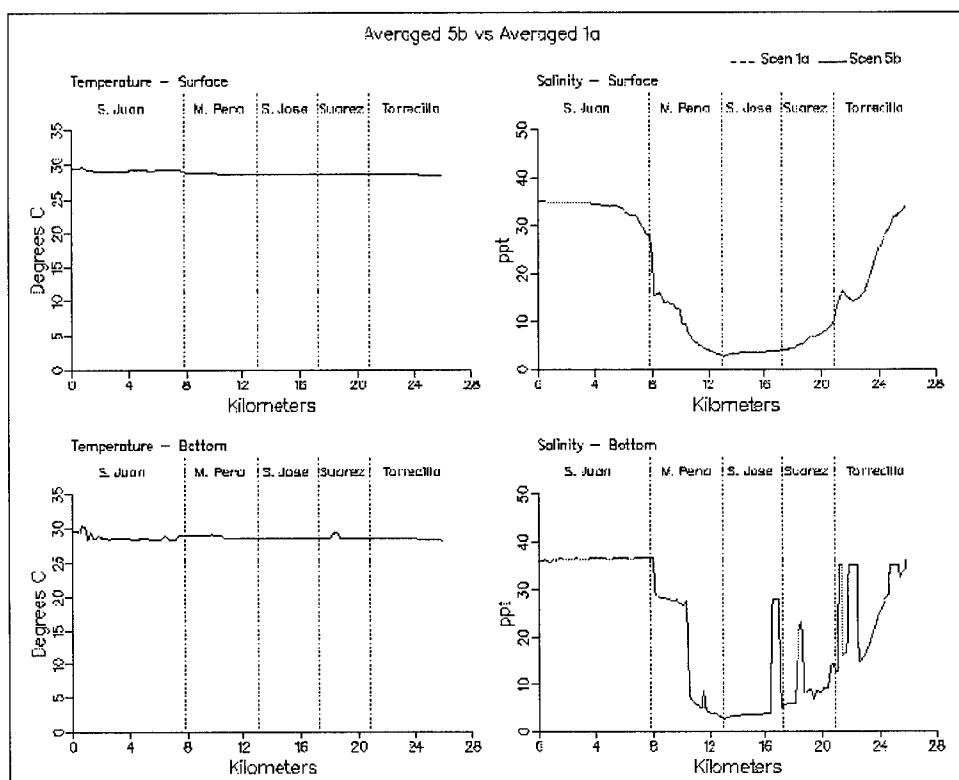


Figure 8-43. Simulation averaged transect plots comparing Scenario 5b with Scenario 1a (Sheet 1 of 11)

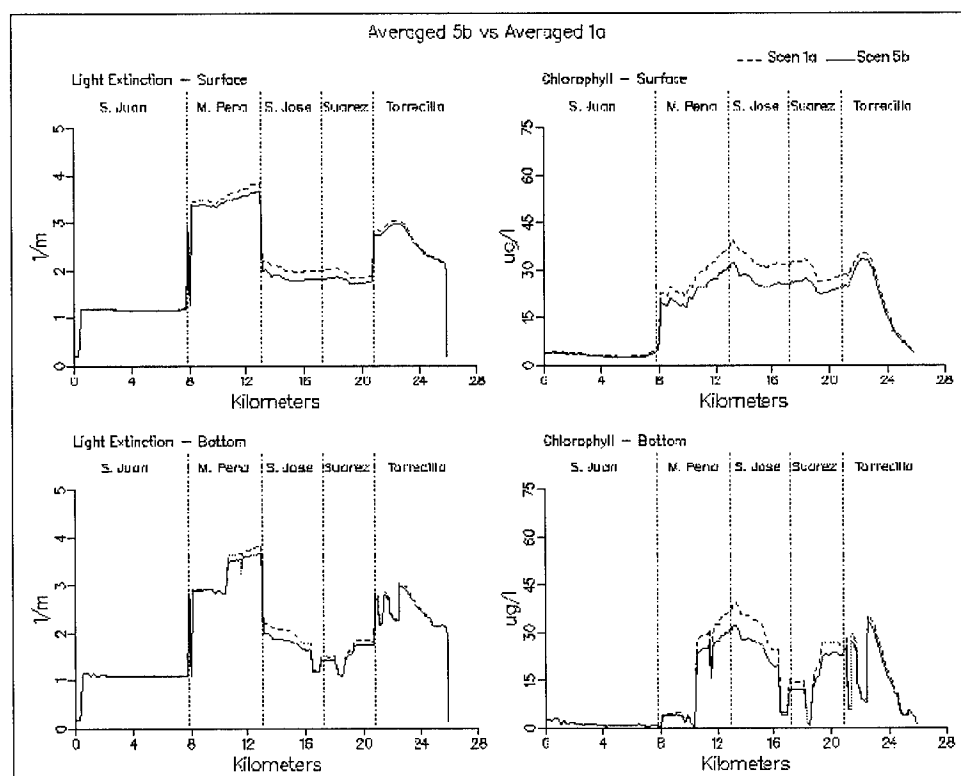


Figure 8-43. (Sheet 2 of 11)

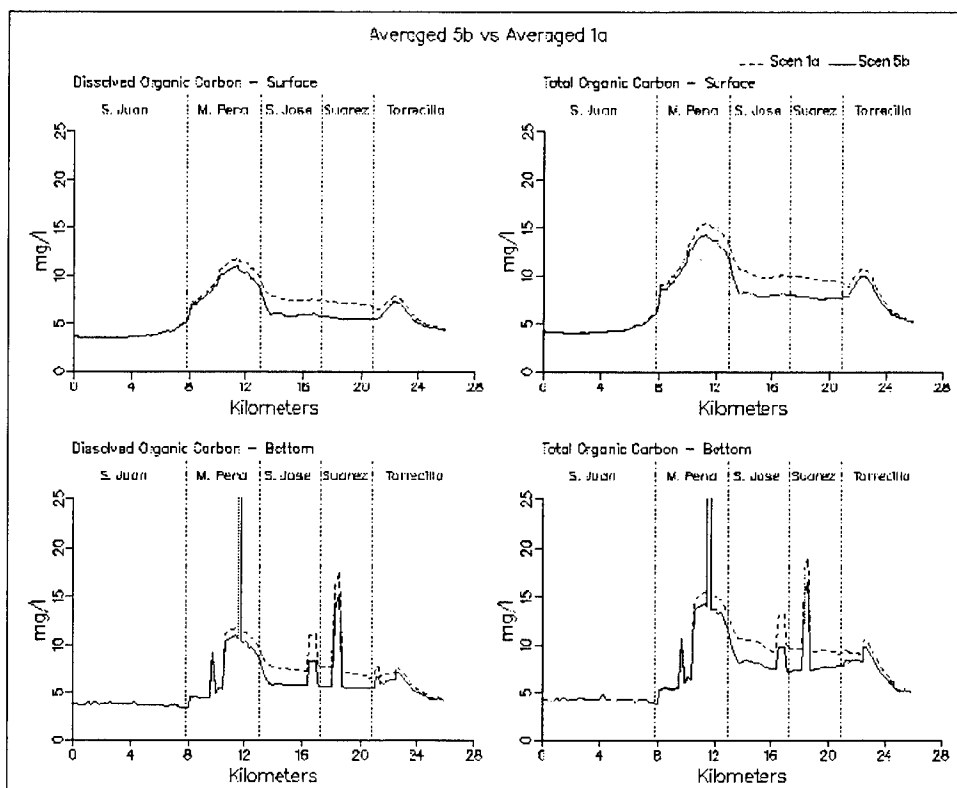


Figure 8-43. (Sheet 3 of 11)

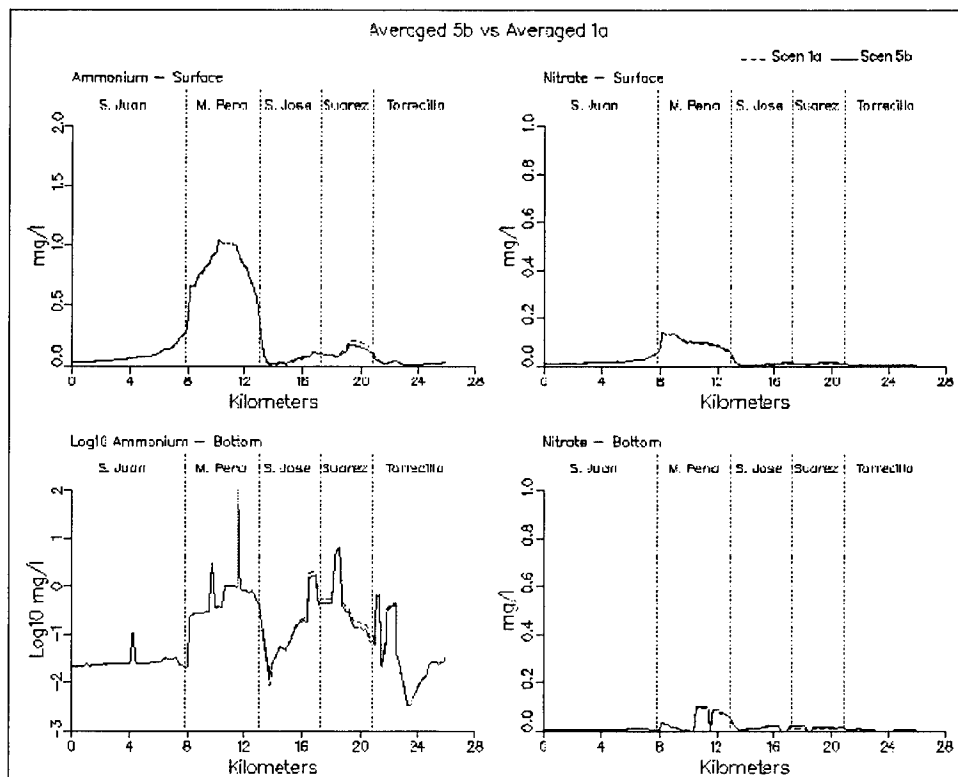


Figure 8-43. (Sheet 4 of 11)

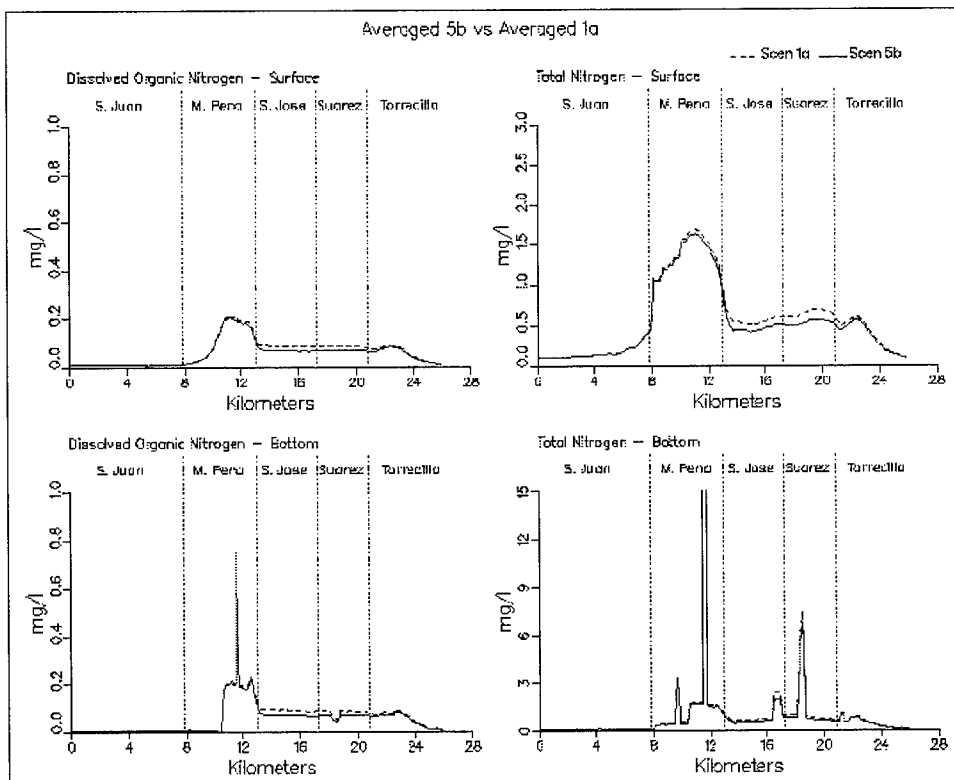


Figure 8-43. (Sheet 5 of 11)

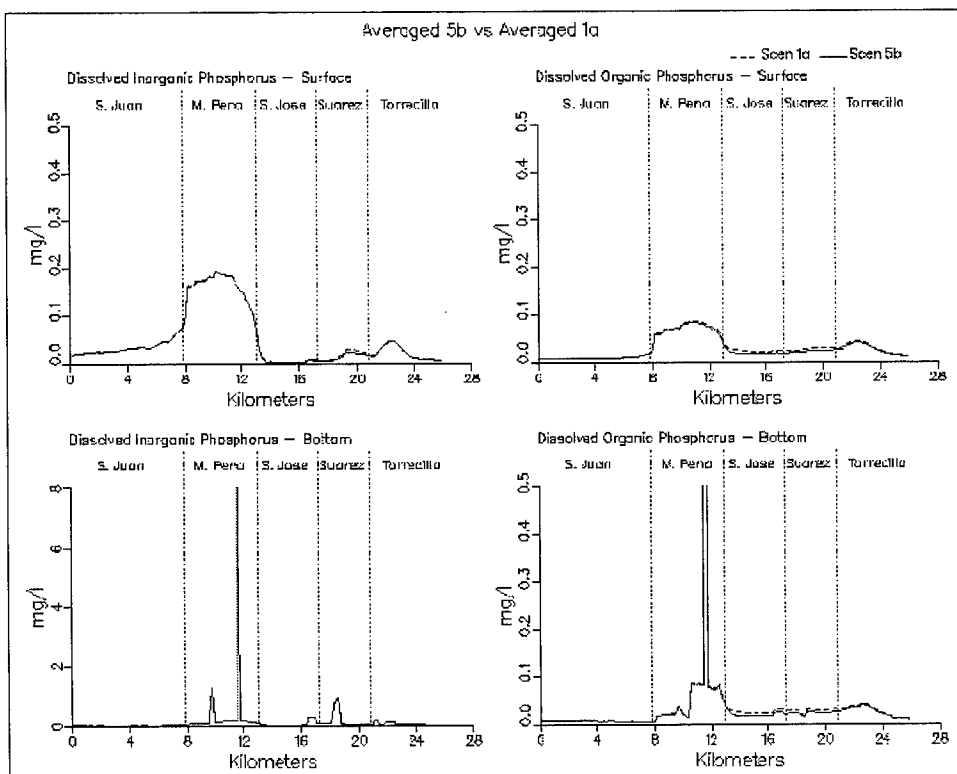


Figure 8-43. (Sheet 6 of 11)

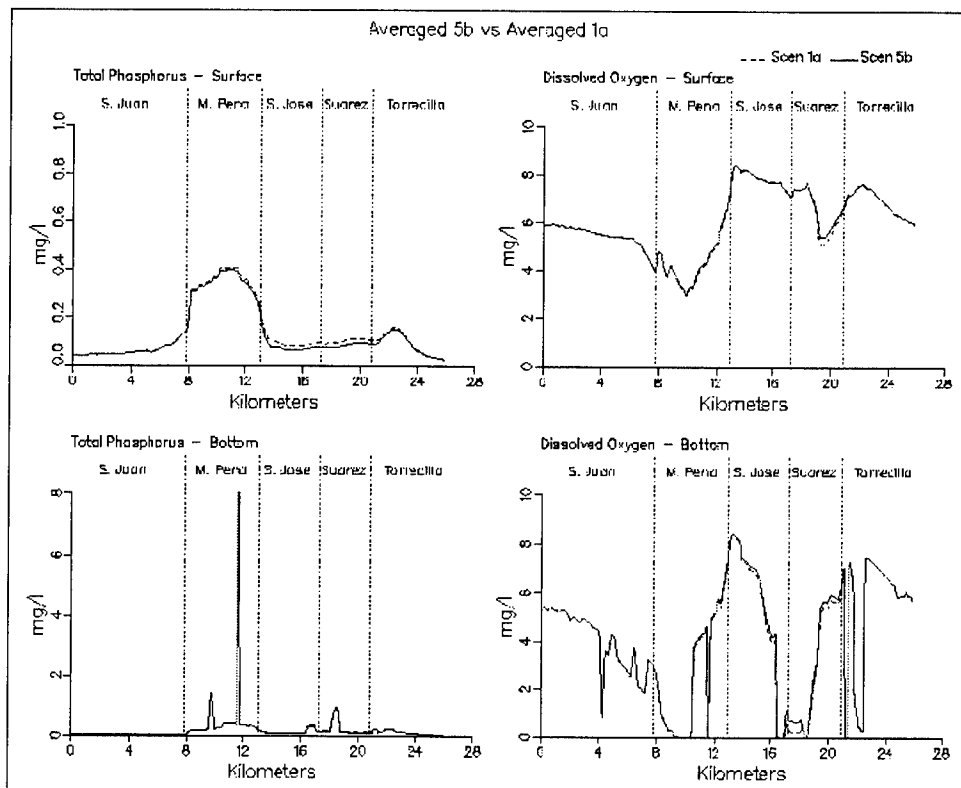


Figure 8-43. (Sheet 7 of 11)

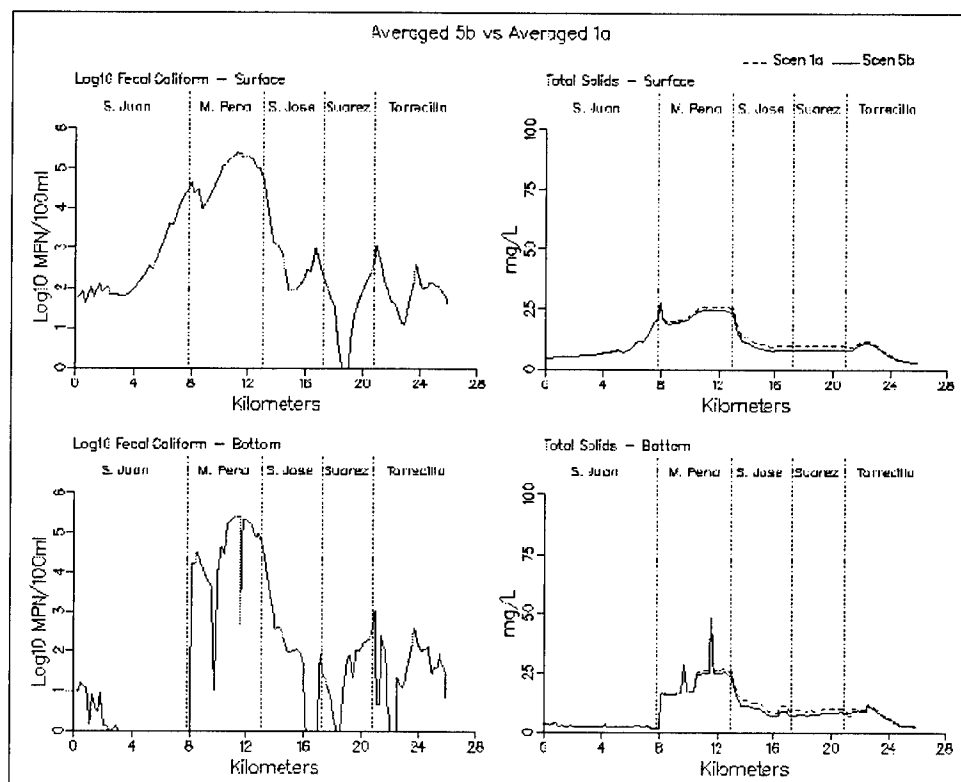


Figure 8-43. (Sheet 8 of 11)

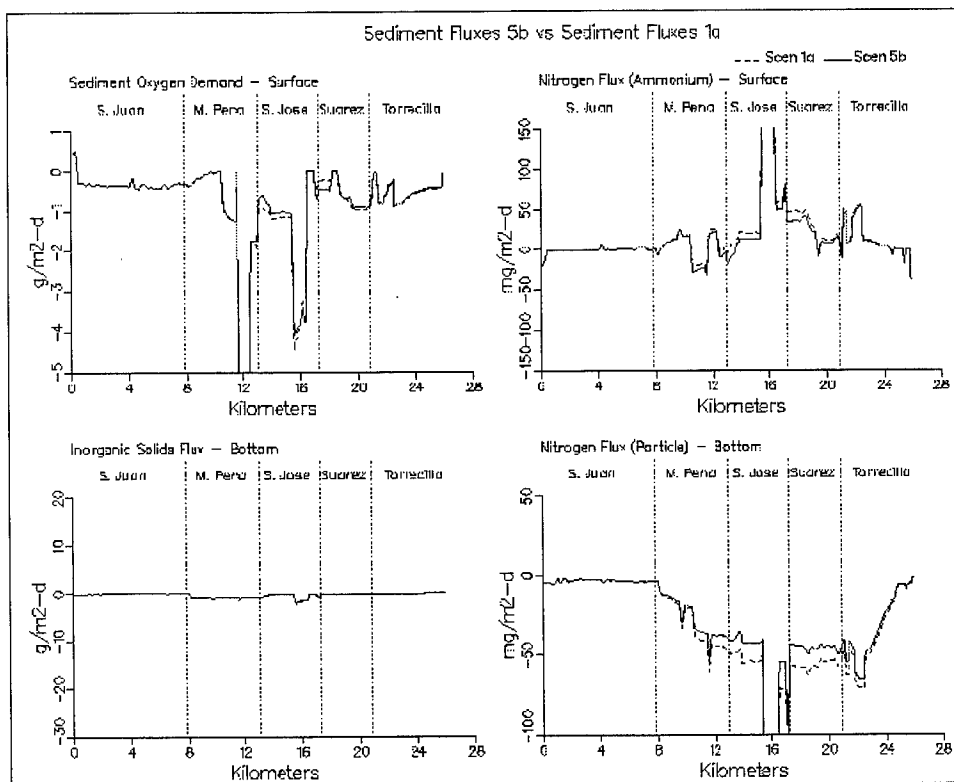


Figure 8-43. (Sheet 9 of 11)

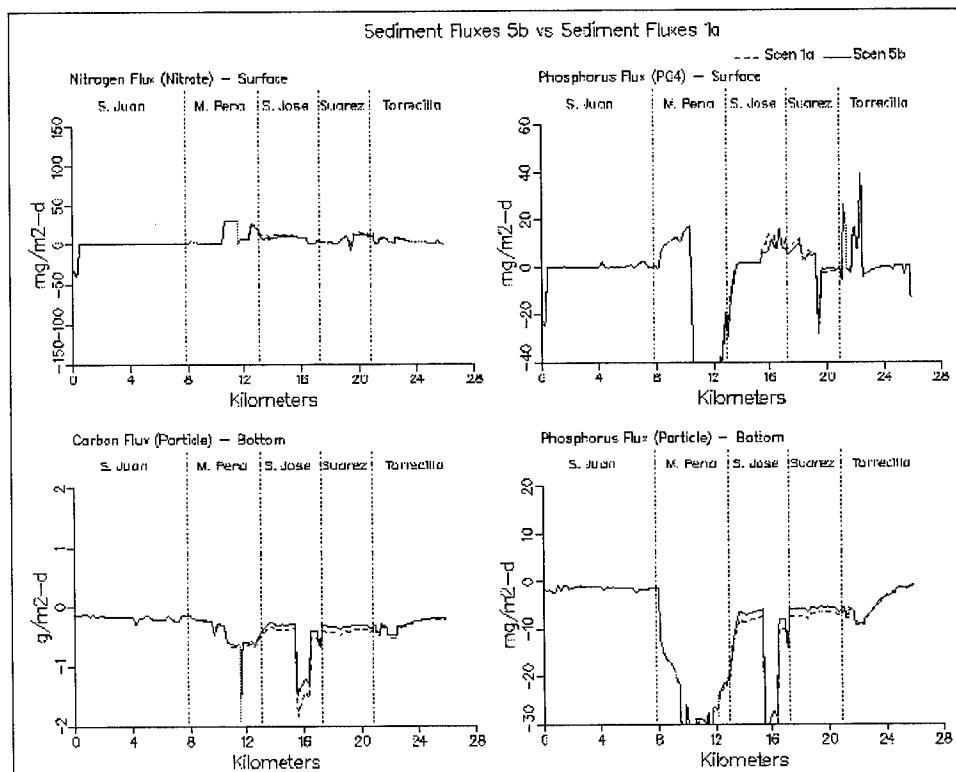


Figure 8-43. (Sheet 10 of 11)

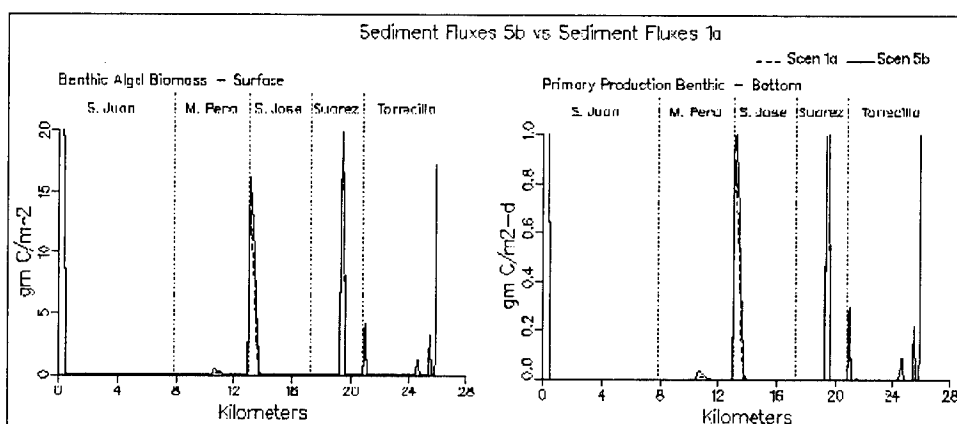


Figure 8-43. (Sheet 11 of 11)

Organic carbon concentrations decreased in Caño Martín Peña, Laguna San José, Canal Suárez, and Laguna La Torrecilla in Scenario 6a when compared to 1a. Dissolved organic carbon levels decreased by 8 mg/l in eastern Caño Martín Peña, 4 mg/l in Laguna San José, 3 mg/l in Canal Suárez, and 1 mg/l in upper Laguna La Torrecilla. Similar decreases in total organic carbon levels occurred in Scenario 6a. Comparison of Scenario 6a results with those of 1c indicates that dissolved organic carbon levels decreased by 1 mg/l in Caño Martín Peña and 1.5 mg/l in Laguna San José. In Scenario 6a, Laguna San José exported 2558 kg/day of carbon to Caño Martín Peña and imported 174 kg/day from Canal Suárez.

Caño Martín Peña surface ammonium levels in Scenario 6a were much lower than those of 1a and slightly lower than those of 1c as a result of the removal of the un-sewered loadings. In Scenario 6a, the maximum ammonium concentration in Caño Martín Peña occurs in the western end and is the result of Rio Piedras inflows. Caño Martín Peña nitrate concentrations decreased in Scenario 6a by 0.1 mg/l in comparison to Scenario 1a levels but were identical to Scenario 1c levels. Dissolved organic nitrogen decreased in Caño Martín Peña, Laguna San José, Canal Suárez, and Laguna La Torrecilla in Scenario 6a. The greatest decrease occurred in eastern Caño Martín Peña. When compared to 1a results, dissolved organic nitrogen concentrations decreased 0.18 mg/l at this location in Scenario 6a. However, when compared to Scenario 1c, it is evident that most of this decrease is the result of the channelization of Caño Martín Peña as the dissolved organic nitrogen levels in Scenario 1c are only 0.02 mg/l higher than those of 6a. In Scenario 6a, Laguna San José dissolved organic nitrogen levels were half of what they had been in Scenario 1a. These levels were also 0.03 mg/l lower than they had been in Scenario 1c. Total nitrogen levels in Scenario 6a were significantly lower in Scenario 6a than in 1a as a result of the decreases in ammonium, dissolved organic nitrogen, and particulate organic nitrogen. In Scenario 6a, Laguna San José discharged 161 kg/day of nitrogen to Caño Martín Peña and imported 7 kg/day from Canal Suárez.

Scenario 6a phosphorus levels indicated large decreases in Caño Martín Peña when compared to results for Scenario 1a. Dissolved inorganic phosphorus levels decreased from as much as 0.2 mg/l in Caño Martín Peña in 1a to 0.04 mg/l in 6a. However, comparison of results from 1c to those of 6a indicates that this decrease results from the channelization of Caño Martín Peña and not from the removal of the un-sewered loads as the concentrations for dissolved inorganic phosphorus in Caño Martín Peña in Scenarios 1c and 6a are identical. Scenario 6a dissolved organic phosphorus levels and total phosphorus levels in Caño Martín Peña and Laguna San José also indicate decreases when compared to Scenario 1a. The largest decreases occur in Caño Martín Peña and are a result of both the channelization and loading reductions as dissolved organic phosphorus and total phosphorus levels are lower in Scenario 6a than in Scenario 1c. In Scenario 6a, Laguna San José exports 14.6 kg/day of phosphorus to Caño Martín Peña and imports 2.5 kg/day from Canal Suárez.

Dissolved oxygen levels in Scenario 6a increased significantly in Caño Martín Peña when compared to Scenario 1a results. Dissolved oxygen levels decreased in Laguna San José, Canal Suárez, and Laguna La Torrecilla as a result of lower algal photosynthesis. Both surface and bottom dissolved oxygen results from Scenario 6a are nearly identical to the results for Scenario 1c which indicates that, at least along the transect, the removal of the un-sewered loads and the storm water loads had less of an effect than channelization of Caño Martín Peña. It must be remembered that surface dissolved oxygen levels in Scenario 1c and 6a are relatively high and cannot go any higher without algal photosynthesis. Dissolved oxygen levels along the bottom of Laguna San José in Scenario 6a did increase slightly when compared to Scenario 1c indicating that the loading removal did have some effect.

Fecal coliform levels in Scenario 6a exhibited the same behavior as those of 1a except for Caño Martín Peña where levels were one order of magnitude lower. Total solids transects for Scenario 6a were lower than the results for Scenario 1a. Scenario 6a results exhibited the same pattern as the results of Scenario 1c but were slightly lower. The decrease in total solids that occurs between Scenarios 1c and 6a results from a decrease in the solids load at Baldeorioty de Castro Pump Station and the decrease in algae brought upon by lower nutrient levels.

In summary, the conditions simulated in Scenario 6a improved water quality throughout the interior portions of the system. Opening Caño Martín Peña established a clockwise circulation through the interior system which promotes flushing. The most significant feature that the loading reductions added was a decrease in chlorophyll levels in Laguna San José in turn decreasing levels in Canal Suárez and Caño Martín Peña. Decreases in algae levels in these bodies translated into decreases in organic carbon, nitrogen, phosphorus, and total solids.

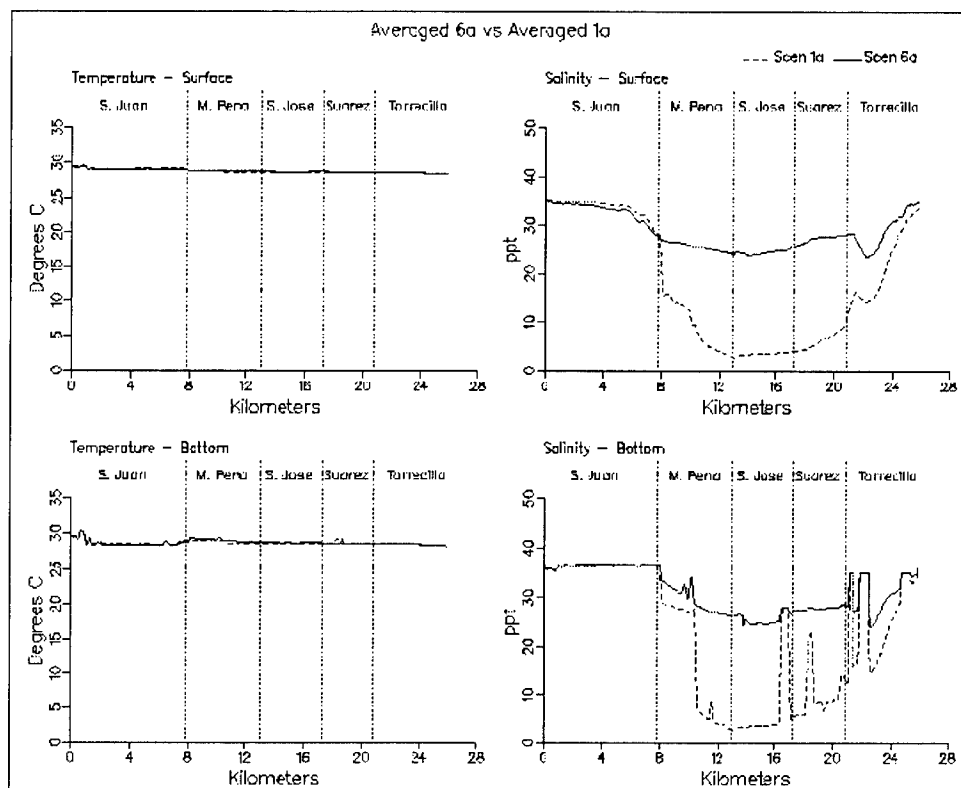


Figure 8-44. Simulation averaged transect plots comparing Scenario 6a with Scenario 1a (Sheet 1 of 11)

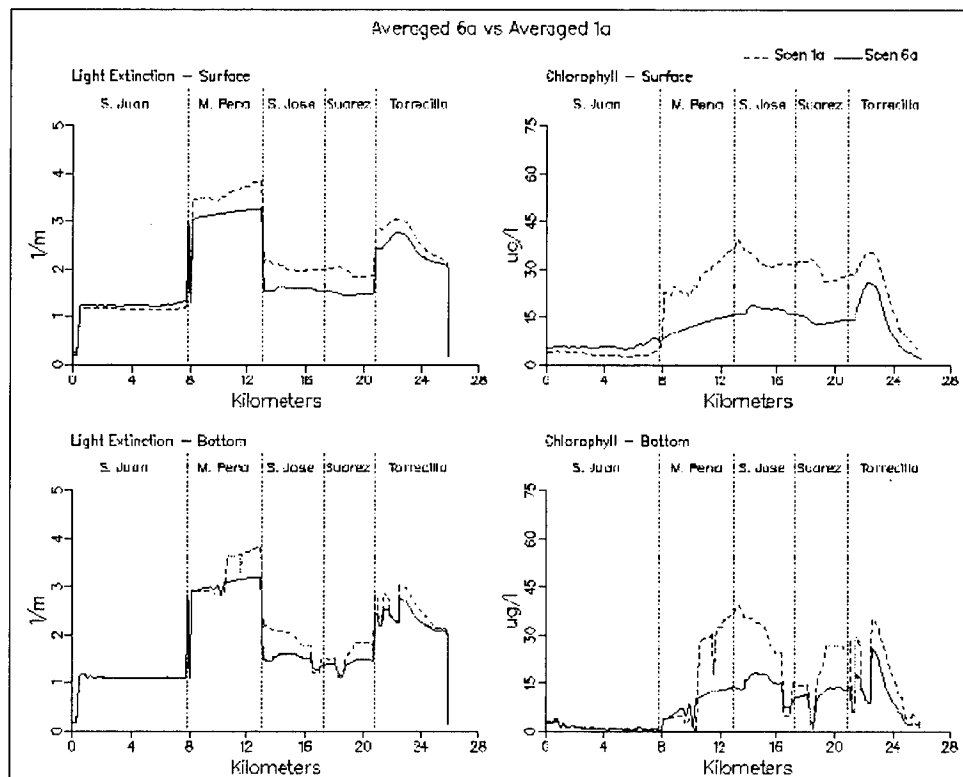


Figure 8-44. (Sheet 2 of 11)

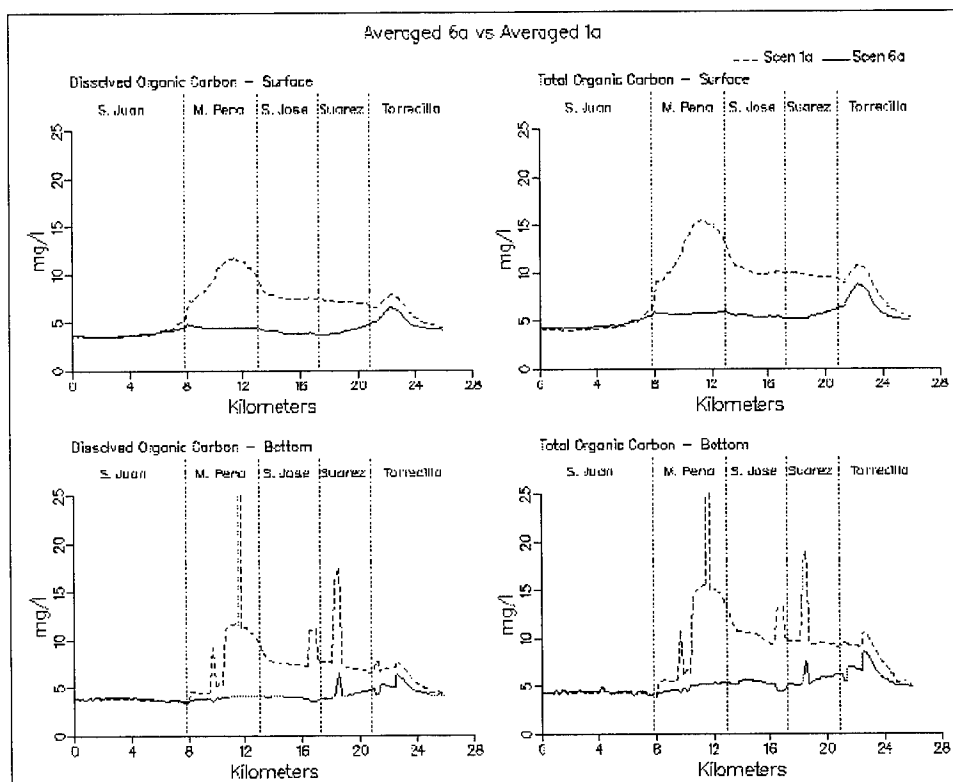


Figure 8-44. (Sheet 3 of 11)

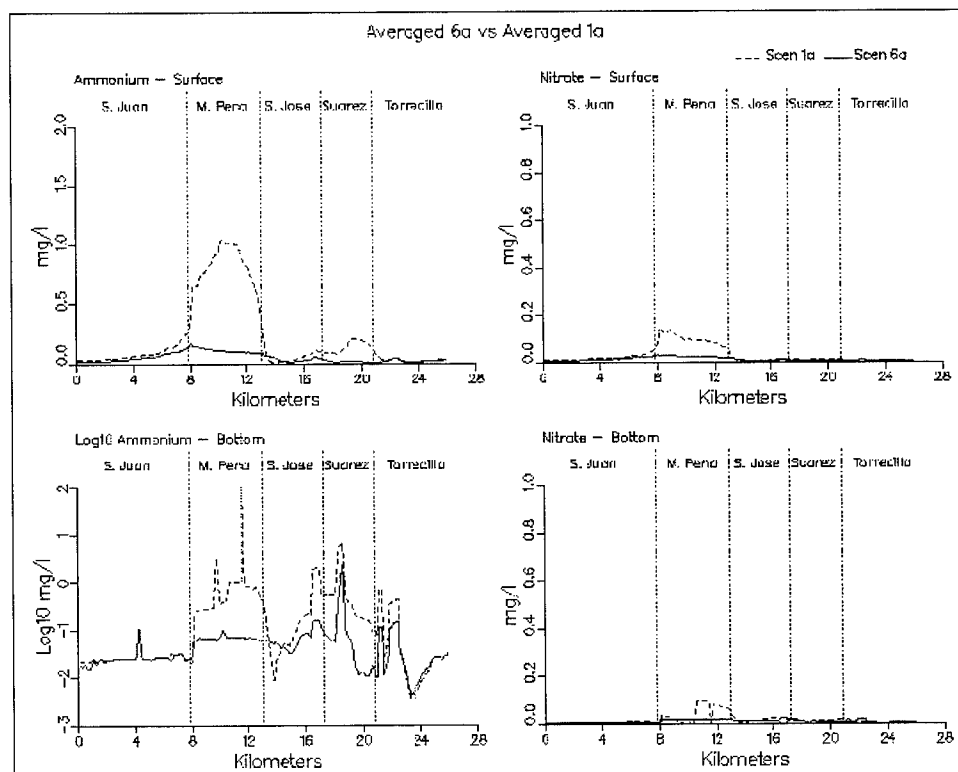


Figure 8-44. (Sheet 4 of 11)

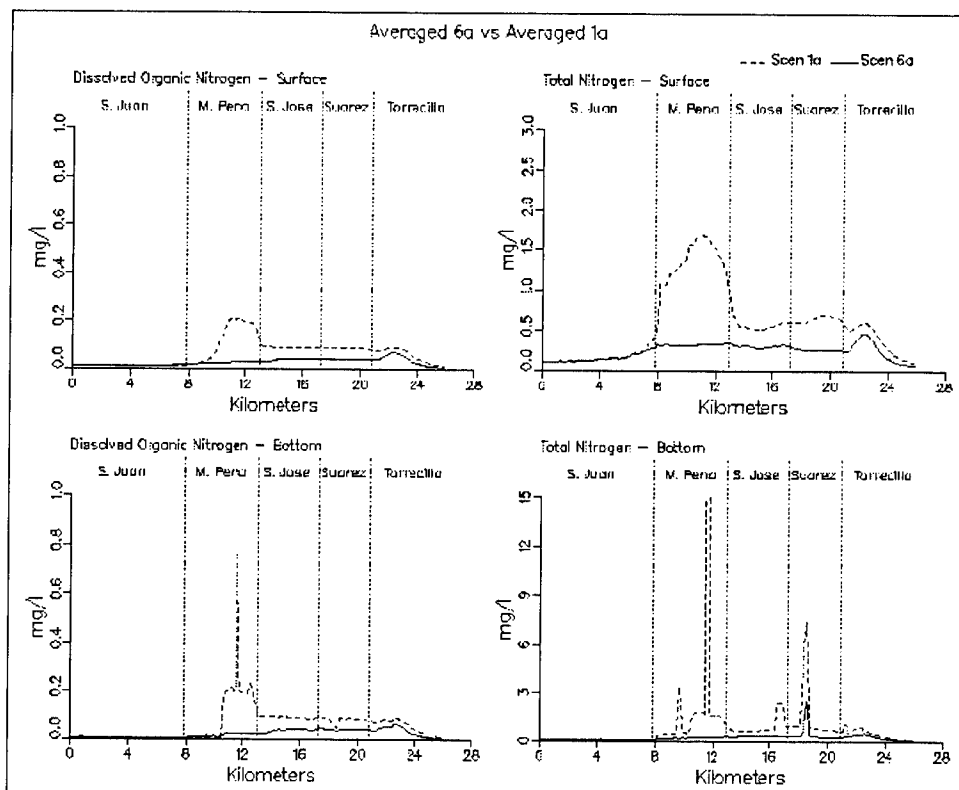


Figure 8-44. (Sheet 5 of 11)

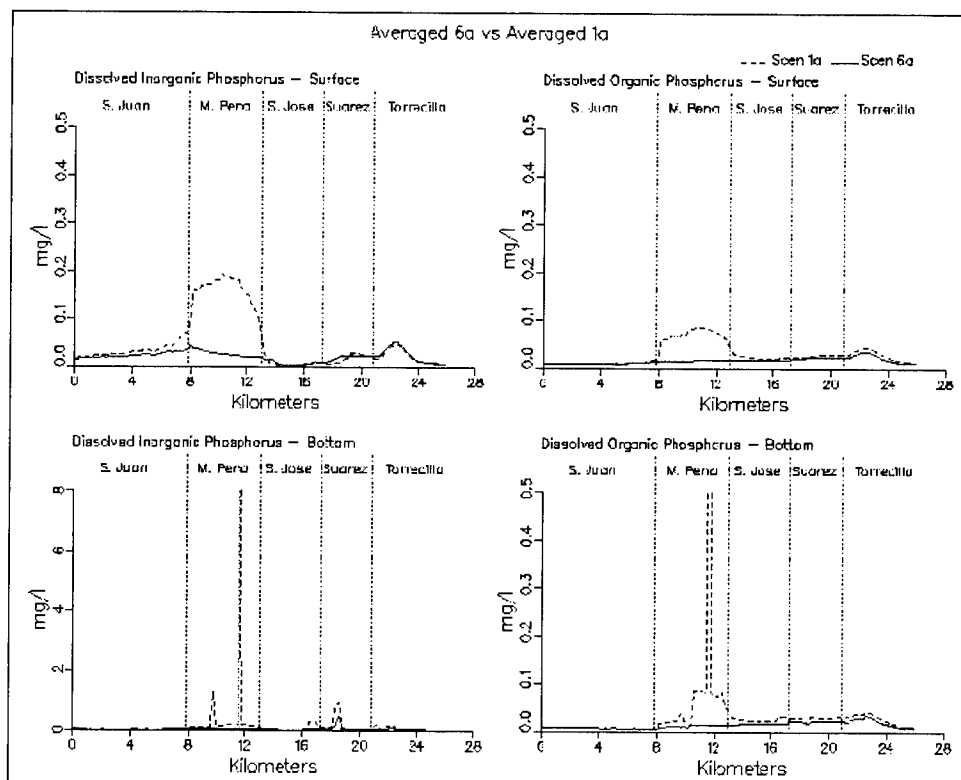


Figure 8-44. (Sheet 6 of 11)

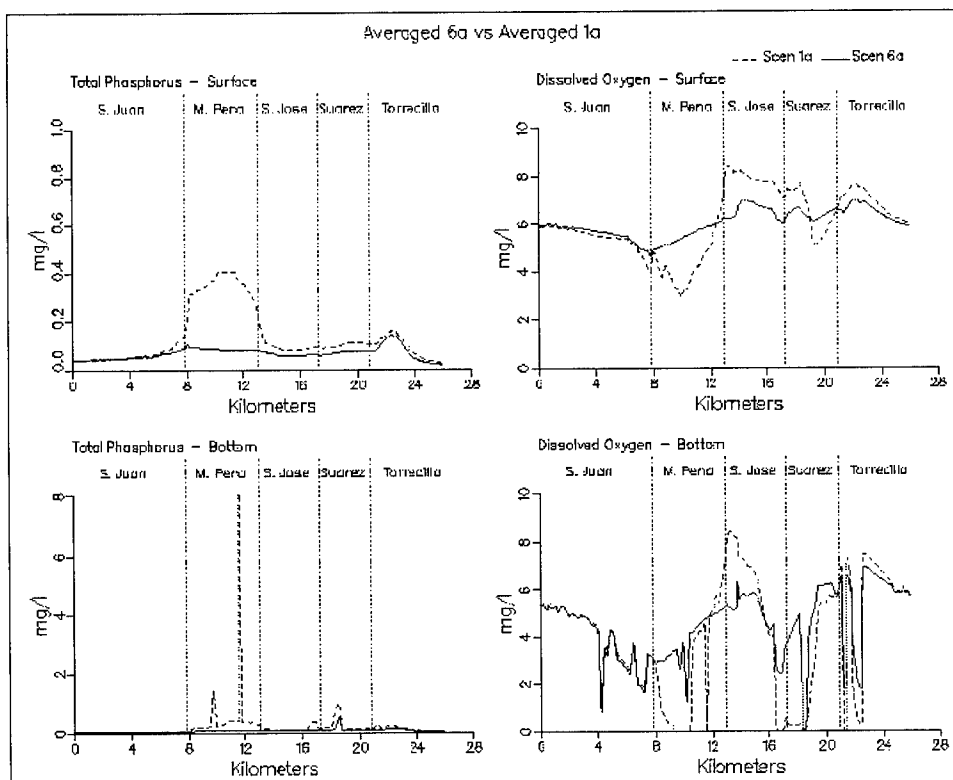


Figure 8-44. (Sheet 7 of 11)

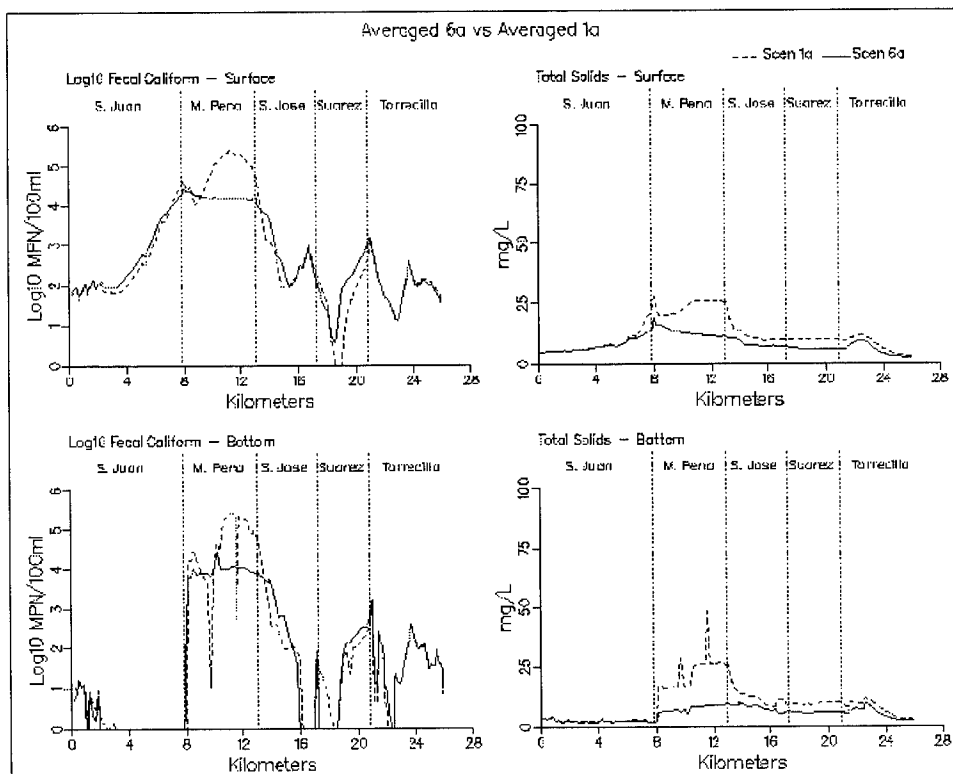


Figure 8-44. (Sheet 8 of 11)

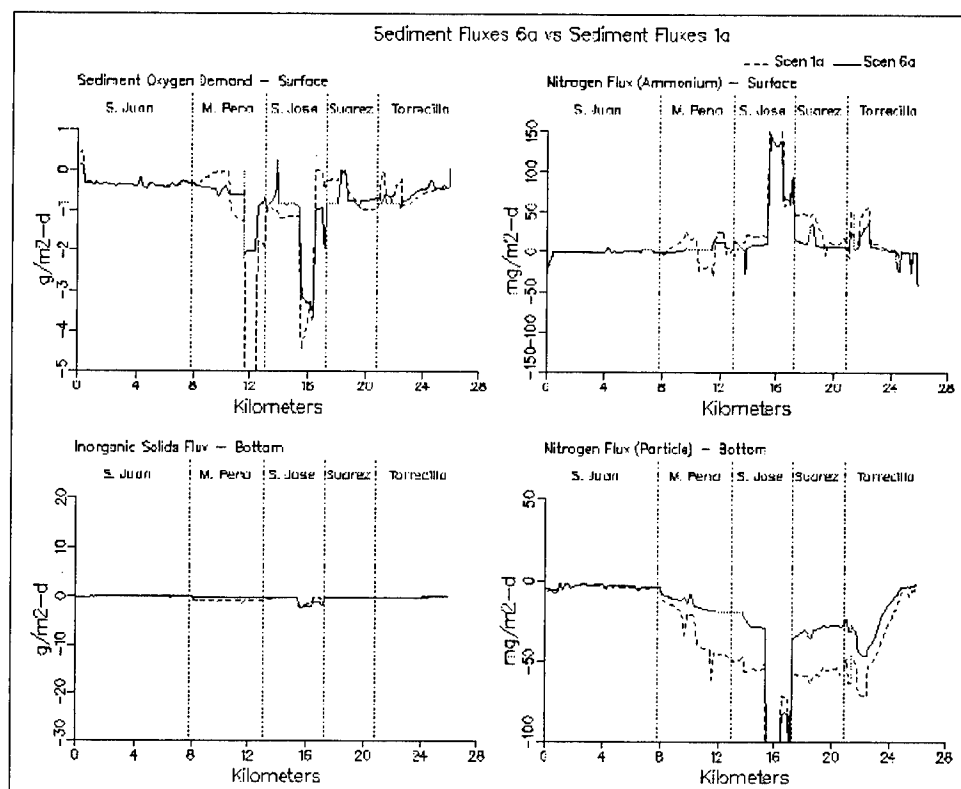


Figure 8-44. (Sheet 9 of 11)

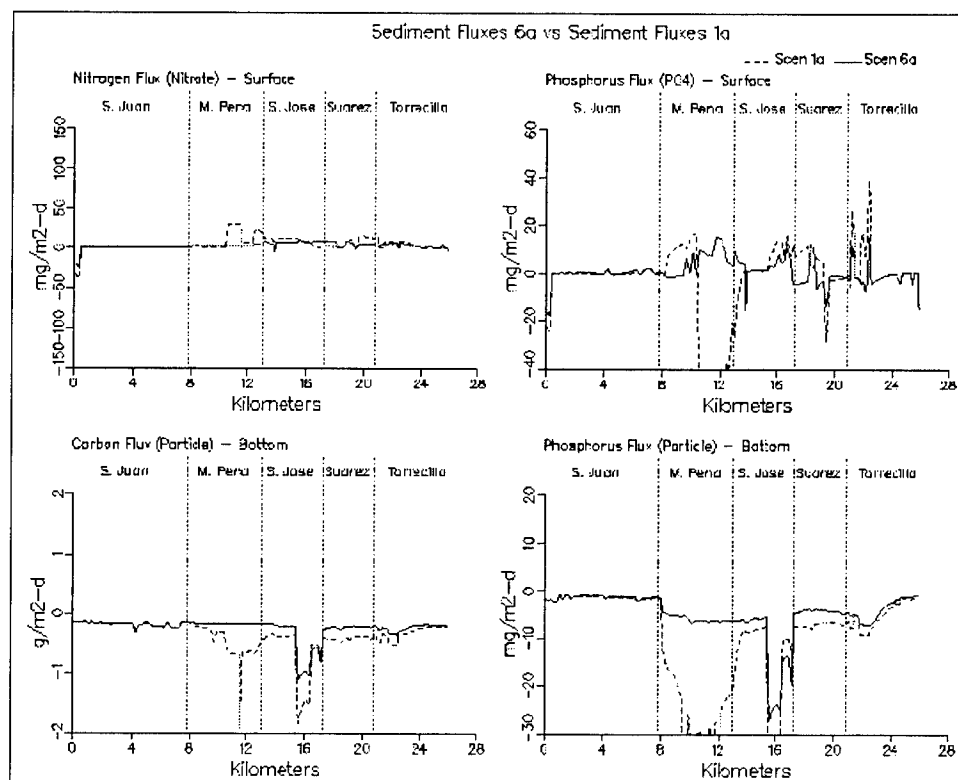


Figure 8-44. (Sheet 10 of 11)

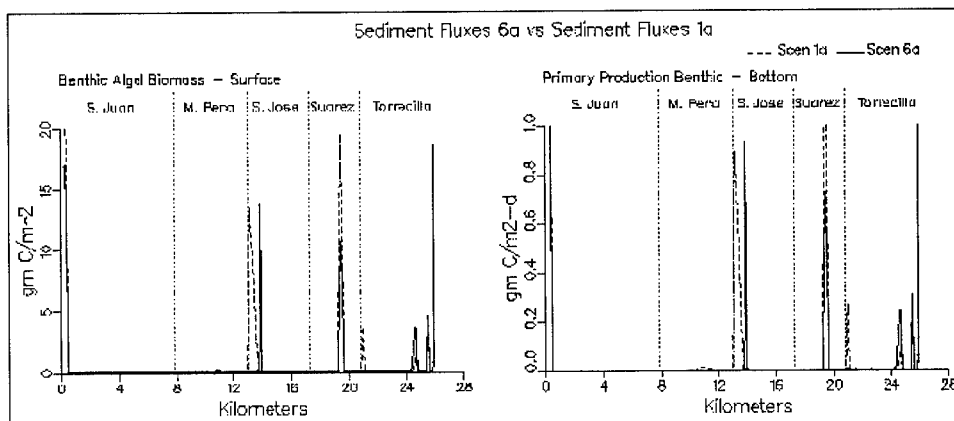


Figure 8-44. (Sheet 11 of 11)

Scenario 6b

Scenario 6b combines all of the loading reductions and channelization of Scenario 6a with the filling of anoxic dredge material borrow pits in Scenario 2. Flows from Laguna San José to Caño Martín Peña were $3.05 \text{ m}^3/\text{s}$ and flows from Canal Suárez into Laguna San José were $0.4 \text{ m}^3/\text{s}$. Since Scenario 6b is a hybrid version of Scenario 6a, this discussion will focus more on the changes that occurred between Scenarios 6a and 6b, than between 6b and 1a.

Temperature results from Scenario 6b indicate that surface temperatures are slightly cooler in San Juan Bay (see Figure 8-45) compared with Scenario 1a. Salinity in Laguna San José increased in Scenario 6b over what it was in either Scenarios 1a or Scenario 2 but is still below what it was for Scenario 1c. The reason for the increase is obviously the channelization of Caño Martín Peña which is why the salinity is higher than it was in either Scenario 1a or 2. The reason that the salinity in Scenario 6b is lower than that of Scenario 1c appears to be the effects of spin-up runs without nudging on. As discussed earlier, nudging acts as a pseudo-salinity-boundary condition inside Laguna San José. Without nudging, the cells in the anoxic holes freshened up. While the opening of Caño Martín Peña allowed more saltwater intrusion into Laguna San José, the freshwater inflows diluted the waters of the lagoon which resulted in a decrease in the salinity of San Juan Bay.

Scenario 6b chlorophyll levels indicated the same behavior as observed in Scenario 6a. There was a slight decrease of $1 \text{ } \mu\text{g/l}$ to $2 \text{ } \mu\text{g/l}$ in surface chlorophyll levels in Caño Martín Peña and Laguna San José. This decrease resulted from the additional reduction in nutrient releases from the anoxic holes. When comparing Scenario 6b to 6a, sediment ammonium releases decreased in Laguna San José and dissolved inorganic phosphorus releases decreased in eastern Caño Martín Peña. Phytoplankton primary production in Laguna San José decreased in Scenario 6b to 3470 kg C/day

from 3972 kg C/day in Scenario 6a. For comparison, Laguna San José phytoplankton primary production was 6093 kg C/day in Scenario 1a.

Dissolved and total organic carbon results for Scenario 6b are similar to those of 6a. Both dissolved and total organic carbon levels are slightly lower in San Juan Bay and slightly higher in Canal Suárez and upper Laguna La Torrecilla. Laguna San José organic carbon exports to Caño Martín Peña were 2650 kg/day and imports from Canal Suárez were 190 kg/day.

Scenario 6b surface ammonium results were very similar to those of 6a. Slight decreases in Laguna San José occurred as a result of decreases in sediment ammonium fluxes. There were also slight decreases in bottom ammonium levels mainly in eastern Laguna San José and in Canal Suárez. Nitrate levels were unchanged between Scenario 6a and 6b. Dissolved organic nitrogen and total nitrogen also exhibited no change. Nitrogen exports from Laguna San José via Caño Martín Peña in Scenario 6b were 167 kg/day and imports from Canal Suárez were 7.3 kg/day.

Dissolved inorganic phosphorus levels in Scenarios 6b were slightly lower than those of 6a. The largest decreases, 0.03 mg/l, occurred in Canal Suárez and Laguna La Torrecilla as a result of decreases in sediment fluxes in those regions. A slight decrease was observed in the surface waters of San Juan Bay and appears to be the result of decreased releases in Caño Martín Peña. Dissolved organic phosphorus transects for 6b and 6a were identical. Total phosphorus plots for 6a and 6b appear to be the same except for the differences due to dissolved inorganic phosphorus. Phosphorus exports in Scenario 6b from Laguna San José via Caño Martín Peña were 15.3 kg/day while imports from Canal Suárez were 1.6 kg/day.

Dissolved oxygen results for Scenario 6b were similar to those of 6a. Surface dissolved oxygen levels show increases over those of 6a but these are due to an increase in the saturation concentration of dissolved oxygen resulting from decreased salinity. Since the reason for the decreases in salinity are not fully understood at present, it is felt that the conditions of Scenario 6b did not improve the surface dissolved oxygen significantly. The conditions of Scenario 6b did improve the bottom dissolved oxygen in Laguna San José and Canal Suárez. Fecal coliform and total solids levels in Scenario 6b were not appreciably different from levels in 6a.

In summary, Scenario 6b indicated some improvements in water quality over Scenario 6a. Chlorophyll levels decreased slightly as did some nutrient releases. Significant effects were observed in dissolved oxygen levels in the locations where the anoxic holes in eastern Laguna San José and Canal Suárez were filled in.

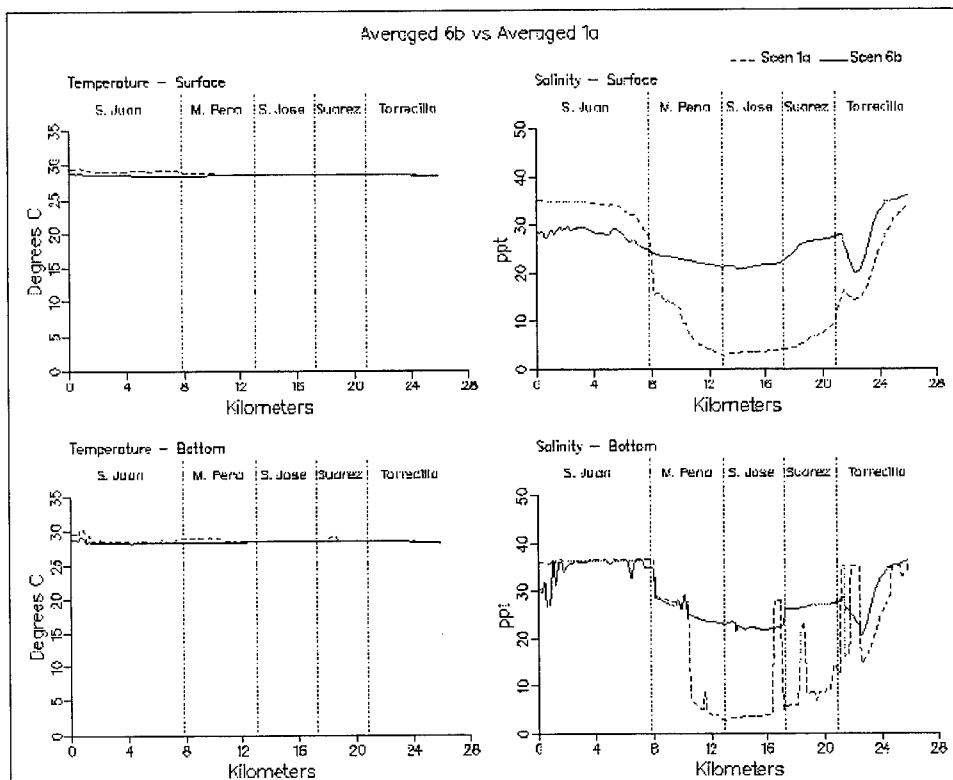


Figure 8-45. Simulation averaged transect plots comparing Scenario 6b with Scenario 1a (Sheet 1 of 11)

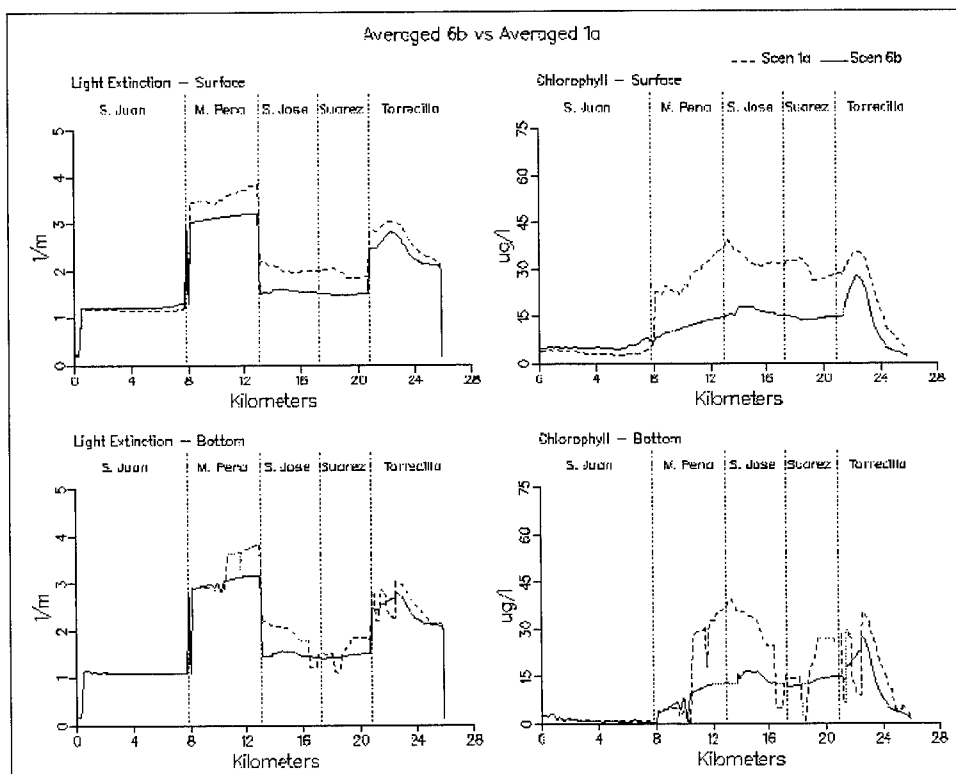


Figure 8-45. (Sheet 2 of 11)

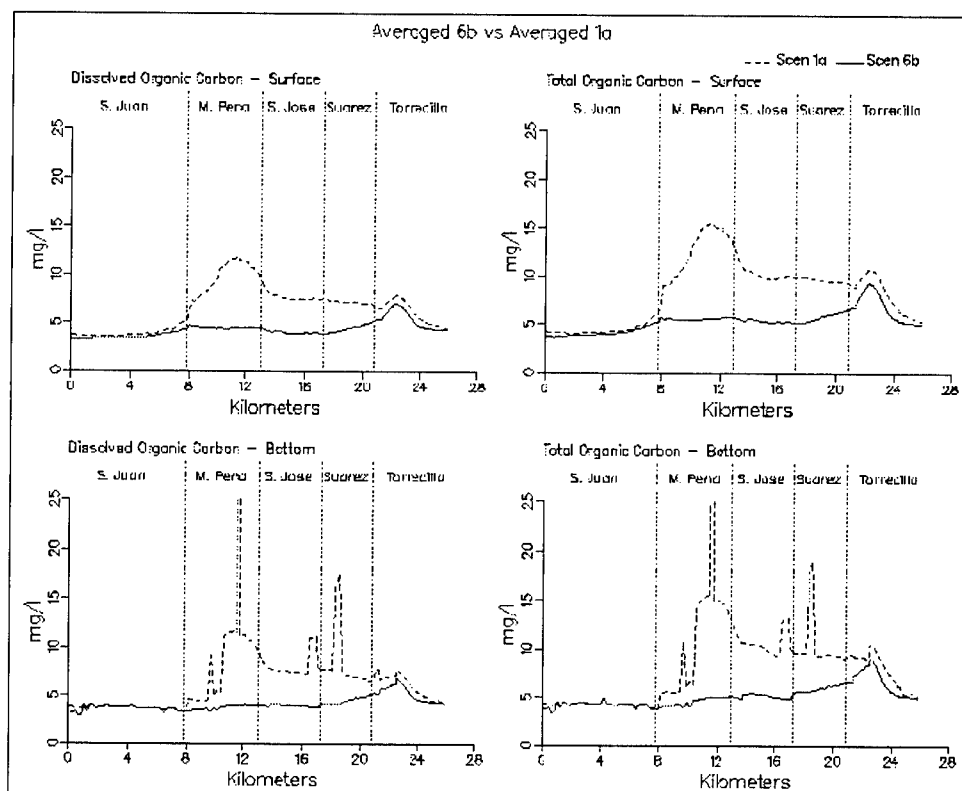


Figure 8-45. (Sheet 3 of 11)

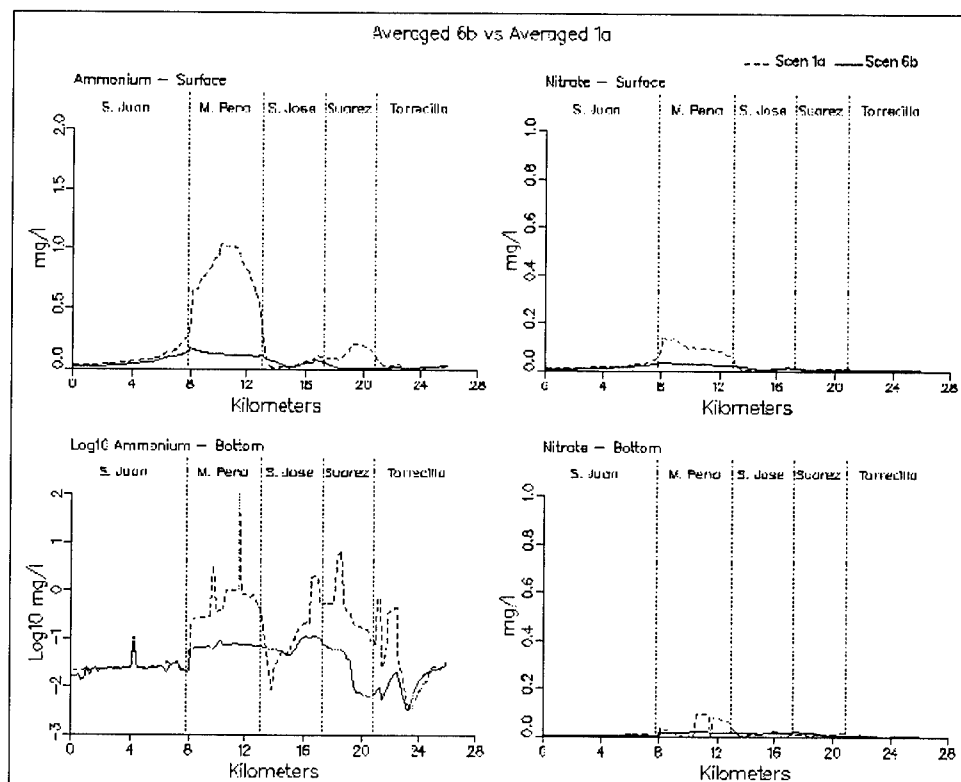


Figure 8-45. (Sheet 4 of 11)

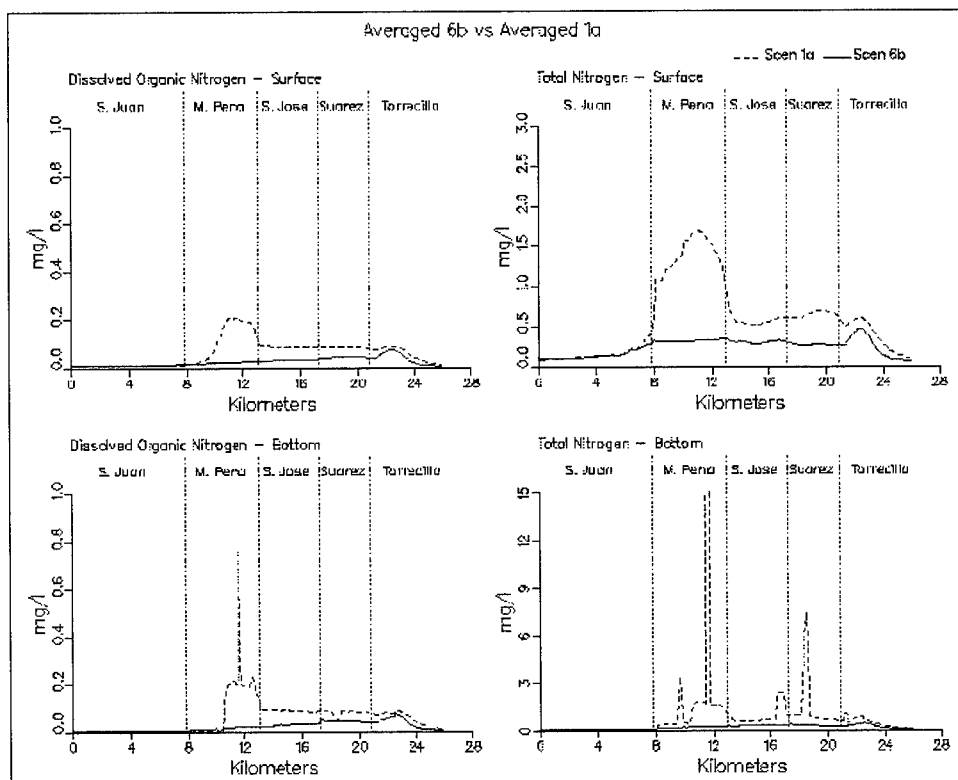


Figure 8-45. (Sheet 5 of 11)

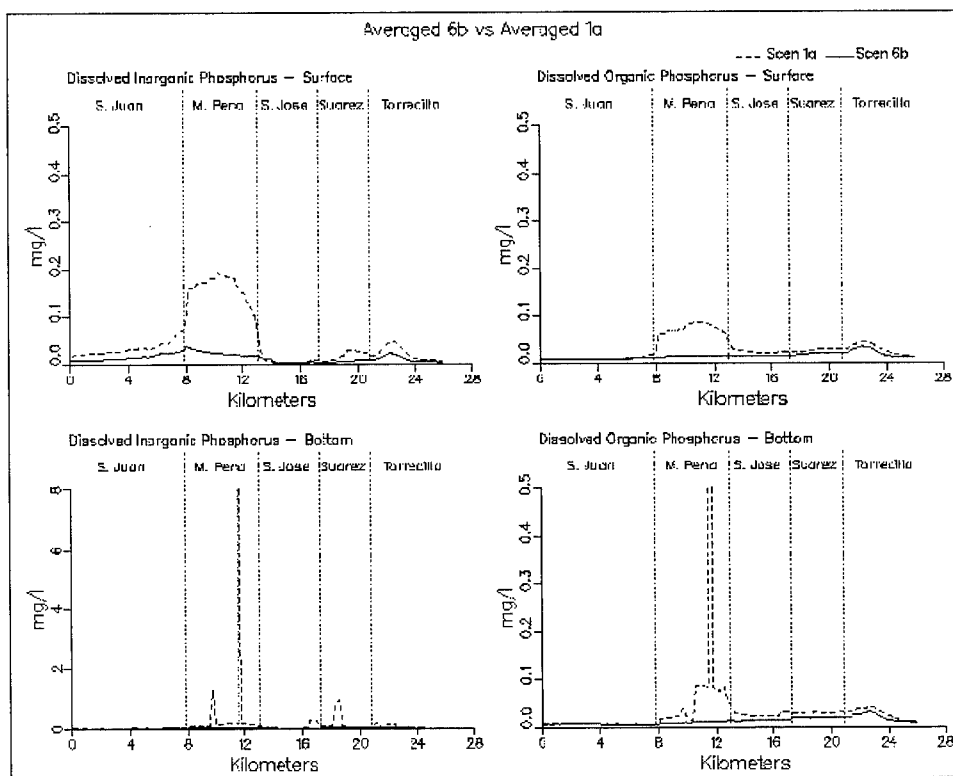


Figure 8-45. (Sheet 6 of 11)

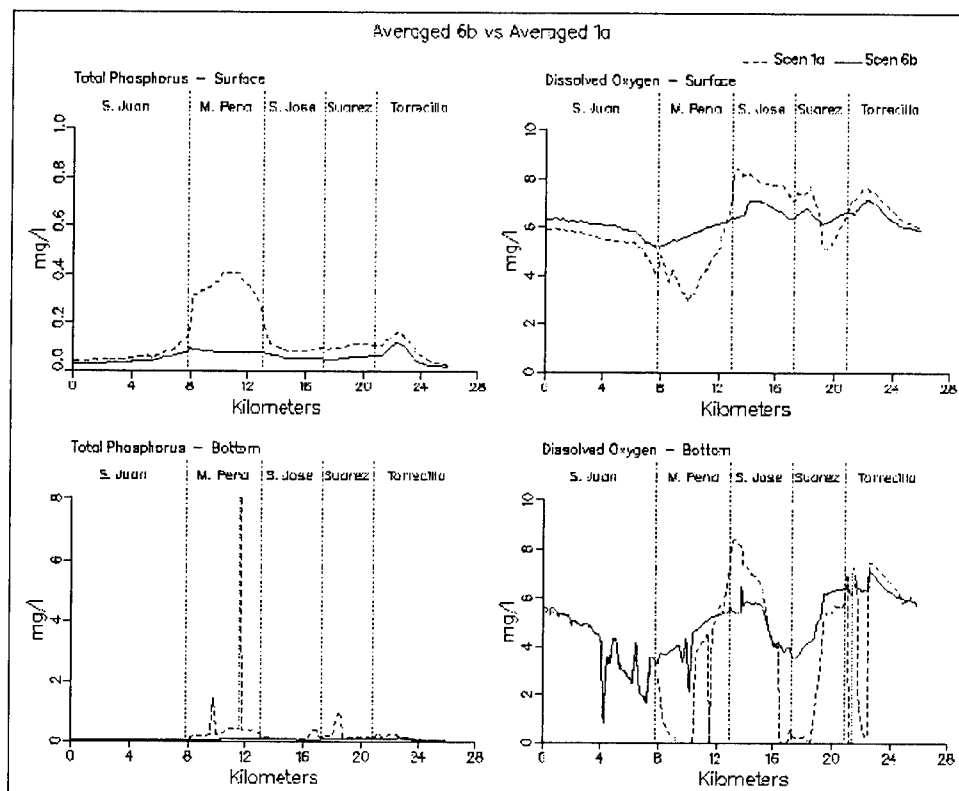


Figure 8-45. (Sheet 7 of 11)

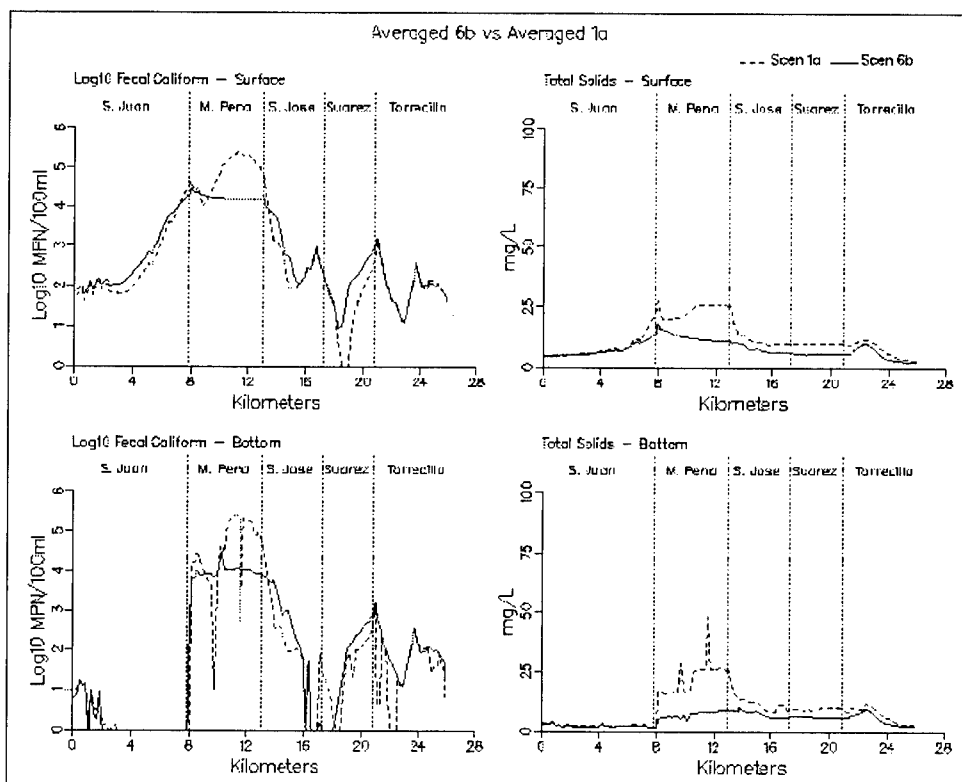


Figure 8-45. (Sheet 8 of 11)

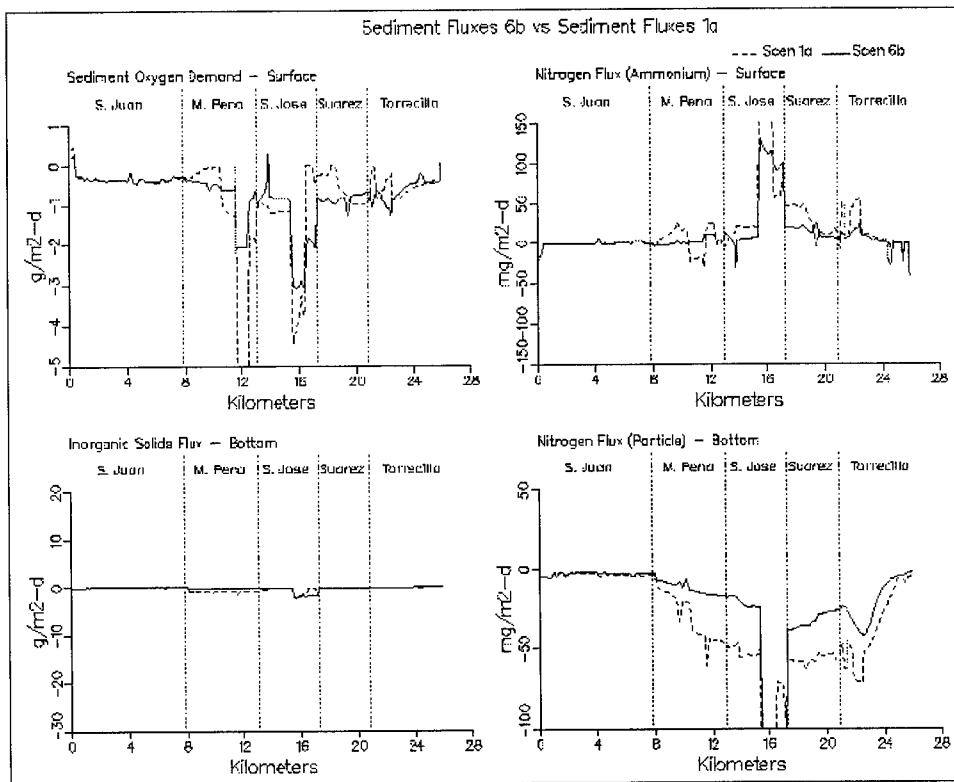


Figure 8-45. (Sheet 9 of 11)

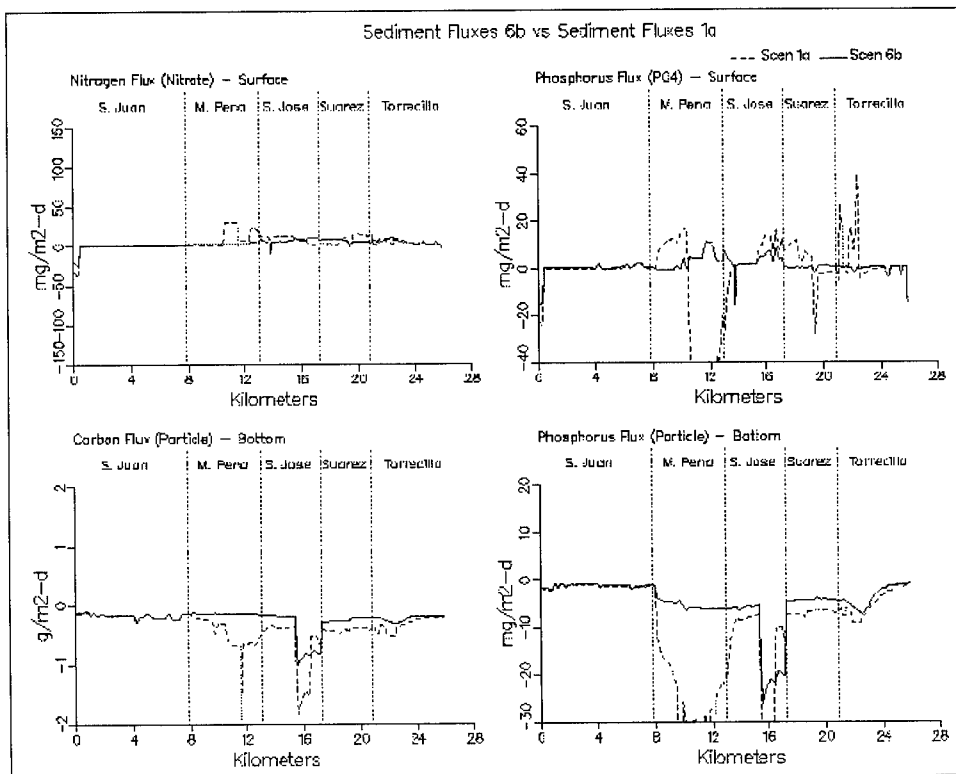


Figure 8-45. (Sheet 10 of 11)

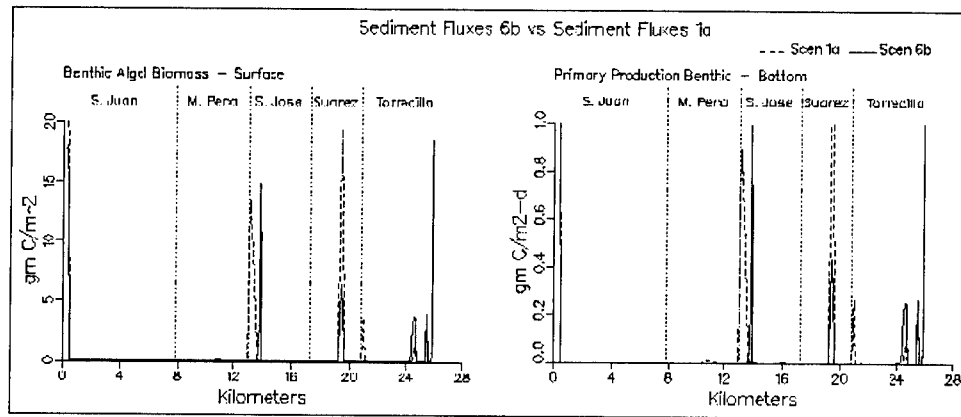


Figure 8-45. (Sheet 11 of 11)

9 Conclusions and Recommendations

A three-dimensional, coupled, hydrodynamic and water quality model of the SJBE system was calibrated using field observations for the summer of 1995. Overall, given the complexity of this system with the multiple ocean inlets, connecting channels, and lagoons, the calibrated model reproduces the observations reasonably well.

Following adjustments and calibration, the model was applied for scenarios to evaluate the effectiveness of various alternatives to increase flushing and reduce loadings for improving water quality. The impacts of each management alternative that was simulated are summarized in Table 9-1 in terms of fluxes of material from one region of the system to another over the scenario simulation duration. As an alternative for comparison, Appendix B contains a summary of the volume-weighted, scenario-average constituent concentrations and the percent change from the base (1a) concentration for all scenarios so that one can easily compare how each alternative affects water quality in an average sense.

All of the alternatives offer some benefits for improving water quality. However, improvements in some areas of the SJBE system can result in degradation to other areas. For example, Scenario 1c provides much improvement to Caño Martín Peña and Laguna San José, but at the expense of flushing more carbon, nitrogen, and phosphorus into San Juan Bay.

Clearly, alternatives were simulated that provide dramatic improvements to water quality. However, the improvements come with costs, including construction costs as well as changes in habitat. For example, it is possible to improve water quality through increased flushing (e.g., Scenarios 1b, 1c, and 3), but this will increase the salinity of Laguna San José and could result in loss of mangrove habitat. Stakeholders must first decide if altering the salinity of Laguna San José is acceptable in terms of habitat and how much mangrove loss is acceptable.

There is not an unequivocally best alternative for improving water quality since a *best* alternative will involve trade-offs, such as water-quality improvement in one area versus degradation in another, costs, habitat

Table 9-1.
Summary of Impacts for Each Management Scenario

Scenario	Flux from Laguna San José to Caño Martín Peña				Flux from Laguna San José to Canal Suárez				Laguna San José Primary Production	San Juan Bay Primary Production
	Flow, m ³ /s	C, kg/d	N, kg/d	P, kg/d	Flow, m ³ /s	C, kg/d	N, kg/d	P, kg/d	As C, kg/day	As C, kg/day
1a	0.5	454	8	2	1.98	1631	138	20	6093	3586
1b	1.45	1311	54	9	1.08	769	71	10	5825	4065
1c	3.05	3530	187	15	-0.4	-166	-5	-2	5860	5300
2	0.5	329	8.8	2	1.98	1060	18	13	1584	2264
3	0.1	-35	-38	-9	2.5	2261	178	23	6450	3060
4	2.55	2415	141	32	-0.2	-73	-2	-1	6675	4957
5a	0.5	513	27	6	1.98	1563	130	19	5741	3263
5b	0.5	369	10	1	1.98	1240	110	15	4541	3347
6a	3.05	2558	161	15	-0.4	-175	-7	-3	3973	4574
6b	3.05	2650	167	15	-0.4	-190	-7	-2	3470	3968

Note: C, N, and P fluxes are rounded off to near whole number

considerations, and other considerations. Even though trade-offs can be assessed to find the optimal solution, politics will eventually enter the decision process and can affect the final selection. However, if one studies the table in Appendix B and does not consider other factors, such as habitat considerations, it is clear that alternative 6b provides the best overall water quality, especially the best DO conditions.

In order to find the preferred alternative for water quality improvement, it is recommended that the stakeholders first specify the bounds of acceptable results in terms of water quality standards, construction/remediation costs, habitat, etc. For example, the stakeholders may decide that it is acceptable to degrade water quality slightly in San Juan Bay as long as water quality standards are satisfied. The stakeholders may decide that it is acceptable to increase the salinity of Laguna San José, thus favoring flushing alternatives involving enlargement of Caño Martín Peña. Conversely, the stakeholders may decide that the preference is to hold steady or even decrease the salinity of Laguna San José. In this case, alternative 4 (i.e., tide gate and removal of bridge constriction in Canal Suárez) may be preferred. Alternative 1c may result in more mangrove loss along Caño Martín Peña than alternative 1b, a consequence to consider.

Assuming that an increase in the salinity of Laguna San José is acceptable and ignoring mangrove losses, a combination of alternatives 1c, 2, and loading reductions seems intuitively appropriate. It is possible that material removed from Caño Martín Peña could be placed in the dredged borrow pits, thus solving two problems while providing added water quality benefits. Additionally, it seems logical that channel improvements in Caño Martín Peña would be accomplished concurrently with removal of un-sewered, untreated wastes in that area. The combination scenario, e.g., dredging of Caño Martín Peña, filling borrow pits, and removal of un-sewered loads (with the inclusion of the pumping station loads removed), was simulated with Scenario 6b which provided the most improvement in water quality. Based upon this logic and the degree of water-quality improvement, one would have to conclude that alternative 6b is preferred.

However, upon review of the results of Scenario 5b, the relatively minor benefits in water quality gained by removal of the Baldeorioty de Castro Pump Station loads may not warrant the cost of this additional waste treatment. Therefore, a preferred alternative may be 6b with the Baldeorioty de Castro Pump Station loads included.

10 References

- American Society of Civil Engineers. (1961). "Effect of water temperature on stream reaeration," *Journal of the Sanitary Engineering Division* 87(SA6), 59-71.
- Ammerman, J., and Azam, F. (1985). "Bacterial 5'-nucleodase in aquatic ecosystems: a novel mechanism of phosphorus regeneration," *Science* 227, 1338-40.
- Bird, D., and Kalff, J. (1984). "Empirical relationships between bacterial abundance and chlorophyll concentration in fresh and marine waters," *Canadian Journal of Fisheries and Aquatic Science* 41, 1015-23.
- Bloss, S., Lehfeldt, R., and Patterson, J. C. (1988). "Modeling turbulent transport in stratified estuary," *Journal of Hydraulic Engineering, Am. Soc. Civil Eng.* 114(9), 1113-33.
- Boni, L., Carpena, E., Wynne, D., and Reti, M. (1989). "Alkaline phosphatase activity in *Protophylla* *Tamarensis*," *Journal of Plankton Research* 11, 879-85.
- Cerco, C. F. (1995a). "Simulation of long-term trends in Chesapeake Bay eutrophication," *J. Environ. Eng., Am. Soc. Civil Eng.* 121(4), 298-310.
- Cerco, C. F. (1995b). "Response of Chesapeake Bay to nutrient load reductions," *J. Environ. Eng., Am. Soc. Civil Eng.* 121(8), 549-57.
- Cerco, C. F., and Bunch, B. (1997). "Passaic River tunnel diversion model study, report 5, water quality modeling," Technical Report HL-96-2, U.S. Army Engineer Waterways Experiment Station, Vicksburg, MS.
- Cerco, C. F., and Cole, T. (1993). "Three-dimensional eutrophication model of Chesapeake Bay," *J. Environ. Eng., Am. Soc. Civil Eng.* 119(6), 1006-25.
- Cerco, C. F., and Cole, T. M. (1994). "Three-dimensional eutrophication model of Chesapeake Bay," Technical Report EL-94-4, U.S. Army Engineer Waterways Experiment Station, Vicksburg, MS.

- Cerco, C. F., and Cole, T. M. (1995). "User's guide to the CE-QUAL-ICM three-dimensional eutrophication model," Technical Report EL-95-15, U.S. Army Engineer Waterways Experiment Station, Vicksburg, MS.
- Cerco, C., and Seitzinger, S. (1997). "Measured and modeled effects of benthic algae on eutrophication in Indian River-Rehoboth Bay, Delaware," *Estuaries* 20(1), 231-48.
- Cerco, C. F., Bunch, B., Cialone, M. A., and Wang, H. (1994). "Hydrodynamic and eutrophication model study of Indian River and Rehoboth bay, Delaware," Technical Report EL-94-5, U.S. Army Engineer Waterways Experiment Station, Vicksburg, MS.
- Cerco, C. F., Bunch B., and Letter, J. (1999). "Impact of flood-diversion tunnel on Newark Bay and adjacent waters," *J. Environ. Eng., Am. Soc. Civil Eng.* 125(4), 328-38.
- Chrost, R., and Overbeck, J. (1987). "Kinetics of alkaline phosphatase activity and phosphorus availability for phytoplankton and bacterioplankton in Lake Plubsee (north German eutrophic lake)," *Microbial Ecology* 13, 229-48.
- Cole, J., Findlay, S., and Pace, M. (1988). "Bacterial production in fresh and saltwater ecosystems: a cross-system overview," *Marine Ecology Progress Series* 43, 1-10.
- DiToro, D. (1980). "Applicability of cellular equilibrium and Monod theory to phytoplankton growth kinetics," *Ecological Modelling* 8, 201-18.
- DiToro, D., and Fitzpatrick, J. (1993). "Chesapeake Bay sediment flux model," Contract Report EL-93-2, U.S. Army Engineer Waterways Experiment Station, Vicksburg, MS.
- Droop, M. (1973). "Some thoughts on nutrient limitation in algae," *Journal of Phycology* 9, 264-72.
- Edinger, J., Brady, D., and Geyer, J. (1974). "Heat exchange and transport in the environment," Report 14, Department of Geography and Environmental Engineering, Johns Hopkins University, Baltimore, MD.
- Ellis, S. R., and Gómez-Gómez, F. (1976). "Hydrologic Characteristics of Lagoons at San Juan, Puerto Rico, During a January 1974 Tidal Cycle," U.S. Geological Survey, WRI-38-75.
- Fagerburg, T. L. (1998). "San Juan Bay Estuary study: hydrodynamic field data collection," Miscellaneous Paper CHL-98-3, U.S. Army Engineer Waterways Experiment Station, Vicksburg, MS.

- Garratt, J. R. (1977). "Review of drag coefficients over oceans and continents," *Monthly Weather Review* 105, 915-29.
- Genet, L., Smith, D., and Sonnen, M. (1974). "Computer program documentation for the dynamic estuary model," U.S. Environmental Protection Agency, Systems Development Branch, Washington, DC.
- Gómez-Gómez, F., Quinones, F., and Ellis, S. (1983). "Hydrologic characteristics of lagoon at San Juan, Puerto Rico, during an October 1974 tidal cycle," U.S. Geological Survey Water Resources Investigations Open File Report 82-8349, San Juan, PR.
- Hall, R. W., and Dortch, M. S. (1994). "New York Bight study, development and application of a eutrophication/general water quality model," Technical Report CERC-94-4, Report 2, U.S. Army Engineer Waterways Experiment Station, Vicksburg, MS.
- HydroQual. (1987). "A steady-state coupled hydrodynamic/water quality model of the eutrophication and anoxia process in Chesapeake Bay," Final Report, HydroQual Inc., Mahwah, NJ.
- Johnson, B. H. (1980). "VAHM - a vertically averaged hydrodynamic model using boundary-fitted coordinates," Miscellaneous Paper HL-80-3, U.S. Army Engineer Waterways Experiment Station, Vicksburg, MS.
- Johnson, B. H., Heath, R. E., Hsieh, B. B., Kim, K. W., and Butler, H. L. (1991). "Development and verification of a three-dimensional numerical hydrodynamic, salinity, and temperature model of Chesapeake Bay," Technical Report HL-91-7, U.S. Army Engineer Waterways Experiment Station, Vicksburg, MS.
- Johnson, B. H., Kim K. W., Heath, R. E., Hsieh, B. B., and Butler, H. L. (1993). "Validation of three-dimensional hydrodynamic model of Chesapeake Bay," *J. of Hyd. Eng., Am. Soc. Civil Eng.* 119(1), 2-20.
- Kennedy, R. H., Hains, J. J., Boyd, W. A., Lemons, J., Herrmann F., Honnell, D., Howell, P., Way, C., Fernandez, F., Miller-Way, T., and Twilley, R. R. (1996). "San Juan Bay and Estuary study: water quality data collection," Miscellaneous Paper EL-96-9, U.S. Army Engineer Waterways Experiment Station, Vicksburg, MS.
- Leonard, B. (1979). "A stable and accurate convection modelling procedure based on quadratic upstream interpolation," *Computer Methods in Applied Mechanics and Engineering* 19, 59-98.
- Mark, D. J., Scheffner, N. W., Butler, H. L., Bunch, B. W., and Dortch, M. S. (1993). "Hydrodynamic and water quality modeling of lower Green Bay, Wisconsin," Technical Report CERC-93-16, U.S. Army Engineer Waterways Experiment Station, Vicksburg, MS.

- Matavulj, M., and Flint, K. (1987). "A model for acid and alkaline phosphatase activity in a small pond," *Microbial Ecology* 13, 141-58.
- Metcalf & Eddy., Inc. (1979). "*Wastewater engineering: treatment/disposal/reuse*. McGraw Hill Book Company, New York, NY.
- Mississippi Department of Environmental Quality, Mississippi Soil and Water Conservation Commission, USDA Soil Conservation Service (1994). "Planning and design manual for the control of erosion, sediment, & stormwater," Mississippi Department of Environmental Quality, Jackson, MS.
- Monod, J. (1949). "The growth of bacterial cultures," *Annual Review of Microbiology* 3, 371-94.
- Morel, F. (1983). *Principles of aquatic chemistry*, John Wiley and Sons, New York, NY, 150.
- O'Connor, D. (1983). "Wind effects on gas-liquid transfer coefficients," *Journal of the Environmental Engineering Division* 190, 731-52.
- O'Connor, D., and Dobbins, W. (1958). "Mechanisms of reaeration in natural streams," *Transactions of the American Society of Civil Engineers* 123, 641-66.
- Odum, E. (1971). *Fundamentals of ecology*, 3rd ed., W. B. Saunders, Philadelphia, PA, pp 106-7.
- Parsons, T., Takahashi, M., and Hargrave, B. (1984). *Biological oceanographic processes*. 3rd ed., Pergamon Press, Oxford.
- Redfield, A., Ketchum, B., and Richards, F. (1966). "The influence of organisms on the composition of sea-water." *The Sea Volume II*. Interscience Publishers, New York, 26-48.
- Rodi, W. (1980). "Turbulence models and their application in hydraulics: a state of the art review," *IAHR*, Delft, The Netherlands.
- Sheng, Y. P. (1986). "A three-dimensional mathematical model of coastal, estuarine and lake currents using boundary-fitted grid," Report No. 585, A.R.A.P. Group of Titan Research and Technology, Princeton, NJ.
- Stumm, W., and Morgan, J. (1981). *Aquatic chemistry*. 2nd ed., Wiley Interscience, New York.
- Tchobanoglous, G., and Schroeder, E. (1987). *Water quality*. Addison Wesley, Reading, MA.

- Thomann, R., and Fitzpatrick, J. (1982). "Calibration and verification of a mathematical model of the eutrophication of the Potomac Estuary," HydroQual Inc., Mahwah, NJ.
- Tuffey, T., Hunter, J., and Matulewich, V. (1974). "Zones of nitrification," *Water Resources Bulletin* 10, 555-64.
- U.S. Environmental Protection Agency. (1993). "National Estuary Program: bringing our estuaries new life," Technical Report EPA-842-F-93-002, Office of Wetlands, Oceans, and Watersheds, Washington, DC.
- Wen, C., Kao, J., Wang, L., and Liaw, C. (1984). "Effect of salinity on reaeration coefficient of receiving waters," *Water Science and Technology* 16, 139-54.
- Westerlink, J. J., Luettich, R. A., Baptista, A. M., Scheffner, N. W., and Farrar, P. (1992). "Tide and storm surge predictions using a finite element model," *Journal of Hydraulic Engineering, Am. Soc. Civil Eng.*, 118, 1373-90.
- Westrich, J., and Berner, R. (1984). "The role of sedimentary organic matter in bacterial sulfate reduction: the G model tested," *Limnology and Oceanography* 29, 236-49.
- Wezernak, C., and Gannon, J. (1968). "Evaluation of nitrification in streams," *Journal of the Sanitary Engineering Division* 94(SA5), 883-95.

Appendix A

Transformed Horizontal Momentum Diffusion Terms

X - Horizontal Diffusion

$$\begin{aligned}
 &= \frac{Y_\eta}{J^2} \left(\frac{A_h G_{22}}{J} \left[(X_\xi H \bar{u})_\xi + (X_\eta H \bar{v})_\xi \right] \right)_\xi \\
 &+ \frac{Y_\eta}{J^2} \left(\frac{A_h G_{11}}{J} \left[(X_\xi H \bar{u})_\eta + (X_\eta H \bar{v})_\eta \right] \right)_\eta \\
 &- \frac{X_\eta}{J^2} \left(\frac{A_h G_{11}}{J} \left[(Y_\xi H \bar{u})_\eta + (Y_\eta H \bar{v})_\eta \right] \right)_\eta \\
 &- \frac{Y_\eta}{J^2} \left(\frac{A_h G_{12}}{J} \left[(X_\xi H \bar{u})_\eta + (X_\eta H \bar{v})_\eta \right] \right)_\xi \\
 &- \frac{Y_\eta}{J^2} \left(\frac{A_h G_{12}}{J} \left[(X_\xi H \bar{u})_\xi + (X_\eta H \bar{v})_\xi \right] \right)_\eta \\
 &+ \frac{X_\eta}{J^2} \left(\frac{A_h G_{12}}{J} \left[(Y_\xi H \bar{u})_\eta + (Y_\eta H \bar{v})_\eta \right] \right)_\xi \\
 &+ \frac{X_\eta}{J^2} \left(\frac{A_h G_{12}}{J} \left[(Y_\xi H \bar{u})_\xi + (Y_\eta H \bar{v})_\xi \right] \right)_\eta
 \end{aligned}$$

Y - Horizontal Diffusion

$$\begin{aligned}
&= \frac{X_\xi}{J^2} \left(\frac{A_h G_{11}}{J} \left[(Y_\eta H \bar{v})_\eta + (Y_\xi H \bar{u})_\eta \right] \right)_\eta \\
&- \frac{Y_\xi}{J^2} \left(\frac{A_h G_{11}}{J} \left[(X_\eta H \bar{v})_\eta + (X_\xi H \bar{u})_\eta \right] \right)_\eta \\
&+ \frac{X_\xi}{J^2} \left(\frac{A_h G_{22}}{J} \left[(Y_\eta H \bar{v})_\xi + (Y_\xi H \bar{u})_\xi \right] \right)_\xi \\
&- \frac{Y_\xi}{J^2} \left(\frac{A_h G_{22}}{J} \left[(X_\eta H \bar{v})_\xi + (X_\xi H \bar{u})_\xi \right] \right)_\xi \\
&- \frac{X_\xi}{J^2} \left(\frac{A_h G_{12}}{J} \left[(Y_\eta H \bar{v})_\eta + (Y_\xi H \bar{u})_\eta \right] \right)_\xi \\
&- \frac{X_\xi}{J^2} \left(\frac{A_h G_{12}}{J} \left[(Y_\eta H \bar{v})_\xi + (Y_\xi H \bar{u})_\xi \right] \right)_\eta \\
&+ \frac{Y_\xi}{J^2} \left(\frac{A_h G_{12}}{J} \left[(X_\eta H \bar{v})_\eta + (X_\xi H \bar{u})_\eta \right] \right)_\xi \\
&+ \frac{Y_\xi}{J^2} \left(\frac{A_h G_{12}}{J} \left[(X_\eta H \bar{v})_\xi + (X_\xi H \bar{u})_\xi \right] \right)_\eta
\end{aligned}$$

Replacing $H\bar{u}$ and $H\bar{v}$ with \bar{U} and \bar{V} , respectively, the same expressions apply in the external mode equations.

Appendix B

Scenario Average Concentrations and Percent Change from Base Condition

Surface Salinity (PPT)											
Region	SC 1a	SC 1b	%	SC 1c	%	SC 2	%	SC 3	%	SC 4	%
San Juan Bay Cano Martin Pena	33.7 20.7	33.4 19.5	-1 -6	33.0 27.5	-2 33	26.0 18.2	-23 -12	33.9 23.8	1 15	32.8 16.9	-3 -19
Laguna San Jose Canal Suarez	3.2 5.5	6.0 10.0	90 81	22.7 27.3	619 396	0.5 1.8	-86 -67	7.7 12.4	144 126	5.2 26.0	65 373
Laguna La Torrecilla Laguna de Pinones	18.6 13.8	22.1 17.5	19 26	26.2 22.1	41 59	16.1 6.6	-14 -52	19.5 13.2	5 -5	26.2 22.4	41 61
Note: "SC" denotes Scenario.											

Surface Salinity (PPT)									
Region	SC 1a	SC 5a	%	SC 5b	%	SC 6a	%	SC 6b	%
San Juan Bay Cano Martin Pena	33.7 20.7	33.7 20.7	0 0	33.7 20.7	0 0	33.0 27.5	-2 33	26.4 24.9	-22 20
Laguna San Jose Canal Suarez	3.2 5.5	3.2 5.5	0 0	3.2 5.5	0 0	22.7 27.3	619 396	19.9 25.8	529 369
Laguna La Torrecilla Laguna de Pinones	18.6 13.8	18.6 13.8	0 0	18.6 13.8	0 0	26.2 22.1	41 59	25.6 16.5	38 19

**Surface
Chlorophyll ($\mu\text{g/L}$)**

Region	SC 1a	SC 1b	%	SC 1c	%	SC 2	%	SC 3	%	SC 4	%
San Juan Bay Cano Martin Pena	3.95 13.53	4.78 16.76	21 24	7.44 11.66	88 -14	2.50 4.44	-37 -67	3.27 9.41	-17 -30	6.13 18.80	55 39
Laguna San Jose Canal Suarez	32.30 31.31	29.86 27.51	-8 -12	25.26 16.13	-22 -48	8.50 6.82	-74 -78	33.99 30.37	5 -3	34.00 13.53	5 -57
Laguna La Torrecilla Laguna de Pinones	26.90 38.26	17.70 19.78	-34 -48	18.22 33.79	-32 -12	17.49 32.62	-35 -15	26.18 38.55	-3 1	18.39 33.78	-32 -12

**Surface
Chlorophyll ($\mu\text{g/L}$)**

Region	SC 1a	SC 5a	%	SC 5b	%	SC 6a	%	SC 6b	%
San Juan Bay Cano Martin Pena	3.95 13.53	3.63 12.19	-8 -10	3.67 11.31	-7 -16	6.10 8.65	54 -36	5.42 8.06	37 -40
Laguna San Jose Canal Suarez	32.30 31.31	30.28 29.86	-6 -5	22.99 25.73	-29 -18	15.74 13.76	-51 -56	14.90 13.98	-54 -55
Laguna La Torrecilla Laguna de Pinones	26.90 38.26	26.34 37.98	-2 -1	24.95 37.27	-7 -3	18.15 33.75	-33 -12	18.48 33.62	-31 -12

**Surface
Total Nitrogen (mg/L)**

Region	SC 1a	SC 1b	%	SC 1c	%	SC 2	%	SC 3	%	SC 4	%
San Juan Bay Cano Martin Pena	0.1443 0.8100	0.1458 0.6238	1 -23	0.1640 0.3496	14 -57	0.1250 0.6967	-13 -14	0.1366 0.7645	-5 -6	0.1668 0.6863	16 -15
Laguna San Jose Canal Suarez	0.5809 0.6267	0.5553 0.5238	-4 -16	0.4568 0.2985	-21 -52	0.1789 0.1268	-69 -80	0.6085 0.5607	5 -11	0.6019 0.2694	4 -57
Laguna La Torrecilla Laguna de Pinones	0.4828 0.6610	0.3290 0.3585	-32 -46	0.3432 0.5881	-29 -11	0.3260 0.5854	-32 -11	0.4758 0.6680	-1 1	0.3466 0.5883	-28 -11

**Surface
Total Nitrogen (mg/L)**

Region	SC 1a	SC 5a	%	SC 5b	%	SC 6a	%	SC 6b	%
San Juan Bay Cano Martin Pena	0.1443 0.8100	0.1321 0.4756	-9 -41	0.1393 0.6800	-4 -16	0.1445 0.2883	0 -64	0.1315 0.2863	-9 -65
Laguna San Jose Canal Suarez	0.5809 0.6267	0.5453 0.5923	-6 -5	0.4296 0.5102	-26 -19	0.2945 0.2537	-49 -60	0.2947 0.2568	-49 -59
Laguna La Torrecilla Laguna de Pinones	0.4828 0.6610	0.4731 0.6563	-2 -1	0.4487 0.6446	-7 -2	0.3420 0.5875	-29 -11	0.3420 0.5986	-29 -9

**Surface
Total Phosphorus (mg/L)**

Region	SC 1a	SC 1b	%	SC 1c	%	SC 2	%	SC 3	%	SC 4	%
San Juan Bay Cano Martin Pena	0.0594 0.2270	0.0587 0.1677	-1 -26	0.0585 0.0943	-1 -58	0.0415 0.2190	-30 -4	0.0574 0.2304	-3 2	0.0639 0.1778	8 -22
Laguna San Jose Canal Suarez	0.0989 0.0949	0.0918 0.0798	-7 -16	0.0919 0.0748	-7 -21	0.0998 0.0790	1 -17	0.1055 0.0884	7 -7	0.1140 0.0804	15 -15
Laguna La Torrecilla Laguna de Pinones	0.1239 0.1034	0.0944 0.0728	-24 -30	0.1063 0.0934	-14 -10	0.0943 0.0788	-24 -24	0.1157 0.0974	-7 -6	0.1066 0.0929	-14 -10

**Surface
Total Phosphorus (mg/L)**

Region	SC 1a	SC 5a	%	SC 5b	%	SC 6a	%	SC 6b	%
San Juan Bay Cano Martin Pena	0.0594 0.2270	0.0568 0.1610	-4 -29	0.0592 0.2232	0 -2	0.0546 0.0830	-8 -63	0.0382 0.0765	-36 -66
Laguna San Jose Canal Suarez	0.0989 0.0949	0.0939 0.0907	-5 -4	0.0696 0.0770	-30 -19	0.0601 0.0674	-39 -29	0.0541 0.0496	-45 -48
Laguna La Torrecilla Laguna de Pinones	0.1239 0.1034	0.1227 0.1029	-1 0	0.1184 0.1009	-4 -2	0.1061 0.0932	-14 -10	0.0916 0.0811	-26 -22

**Surface
Fecal Coliform (MPN/ml)**

Region	SC 1a	SC 1b	%	SC 1c	%	SC 2	%	SC 3	%	SC 4	%
San Juan Bay Cano Martin Pena	1748.2 62863.0	1784.4 54475.0	2 -13	1810.6 32547.0	4 -48	1903.2 64263.0	9 2	1732.3 61782.0	-1 -2	1830.9 61210.0	5 -3
Laguna San Jose Canal Suarez	6534.3 41.4	6762.1 59.5	3 44	6981.6 114.3	7 176	6471.7 74.4	-1 80	7025.5 457.8	8 1005	5170.6 130.8	-21 216
Laguna La Torrecilla Laguna de Pinones	2235.9 745.9	2235.8 747.2	0 0	2243.0 749.6	0 0	2229.0 743.8	0 0	2093.5 743.8	-6 0	2259.2 750.0	1 1

**Surface
Fecal Coliform (MPN/ml)**

Region	SC 1a	SC 5a	%	SC 5b	%	SC 6a	%	SC 6b	%
San Juan Bay Cano Martin Pena	1748.2 62863.0	1730.9 53056.0	-1 -16	1748.2 62862.0	0 0	1718.4 30888.0	-2 -51	1839.3 31832.0	5 -49
Laguna San Jose Canal Suarez	6534.3 41.4	6478.3 41.4	-1 0	4088.6 41.4	-37 0	4196.6 114.0	-36 175	4287.9 129.5	-34 213
Laguna La Torrecilla Laguna de Pinones	2235.9 745.9	2235.9 745.9	0 0	2235.9 745.9	0 0	2243.0 749.6	0 0	2243.1 748.4	0 0

**Water Column
Dissolved Oxygen (mg/L)**

Region	SC 1a	SC 1b	%	SC 1c	%	SC 2	%	SC 3	%	SC 4	%
San Juan Bay Cano Martin Pena	4.2 2.8	4.2 3.0	-1 8	4.1 4.0	-2 42	4.8 3.2	15 14	4.2 2.9	1 3	4.1 3.0	-3 7
Laguna San Jose Canal Suarez	5.3 2.8	5.3 3.3	1 21	5.4 4.3	1 55	7.6 5.1	44 86	5.3 4.8	1 75	5.1 4.8	-5 74
Laguna La Torrecilla Laguna de Pinones	4.4 7.3	4.6 7.2	5 -2	4.5 6.9	2 -5	6.7 7.6	50 4	4.3 7.3	-3 0	4.5 6.9	3 -5

**Water Column
Dissolved Oxygen (mg/L)**

Region	SC 1a	SC 5a	%	SC 5b	%	SC 6a	%	SC 6b	%
San Juan Bay Cano Martin Pena	4.2 2.8	4.2 2.8	0 2	4.2 2.8	0 0	4.1 4.0	-2 43	4.7 4.4	12 59
Laguna San Jose Canal Suarez	5.3 2.8	5.3 2.8	0 1	5.4 3.0	2 10	5.4 4.3	2 57	6.1 5.8	15 109
Laguna La Torrecilla Laguna de Pinones	4.4 7.3	4.4 7.3	0 0	4.5 7.3	1 0	4.5 6.9	2 -5	6.2 7.1	41 -2

**Water Column
Bottom Dissolved Oxygen (mg/L)**

Region	SC 1a	SC 1b	%	SC 1c	%	SC 2	%	SC 3	%	SC 4	%
San Juan Bay Cano Martin Pena	4.0 2.3	3.9 2.5	-2 8	3.9 3.7	-3 62	4.4 2.6	12 13	4.0 2.3	1 1	3.8 2.5	-4 8
Laguna San Jose Canal Suarez	5.0 1.4	5.1 1.8	0 23	5.0 2.5	0 76	7.5 2.6	48 83	5.0 3.9	0 171	4.7 3.0	-7 109
Laguna La Torrecilla Laguna de Pinones	5.2 7.3	5.3 7.2	2 -2	5.1 6.9	-2 -5	6.4 7.6	22 4	5.1 7.3	-2 0	5.1 6.9	-2 -5

**Water Column
Bottom Dissolved Oxygen (mg/L)**

Region	SC 1a	SC 5a	%	SC 5b	%	SC 6a	%	SC 6b	%
San Juan Bay Cano Martin Pena	4.0 2.3	3.9 2.4	0 2	3.9 2.3	0 0	3.9 3.8	-3 63	4.3 4.2	9 83
Laguna San Jose Canal Suarez	5.0 1.4	5.1 1.5	0 1	5.1 1.6	2 11	5.1 2.6	1 79	5.4 4.6	8 224
Laguna La Torrecilla Laguna de Pinones	5.2 7.3	5.2 7.3	0 0	5.3 7.3	0 0	5.1 6.9	-2 -5	5.9 7.1	13 -2

Water Column Salinity (PPT)											
Region	SC 1a	SC 1b	%	SC 1c	%	SC 2	%	SC 3	%	SC 4	%
San Juan Bay Cano Martin Pena	35.9 30.2	35.9 29.7	0 -2	35.7 31.5	-1 4	29.9 27.0	-17 -11	35.9 31.0	0 3	35.7 28.1	0 -7
Laguna San Jose Canal Suarez	7.2 9.6	9.6 13.6	34 42	24.1 27.6	235 188	0.5 2.1	-93 -78	11.2 14.9	55 55	9.0 27.6	25 188
Laguna La Torrecilla Laguna de Pinones	23.7 13.8	26.1 17.5	10 26	29.0 22.1	23 59	15.3 6.6	-35 -52	24.2 13.2	2 -5	29.1 22.4	23 61

Water Column Salinity (PPT)									
Region	SC 1a	SC 5a	%	SC 5b	%	SC 6a	%	SC 6b	%
San Juan Bay Cano Martin Pena	35.9 30.2	35.9 30.2	0 0	35.9 30.2	0 0	35.7 31.5	-1 4	30.6 28.6	-15 -5
Laguna San Jose Canal Suarez	7.2 9.6	7.2 9.6	0 0	7.2 9.6	0 0	24.1 27.6	235 188	20.4 26.0	184 171
Laguna La Torrecilla Laguna de Pinones	23.7 13.8	23.7 13.8	0 0	23.7 13.8	0 0	29.0 22.1	23 59	24.8 16.5	5 19

Water Column Chlorophyll (µg/L)											
Region	SC 1a	SC 1b	%	SC 1c	%	SC 2	%	SC 3	%	SC 4	%
San Juan Bay Cano Martin Pena	3.95 13.53	4.78 16.76	21 24	7.44 11.66	88 -14	2.50 4.44	-37 -67	3.27 9.41	-17 -30	6.13 18.80	55 39
Laguna San Jose Canal Suarez	32.30 31.31	29.86 27.51	-8 -12	25.26 16.13	-22 -48	8.50 6.82	-74 -78	33.99 30.37	5 -3	34.00 13.53	5 -57
Laguna La Torrecilla Laguna de Pinones	26.90 38.26	17.70 19.78	-34 -48	18.22 33.79	-32 -12	17.49 32.62	-35 -15	26.18 38.55	-3 1	18.39 33.78	-32 -12

Water Column Chlorophyll (µg/L)									
Region	SC 1a	SC 5a	%	SC 5b	%	SC 6a	%	SC 6b	%
San Juan Bay Cano Martin Pena	3.95 13.53	3.63 12.19	-8 -10	3.67 11.31	-7 -16	6.10 8.65	54 -36	5.42 8.06	37 -40
Laguna San Jose Canal Suarez	32.30 31.31	30.28 29.86	-6 -5	22.99 25.73	-29 -18	15.74 13.76	-51 -56	14.90 13.98	-54 -55
Laguna La Torrecilla Laguna de Pinones	26.90 38.26	26.34 37.98	-2 -1	24.95 37.27	-7 -3	18.15 33.75	-33 -12	18.48 33.62	-31 -12

**Water Column
Total Nitrogen (mg/L)**

Region	SC 1a	SC 1b	%	SC 1c	%	SC 2	%	SC 3	%	SC 4	%
San Juan Bay	0.0753	0.0728	-3	0.0843	12	0.0591	-21	0.0727	-3	0.0815	8
Cano Martin Pena	0.6112	0.3230	-47	0.2262	-63	0.5754	-6	0.3382	-45	0.3875	-37
Laguna San Jose	0.9073	0.7942	-12	0.5038	-44	0.1964	-78	0.8004	-12	1.0316	14
Canal Suarez	2.0877	1.7914	-14	0.7041	-66	0.1433	-93	0.5963	-71	0.2971	-86
Laguna La Torrecilla	0.6469	0.3869	-40	0.4045	-37	0.3787	-41	0.6861	6	0.4076	-37
Laguna de Pinones	0.6610	0.3585	-46	0.5881	-11	0.5854	-11	0.6680	1	0.5883	-11

**Water Column
Total Nitrogen (mg/L)**

Region	SC 1a	SC 5a	%	SC 5b	%	SC 6a	%	SC 6b	%
San Juan Bay	0.0753	0.0709	-6	0.0731	-3	0.0763	1	0.0634	-16
Cano Martin Pena	0.6112	0.2822	-54	0.4977	-19	0.1879	-69	0.1828	-70
Laguna San Jose	0.9073	0.8577	-5	0.6790	-25	0.3250	-64	0.2985	-67
Canal Suarez	2.0877	2.0222	-3	1.8416	-12	0.6421	-69	0.2791	-87
Laguna La Torrecilla	0.6469	0.6340	-2	0.6009	-7	0.4028	-38	0.3991	-38
Laguna de Pinones	0.6610	0.6563	-1	0.6446	-2	0.5875	-11	0.5986	-9

**Water Column
Total Phosphorus (mg/L)**

Region	SC 1a	SC 1b	%	SC 1c	%	SC 2	%	SC 3	%	SC 4	%
San Juan Bay	0.0383	0.0370	-3	0.0375	-2	0.0241	-37	0.0375	-2	0.0396	3
Cano Martin Pena	0.1609	0.1154	-28	0.0677	-58	0.1501	-7	0.1324	-18	0.1320	-18
Laguna San Jose	0.1396	0.1219	-13	0.0936	-33	0.1001	-28	0.1271	-9	0.1654	18
Canal Suarez	0.2856	0.2551	-11	0.1481	-48	0.0841	-71	0.0955	-67	0.0892	-69
Laguna La Torrecilla	0.1690	0.1119	-34	0.1205	-29	0.1051	-38	0.1759	4	0.1194	-29
Laguna de Pinones	0.1034	0.0728	-30	0.0934	-10	0.0788	-24	0.0974	-6	0.0929	-10

**Water Column
Total Phosphorus (mg/L)**

Region	SC 1a	SC 5a	%	SC 5b	%	SC 6a	%	SC 6b	%
San Juan Bay	0.0383	0.0373	-2	0.0381	0	0.0361	-6	0.0230	-40
Cano Martin Pena	0.1609	0.1203	-25	0.1598	-1	0.0606	-62	0.0528	-67
Laguna San Jose	0.1396	0.1341	-4	0.1057	-24	0.0625	-55	0.0538	-61
Canal Suarez	0.2856	0.2806	-2	0.2622	-8	0.1407	-51	0.0513	-82
Laguna La Torrecilla	0.1690	0.1675	-1	0.1622	-4	0.1202	-29	0.1046	-38
Laguna de Pinones	0.1034	0.1029	0	0.1009	-2	0.0932	-10	0.0811	-22

Water Column Fecal Coliform (MPN/ml)											
Region	SC 1a	SC 1b	%	SC 1c	%	SC 2	%	SC 3	%	SC 4	%
San Juan Bay Cano Martin Pena	265.4 25974.0	270.4 25409.0	2 -2	335.4 19081.0	26 -27	292.1 26954.0	10 4	264.9 25689.0	0 -1	272.5 26534.0	3 2
Laguna San Jose Canal Suarez	2994.6 3.6	3086.6 13.8	3 281	3488.0 47.7	16 1219	4061.0 31.7	36 775	3281.5 283.1	10 7723	2562.1 28.9	-14 700
Laguna La Torrecilla Laguna de Pinones	1071.0 745.9	1071.4 747.2	0 0	1080.3 749.6	1 0	1781.6 743.8	66 0	1011.0 743.8	-6 0	1086.1 750.0	1 1

Water Column Fecal Coliform (MPN/ml)									
Region	SC 1a	SC 5a	%	SC 5b	%	SC 6a	%	SC 6b	%
San Juan Bay Cano Martin Pena	265.4 25974.0	264.4 22905.0	0 -12	265.4 25974.0	0 0	319.8 17729.0	21 -32	345.6 18320.0	30 -29
Laguna San Jose Canal Suarez	2994.6 3.6	2969.6 3.6	-1 0	1808.7 3.6	-40 0	2065.2 47.6	-31 1214	2827.9 79.1	-6 2084
Laguna La Torrecilla Laguna de Pinones	1071.0 745.9	1071.0 745.9	0 0	1071.0 745.9	0 0	1080.3 749.6	1 0	1792.2 748.4	67 0

REPORT DOCUMENTATION PAGE

Form Approved
OMB No. 0704-0188

Public reporting burden for this collection of information is estimated to average 1 hour per response, including the time for reviewing instructions, searching existing data sources, gathering and maintaining the data needed, and completing and reviewing the collection of information. Send comments regarding this burden estimate or any other aspect of this collection of information, including suggestions for reducing this burden, to Washington Headquarters Services, Directorate for Information Operations and Reports, 1215 Jefferson Davis Highway, Suite 1204, Arlington, VA 22202-4302, and to the Office of Management and Budget, Paperwork Reduction Project (0704-0188), Washington, DC 20503.

1. AGENCY USE ONLY (Leave blank)		2. REPORT DATE April 2000	3. REPORT TYPE AND DATES COVERED Final report
4. TITLE AND SUBTITLE Hydrodynamic and Water Quality Model Study of San Juan Bay Estuary			5. FUNDING NUMBERS
6. AUTHOR(S) Barry W. Bunch, Carl F. Cerco, Mark S. Dortch, Billy H. Johnson, Keu W. Kim			
7. PERFORMING ORGANIZATION NAME(S) AND ADDRESS(ES) U.S. Army Engineer Research and Development Center 3909 Halls Ferry Road, Vicksburg, MS 39180-6199			8. PERFORMING ORGANIZATION REPORT NUMBER ERDC TR-00-1
9. SPONSORING/MONITORING AGENCY NAME(S) AND ADDRESS(ES) U.S. Army Engineer District, Jacksonville P.O. Box 4970 Jacksonville, FL 32232-0019			10. SPONSORING/MONITORING AGENCY REPORT NUMBER
11. SUPPLEMENTARY NOTES			
12a. DISTRIBUTION/AVAILABILITY STATEMENT Approved for public release; distribution is unlimited.			12b. DISTRIBUTION CODE
13. ABSTRACT (Maximum 200 words) <p>This report describes a three-dimensional hydrodynamic and water quality model study of the San Juan Bay and Estuaries system conducted to evaluate the effectiveness of various management alternatives for improving water quality. Alternatives included methods to increase flushing, reduce pollutant loadings, and combinations of the two. The CH3D-WES hydrodynamic model and the CE-QUAL-ICM water quality model were employed in the study. The models were indirectly coupled and were adjusted and calibrated against data collected during the summer of 1995. Analysis of various management scenarios revealed that a combination of widening and deepening of Cano Martín Peña, filling of dredged submerged borrow pits, and removal of un-sewered loads in Cano Martín Peña provided the greatest water quality benefits.</p>			
14. SUBJECT TERMS Estuary Loadings Water quality Flushing Model Hydrodynamic San Juan Bay			15. NUMBER OF PAGES 298
			16. PRICE CODE
17. SECURITY CLASSIFICATION OF REPORT UNCLASSIFIED	18. SECURITY CLASSIFICATION OF THIS PAGE UNCLASSIFIED	19. SECURITY CLASSIFICATION OF ABSTRACT	20. LIMITATION OF ABSTRACT